UNIVERSITÀ DEGLI STUDI DI NAPOLI
FEDERICO II

SCUOLA POLITECNICA E DELLE SCIENZE DI BASE

Enzyme immobilization: design of nanoscaled supported biocatalysts and miniaturized enzyme reactors for biofuel production and green organic synthesis

Giulio Pota

Supervisor
Prof. A. Costantini

Co-supervisor
Prof. G. Vitiello
Dr. Valeria Califano

Scientific Committee
Dr. Eng. Gianluca Landi
Prof. Fernando López Gallego

A thesis presented for the degree of Doctor of Philosophy in Products and Industrial Processes Engineering

2022/2023

Chapter 1

Introduction

Contents

1. Biocatalysis for the ecological transition

1.1. Motivation

1.1.1. The anthropogenic contribution to climate change

In the last 65 years, climate change has become the main threat for ecosystems all over the world. It is identified with the combination global warming, changes in precipitation patterns, and increased occurrence of extreme weather events.[1] The consequences of climate change are multiple and potentially unmanageable. First, those events will cause massive immigration with related social and economic tensions. More specifically, the increasing inhospitality of Sub-Saharan Africa, South Asia, and Latin America (55% of the developing world's population) will force 143 million people to migrate within their countries by 2050 to escape the slow-onset impacts of climate change.[2] The second main consequence is the reduction in biodiversity, seriously threatening a plethora of animal and vegetable species.[3] Last but not least, climate change makes us more stupid. Indeed, worse quality of water and air, increased environmental pollution, change in the distribution of pathogens and alteration in food production seriously affect human health, resulting in mental diseases as well.[4] Evolutionary studies have also shown that brain size noticeably decreased during Holocene warmer periods with respect to glacial eras.[5] Moreover, mankind lacks the capacity to rapidly adapt to new environmental conditions. In detail, *Homo sapiens* species evolved as the CO_2 concentration in the atmosphere was about 280 ppm, almost half of the current value. This means severe reduction of the theoretical brain functions and of cognitive capacity.[6] CO_2 is the main actor of climate changes since it is the most abundant greenhouse gas (together with CH_4 and N_2O) whose concentration has dramatically increased starting from the industrial revolution. Indeed, in the last 9000 years (from the Early Holocene on), CO_2 concentration was kept almost steady at 280 ppm. On the contrary, it experienced an exponential growth to 420 ppm in the last 150 years (**Figure 1.1**).

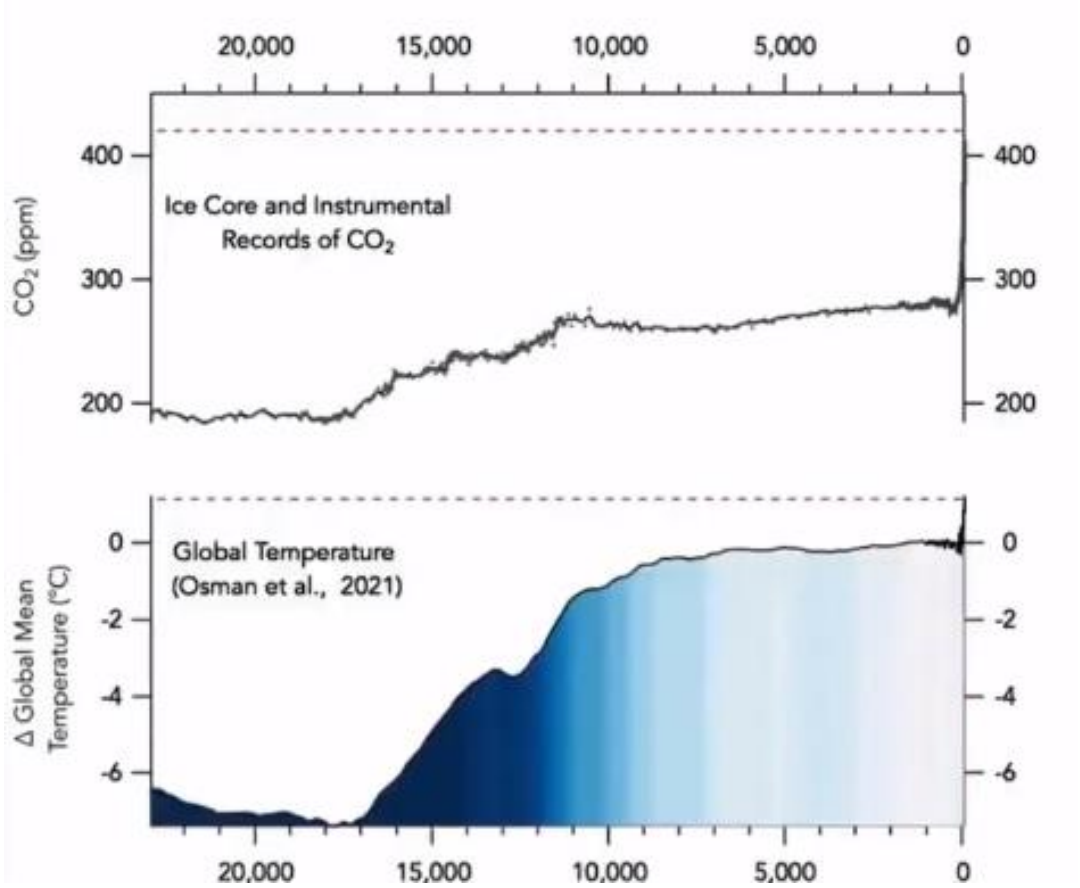

Figure 1.1. Time trends for CO_2 concentration and anomaly in the global mean temperature. On the x axis, time is reported backwards starting from outbreak of the industrial revolution, chosen as reference value. [7]

The anomaly in the global mean temperature shares the same trend as CO_2, reaching the impressive value of +1.1°C in 2020.[8] Even if there still survive some negationist voices, massive emission of greenhouse gases is attributed to uncontrolled anthropogenic activities, especially extraction [9] and burning of fossil fuels,[6,9–11] responsible for 86% of carbon dioxide emissions in the past 10 years.[12] As a matter of fact, with the Paris Agreement (COP21) governments committed to limit temperature increase to 1.5°C above pre-industrial levels and to reduce GHG emissions of 43% by 2030.[13] This would mean that 58% of oil, 59% of gas, and 89% of coal reserves should be unextractable.[14] Furthermore, the 2021 Glasgow Climate

Change Conference (COP26) officially recognized the need to reduce and progressively stop using fossil fuels as sources of energy,[15] promoting a series of anti-fossil fuels norms to respect the COP21 purposes by 2030, with the ambition of reaching net zero carbon by 2050.[16] At Dubai COP28 held in December 2023, the EU and its countries pushed parties to agree on transitioning away from fossil energy: parties agreed to progressively move away from fossil fuels in the energy sector by 2050.[17] This commitment prescribes a radical change in energy production, intensely pushing toward the ecologic transition. One of the suitable green strategies could be to encourage the use of biofuels.

1.2. Biofuels

1.2.1. Classification

Biofuels are produced from biomass, especially of vegetable origin, and they represent a valid alternative to petroleum-based fuels.[18] Depending on the feedstock they originate, biofuels can be distinguished into three categories. 1st generation biofuels are obtained from food crops such as corn, sugar cane, and vegetable oils, after a series of extraction and processing steps to obtain sugar, starch, and edible oils. Fermentation, distillation or transesterification stages are needed to transform these substrates into bioalcohols or biodiesel. As might be expected, the use of food crops opens to ethical concerns, which limits the spread of this class of biofuels.[19] 2nd generation biofuels are derived from non-edible lignocellulosic biomass, made of carbohydrates (cellulose, hemicellulose) and lignin. As a matter of fact, the cost of this biomass is sensitively lower than edible crops.[20] Although the enhanced complexity to be produced, 2nd generation biofuels are environmentally and socially friendly since they don't compete with food items.[21] The major concerns are about the huge need for water to grow some crops and the potential reduction of biodiversity.[22] 3rd generation biofuels are mainly produced from algae. Potentially, they are extremely advantageous over the previous classes of biofuels since algae cultivation is rather cheap and their average lipid content is about 90% on dry weight.

This makes algae suitable biomass for biodiesel production. Moreover, they are able to adapt and grow easily in harsh conditions. Finally, biodiesel from waste cooking oil is another important 3rd generation biofuel. The valorization of this waste could be a forefront solution to couple energy production with reduced water contamination.[23] The Biotechnology Industry Organization estimates that biofuels are accounted for the reduction of CO_2 emissions by 589.3 million tons and their impact on the energetic transition will increase more and more, especially for transportation, which contributes to 19% CO_2 and 70% CO emission worldwide.[24,25]

1.2.2. Bioethanol

Bioethanol is the most used biofuel worldwide and it is expected to be more and more common in the future as a surrogate of petroleum-derived fuels. Bioethanol production began in the early 20th century, but then it almost completely stopped due to high production costs and prohibitionism. The energy crisis of 1973 refed the interest towards biofuels.[26] The main actor in bioethanol production worldwide is the European Union with 5.35 billion liters in 2022, and the data are expected to increase especially after the approval of the Green Deal and the Russian invasion of Ukraine.[27] Octane number of 108 and 80% less CO_2 emission than gasoline make bioethanol a very performing and sustainable fuel for internal combustion.[25] Indeed, the presence of oxygen ensures cleaner combustion although the heating power (26-28 MJ/liter) is lower than traditional hydrocarbons (32-34) MJ/liter.[28] The higher costs with respect to fossil fuels are to be attributed to the production process, which prescribes the pretreatment of the biomass, that means extraction of the different components (i.e. biorefinery), [29] the hydrolysis of the carbohydrates into monosaccharides, the fermentation and, finally, distillation (**Figure 1.2**).[30] Therefore, the quality of the final product depends on the efficiency of each step. In particular, biomass pre-treatment and hydrolysis steps are the key steps for high yields and quality.

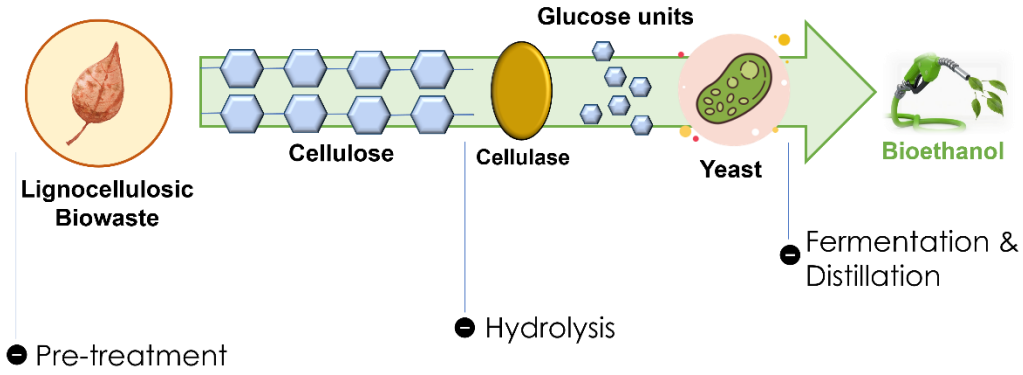

Figure 1.2. Graphical overview of the bioethanol production process. In this case, enzymatic hydrolysis is shown.

Pre-treatment can be mechanical, chemical, microbial and physic-chemical, with efficiency depending on the nature of the starting feedstock. Hydrothermal treatments with different severity factors are performed to remove hemicellulose,[31] whereas the cleavage of β-O-4 bonds in lignin polymer requires alkaline environment.[32] Moreover, alkaline delignification usually results in highly hydrolyzable cellulose.[33] On the contrary, the traditional way to hydrolyze cellulose is with sulfuric acid and high temperature.[34,35] This method is fast and effective, resulting in 90% cellulose conversion into sugars,[36] but it leads to supplementary disposal costs and possible sugar degradation. A sustainable alternative is enzymatic hydrolysis. Indeed, enzymes work at a mild environment, hence less equipment maintenance cost will be needed. Cellulose is hydrolyzed by cellulase, a group of three proteins which work synergistically and sequentially to achieve depolymerization into glucose.[37] The high cost of production, together with the intrinsic lability of the proteins and some concentration unbalances in the enzyme mixture limit the commercialization at an industrial-scale level. Detailed insight into cellulolytic enzymes is provided in the next chapter.

1.2.3. Biodiesel

Biodiesel is the second most used biofuel worldwide, with the European Union being the first producer with 15.46 billion liters.[27] It is composed of fatty acids alkyl esters (FAAE), obtained from the transesterification (alcoholysis) of triglycerides obtained from vegetable oils, waste cooking oils and algae (**Figure 1.3**).

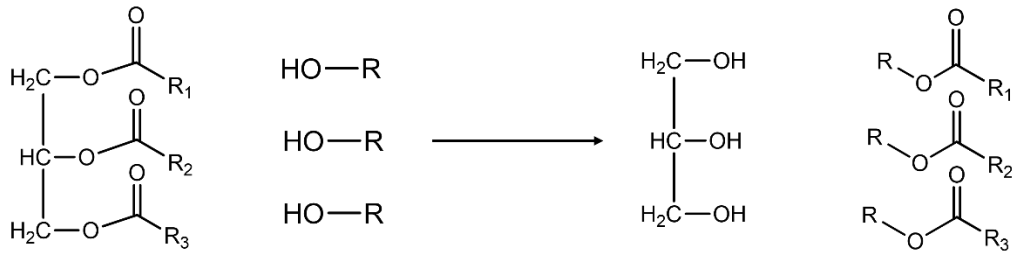

Figure 1.3. Scheme of the transesterification reaction

Current engines and cars can properly burn biodiesel, which is sulfur-free, non-toxic, biodegradable and with enhanced lubricant capacity.[38] However, just like bioethanol, commercialization is limited by production costs, estimated as 3-fold traditional diesel.[39] 25% of the total cost is attributed to the separation from the byproduct glycerol.[40] Transesterification is an environmentally friendly process performed at mild temperatures with or without catalysts. Homogeneous catalysis is usually performed with strong bases (KOH, NaOH, Sodium methylate) or acids (H_2SO_4, HCl). However, this method is definitely not sustainable. Moreover, catalyst removal is tricky and contributes to cost enhancement.[40] Solid-base (CaO, MgO, zeolites, alkaline earth metal oxides, Al_2O_3, aluminosilicates, ZrO_2) and solid-acid (Nafion-NR50, sulfated zirconia, tungstate zirconia) are commonly used as heterogeneous catalysts, usually in fixed-bed reactors.[41,42] Separability and reusability benefit from this method, but catalyst preparation is often costly and leakage of active sites is still an issue. A greener alternative is enzyme catalysis. Indeed, lipase enzymes behave as biocatalysts for transesterification, promoting the cleavage of ester bonds in triglycerides.[43] The use of biocatalysts reduces the number of reaction steps, requires less energy and it is performed at low temperatures, resulting in a cost-effective

process. Moreover, enzyme catalysis ensures high selectivity and thus highly pure biodiesel. However, the protein suffers from denaturation if the alcohol:oil ratio is fixed higher than 4:1. Other key disadvantages are inhibition by glycerol and the cost of production.[44] Nevertheless, enzyme immobilization can provide reusability and shield protein from conformational modification.[45] Further details about lipase immobilization are provided in the next chapter.

1.3. Enzyme catalysis

1.3.1. Advantages and drawbacks

The metabolism of living cells, tissues and organs involves a multitude of biochemical reactions. However, these biochemical pathways need to be sped up at a pace to sustain life. The biomacromolecules committed to this duty are the enzymes. It deals with some particular protein which have adapted to accomplish their duty under mild environmental conditions typical of biological systems.[46] As for traditional catalysts, biocatalysts action consists of the reduction of the free energy barrier to be overcome for converting a reagent (usually called substrate) into a product, according to the transition state theory (**Figure 1.4**).[47]

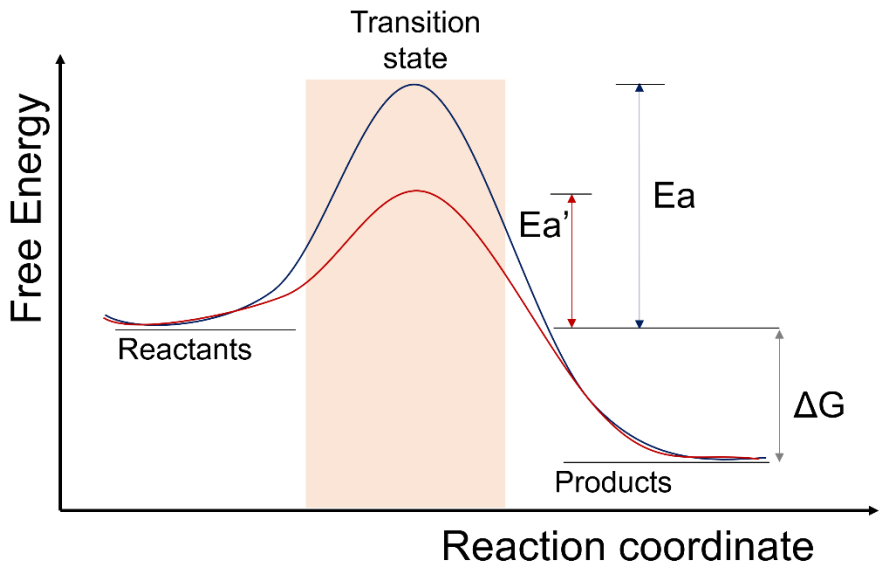

Figure 1.4. Comparison between uncatalyzed (blue) and catalyzed (red) reaction mechanisms for a spontaneous reaction (ΔG<0). *Ea* and *Ea'* refers to the activation energies with and without catalyst, respectively.

More specifically, a catalyst does not alter the *ΔG* between products and reactants, but the interaction with the substrate results in the decrease of the activation energy *Ea*, that is the free energy difference between the activated complex and the reactants. Therefore, the lower the *Ea*, the higher the reaction rate. From the beginning of the 19th century on, when further investigations on yeast fermentations led to the discovery of the enzymes and to the birth of enzymology,[48] biocatalysis has increasingly gained weight among the scientific community and the industrial world as well. Indeed, within the first decades of the 21st century companies operating in different sectors like food, agro, biofuel, pharmaceutical, textile, leather, cosmetics, and waste management have started to replace traditional inorganic catalysts with enzymes.[49] Enzymes exhibit rather distinct properties with respect to inorganic catalysts, which make them interesting as potential process catalysts (**Table 1.1**).

Table 1.1. Advantages and drawbacks of enzymes with respect to traditional inorganic catalysts.[50]

Advantages	**Drawbacks**
High (chemo-, regio-, enantio-) selectivity	Instability (thermal, pH)
Nontoxic nature	Incompatibility with organic solvents
Mutual compatibility	Substrate and product inhibition
Biodegradability	Requirement of co-factors
Energy efficiency	High costs of production

Indeed, the complex molecular structure is responsible for high specificity, which is a mandatory requirements for pharmaceutical or fine chemistry; moreover, the exquisitely selective affinity with the substrate ensures faster kinetics than traditional catalysts. As protein molecules, they perform the best under physiological conditions (mild temperatures, pH, ionic strength). With growing limitations imposed by national and international institutions, the possibility to set up industrial processes characterized by lower environmental impact, requiring less expensive reactors and no by-product disposal, is very appealing.[51] However, the molecular complexity is associated with intrinsic poor stability of the biocatalysts, which are very sensitive to temperature overshoots, organic solvents, and pH variations. Furthermore, the production process includes expression into a host organism, cell lysis and purification, which means high costs.[49] As a matter of fact, research on several technological interventions such as protein engineering,[52] with the possibility of designing tailor-made biocatalysts, and immobilization is gaining even more attention in both industrial and academic world, paving the way for the biocatalytic translation of most of the industrially important catalytic processes. [53]

1.3.2. The industrial use of enzymes

The inception of biocatalysis can be traced back more than a century ago, marked by a breakthrough when scientists discerned the ability of entire living cells to execute significant chemical transformations, exemplified by the synthesis of a precursor to L-ephedrine. Advancing into the second wave, occurring in the latter part of the 20th century, the utilization of enzymes, along with a screening of substrates and media, coupled with initial protein engineering technologies, facilitated the expansion of enzyme substrate capabilities to encompass unconventional compounds. The third phase, emerging in the late 1990s and dubbed "direct evolution," witnessed the incorporation of sophisticated molecular biology and high-throughput screening techniques to rapidly and extensively modify biocatalysts. Presently, we stand on the brink of the fourth wave, characterized by intensified protein engineering endeavors

that empower biocatalysis to delve into innovative and frequently non-natural reactions.[54] Enzymes are suitable for use in a plethora of industrial applications. The major share of the global market of industrial enzymes is owned by Europe and the United States since the majority of pharmaceutical and fine chemicals are produced in Western countries.[55] In 2022, the global industrial enzymes market was estimated at 5.6 billion USD, whereas the growth predictions calculated a compounded annual growth rate (CAGR) of 6.4% from 2020 to 2027.[56] The main contribution to the market growth comes from the developing economies of Asia, Eastern Europe, and Africa, especially for the rising demand for detergents and pharmaceutical products (**Figure 1.5**).

Figure 1.5. Planisphere reporting the world industrial enzyme market.[56]

Current industrial scale biocatalytic applications are dominated by pharmaceutical, [57] food and beverages,[58] detergent,[59] and biofuels,[60,61] as reported in **Figure 1.6.**

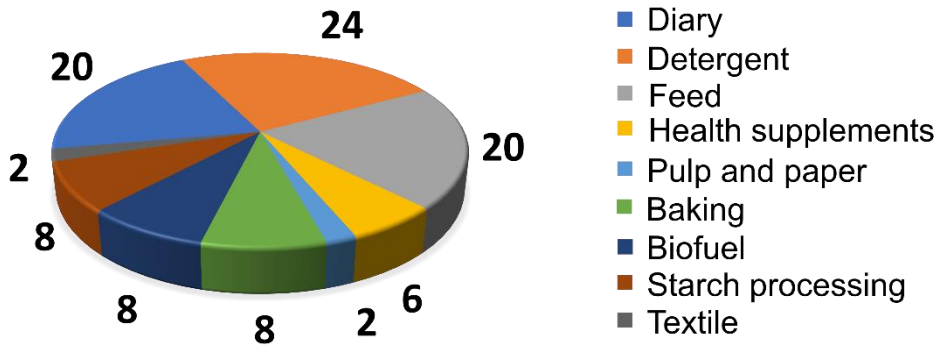

Figure 1.6. Industrial enzyme sales by sector. [62]

However, recent analyses have predicted a future increment of the production of technical enzymes, giving a boost to new sectors such as textile, paper and pulp, leather, and biodiesel, due to the even more severe environmental rules which impose a reduction of waste and toxic by-products.[63] Moreover, petroleum-based chemicals are being replaced by bioderived compounds, thanks to the rising use of enzymes in organic synthesis. The global industrial enzymes market consists of various enzymes, which can be broadly categorized as carbohydrases, proteases, lipases, and others, carbohydrases accounting for 47% of the total.[56] Indeed, this class of enzymes includes cellulases, amylases, and other hydrolases involved in the hydrolysis of polysaccharides. Therefore, they are frequently used in both food and biofuels applications.

1.3.3. Enzyme immobilization

Biocatalysts could seriously trigger the ecological transition of the chemical industry. However, there is the need to make enzymatic processes commercially competitive with respect to the traditional ones. First, reducing protein intrinsic lability could lead to higher productivity. Indeed, the high sensitivity to the operating parameters could result in protein inactivation (in case of temperature overshoots, for example). Among the possible strategies, protein engineering is a suitable method

to improve the conformational stability of the enzymes. But above all, reusability is the key to reduce processing costs. These drawbacks can be overcome by enzyme immobilization that is the attachment of the protein onto an insoluble support, that can be achieved either with physical or chemical methods. Indeed, immobilization usually results in increased pH, temperature and organic solvent tolerance.[64,65] Moreover, supported biocatalysts are easily separable from the reactors, thus enhancing product purity. The cost contribution from immobilized enzymes is to be taken into account when designing a biocatalytic process. It depends on the reaction kinetics, specificity and productivity, measured as kg of product per kg of enzyme. Therefore, the operational stability of the biocatalyst severely affects the overall productivity. More specifically, guidelines for competitive processes prescribe productivity values within 2000–10000 $kg_{product}/kg_{enzyme}$ interval for commodity bulk items, whereas the threshold decreases to 50–100 $kg_{product}/kg_{enzyme}$ high-value pharma products.[66] The interest towards enzyme immobilization started from 1950s, when the first literature reports about proteins bound to polymeric materials appeared.[67] From that time on, several immobilization techniques have been developed, allowing more and more enzymes to be immobilized. The advancements in this technology broadened the scope of biocatalysis, introducing the industrial use of supported enzymes to the production of chemicals and active pharmaceutical ingredients (APIs).[68] In the end, the feasibility of a biocatalytic process lies in a trade-off between the advantages (in terms of both sustainability and process simplification) and the overall costs, which include protein production and disposal as well as the eventual regeneration of the carrier.

2. Principles of biocatalysis

In this chapter, the fundamentals of enzyme catalysis are reported. More specifically, introductory concepts dealing with protein-ligand interaction, kinetics and thermodynamical aspects are reported. This paragraph is an adaptation from chapters

4, 5 and 6 of R.A. Copeland's book "Enzymes. A practical introduction to structure, mechanism and data analysis".[46]

2.1. Enzyme-substrate binding equilibria

The first step of enzyme catalysis prescribes that enzyme and substrate must encounter one another and form a binary complex, accomplished through the binding of the substrate to a specific region of the protein known as active site. In the simplifying hypothesis of single binding site for the protein, it is possible to write the following mass conservation equations:

$$[E] = [ES] + [E_f] \quad (2.1)$$

$$[S] = [ES] + [S_f] \quad (2.2)$$

Where *E* and *S* are the total concentrations of enzyme and substrate, respectively; E_f and S_f are the concentrations of unbound protein and substrate, respectively, whereas ES is the concentration of substrate-protein binary complex. Indeed, an equilibrium is established in solution as protein and substrate interact with each other, described by the dissociation constant K_d:

$$K_d = \frac{[E_f]\cdot[S_f]}{[ES]} \quad (2.3)$$

Even if it seems unusual, backward description of the complexation equilibrium correlates the value of K_d with the intensity of the interaction: the lower K_d, the tighter the bond. This aspect appears clearer as K_d is related to the Gibbs free energy of binding $\Delta G_{binding}$:

$$\Delta G_{binding} = RTln(K_d) \quad (2.4)$$

As a matter of fact, lower values for K_d mean more negative values for $\Delta G_{binding}$. One of the possible ways to treat the equilibrium by means of the kinetic approach.

2.1.1. The kinetic approach to equilibrium

In the hypothesis of reversible bimolecular binding, the equilibrium is described as follows:

$$(2.5) \quad E + S \underset{k_{off}}{\overset{k_{on}}{\rightleftarrows}} ES$$

Where k_{on} is the 2nd-order rate constant for complex association, whereas k_{off} is the 1st-order rate constant for complex dissociation. So, the dissociation constant K_d is equal to the ratio between direct and reverse reaction constants:

$$(2.6) \quad K_d = \frac{k_{on}}{k_{off}}$$

Generally speaking, high substrate concentrations are needed to achieve high degrees of binding with the receptor. Therefore, substrate concentration is usually much higher than enzyme concentration and can be assumed constant ($[S_f] \approx [S]$). This allows for a simplification of the system, approximating complex-association mechanism to a 1st-order kinetics. Is it possible to fit the time profile for the enzyme-substrate complex to the following equation:

$$(2.7) \quad [ES]_{(t)} = [ES]_{eq}(1 - e^{-k_{obs}t})$$

$[ES]_{(t)}$ and $[ES]_{eq}$ refers to the concentration values of the complex at time *t* and at the equilibrium, respectively. From this fit it is possible to estimate k_{obs}, which is the observed kinetic constant. For a reversible binding, k_{obs} grows linearly with substrate concentration:

$$(2.8) \quad k_{obs} = k_{off} + k_{on}[S_f]$$

However, monitoring the complexation kinetics is experimentally tricky since binding is usually accomplished in few milliseconds. A suitable strategy could be the analysis of substrate-enzyme interactions after the equilibrium is reached.

2.1.2. Derivation of the Langmuir isotherm

Under conditions of dynamic equilibrium, the rate of production of the binary complex (equation 1.9) is equal to the opposite rate of decomplexation (equation 1.10), meaning that the concentration of the complex is kept constant.

$$\frac{d[ES]}{dt} = k_{on}[S_f][E_f] \quad (2.9)$$

$$-\frac{d[ES]}{dt} = k_{off}[ES] \quad (2.10)$$

From the comparison between the equations above:

$$k_{on}[S_f][E_f] = k_{off}[ES] \quad (2.11)$$

Isolating the complex concentration leads to:

$$[ES] = \frac{k_{on}}{k_{off}}[S_f][E_f] = K_a[S_f][E_f] \quad (2.12)$$

With K_a is the association constant, the reciprocal of K_d.

However, in expression 2.12 complex concentration is related to both unbound substrate and enzyme, whose measurements is not always so easy. Therefore, it is better to refer to the total enzyme and substrate concentration, since these quantities are known by the experimenter from the beginning. From the manipulation of the mass conservation equation for the protein (2.1), it is possible to express the concentration of unbound protein as:

$$[E_f] = \frac{[E]}{1+\frac{[ES]}{[E_f]}} \quad (2.13)$$

Substituting this expression in equation 2.12 and considering constant substrate concentration:

$$[ES] = K_a[S]\frac{[E]}{1+\frac{[ES]}{[E_f]}} = \frac{[E][S]}{\frac{1}{K_a}+[S]} = \frac{[E][S]}{K_d+[S]} \quad (2.14)$$

The described formula characterizes a square hyperbola commonly observed in saturable binding scenarios within various chemical, physical, and biochemical

contexts. Referred to as the Langmuir isotherm equation, this equation effectively captures the behavior of binding. As a result of the equation's apt description of the data, graphs depicting $[ES]$ in relation to the overall substrate concentration are sometimes denoted as binding isotherms **(Figure 2.1)**.

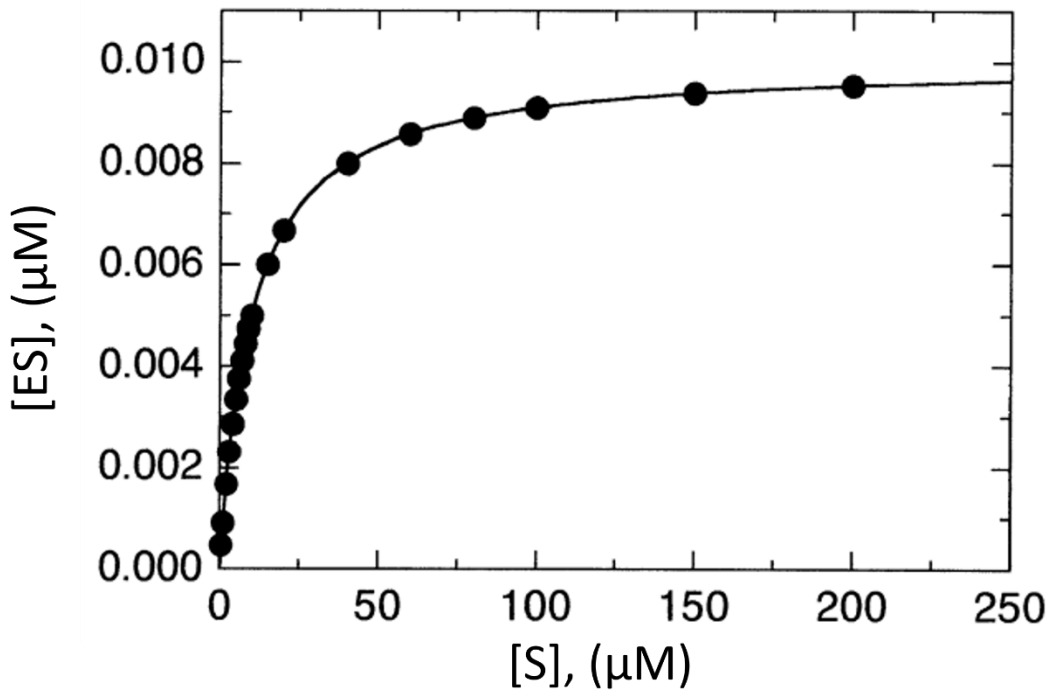

Figure 2.1. Langmuir isotherm for formation of the binary ES complex as a function of substrate concentration.

The curve fitted through the data in each instance represents the nonlinear optimal fit to Equation 2.14. This fitting process allows researchers to derive estimations for both K_d and the overall receptor concentration $[S]$.

2.2. Kinetics of single-substrate enzyme reactions

The most commonly used method to elucidate enzyme mechanism is to unveil the kinetic aspects of single-substrate reactions. More specifically, rapid equilibrium and

steady state models are herein reported to define the concept of catalytic efficiency and substrate affinity.

2.2.1. Time course of enzyme reaction: the influence of substrate concentration on velocity

The reaction progress curves are described by 1st-order kinetics, as graphically reported in **Figure 2.2.**

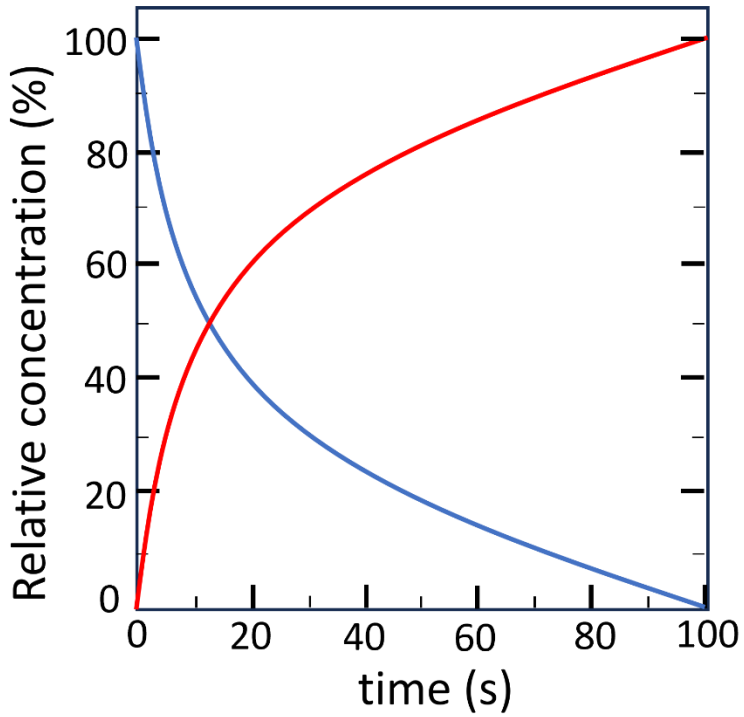

Figure 2.2. Relative concentration curves for substrate S (blue curve) and product P (red curve).

For a 1st-order kinetics, the expression of velocity is:

$$(2.15)\quad v = -\frac{d[S]}{dt} = +\frac{d[P]}{dt} = k[S] = k[S_0]e^{-kt}$$

with k as the pseudo-first order kinetic constant. If $\Delta[S] \leq 0.10[S_0]$, substrate consumption (and thus product production) can be approximated to a linear curve,

with a slope equal to the initial velocity $v_0 = -\frac{\Delta[S]}{\Delta t}$. According to equation 2.15, reaction velocity should grow linearly with initial substrate concentration. However, experimental measurements reveal that two different dependencies exist. For low initial substrate concentration, v_0 grows linearly with $[S_0]$, as in the case of 1st-order kinetics; on the other hand, v_0 approaches to a plateau value as $[S_0]$ becomes high, suggesting the occurrence of a typical saturation condition described by a 0-order kinetics (**Figure 2.3**).

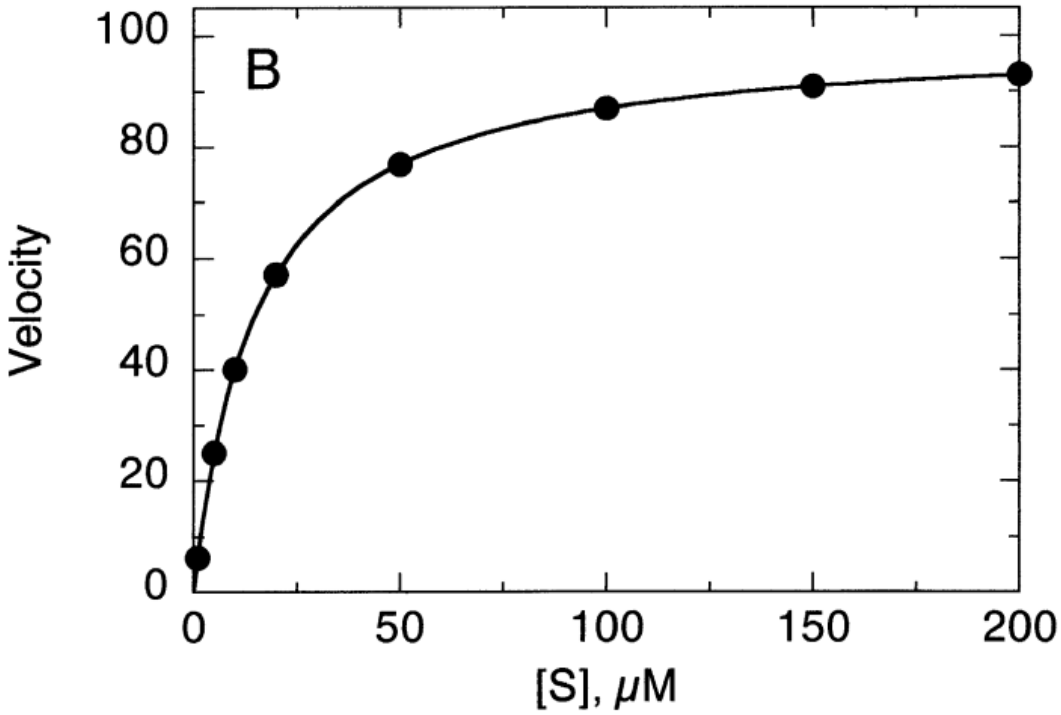

Figure 2.3. Trend for reaction initial velocity over initial substrate concentration.

2.2.2. The Michaelis-Menten model

The first attempt to quantify the dependence of velocity from substrate concentration resulted in the Brown model. According to Brown, velocity can be linearly proportional to the concentration of the ES complex, according to the following reaction scheme:

$$E + S \underset{k_{-1}}{\overset{k_1}{\rightleftarrows}} ES \overset{k_2}{\rightarrow} E + P$$

$$(2.16)\quad v = k_2\,[ES]$$

The outcome of this model is that kinetics is strictly dependent on binary complex formation. However, a proper mathematical framework was needed for Brown model to be fairly used during experiments. This effort resulted in the Michalis-Menten model, which originated from a new approach based on two main hypotheses: 1) rapid equilibrium formation between reactants and complex; 2) slower conversion of ES to P and back to $E + S$, with $k_2 \ll k_1$. Since reactions are usually performed in a large excess of substrate, it is possible to assume $[S_f] \approx [S]$. The constant dissociation for this system is:

$$(2.17)\quad K_S = \frac{[E_f]\cdot[S]}{[ES]}$$

Using mass balance equation 2.1 and substituting the expression of E_f in 2.17, the following expression for ES is obtained:

$$(2.18)\quad [ES] = \frac{[E]\cdot[S]}{K_S+[S]}$$

ES complex is transformed following Brown scheme:

$$E + S \underset{K_S}{\rightleftarrows} ES \overset{k_{cat}}{\longrightarrow} E + P$$

Substituting the expression 2.18 in 2.16 with k_{cat} replacing k_2:

$$(2.19)\quad v = k_{cat}\,[ES] = k_{cat}\,\frac{[E]\cdot[S]}{K_S+[S]}$$

This equation describes the reaction velocity as a hyperbolic function of $[S]$, with plateau value (for $[S]\rightarrow\infty$) equal to $k_{cat}[E]$. This quantity is known as v_{max}. The final expression for velocity is thus reported below:

$$(2.20)\quad v = \frac{v_{max}\cdot[S]}{K_S+[S]}$$

Equation 2.20 is known as the Michaelis-Menten equation. The take-home message from this paragraph is that a good description of enzyme kinetics can be provided by the sequence of rapid equilibrium complex formation with slow chemical transformation.

2.2.3. The Haldan-Briggs model

An upgrade to Michaelis-Menten model was provided by Briggs and Haldan. They untied the description of the kinetics from the occurrence of a rapid equilibrium ($k_2 \ll k_{-1}$). Haldan-Briggs description is built under steady state conditions for ES complex, that means constant concentration. Three main hypotheses are considered:

1. Only binary enzyme/substrate complexes are possible:

$$[E] = [E_f] + [ES] \quad (2.21)$$

2. The protein behaves purely as a catalyst, meaning very low concentration with respect to the substrate:

$$[S] \gg [E] \;\rightarrow\; [S_f] \approx [S]$$

3. The reaction progress is characterized by three different phases (**Figure 2.4**):
    - *a)* Little product formation, rapid burst of formation for ES complex;
    - *b)* constant concentration for ES. This is the phase of the steady state;
    - *c)* post-steady state phase of decomplexation and significant substrate consumption;

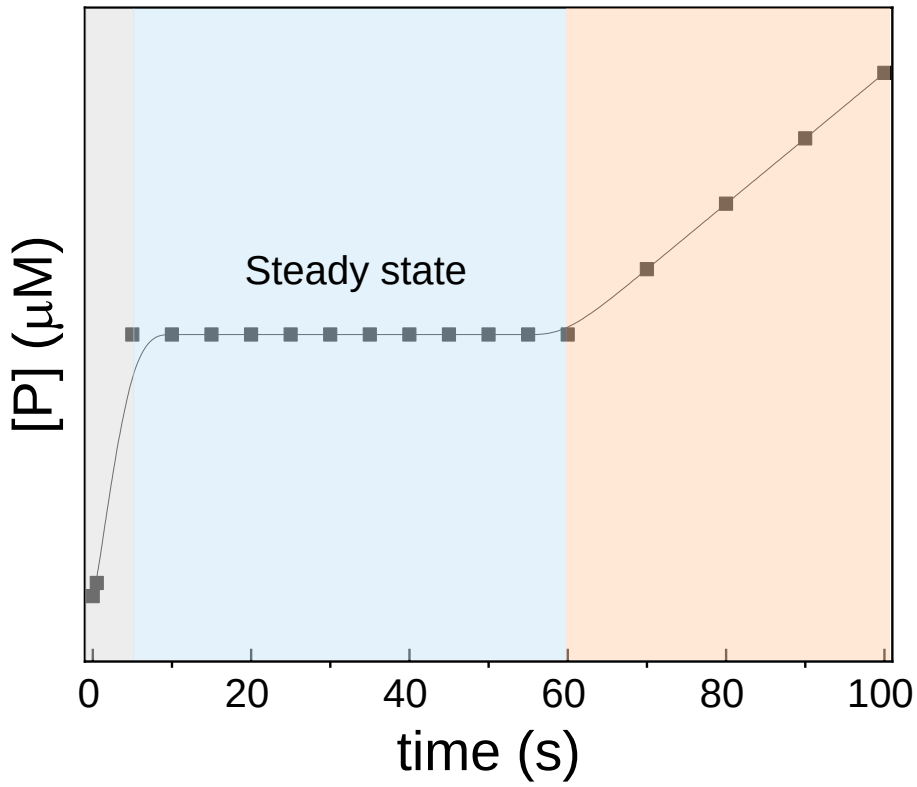

Figure 2.4. Product molar concentration over the time of reaction. Phase a, b and c in the graph are filled in grey, light blue and orange, respectively.

Constant ES concentration in the steady state phase means that the rate of production (provided by complexation) is balanced by the rate of consumption (provided by decomplexation and chemical reaction):

$$(2.22)\quad \frac{d[ES]}{dt} = k_1\left[E_f\right][S] - k_{-1}[ES] - k_2[ES] = 0$$

It is possible to isolate $[ES]$:

$$(2.23)\quad [ES] = \frac{[E_f][S]}{\frac{k_{-1}+k_2}{k_1}} = \frac{[E_f][S]}{K_m}$$

with K_m grouping all the kinetic constants:

$$(2.24)\quad K_m = \frac{k_{-1}+k_2}{k_1}$$

Mass conservation equation for the protein (2.1) allows to insert total enzyme concentration in the expression of $[ES]$:

$$(2.25)\quad [ES] = [E]\frac{[S]}{[S]+K_m}$$

It is now possible to report an expression for enzyme velocity substituting [ES] in equation 2.19 with the expression reported in equation 2.25:

$$(2.26)\quad v = k_{cat}\,[ES] = k_{cat}[E]\frac{[S]}{[S]+K_m} = \frac{v_{max}\,[S]}{[S]+K_m}$$

with $k_{cat} = k_2$ and $v_{max} = k_{cat}[E]$.

Equation 2.26 is a hyperbolic function of $[S]$ as the expression of velocity for Michaelis and Menten, but here K_m constant has a different meaning. More specifically, it is the substrate concentration value for which reaction velocity is half v_{max}. Therefore, it measures the stability of $[ES]$ complex, which is critical for high reaction velocity, and thus the substrate binding affinity for the protein: the lower K_m, the stronger the bond. The calculation of K_m is important to monitor whether changes in the chemical environment (temperature, pH, ionic strength) can affect the capacity of the protein to bind to the substrate. k_{cat} constant is known as turnover number, literally the units of molecules of product produced per unit time per molecules of enzyme present (time^{-1} in units). It is usually calculated for $[S] \gg K_m$, that means $v \approx v_{max}$. This parameter describes how the chemical reaction is affected after substrate binding and gives an idea of the maximum velocity an enzyme-catalyzed reaction can achieve. However, substrate concentration *in vivo* uses to be much lower than K_m, leading to linear dependence of v on $[S]$:

$$(2.27)\quad v = \frac{k_{cat}}{K_m}\,[E][S] = k_{cat}\frac{k_1}{k_{-1}+k_{cat}}[E][S]$$

More specifically, the intensity of *v* depends on k_1, which is the diffusional rate of encounter of the free enzyme with the substrate. Nevertheless, the best way to

investigate the catalytic efficiency of an enzyme is to calculate the ratio $\frac{k_{cat}}{K_m}$ that gives the most immediate measure of substrate selectivity. Furthermore, the rate determining step could be either complex formation ($k_1 \ll k_{cat}$) or chemical reaction ($k_1 \gg k_{cat}$). In the former case, the reaction is under diffusive control; in the latter case, it is under kinetical control. Moreover, high values for $\frac{k_{cat}}{K_m}$ ($\sim 10^8$-10^9 $M^{-1}s^{-1}$) define conditions of kinetic perfections, meaning that all the complex is consumed as fast as is formed.

2.2.4. Determination of the kinetic parameters

After measuring the initial velocity of an enzymatic reaction by varying the substrate concentration, it is possible to estimate kinetic parameters through various methodologies. The most accurate method for determining K_m and v_{max} is to perform a non-linear fitting of the collected experimental data using the Michaelis-Menten (Haldan-Briggs) equation. However, this type of analysis requires as accurate as possible initial guess values for the mentioned parameters, which can be obtained graphically by linearizing the model beforehand.

Haldan-Briggs model can be linearized by inverting both 1st and 2nd members of equation 2.26:

$$(2.28)\quad \frac{1}{v} = \frac{K_m}{v_{\max}[S]} + \frac{1}{v_{\max}}$$

Plotting $\frac{1}{v}$ versus $\frac{1}{[S]}$, a linear curve is obtained (**Figure 2.5**).

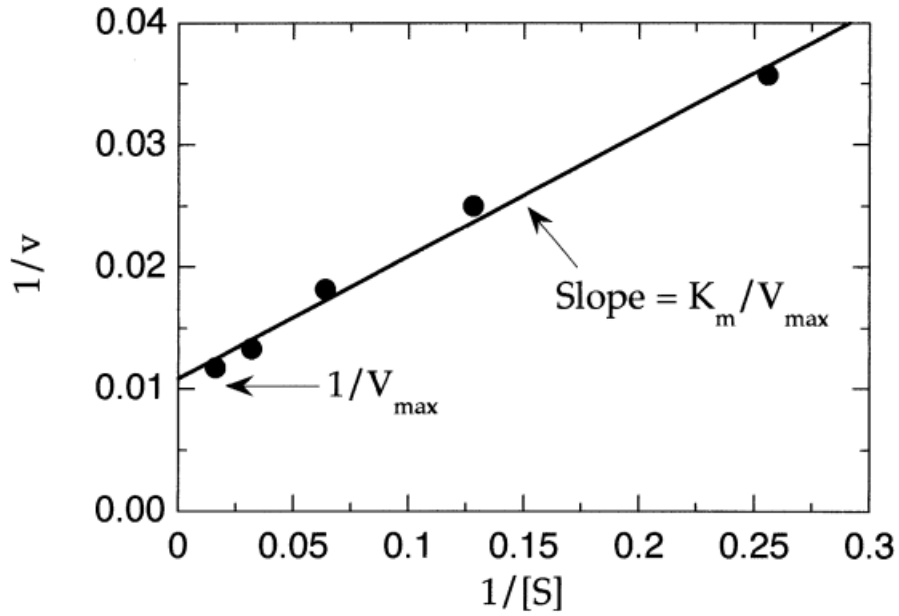

Figure 2.5. Lineweaver-Burk plot for an enzyme reaction.

In detail, the intercept of the curve gives $\frac{1}{v_{\max}}$, whereas the slope is equal to $\frac{K_m}{v_{\max}}$. This method is known as Lineweaver-Burk linearization and gives an approximate evaluation of the kinetic parameters. Even if it is a good strategy to extrapolate a first estimation, this method suffers from some limitations. Indeed, data transformation enhances the sensitivity to noise and experimental errors. Moreover, data collected at low substrate concentrations could be overestimated. It is important to be aware of these drawbacks and maybe try other linearization methods, such as the Hanes-Wolff transformation. More specifically, the Hanes-Wolff equation is obtained by multiplying both members of Lineweaver-Burk equations for $[S]$:

$$(2.29)\quad \frac{[S]}{v} = \frac{K_m}{v_{\max}} + \frac{[S]}{v_{\max}}$$

A linear plot is obtained by graphing $\frac{[S]}{v}$ as a function of $[S]$, as reported in **figure 2.6**.

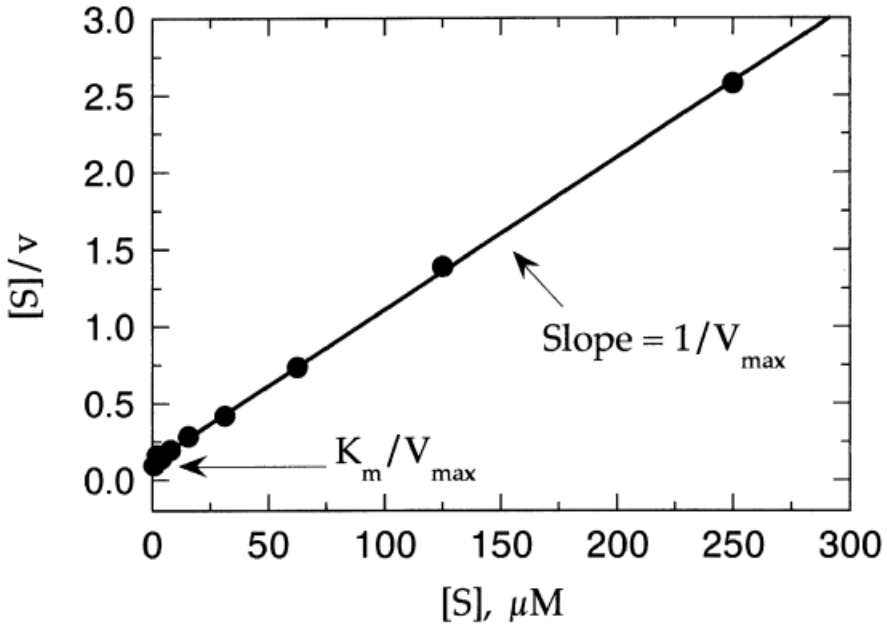

Figure 2.6. Hanes-Wolff linearization plot.

The slope of the curve is equal to $\frac{1}{v_{\max}}$, whereas the intercept gives the ratio $\frac{K_m}{v_{\max}}$.

2.3. Factors affecting the catalytic activity

2.3.1. The influence of pH

The catalytic activity of an enzyme is a direct consequence of its three-dimensional conformation. Any external factor capable of modifying the enzyme's conformation results in an alteration of its catalytic activity. The pH of the solution in which the enzyme operates is among the environmental parameters of greatest relevance in determining its conformation. Indeed, proteins are amphoteric substances, meaning they can function as both acids and bases, as the ionization state of ionizable residues varies with pH. This variation can affect the ionic and electrostatic bonds that contribute to stabilizing the protein's conformation. In cases where one of the ionizable groups directly contributes to the functionality of the active site, changes in its ionization state can completely nullify enzymatic activity. The isoelectric point (*pI*) of a protein is defined as the pH value at which the protein has a net charge of

zero. It is characteristic of each protein and depends on the number, type, and arrangement of acidic and basic amino acids within the molecule. If *pH* > *pI*, the protein is negatively charged. If *pH* < *pI*, the protein is positively charged.

To simplify the explication of activity dependence on pH, let's consider that a single protein functionality included in the active site can be deprotonated twice, exerting weak acidic behavior:

$$[E] \rightleftarrows [E^-] + [H^+]$$

$$[E^-] \rightleftarrows [E^{2-}] + [H^+]$$

Each of the two equilibria is described by an acidic dissociation constant:

$$(2.30)\quad K_1 = \frac{[E^-][H^+]}{[E]}$$

$$(2.31)\quad K_2 = \frac{[E^{2-}][H^+]}{[E^-]}$$

Doing the hypothesis that the single-deprotonated form E^- is the only active, under saturating conditions $v_{\max}$ is only proportional to E^-:

$$(2.32)\quad v_{\max} = k_{cat}[E^-]$$

Therefore, the molar fraction of active protein is equal to:

$$(2.33)\quad \frac{[E^-]}{[E_{tot}]} = \frac{[E^-]}{[E^-]+[E^{2-}]+[E]} = \frac{1}{1+\frac{[E^{2-}]}{[E^-]}+\frac{[E]}{[E^-]}}$$

Substituting the values for $\frac{[E^{2-}]}{[E^-]}$ and $\frac{[E]}{[E^-]}$ according to the equilibrium equations:

$$(2.34)\quad \frac{[E^-]}{[E]} = \frac{1}{1+\frac{K_2}{[H^+]}+\frac{[H^+]}{K_1}}$$

Finally, the $v_{\max}$ expression becomes:

$$(2.35)\quad v_{\max} = \frac{k_{cat}[E_{tot}]}{1+\frac{K_2}{[H^+]}+\frac{[H^+]}{K_1}}$$

This equation describes a bell curve as in **figure 2.7**.

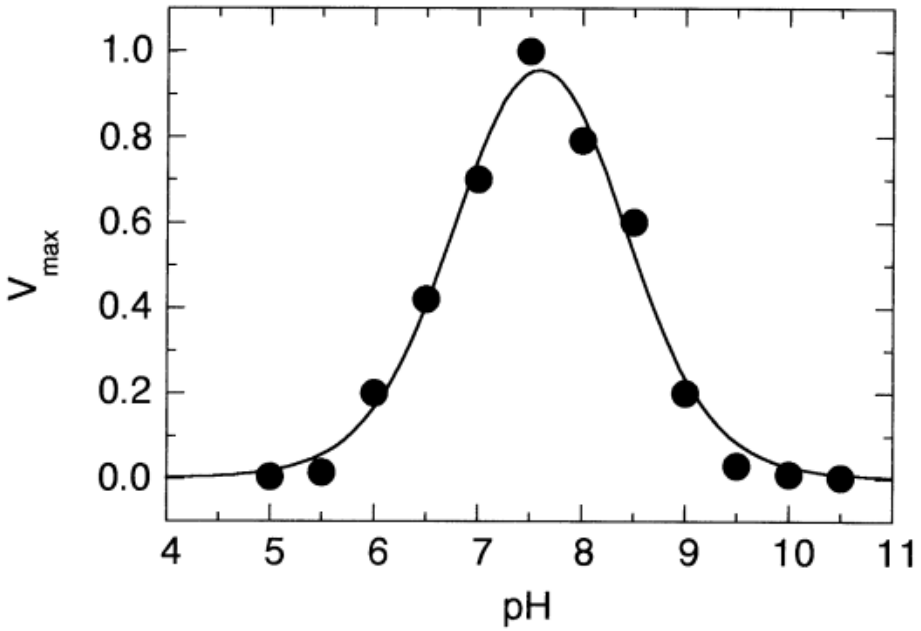

Figure 2.7. The effects of pH on the maximum velocity of a typical enzymatic reaction.

The maximum is found by calculating $[H^+]_{max}$ as imposing $\frac{dv_{max}}{d[H^+]} = 0$. Therefore, the pH_{max} is equal to:

$$(2.36)\quad pH_{max} = -\log[H^+]_{max} = -\log(K_1K_2)^{\frac{1}{2}} = \frac{1}{2}(pK_1 + pK_2)$$

Generally, it is observed that protein conformation remains stable across a relatively wide pH range, approximately spanning 4 to 5 pH units. However, within this range, the enzymatic reaction velocity fluctuates in response to changes in pH, as clearly shown by **Figure 2.7**. For this reason, enzyme reactions are usually performed in buffered systems.

2.3.2. The effect of temperature

It is well known that the rate of a chemical reaction depends exponentially on temperature, according to the Arrhenius equation. It is true for catalytic reactions and

thus for enzymatic reactions as well. However, the effects of temperature on enzyme activity results from the competition between higher catalytic efficiency and protein denaturation, which seriously affect the capacity to bind the substrate. This feature is perfectly described by the non-monotonous profile in **Figure 2.8 A.**

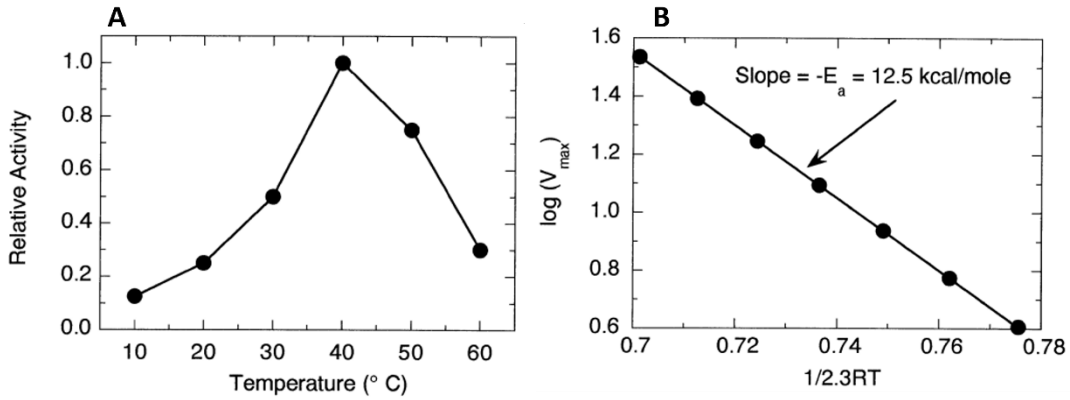

Figure 2.8. Relative activity profile versus temperature for an enzyme reaction (A). Linearized Arrhenius plot , with the slope being the activation energy of the reaction (B).

If we restrict the analysis to a thermal interval not affected by denaturation, Arrhenius model is applied to enzyme kinetics as well:

$$(2.37)\quad k_{cat} = Ae^{\frac{-E_a}{RT}}$$

The logarithm function allows the linearization of this equation:

$$(2.38)\quad \log(k_{cat}) = -E_a \frac{1}{2.3RT} + \log(A)$$

The plot of $\log(k_{cat})$ versus $\frac{1}{2.3RT}$ results in a linear curve with negative slope equal to the activation energy of the reaction. The same trend is exhibited by v_{max} since, under saturating conditions, $v_{max} = k_{cat}[E]$, as shown in **Figure 2.8 B**. Therefore, the higher the temperature, the lower $\frac{1}{2.3RT}$ and thus the higher v_{max}.

2.3.3. Competitive, noncompetitive, substrate inhibition

Catalytic activity can be negatively affected by the capacity of some molecules to modify the enzyme conformation after binding to a specific portion of the protein. These molecules are called inhibitors and inhibition can be reversible or irreversible. Irreversible inhibitors permanently distort enzyme conformation, completely compromising substrate binding. However, most of the inhibitors act reversibly and, according to the nature of inhibition, they can be referred to as competitive, noncompetitive and uncompetitive. Competitive inhibitors exhibit similar structures as the substrates and compete with the substrates themselves in binding to the active sites. This situation is described by the following equilibria:

$$[E] + [S] \underset{K_m}{\rightleftarrows} [ES]$$

$$[E] + [I] \underset{K_I}{\rightleftarrows} [EI]$$

Where $[I]$ and $[EI]$ are the inhibitor and inhibitor-enzyme binary complex concentrations, respectively, whereas K_I is the dissociation constant for this equilibrium. In this case, the mass conservation equation is the following:

$$[E_{tot}] = [E] + [EI] + [ES] \quad (2.39)$$

So, free enzyme concentration is equal to:

$$[E] = [E_{tot}] - [EI] - [ES] \quad (2.40)$$

Equation 2.40 can be used to derive the expression of $[ES]$ from the complexation equilibrium. Indeed:

$$[ES]K_m = [E][S] = [S]([E_{tot}] - [EI] - [ES]) = [S][E_{tot}] - [S][EI] - [S][ES] \quad (2.41)$$

According to the enzyme-inhibitor complexation equilibrium:

$$[EI] = \frac{[E][I]}{K_I} \quad (2.42)$$

Expression 2.42 can be substituted in equation 2.41:

(2.43) $[ES]K_m = [S][E_{tot}] - [S]\frac{[E][I]}{K_I} - [S][ES] = [S][E_{tot}] - [ES][I]\frac{K_m}{K_I} - [S][ES]$

Isolating $[ES]$:

(2.44) $[ES] = \frac{[S][E_{tot}]}{K_m + \frac{K_m}{K_I}[I] + [S]}$

Therefore, the expression of velocity becomes:

(2.45) $v = k_{cat}[ES] = k_{cat}\frac{[S][E_{tot}]}{K_m + \frac{K_m}{K_I}[I] + [S]} = \frac{v_{max}[S]}{K'_m + [S]}$

With $K'_m = K_m(1 + \frac{[I]}{K_I})$

The mathematical formalism of the velocity expression in the presence of a competitive inhibitor is the same as the classical Michaelis-Menten equation, but the new dissociation constant K'_m is always higher than K_m due to the additive contribution of $\frac{[I]}{K_I}$ factor. However, the value of v_{max} remains the same. So, the effect of competitive inhibitors can be reduced by increasing substrate concentration. On the other hand, this is not possible for non-competitive inhibitors. As a matter of fact, the molecules of non-competitive inhibitors have a different shape from that of the substrate. They form complexes with the enzyme at points other than the active site (in fact, they are also called "allosteric"). The formation of the complex can alter the entire conformation of the enzyme, even at the active site. The enzyme can also form ternary complexes ESI, but only the ES complex evolves into a product, as described by the following equilibria:

$$[E] + [S] \underset{K_m}{\rightleftarrows} [ES]$$

$$[E] + [I] \underset{K_I}{\rightleftarrows} [EI]$$

$$[EI] + [S] \underset{K_I}{\rightleftarrows} [ESI]$$

$$[ES] + [I] \underset{K_I}{\rightleftarrows} [ESI]$$

The fact that a portion of the enzyme molecules is complexed with the inhibitor in the form of EI and ESI reduces the possibility of complexing with the substrate and, therefore, the rate of the enzymatic reaction. The analytic expression of velocity in case of noncompetitive inhibition is obtained the same way as before. In this case, the mass balance equation for the protein is:

$$(2.46)\quad [E_{tot}] = [E] + [EI] + [ES] + [ESI]$$

So, free enzyme concentration is equal to:

$$(2.47)\quad [E] = [E_{tot}] - [EI] - [ES] - [ESI]$$

Substituting this expression in equation 2.23:

$$(2.48)\quad [ES]K_m = [S][E_{tot}] - [S]\frac{[E][I]}{K_I} - [S][ES] - [S]\frac{[ES][I]}{K_I} = [S][E_{tot}] - [ES][I]\frac{K_m}{K_I} - [S][ES] - [S]\frac{[ES][I]}{K_I}$$

Isolating $[ES]$:

$$(2.49)\quad [ES] = \frac{[S][E_{tot}]}{(K_m+[S])(\frac{[I]}{K_I}+1)}$$

Therefore, the final expression for v is:

$$(2.50)\quad v = \frac{\frac{k_{cat}[E_{tot}]}{(\frac{[I]}{K_I}+1)}}{(K_m+[S])}[S] = \frac{\frac{v_{max}}{(\frac{[I]}{K_I}+1)}}{(K_m+[S])}[S] = \frac{v'_{max}[S]}{(K_m+[S])}$$

The kinetic equation remains formally $K_m$unchanged compared to that of the uninhibited enzyme. The value remains identical to what is observed in the absence of the inhibitor, as the equilibrium of complex formation between E and S is not affected by the presence of the inhibitor. The value of the maximum velocity v'_{max} is always lower than that observed in the absence of the inhibitor since, regardless of the concentration of S, if the inhibitor is present, a portion of the enzyme is still

complexed with it to form EI and ESI, and the condition for which the entire enzyme is present in the form of the ES complex is never reached. Allosteric inhibition requires a significant complexity of the enzyme molecule, which must possess two distinct active sites. The presence of enzymes whose activity is modulated by inhibitor concentration levels represents an advantage for the host organism. Nonhyperbolic behavior may also arise due to substrate inhibition, which occurs when an additional molecule of substrate can attach to the ES complex, resulting in the formation of an inactive ternary complex ESS, as shown by the following equilibria:

$$[E] + [S] \underset{K_m}{\rightleftarrows} [ES]$$

$$[ES] + [S] \underset{K_S}{\rightleftarrows} [ESS]$$

In this case, the usual mass balance equation for the protein becomes:

$$[E_{tot}] = [E] + [ES] + [ESS] \quad (2.51)$$

So, free enzyme concentration is equal to:

$$[E] = [E_{tot}] - [ES] - [ESS] \quad (2.52)$$

Substituting this expression in equation 2.23:

$$[ES]K_m = [S][E_{tot}] - [S][ES] - \frac{[S]^2[ES]}{K_S} \quad (2.53)$$

Isolating $[ES]$:

$$[ES] = \frac{[S][E_{tot}]}{K_m + [S] + \frac{[S]^2}{K_S}} \quad (2.54)$$

It is possible to find now an analytical expression for v:

$$v = k_{cat}[ES] = \frac{v_{max}[S]}{K_m + [S] + \frac{[S]^2}{K_S}} \quad (2.55)$$

Since the creation of the ES complex must happen before the inhibitory ternary complex is formed, substrate inhibition typically occurs only at elevated substrate concentrations. It manifests as a measured velocity at these high substrate concentrations that is lower than anticipated **(figure 2.9)**.

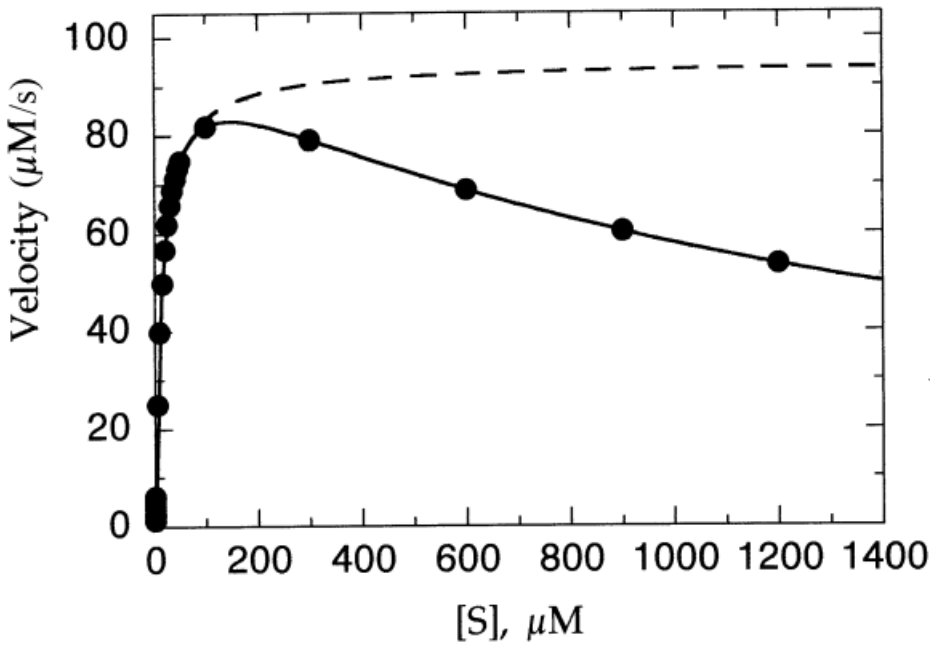

Figure 2.9. Trend of reaction velocity as a function of substrate concentration for the case of substrate inhibition.

3. Aim of the work

The focus of this thesis is double. The first part of the experimental work was oriented in enzyme immobilization onto nanostructured materials for two kinds of applications namely biofuel production and organic synthesis. Two different enzyme families were chosen for immobilization: cellulolytic enzymes and lipases. The former were committed to the hydrolysis of cellulose (the first stage for bioethanol production); the latter were alternatively used for both biodiesel production and

organic synthesis. The selected carriers were mesoporous silica nanoparticles produced by sol-gel route. The supported biocatalyst underwent extended physic-chemical characterization to shed light on spatial distribution, conformation and amount of the immobilized protein. The effectiveness of physical immobilization in preserving the capacity of binding the substrates, ensuring reusability and thermal stability as well was assessed through functionality assays. The second part of the work mainly focused on the design of miniaturized enzyme reactors for enantio-selective organic synthesis. Part of the research program was spent in the Heterogeneous Biocatalysis Lab headed by Ikerbasque Professor Dr. Fernando Lopez-Gallego from CIC biomaGUNE (Donostia/San Sebastian, Spain), who supervised the application of enzymes the enantio-selective synthesis of β-hydroxyacids in both batch and continuous flow reactors.

3.1. Organization of the contents

The present thesis is organized into 7 chapters.

Chapter 1 is the opening section, introducing the objectives, the organization of the thesis and exposes the principles of biocatalysis. This chapter also provides the collection of both published and under review papers, the academic activities and other relevant achievements of this PhD project.

Chapter 2 offers an extended overview of enzyme immobilization, including the state of the art with specific focus on cellulolytic enzymes (i.e. cellulases) and lipases. The main techniques of immobilization are presented in detail, highlighting both pros and cons of each one.

Chapter 3 deals with the synthesis of mesoporous silica nanoparticles, the possible functionalization strategies and their applications as carriers for proteins.

Chapter 4 is a resume of the experimental techniques used to characterize the synthesized carrier and the supported biocatalysts.

Chapter 5 is a collection of published and under-review papers produced during the three years of the PhD project. The common thread of the chapter is the design of nanoscaled supported biocatalysts by immobilization into MSNs.

- Section **1** focuses on the insight into the physical immobilization of β-glucosidase into MSNs. The mechanism of immobilization is investigated and the immobilization conditions are tuned in order to maximize the yield of immobilization. The supported biocatalysts are finally tested in the hydrolysis of cellobiose to produce glucose. Part of the work was carried out in the Heterogeneous Biocatalysis laboratory (Donostia/San Sebastian, Spain)
- Section **2** deals with the co-immobilization of cellulase and supplementary β-glucosidase for the hydrolysis of biomass-derived cellulose. The weight ratio between the enzymes was optimized to maximize glucose production, whereas pore geometry was properly designed to fit the size of both the proteins.
- In Section **3**, the immobilization of *Candida rugosa* lipase (CRL) into hydrophobic MSNs for biodiesel production. The carriers were properly functionalized with a silane agent through chemical vapor deposition in order to provide lipase interfacial activation.
- Section **5d** reports the immobilization of *Candida antarctica* lipase B (CALB) and *Rhizomucor miehei* lipase (RML) into hydrophobic MSNs for the production of β-hydroxyacids. This project was carried out at the Heterogeneous Biocatalysis Laboratory from CIC-biomaGUNE, under the supervision of Ikerbasque Prof. Fernando Lopez-Gallego.

In **Chapter 6,** the design of a series of packed bed reactors to enantioselectively convert β-ketoesters into β-hydroxyacids. This work was supervised by Prof. Fernando Lopez-Gallego as well. Moreover, the preliminary steps to transpose

cellulose hydrolysis from batch to continuous flow miniaturized reactors are presented.

Chapter 7 resumes the main outlooks of the present thesis and briefly introduces some possible future perspectives.

4. Publications and relevant achievements

4.1 Published papers

1. Pota, G., Bifulco, A., Parida, D., Zhao, S., Rentsch, D., Amendola, E., ... & Costantini, A. (2021). Tailoring the hydrophobicity of wrinkled silica nanoparticles and of the adsorption medium as a strategy for immobilizing lipase: An efficient catalyst for biofuel production. *Microporous and Mesoporous Materials*, 328, 111504.

2. Pota, G., Sapienza Salerno, A., Costantini, A., Silvestri, B., Passaro, J., & Califano, V. (2022). Co-immobilization of cellulase and β-glucosidase into mesoporous silica nanoparticles for the hydrolysis of cellulose extracted from Eriobotrya japonica Leaves. *Langmuir*, *38*(18), 5481-5493.

3. Pota, G., Gallucci, N., Cavasso, D., Krauss, I. R., Vitiello, G., López-Gallego, F., ... & Califano, V. (2023). Controlling the Adsorption of β-Glucosidase onto Wrinkled SiO_2 Nanoparticles To Boost the Yield of Immobilization of an Efficient Biocatalyst. *Langmuir*, 39(4), 1482-1494.

4.2 Submitted papers

4.3 Academic activity

- Subject expert in Chemistry at the Department of Chemical, Materials and Production engineering of the University of Naples Federico II

- Assistant for the course of Chemistry (CHIM-07) held in the faculty of engineering at the University of Naples Federico II
- Co-supervisor of more than 10 Bachelor theses in Chemical and Biomedical engineering, supervised by Prof. Vitiello and Prof. Costantini.
- Co-supervisor of 6 Master thesis in Chemical Engineering supervised by Prof. Luciani, Costantini and Vitiello.
- Co-supervisor of Master thesis in Chemical Engineering entitled: *"Honeycomb microreactors loaded with β-glucosidase adsorbed into Wrinkled nano-SiO_2: a study of the operating parameters for the hydrolysis of cellobiose"*, supervised by Prof. Costantini
- Co-supervisor of Master thesis in Chemical Engineering entitled: *"Enzymatic conversion of lignocellulosic biomass: biomass pretreatment and cellulase immobilization into mesoporous silica nanoparticles"*, supervised by Prof. Costantini
- Co-supervisor of Master thesis in Chemical Engineering entitled: *"Physical adsorption of Cellulase and β-Glucosidase into Mesoporous Silica Nanoparticles: free and immobilized nanoparticles into a honeycomb cordierite monolith for the hydrolysis of cellulose"*, supervised by Prof. Costantini
- Co-supervisor of Master thesis in Chemical Engineering entitled: *"Wood-derived cathodes for quasi-solid Al-air batteries"*, supervised by Prof. Costantini

4.4 Oral and poster presentations to national and international conferences

- 31st Conference of the European Society for Biomaterials (ESB), 5-9/09/2021, virtual, oral presentation: "Multifunctional bioinspired melanin-CeO_2 hybrid nanozymes for regenerative medicine"
- 2021 EUSMI / SoftComp Annual Meeting, 31/05-02/06/2021, virtual, oral presentation: "On the interaction of β-glucosidase with Wrinkled SiO_2 nanoparticles: the protein corona formation"
- XXVII Congresso Nazionale della Società Chimica Italiana, 14-23/09/2021, virtual, oral presentation: "Mesoporous Silica Nanoparticles: a powerful platform for biocatalysis"
- Conferenza Nazionale Biomateriali SIB2021, 11-14/07/2021, Lecce, oral presentation: "Multifunctional bioinspired melanin-CeO_2 for wound healing application"
- I congresso nazionale della divisione "Chimica per le tecnologie" della Società Chimica Italiana, 4-7/09/2022, Napoli, Flash presentation and Poster: "Co-immobilization of cellulase and β-glucosidase into mesoporous silica nanoparticles for the hydrolysis of cellulose extracted from *Eriobotrya japonica* leaves". Winner of the best poster award.
- 2023 EUSMI / SoftComp Annual Meeting, 22-25/05/2023, Ancona, oral presentation: "Cellulase and β-glucosidase co-adsorbed into mesoporous silica nanoparticles: a nanostructured biocatalyst for cellulose hydrolysis"
- 6th EuChemS Conference on Green and Sustainable Chemistry, 03-06/09/2023, Salerno, oral presentation: "*Candida rugosa* lipase immobilized into hydrophobic mesoporous silica nanoparticles as an effective biocatalyst for biodiesel production"

4.5 Staying at other international research institutions

- Institution: Centre for Cooperative Research in Biomaterials (CIC biomaGUNE), San Sebastian (Spain)
- Time: from 05/2022 to 11/2022 (7 months)
- Tutor: IKERBASQUE Professor Dr. Fernando Lopez-Gallego
- Activity: Immobilization of multienzyme systems for the enantioselective synthesis of β-hydroxyacids

References

(1) Organization, W. H. COP24 Special Report: Health and Climate Change. **2018**.

(2) Rigaud, K. K.; De Sherbinin, A.; Jones, B.; Bergmann, J.; Clement, V.; Ober, K.; Schewe, J.; Adamo, S.; McCusker, B.; Heuser, S. Groundswell: Preparing for Internal Climate Migration. **2018**.

(3) Thuiller, W.; Lavergne, S.; Roquet, C.; Boulangeat, I.; Lafourcade, B.; Araujo, Miguel. B. Consequences of Climate Change on the Tree of Life in Europe. *Nature* **2011**, *470* (7335), 531–534. https://doi.org/10.1038/nature09705.

(4) Ruszkiewicz, J. A.; Tinkov, A. A.; Skalny, A. V.; Siokas, V.; Dardiotis, E.; Tsatsakis, A.; Bowman, A. B.; da Rocha, J. B. T.; Aschner, M. Brain Diseases in Changing Climate. *Environmental Research*. Academic Press Inc. October 1, 2019. https://doi.org/10.1016/j.envres.2019.108637.

(5) Stibel, J. M. Climate Change Influences Brain Size in Humans. *Brain Behav Evol* **2023**, *98* (2), 93–106. https://doi.org/10.1159/000528710.

(6) Karnauskas, K. B.; Miller, S. L.; Schapiro, A. C. Fossil Fuel Combustion Is Driving Indoor CO2 Toward Levels Harmful to Human Cognition. *Geohealth* **2020**, *4* (5). https://doi.org/10.1029/2019GH000237.

(7) Osman, M. B.; Tierney, J. E.; Zhu, J.; Tardif, R.; Hakim, G. J.; King, J.; Poulsen, C. J. Globally Resolved Surface Temperatures since the Last Glacial Maximum. *Nature* **2021**, *599* (7884), 239–244. https://doi.org/10.1038/s41586-021-03984-4.

(8) Lee, H.; Calvin, K.; Dasgupta, D.; Krinner, G.; Mukherji, A.; Thorne, P.; Trisos, C.; Romero, J.; Aldunce, P.; Ruane, A. C. CLIMATE CHANGE 2023 Synthesis Report Summary for Policymakers. *CLIMATE CHANGE 2023 Synthesis Report: Summary for Policymakers* **2024**.

(9) Soeder, D. J. *Fracking and the Environment: A Scientific Assessment of the Environmental Risks from Hydraulic Fracturing and Fossil Fuels*; Springer International Publishing, 2020. https://doi.org/10.1007/978-3-030-59121-2.

(10) Hansen, G.; Stone, D. Assessing the Observed Impact of Anthropogenic Climate Change. *Nat Clim Chang* **2016**, *6* (5), 532–537. https://doi.org/10.1038/nclimate2896.

(11) Abbass, K.; Qasim, M. Z.; Song, H.; Murshed, M.; Mahmood, H.; Younis, I. A Review of the Global Climate Change Impacts, Adaptation, and Sustainable Mitigation Measures. *Environmental Science and Pollution Research*. Springer Science and Business Media Deutschland GmbH June 1, 2022, pp 42539–42559. https://doi.org/10.1007/s11356-022-19718-6.

(12) Canadell, J. G.; Monteiro, P. M. S.; Costa, M. H.; Da Cunha, L. C.; Cox, P. M.; Eliseev, A. V; Henson, S.; Ishii, M.; Jaccard, S.; Koven, C. Global Carbon and Other Biogeochemical Cycles and Feedbacks. 2021.

(13) UNFCCC. Conference of the Parties. In *ADOPTION OF THE PARIS AGREEMENT*; 2015.

(14) Turiel, A. The Energy Crisis in the World Today: Analysis of the World Energy Outlook 2021. **2022**.

(15) van Asselt, H.; Green, F. COP26 and the Dynamics of Anti-Fossil Fuel Norms. *Wiley Interdiscip Rev Clim Change* **2023**, *14* (3). https://doi.org/10.1002/wcc.816.

(16) Wang, Y.; Liu, Y.; Gu, B. COP26: Progress, Challenges, and Outlook. Springer 2022.

(17) Wise, J. COP28 Decision to "Transition Away" from Fossil Fuels Is Hailed as Milestone but Loopholes Are Decried. *BMJ* **2023**, *383*, p2941. https://doi.org/10.1136/BMJ.P2941.

(18) Sakthivel, R.; Abbhijith, H.; Harshini, G. V.; Vardhan, M. S.; Shadangi, K. P. Biofuels: Classification, Conversion Technologies, Optimization Techniques and Applications. In *Biorefineries: Production of Fuels and Platform Chemicals*; Wiley Blackwell, 2024; pp 1–30. https://doi.org/10.1002/9781119724872.ch1.

(19) Aro, E.-M. From First Generation Biofuels to Advanced Solar Biofuels. *Ambio* **2016**, *45* (Suppl 1), 24–31.

(20) Lee, R. A.; Lavoie, J.-M. From First-to Third-Generation Biofuels: Challenges of Producing a Commodity from a Biomass of Increasing Complexity. *Animal Frontiers* **2013**, *3* (2), 6–11.

(21) Sims, R. E. H.; Mabee, W.; Saddler, J. N.; Taylor, M. An Overview of Second Generation Biofuel Technologies. *Bioresour Technol* **2010**, *101* (6), 1570–1580.

(22) Carriquiry, M. A.; Du, X.; Timilsina, G. R. Second Generation Biofuels: Economics and Policies. *Energy Policy* **2011**, *39* (7), 4222–4234. https://doi.org/10.1016/j.enpol.2011.04.036.

(23) Sakthivel, R.; Ramesh, K.; Purnachandran, R.; Shameer, P. M. A Review on the Properties, Performance and Emission Aspects of the Third Generation Biodiesels. *Renewable and Sustainable Energy Reviews* **2018**, *82*, 2970–2992.

(24) The Renewable Fuel Standard: A Decade's Worth of Carbon Reductions. *Biotechnology Industry Organization* **2014**.

(25) Aditiya, H. B.; Mahlia, T. M. I.; Chong, W. T.; Nur, H.; Sebayang, A. H. Second Generation Bioethanol Production: A Critical Review. *Renewable and Sustainable Energy Reviews*. Elsevier Ltd December 1, 2016, pp 631–653. https://doi.org/10.1016/j.rser.2016.07.015.

(26) Balat, M. New Biofuel Production Technologies. *Energy Educ Sci Technol Part A* **2009**, *22* (2), 147–161.

(27) Flach, B.; Lieberz, S.; Bolla, S. *European Union: Biofuels Annual*; 2022.

(28) Krylova, A. Y.; Kozyukov, E. A.; Lapidus, A. L. Ethanol and Diesel Fuel from Plant Raw Materials: A Review. *Solid Fuel Chemistry* **2008**, *42*, 358–364.

(29) Awasthi, M. K.; Sindhu, R.; Sirohi, R.; Kumar, V.; Ahluwalia, V.; Binod, P.; Juneja, A.; Kumar, D.; Yan, B.; Sarsaiya, S. Agricultural Waste Biorefinery Development towards Circular Bioeconomy. *Renewable and Sustainable Energy Reviews* **2022**, *158*, 112122.

(30) Azhar, S. H. M.; Abdulla, R.; Jambo, S. A.; Marbawi, H.; Gansau, J. A.; Faik, A. A. M.; Rodrigues, K. F. Yeasts in Sustainable Bioethanol Production: A Review. *Biochem Biophys Rep* **2017**, *10*, 52–61.

(31) Garrote, G.; Domínguez, H.; Parajó, J. C. Interpretation of Deacetylation and Hemicellulose Hydrolysis during Hydrothermal Treatments on the Basis of the Severity Factor. *Process Biochemistry* **2002**, *37* (10), 1067–1073.

(32) Iravani, S.; Varma, R. S. Greener Synthesis of Lignin Nanoparticles and Their Applications. *Green Chemistry* **2020**, *22* (3), 612–636. https://doi.org/10.1039/c9gc02835h.

(33) Refaat, A. A. Biofuels from Waste Materials. *Comprehensive Renewable Energy* **2012**, 217–261. https://doi.org/10.1016/B978-0-08-087872-0.00518-7.

(34) Kim, J. S.; Lee, Y. Y.; Torget, R. W. Cellulose Hydrolysis under Extremely Low Sulfuric Acid and High-Temperature Conditions. In *Twenty-Second Symposium on Biotechnology for Fuels and Chemicals*; Springer, 2001; pp 331–340.

(35) Mosier, N. S.; Ladisch, C. M.; Ladisch, M. R. Characterization of Acid Catalytic Domains for Cellulose Hydrolysis and Glucose Degradation. *Biotechnol Bioeng* **2002**, *79* (6), 610–618. https://doi.org/10.1002/bit.10316.

(36) DEMİRBAŞ, A. Bioethanol from Cellulosic Materials: A Renewable Motor Fuel from Biomass. *Energy sources* **2005**, *27* (4), 327–337.

(37) Zhang, H.; Han, L.; Dong, H. An Insight to Pretreatment, Enzyme Adsorption and Enzymatic Hydrolysis of Lignocellulosic Biomass: Experimental and Modeling Studies. *Renewable and sustainable energy reviews* **2021**, *140*, 110758.

(38) Babadi, A. A.; Rahmati, S.; Fakhlaei, R.; Barati, B.; Wang, S.; Doherty, W.; Ostrikov, K. K. Emerging Technologies for Biodiesel Production:

Processes, Challenges, and Opportunities. *Biomass Bioenergy* **2022**, *163*, 106521.

(39) Mathew, G. M.; Raina, D.; Narisetty, V.; Kumar, V.; Saran, S.; Pugazhendi, A.; Sindhu, R.; Pandey, A.; Binod, P. Recent Advances in Biodiesel Production: Challenges and Solutions. *Science of the Total Environment* **2021**, *794*, 148751.

(40) Sitepu, E. K.; Heimann, K.; Raston, C. L.; Zhang, W. Critical Evaluation of Process Parameters for Direct Biodiesel Production from Diverse Feedstock. *Renewable and Sustainable Energy Reviews* **2020**, *123*, 109762.

(41) Védrine, J. C. Heterogeneous Catalysis on Metal Oxides. *Catalysts* **2017**, *7* (11), 341.

(42) Furuta, S.; Matsuhashi, H.; Arata, K. Biodiesel Fuel Production with Solid Amorphous-Zirconia Catalysis in Fixed Bed Reactor. *Biomass Bioenergy* **2006**, *30* (10), 870–873.

(43) Adlercreutz, P. Immobilisation and Application of Lipases in Organic Media. *Chem Soc Rev* **2013**, *42* (15), 6406–6436.

(44) Tan, T.; Lu, J.; Nie, K.; Deng, L.; Wang, F. Biodiesel Production with Immobilized Lipase: A Review. *Biotechnology Advances*. September 2010, pp 628–634. https://doi.org/10.1016/j.biotechadv.2010.05.012.

(45) Amini, Z.; Ong, H. C.; Harrison, M. D.; Kusumo, F.; Mazaheri, H.; Ilham, Z. Biodiesel Production by Lipase-Catalyzed Transesterification of Ocimum Basilicum L.(Sweet Basil) Seed Oil. *Energy Convers Manag* **2017**, *132*, 82–90.

(46) Copeland, R. A. *Enzymes: A Practical Introduction to Structure, Mechanism, and Data Analysis*; John Wiley & Sons, 2023.

(47) Laidler, K. J.; King, M. C. The Development of Transition-State Theory. *J. phys. Chem* **1983**, *87* (15), 2657–2664.

(48) Reetz, M. T. Biocatalysis in Organic Chemistry and Biotechnology: Past, Present, and Future. *J Am Chem Soc* **2013**, *135* (34), 12480–12496.

(49) May, O. Industrial Enzyme Applications–Overview and Historic Perspective. *Industrial enzyme applications* **2019**, 1–24.

(50) Chansekaran, M. *Enzymes in Food and Beverage Processing*.

(51) Illanes, A. Enzyme Biocatalysis. *Principles and Applications. Editorial Springer-Verlag New York Inc., United States* **2008**, 1–56.

(52) Victorino da Silva Amatto, I.; Gonsales da Rosa-Garzon, N.; Antônio de Oliveira Simões, F.; Santiago, F.; Pereira da Silva Leite, N.; Raspante Martins, J.; Cabral, H. Enzyme Engineering and Its Industrial Applications. *Biotechnology and Applied Biochemistry*. John Wiley and Sons Inc April 1, 2022, pp 389–409. https://doi.org/10.1002/bab.2117.

(53) Maghraby, Y. R.; El-Shabasy, R. M.; Ibrahim, A. H.; Azzazy, H. M. E.-S. Enzyme Immobilization Technologies and Industrial Applications. *ACS Omega* **2023**, *8* (6), 5184–5196.

(54) Basso, A.; Serban, S. Industrial Applications of Immobilized Enzymes—A Review. *Molecular Catalysis*. Elsevier B.V. December 1, 2019. https://doi.org/10.1016/j.mcat.2019.110607.

(55) Sarrouh, B.; Santos, T. M.; Miyoshi, A.; Dias, R.; Azevedo, V. Up-to-Date Insight on Industrial Enzymes Applications and Global Market. *J Bioprocess Biotech* **2012**, *4*, 002.

(56) *Industrial Enzymes Market Size, Share & Trends Analysis Report By Product, By Source (Plants, Animals), By Application (Food & Beverages,*

Detergents, Animal Feed), By Region, And Segment Forecasts (2023-2030); 2023.

(57) Sun, H.; Zhang, H.; Ang, E. L.; Zhao, H. Biocatalysis for the Synthesis of Pharmaceuticals and Pharmaceutical Intermediates. *Bioorg Med Chem* **2018**, *26* (7), 1275–1284.

(58) Bilal, M.; Iqbal, H. M. N. State-of-the-Art Strategies and Applied Perspectives of Enzyme Biocatalysis in Food Sector—Current Status and Future Trends. *Crit Rev Food Sci Nutr* **2020**, *60* (12), 2052–2066.

(59) Kumar, D.; Savitri, T. N.; Verma, R.; Bhalla, T. C. Microbial Proteases and Application as Laundry Detergent Additive. *Res J Microbiol* **2008**, *3* (12), 661–672.

(60) Soni, S. K.; Sharma, A.; Soni, R. Microbial Enzyme Systems in the Production of Second Generation Bioethanol. *Sustainability* **2023**, *15* (4), 3590.

(61) Kalita, P.; Basumatary, B.; Saikia, P.; Das, B.; Basumatary, S. Biodiesel as Renewable Biofuel Produced via Enzyme-Based Catalyzed Transesterification. *Energy Nexus* **2022**, *6*, 100087.

(62) *Global Enzyme Market Size, Share & Trends Analysis Report By Type (Industrial And Specialty), By Product (Carbohydrase And Proteases), And By Source (Microorganisms, Plant And Animals) Forecast Period (2022-2028)*; 2023.

(63) Chapman, J.; Ismail, A. E.; Dinu, C. Z. Industrial Applications of Enzymes: Recent Advances, Techniques, and Outlooks. *Catalysts*. MDPI June 5, 2018. https://doi.org/10.3390/catal8060238.

(64) Mateo, C.; Palomo, J. M.; Fernandez-Lorente, G.; Guisan, J. M.; Fernandez-Lafuente, R. Improvement of Enzyme Activity, Stability and

Selectivity via Immobilization Techniques. *Enzyme Microb Technol* **2007**, *40* (6), 1451–1463.

(65) DiCosimo R, McAuliffe J, Poulose AJ, B. G. Industrial Use of Immobilized Enzymes. *Chem Soc Rev* **2013**, 42, 6437–6474,. https://doi.org/10.1039/c3cs35506c.

(66) DiCosimo, R.; McAuliffe, J.; Poulose, A. J.; Bohlmann, G. Industrial Use of Immobilized Enzymes. *Chem Soc Rev* **2013**, *42* (15), 6437–6474.

(67) Mosbach, K. Enzymes Bound to Artificial Matrixes. **1971**, *224* (3), 26–33. https://doi.org/10.2307/24927745.

(68) Savile, C. K.; Janey, J. M.; Mundorff, E. C.; Moore, J. C.; Tam, S.; Jarvis, W. R.; Colbeck, J. C.; Krebber, A.; Fleitz, F. J.; Brands, J. Biocatalytic Asymmetric Synthesis of Chiral Amines from Ketones Applied to Sitagliptin Manufacture. *Science (1979)* **2010**, *329* (5989), 305–309.

Chapter 2

Enzyme immobilization

Contents

1. Fundamentals of enzyme immobilization

Four decades ago, the advent of immobilization offered a highly effective solution to address the challenges associated with enzyme solubility. In essence, enzyme immobilization involves integrating an enzyme into a solid material while preserving its catalytic activity. Both rational and random immobilization protocols have demonstrated their utility in achieving this objective. Following immobilization, enzymes function as heterogeneous biocatalysts, facilitating easy separation from reactants upon completion of the reaction. They can be efficiently reused for multiple operational cycles and seamlessly integrated into flow bioreactors to enhance chemical biomanufacturing processes. The immobilization of unstable enzymes through rational immobilization–stabilization strategies provides simultaneous enhancement of stability and preservation of the catalytic activity. In this context, the choice of carrier is fundamental since there is no perfect support for every enzyme. Indeed, the selected carrier should match the size of the protein and both actors are expected to exhibit chemical affinity with each other. Moreover, immobilization can be pursued either with physical (adsorption, entrapment/encapsulation) or chemical methods (covalent immobilization, cross-linked enzyme aggregates, CLEA).[1] In this paragraph, the fundamental aspects of enzyme immobilization, including the immobilization strategies and the chemical nature of the carriers, are explored. A graphical portrait of the main immobilization technique is reported in **Figure 1.1.**

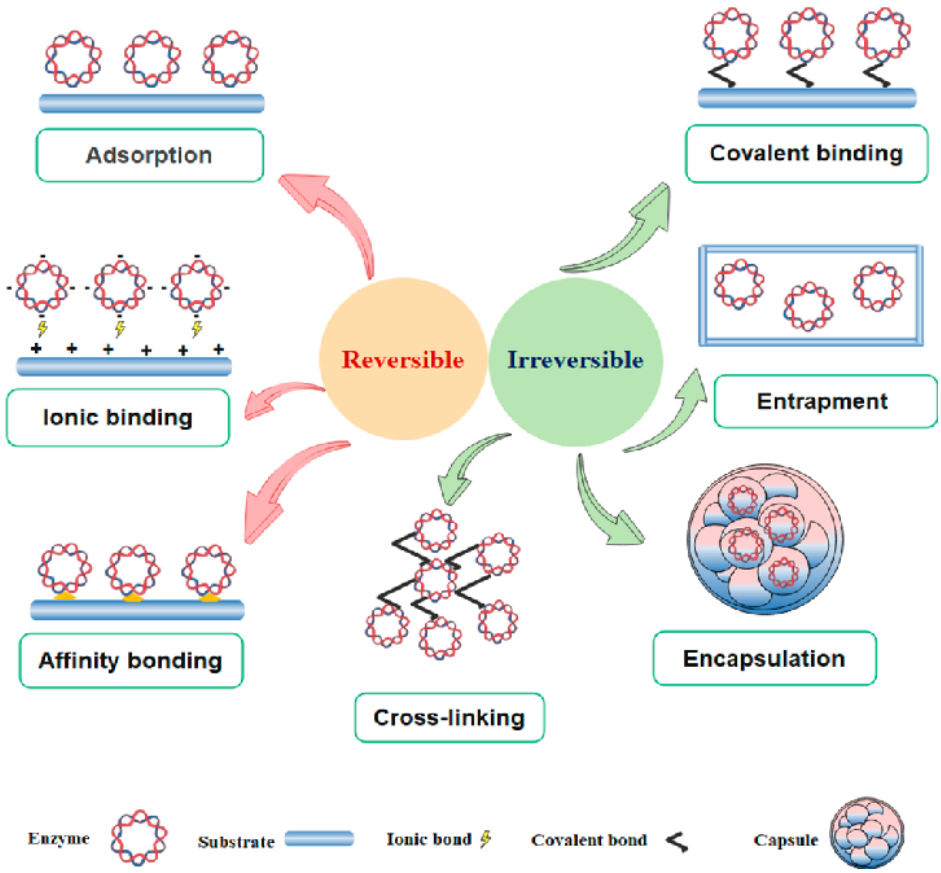

Figure 1.1. Most used immobilization techniques.[2]

1.1. Immobilization on pre-existing carriers

1.1.1. The choice of the carrier

Careful consideration is essential when selecting carrier matrices for enzyme immobilization through adsorption and covalent binding. The cost of these matrices is particularly relevant if compared to overall process expenses, ideally requiring affordability for disposal. In instances where high-value products are manufactured on a smaller scale, the use of relatively expensive supports and immobilization techniques may be feasible, but such approaches may not be economical for large-scale production of low added-value materials. Significant cost savings can be achieved when the carrier allows regeneration after the useful lifespan of the immobilized enzyme. The maximum binding capacity is determined by the surface

density of binding sites and the volumetric surface area available to the enzyme, considering steric factors. The actual capacity is influenced by the number of potential coupling sites in the enzyme molecules, as well as the electrostatic charge distribution and surface polarity on both the enzyme and support. The nature of the support significantly impacts an enzyme's expressed activity and apparent kinetics, including its form, shape, density, porosity, pore size distribution, operational stability, and particle size distribution. The choice of supporting matrix also affects the configuration of the reactor in which the immobilized biocatalyst is employed. An ideal support is characterized by being inexpensive, inert, physically robust, and stable. It enhances enzyme specificity, expressed by $\frac{k_{cat}}{K_m}$, minimizes product inhibition, adjusts the optimum pH value for the process, and deters microbial growth and non-specific adsorption. Some matrices possess additional properties suitable for specific purposes, such as ferromagnetism (e.g., magnetic iron oxide), catalytic surfaces (e.g., MnO_2), or a reductive surface environment (e.g., TiO_2 for enzymes susceptible to oxidation). While most supports may not exhibit all these features, a comprehensive understanding of immobilized enzyme properties allows for the appropriate engineering of the system to approach these optimal qualities.[3] Certain protocols for enzyme immobilization can induce crucial stabilizing effects, even when the 3D structure of the enzyme is not stabilized. In these instances, the root causes of inactivation seen in soluble native enzymes are mitigated. A notable example is the immobilization of enzymes within porous supports (**Figure 1.2**). Within the porous structure, the occurrence of hydrophobic interfaces, which could arise in an enzymatic reactor, is prevented. Consequently, these interfaces cannot lead to the inactivation of the immobilized enzyme molecules. For instance, during vigorous stirring, often necessary for industrial processes to ensure optimal mixing and pH control or in aerated systems, the use of porous carriers for enzyme immobilization proves effective in preventing contact between gas bubbles and the enzyme surface. Such contact, if it were to occur, could result in enzyme unfolding.

Additionally, the porous structure prevents the formation of hydrophobic interfaces in vigorously stirred biphasic systems within the immobilized biocatalyst.

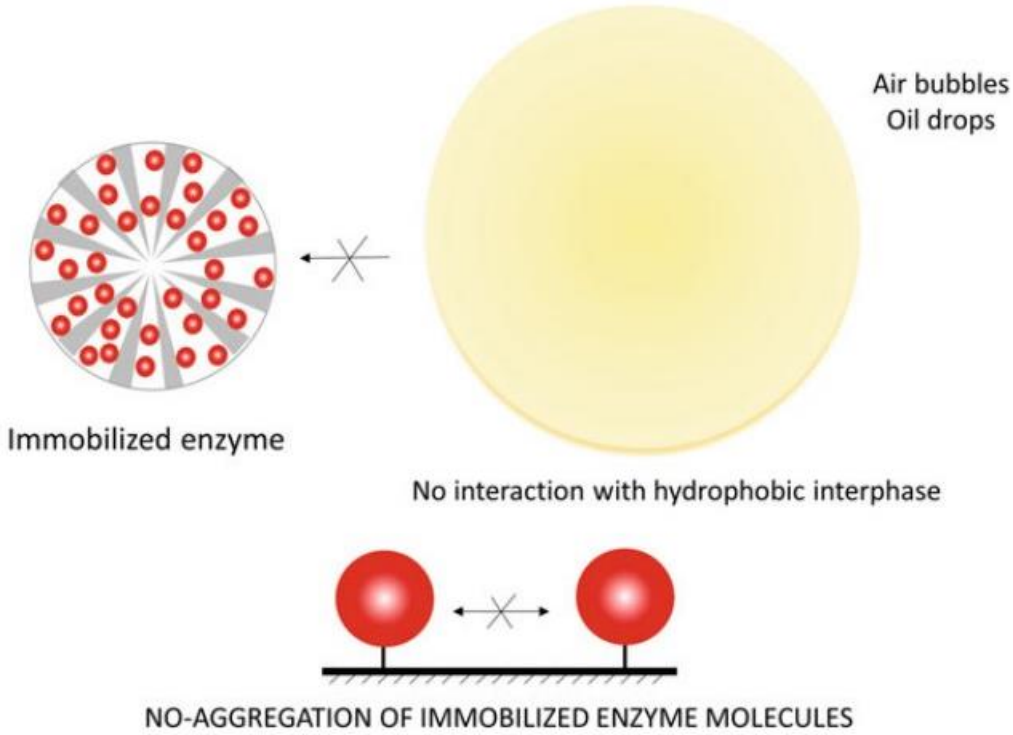

Figure 1.2. The stabilization effects arising from the immobilization into porous carriers.[1]

Moreover, enzymes securely bound to the surface of porous supports are resistant to aggregation processes. These immobilized enzymes exhibit stability, resisting undesirable aggregation in the presence of cosolvents, extreme pH values, high temperatures, and similar conditions. The stabilizing effects achieved through immobilization within porous supports are notable for their independence from the specific immobilization chemistry used to attach the enzyme to the support surface. In contrast, the immobilization of enzymes on non-porous supports (e.g., magnetic nanoparticles) does not yield these stabilizing effects, as the enzymes are exposed to the reaction bulk, making them susceptible to contact with hydrophobic interfaces and potential interparticle aggregation issues.[1]

1.1.2. Adsorption

Adsorption consist of protein binding onto the support's surface thanks to either weak interaction, such as van Der Walls forces or hydrogen bonding, or ionic interactions. van Der Walls forces usually involve hydrophobic supports and enzymes with lipophilic regions (lipases), whereas carriers with polar functionalities are expected to bind glycosylated proteins through hydrogen bonding. The advantages of this technique are the absence of any chemical linking step, reducing the probability of denaturation and thus of active site modification. However, weak interactions do not ensure permanent binding. Therefore, the integrity of the biocatalyst can be undermined by leakage phenomena occurring as a consequence of changes in the chemical environment (pH, ionic strength), especially as the enzyme reaction are carried out in aqueous media.[4] Hydrophobic interactions (another way to say van Der Walls interaction) are not strong enough to provide efficient binding. Indeed, the mechanism of adsorption is better explained by introducing entropy change, that is the enhancement of the entropy of the system as protein chains remove a number of water molecules from both the carrier and their own surface. So, $\Delta S > 0$ makes this process spontaneous due to the increasing reorientational mobility of water molecules.[5] The main requirement for this immobilization strategy to be properly performed is the presence of hydrophobic moieties in both carrier and enzyme. As a matter of fact, strongly hydrophobic carriers such as EP-100 polypropylene,[6,7] Accurel® MP1004 polypropylene,[6,8] octyl-silica,[9,10] and octyl-agarose[11,12]are used for lipase immobilization, since they mimic natural lipase's substrates, inducing a conformational change known as interfacial activation.[13] On the other hand, most of enzymes are mainly hydrophilic due to the great abundance of polar aminoacidic residues. This feature favors the adsorption onto hydrophilic carriers, such as cellulose,[14] clay,[15] sol-gel silica,[16] and Celite.[17] It is a significantly porous diatomaceous earth containing silica SiO_2/metal oxides, commonly utilized for the immobilization of enzymes owing to its chemical inertness and distinctive interconnected pore architecture. Frequently, formulations include additives like

sugars, PEG, or albumin to enhance enzyme stability. The belief is that these polar compounds shield enzymes from the adverse effects of organic solvents and positively impact the distribution of water within the enzyme's microenvironment. In enzyme conformation there are seven amino acids side chains that can behave as Bronsted acids or bases depending on the pH of the medium, namely tyrosine, histidine, cysteine, lysine, arginine, aspartic and glutamic acids.[18] Indeed, functional groups of these amino acids such as amino or carboxyl can be either protonated or deprotonated. The resulting charge of the protein results from the balance between negatively and positively charged groups. More specifically, the zero point charge for a protein is known ad isoelectric point pI. An enzyme is negatively or positively charged depending on whether $pH > pI$ or $pH < pI$, respectively. When adsorption occurs at a pH lower than the pI of the enzyme but higher than the point of zero charge of the carrier, the protein acquires a positive charge. The intensity of this positive charge directly correlates with the strength of the electrostatic attraction between the protein and the surface, while simultaneously increasing the repulsion between adsorbed molecules.[19] So, in the case of a non-charged carrier, the surface can be modified with a properly charged ion exchanger, such as cationic polymer polyethyleneimine (PEI), To begin with, the adhesion of enzymes is notably robust due to the presence of multiple cation groups at various distances in PEI, which can conform to the spacing between enzyme groups. Additionally, the polymer assumes a random coil configuration, preventing any distortion of the enzyme during interaction through multiple points. Furthermore, the three-dimensional adsorption provided by the PEI-formed polymeric bed surpasses the two-dimensional adsorption of conventional supports, facilitating the immobilization of over 80% of proteins present in a crude protein extract.[20] Ionic-driven immobilization can be induced by the functionalization of the carrier with ion-bearing groups. Indeed, Co^{2+}, Cu^{2+}, Ni^{2+} metal cations can be complexed by imidazole rings of protein's histidine (His) moieties (**Figure 1.3**).

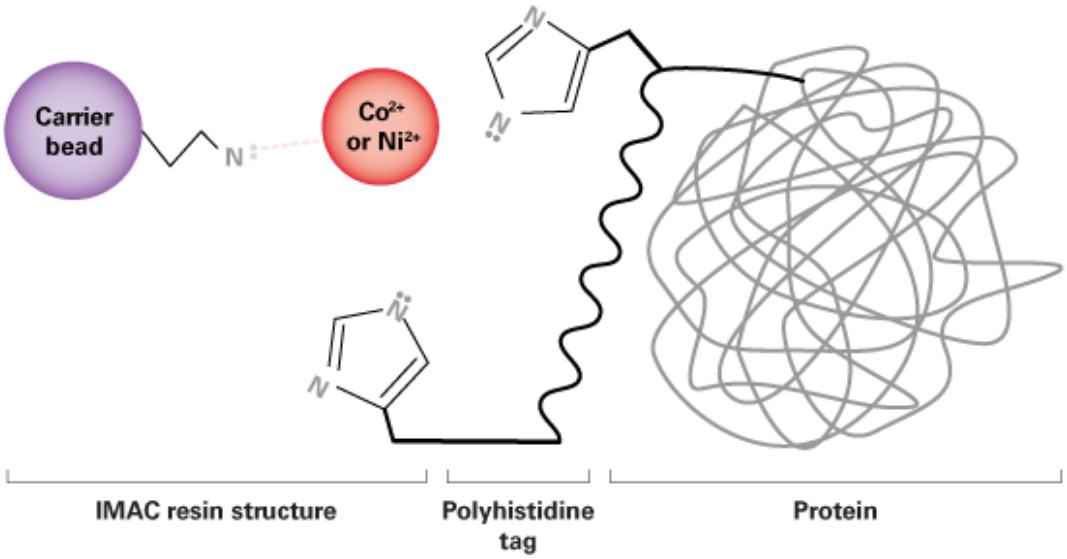

Figure 1.3. Electrostatic binding of His-tagged protein to transition metal cations bared by a carrier.[21]

Therefore, natural protein conformation needs to exhibit accessible histidine chains or, genetic modifications are necessary to induce the expression of a supplementary histidine portion (His-tag).[22] The effectiveness of ionic immobilization relies significantly on both the pH level and salt concentrations not only during the immobilization process but also upon application. Much like the leaching observed in aqueous environments for enzymes immobilized through hydrogen bonds, elevated salt concentrations can result in ion exchange, causing the washing out of enzymes immobilized through ionic interactions. Ionic-driven physisorption is at the basis of immobilization into mesoporous silica nanoparticles (MSNs). Indeed, MSNs usually exhibit zero point charge at low pH (< 3). This is very useful since it allows to perform immobilization in a wide pH range, higher than the pH of zero point charge but lower than the pI of proteins. Moreover, sol-gel synthesis is the proper strategy to adapt pore size to enzyme dimension.[23]

1.1.3. Covalent immobilization

Binding an enzyme covalently to a carrier offers the advantage of securely anchoring the enzyme. This results in minimal enzyme leaching in aqueous environments and eliminates the risk of protein contamination in the final product. Generally, when working in aqueous solutions or dealing with denaturing factors, it is advisable to opt for covalent immobilization. This preference stems from the formation of multiple covalent bonds between the enzyme and the carrier, which reduces conformational flexibility and thermal vibrations, thereby preventing protein unfolding and denaturation (**Figure 1.4**).

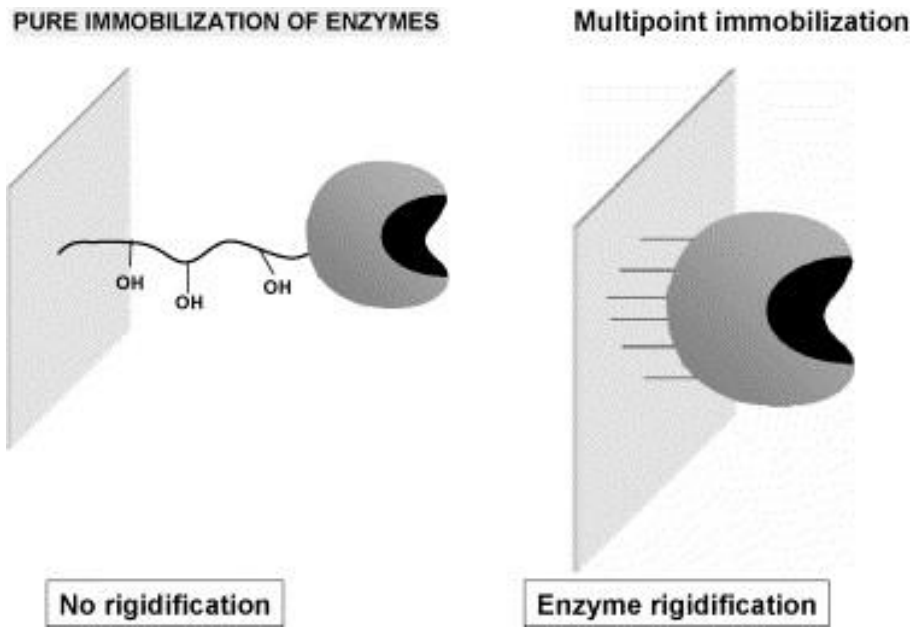

Figure 1.4. Effect of immobilization on enzyme stability.[24]

In contrast, enzymes that are adsorbed should be employed in organic solvents or pure hydrophobic reactants to prevent leaching, while covalently immobilized enzymes can be utilized in various media. So, both enzyme and carrier should bear proper functionalities on their surfaces. The choice of the carrier is of primary importance for providing effective protein stabilization. Therefore, a series of requirements should be satisfied:

• to ensure effective interaction with the enzyme surface, the support must offer a substantial internal surface area with good geometrical congruence. If the support consists of extremely thin fibers, smaller than the protein itself, achieving a strong interaction between the enzyme and the support becomes challenging;

• the support should provide a high superficial density of reactive groups. An abundant presence of reactive groups beneath the protein surface is crucial for establishing an intense multipoint covalent attachment.

• Minimal steric hindrances should be present in the reactive groups of both the protein and the support to facilitate the immobilization process. Following the initial immobilization, achieving multipoint covalent attachment relies on the contact between groups bound to rigid structures.

• The support's reactive groups should be compatible with those frequently found on the enzyme surface.

• Stability of the reactive groups involved in the immobilization process is essential to allow for extended enzyme–support reaction periods.

• Achieving a final inert surface in the support post-immobilization should be straightforward. This can be accomplished by either destroying or blocking any remaining reactive groups in the support without adversely affecting the enzyme.[24]

Several functionalities can be grafted to the surface of the support to covalently bind enzymes, such as -NH_2, -OH, -COOH, -SH and this step is usually termed derivatization. However, functionalization must be followed by activation through bifunctional agents like glutaraldehyde and carbodiimide, bearing glyoxylic, amino or epoxy groups. Most commonly, amino groups of proteins are employed for covalent immobilization, the very common lysine ε-NH_2, even if carboxyl functionalities and sugar moieties in glycosylated enzymes as well.[25] Covalent binding is usually accomplished by nucleophilic addition of the amino groups from

the protein to carbonyl groups of aldehydes from the carrier. A permanent bond originates from the following reduction of the formed imine ($NaBH_4$) through reductive amination. Over time, carriers such as agarose, glyoxyl agarose, and aminated glyoxyl agarose (specifically noted for its high nucleophilicity due to the primary amino group) have demonstrated their effectiveness. More specifically, modified aminated nucleophilic agarose (MANA) was proved to be particularly suitable for covalent attachment for its nucleophilic properties.[26] Epoxy-functionalization with Eupergit C and Eupergit C 250 L is usually carried out with methacrylic carriers such as Sepabeads®.[27] The length of the polymer-enzyme spacer arm determines the stability of the supported biocatalysts. Indeed, the longer the spacer arm, the more flexible is the immobilized protein conformation, suggesting less influence on the catalytic activity. However, restriction of the conformational mobility is mandatory if thermal stabilization is desired and this is achieved with short spacers.[28]

1.2. Enzyme encapsulation

Enzyme encapsulation refers to the process of enclosing or entrapping enzymes within a protective material or structure.[4] The goal is to create a microenvironment that shields the enzyme from external factors, such as harsh chemicals or extreme conditions, while still allowing the substrate and product molecules to interact with the enzyme. This protective encapsulation can enhance the stability and functionality of the enzyme, extending its activity and making it more suitable for various applications, such as biocatalysis or controlled release in drug delivery systems. Encapsulation materials can vary and may include polymers,[29] lipids,[30] or other biocompatible substances like silica nanostructures.[31] More specifically, silica-based porous materials stand as interesting devices for enzyme entrapment due to the possibility of properly tuning pore size and morphology through sol-gel synthesis. The sol–gel material is a chemically inert glass that can be shaped in any desired way. It can be designed to be thermally and mechanically very stable, but the

standard sol–gel is brittle. Although sol–gels are porous, diffusion of the substrate to the enzyme can be restricted and care has to be taken to avoid this.[32]

1.3. Cross-linked enzyme aggregates (CLEA)

Cross-Linked Enzyme Aggregates (CLEAs) belongs to the immobilization strategies in absence of carriers. They consist of insoluble, aggregated structures produced through inter-enzyme cross-linking.[33] This approach combines the benefits of both enzyme immobilization and cross-linking techniques. This can be achieved by various methods, including precipitation and subsequent cross-linking, resulting in a stable and easily recoverable enzyme form (**Figure 1.5**).

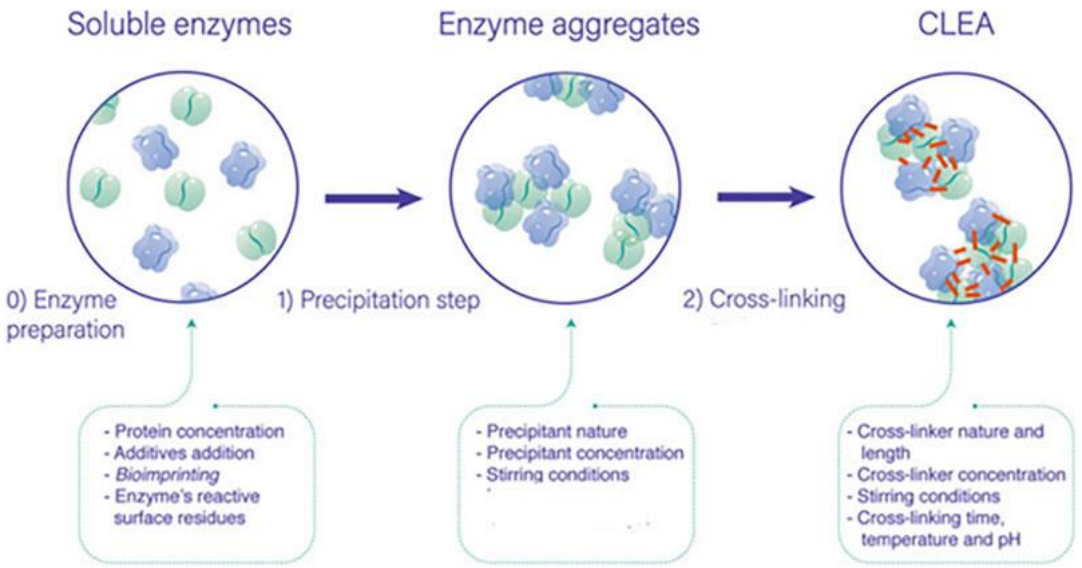

Figure 1.5. Sequence scheme for CLEA preparation.[34]

Covalent bonds are usually provided by bifunctional chemical cross-linkers such as glutaraldehyde. Cross-linking takes place through the interaction of free amino groups located on the surface of adjacent enzyme molecules with oligomers or polymers formed from aldol condensations of glutaraldehyde. This process can encompass both the formation of Schiff's base and a Michael-type 1,4 addition to α,β-unsaturated aldehyde moieties.[35] The cross-linking helps protect the enzyme from denaturation, making them more resistant to harsh conditions such as changes

in temperature, pH, or the presence of organic solvents. Glutaraldehyde is the most used cross-linker, even if other examples were used in the preparation of CLEAs, such as dextran polyaldehyde,[36] diepoxides,[37] *p*-benzoquinone,[38] L-lysine[39] and pectine.[40] One of the advantages of CLEAs is their ease of separation and reusability. The aggregated form allows for simple recovery from reaction mixtures, and the cross-linking ensures that the enzymes remain attached to the aggregate, reducing at the minimum the rate of catalyst leakage. CLEAs are very versatile biocatalytic structures. Indeed, can be created from various enzymes and used in a wide range of applications, including biocatalysis, industrial processes, and biotechnology. Moreover, the extended ease of reusability can contribute to environmentally friendly processes by allowing the reuse of enzymes, reducing the need for frequent enzyme replenishment, and minimizing waste. The main drawbacks of this immobilization strategy are the possibility of massive protein chemical modification since excessive cross-linking might affect the accessibility of the active site to substrates. Moreover, if the protein network is too dense, mass transfer limitations can occur, resulting in both reduced substrate accessibility and limited diffusion of both reactants and products.[41]

1.4. Characterization of immobilized enzymes

(from "Parameters for the evaluation of immobilized enzymes under process conditions" by A. Illanes and L. Wilson").[42]

The evaluation of the immobilization strategy requires a preventive characterization of the supported biocatalyst as a basic step for the future industrial scale up of the process. Indeed, both activity and stability of the obtained supported biocatalyst need to be properly assessed, to unveil the occurrence of inactivation or mass transfer limitation as a consequence of the immobilization.

1.4.1. Characterization prior to use

Three parameters need to be assessed as soon as possible after producing a biocatalyst. The first one is the immobilization yield in terms of protein Y_p, calculated as the percentage ratio between the immobilized protein P_I and the offered protein P_o:

$$(1.1) \quad Y_p(\%) = \frac{P_I}{P_o} \cdot 100$$

The second one is the immobilization yield in terms of activity Y_a:

$$(1.2) \quad Y_a(\%) = \frac{a_I}{a_o} \cdot 100$$

where a_I and a_o are the activities of the immobilized and the offered protein, respectively. Even if $Y_p \leq 100\%$ always, there might be some cases for which $Y_a(\%) > 100\%$, such as hyperactivation of lipases after immobilization onto hydrophobic supports. The third main parameter is the specific activity of the biocatalyst a_{sp}, namely the enzyme activity per unit mass of the biocatalyst:

$$(1.3) \quad a_{sp} = \frac{a_I}{m_{cat}}$$

where m_{cat} is the mass of the biocatalyst.

1.4.2. Characterization under process conditions

The residual activity of the enzyme r_a is defined as the ratio between the specific activity at time t and the initial specific activity:

$$(1.4) \quad r_a = \frac{a}{a_0}$$

It is calculated by measuring the specific activity under standard operating conditions. The collected experimental data of r_a are plotted versus time and fitted by the inactivation models proposed by Henley and Sadana, selecting the best fitting one. The first proposed model is based on a one-stage first-order mechanism:

$$E \xrightarrow{k_D} E^*$$

according to which, the native protein E is irreversibly converted into a completely inactive form E^*. The analytical expression for r_a over time is the one reported below:

$$(1.5) \quad r_a = e^{-k_D t}$$

So, fitting the experimental data with expression 1.5 provides the value of the first-order inactivation rate constant k_D. On the other hand, two-stage inactivation mechanism proposes that a less active intermediate species E_1 is formed before evolving into completely inactive form E^*:

$$E \overset{k_1}{\rightarrow} E_1 \overset{k_2}{\rightarrow} E^*$$

This model prescribes a more complicated expression for r_a:

$$(1.6) \quad r_a = \left(1 + A\frac{k_1}{k_2 - k_1}\right) e^{-k_1 t} - A\frac{k_1}{k_2 - k_1} e^{-k_2 t}$$

Again, non-linear regression of experimental data gives the inactivation parameters k_1, k_2 and A, the last being the specific activity ratio of E_1 and E. It is also useful to assess the stability of the biocatalyst under different inactivating conditions, for example simulating variation in temperature or pH and calculating the residual activity. The time needed to halve the initial protein activity is termed half-life $t_{1/2}$ that in case of one-stage first-order inactivation is expressed as follows:

$$(1.7) \quad t_{1/2} = \frac{\ln(2)}{k_D}$$

The calculation of the half-time can be useful to compare the stability of immobilized and soluble proteins in the same operating conditions. More specifically, by dividing the half-lives of immobilized $(t_{1/2}, ie)$ and soluble $(t_{1/2}, se)$ enzyme, the stabilization factor is obtained:

$$(1.8) \quad SF = \frac{t_{1/2}, ie}{t_{1/2}, se}$$

A comprehensive assessment of both activity and stability of the supported biocatalyst is obtained by calculating the catalytic potential CP, that is the integral of the integral of the specific activity function $a(t)$ over the 0-t_f interval, where t_f is the chosen time for the biocatalyst to be replaced:

$$CP = \int_{t=0}^{t=t_f} a(t)dt \quad (1.9)$$

Usually, $t_{1/2} < t_f < 3t_{1/2}$.

1.5. Nanomaterials as carriers: the importance of colloidal stability

Nanomaterials and mesoporous materials have recently become popular choices for immobilizing enzymes. These materials offer significant specific surface area, a high capacity for loading proteins, excellent dispersibility, low mass transfer restrictions.[43] These characteristics make them appealing as biocatalytic carriers for various applications in biocatalysis. More specifically, the use of a nanosized carrier results in redefining the nature of the catalytic processes as *quasi*-homogeneous that means that the reaction rates are comparable to those achieved by homogeneous catalysts and the physical properties (such as the diffusivity) lie in between colloidal and molecular domain.[44] Furthermore, the co-immobilization of distinct enzymes onto a single particle offers precise control over inter-enzyme distances and substrate channeling. This enables rapid execution of multi enzymatic cascade reactions at an inter-colloidal level, remarkably reducing the diffusion paths.[45] The colloidal stability of supported systems significantly influences the catalytic performance of immobilized enzymes. [43,46] Indeed, fast self-aggregation or precipitation processes in the reaction media can impede substrate access and induce unfavorable conformational changes, leading to a drastic reduction in biocatalytic activity.[47] These dynamics, influenced by factors like ionic force and pH values, underscore the importance of robust immobilization on nanoparticles for designing high-performance biocatalysts with enhanced stability, reduced preparation costs, and

increased reusability. Protein-nanoparticle interactions are complex and involve a dynamic interplay of polar and nonpolar mechanisms, resulting in the formation of a surface protein corona layer.[48–50] However, the use of porous nanoparticles potentially allows migration of the protein corona into their pores. [51] All these factors are to be taken into account when designing a nanoscaled supported biocatalysts.

2. Immobilization of cellulolytic enzymes

2.1. Waste-to-energy strategies: the role of lignocellulosic biowaste

Fossil fuels depletion is accelerating dramatically since currently exploited fields are expected to completely run out in 50 and 130 years for oil&gas and coal, respectively.[52] Nevertheless, predictions for global energy demand claim 28% growth in the next 25 days, reaching the impressive value of 215 billion kWh.[53] This picture paves the way to find alternatives and carbon-neutral sources of energy as soon as possible. A suitable and very easy choice is the exploitation of lignocellulosic biomass, which is the most abundant biowaste worldwide with 200 billion metric tons per year production.[54] The biomass is mainly composed of three components: cellulose, accounting for 40-60% of total, is characterized by linear chains of glucose molecules bound by β-1,4-glycosydic bonds; hemicellulose, a polymer of both pentose and hexose monosaccharides , accounting for 20-30% of the total; lignin, an aromatic polyphenolic polymer made of coniferyl, sinapyl, and p-coumaryl alcohol units, wrapping together hemicellulose and cellulose, as described in **Figure 1.6**.[55]

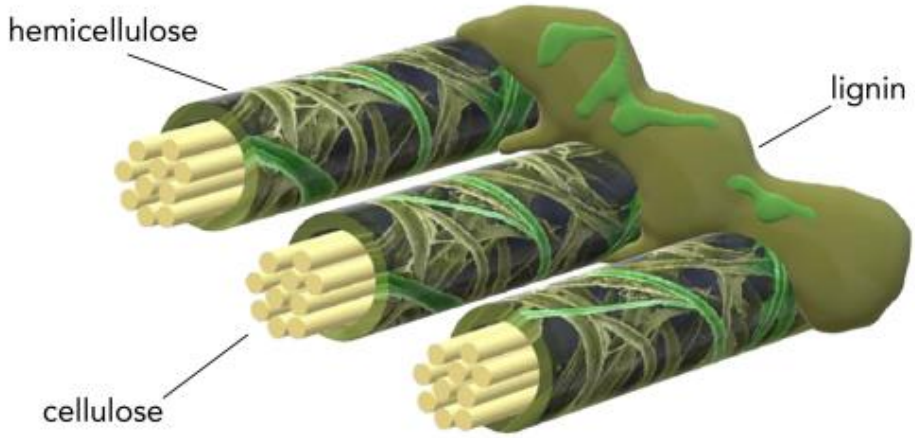

Figure 1.6. Spatial organization of cellulose, hemicellulose and lignin within vegetable biomass.

In particular, cellulose is a reservoir of soluble sugars, which can be released by hydrolysis and fermented by yeast (i.e. *Saccharomyces cerevisiae)* to obtain bioalcohols that are second-generation biofuels. However, the purity of the biofuels as well as the final yield depends on the fermentability of the biomass that means providing proper separation of the components and cellulose isolation before the hydrolysis step. This phase is known as biorefinery and, in analogy with the fractionation of the several components of crude oil on the basis of the boiling point, consists of a series of pre-treatments necessary to separate the biomass constituents.[56] Physical, thermal and chemical pre-treatments are currently used to detach lignin and hemicellulose from cellulose core. Traditional processes for hydrolysis of cellulose are usually carried out in acid conditions by means of diluted H_2SO_4 or concentrated HCl,[57,58] but the harshness of the reaction system imposes expensive corrosion-resistant reactors and accurate pre-disposal strategies. Therefore, there is a need to find new environmentally-friendly ways to hydrolyze cellulose, such as enzymatic processes.

2.1.1. Cellulase enzymes for the valorization of lignocellulosic biomass

Cellulase (EC 3.2.1.4, 4-β-D-glucan 4-glucanohydrolase) is a class of enzymes deputed to depolymerize cellulose through the hydrolysis of β-1,4-glycosidic bonds.[59] The structure of the protein comprises a catalytic domain (CD) and a carbohydrate-binding domain (CBD), linked by a flexible connector (**Figure 1.7**).

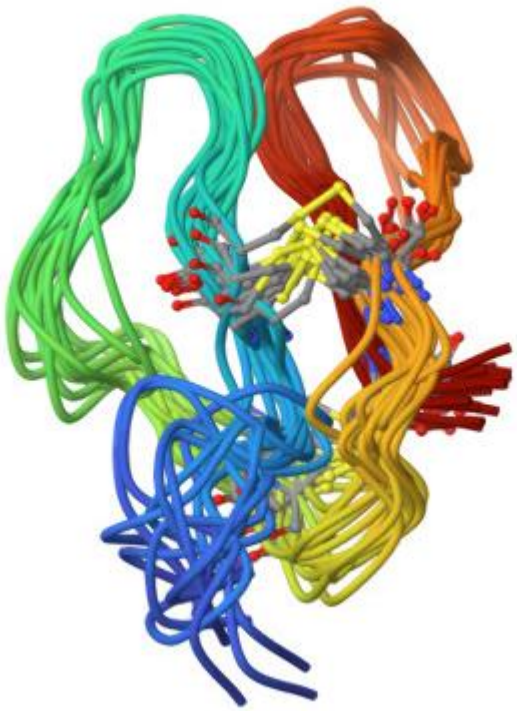

Figure 1.7. 3-D structure of CBD from *T.reesei.*[60]

The CD governs enzymatic activity, whereas the CBD aids in the binding of the enzyme to the cellulose substrate. The connector that links these domains imparts flexibility and influences the overall conformation of the cellulase.[61] It is made up of three different proteins namely endo-glucanase, exo-glucanase and β-glucosidase, that work sequentially and synergistically to break down cellulose chains. More specifically, endo-glucanase and exo-glucanase work on insoluble cellulose, generating soluble oligomers such as cellobiose and cellotriose. The hydrolysis of the β-glycosidic bond in these soluble oligosaccharides is carried out by β-glucosidase, resulting in the production of glucose.[62] Cellulase is usually produced

by microorganisms, especially filamentous fungi like *Aspergillus, Penicillium* and *Trichoderma.* The high use in both industrial (textile, paper pulping) and academic fields makes it one of the most demanded enzymes, covering 20% of global enzyme market.[63] The implementation of an enzymatic process for cellulase hydrolysis brings consistent advantages such as lower environmental impact, due to the milder reaction conditions with respect to traditional processes and the absence of toxic residues, which contribute to keep the operating costs low. However, the large scale use of the protein mixture is still far from being conventional since some challenges are to be faced. First, high glucose yields require high substrate concentrations, but this leads to massive product inhibition, especially by disaccharide cellobiose which is a severe inhibitor for both endoglucanase and exoglucanase.[64] Second, lignin exerts physical inhibition towards cellulase by sterically hindering cellulose functionalities or by leading to non-catalytic binding.[65] Therefore, accurate delignification is needed to allow cellulase to properly work. Last but not least, microorganisms do not provide adequate amounts of any single cellulase component to achieve satisfying performances. More specifically, cellulase from the widely used *Trichoderma reseii* fungus is deficient in β-glucosidase. Lack of β-glucosidase severely affects the overall reaction rate since cellobiose hydrolysis is the bottleneck of the whole reaction cascade. Therefore, it needs to be supplemented with a heterologous aliquot.[66] Finally, the high cost of production, approximately equal to 10 $/Kg (ten times higher than vegetable proteins like soy),[67] and the exigence to reduce waste to improve the circularity of the process, suggest the need to develop some strategies for reusing the catalyst in multiple operating cycles, such as immobilization.

2.1.2. Cellulase immobilization

Immobilization of cellulase usually affects several aspects related to the protein functionality. For instance, the protein microenvironment could be remarkably altered whereas conformational modifications might involve the active site. This can

positively or negatively influence substrate accessibility (due to steric hindrance) and substrate/protein interaction, resulting in higher or lower activity than free protein, respectively.[68,69] Thermal and operational stability are usually improved by immobilization since protein-matrix interaction provide enhanced structural rigidity to aminoacidic chains, improving the resistance to high temperature,[70] organic solvents,[71] pH values far from the optimal ones,[72] and inhibitors.[73] Moreover, if the immobilization strategy is able to avoid protein leakage, the reusability of the biocatalyst can be extended to multiple consecutive reaction cycles.[74] A plethora of materials can be successfully used as carriers for cellulase immobilization, both inorganic and organic. Interest in organic materials as supports for cellulase immobilization has grown significantly. These materials can be broadly categorized into two primary groups: natural polysaccharides and synthetic polymers. Natural polysaccharide carriers (chitosan,[75] alginate)[76] are generally cost-effective, non-toxic, biodegradable, and biocompatible, making them highly desirable for immobilization processes. On the other hand, synthetic polymer carriers (polyacrylonitrile,[77] polymethyl methacrylate,[78] polystyrene,[79] polysulfone)[80] exhibit diverse physical and chemical properties, providing versatility in cellulase immobilization processes. Typically, these materials offer greater stability and mechanical strength compared to natural polysaccharide carriers, making them particularly valuable in applications where durability is a critical factor. Extensive research has been conducted on the utilization of inorganic materials as supports for cellulase immobilization, attributed to their notable characteristics such as high stability, rigidity, and porosity. These materials frequently exhibit substantial surface areas, fostering robust interactions with cellulase via mechanisms such as hydrogen bonding, electrostatic interactions, or covalent bonding.[25] Common inorganic carriers employed in cellulase immobilization encompass silica,[81] magnetic nanoparticles, metal and metal oxide nanoparticles, carbon-based materials and clay minerals.[25] Covalent binding is usually adopted for binding cellulase to functionalized Fe_3O_4 magnetite nanoparticles. Indeed, magnetite is poorly stable in

aqueous solution thus functionalization helps suspensibility. Lima et al. efficiently immobilized cellulase onto PMMA-encapsulated Fe_3O_4 nanoparticles using glutaraldehyde as chemical linker. The immobilized cellulase displayed a wider range of temperature stability compared to its free form and demonstrated excellent reusability, maintaining 69% of its initial enzyme activity over eight usage cycles. The magnetic support proved to be promising for cellulase immobilization, enabling swift and convenient recovery of the biocatalyst with a single magnet.[82] High surface area and ease of functionalization make metal-oxide nanoparticles suitable carrier for cellulase immobilization. For instance, Kumar et al. immobilized both physically and covalently crude cellulase extract onto five types of nanoparticles, namely ZnO, MgO, Ag_2O, SiO_2, Fe_2O_3. The best results were obtained for cellulase bound to Fe_2O_3, which exhibited elevated immobilization efficiency ranging from 60% to 80%. The immobilized enzyme was employed in two consecutive cycles of saccharification on alkali-treated paddy straw, achieving a 55% recovery of the enzyme.[83]

2.1.3. Silica mesostructures as ideal carriers for cellulolytic enzymes

Mesoporous silica nanoparticles (MSNs) present a distinctive prospect in the realm of biocatalysis owing to their exceptional attributes. The adjustable pore size within the mesopore range enables the immobilization of substantial enzyme molecules. The expansive surface area enhances catalytic efficiency by facilitating higher enzyme loading and precise dispersion of biocatalyst molecules. The readily adjustable pore morphology provides the opportunity to establish a suitable environment for hosting enzymes. The constraining impact of mesopores can enhance enzyme stability and fortify resistance to extreme pH and temperatures. Cellulase was first adsorbed into SBA-15 with different pore size and the catalytic performance was found to depend on pore diameter.[84] Cellulase was also immobilized onto organo-functionalized MSNs to enhance hydrophobic interaction between protein and matrix. Vinyl functionalized MSNs created an optimal

microenvironment for cellulase activity, while amino-functionalization caused a decrease in carboxymethylcellulose (CMC) hydrolysis rate due to the involvement of carboxyl groups enzyme active sites in amide bond formation with the support.[85] Covalent immobilization was effectively carried out onto aminated silica mesocellular foams, resulting in a supported biocatalyst exerting higher activity than soluble enzyme and good reusability due to the stabilization of protein conformation by weak interactions. Chemical coupling was accomplished thanks to glutaraldehyde. Glutaraldehyde is ad effective linker for amine-functionalized silica. Indeed, it exhibits two carbonyl groups, one binding amine groups of the support and the other binding ε-amino groups of lysine residues, preserving the enzyme catalytic sites.[86] Recently, I and my research group have successfully immobilized cellulase into WSNs (**Figure 1.8 A, B**). The obtained biocatalyst was tested in the hydrolysis of CMC and exhibited high glucose production and reusability.

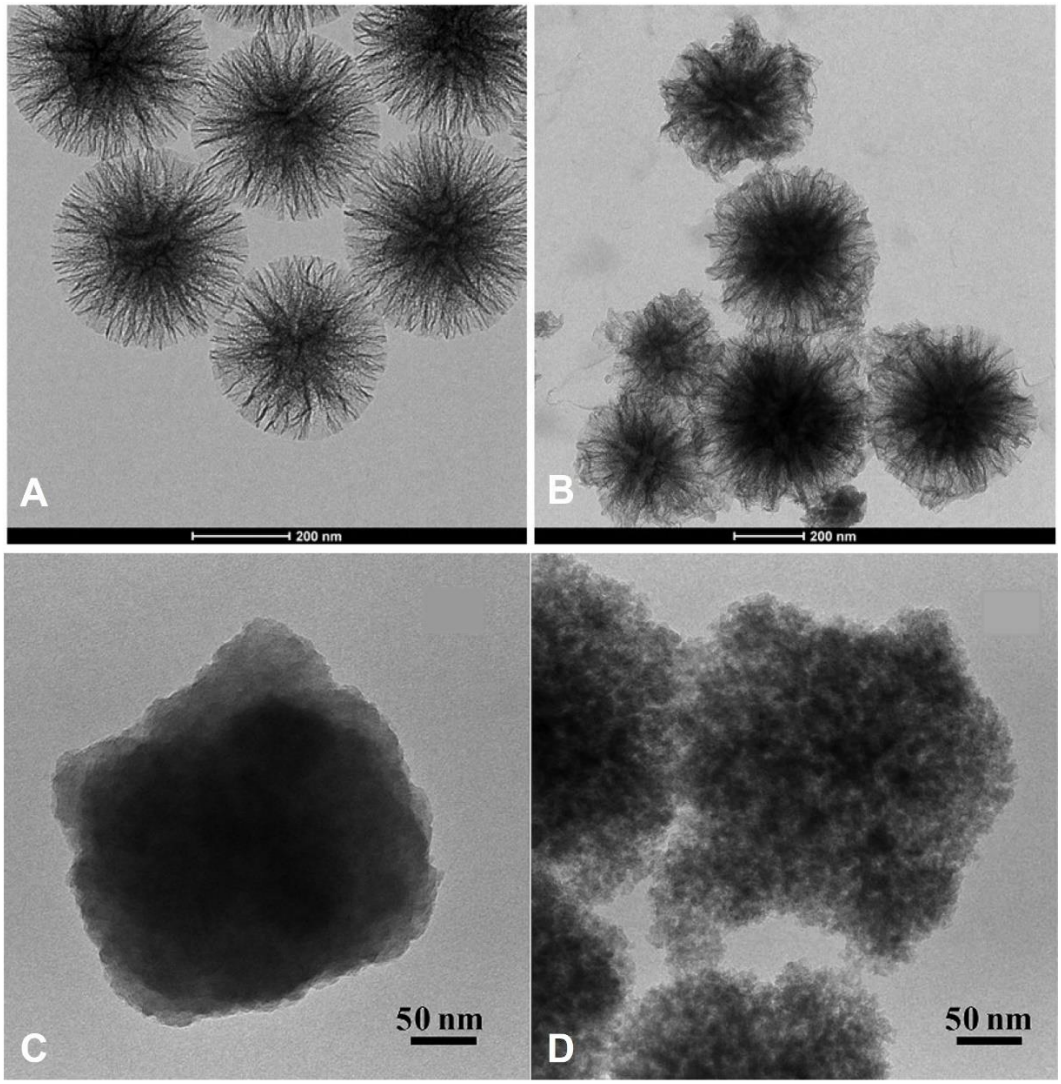

Figure 1.8. TEM images of bare (A) and cellulase-loaded WSNs (B).[74] Novel MSNs obtained with tannic acid as surfactant (C) an loaded with β-glucosidase (D).[87]

The synthesis of the support was modified to obtain a higher inter-wrinkle distance in order to properly host a bulky enzyme as cellulase.[74] Immobilization of β-glucosidase is critical for the enzyme recovery since it is not adsorbable onto cellulose surface. BG was first physically immobilized into SBA-15 in acidic medium to maximize the differences in terms of surface potential between enzyme and support. Immobilized enzyme retained 95% activity if compared to free BG

since the protein settled at the pore entrance, making cellobiose diffusion path shorter.[88] Covalent immobilization of BG into aminated micro-sized aggregates was accomplished through glutaraldehyde activation. 29 nm pores led to high values for enzyme loading, 2-fold the one obtained by physical immobilization onto the same support.[90] MSNs obtained with green surfactant tannic acid worked as optimal support for BG (**Figure 1.8 C, D**). A proper tuning of pore size resulted in a high performing biocatalyst, able to reach 100% cellobiose conversion in 24 h.[87] However, the analysis of kinetic parameters revealed the occurrence of diffusive limitations caused by pore blocking (crowding effect). This problem was overcome replacing MSNs with WSNs.[91] Radial porosity allowed for proper filling of the inner core of the NPs, avoiding pore entrance to be blocked and maximizing both cellobiose and glucose diffusion.[92] As previously stated, single-microorganism cellulase cocktail is often scarce in terms of BG and this make integration with supplementary BG a mandatory strategy to avoid cellobiose inhibition and increase the overall yield in glucose. A suitable strategy to improve the catalytic performance of immobilized cellulolytic enzymes is the co-immobilization of BG and cellulase. Several attempts were done to attach this multienzyme system onto different matrices, such as polyurethane foams,[93] pH-responsive copolymers,[94] and polymer brushes through one-pot or sequential immobilization. [95] However, literature lacks similar examples about immobilization onto silica-based supports.

3. Immobilization of lipases

3.1. Lipase as multifunctional powerful biocatalyst

3.1.1. The role of lipase in biodiesel production

Diesel is the most burned fuel in the world, with a 29.0% share, defeating gasoline by 5%. Even if its use is being reduced in the Western world (especially in the European Union), the economic growth of developing countries has led diesel consumption to globally increase of 2.6%, according to estimates by the Energy

Institute for 2023.[96] However, as mentioned in the paragraph dedicated to lignocellulosic biomass, the ecological transition imposes the need to reduce fossil fuel consumption and valorizing carbon contained in food waste perfectly fits this purpose. A suitable example is waste cooking oil (WCO), whose global production is estimated to be approximately 15 million tons, with the European Union (EU) close to 1 million tons per year.[97] One of the best strategies to give new life to WCO can be a the use as substrate for biodiesel production. Indeed, as a mixture of fatty acids alkyl esters (FAAE), biodiesel is biodegradable, less toxic than traditional diesel and its closed carbon cycle does not contribute to global warming. Moreover, the high oxygen content and the absence of sulfur result in cleaner combustion.[98] It can be produced from the transesterification of vegetable oils and thus of WCO with short-chain alkyl alcohols. Lipases (E.C. 3.1.1.3, triacylglycerol acyl hydrolases) represent environmentally friendly biocatalysts highly favored in transesterification processes when compared to chemical catalysts. This preference stems from their diverse substrate specificity, the requirement for fewer reaction conditions, reduced energy consumption, generation of purer products, and the ease of recovering biodiesel and glycerol. Additionally, lipases are known for their ecological compatibility and compatibility with a wide range of feedstock oils, particularly those abundant in free fatty acids (FFA), such as WCO.[99] Indeed, FFA can be esterified into FAAE by the enzyme.[100]

3.1.2. Lipase as biocatalyst in organic synthesis

In the last 40 years, environmental needs have led the chemical industry to evolve into a more sustainable way, preventing the generation of toxic waste. In this context, flow biocatalysis gained weight thanks to the easier scalability, higher productivity which are consequences of enhanced mass transfer, better control of the reaction parameters.[101] Moreover, the use of plug flow reactors avoids harsh mixing and makes the reusability of the biocatalyst easier. The pioneering work by Zaks and Klibanov assessing the stability of lipase in organic solvents paved the way for the

use of lipase in organic synthesis.[102] More specifically, lipase-catalyzed self-condensation has become a suitable strategy to produce poly-hydroxy alkanoates (PAHs) with tailor-made structures and properties, thanks to higher enantio-, chemo- and regio-selectivity associated with metal-free residues if compared to metal catalyst and few by-products.[103] Otherwise, Lipase-catalyzed hydrolysis of bioavailable substrates as β-keto esters can lead to enantiopure β-hydroxy acids, valuable intermediates of various active pharmaceutical ingredients and bioactive natural products.[104] More specifically, 3-hydroxybutyric acid (3HBA) is an essential metabolite in the catabolism of fatty acids, exhibiting antimicrobial and antiviral activity, as well as insecticidal properties.[105] Moreover, it can be used as monomers for the synthesis of poly hydroxybutyrate (PHB), a biocompatible and biodegradable polymer obtained from the condensation of β-hydroxy acids or their ester derivatives and exhibits similar mechanical properties as PET but higher hydrophobicity and oxygen barrier effects.[106]

3.2. Lipase immobilization

3.2.1. Interfacial adsorption onto hydrophobic supports

(from G. Fernandez-Lorente et al. "Immobilization of lipases by adsorption on hydrophobic supports")[107]

Differently from cellulase, lipases exhibit a very complex catalytic mechanism, which involves partial reorganization of the enzyme conformation. More specifically, when dissolved in aqueous solution the active site of the protein is usually covered by a peptide chain termed lid, characterized by several hydrophobic aminoacidic residues in its internal face. The lid usually shields the active sites of the protein from the polar and hydrophilic environment of the solvent. The closed-lid conformation is usually in equilibrium with the open-lid (and active) conformation, if hydrogen bonds or ionic interaction allow lid stabilization. Furthermore, lipases tend to form dimers in aqueous solution through the interaction of the active centers of two molecules in the open form, which are in equilibrium

with the monomer.[108,109] However, in the presence of oil drops (which are the natural substrates for the proteins), hydrophobic interactions between the internal face of the lid and the surface of the substrate occur, providing the active site with substrate accessibility (**Figure 1.9**).

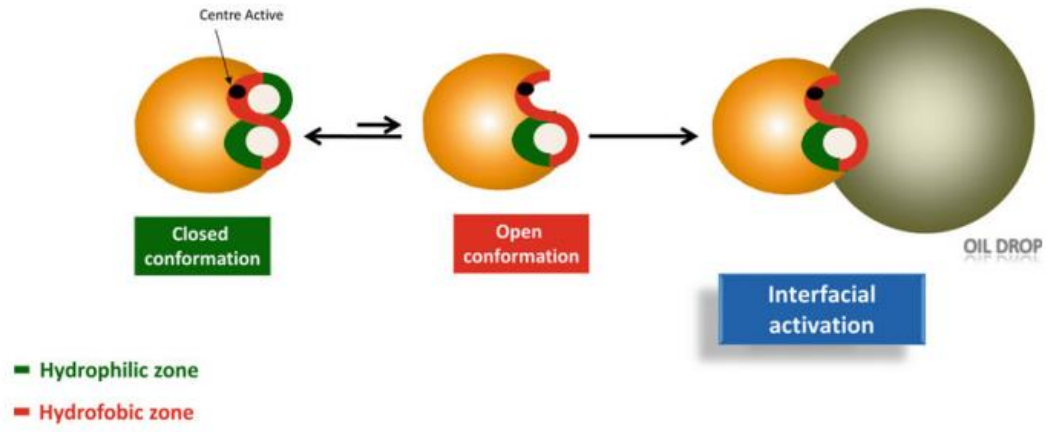

Figure 1.9. Mechanism of interfacial activation.[107]

The strength of this mechanism, known as interfacial activation, depends on the nature of the lipase, whether or not it has a large lid surface. For instance, the lid in lipase from *Candida antarctica* B is very small and does not isolate completely the active site, whereas even a remarkably complex double lid is typical *Geobacillus thermocatenulatus* lipase.[110] The dynamics of interfacial activation can be stimulated by immobilizing the enzyme onto hydrophobic supports (**Figure 1.10**).

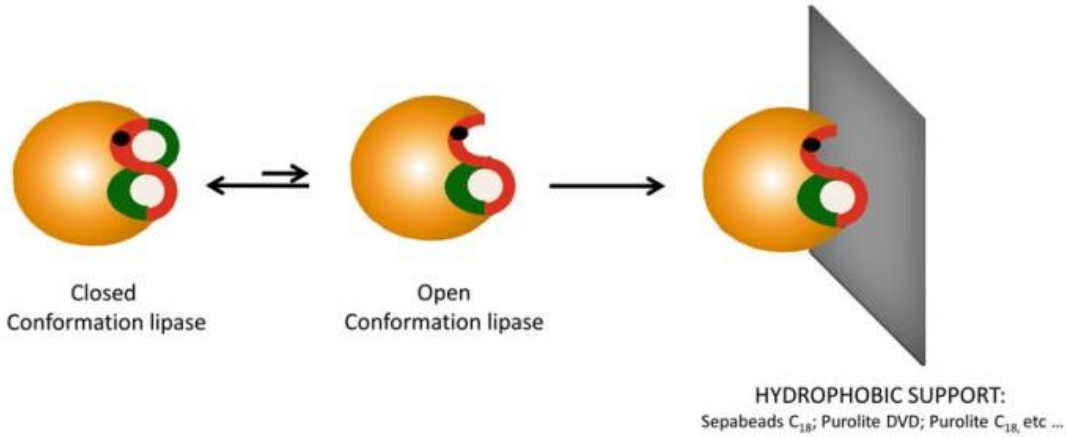

Figure 1.10. Immobilization on hydrophobic supports via interfacial activation.[107]

This one-stage simple immobilization strategy allows to easily adsorb the protein in its active form, resulting in hyperactivation and, frequently, higher stability and enantioselectivity with respect to soluble lipases. Another important advantage of interfacial adsorption on hydrophobic supports is the gain in stability towards organic solvents, which makes lipase a powerful catalyst for chemical synthesis.

3.2.2. Carriers for lipase immobilization

As previously introduced, lipase immobilization is usually performed through interfacial adsorption onto hydrophobic supports. Several carriers are usually employed, characterized by different chemical and morphological features. Zeolite-imidazole metal-organic framework (ZIF-8) was effectively employed as a carrier to immobilize *Burkholderia cepacia* lipase (BCL). The immobilized lipase demonstrated an impressive activity recovery of 1279%, marking a 12-fold enhancement compared to its free form. In the transesterification process for biodiesel production, BCL-ZIF-8 served as a biocatalyst and achieved a high yield of 93.4%, proved to be perfectly reusable up to eight consecutive cycles.[111] Highly porous inorganic carriers are frequently chosen since they are easily produced from cheap precursors and both chemical and morphological features can be finely tuned. A hydrophobic type Y zeolite, employed as a substrate for immobilizing *Candida*

cylindracea lipase, maintained its catalytic activity over the course of seven cycles in the hydrolysis of palm oil.[112] Hierarchical porosity is the fundamental feature of activated carbon. The high protein loading capacity, together with the reduced mass transfer limitations due to easy substrate/product diffusion, makes it a suitable support for protein immobilization. Indeed, CALB lipase was immobilized on both activated carbon powder and cloth for the transesterification of palm oil. As expected, higher yields in biodiesel were achieved as the protein was immobilized onto the granular carbon.[113] Magnetite (Fe_3O_4) nanoparticles possesses a surface that can be chemically modified, offering a substantial enzyme loading capacity, a large specific surface area, minimal mass transfer resistance, high binding capacity, and excellent reusability. Moreover, separability can be easily achieved by imposing and external magnetic field. Chemical coupling with proteins can be pursued in different ways such as grafting with glutaraldehyde and carbodiimides, after functionalization with amino or carboxyl groups. For instance, the chemistry of N-(3-dimethylaminopropyl)-N-ethylcarbodiimide (EDC) and N-hydroxysuccinimide (NHS) was used to covalently bind *Candida rugosa* lipase (CRL) on Fe_3O_4-chitosan and *Thermomyces lanuginosus* lipase (TRL) on APTES-Fe_3O_4.[114,115] Macroporous resins repeatedly prove to be effective carriers for the immobilization of lipases. To enhance both the activity and operational stability of *Yarrowia lipolytica* lipase LIP2 (YlLIP2), an immobilization strategy was implemented, employing macroporous resins as the carrier. Among the various supports tested, cation-exchange resin D152H proved to be the most effective. Under optimized conditions, the immobilization efficiency reached 89.81%, and the specific activity was measured at 809.751 U/g. This specific activity was 2.1 times higher compared to the free lipase.[116] Natural polymers like chitin, cellulose, chitosan or agarose are successfully used as enzyme carriers. In particular, agarose beads bearing hydrophobic functionalities were employed as supports for multi-enzyme co-immobilization. More specifically, Arana-Peña et al. carried out sequential coimmobilization on octyl-glyoxyl (OCGLX) agarose of CALB, RML and phospholipase lecitase ultra

(LEU) through both covalent bond and interfacial activation, proving the possibility to selectively reuse the most stable of the three proteins (CALB) after the inactivation of the others.[117] Poly-acrylic resins are among the most used supports due to the number of advantages the bring to the supported biocatalyst. Indeed, they are very rigid, exhibit heterogeneous pore distribution, and different hydrophobic moieties (octadecyl, divinyl benzene) do not swell in water and do not shrink in organic solvents or after drying. As a matter of fact, the most used commercial enzyme known as Novozyme 435 is obtained by adsorption of CALB on Lewatit VP OC 1600, a macroporous resin formed by poly(methyl methacrylate) crosslinked with divinylbenzene.[118]

3.2.3. Immobilization of lipase onto mesoporous silica nanoparticles

Silica, when employed as a carrier, provides robust mechanical strength, excellent resistance to organic solvents, and thermal stability. Various mesoporous silica materials, including MCM-41 and SBA-15, find widespread application in enzyme immobilization. Pore-structured materials are recognized for their versatility in diverse applications, particularly in catalysis. However, achieving control over homogeneity and pore size during their synthesis remains a challenge, especially in the mesoporous size range of 10–50 nm. Larger pore sizes have the capability to accommodate relatively large entities such as protein molecules, including enzymes, facilitating their diffusion through the porous medium. Silica-based supports need to be hydrophobized to favor lipase immobilization in the open form and avoid accumulation of glycerol in the biocatalyst's active sites.[119] Lipase immobilized into bare SBA-15 succeeded in convert oils into biodiesel but experienced a huge loss in activity after one reuse cycle.[120] Functionalization with octadecyl groups led to complete retention of activity with respect to free enzyme and 93% retention after 5 reuse cycles.[121] Adequate tuning of alkyl chain length and enzyme loading allowed for successful implementation in continuous flow reactors. MSNs hydrophobized with trimethoxysilane and enzyme loading of 100 mg/g of support did not experience

pore blocking, leading to a 1.14-fold hyperactivation of the protein if compared to free enzyme. 99% and 64% biodiesel production were reached at the beginning and after 24 h, respectively.[122] Covalent immobilization is the most used method to attach lipase onto silica since it prevents the protein to leak from the support even if the enzyme activity is often undermined. Lipase immobilization onto epoxy-functionalized MSNs was reported as successful for vegetable oil transesterification. More specifically, lipase covalently attached onto epoxy-grafted SBA-15 experienced the highest activity and reusability if compared to other immobilization strategies.[123]

References

(1) Guisan, J. M.; López-Gallego, F.; Bolivar, J. M.; Rocha-Martín, J.; Fernandez-Lorente, G. The Science of Enzyme Immobilization. *Immobilization of Enzymes and Cells: Methods and Protocols* **2020**, 1–26.

(2) Maghraby, Y. R.; El-Shabasy, R. M.; Ibrahim, A. H.; Azzazy, H. M. E.-S. Enzyme Immobilization Technologies and Industrial Applications. *ACS Omega* **2023**, *8* (6), 5184–5196.

(3) Chaplin, M. F.; Bucke, C. *Enzyme Technology*; CUP Archive, 1990.

(4) Hanefeld, U.; Gardossi, L.; Magner, E. Understanding Enzyme Immobilisation. *Chem Soc Rev* **2009**, *38* (2), 453–468. https://doi.org/10.1039/b711564b.

(5) Czeslik, C.; Jackler, G.; Royer, C. *Driving Forces for the Adsorption of Enzymes at the Water/Silica Interface Studied by Total Internal Reflection Fluorescence Spectroscopy and Optical Reflectometry*; IOS Press, 2002; Vol. 16.

(6) Gitlesen, T.; Bauer, M.; Adlercreutz, P. Adsorption of Lipase on Polypropylene Powder. *Biochimica et Biophysica Acta (BBA)-Lipids and Lipid Metabolism* **1997**, *1345* (2), 188–196.

(7) Persson, M.; Wehtje, E.; Adlercreutz, P. Factors Governing the Activity of Lyophilised and Immobilised Lipase Preparations in Organic Solvents. *ChemBioChem* **2002**, *3* (6), 566–571.

(8) Salis, A.; Sanjust, E.; Solinas, V.; Monduzzi, M. Commercial Lipase Immobilization on Accurel MP 1004 Porous Polypropylene. *Biocatal Biotransformation* **2005**, *23* (5), 381–386.

(9) Vescovi, V.; dos Santos, J. B. C.; Tardioli, P. W. Porcine Pancreatic Lipase Hydrophobically Adsorbed on Octyl-Silica: A Robust Biocatalyst for Syntheses of Xylose Fatty Acid Esters. *Biocatal Biotransformation* **2017**, *35* (4), 298–305.

(10) Salis, A.; Sanjust, E.; Solinas, V.; Monduzzi, M. Characterisation of Accurel MP1004 Polypropylene Powder and Its Use as a Support for Lipase Immobilisation. *J Mol Catal B Enzym* **2003**, *24*, 75–82.

(11) Arana-Peña, S.; Mendez-Sanchez, C.; Rios, N. S.; Ortiz, C.; Gonçalves, L. R. B.; Fernandez-Lafuente, R. New Applications of Glyoxyl-Octyl Agarose in Lipases Co-Immobilization: Strategies to Reuse the Most Stable Lipase. *Int J Biol Macromol* **2019**, *131*, 989–997.

(12) Arana-Peña, S.; Lokha, Y.; Fernández-Lafuente, R. Immobilization of Eversa Lipase on Octyl Agarose Beads and Preliminary Characterization of Stability and Activity Features. *Catalysts* **2018**, *8* (11), 511.

(13) Verger, R. 'Interfacial Activation'of Lipases: Facts and Artifacts. *Trends Biotechnol* **1997**, *15* (1), 32–38.

(14) Liu, Y.; Chen, J. Y. Enzyme Immobilization on Cellulose Matrixes. *J Bioact Compat Polym* **2016**, *31* (6), 553–567.

(15) An, N.; Zhou, C. H.; Zhuang, X. Y.; Tong, D. S.; Yu, W. H. Immobilization of Enzymes on Clay Minerals for Biocatalysts and Biosensors. *Appl Clay Sci* **2015**, *114*, 283–296.

(16) Popat, A.; Hartono, S. B.; Stahr, F.; Liu, J.; Qiao, S. Z.; Lu, G. Q. M. Mesoporous Silica Nanoparticles for Bioadsorption, Enzyme Immobilisation, and Delivery Carriers. *Nanoscale* **2011**, *3* (7), 2801–2818.

(17) Koszelewski, D.; Müller, N.; Schrittwieser, J. H.; Faber, K.; Kroutil, W. Immobilization of ω-Transaminases by Encapsulation in a Sol–Gel/Celite Matrix. *J Mol Catal B Enzym* **2010**, *63* (1–2), 39–44.

(18) Copeland, R. A. *Enzymes: A Practical Introduction to Structure, Mechanism, and Data Analysis*; John Wiley & Sons, 2023.

(19) Yiu, H. H. P.; Wright, P. A. Enzymes Supported on Ordered Mesoporous Solids: A Special Case of an Inorganic-Organic Hybrid. *J Mater Chem* **2005**, *15* (35–36), 3690–3700. https://doi.org/10.1039/b506090g.

(20) Virgen-Ortíz, J. J.; Dos Santos, J. C. S.; Berenguer-Murcia, Á.; Barbosa, O.; Rodrigues, R. C.; Fernandez-Lafuente, R. Polyethylenimine: A Very Useful Ionic Polymer in the Design of Immobilized Enzyme Biocatalysts. *Journal of Materials Chemistry B*. Royal Society of Chemistry 2017, pp 7461–7490. https://doi.org/10.1039/c7tb01639e.

(21) Takara Bio Blog Team. *Takarabio.com*. When your his-tagged constructs don't bind—troubleshooting your protein purification woes.

(22) Andrés-Sanz, D.; Diamanti, E.; Di Silvo, D.; Gurauskis, J.; López-Gallego, F. Selective Coimmobilization of His-Tagged Enzymes on Yttrium-Stabilized Zirconia-Based Membranes for Continuous Asymmetric Bioreductions. *ACS Appl Mater Interfaces* **2022**, *14* (3), 4285–4296.

(23) Popat, A.; Hartono, S. B.; Stahr, F.; Liu, J.; Qiao, S. Z.; Lu, G. Q. M. Mesoporous Silica Nanoparticles for Bioadsorption, Enzyme Immobilisation, and Delivery Carriers. *Nanoscale* **2011**, *3* (7), 2801–2818.

(24) Mateo, C.; Palomo, J. M.; Fernandez-Lorente, G.; Guisan, J. M.; Fernandez-Lafuente, R. Improvement of Enzyme Activity, Stability and

Selectivity via Immobilization Techniques. *Enzyme and Microbial Technology*. May 2, 2007, pp 1451–1463. https://doi.org/10.1016/j.enzmictec.2007.01.018.

(25) Zucca, P.; Sanjust, E. Inorganic Materials as Supports for Covalent Enzyme Immobilization: Methods and Mechanisms. *Molecules*. MDPI AG September 9, 2014, pp 14139–14194. https://doi.org/10.3390/molecules190914139.

(26) Fernandez-Lafuente, R.; Rosell, C. M.; Rodríguez, V.; Santana, C.; Soler, G.; Bastida, A.; Guisán, J. M. Preparation of Activated Supports Containing Low PK Amino Groups. A New Tool for Protein Immobilization via the Carboxyl Coupling Method. *Enzyme Microb Technol* **1993**, *15* (7), 546–550.

(27) Boller, T.; Meier, C.; Menzler, S. EUPERGIT Oxirane Acrylic Beads: How to Make Enzymes Fit for Biocatalysis. *Org Process Res Dev* **2002**, *6* (4), 509–519.

(28) Rodrigues, R. C.; Ortiz, C.; Berenguer-Murcia, Á.; Torres, R.; Fernández-Lafuente, R. Modifying Enzyme Activity and Selectivity by Immobilization. *Chem Soc Rev* **2013**, *42* (15), 6290–6307.

(29) Caruso, F.; Trau, D.; Möhwald, H.; Renneberg, R. Enzyme Encapsulation in Layer-by-Layer Engineered Polymer Multilayer Capsules. *Langmuir* **2000**, *16* (4), 1485–1488.

(30) Walde, P.; Ichikawa, S. Enzymes inside Lipid Vesicles: Preparation, Reactivity and Applications. *Biomol Eng* **2001**, *18* (4), 143–177.

(31) Wang, Y.; Caruso, F. Enzyme Encapsulation in Nanoporous Silica Spheres. *Chemical communications* **2004**, No. 13, 1528–1529.

(32) Livage, J.; Coradin, T.; Roux, C. Encapsulation of Biomolecules in Silica Gels. *Journal of Physics: Condensed Matter* **2001**, *13* (33), R673.

(33) Sheldon, R. A. Cross-Linked Enzyme Aggregates (CLEA® s): Stable and Recyclable Biocatalysts. *Biochem Soc Trans* **2007**, *35* (6), 1583–1587.

(34) Velasco-Lozano, S. Immobilization of Enzymes as Cross-Linked Enzyme Aggregates: General Strategy to Obtain Robust Biocatalysts. *Methods in Molecular Biology* **2020**, *2100*, 345–361. https://doi.org/10.1007/978-1-0716-0215-7_23/COVER.

(35) Sheldon, R. A. Cross-Linked Enzyme Aggregates as Industrial Biocatalysts. *Org Process Res Dev* **2011**, *15* (1), 213–223. https://doi.org/10.1021/op100289f.

(36) Caballero Valdés, E.; Wilson Soto, L.; Aroca Arcaya, G. Influence of the PH of Glutaraldehyde and the Use of Dextran Aldehyde on the Preparation of Cross-Linked Enzyme Aggregates (CLEAs) of Lipase from Burkholderia Cepacia. *Electronic Journal of Biotechnology* **2011**, *14* (3), 10.

(37) Miletić, N.; Loos, K. Over-Stabilization of Chemically Modified and Cross-Linked Candida Antarctica Lipase B Using Various Epoxides and Diepoxides. *Aust J Chem* **2009**, *62* (8), 799–805.

(38) Wang, A.; Zhang, F.; Chen, F.; Wang, M.; Li, H.; Zeng, Z.; Xie, T.; Chen, Z. A Facile Technique to Prepare Cross-Linked Enzyme Aggregates Using p-Benzoquinone as Cross-Linking Agent. *Korean Journal of Chemical Engineering* **2011**, *28*, 1090–1095.

(39) Ayhan, H.; Ayhan, F.; Gülsu, A. Highly Biocompatible Enzyme Aggregates Crosslinked by L-Lysine. *Turk. J. Biochem* **2012**, *37* (1), 14–20.

(40) Talekar, S.; Nadar, S.; Joshi, A.; Joshi, G. Pectin Cross-Linked Enzyme Aggregates (Pectin-CLEAs) of Glucoamylase. *RSC Adv* **2014**, *4* (103), 59444–59453.

(41) Velasco-Lozano, S.; López-Gallego, F.; Mateos-Díaz, J. C.; Favela-Torres, E. Cross-Linked Enzyme Aggregates (CLEA) in Enzyme Improvement – a Review. *Biocatalysis* **2016**, *1* (1). https://doi.org/10.1515/boca-2015-0012.

(42) Illanes, A.; Wilson, L. Parameters for the Evaluation of Immobilized Enzymes Under Process Conditions. In *Methods in Molecular Biology*; Humana Press Inc., 2020; Vol. 2100, pp 65–81. https://doi.org/10.1007/978-1-0716-0215-7_3.

(43) Abu-Reziq, R.; Alper, H. Magnetically Separable Base Catalysts: Heterogeneous Catalysis vs. Quasi-Homogeneous Catalysis. *Applied Sciences* **2012**, *2* (2), 260–276.

(44) Kreuzer, L. P.; Männel, M. J.; Schubert, J.; Höller, R. P. M.; Chanana, M. Enzymatic Catalysis at Nanoscale: Enzyme-Coated Nanoparticles as Colloidal Biocatalysts for Polymerization Reactions. *ACS Omega* **2017**, *2* (10), 7305–7312.

(45) Männel, M. J.; Kreuzer, L. P.; Goldhahn, C.; Schubert, J.; Hartl, M. J.; Chanana, M. Catalytically Active Protein Coatings: Toward Enzymatic Cascade Reactions at the Intercolloidal Level. *ACS Catal* **2017**, *7* (3), 1664–1672. https://doi.org/10.1021/acscatal.6b03072.

(46) Männel, M. J.; Kreuzer, L. P.; Goldhahn, C.; Schubert, J.; Hartl, M. J.; Chanana, M. Catalytically Active Protein Coatings: Toward Enzymatic Cascade Reactions at the Intercolloidal Level. *ACS Catal* **2017**, *7* (3), 1664–1672.

(47) Liu, H.-L.; Chen, W.-J.; Chou, S.-N. Mechanisms of Aggregation of Alpha-and Beta-Amylases in Aqueous Dispersions. *Colloids Surf B Biointerfaces* **2003**, *28* (2–3), 215–225.

(48) Wei, Q.; Becherer, T.; Angioletti-Uberti, S.; Dzubiella, J.; Wischke, C.; Neffe, A. T.; Lendlein, A.; Ballauff, M.; Haag, R. Protein Interactions with Polymer Coatings and Biomaterials. *Angewandte Chemie International Edition* **2014**, *53* (31), 8004–8031.

(49) Lynch, I.; Dawson, K. A. Protein-Nanoparticle Interactions. *Nano Today* **2008**, *3* (1–2), 40–47. https://doi.org/10.1016/S1748-0132(08)70014-8.

(50) Camelin, E.; Romero, O.; Piumetti, M.; Ottone, C.; Illanes, A.; Fino, D. Mechanisms of Interaction among Enzymes and Supports. In *Nanomaterials for Biocatalysis*; Elsevier, 2022; pp 105–148.

(51) Diamanti, E.; Arana-Peña, S.; Ramos-Cabrer, P.; Comino, N.; Carballares, D.; Fernandez-Lafuente, R.; López-Gallego, F. Intraparticle Macromolecular Migration Alters the Structure and Function of Proteins Reversibly Immobilized on Porous Microbeads. *Adv Mater Interfaces* **2022**, 2200263.

(52) Newell, R. G.; Raimi, D.; Aldana, G. Global Energy Outlook 2019: The Next Generation of Energy. **2019**.

(53) International Energy Outlook 2017. **2017**.

(54) Ahmad, E.; Khan, T. S.; Alam, M. I.; Pant, K. K.; Ali Haider, M. Understanding Reaction Kinetics, Deprotonation and Solvation of Brønsted Acidic Protons in Heteropolyacid Catalyzed Synthesis of Biorenewable Alkyl Levulinates. *Chemical Engineering Journal* **2020**, *400*, 125916. https://doi.org/10.1016/J.CEJ.2020.125916.

(55) Lorenci Woiciechowski, A.; Dalmas Neto, C. J.; Porto de Souza Vandenberghe, L.; de Carvalho Neto, D. P.; Novak Sydney, A. C.; Letti, L. A. J.; Karp, S. G.; Zevallos Torres, L. A.; Soccol, C. R. Lignocellulosic Biomass: Acid and Alkaline Pretreatments and Their Effects on Biomass Recalcitrance – Conventional Processing and Recent Advances. *Bioresour*

Technol **2020**, *304*, 122848. https://doi.org/10.1016/J.BIORTECH.2020.122848.

(56) Patel, A.; Shah, A. R. Integrated Lignocellulosic Biorefinery: Gateway for Production of Second Generation Ethanol and Value Added Products. *Journal of Bioresources and Bioproducts* **2021**, *6* (2), 108–128. https://doi.org/10.1016/J.JOBAB.2021.02.001.

(57) Thompson, D. R. G. H. E. Design and Evaluation of a Plug Flow Reactor for Acid Hydrolysis of Cellulose. *Industrial & Engineering Chemistry Process Design and Development* **1979**, *18* (3).

(58) Fan, L.; Gharpuray, M. M.; Lee, Y.-H. Acid Hydrolysis of Cellulose. **1987**, 121–148. https://doi.org/10.1007/978-3-642-72575-3_4.

(59) Klein-Marcuschamer, D.; Oleskowicz-Popiel, P.; Simmons, B. A.; Blanch, H. W. The Challenge of Enzyme Cost in the Production of Lignocellulosic Biofuels. *Biotechnol Bioeng* **2012**, *109* (4), 1083–1087. https://doi.org/10.1002/BIT.24370.

(60) Mattinen, M.-L. *THREE-DIMENSIONAL STRUCTURES OF THREE ENGINEERED CELLULOSE-BINDING DOMAINS OF CELLOBIOHYDROLASE I FROM TRICHODERMA REESEI, NMR, 14 STRUCTURES*. Worldwide Protein Data Bank.

(61) Dong, C. Di; Patel, A. K.; Madhavan, A.; Chen, C. W.; Singhania, R. R. Significance of Glycans in Cellulolytic Enzymes for Lignocellulosic Biorefinery – A Review. *Bioresour Technol* **2023**, *379*, 128992. https://doi.org/10.1016/J.BIORTECH.2023.128992.

(62) Gunjikar, T. P.; Sawant, S. B.; Joshi, J. B. Shear Deactivation of Cellulase, Exoglucanase, Endoglucanase, and β-Glucosidase in a Mechanically Agitated Reactor. *Biotechnol Prog* **2001**, *17* (6), 1166–1168. https://doi.org/10.1021/BP010114U.

(63) Singh, A.; Bajar, S.; Devi, A.; Pant, D. An Overview on the Recent Developments in Fungal Cellulase Production and Their Industrial Applications. *Bioresource Technology Reports*. Elsevier Ltd June 1, 2021. https://doi.org/10.1016/j.biteb.2021.100652.

(64) Andrić, P.; Meyer, A. S.; Jensen, P. A.; Dam-Johansen, K. Reactor Design for Minimizing Product Inhibition during Enzymatic Lignocellulose Hydrolysis: I. Significance and Mechanism of Cellobiose and Glucose Inhibition on Cellulolytic Enzymes. *Biotechnol Adv* **2010**, *28* (3), 308–324. https://doi.org/10.1016/J.BIOTECHADV.2010.01.003.

(65) Vermaas, J. V.; Petridis, L.; Qi, X.; Schulz, R.; Lindner, B.; Smith, J. C. Mechanism of Lignin Inhibition of Enzymatic Biomass Deconstruction. *Biotechnol Biofuels* **2015**, *8* (1). https://doi.org/10.1186/s13068-015-0379-8.

(66) Saini, J. K.; Singhania, R. R.; Satlewal, A.; Saini, R.; Gupta, R.; Tuli, D.; Mathur, A.; Adsul, M. Improvement of Wheat Straw Hydrolysis by Cellulolytic Blends of Two Penicillium Spp. *Renew Energy* **2016**, *98*, 43–50. https://doi.org/10.1016/J.RENENE.2016.01.025.

(67) Klein-Marcuschamer, D.; Oleskowicz-Popiel, P.; Simmons, B. A.; Blanch, H. W. The Challenge of Enzyme Cost in the Production of Lignocellulosic Biofuels. *Biotechnol Bioeng* **2012**, *109* (4), 1083–1087. https://doi.org/10.1002/bit.24370.

(68) Hosseini, S. H.; Hosseini, S. A.; Zohreh, N.; Yaghoubi, M.; Pourjavadi, A. Covalent Immobilization of Cellulase Using Magnetic Poly(Ionic Liquid) Support: Improvement of the Enzyme Activity and Stability. *J Agric Food Chem* **2018**, *66* (4), 789–798. https://doi.org/10.1021/ACS.JAFC.7B03922/ASSET/IMAGES/MEDIUM/JF-2017-03922R_0012.GIF.

(69) Zhou, J. Immobilization of Cellulase on a Reversibly Soluble−Insoluble Support: Properties and Application. *J Agric Food Chem* **2010**, *58* (11), 6741–6746. https://doi.org/10.1021/jf100759c.

(70) Poorakbar, E.; Shafiee, A.; Saboury, A. A.; Rad, B. L.; Khoshnevisan, K.; Ma'mani, L.; Derakhshankhah, H.; Ganjali, M. R.; Hosseini, M. Synthesis of Magnetic Gold Mesoporous Silica Nanoparticles Core Shell for Cellulase Enzyme Immobilization: Improvement of Enzymatic Activity and Thermal Stability. *Process Biochemistry* **2018**, *71*, 92–100. https://doi.org/10.1016/J.PROCBIO.2018.05.012.

(71) Sannino, F.; Costantini, A.; Ruffo, F.; Aronne, A.; Venezia, V.; Califano, V. Covalent Immobilization of β-Glucosidase into Mesoporous Silica Nanoparticles from Anhydrous Acetone Enhances Its Catalytic Performance. *Nanomaterials* **2020**, *10* (1), 108.

(72) Wang, Y.; Chen, D.; Wang, G.; Zhao, C.; Ma, Y.; Yang, W. Immobilization of Cellulase on Styrene/Maleic Anhydride Copolymer Nanoparticles with Improved Stability against PH Changes. *Chemical Engineering Journal* **2018**, *336*, 152–159. https://doi.org/10.1016/J.CEJ.2017.11.030.

(73) Qi, B.; Luo, J.; Wan, Y. Immobilization of Cellulase on a Core-Shell Structured Metal-Organic Framework Composites: Better Inhibitors Tolerance and Easier Recycling. *Bioresour Technol* **2018**, *268*, 577–582. https://doi.org/10.1016/J.BIORTECH.2018.07.115.

(74) Costantini, A.; Venezia, V.; Pota, G.; Bifulco, A.; Califano, V.; Sannino, F. Adsorption of Cellulase on Wrinkled Silica Nanoparticles with Enhanced Inter-Wrinkle Distance. *Nanomaterials* **2020**, *10* (9), 1799. https://doi.org/10.3390/nano10091799.

(75) Verma, M. L.; Kumar, S.; Das, A.; Randhawa, J. S.; Chamundeeswari, M. Chitin and Chitosan-Based Support Materials for Enzyme Immobilization and Biotechnological Applications. *Environ Chem Lett* **2020**, *18* (2), 315–323. https://doi.org/10.1007/S10311-019-00942-5/METRICS.

(76) Andriani, D.; Sunwoo, C.; Ryu, H. W.; Prasetya, B.; Park, D. H. Immobilization of Cellulase from Newly Isolated Strain Bacillus Subtilis TD6 Using Calcium Alginate as a Support Material. *Bioprocess Biosyst Eng* **2012**, *35* (1–2), 29–33. https://doi.org/10.1007/S00449-011-0630-Z/FIGURES/8.

(77) Hung, T. C.; Fu, C. C.; Su, C. H.; Chen, J. Y.; Wu, W. T.; Lin, Y. S. Immobilization of Cellulase onto Electrospun Polyacrylonitrile (PAN) Nanofibrous Membranes and Its Application to the Reducing Sugar Production from Microalgae. *Enzyme Microb Technol* **2011**, *49* (1), 30–37. https://doi.org/10.1016/J.ENZMICTEC.2011.04.012.

(78) Ho, K. M.; Mao, X.; Gu, L.; Li, P. Facile Route to Enzyme Immobilization: Core-Shell Nanoenzyme Particles Consisting of Well-Defined Poly(Methyl Methacrylate) Cores and Cellulase Shells. *Langmuir* **2008**, *24* (19), 11036–11042. https://doi.org/10.1021/LA8016529/SUPPL_FILE/LA8016529_SI_001.PDF.

(79) Ahirwar, R.; Sharma, J. G.; Nahar, P.; Kumar, S. Immobilization Studies of Cellulase on Three Engineered Polymer Surfaces. *Biocatal Agric Biotechnol* **2017**, *11*, 248–251. https://doi.org/10.1016/J.BCAB.2017.07.014.

(80) Wei, P.; Qin Zhang, H.; Zhen Wan, Y.; Dun Liu, J.; Gang Zhang, Y. *Immobilization of Cellulase Using Polysulfone Membrane*; 2009; Vol. 21.

(81) Califano, V.; Costantini, A. Immobilization of Cellulolytic Enzymes in Mesostructured Silica Materials. *Catalysts* **2020**, *10* (6), 706.

(82) Lima, J. S.; Araú Jo, P. H. H.; Sayer, C.; Souza, A. A. U.; Viegas, A. C.; Débora De Oliveira, •. Cellulase Immobilization on Magnetic Nanoparticles Encapsulated in Polymer Nanospheres. https://doi.org/10.1007/s00449-016-1716-4.

(83) Kumar, A.; Singh, S.; Tiwari, R.; Goel, R.; Nain, L. Immobilization of Indigenous Holocellulase on Iron Oxide (Fe2O3) Nanoparticles Enhanced Hydrolysis of Alkali Pretreated Paddy Straw. *Int J Biol Macromol* **2017**, *96*, 538–549.

(84) Takimoto, A.; Shiomi, T.; Ino, K.; Tsunoda, T.; Kawai, A.; Mizukami, F.; Sakaguchi, K. Encapsulation of Cellulase with Mesoporous Silica (SBA-15). **2008**. https://doi.org/10.1016/j.micromeso.2008.05.046.

(85) Hartono, S. B.; Qiao, S. Z.; Liu, J.; Jack, K.; Ladewig, B. P.; Hao, Z.; Lu, G. Q. M. Functionalized Mesoporous Silica with Very Large Pores for Cellulase Immobilization. *The Journal of Physical Chemistry C* **2010**, *114* (18), 8353–8362.

(86) Kannan, K.; Jasra, R. V. Improved Catalytic Hydrolysis of Carboxy Methyl Cellulose Using Cellulase Immobilized on Functionalized Meso Cellular Foam. *Journal of Porous Materials* **2011**, *18* (4), 409–416.

(87) Venezia, V.; Sannino, F.; Costantini, A.; Silvestri, B.; Cimino, S.; Califano, V. Mesoporous Silica Nanoparticles for β-Glucosidase Immobilization by Templating with a Green Material: Tannic Acid. *Microporous and Mesoporous Materials* **2020**, *302*, 110203.

(88) Gómez, J. M.; Romero, M. D.; Fernández, T. M.; García, S. Immobilization and Enzymatic Activity of β-Glucosidase on Mesoporous SBA-15 Silica. *Journal of Porous Materials* **2010**, *17* (6), 657–662.

(89) Gómez, J. M.; Romero, M. D.; Fernández, T. M.; Díez, E. Immobilization of β-Glucosidase in Fixed Bed Reactor and Evaluation of the Enzymatic Activity. *Bioprocess Biosyst Eng* **2012**, *35* (8), 1399–1405.

(90) Ivetić, D. Ž.; Srdić, V. V; Antov, M. G. Immobilization of β-Glucosidase onto Mesoporous Silica Support: Physical Adsorption and Covalent Binding of Enzyme. *Journal of the Serbian Chemical Society* **2014**, *79* (5), 533–543.

(91) Califano, V.; Sannino, F.; Costantini, A.; Avossa, J.; Cimino, S.; Aronne, A. Wrinkled Silica Nanoparticles: Efficient Matrix for β-Glucosidase Immobilization. *The Journal of Physical Chemistry C* **2018**, *122* (15), 8373–8379.

(92) Califano, V.; Costantini, A.; Silvestri, B.; Venezia, V.; Cimino, S.; Sannino, F. The Effect of Pore Morphology on the Catalytic Performance of β-Glucosidase Immobilized into Mesoporous Silica. *Pure and Applied Chemistry* **2019**, *91* (10), 1583–1592.

(93) Chakrabarti, A. C.; Storey, K. B. Enhanced Glucose Production from Cellulose Using Coimmobilized Cellulase and β-Glucosidase. *Appl Biochem Biotechnol* **1989**, *22* (3), 263–278.

(94) Liu, J.; Cao, X. Biodegradation of Cellulose by β-Glucosidase and Cellulase Immobilized on a PH-Responsive Copolymer. *Biotechnology and bioprocess engineering* **2014**, *19* (5), 829–837.

(95) Wang, G.; Zhang, K.; Xin, J.-Y.; Zhao, C.-W.; Ma, Y.-H.; Yang, W.-T. Facile Construction of Synergistic β-Glucosidase and Cellulase Sequential Co-Immobilization System for Enhanced Biomass Conversion. *Chinese Journal of Polymer Science* **2020**, *38*, 1277–1285.

(96) *In Partnership with Statistical Review of World Energy 2023 | 72 Nd Edition*.

(97) Mannu, A.; Ferro, M.; Di Pietro, M. E.; Mele, A. Innovative Applications of Waste Cooking Oil as Raw Material. *Sci Prog* **2019**, *102* (2), 153–160. https://doi.org/10.1177/0036850419854252.

(98) Suzihaque, M. U. H.; Alwi, H.; Kalthum Ibrahim, U.; Abdullah, S.; Haron, N. Biodiesel Production from Waste Cooking Oil: A Brief Review. *Mater Today Proc* **2022**, *63*, S490–S495. https://doi.org/10.1016/j.matpr.2022.04.527.

(99) Hama, S.; Noda, H.; Kondo, A. How Lipase Technology Contributes to Evolution of Biodiesel Production Using Multiple Feedstocks. *Curr Opin Biotechnol* **2018**, *50*, 57–64. https://doi.org/10.1016/J.COPBIO.2017.11.001.

(100) Liang, X. Synthesis of Biodiesel from Waste Oil under Mild Conditions Using Novel Acidic Ionic Liquid Immobilization on Poly Divinylbenzene. *Energy* **2013**, *63*, 103–108.

(101) Benítez-Mateos, A. I.; Contente, M. L.; Roura Padrosa, D.; Paradisi, F. Flow Biocatalysis 101: Design, Development and Applications. *Reaction Chemistry and Engineering*. Royal Society of Chemistry April 1, 2021, pp 599–611. https://doi.org/10.1039/d0re00483a.

(102) Zaks, A.; Klibanov, A. M. Enzyme-Catalyzed Processes in Organic Solvents. *Proceedings of the National Academy of Sciences* **1985**, *82* (10), 3192–3196.

(103) Liu, Y.; Song, L.; Feng, N.; Jiang, W.; Jin, Y.; Li, X. Recent Advances in the Synthesis of Biodegradable Polyesters by Sustainable Polymerization: Lipase-Catalyzed Polymerization. *RSC Adv* **2020**, *10* (59), 36230–36240. https://doi.org/10.1039/d0ra07138b.

(104) Orrego, A. H.; Rubanu, M. G.; López, I. L.; Andrés-Sanz, D.; García-Marquina, G.; Pieslinger, G. E.; Salassa, L.; López-Gallego, F. ATP-

Independent and Cell-Free Biosynthesis of β-Hydroxy Acids Using Vinyl Esters as Smart Substrates. *Angewandte Chemie - International Edition* **2023**, *62* (13). https://doi.org/10.1002/anie.202218312.

(105) Newman, J. C.; Verdin, E. β-Hydroxybutyrate: A Signaling Metabolite. *Annu Rev Nutr* **2017**, *37*, 51–76.

(106) Gabirondo, E.; Sangroniz, A.; Etxeberria, A.; Torres-Giner, S.; Sardon, H. Poly(Hydroxy Acids) Derived from the Self-Condensation of Hydroxy Acids: From Polymerization to End-of-Life Options. *Polym Chem* **2020**, *11* (30), 4861–4874. https://doi.org/10.1039/d0py00088d.

(107) Fernandez-Lorente, G.; Rocha-Martín, J.; Guisan, J. M. Immobilization of Lipases by Adsorption on Hydrophobic Supports: Modulation of Enzyme Properties in Biotransformations in Anhydrous Media. In *Methods in Molecular Biology*; Humana Press Inc., 2020; Vol. 2100, pp 143–158. https://doi.org/10.1007/978-1-0716-0215-7_9.

(108) Palomo, J. M.; Muñoz, G.; Fernández-Lorente, G.; Mateo, C.; Fernández-Lafuente, R.; Guisán, J. M. Interfacial Adsorption of Lipases on Very Hydrophobic Support (Octadecyl–Sepabeads): Immobilization, Hyperactivation and Stabilization of the Open Form of Lipases. *Journal of Molecular Catalysis B: Enzymatic* **2002**, *19*, 279–286.

(109) Fernandez-Lafuente, R.; Armisén, P.; Sabuquillo, P.; Fernández-Lorente, G.; Guisán, J. M. Immobilization of Lipases by Selective Adsorption on Hydrophobic Supports. *Chemistry and physics of lipids* **1998**, *93* (1–2), 185–197.

(110) Rodrigues, R. C.; Fernandez-Lafuente, R. Lipase from Rhizomucor Miehei as an Industrial Biocatalyst in Chemical Process. *J Mol Catal B Enzym* **2010**, *64* (1–2), 1–22.

(111) Adnan, M.; Li, K.; Wang, J.; Xu, L.; Yan, Y. Hierarchical ZIF-8 toward Immobilizing Burkholderia Cepacia Lipase for Application in Biodiesel Preparation. *Int J Mol Sci* **2018**, *19* (5), 1424. https://doi.org/10.3390/ijms19051424.

(112) Knezevic, Z.; Mojovic, L.; Adnadjevic, B. Palm Oil Hydrolysis by Lipase from Candida Cylindracea Immobilized on Zeolite Type Y. *Enzyme Microb Technol* **1998**, *22* (4), 275–280. https://doi.org/10.1016/S0141-0229(97)00187-7.

(113) Naranjo, J. C.; Córdoba, A.; Giraldo, L.; García, V. S.; Moreno-Piraján, J. C. Lipase Supported on Granular Activated Carbon and Activated Carbon Cloth as a Catalyst in the Synthesis of Biodiesel Fuel. *J Mol Catal B Enzym* **2010**, *66* (1–2), 166–171. https://doi.org/10.1016/j.molcatb.2010.05.002.

(114) Kuo, C. H.; Liu, Y. C.; Chang, C. M. J.; Chen, J. H.; Chang, C.; Shieh, C. J. Optimum Conditions for Lipase Immobilization on Chitosan-Coated Fe 3O4 Nanoparticles. *Carbohydr Polym* **2012**, *87* (4), 2538–2545. https://doi.org/10.1016/j.carbpol.2011.11.026.

(115) Raita, M.; Arnthong, J.; Champreda, V.; Laosiripojana, N. Modification of Magnetic Nanoparticle Lipase Designs for Biodiesel Production from Palm Oil. *Fuel Processing Technology* **2015**, *134*, 189–197. https://doi.org/10.1016/j.fuproc.2015.01.032.

(116) Yan, Y.; Zhang, X.; Chen, D. Enhanced Catalysis of Yarrowia Lipolytica Lipase LIP2 Immobilized on Macroporous Resin and Its Application in Enrichment of Polyunsaturated Fatty Acids. *Bioresour Technol* **2013**, *131*, 179–187. https://doi.org/10.1016/J.BIORTECH.2012.12.092.

(117) Arana-Peña, S.; Mendez-Sanchez, C.; Rios, N. S.; Ortiz, C.; Gonçalves, L. R. B.; Fernandez-Lafuente, R. New Applications of Glyoxyl-Octyl Agarose in Lipases Co-Immobilization: Strategies to Reuse the Most

Stable Lipase. *Int J Biol Macromol* **2019**, *131*, 989–997. https://doi.org/10.1016/J.IJBIOMAC.2019.03.163.

(118) Ortiz, C.; Luján Ferreira, M.; Barbosa, O.; S dos Santos, J. C.; Rodrigues, R. C.; Berenguer-Murcia, Á.; Briand, L. E.; Fernandez-Lafuente, R. Catalysis Science & Technology MINI REVIEW Novozym 435: The "Perfect" Lipase Immobilized Biocatalyst? *Cite this: Catal. Sci. Technol* **2019**, *9*, 2380. https://doi.org/10.1039/c9cy00415g.

(119) Rodrigues, R. C.; Virgen-Ortíz, J. J.; Dos Santos, J. C. S.; Berenguer-Murcia, Á.; Alcantara, A. R.; Barbosa, O.; Ortiz, C.; Fernandez-Lafuente, R. Immobilization of Lipases on Hydrophobic Supports: Immobilization Mechanism, Advantages, Problems, and Solutions. *Biotechnology advances* **2019**, *37* (5), 746–770.

(120) Katiyar, M.; Abida, K.; Ali, A. Candida Rugosa Lipase Immobilization over SBA-15 to Prepare Solid Biocatalyst for Cotton Seed Oil Transesterification. *Materials Today: Proceedings* **2021**, *36*, 763–768.

(121) Deon, M.; Carminatti Ricardi, N.; Carvalho de Andrade, R.; Hertz, P. F.; Nicolodi, S.; Costa, T. M. H.; Bussamara, R.; Benvenutti, E. V.; de Menezes, E. W. Designing a Support for Lipase Immobilization Based On Magnetic, Hydrophobic, and Mesoporous Silica. *Langmuir* **2020**, *36* (34), 10147–10155.

(122) Kalantari, M.; Yu, M.; Liu, Y.; Huang, X.; Yu, C. Engineering Mesoporous Silica Microspheres as Hyper-Activation Supports for Continuous Enzymatic Biodiesel Production. *Materials Chemistry Frontiers* **2019**, *3* (9), 1816–1822.

(123) Babaki, M.; Yousefi, M.; Habibi, Z.; Mohammadi, M.; Yousefi, P.; Mohammadi, J.; Brask, J. Enzymatic Production of Biodiesel Using Lipases Immobilized on Silica Nanoparticles as Highly Reusable

Biocatalysts: Effect of Water, t-Butanol and Blue Silica Gel Contents. *Renewable Energy* **2016**, *91*, 196–206.

Chapter 3

Design of nanostructured carriers by sol-gel chemistry

Contents

1. The basics of sol-gel chemistry

The information reported in this paragraph are mainly contained in the works by Danks, Wright and Cushing. [1, 2, 3]

1.1. A powerful technique to produce nanomaterials

Nanomaterials are defined as solids with at least one dimension lower than 100 nm. In recent years, the growing interest in the nanoscale fed the rise of a new discipline known as nanotechnology, gathering synthesis, characterization and application of nanomaterials.[4] This enthusiasm towards nanoscaled materials is powered by the interesting properties they exhibit with respect to the corresponding bulk phases. Two are the main size effects, affecting the reactivity and the physic-chemical properties of nanomaterials: *a)* quantum confinement, mostly concerning optical and electronic properties; *b)* surface effects, determined by the high surface-to-volume ratio, which means high number of atoms exposed on the surface and thus high reactivity.[5] Nanomaterials are usually produced through either top-down (i.e. from the bulk phase) or bottom-up approaches, meaning that molecular precursors properly react with each other to build a solid. Bottom-up approaches are usually preferred to top-down ones due to higher product purity, precise control of the properties, higher energy efficiency, wide choice of molecular precursors and easy scalability. Bottom-up synthesis of nanomaterials is usually carried through wet-chemistry routes, such as coprecipitation, hydrothermal processing, solvothermal method and sol-gel chemistry.[3] More specifically, fine chemical and morphological tuning of material size, together with process advantages such as low reaction time and operating temperatures, make sol-gel strategy the most interesting among the others. It consists of the formation of colloidal suspensions (termed “sol”), which subsequently evolve into gels and solid materials, with the morphological features of the final product depending on both the nature of the precursor, the reaction conditions and the post-processing steps.

1.2. Introduction to sol-gel chemistry

A colloidal suspension is defined by IUPAC as a dispersion of particles in a medium, with particle size included in 1 nm – 1 μm interval along at least one direction. As previously mentioned, a sol is a suspension of colloidal particles subjected to Brownian motion. In the hypothesis of spherical bodies, the particles are perfectly suspended if the surface drag force $\boldsymbol{F_D}$ and the Archimedes' buoyant force $\boldsymbol{F_A}$ perfectly balance the weight force $\boldsymbol{F_W}$ of the colloid:

$$\boldsymbol{F_D + F_A + F_W = 0}$$

$$(1.1) \quad 6\pi\mu r v + \frac{4}{3}\pi r^3 \rho_m g - \frac{4}{3}\pi r^3 \rho_b g = 0$$

where r is the radius of the particle, ρ_m and ρ_b are the viscosity of the medium and of the body, respectively whereas v is the sedimentation velocity, whose expression is derived as:

$$(1.2) \quad v = \frac{2r^2(\rho_b - \rho_m)g}{9\mu}$$

So, sedimentation velocity is proportional to the square radius. Therefore, if the particle size increases from the nanoscale (10^{-9}) to the microscale (10^{-6}), the sedimentation velocity increases by six orders of magnitude. However, in a multiparticle system like a suspension the stability is strictly dependent on aggregation. Colloidal aggregation refers to the process by which colloidal particles come together to form larger clusters or aggregates. This phenomenon is influenced by various factors, such as surface tension and capillary forces, curvature effects van der Walls attraction and electrostatic forces. Assuming that a solid colloid can behave the same as a liquid droplet, the role of curvature effects is described by Kelvin equation:

$$(1.3) \quad RTln\left(\frac{p_r}{p_0}\right) = \frac{2\gamma M}{\rho r}$$

where p_r and p_0 are the pressures on a curved surface of curvature radius r and on a flat surface, respectively. γ, M and ρ are the surface tension, the molecular weight and the density of the solid. According to this equation, small particles should coalesce due to the higher pressure difference linked to the high curvature. A colloidal sol usually experiences aggregation if the van der Walls attractive forces, depending on d^{-6}, overcome the electrostatic Coulombian repulsions, proportional to d^{-1}, where d is the interparticle distance. A way to support aggregation against repulsion is to make the diffuse layer thinner, and this can be achieved by increasing the ionic strength of the solution. Gel formation is the outcome of a two-step sequence of processes: nucleation and growth. More specifically, the rate of growth of the initial nuclei determines the size of the resulting colloids and it depends on the concentration of the reactants, the medium viscosity, the inhibitory effects of impurities loaded in the particle surface. Colloids are obtained if the rate of nucleation is much higher than the rate of growth. After a gel is formed, it usually undergoes a phase of syneresis (aging), during which polycondensation reactions continue and all the solvent molecules are expelled from the gel network. Simultaneously, phase transformation and Ostwald ripening might occur. In Ostwald ripening, smaller particles tend to dissolve and redeposit onto larger particles, resulting in an overall increase in the size of the larger particles and a decrease in the size of the smaller particles. This process is driven by differences in the chemical potential of the smaller and larger particles. Ostwald ripening is more commonly associated with systems where there is a wide distribution of particle sizes and is common in crystal growth during coprecipitation synthesis. The phenomenon is accurately described by the Lifshitz-Slyozov-Wagner (LSW) theory, which is traceable back to the Gibbs-Thomson equation:

$$C_e = C_\infty e^{\frac{2\sigma V_m}{rRT}} \quad (1.4)$$

According to this relationship, the solubility C_e of a solid of radius r exponentially increases with particle size reduction. In equation 1.4, C_∞ is the solubility of a solid

with infinite size, V_m and σ are the molar volume and the surface energy, respectively. LSW theory can be developed by three principles:

i) In diffusion controlled processes, the average radius of growing particles is proportional to the cube root of time:

$$\bar{r}(t) = \sqrt[3]{Kt} \quad (1.5)$$

where K is the coarsening rate, proportional to solute diffusivity;

ii) The number of nucleated particles N decays as:

$$N(t) = \frac{0.22Q_0}{\bar{r}(t)^3} \quad (1.6)$$

where Q_0 is the value of the supersaturation concentration;

iii) The size distribution of particles $f(r,t)$ is calculated as:

$$f(r,t) = \frac{N(t)}{\bar{r}(t)} p_0(\rho_{(t)}) \quad (1.7)$$

with p_0 depending on the ratio $\rho(t) = \frac{\bar{r}}{\bar{r}(t)}$

If a solid dry gel is wanted, the process continues with drying, leading ether to a xerogel (collapse of the porous network) or an aerogel if the solvent removal is accomplished under supercritical conditions. Finally, condensation of surface M-OH groups is obtainable by calcinating the sample at high temperatures (up to 800°C). The reactivity of the precursor is a key parameter for the progress of hydrolysis and condensation reactions. It is strictly related to the chemical nature of the reactant, whether it is an alkoxide, a metal-organic precursor or a solvated metal cation. More specifically, an effective description is provided by Livage's partial-charge model. According to this theory, the partial charge δ on an atom i, is given by:

$$\delta_i = \frac{(\bar{\chi} - \chi_i^0)}{k\sqrt{\chi_i^0}} \quad (1.8)$$

where χ_i^0 is the electronegativity of the atom, k constant is equal to 1.36 and $\bar{\chi}$ is the mean electronegativity of the system.

1.3. Reaction mechanisms of silica sol-gels

Sol-gel silicates are usually produced through hydrolysis and condensation of silicon alkoxides, and the final result depends on a series of parameters such as nature and concentration of precursor and co-solvent, amount of water, pH and temperature.

1.3.1. Hydrolysis

Hydrolysis of silicon alkoxides belongs to nucleophilic substitution bimolecular reactions, known as S_N2, that involves the substitution of one nucleophile for another in a molecule, as described in the mechanism reported below:

$$Nu- + R-X \rightarrow Nu-R + X-$$

where Nu- is the nucleophile species, R-X is the alkoxide and X- is the leaving group. In this case, water is the nucleophile and the leaving group is an alcohol. This process can be catalyzed by acids or alkaline catalysts, as reported in **Scheme 1**:

Acid catalysis

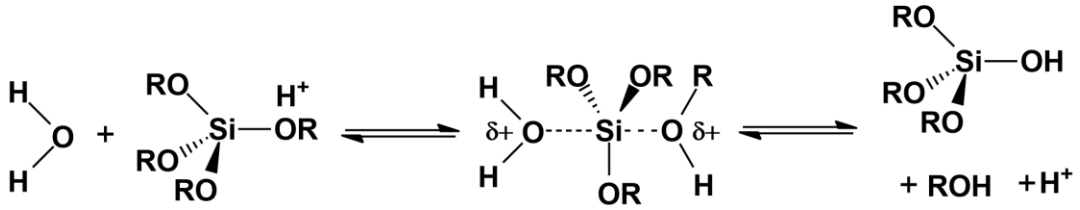

Base catalysis

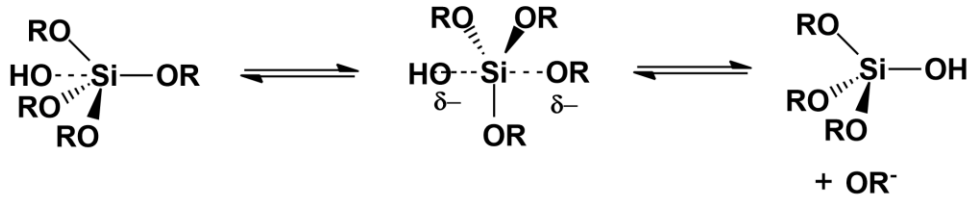

Scheme 1.1. Acid and base catalyzed hydrolysis of silicon alxoxides

In both mechanisms, a pentacoordinate transition state is formed and the number of hydrolyzed alkoxy groups is strictly dependent on the Si/H_2O molar ratio. The rate

determining step for hydrolysis is the formation of the transition state. More specifically, the more stable is the intermediate, the faster is hydrolysis. The stability of the transition state is related to the electron donating power of the silicon's substituents. In the case of acidic hydrolysis, the positive charge density on silicon increases with the number of alkyl groups replaced by hydroxyls, since -OR groups exhibit more donating power than -OH groups. Therefore, the hydrolysis rate decreases with the number of attached -OH. On the contrary, progressive alcohol expulsion and hydroxyl substitution lead to increased reaction rate in basic hydrolysis, since the negatively charged transition state isstabilized by less-donating groups. Fast hydrolysis is expected to be performed at pH values far from the isoelectric point of silica, which is at $pH \sim 2.2$. The nature of the precursor is another critical factor for the rate of hydrolysis. More specifically, steric hindrance affects the nucleophile accessibility towards the transition state, resulting in slower reactions. Indeed, the fastest-hydrolyzing alkoxide is tetramethoxy silane (TMOS) followed by tetraethoxy silane (TEOS) (**Figure 1.1**).

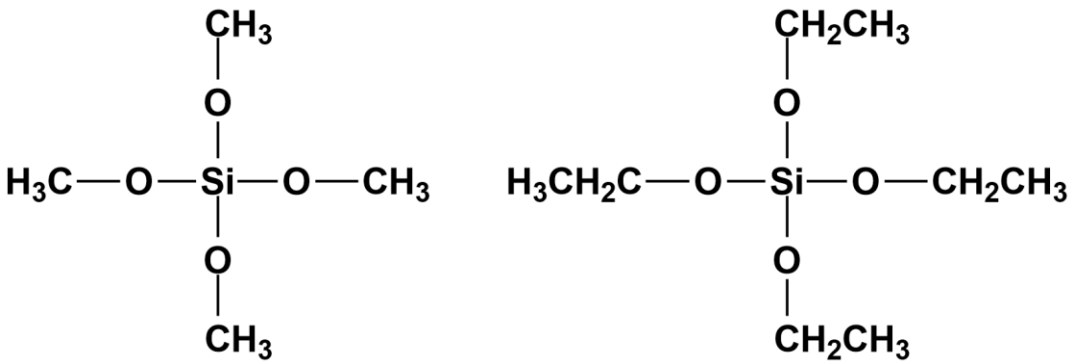

Figure 1.1. Molecular structures of TMOS (left) and TEOS (right)

Furthermore, alkoxides are rather hydrophobic. So, they require a co-solvent to be properly mixed with water and allowed to react (**Figure 1.2**). Several co-solvents are used such as alcohols, formamide, dimethylformamide (DMF), dioxane and tetrahydrofuran. It is usually preferable to use as co-solvent the same alcohol as the leaving one, in order to avoid transesterification reaction

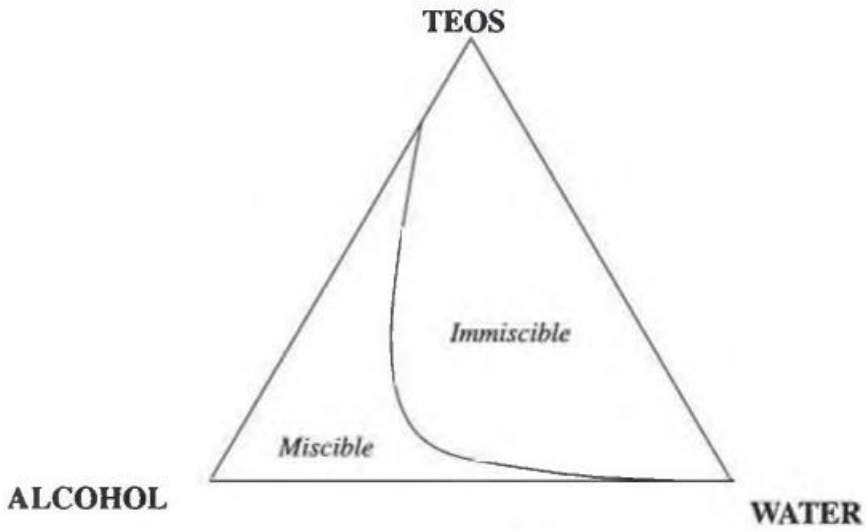

Figure 1.2. Ternary phase diagram for ethanol/TEOS/water mixtures.[6]

In detail, the hydrolysis of TEOS requires four water molecules to respect stoichiometry:

$$Si(OEt)_4 + 4H_2O \rightleftharpoons Si(OH)_4 + 4EtOH$$

However, it is possible to use $H_2O{:}TEOS \leq 4$ since hydrolysis occurs simultaneously with condensation, and water is a product of this reaction. Moreover, too high $H_2O{:}TEOS$ ratios lead to excessive dilution of the precursor, resulting in lower reaction rates. The same effect is achieved as the co-solvent concentration is increased (**Figure 1.3**).

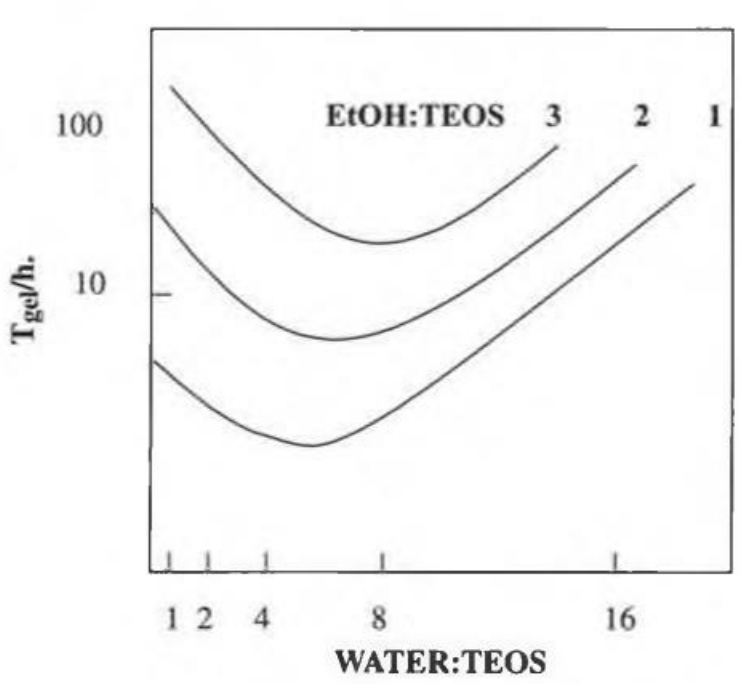

Figure 1.3. Time to gelation (T_{gel}) plotted against the $H_2O{:}TEOS$ molar ratio, parametric for $EtOH{:}TEOS$ ratio.[6]

1.3.2. (Poly)Condensation of hydrolyzed alkoxides

Condensation reactions follow hydrolysis. During condensation, the hydroxyl groups generated in the hydrolysis step react with each other, leading to the formation of bridges between the metal atoms. This process results in the elimination of water molecules, and the metal atoms become connected by oxygen bridges (reaction A). On the other hand, if the hydroxyl of one hydrolyzed alkoxide reacts with a non-completely hydrolyzed precursor, an alcohol molecule can be expelled (alcohol condensation, reaction B).

(A) $Si(OEt)_3OH + HOSi(OEt)_3 \rightleftharpoons (EtO)_3SiOSi(OEt)_3 + H_2O$

(B) $Si(OEt)_3OR + HOSi(OEt)_3 \rightleftharpoons (EtO)_3SiOSi(OEt)_3 + ROH$

Condensation can be acid or base catalyzed, just like hydrolysis (**Scheme 1.2**):

Acid catalysis

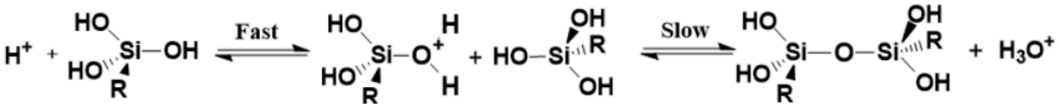

Basic catalysis

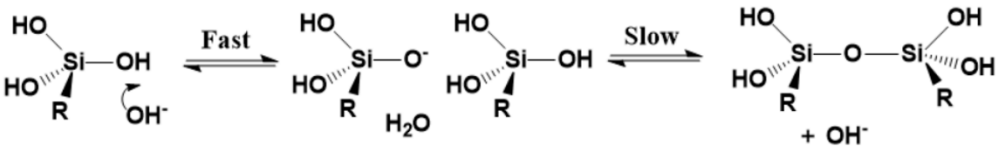

Scheme 1.2. Acidic and basic catalysis for condensation reactions

In both cases, the reaction results from a two-step series of fast proton/hydroxyl attachment, with the formation of a charged intermediate, followed by a slow nucleophilic attack of a second neutral silicon species. A siloxane Si-O-Si bond originates from the reaction. The pH of the system severely affects the morphology of the resulting gel. More specifically, in acidic conditions the first hydrolysis step is the fastest, meaning that condensation begins before hydrolysis is completed and involves terminal silanols (Si-OH), evolving into network-like gels. Differently, under alkaline conditions the hydrolysis rate grows along the process, resulting in the complete hydrolysis of the alkoxide before condensation begins. In this condition, more condensation sites are available for each silicon atom. Therefore, branched agglomerates in sols are formed, that eventually cross-link to form colloidal gels (**Figure 1.4**).

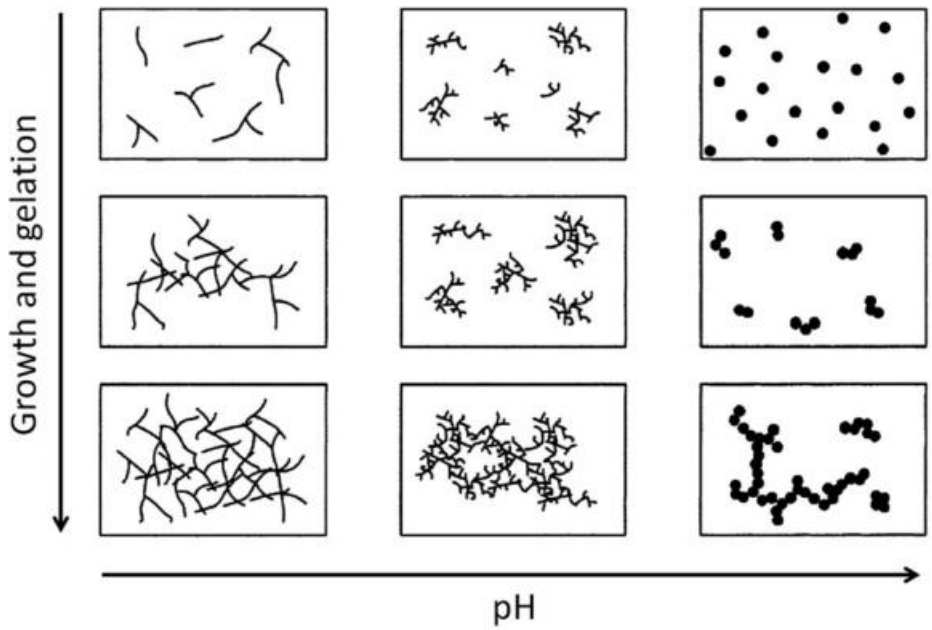

Figure 1.4. Effect of pH on the morphology of sols and corresponding gels.[3]

Although it is modeled as a series of distinct reactions, in real systems hydrolysis and condensation occur simultaneously, which makes the development of a comprehensive kinetics impossible.

1.3.3. Gelation

The term gelation refers to the extended cross-linking occurring between sol particles, associated with a massive increase in viscosity. Afterwards, further cross-linking and inclusion of last-standing sol particles in the gel matrix lead to an increase in elasticity, as shown in **Figure 1.5**.

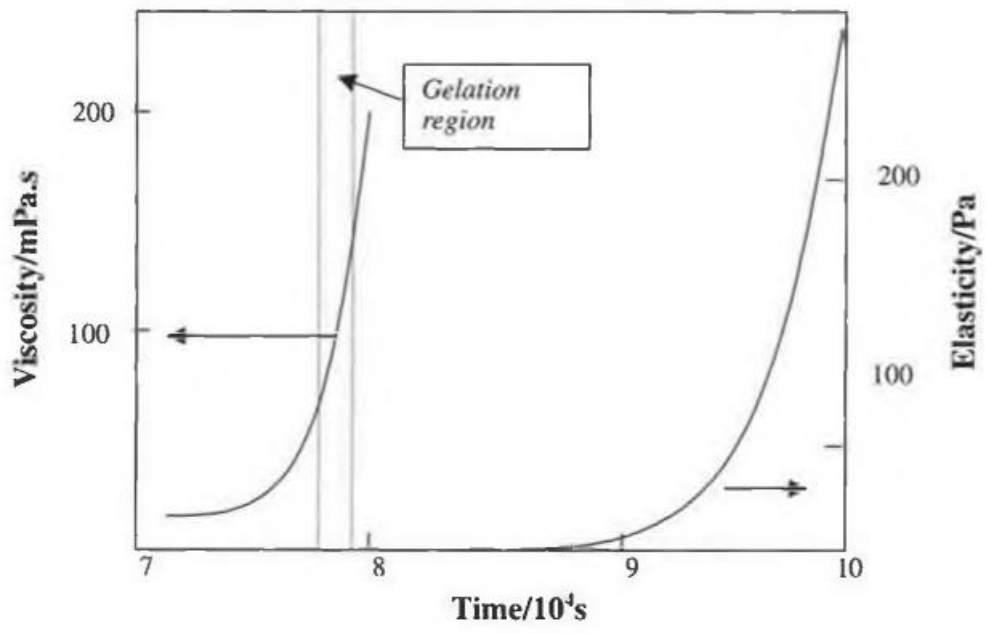

Figure 1.5. Viscosity and Elasticity profiles over time. An individual gelation point is not pointed out. On the contrary, a time interval including the inflection point of the viscosity curve is defined as gelation region.

The gelation theory by Flory and Stockmayer states that the chain density at the surface of a growing polymer particle increases indefinitely with the growth of the particle. On the other hand, percolation model can be used to describe gel formation through cross-linking between sol particles. It is based on random bond formation between the particles (random filling of sites) and no correlations between successive bond formation are considered. However, gelation through particle clustering can be described by Smoluchowski equation:

$$(1.9) \quad \frac{dn_s}{dt} = \frac{1}{2}\sum_{i+j=s} K(i,j)n_i n_j - n_s \sum_{j=1}^{\infty} K(i,j)n_j$$

It states that the number of clusters of size s increases and decreases over time due to formation by aggregation of clusters of sizes i and j and loss by further aggregation, respectively.

1.3.4. Ageing: syneresis and ripening

Even if hydrolysis and condensation are recognized as the main steps of sol-gel processing, further physic and chemical modification are experienced by the system during the following stages. Indeed, trans-pore cross-linking reaction can continue even for a month at room temperature, with the rate depending on pH and gel composition. This behaviour is proved by NMR analysis, which assesses an enhancement in the amount of Q^3 and Q^4 silica species, that means Si bound to three and four other Si atoms by oxygen links, respectively. This result in stiffening (as new covalent bonds are formed within the gel) and shrinkage of the structure. In detail, shrinkage leads to solvent removal from the gel which is transformed into a solid monolith. This process is known as syneresis. As anticipated in paragraph 1.2 when describing the curvature effects in particle growth, ageing phase can involve ripening phenomena as well. Ripening (or coarsening) is defined as the clustering of two or more individual particles. It occurs through the dissolution of the particle surface and the redeposition of the dissolved matter into the curved region originating from the contact between the particles (known as necks, **Figure 1.6**).

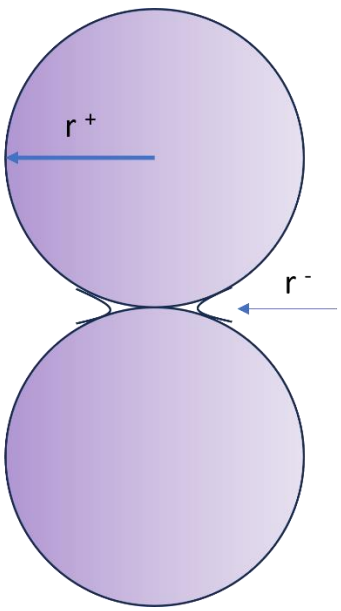

Figure 1.6. Radii of curvature for particles (r^+) and necks (r^-).

More specifically, the solubility of a solid depends on the radius of curvature of the interface. Indeed, if r is the radius of curvature of a solid-liquid interface with interfacial tension γ_{SL}, the solubility S of the solid is related to the solubility of a flat surface S_0 by Kelvin equation:

$$S = S_0 e^{\frac{2\gamma_{SL}V_m}{RTr}} \quad (1.10)$$

with V_m and T as molar volume of the solid and temperature, respectively. Therefore, small particles exhibit higher solubility and the dissolved material is accumulated in the neck region.

1.3.5. Drying

The drying of a gelled sample involves four main stages, each characterized by distinct phenomena. Initially, the gel undergoes shrinkage equivalent to the volume of evaporated liquid (usually water). Occurs in flexible and compliant gels capable of adjusting to reduced volume. Gels may shrink faster than water evaporates under rapid cross-linking and syneresis, impacting pore size distribution. The first phase is known as constant rate period. Afterwards, the gel becomes stiff, resisting to further shrinkage, causing the liquid to recede into the porous structure. The increased stiffness is due to additional cross-linking and a more compact structure. However, capillary stress may lead to cracking unless the gel has optimal cross-linking and aging. This second phase is known as critical point. The third phase is termed first falling-rate period. It consists of further drying as a consequence of bulk liquid receding into capillary pores and thin liquid film formation along pore walls, driven by capillary forces. However, this phase is critical for cracking occurrence due to capillary stress. The last phase, known as second falling-rate period, is characterized by vaporization of the liquid film before it reaches the surface of the pore. Prediction of drying rate is complex and depends on various factors, including pore-size distribution and temperature differentials. The sintering process is a crucial determinant of the size and morphology of the sol-gel product, involving the collapse

of the pore network and the volatilization of organic species. Because the gels have an amorphous structure, the sintering process is predominantly influenced by viscous flow and the sintering rate ε, which is the rate of contraction of the porous network, is calculated as:

$$\varepsilon = \frac{\gamma_{SV} \sqrt[3]{N}}{\mu} \quad (1.11)$$

where γ_{SV} is the gel's surface energy, μ the viscosity and N the number of pores per unit volume. The way drying is accomplished widely affects the properties of the final product. For instance, lower regions tend to have filled pores, causing lower concave surfaces due to residual capillary stress. Soluble materials transported along liquid films may deposit as a white efflorescence near the surface. Moreover, surface layers may exhibit slight cloudiness in partially dried samples. However, avoiding or at least reducing cracking is a mandatory requirement for preserving the integrity of the gel's properties. Cracking magnitude can be reduced by supercritical drying, even if it requires high temperature and pressures; freeze-drying, even if vacuum sublimation can be responsible for extensive fracturing; the use of drying control chemical additives (DCCAs) but gel properties could be severely modified since they are difficult to remove; expand pore size, in order to reduce capillary stress.

1.4. Chemical control of the sol-gel process

The characteristics of sol-gel materials, including transparency, porosity, pore size distribution and surface functionality are significantly influenced by the chosen preparation method. It is possible to precisely adjust the properties of the final material by carefully manipulating the conditions throughout the consecutive stages of the process.

1.4.1. *Nature of the precursor, pH, co-solvent and water content as controlling parameters for hydrolysis and condensation*

Among the factors that affect the rate of hydrolysis and condensation, steric hindrance of the silicon alkoxide precursor is one of the most influential. Indeed, reaction rates are notably reduced by stable modifying ligands, which usually exhibit extended branching and long alkyl chains, resulting in less-condensed gels. A similar effect is obtained by using a longer-chained alcohol as co-solvent, since transesterification results in the substitution of the leaving alcohol groups with co-solvent molecules. In the specific case of colloidal gels, the design of structures with wider pores is accomplished by starting with pre-condensed phases like sol particles or water glass. The nature of the selected catalytic route is another structure-determining parameter, since it modulates the selectivity of the reaction system. More specifically, in the case of acid catalysis, hydrolysis starts very fast but promptly decelerates, due to the substitution of electron donating ether -OR with -OH groups, which exert lower capacity of stabilization towards the positively charges transition state. Slow hydrolysis enhances the possibility of condensation between Si-OR and Si-OH groups, leading to chain elongation and linear polymer formation due to the high reactivity of terminal Si-OR groups. The hydrolysis of side Si-OR groups might result in random cross-linking of chains, that entangle with each other to give dense gel characterized by small-sized pores. On the other hand, base catalysis shifts the selectivity of the process towards hydrolysis, which terminates before the beginning of condensation. Condensation between completely hydrolyzed precursors results fast binding between highly cross-linked polymers, giving fast gelation to porous networks. The hydrophobicity of the final product can be enhanced by using HF instead of HCl as catalyst. Indeed, a portion of surface silanols are replaced by strongly hydrophobic Si-F groups. Water content directly affects the reaction rates. In detail, at low water concentrations ($\frac{H_2O}{Si} < 2$), condensation between only partially hydrolyzed precursors occurs, resulting in esterified polymer chains whatever the catalytic strategy. Increasing water content so that $4 < \frac{H_2O}{Si} < 10$, different behaviours are experienced whether the catalysis is acid or basic. In the

former situation, hydroxylated linear chains are obtained; in the latter case, phase separation may occur due to the co-existence of hydroxylated polymers and unreacted monomers. Further dilution of the alkoxides ($25 < \frac{H_2O}{Si} < 50$) leads to the separation of polymeric strands and makes intermolecular condensation difficult. In this case, spherical particles are likely formed rather than network structures. The activity of the catalysts and thus the reaction rate can be properly tuned by adding a specific amount of co-solvent, like alcohols, THF, dioxane. As a matter of fact, the presence of the co-solvent attenuates the acidity or basicity of the reaction medium by interrupting water hydrogen bonds and increasing, as a consequence, the degree of solvation of H^+ and OH^- ions. More specifically, the catalyst activity exhibits a non-monotonous trend with the co-solvent amount, as shown in **Figure 1.7**.

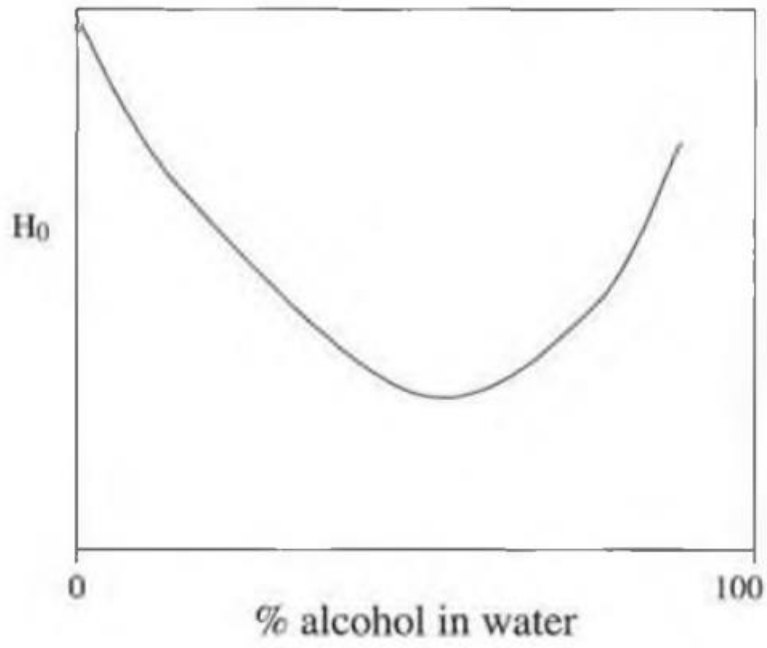

Figure 1.7. Trend of catalyst activity H_0, defined as the moles of product over the mass of catalyst per time unit, versus alcohol v% in water.

Focusing more on the role of the alcohols as co-solvents, under neutral-pH conditions silicates are usually negatively charged since the isoelectric point is at

very low pH (~2.2). Therefore, surface silanol groups are deprotonated and the condensation is achieved by nucleophilic addition of $Si\text{-}O^-$. Alcohol molecules and polar protic solvents can reduce the reactivity by establishing hydrogen bonds with deprotonated silanols, resulting in highly branched structures and less dense gels.

1.4.2. Organic templates as structuring agents

When non-solvent organic molecules are introduced into a sol, they become captured during gelation and remain incorporated in the resulting xerogel. This approach is effective for organizing silica at the molecular level by interacting with organic additives. A typical example is the use of surfactant or, generally, amphiphilic molecules to produce mesoporous structures. Cetyltrimethylammonium bromide (CTAB) surfactant is one of the most used tuning silicate structures. As the surfactant is added to the reaction medium, a lamellar phase made of rod-like micelles is formed. Deprotonated silanols $Si\text{-}O^-$ starts reacting to form siloxane bridges Si-O-Si. This increases the repulsion between the positively charged polar heads of surfactant molecules, which self-assemble into hexagonal phases composed of rod-like micelles. So, silica oligomer chains exposing negatively charged groups keep growing around CTAB supramolecular organization, resulting in honeycomb-like structures (**Figure 1.8**). Following heat treatment is necessary to remove the template and free the pore structure.

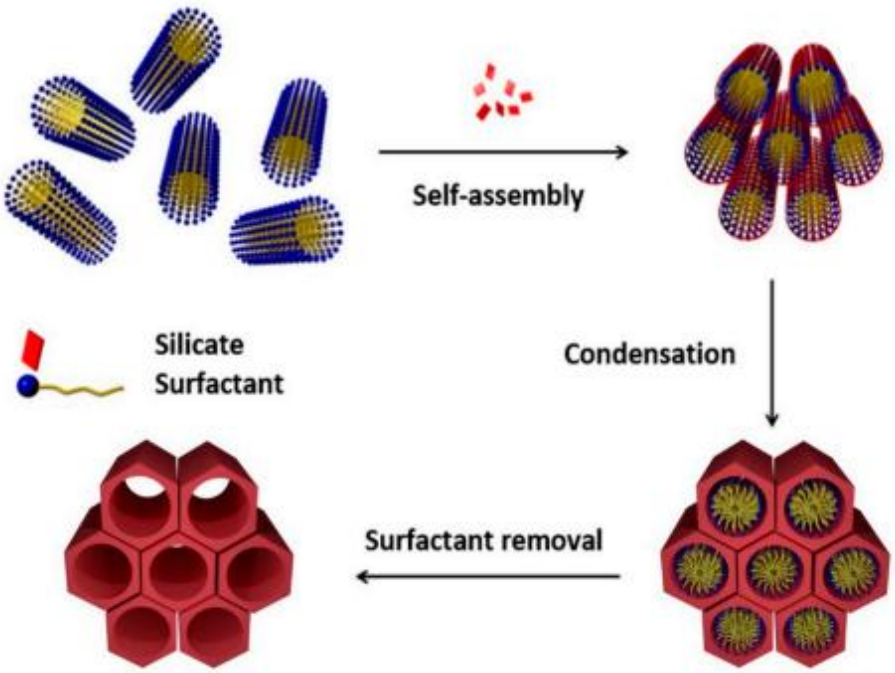

Figure 1.8. Graphical scheme of the synthesis of MCM-41 ordered mesoporous silica.[7]

1.4.3. Entrapment strategy for designing functional materials

One of the advantages of sol-gel strategy is the mild reaction temperature, which allow the functionalization of the inorganic matrix with organic thermolabile species like biomolecules (carbohydrates, proteins). In detail, the guest molecules are added in the preformed silica sol and remains immobilized within the final xerogel network as gelation occurs (**Figure 1.9**).

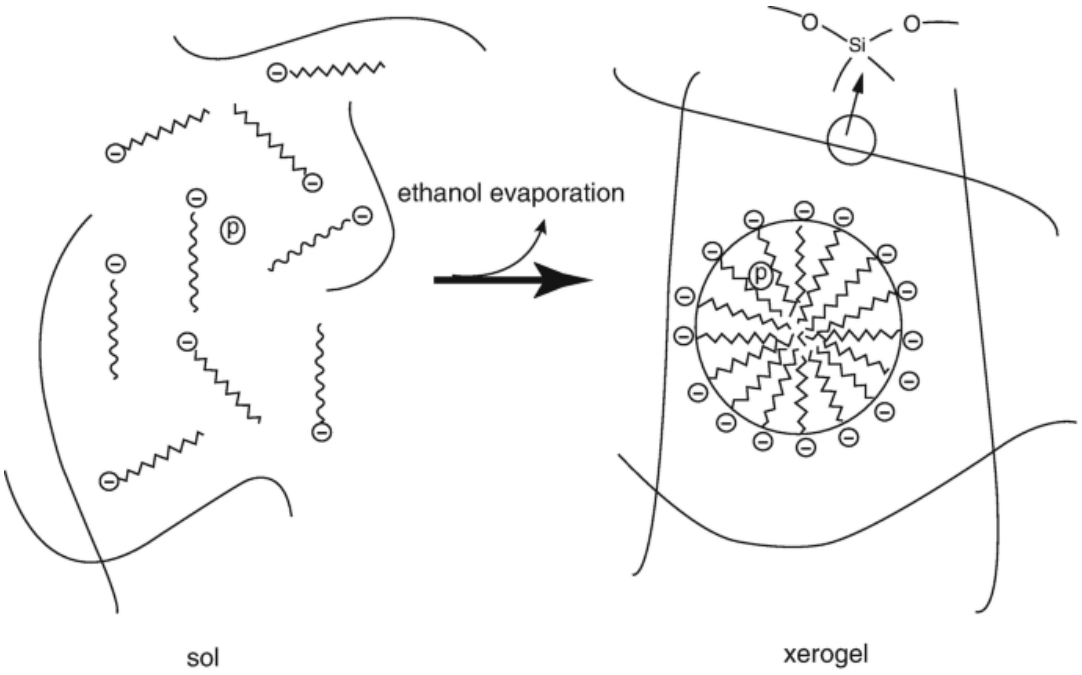

Figure 1.9. Scheme of entrapment of a sodium dodecyl sulfate (SDS) micelle in sol-gel silica gel.[8]

The efficiency of encapsulation depends on the relative size of the molecule and the pore and the strength of the mutual interaction. A suitable strategy to avoid leakage of the guest into the liquid phase is to derivatize the molecule with alkoxysilane functionalities, in order couple physical immobilization with chemical binding to the growing silica skeleton.

1.4.4. Synthesis of hybrid materials

To meet the physical and mechanical requirements for various applications, polymeric materials are often utilized in blends or composites. The properties of these composite materials are not only influenced by the individual components but are also heavily dependent on the phase morphology, particularly the interfacial properties, making the degree of phase separation crucial. The sol-gel method offers the advantage of achieving nanoscale mixing of organic and inorganic polymers, sometimes even at a molecular level. This intimate mixing results in hybrid materials

that are frequently highly transparent compared to other composites, as light scattering due to domain formation is significantly reduced. Five major classes of hybrids have been identified: (1) pre-formed soluble organic polymers entrapped in a xerogel; (2) pre-formed embedded polymers with covalent links to the inorganic network; (3) mutually interpenetrating organic and inorganic networks; (4) interpenetrating networks with covalent links between the organic and inorganic phases; and (5) non-shrinking sol-gel composites (**Figure 1.10**).

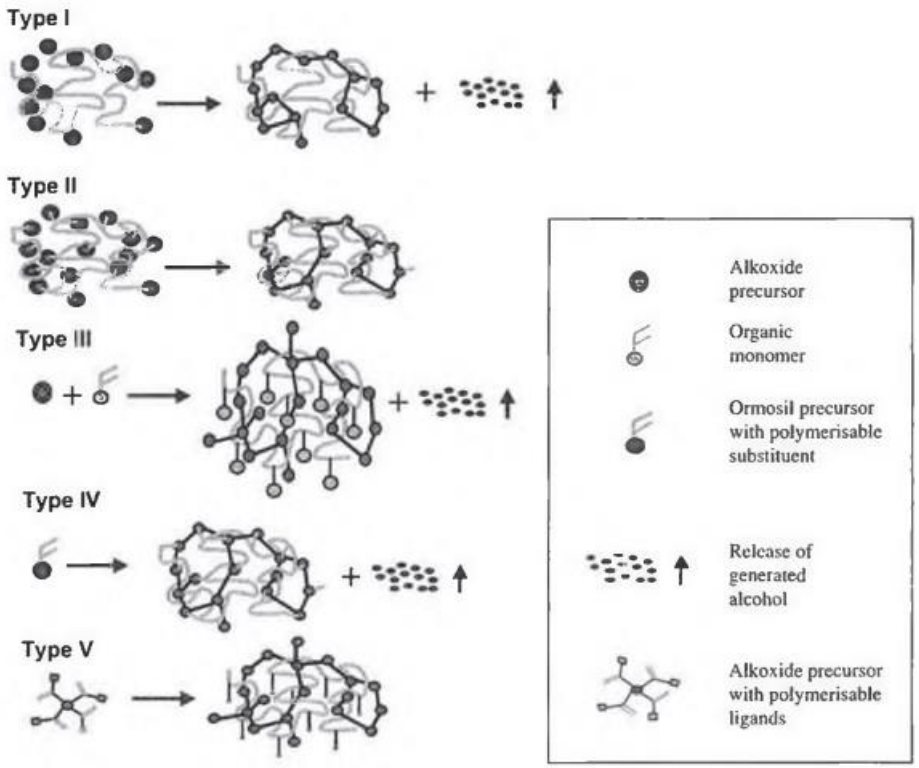

Figure 1.10. Novak's classification of hybrid materials.

Transparent and uniform hybrids of type (1) have been successfully produced for various polymers featuring basic functional groups, including polyamines and poly(vinyl pyridines). These polymers remain soluble in hydrolyzing acidic sols. Type (2) materials are typically derived from the hydrolysis of a tetra-alkoxysilane in the presence of a preformed polymer that is soluble and functionalized with

trialkoxysilane groups. These preformed polymers can be generated through hydrosilylation of terminal double bonds or by coupling reactive groups in the polymer with functionalized trialkoxysilanes. Alternative methods for preparing such materials include co-condensation of a tetraalkoxysilane and a hydroxy- or alkoxy-silane-terminated polymer, such as polydimethyl siloxane and aminopropyltriethoxysilane-endcapped poly(methyl oxazoline), respectively. Additionally, hydroxylated polymers like polyvinyl alcohol and cellulose can be employed, becoming linked to the network during the drying process through the formation of silylether bonds. Given the limited number of polymers soluble in the tricomponent sol-gel solution, efforts have concentrated on simultaneously forming an organic and an inorganic matrix. In the pursuit of new materials for contact lenses, Schmidt synthesized high-quality composites with superior hardness, transparency, and wettability through the co-condensation of 3-glycidoxypropyltrimethylsilane and titanium alkoxides. However, the brittleness arising from the ionic character of the glass was addressed by increasing the organic content through the addition of methacrylates along with a trialkylsilyl-functionalized propylmethacrylate to the polymerizing mixture, resulting in a type (4) material possessing the necessary elasticity for manufacturing and handling. Non-shrinking hybrids of type (5) were successfully obtained by replacing these ligands with polymerizable alcohols. This precursor, upon hydrolysis, generates two polymerizable components simultaneously—an inorganic and an organic monomer—eliminating the need for evaporation. The organic/inorganic ratio can be precisely adjusted by selecting appropriate ligands for silicon. Non-shrinking hybrids with glass contents reaching up to 50% were achieved using poly(silylic acid) oligomers esterified with a polymerizable alcohol.

1.5. Advantage and drawbacks of sol-gel synthesis

Sol-gel synthesized materials hold particular value and interest for several reasons.

Low temperatures are required for all stages, minimizing thermal degradation and enabling high purity and stoichiometry. Indeed, mild chemical conditions allow for the entrapment of pH-sensitive organic and biological species without compromising their functions. Moreover, metal alkoxides can be easily purified to high levels, contributing to product purity. The high miscibility of organometallic precursors involving different metals allow accurate doping of the final gel. As for the design of the desired morphology, the method allows for the preparation of highly porous and nanocrystalline materials, whereas control over hydrolysis rates, colloid particle size, and final material properties is achievable through chemical modification of precursors. More specifically, pore-size tuning is achievable by entrapment and following removal of surfactant species. Functionalized precursors enable the covalent attachment of organic and biological species to porous silicate glass structures. Further control over pore size and mechanical strength is possible by adjusting ageing and drying conditions. Organometallic precursors with polymerizable organic ligands enable the production of organic-inorganic hybrid materials. The use of liquid precursors allows the casting of ceramic materials in complex shapes, producing thin films, fibers, and monoliths without machining or melting. Finally, the optical quality of sol-gel materials is often good, making them suitable for optical components. However, some drawbacks are to be taken into account. Indeed, the precursors are often expensive and sensitive to moisture, restricting large-scale production to specialized applications like optical coatings. The process is time-consuming, especially when precise aging and drying are essential, leading to higher material volumes in processing lines. Additionally, challenges such as dimensional change during densification and issues with shrinkage and stress cracking during drying require careful consideration. While these limitations exist, it underscores the importance of optimizing sol-gel materials to maximize their benefits in applications where they offer unique properties not achievable through other methods.

2. Mesoporous silica nanoparticles

Mesoporous silica nanoparticles (MSNs) are a type of nanomaterial with a unique structure characterized by ordered and regularly spaced pores within the silica matrix. These nanoparticles have gained significant attention in various scientific and technological applications due to their distinct properties and versatile features, such as high specific surface area and pore volume, adjustable sizes and shapes, straightforward surface functionalization, along with favorable physicochemical properties including abundant surface groups, colloidal stability, and high dispersibility. All these properties are provided by the unique surface chemistry and pore architecture, which can be finely tuned by adjusting the synthesis conditions. [9] The information reported in this paragraph is mainly contained in the works by Popat,[10] Kankala,[11] and Lee.[12]

2.1. Historical background

The first example of MSNs was provided by the scientist of Mobil Research and Development Corporation. More specifically, Kresge and co-workers reported the synthesis of a mesoporous solid, from the calcination of aluminosilicate gels in the presence of surfactants, by means of a liquid-crystal 'templating' mechanism, in which the silicate material forms inorganic walls between ordered hexagonal arrays of surfactant micelles (a graphical sketch of the process is reported in paragraph 1.4.2, **Figure 1.8**).[13] The obtained material was termed Mobile Composition of Matter (MCM)-41and is part of the MCM series, together with three-dimensional cubic-shaped MCM-48,[14] and lamellar-structured MCM-50.[15] Micro-mesoporous silicates with high surface area (~900 m^2 /g) were produced few years before by Yanagisawa et al. by reaction of kanemite ($NaHSi_2O_5 \cdot 3H_2O$) with alkyltrimethylammonium chloride solutions.[16] Surfactants are the key factors for the synthesis of porous architectures and depending on the neat charge they can be classified as: cationic, such as cetyltrimethylammonium bromide (CTAB); anionic,

like sodium dodecyl sulphate (SDS) and long-chained carboxylic acids; non-ionic, such as polyethylene oxide-(PEO) and polypropylene oxide-(PPO)based copolymers, Pluronic F123. Anionic surfactants are widely used. Indeed, a series of mesoporous silicates is named after them, namely the anionic surfactant-templated mesoporous silicas (AMS).[17] Zhao at al. efficiently designed hexagonal mesoporous silica structures with uniform pore sizes up to approximately 300 Å using poly(alkylene oxids) of different lengths as surfactants. These materials were called Santa Barbara amorphous (SBA)-15, and inaugurated SBA-type material series.[18] The peculiar pore structure, together with the wide availability of surface silanol groups, make them very powerful players in the fields of drug delivery and encapsulation of biomolecules.

2.2. Synthesis, functionalization and applications

2.2.1. Synthesis strategies

The synthesis strategies of MSNs can be generally grouped into surfactant-templating approach. It consists of the use of surfactants at their critical micelle concentrations (CMC). For higher concentrations than CMC, the amphiphilic molecules organize in micelles to provide a structure-orienting pattern for the inorganic skeleton. More specifically, silica originates from the sol-gel reaction series of alkoxide precursors, added in the surfactant solution. Finally, a surfactant-removal step (by washing or calcination) is required to free the pore architecture (**Figure 2.1**).

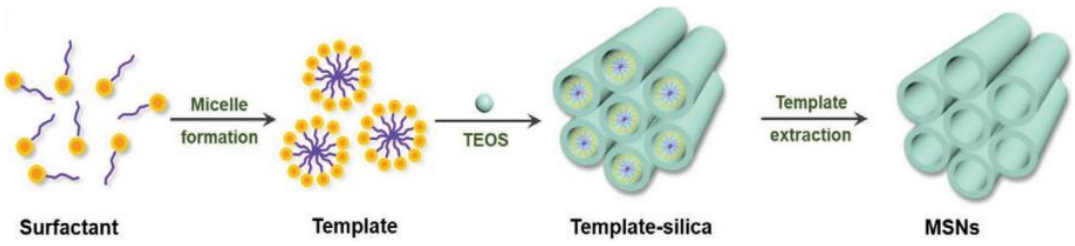

Figure 2.1. Surfactant-templating approach for the synthesis of MSNs.[19]

As previously mentioned in general for sol-gel processes, the reactivity of the precursor is strictly dependent on pH, as described by **Figure 2.2**.

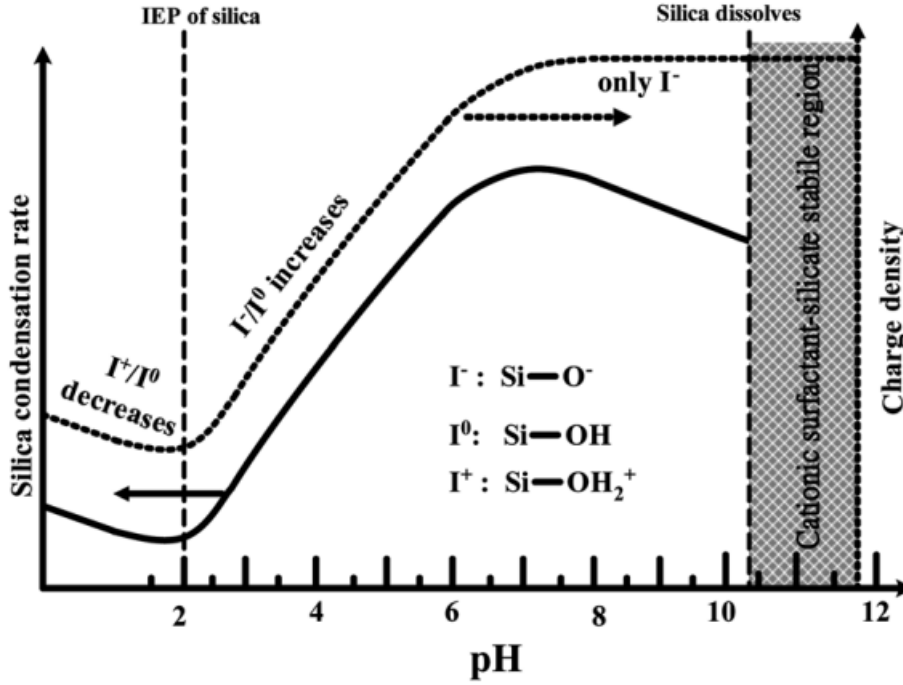

Figure 2.2. Silica condensation rate against pH value.[19]

The amount of positively charged silanols grows as pH decreases for $pH < pI$. For $pH > pI$, silanols are deprotonated and thus negatively charged, and the absolute value of the charge increases with pH. In the region of $pI < pH < 7$ the growing amount of nucleophilic species results in faster condensation, with the maximum centered at around $pH = 7$. However, $pH > 7$ favor silica dissolution and lower reaction rates are recorded. Nevertheless, synthesis of MSNs is usually performed in $10 < pH < 12$ interval. This is justified by the complete deprotonation of silanols ($Si\text{-}O^-$), which strongly bind cationic surfactants through electrostatic interactions or hydrogen bonding, contributing to stabilize the growing silica structure. The marked sensitivity of the silicate reactivity with the pH value paved the way for a new synthesis method known as fast self-assembling method, reported in **Figure 2.3**. In detail, pre-condensed silica particles are obtained through initial nucleation at $pH \sim$

pI. Afterwards, sudden neutralization or basification leads to fast simultaneous assembling-growth of the silica–surfactant nuclei.[20]

Figure 2.3. Fast pH-change for the induction of self-assembly in the synthesis of cationic surfactant-templated MSNs.[19]

There is a notable tendency for surfactant-silica nanoparticles to aggregate, especially when surface silanols play an active role in condensation reactions to form Si-O-Si bridging bonds between nanoparticles. Preventing aggregation is crucial for achieving a stable colloidal suspension of MSNs. While the high dilution method can be employed to create a stable colloidal suspension within the range of tens to hundreds of nanometers, the collection of highly-diluted MSNs demands significant time and energy. To mitigate the irreversible aggregation of MSNs during synthesis,

it's essential to prevent the direct contact of silanol groups. Suzuki et al. addressed this challenge by utilizing a binary surfactant mixture, employing a cationic surfactant as a mesostructural directing agent and a non-ionic triblock polymer (Pluronic F127) as a steric stabilizer (**Figure 2.4**). [21]

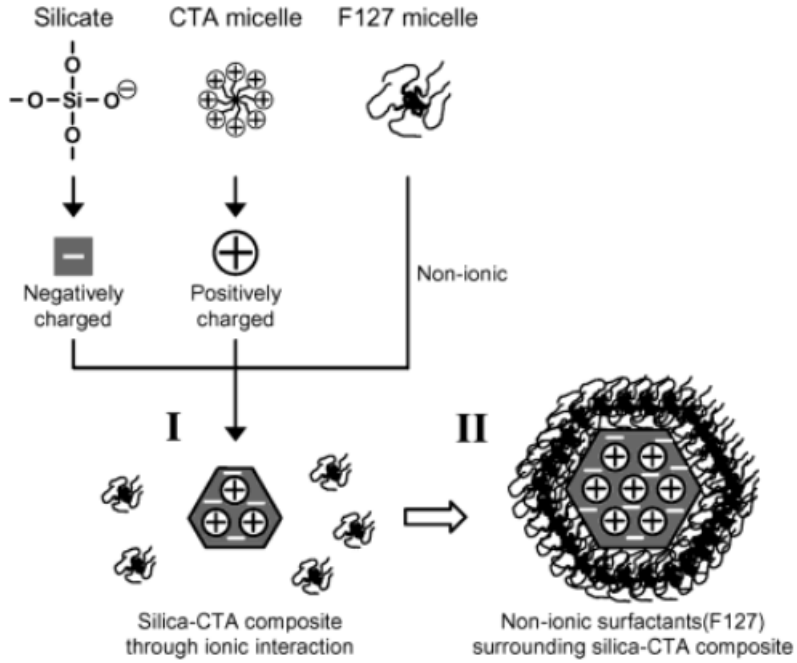

Figure 2.4. Schematic representation of the functions of two surfactants.[21]

Pluronic F127, anchored to the cationic surfactant-silicate nanoparticles and inhibiting grain growth, offers a method to prepare a stable and concentrated colloidal suspension of MSNs with a diameter below 50 nm. Other surface-protecting agents, such as PEG, triethanolamine (TEA), and the amino acid L-lysine, have also been employed to stabilize and reduce the size of MSNs. The synthesis of uniformly sized spherical silica particles was first achieved by Stober et. al. through the hydrolysis and condensation of alkyl silicates in alcoholic solutions, using NH_4OH as a morphological catalyst. The suspended particle sizes achieved range from less than 0.05 μm to 2 μm in diameter.[22] This strategy, known as the Stober method, was then modified by adding cationic surfactants to an alkaline hydro-

alcoholic mixture and became a suitable route to produce MSNs. For instance, well-dispersed pseudo-hexagonal MSNs were obtained by Lin et al. using TEOS as alkoxide precursor and CTAB as surfactant. In detail, separating the nucleation and growth phases in dilute alkaline solutions resulted in homogeneous particles of 110 nm in diameter.[23] Moreover, pH seems to be the key parameter for controlling particle growth. Indeed, the higher the pH, the higher the particle size. This phenomenon can be explained by taking into account the different reaction rates for silicates in alkaline media. More specifically, at highly alkaline pH the condensation rate decreases with increasing pH (**Figure 2.2**). Therefore, lower pH means faster condensation and thus more small nuclei. On the other hand, at higher pH completely hydroxylated alkoxides react with less growing nuclei, resulting in bigger particles.[24] Besides accelerating the sol-gel reactions, the chemical nature of the morphological catalyst is a critical factor for tuning particle size as well. It was demonstrated that replacing ammonia with alkylamines like triethanolamine (TEA) leads to smaller particles. As a matter of fact, TEA is a chelating agent for silicates, acting as steric inhibitor for particle growth: the more TEA is added, the smaller the MSNs (**Figure 2.5**).[25]

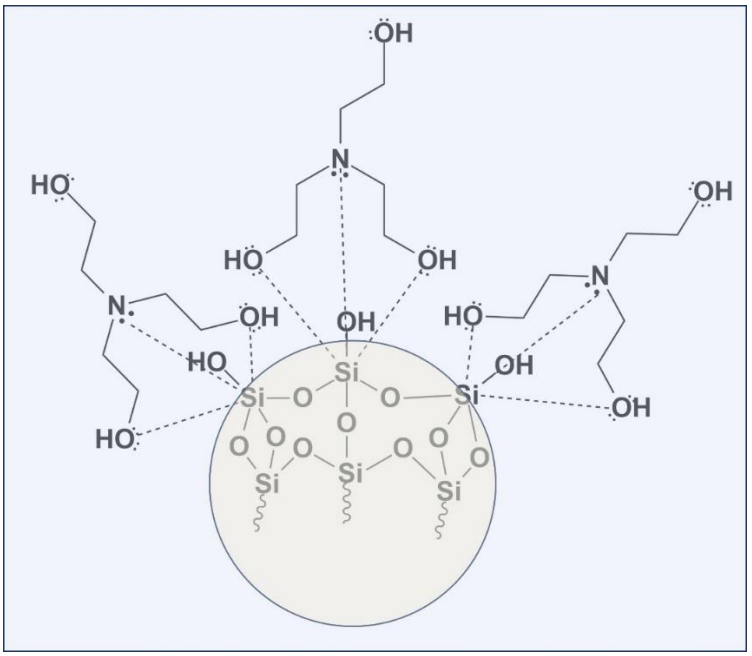

Figure 2.5. Surface TEA-silicate complexes on the surface of the growing particle.

The length of the alkoxide's alkyl chain can affect the particle size as well. Indeed, short-chained alkoxides lead to faster hydrolysis and thus to more growing nuclei, resulting in smaller particles, as reported by Yamada et al.[26] More specifically, four different alkoxides were used namely TMOS, TEOS, TPOS and TBOS and the higher the length of the alkyl chain, the bigger the particles (**Figure 2.6**) due to the decrease in hydrolysis rate caused by enhanced steric hindrance.

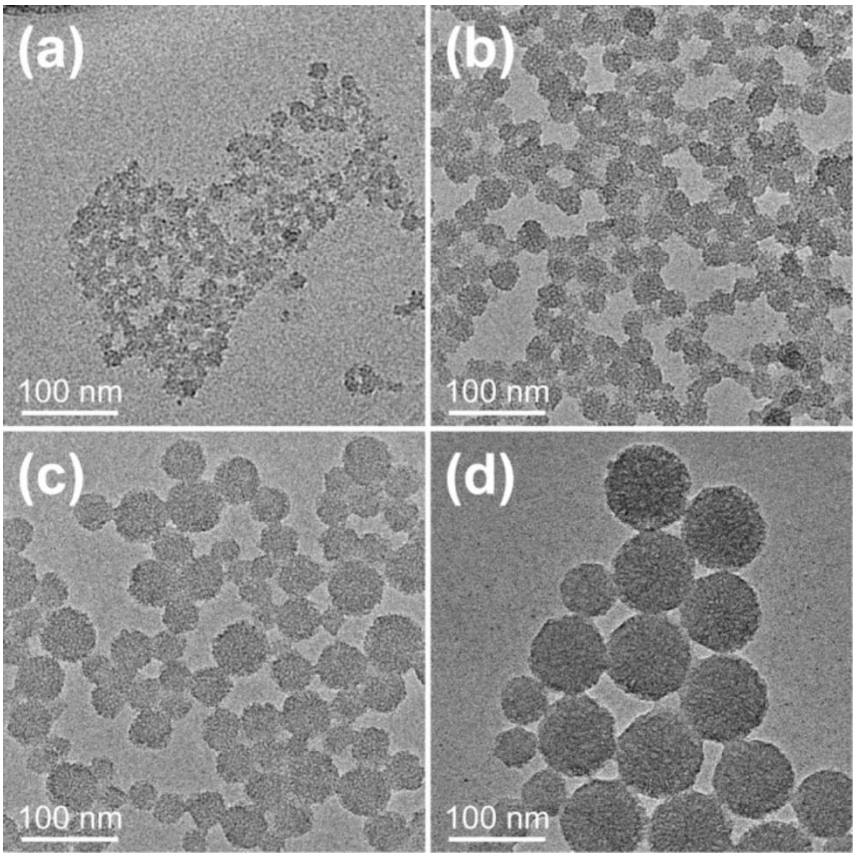

Figure 2.6. TEM images of MSNs produced using TMOS (a), TEOS (b), TPOS (c), TBOS (d).[26]

The application of MSNs as carriers for cargo delivery or immobilization of biomolecules requires fine tuning of pore size, since it should properly match the size of the guest molecule. A suitable strategy to modulate pore morphology is to

change surfactant, replacing the widely used quaternary ammonium salts (CTAB, for instance) with larger templating agents such as 1,3,5-trimethylbenzene (TMB) or nonionic polymers like Pluronic P65, P123, and F127. [27,28] In **Figure 2.7**, reported pore size distributions prove that average pore size shifts towards higher diameters with increasing amounts of employed swelling agent, whether it is TMB or N,N-dimethylhexadecylamine (DMHA).

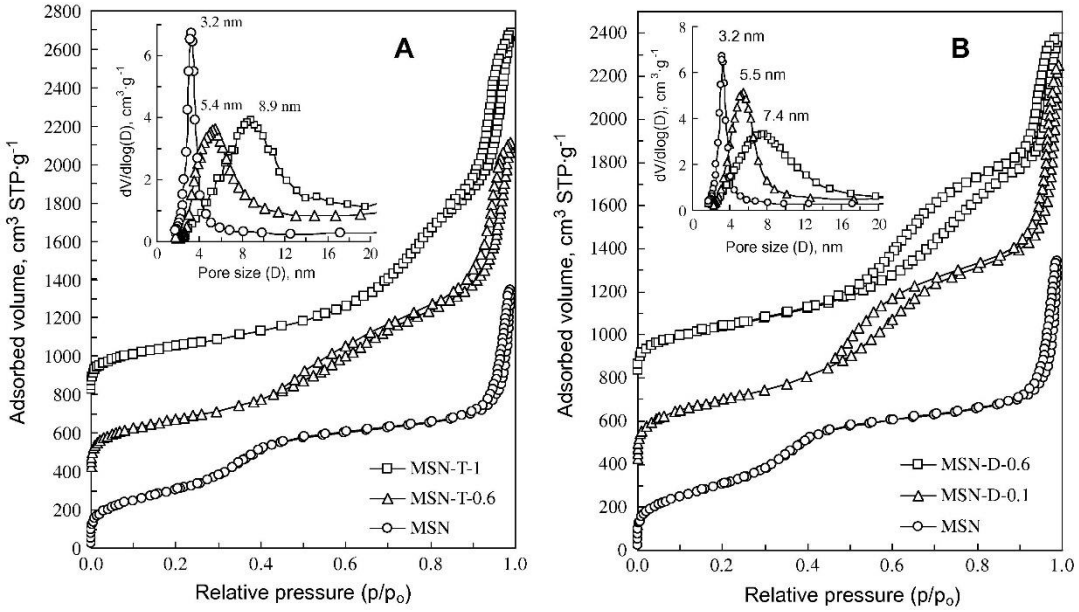

Figure 2.7. N_2 physisorption hysteresis and pore size distributions (inset) for MSNs prepared with TMB (A) and DMHA (B).[27]

Surfactant removal stage is fundamental for benefitting from the whole pore architecture of MSNs, and a proper removal strategy has to be selected. Calcination is the easiest way to eliminate templating agents since it consists of high-temperature treatment under nitrogen or air treatment. However, MSNs are almost always produced through sol-gel routes, which means they load huge amounts of solvents within the three-dimensional gel network. Therefore, high temperature treatments could lead to fast solvent evaporation and thus massive shrinkage. Moreover, surface silanol might condense with each other, leading to inter-particle siloxane bridge formation and sintering, resulting in consistent reduction of porosity and surface

area.[29] Preservation of morphology can be achieved by performing liquid-phase extraction of surfactant, known as "liquid-phase calcination",[30] which exploits the high solubility of surfactants in boiling solvents as ethanol. This strategy can be coupled with surface functionalization by suspending MSNs in ethanol and silanes to facilitate the simultaneous exchange process of surfactant and silyl groups. This leads to a more consistent monolayer coverage on the surface and an increased quantity of surface attachments of silane.[31] A special mention is deserved by wrinkled silica nanoparticles (WSNs), which are mesoporous silica nanoparticles with hierarchical central-radial pore structure. Even if the synthesis of such nanostructures was repeatedly reported in the literature before,[32,33] it was the work by pioneers Moon and Lee that shed light on the mechanism of formation.[34] The synthesis is carried out in a cetylpyridinium bromide (CPB)-stabilized bicontinuous microemulsion which provides a continuous network of both oil and water phases instead of having distinct droplets of oil dispersed in water or vice versa. More specifically, the reaction system is termed Winsor III, that means microemulsion in the middle of an excess oil layer on the top and an excess water-based layer on the bottom. The key feature of a bicontinuous microemulsion is that provides a large interfacial area, making it as a suitable template for materials synthesis. In detail, CPB surfactant is dissolved in water with the morphological catalyst urea. Afterwards, the microemulsion originates from the addition of a non-polar phase made of an equal amount of cyclohexane and isopropanol, acting as co-solvent. The silica precursor is the TEOS, which diffuses in the oil layer and starts reacting, following the sol-gel route of hydrolysis and condensation, as soon as it reaches the oil-water interfaces. After 16 h at 70°C, a wrinkled highly porous structure is obtained (**Figure 2.8**).

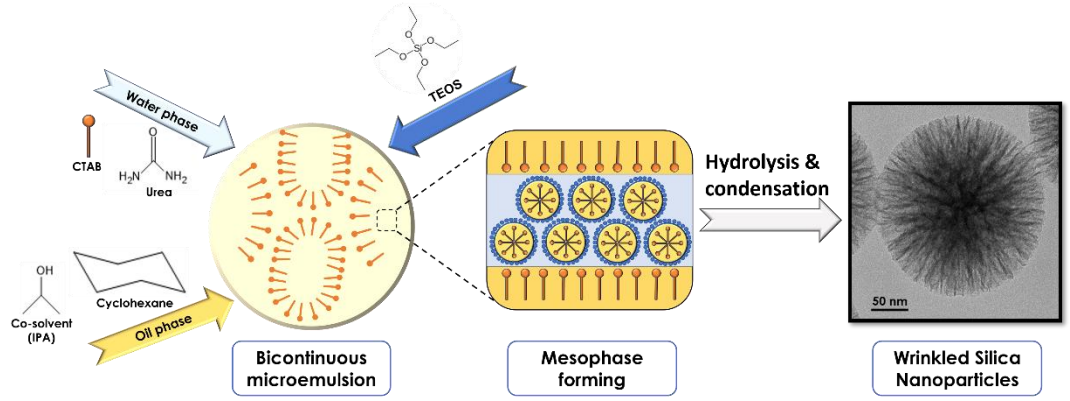

Figure 2.8. Reaction scheme for the synthesis of WSNs but replacing CPB with CTAB in the role of surfactant.

A key feature for tuning pore size is the choice of the co-solvent. Indeed, the higher the chain length of the selected alcohol, the higher the inter-wrinkled distance and thus the larger the pores, as reported in **Figure 2.9**.

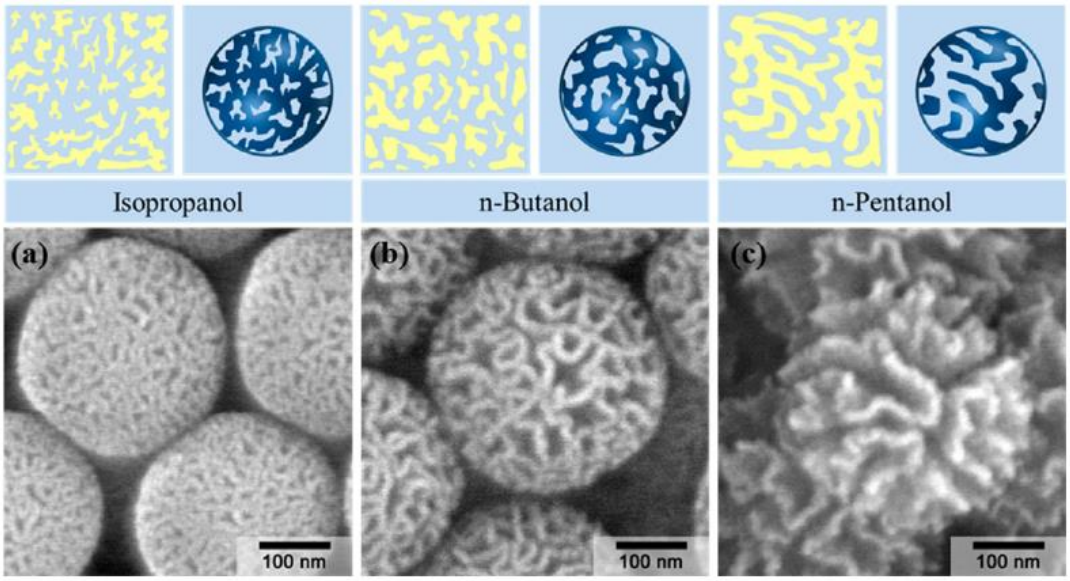

Figure 2.9. Schematic illustrations of microemulsion phases of reaction mixtures with identical molar amounts of different cosolvents.[34]

2.2.2. Surface functionalization for protein binding

MPS exhibits a clearly defined structure and a high density of surface silanol groups, which are sites of chemical modification with various organic functional groups to immobilize biomolecules, such as enzymes. The surface functional groups serve multiple purposes in enzyme immobilization: (i) altering the surface charge of MPS to regulate electrostatic interactions with the adsorbed enzyme, (ii) forming chemical links with the amino acid groups of the targeted enzyme, and (iii) reducing the size of the pore entrance to trap enzymes within the nanochannels. The functionalization of MSNs with organosilanes is termed silanization and it is usually achieved through three alternative strategies. The first one is the grafting of organosilanes onto the silica surface through S_N2 reaction. This results in the organic chain of the silanes exposed onto the surface of the nanostructures. The second strategy is called co-condensation. In this single-step procedure, organosilanes are directly introduced into the synthesizing gel solution alongside the silica source. A portion of the silica precursor in the sol—gel mixture is substituted with varying ratios of organosilanes. Subsequently, the removal of surfactant molecules occurs through extraction using an acidic, salt, or organic solvent. Co-condensation offers advantages such as a high loading density of organosilanes and the even distribution of functional groups, achieved without significant reductions in surface area, pore size, and pore volume. Nevertheless, a drawback of this method is the extraction efficiency for block copolymer systems, which is only approximately 80%. Another concern is that the functional groups may undergo degradation under the harsh conditions of sol—gel reactions and surfactant extraction. The introduction of a reactive vinyl group into MPS opens up the possibility of generating a diverse range of functional groups through post-modification of the initial functional groups. The third strategy is the surfactant displacement or liquid-phase calcination, as it was previously mentioned. Functionalization is usually performed with trialkoxyorganosilanes, as described in **Figure 2.10**.

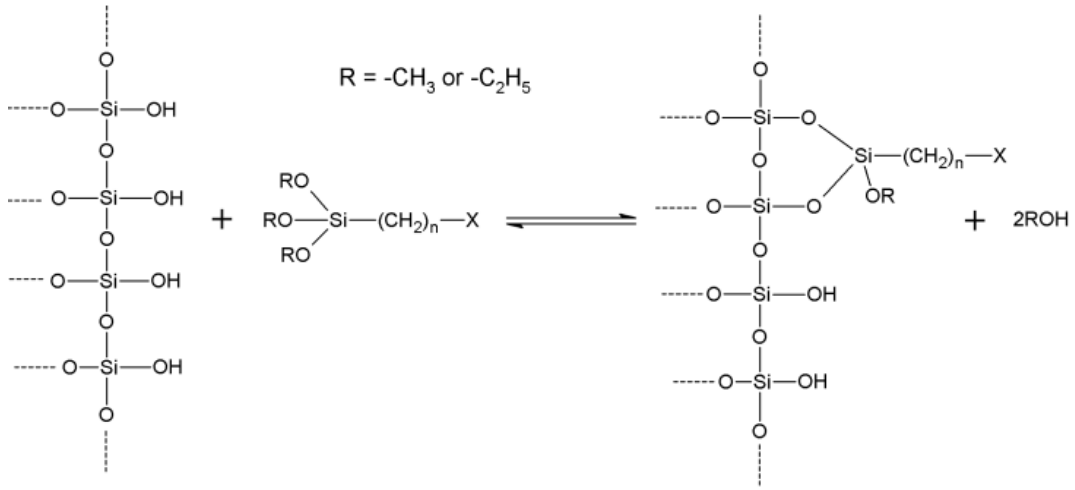

Figure 2.10. Grafting of surface silanol groups with trialkoxyorganosilanes. X is a specific functional group useful for protein immobilization.[35]

Amine functionality are widely used and aminopropyltriethoxysilane (APTES) is the most used organosilane for surface functionalization due to the cost-effectiveness and the versatile reactivity of amino-groups. Moreover, it provides hydrophilicity of the support, which is usually required for carriers. Carboxyl groups can be used too for protein attachment but the cost of production is rather high. Therefore, it is preferable to graft amino-silanes and then perform further functionalization with derivatizing agents such as glutaric anhydride or by hydrolysis of nitrile and cyano groups. Epoxy functionalities (glycidyloxypropyl-trialkoxysilanes) are frequently used as well because of the high reactivity of the epoxide ring. Indeed, ring opening is usually provided by reaction with amine groups from proteins. Sulphonic acid groups can be inserted by post-oxidation of previously grafted mercapto-groups, the same way as phosphoric acid groups come from the hydrolysis of the diethylestersilanes. Non-covalent immobilization is usually required for lipase, a class of enzymes which are sensitive to interfacial activation as adsorbed onto hydrophobic surfaces. Proper hydrophobization is achieved by choosing phenyl-trialkoxysilanes of halide-trialkoxysilanes.

2.2.3. Activation routes

Functionalized supports often lack direct reactivity with proteins. Only epoxy- or aldehyde-functionalized supports can directly couple with enzymes. Otherwise, supports must be activated using specific reagents to ensure reactivity with protein functional groups. Support activation involves inserting electrophilic functions on the support surface or modifying introduced functions into desired electrophilic moieties. Commonly, protein surface functions are nucleophilic or made nucleophilic by pH adjustment to $6 < pH < 9$ interval, often using phosphate-based buffers. Tris buffers are unsuitable due to competition with protein amino groups. Excessively high pH wastes electrophilic moieties. Although higher pH accelerates immobilization, hydroxide ions and nucleophiles, can compromise it. Optimal pH balances support electrophilic power and protein nucleophilic character. Dilute $NaHCO_3$ ($pH \sim 8$) suits unreactive carriers; reactive ones perform best at $pH \sim 8$. The primary targeted protein function is $–NH_2$. More specifically, N-terminal α-amino group, and lysine ε-amino group due to their widespread presence and optimal reactivity. Lysine ε-amino groups require alkaline media ($pH > 9 - 10$) for non-dissociated form. Chemical amination or α-amino groups with lower pKa ($\sim 7 - 8$) offer alternatives. Carboxylic groups require activation; other groups (alcoholic, phenolic, imidazole, thiol) have limited use due to lower frequency. The molecular spacers exert a very important role in tuning catalytic features. Indeed, short spacers rigidify protein structure for stabilization, while long spacers preserve native structure. Moderate stiffening often stabilizes tertiary/quaternary structures. Multipoint enzyme coupling can lead to inactive preparations due to hindered conformational changes and excessive crowding of electrophilic functions on the carrier surface. One of the most popular bifunctional supports for covalent immobilization is glutaraldehyde, due to the double carbonyl functionality of its structure. Furthermore, it can assume at least four different forms as the canonic one and even polymerize in aqueous media, as shown in **Figure 2.11**.

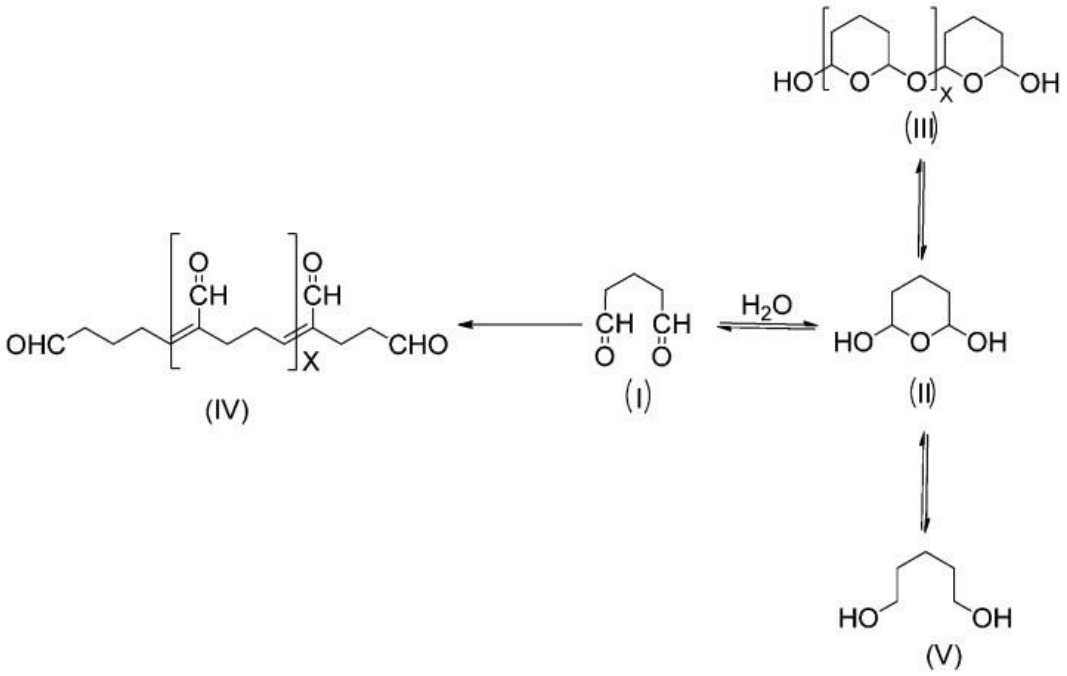

Figure 2.11. Chemical behaviour of glutaraldehyde in aqueous solution.[36]

Two alternative reaction pathways are proposed, namely Schiff-base formation and Michael-type addition with aminated support and protein's -NH_2 groups, as described in **Figure 2.12 A** and **B**, respectively.[36] Even if the former mechanism is the more proposed in literature, some concerns about its probability occur, especially due to the wide possible form glutaraldehyde can exhibit in water, as described by **Figure 2.11**, including α,β-unsaturated aldehydes. As a matter of fact, α,β-unsaturated oligomers can evolve into secondary amines after Michael addition to the double bond.

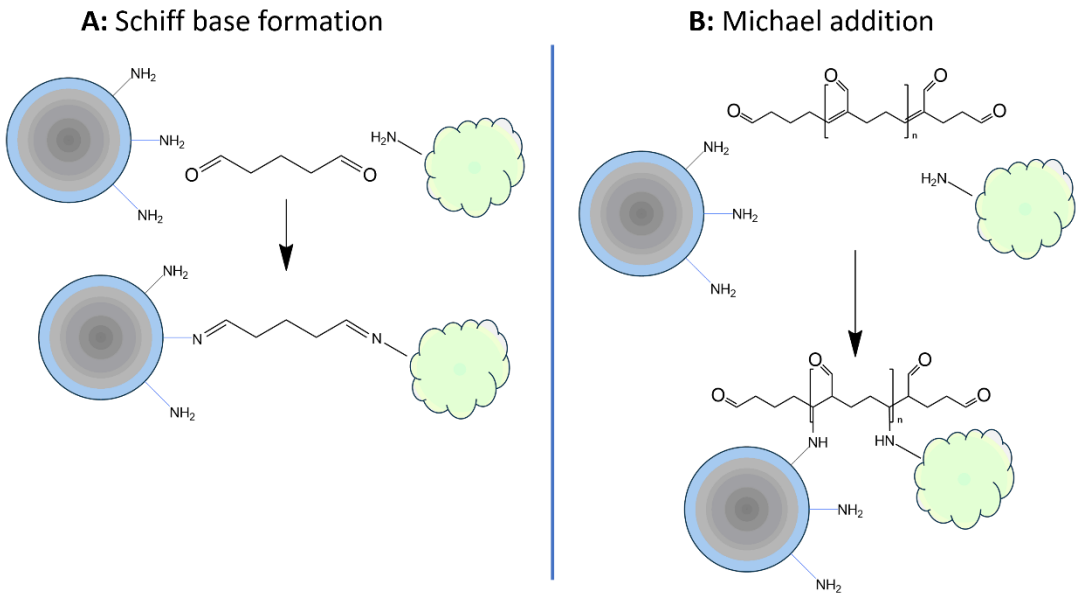

Figure 2.12. Schiff base formation (A) and Michael-type addition (B) in chemical coupling between aminated support (blue and grey particle) and enzyme (green cloud).

Carbodiimides are expensive reagents deputed to the activation of carboxyl-derivatized supports, with the aim of binding to nucleophilic groups like lysine ε-NH_2. A popular carbodiimide, 1-ethyl-3-(3-dimethylaminopropyl)carbodiimide (EDC), is widely used. The electrophilic central carbon atom of EDC is susceptible to nucleophilic attack by the -COOH group from the support, forming an amine-reactive O-acylisourea. Isourea ester intermediates are unstable and prone to hydrolysis. N-hydroxysuccinimide (NHS) stabilizes the intermediate into a more stable, amine-reactive NHS ester. This stabilized form is commercially available as an active succinylated support, enhancing coupling efficiency up to 20-fold (**Figure 2.13**).

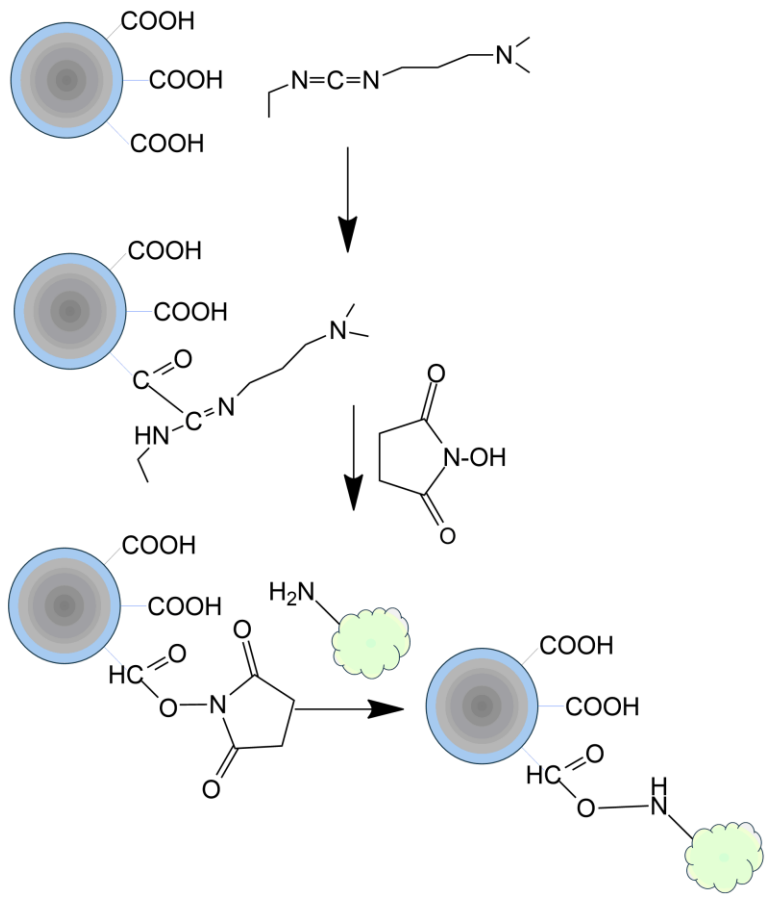

Figure 2.13. Mechanism of covalent attachment of proteins onto carboxylated supports through EDC/NHS chemistry.

References

(1) Danks, A. E.; Hall, S. R.; Schnepp, Z. The Evolution of "sol-Gel" Chemistry as a Technique for Materials Synthesis. *Mater Horiz* **2016**, *3* (2), 91–112. https://doi.org/10.1039/c5mh00260e.

(2) Wright, D. J.; Sommerdijk, N. A. J. M. *Sol-Gel Materials Chemistry and Applications*; CRC Press, 2018. https://doi.org/https://doi.org/10.1201/9781315273808.

(3) Cushing, B. L.; Kolesnichenko, V. L.; O'Connor, C. J. Recent Advances in the Liquid-Phase Syntheses of Inorganic Nanoparticles. *Chem Rev* **2004**, *104* (9), 3893–3946. https://doi.org/10.1021/cr030027b.

(4) *Springer Handbook of Nanomaterials*.

(5) Roduner, E. Size Matters: Why Nanomaterials Are Different. https://doi.org/10.1039/b502142c.

(6) *SILICA SOL-GELS: REACTION MECHANISMS*.

(7) Martínez-Edo, G.; Balmori, A.; Pontón, I.; Del Rio, A. M.; Sánchez-García, D. Functionalized Ordered Mesoporous Silicas (MCM-41): Synthesis and Applications in Catalysis. *Catalysts 2018, Vol. 8, Page 617* **2018**, *8* (12), 617. https://doi.org/10.3390/CATAL8120617.

(8) Sakka, S. *Handbook of Sol-Gel Science and Technology. 1. Sol-Gel Processing*; Springer Science & Business Media, 2005; Vol. 1.

(9) Popat, A.; Hartono, S. B.; Stahr, F.; Liu, J.; Qiao, S. Z.; Lu, G. Q. Mesoporous Silica Nanoparticles for Bioadsorption, Enzyme Immobilisation, and Delivery Carriers. *Nanoscale* **2011**, *3* (7), 2801–2818. https://doi.org/10.1039/c1nr10224a.

(10) Popat, A.; Hartono, S. B.; Stahr, F.; Liu, J.; Qiao, S. Z.; Lu, G. Q. Mesoporous Silica Nanoparticles for Bioadsorption, Enzyme Immobilisation, and Delivery Carriers. *Nanoscale*. July 2011, pp 2801–2818. https://doi.org/10.1039/c1nr10224a.

(11) Kankala, R. K.; Han, Y. H.; Na, J.; Lee, C. H.; Sun, Z.; Wang, S. Bin; Kimura, T.; Ok, Y. S.; Yamauchi, Y.; Chen, A. Z.; Wu, K. C. W. Nanoarchitectured Structure and Surface Biofunctionality of Mesoporous Silica Nanoparticles. *Advanced Materials*. Wiley-VCH Verlag June 1, 2020. https://doi.org/10.1002/adma.201907035.

(12) Lee, C. H.; Lin, T. S.; Mou, C. Y. Mesoporous Materials for Encapsulating Enzymes. *Nano Today*. April 2009, pp 165–179. https://doi.org/10.1016/j.nantod.2009.02.001.

(13) Kresge, C. T.; Leonowicz, M. E.; Roth, W. J.; Vartuli, J. C.; Beckt, J. S. *LETTERS TO NATURE Ordered Mesoporous Molecular Sieves Synthesized by a Liquid-Crystal Template Mechanism*; 1992.

(14) Monnier, A.; Schüth, F.; Huo, Q.; Kumar, D.; Margolese, D.; Maxwell, R. S.; Stucky, G. D.; Krishnamurty, M.; Petroff, P.; Firouzi, A.; Janicke, M.; Chmelka, B. F. Cooperative Formation of Inorganic-Organic Interfaces in the Synthesis of Silicate Mesostructures. *Science (1979)* **1993**, *261* (5126), 1299–1303. https://doi.org/10.1126/SCIENCE.261.5126.1299.

(15) Molaei, S.; Ghadermazi, M. Silver Complex Anchored on Ordered Mesoporous Coated Cobalt Ferrite Nanoparticles as Highly Reusable Catalyst for Synthesis of Tetrazole. *Applied Surface Science Advances* **2023**, *18*, 100519. https://doi.org/10.1016/j.apsadv.2023.100519.

(16) Bcsj.63.988.

(17) Zheng, H.; Gao, C.; Che, S. Amino and Quaternary Ammonium Group Functionalized Mesoporous Silica: An Efficient Ion-Exchange Method to Remove Anionic Surfactant from AMS. *Microporous and Mesoporous Materials* **2008**, *116* (1–3), 299–307. https://doi.org/10.1016/J.MICROMESO.2008.04.016.

(18) Zhao, D.; Feng, J.; Huo, Q.; Melosh, N.; Fredrickson, G. H.; Chmelka, B. F.; Stucky, G. D. Triblock Copolymer Syntheses of Mesoporous Silica with Periodic 50 to 300 Angstrom Pores. *Science (1979)* **1998**, *279* (5350), 548–552. https://doi.org/10.1126/SCIENCE.279.5350.548/ASSET/F429A4F4-

DACE-4061-B204-8E1CEA6F9EC7/ASSETS/GRAPHIC/SE0286194007.JPEG.

(19) Wu, S.-H.; Mou, C.-Y.; Lin, H.-P. Chemical Society Reviews Synthesis of Mesoporous Silica Nanoparticles †. *This journal is Cite this: Chem. Soc. Rev* **2013**, *42* (9), 3862. https://doi.org/10.1039/c3cs35405a.

(20) Fowler, C. E.; Khushalani, D.; Lebeau, B.; Mann, S. Nanoscale Materials with Mesostructured Interiors. *Advanced Materials* **2001**, *13* (9), 649–652. https://doi.org/10.1002/1521-4095(200105)13:9<649::AID-ADMA649>3.0.CO;2-G.

(21) Suzuki, K.; Ikari, K.; Imai, H. Synthesis of Silica Nanoparticles Having a Well-Ordered Mesostructure Using a Double Surfactant System. *J Am Chem Soc* **2003**, *126* (2), 462–463. https://doi.org/10.1021/ja038250d.

(22) Stober, W.; Fink, A.; Ernst Bohn, D. *Controlled Growth of Monodisperse Silica Spheres in the Micron Size Range 1*; 1968; Vol. 26.

(23) Lin, Y.-S.; Tsai, C.-P.; Huang, H.-Y.; Kuo, C.-T.; Hung, Y.; Huang, D.-M.; Chen, Y.-C.; Mou, C.-Y. Well-Ordered Mesoporous Silica Nanoparticles as Cell Markers. *Chemistry of Materials* **2005**, *17* (18), 4570–4573. https://doi.org/10.1021/cm051014c.

(24) Lu, F.; Wu, S. H.; Hung, Y.; Mou, C. Y. Size Effect on Cell Uptake in Well-Suspended, Uniform Mesoporous Silica Nanoparticles. *Small* **2009**, *5* (12), 1408–1413. https://doi.org/10.1002/smll.200900005.

(25) Pan, L.; He, Q.; Liu, J.; Chen, Y.; Ma, M.; Zhang, L.; Shi, J. Nuclear-Targeted Drug Delivery of TAT Peptide-Conjugated Monodisperse Mesoporous Silica Nanoparticles. *J. Am. Chem. Soc* **2012**, *134*, 37. https://doi.org/10.1021/ja211035w.

(26) Yamada, H.; Urata, C.; Aoyama, Y.; Osada, S.; Yamauchi, Y.; Kuroda, K. Preparation of Colloidal Mesoporous Silica Nanoparticles with Different

Diameters and Their Unique Degradation Behavior in Static Aqueous Systems. **2012**. https://doi.org/10.1021/cm3001688.

(27) Fuertes, A. B.; Valle-Vigón, P.; Sevilla, M. Synthesis of Colloidal Silica Nanoparticles of a Tunable Mesopore Size and Their Application to the Adsorption of Biomolecules. *J Colloid Interface Sci* **2010**, *349* (1), 173–180. https://doi.org/10.1016/J.JCIS.2010.05.041.

(28) Han, Y.; Ying, J. Y. Generalized Fluorocarbon-Surfactant-Mediated Synthesis of Nanoparticles with Various Mesoporous Structures. *Angewandte Chemie - International Edition* **2004**, *44* (2), 288–292. https://doi.org/10.1002/ANIE.200460892.

(29) Urata, C.; Aoyama, Y.; Tonegawa, A.; Yamauchi, Y.; Kuroda, K. Dialysis Process for the Removal of Surfactants to Form Colloidal Mesoporous Silica Nanoparticlesw COMMUNICATION Www.Rsc.Org/Chemcomm | ChemComm. **2009**. https://doi.org/10.1039/b908625k.

(30) Cauda, V.; Argyo, C.; G. Piercey, D.; Bein, T. "Liquid-Phase Calcination" of Colloidal Mesoporous Silica Nanoparticles in High-Boiling Solvents. *J Am Chem Soc* **2011**, *133* (17), 6484–6486. https://doi.org/10.1021/ja1067492.

(31) Liu, Y.-H.; Lin, H.-P.; Mou, C.-Y. Direct Method for Surface Silyl Functionalization of Mesoporous Silica. **2004**. https://doi.org/10.1021/la0358421.

(32) Zhang, H.; Li, Z.; Xu, P.; Wu, R.; Jiao, Z. A Facile Two Step Synthesis of Novel Chrysanthemum-like Mesoporous Silica Nanoparticles for Controlled Pyrene Releasew COMMUNICATION Www.Rsc.Org/Chemcomm | ChemComm. *Chem. Commun* **2010**, *46*, 6783–6785. https://doi.org/10.1039/c0cc01673j.

(33) Polshettiwar, V.; Cha, D.; Zhang, X.; Basset, J. M. High-Surface-Area Silica Nanospheres (KCC-1) with a Fibrous Morphology. *Angewandte Chemie - International Edition* **2010**, *49* (50), 9652–9656. https://doi.org/10.1002/ANIE.201003451.

(34) Moon, D.-S.; Lee, J.-K. Tunable Synthesis of Hierarchical Mesoporous Silica Nanoparticles with Radial Wrinkle Structure. *Langmuir* **2012**, *28* (33), 12341–12347.

(35) Zucca, P.; Sanjust, E. Inorganic Materials as Supports for Covalent Enzyme Immobilization: Methods and Mechanisms. *Molecules*. MDPI AG September 9, 2014, pp 14139–14194. https://doi.org/10.3390/molecules190914139.

(36) Barbosa, O.; Ortiz, C.; Angel Berenguer-Murcia, ´; Torres, R.; Rodrigues, R. C.; Fernandez-Lafuente, R. Glutaraldehyde in Bio-Catalysts Design: A Useful Crosslinker and a Versatile Tool in Enzyme Immobilization. **2014**. https://doi.org/10.1039/c3ra45991h.

Chapter 4

Experimental techniques

Contents

1. Morphological and textural characterization

Characterization of nanomaterials involves two main steps: morphological and structural analysis. Morphological characterization cannot be carried out with traditional optical microscopy due to resolution limitations to the wavelength of light. On the other hand, electron microscopy can allow the observation of materials in the nanoscale thanks to the very high resolution provided by the use of electrons instead of photons. In this paragraph, the principles of electron microscopy, together with the main analysis modes, are discussed.

1.1. Electron Microscopy

(This section is based on the works by R.F. Egerton,[1] Z. Wang,[2] N. Kalarikkal et al.,[3] W. Hawkes & John C. H. Spence et al.[4])

Electron microscopy is a morphological characterization technique that allows to unveil the size and the shape of unknown nanomaterials. The origins of this field of analysis are traceable back to the discovery of quantum mechanics and, more specifically, of the double particle-wave nature of electrons. More specifically, according to de Broglie's equation, the wavelength of an electron is inversely proportional to momentum and, thus, to the speed:

$$\lambda = \frac{h}{p} = \frac{h}{mv} \quad (1.1)$$

where h is the Plank constant ($6.626 \cdot 10^{-34}$ J·s), whereas λ, p, m and v are the wavelength, the momentum, the mass and the speed of the electron, respectively. Therefore, hitting the sample to be analyzed with properly accelerated electrons would provide very low resolution limits. To give some numbers, if velocity is fixed at $\sim 10^6$ m/s, $\lambda < 1\, nm$. There are several types of electron microscopes, which differ from each other depending on the nature of the interaction with the atoms of the specimen. Indeed, electrons can be transmitted through the sample, diffracted, absorbed or scattered. The interaction between the incident primary electron and an

atomic nucleus leads to elastic scattering, causing almost no transfer of energy. On the other hand, the interaction between the rapidly moving primary electron and atomic electrons leads to inelastic scattering, wherein the transmitted electron can experience a significant loss of energy. Moreover, most of the electrons are usually scattered forward, even if an aliquot of backscattering is expected.

1.1.1. Transmission electron microscopy (TEM)

In a similar way as light does in a biological optical microscope, in transmission electron microscopy (TEM) electrons penetrate within a thin specimen and are then imaged by the appropriate lenses. A modern transmission electron microscope is described in **Figure 1.1.**

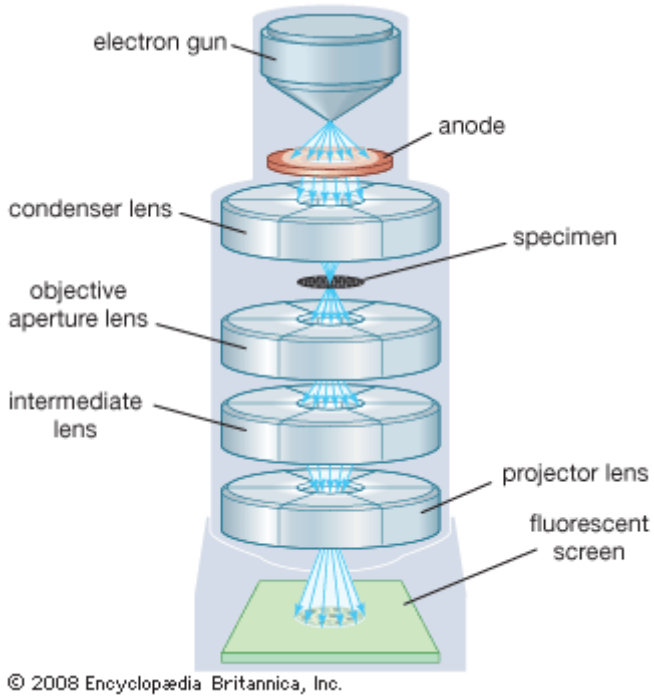

Figure 1.1. Graphical scheme of a transmission electron microscope.[5]

Firstly, it includes an electron gun responsible for generating the electron beam, along with the condenser system that focuses this beam onto the object of interest. Secondly, there is the image-producing system, comprising the objective lens, a

movable specimen stage, and intermediate and projector lenses. This system is crucial for focusing the electrons passing through the specimen to create a real and highly magnified image. Lastly, the TEM features an image-recording system, tasked with converting the electron image into a format perceptible to the human eye. Typically, this system involves a fluorescent screen for image viewing and focusing, as well as a digital camera for producing permanent records. Additionally, the TEM requires a vacuum system, encompassing pumps, associated gauges and valves, as well as power supplies to operate effectively. The electron source, or cathode, consists of a heated V-shaped tungsten filament or, in high-performance instruments, a sharply pointed rod made of materials like lanthanum hexaboride (LaB_6). Encircling the filament is a control grid, often referred to as a Wehnelt cylinder, featuring a central aperture aligned along the column's axis. The cathode's apex is positioned at or slightly above or below this aperture. Both the cathode and control grid are maintained at a negative potential corresponding to the desired accelerating voltage and are electrically insulated from the remainder of the instrument. The electron gun's final electrode is the anode, configured as a disk with a central hole. Electrons emitted from the cathode and shield are accelerated towards the anode. Given sufficient high voltage stabilization, they traverse the central aperture with constant energy. Precise control and alignment of the electron gun are imperative for optimal performance. The intensity and angular aperture of the electron beam are regulated by the condenser lens system situated between the gun and the specimen. While a single lens may converge the beam onto the object, a more common approach involves using a double condenser. In this setup, the first lens is potent, producing a diminished image of the source. Subsequently, the second lens images this reduced source image onto the object. This arrangement optimizes space efficiency between the electron gun and the object stage and enhances flexibility. The size reduction of the source image (and consequently, the final illuminated area on the specimen) can be widely adjusted by controlling the first lens. Utilizing a small spot size minimizes specimen disturbances resulting from heating and

irradiation. The specimen grid is housed in a small holder within a movable specimen stage. Typically, the objective lens has a short focal length, ranging from 1 to 5 mm, and it generates a real intermediate image. This intermediate image is then further magnified by the projector lens or lenses. A single projector lens can offer a magnification range of 5:1. Additionally, by employing interchangeable pole pieces in the projector, a broader range of magnifications can be achieved. In modern instruments, two projector lenses, with one designated as the intermediate lens, are often utilized to enable a more extensive magnification range without a proportional increase in the microscope column's physical length. To maintain image stability and brightness for practical purposes, the microscope is commonly set to achieve a final magnification of 1000–250000× on the screen. If a higher final magnification is needed, it can be attained through photographic or digital enlargement. The quality of the ultimate image in the electron microscope relies significantly on the precision of mechanical and electrical adjustments that align the various lenses with one another and with the illuminating system. These lenses necessitate power supplies with a high degree of stability. For the highest resolution standards, electronic stabilization to better than one part in a million becomes imperative. The operation of a modern electron microscope is managed by a computer, and dedicated software is readily accessible. The electron image, being monochromatic, needs to be rendered visible to the human eye. This can be achieved by directing the electrons onto a fluorescent screen positioned at the microscope column's base. Alternatively, the image can be digitally captured for display on a computer monitor.
A high-voltage electron microscope is a type of electron microscope specifically designed to operate at accelerating voltages exceeding the typical 200–300 kV utilized in conventional transmission electron microscopes. Currently available high-voltage microscopes, produced for commercial use, can accommodate accelerating voltages of up to 1500 kV. These instruments offer several advantages over conventional transmission electron microscopes: (1) the theoretical resolving power improves with higher accelerating voltages; (2) the electron beam easily penetrates

thick specimens; (3) chromatic aberration caused by energy losses and specimen scattering is reduced; and (4) there is a decrease in specimen heating and irradiation damage, particularly for organic samples.

1.1.2. Scanning electron microscopy (SEM)

The scanning electron microscope (SEM), a specific type of electron microscope designed for direct examination of solid object surfaces, employs a focused beam of electrons with relatively low energy as a probe. This electron beam is systematically scanned over the specimen. The electron source and electromagnetic lenses responsible for generating and focusing the beam resemble those used in the transmission electron microscope (**Figure 1.2**).

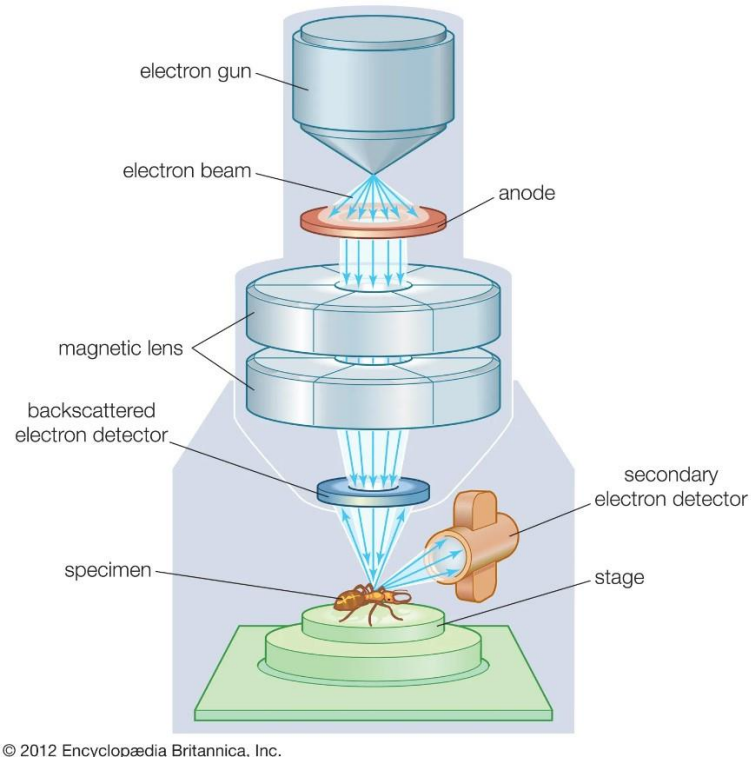

Figure 1.2. Graphical scheme of a scanning electron microscope.[6]

The action of the electron beam prompts the emission of high-energy backscattered electrons and low-energy secondary electrons from the specimen's surface. For SEM

examination, elaborate specimen-preparation techniques are unnecessary, and the microscope can accommodate large and bulky specimens. Ideally, the specimen should be made electrically conducting to obtain a sharp image; this is often achieved by evaporating a thin film of metal, such as gold, onto the specimen in a vacuum. However, if the SEM operates at 1–3 kV of energy, nonconducting specimens can be examined without the need for metallic coating. SEM, with its ability to finely focus an electron beam on a nanometer scale, offers high topographical detail. While SEM alone does not provide chemical information, the electron beam generates X-rays from the sample species. Analyzing these X-rays with an energy-dispersive (EDX) analyzer allows for elemental mapping of the sample's surface layer. In traditional SEM, samples must be coated with a conducting layer to overcome surface charging caused by the electron beam. This coating limits the surface sensitivity of the SEM-EDX combination, requiring high-energy incident beams to penetrate the coating. However, recent SEM techniques use a lower-energy electron beam, eliminating the issue of surface charging and the need for coating. This advancement allows the SEM-EDX combination to function as a surface analytical technique at very low-incident electron energies, such as 1–3 keV.

1.1.3. Energy-Dispersive X-ray Spectroscopy (EDX)

The operational principle of Energy-Dispersive X-ray Spectroscopy (EDX) involves the electron beam striking the specimen surface, causing the electrons within the atoms of that region to enter an excited state. When these electrons return to their ground state, they emit characteristic X-rays. These emitted X-rays are then collected by the X-ray detector, enabling the generation of an image. The X-rays provide information about the elemental composition of the analyzed area. Consequently, EDS can identify elements ranging from carbon to uranium, even in minute quantities down to 1.0 wt%. When integrated with Scanning Electron Microscopy (SEM), the analysis area can be precisely adjusted based on the magnification used for specimen observation. A basic EDX system comprises three primary

components: the X-ray detector, a pulse processor (a box of electronics measuring voltage pulses corresponding to X-ray energies), and a computer. The X-ray detector is strategically positioned to capture X-rays emitted from the specimen. As an X-ray enters the detector, it generates a small current, subsequently converted into a voltage pulse. The size of the voltage pulse is proportional to the energy of the X-ray. The computer records these voltage pulses over a specific duration (e.g., 60 seconds) and presents them as a histogram. The histogram displays a spectrum of measured X-ray energies, allowing for the identification of elements present in the specimen. Since X-rays produced by electron interactions do not result in volume loss of the sample, repeated analysis of the same materials is possible, rendering SEM-EDS analysis non-destructive.

1.1.4. Scanning-transmission electron microscopy (STEM)

The fine-probe/scanning technique is applicable to thin (transmission) specimens, resulting in the creation of a scanning-transmission electron microscope (STEM, **Figure 1.3**). Instead of capturing secondary electrons, the typical approach involves recording primary electrons that scatter in a specific direction and emerge from the beam-exit surface. To match the spatial resolution of a conventional Transmission Electron Microscope (TEM), it is essential to focus the electrons into a probe with sub-nanometer dimensions. To achieve this, the traditional hot-filament electron source is often substituted with a field-emission source. In this setup, electrons are emitted from a sharp tungsten tip under the influence of a strong electric field.

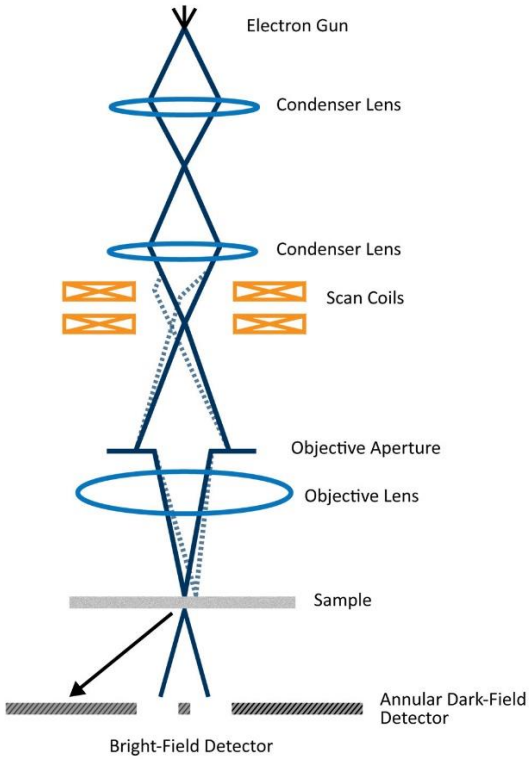

Figure 1.3. Graphical sketch of the main components of a STEM.[4]

1.2. N_2 physisorption: analysis of specific surface area and porosimetry

(This section is based on the works by G. Fagerlund,[7] M. Schmal,[8] P. Barret et al.[9] and S. Fu[10])

Heterogeneous catalysts are usually expected to have large surface areas in order to ensure numerous contact sites for the reactant. Moreover, extended porosity is a mandatory requirement to allow easy diffusion of both substrates and products. As concerns heterogeneous biocatalysts, they are made of an insoluble carrier in which enzymes are loaded. So, the morphology of the carriers needs to be properly designed in order to load huge amounts of proteins. Furthermore, pore size should be adequately tailored to match enzyme dimensions. Specific surface area (SSA) and pore size distribution are usually determined by N_2 physisorption. More specifically,

the Brunauer-Emmett-Teller (BET) model is used to calculate SSA, whereas pore size is derived from the Barrett-Joyner-Halenda (BJH) model.

1.2.1. The Brunauer-Emmet-Teller (BET) theory

The fundamentals of BET theory lie in the physics of adsorption of gases onto porous solids. More specifically, it is known that under equilibrium conditions, at a specific temperature *T*, the physical adsorption of a specific gas by a porous material depends on both the relative vapor pressure of the gas $\frac{p}{p_0}$ and on the total surface area of the material itself. The amount of adsorbed gas at temperature *T* can be related to relative vapor pressure as building the adsorption isotherm. Brunauer identified four different adsorption isotherms (**Figure 1.4**) and the profile of each isotherm is a hallmark of the nature of the solid.

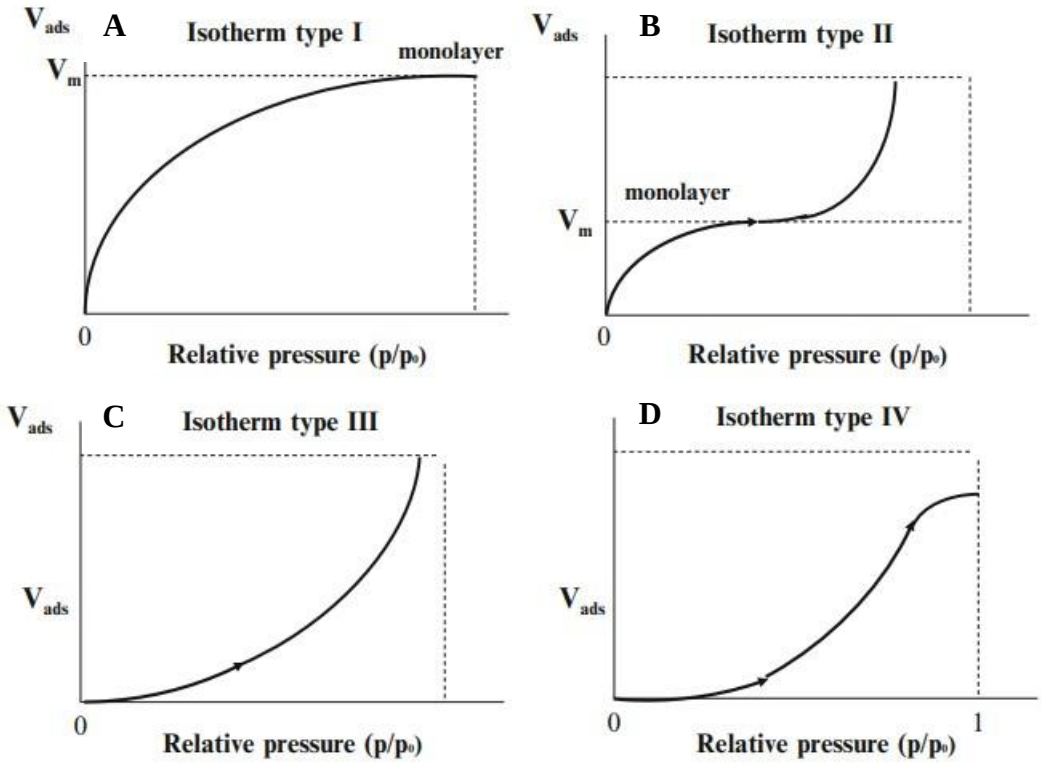

Figure 1.4. Adsorbed volumes V_{ads} plotted against the relative pressure p/p_0. V_m is the volume of the monolayer.[11]

Type I isotherm (**Figure 1.4 A**) is typical of solids with extremely narrow pores, like gels. Type II and type III isotherms (**Figure 1.4 B, C)** describe the adsorption profiles of non-porous solids, whereas the behavior of porous materials is exclusively portraited by type IV isotherms(**Figure 1.4 D)**, obtained by predicting a plateau phase at high $\frac{p}{p_0}$ caused by the phenomenon of capillary condensation that is the formation of a curved meniscus within the pore. The specific surface area SSA is calculated as prescribed by equation 1.2:

$$SSA = \frac{X_m}{M} N_A A_m \quad (1.2)$$

where X_m is the mass of adsorbate forming a monolayer on the unit mass of adsorbent, M is the molecular weight of adsorbate, A_m is the area occupied by one adsorbate molecule in the monolayer and N_A is Avogadro's number. As imaginable, it is rather tricky to estimate X_m. To do this, a series of hypotheses were priorly assumed:

I. The material's surface is composed of numerous discrete adsorption sites, creating a homogeneous surface.

II. At a specific vapor pressure, varying molecules are adsorbed on each site, forming multiple stacked layers.

III. The heat of adsorption and condensation constants in layers above the first are consistent with those of the bulk liquid (a crucial assumption).

IV. The theory is theoretically applicable only to nonporous materials, as at saturation, the number of layers becomes infinite.

V. A molecule beneath another cannot evaporate, representing another crucial assumption.

VI. There is no horizontal interaction between molecules on different sites.

VII. At dynamic equilibrium, the number of molecules evaporating from a layer is equal to the number condensing on the layer below, ensuring a balance between condensation and evaporation.

These assumptions lead to the following equation:

$$\frac{p/p-p_0}{X} = \frac{1}{X_m \cdot C} + \frac{C-1}{X_m \cdot C}\frac{p}{p_0} \quad (1.3)$$

with X as the mass adsorbed at relative vapor pressure p/p_0 whereas C is a constant referring to the relative lifetime of molecules in the condensed state with respect to higher layers (i.e. bulk liquid). In other words, it is an approximated measure of difference between the heat of adsorption in the first layer E_1 and the latent heat of condensation L:

$$E_1 - L \approx RTlnC \quad (1.4)$$

According to equation 1.3, the isotherm can be only of type II or III, and the value of C determines the nature of the isotherm: if $C \leq 2$, type III isotherm is obtained. For higher values of C, the curves gain an inflection point which coincides with $\frac{X}{X_m} = 1$ for $C = 9$ and $C \to \infty$. For high C values, $\frac{X}{X_m} = 1$ means that the first adsorption layer is completed. If $2 < C \leq 9$, the inflection point is placed below monolayer coverage X_m, whereas for $C > 9$ it occurs at coverages up to 16% higher than X_m. The value of X_m is usually estimated graphically from the shape of the curves. Indeed, adsorption isotherms might exhibit a linear region. The adsorption value at the beginning of the linear part (known as B-point) is approximated with X_m. However, this method works well only if C is high enough to have and well recognizable linear region. Indeed, for low C, adsorption occurs simultaneously in both the 1st and the 2nd layers and X_m is not estimable.
In theory, the isotherm of a porous material typically falls into type IV. The primary challenge associated with these isotherms is the tendency to display hysteresis between adsorption and desorption **(Figure 1.5)**.

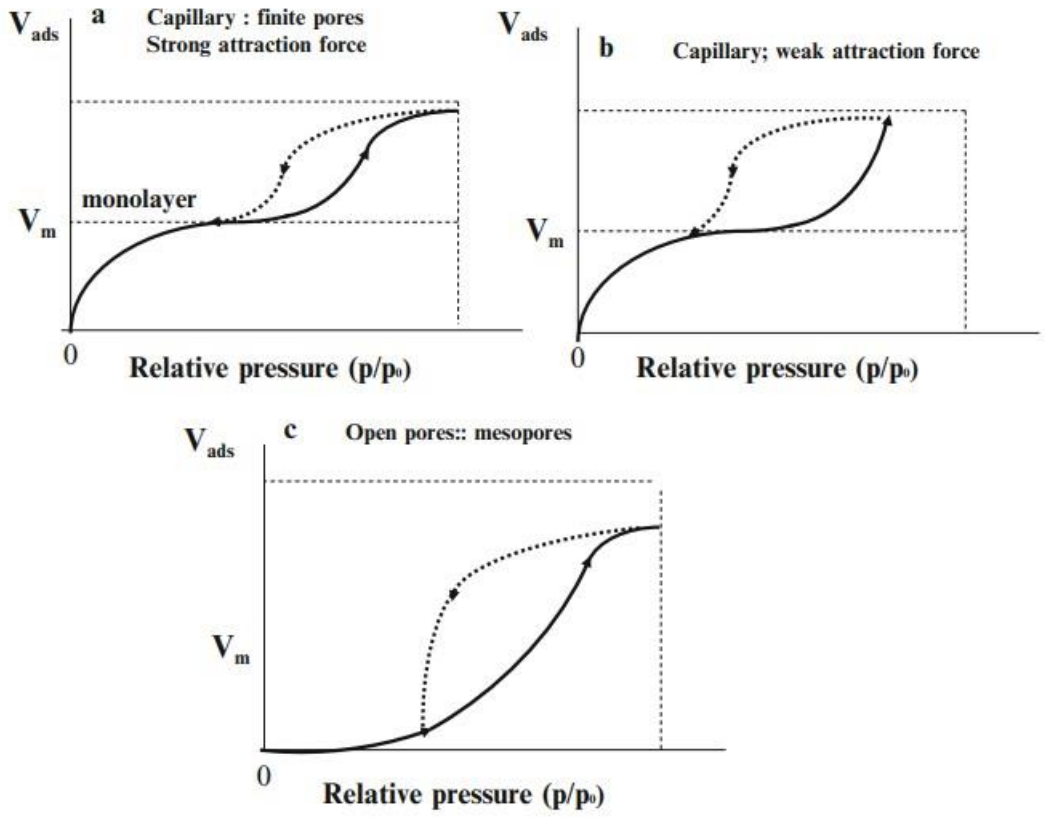

Figure 1.5. Hysteresis curves of adsorption–desorption.[12]

This hysteresis is influenced by capillary condensation in extremely small pores, where the adsorbate can create a curved meniscus with a radius sufficiently small to impact vapor pressure. Nevertheless, the segment of the isotherm utilized for specific surface calculations, ranging from zero pressure to the completion of the first monolayer (approximately at the inflection point), typically shows no hysteresis between adsorption and desorption. Consequently, the same calculation procedure can be applied to determine specific surface from type IV isotherms as from type II isotherms. If $\frac{p}{X(p-p_0)}$ from equation 1.3 is plotted over $p - p_0$, a straight line is obtained only in monolayer-adsorption regime, that is as $0.05 \leq p - p_0 \leq 0.30$ (**Figure 1.6**).

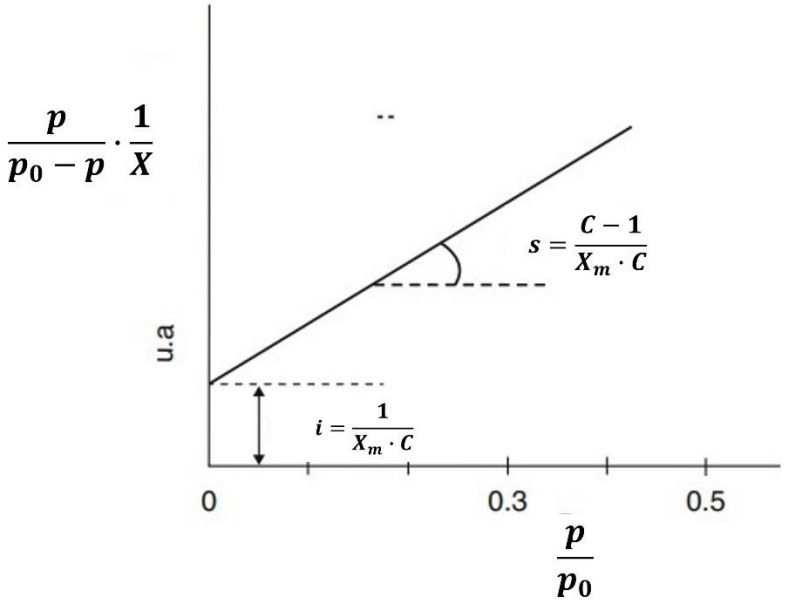

Figure 1.6. Graphical representation of the BET equation 1.3.[7] (Readapted)

The intercept i and the slope s of the line are thus equal to $\frac{1}{X_m \cdot C}$ and $\frac{C-1}{X_m \cdot C}$, respectively. Therefore, it is possible to calculate X_m and C:

$$(1.5) \quad X_m = \frac{1}{s+1}$$

$$(1.6) \quad C = \frac{s}{i} + 1$$

In the assumption of close-packing of the adsorbate molecules, A_m is calculated as:

$$(1.7) \quad A_m = 1.091\left(\frac{M}{\rho N_A}\right)^{2/3}$$

where ρ is the density of the adsorbate. Finally, SSA is calculated as:

$$(1.8) \quad SSA = \frac{N_A A_m}{M} \frac{1}{s+1}$$

Even if it underwent modifications in time, leading to describe adsorption isotherms of all types, the BET theory has solid fundamentals. Indeed, most of measurements are carried out fixing $C \gg 1$. This condition imposes that $\frac{X}{X_m}$ only depends on the area of the adsorbing surface.

1.2.2. The Barrett-Joyner-Halenda (BJH) model

The low-temperature nitrogen adsorption method typically employs the BJH method for calculating pore size distribution. This approach, grounded in the Kelvin equation (1.9), determines pore size distribution directly from the desorption isotherm within the absorption/desorption isotherm curve. However, three key assumptions must be met: (a) the pore passage is rigid and suitable for cylindrical pores, (b) no micropores are present, and (c) at the highest relative pressure, all the relevant pores have been filled. The capillary radius (r_k) is calculated during capillary condensation by applying the Kelvin equation:

$$(1.9) \quad ln\frac{p}{p_0} = -\frac{2\gamma\tilde{v}cos\theta}{r_k RT}$$

where $\frac{p}{p_0}$ represents the equilibrium pressure over the saturated vapor pressure of the adsorbed gas, $\tilde{v}$ is the mole volume of liquid nitrogen, and γ denotes the interfacial tension of liquid nitrogen. Subsequently, a relationship curve between the volume of liquid nitrogen (V) and capillary radius (r_k) is established. This curve serves as the cumulative pore volume distribution, as shown in **figure 1.7**. The derivative of this curve gives the pore size distribution.

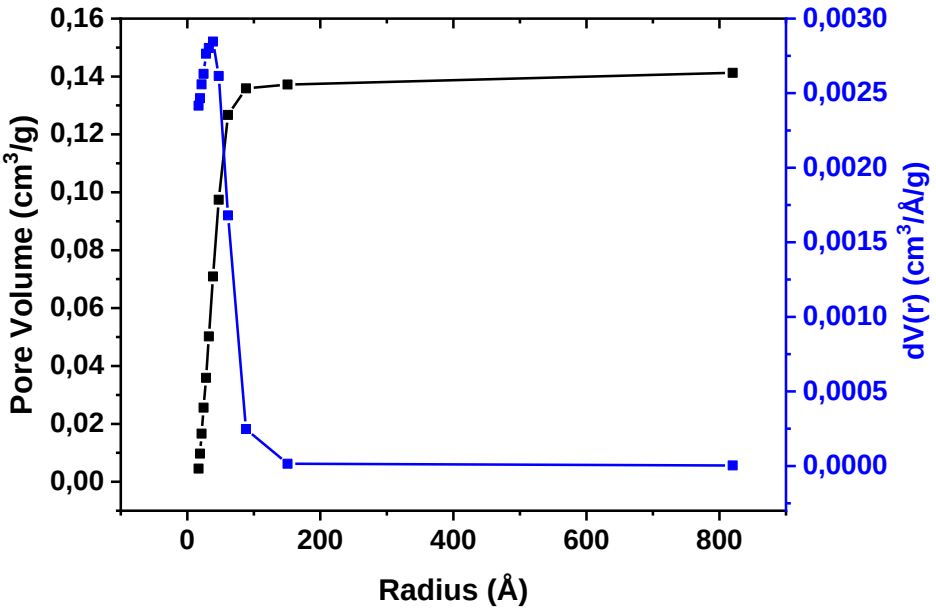

Figure 1.7. Cumulative pore volume (black curve) and pore size distribution (blue curve) for hydrothermally synthesized CeO_2 nanoparticles.[13]

2. Thermal characterization

In this paragraph, the thermal characterization of the materials is presented. More specifically, thermogravimetric analysis (TGA) was performed to assess the amount of enzyme immobilized into the nanocarriers.

(This section is based on the work by P. Gabbott[14])

2.1. Thermogravimetric Analysis

2.1.1. Applications

Thermogravimetric analysis (TGA) is a method employed to assess both the quantity and rate of weight alteration in a substance concerning temperature or time. This analysis occurs within various atmospheres, both reducing, oxidizing and inert, and even in a vacuum. Its primary applications include determining material composition and projecting thermal stability, particularly at temperatures reaching up to 1200°C.

This technique proves valuable for characterizing materials that undergo weight fluctuations due to processes like decomposition, oxidation, or dehydration. Its scope covers the analysis of inorganic materials, metals, polymers, plastics, ceramics, glasses, and composite materials. TGA finds diverse applications, including forecasting the thermal and oxidative stability of materials, elucidating the composition of multicomponent systems, estimating product lifetimes, understanding decomposition kinetics, assessing the impact of reactive or corrosive atmospheres, and determining moisture and volatile content. In the realm of nanotechnology, extensive research has been conducted using TGA to predict the thermal stability of nanomaterials. Moreover, TGA serves as a tool to reveal evidence of surface modification in nanoparticles by other functional groups, along with quantifying the presence of surface-modifying agents attached to the nanoparticles.

2.1.2. The instrument

The instrument is termed thermobalance and it measures changes in weight as a function of time and temperature. **Figure 2.1 A** reports a graphical sketch of the instrument components. The experimental setups usually differ from the type of sample loading. Indeed, the sample can be top-loaded, bottom-loaded or side-loaded. In **Figure 2.1 B,** the section of a side-loading apparatus is represented. It has a horizontal orientation, unlike the other configurations. The sample holder is firmly affixed to the extremity of the balance arm in the horizontal setup.

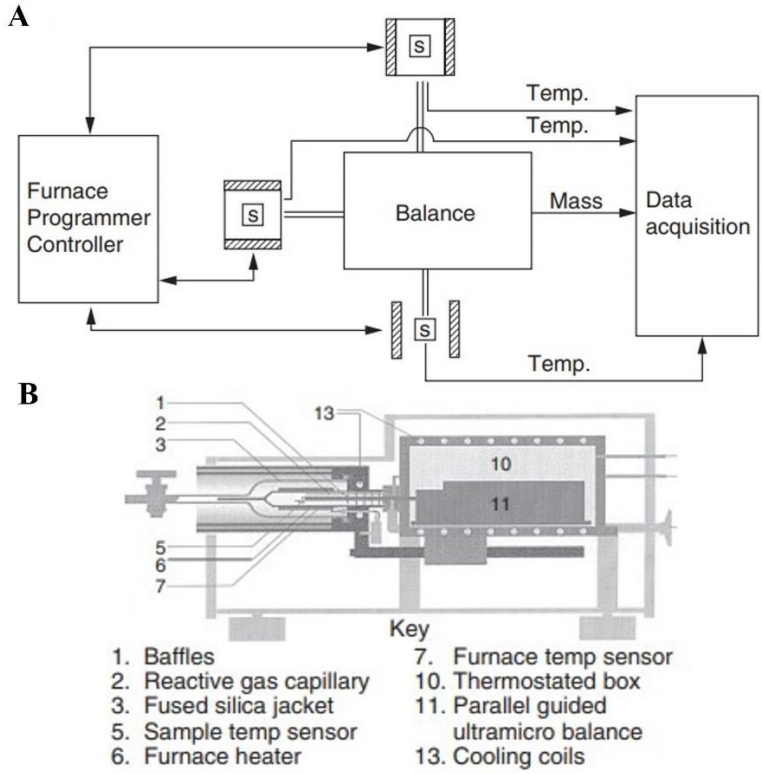

Figure 2.1. General arrangement of components in a thermobalance (A). Side loading model by Mettler-Toledo (B).[15]

Some instruments are equipped with two crucibles, one of which is meant to remain empty during the measurement. Indeed, the decrease in density of a gas during heating at constant pressure leads to an apparent weight gain by the sample. So, TGA thermal profiles are usually automatically corrected by baseline subtraction.

2.1.3. Sample preparation and measurement performance

Sample preparation is critical for collecting reliable data. Indeed, the diffusion rate of reaction products and the reaction progression are significantly influenced by the morphology of the sample. Simultaneously, the sample's morphology plays a role in regulating heat transfer. Additionally, the mass employed in experimental procedures impacts the rate of weight loss, attributable to similar diffusion and heat transfer mechanisms. Ensuring a consistent and reproducible sample preparation

technique is crucial in quality control assessments. When developing quality control methods, it is imperative to examine the method's resilience to external factors, including variations in sample preparation. Maintaining uniform sample masses is fundamental to generate reproducible TGA data. Besides sample preparation, numerous factors can affect TGA measurements. The systematic temperature deviation between actual and measured values, affected by heating rate, can be addressed through calibration, often using thermally conductive pure metals. Real samples like polymers may still show residual temperature dependence post-adjustment. Chemical reactions in samples are influenced by heating rates, with higher rates shifting reactions to higher temperatures. Careful selection of heating rates is crucial, especially when dealing with closely spaced starting temperatures for secondary reactions. Inappropriate rates can lead to overlapping reactions and hinder detection, but judicious choices can help differentiate reactions. Crucible material should not impact the sample reaction, and alumina (aluminum oxide) crucibles are commonly used for TGA measurements due to their ability to withstand temperatures over 1600°C.

2.1.4. Data interpretation

Figure 2.2 reports the typical shape of a TGA curve for thermal decomposition associated with production of volatile compounds.

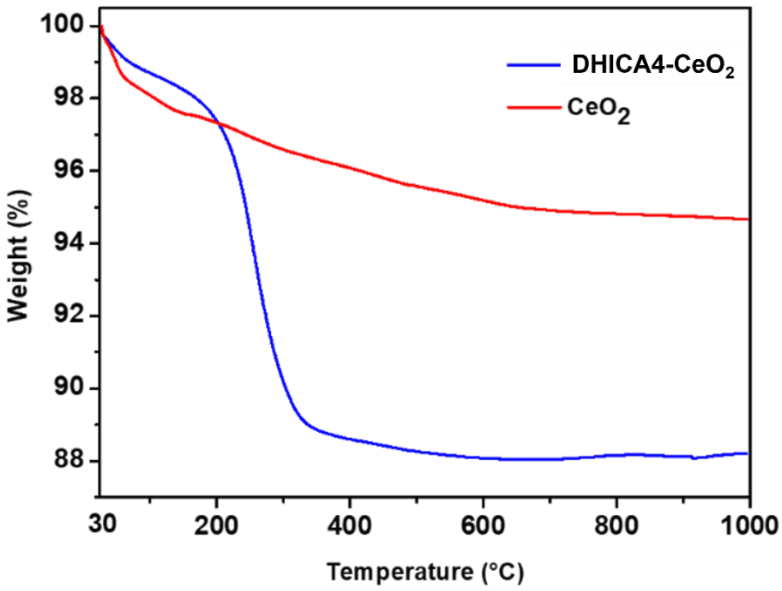

Figure 2.2. TGA curves for bare and melanin-coated CeO_2 nanoparticles recorded under air atmosphere.[13]

This technique is useful to calculate the amount of an organic ligand bound to an inorganic carrier. Indeed, the percentage weight loss of a sample is estimated as follows:

$$(2.1)\quad \Delta w = \frac{w_0 - w_f}{w_0} \cdot 100$$

where w_0 and w_f are the initial and the final sample weight, respectively. The overall percentage amount of ligand can be evaluated as the difference between the weight losses of functionalized and bare carriers. It is better to subtract the moisture content before doing calculation. Further information can be obtained by the analysis of the slope of the thermograms. Indeed, changes in slope may be related to different volatilization phenomena, involving different chemical species. In this case, the differential thermogravimetric (DTG) curve, which is the 1st derivative of TGA curve, can provide the decomposition temperature and rate for every species.

Moreover, single-peak integration results in the evaluation of the content of the volatized compound.

3. Analytical characterization

3.1. Fourier-Transform Infrared (FTIR) Spectroscopy

Infrared spectroscopy provides the characterization of a sample through irradiation with infrared (IR) light. As IR radiation hits a sample, it can be either transmitted or absorbed. Adsorption results in vibration modes in the sample bonds, and each mode occurs at a specific frequency. Therefore, the adsorption (or transmission) spectrum of a sample represents a fingerprint of the sample itself. Moreover, the intensity of the peaks gives an indirect measure of the amount of a specific functionality. This application is especially valuable in scenarios involving surface-modified nanomaterials aimed at enhancing their affinity, reactivity, or compatibility. When examining a nanomaterial with FTIR, it reveals the presence of specific functional groups, guiding the determination of an appropriate surface modification strategy based on the identified groups. Additionally, it proves beneficial in characterizing the conducted surface modification, as the emergence of new groups signifies the success of the reaction.

(This section is based on the works by J. Ojeda et al.[16])

3.1.1. Principles of infrared spectroscopy

Three different regions are usually identified to classify IR radiation, depending on the wavenumber $\tilde{\upsilon}$ ($\frac{2\pi}{\lambda}$):

- near-IR (NIR): 400-10 cm^{-1}
- mid-IR (MIR): 4000-400 cm^{-1}
- far-IR (FIR): 14000-4000 cm^{-1}

Even if IR photons do not have enough energy to result in electronic transition like in UV-vis spectroscopy, they can trigger vibration modes in the atoms involved in

a chemical bond. Chemical bonds exhibit characteristic vibrational frequencies, and upon exposure to infrared (IR) radiation, they absorb the radiation at frequencies corresponding to their vibration modes. The measurement of radiation absorption frequencies generates a spectrum, enabling the identification of functional groups and compounds.

3.1.2. The spectrometer

The main components of a FTIR spectrometer are reported in **Figure 3.1**.

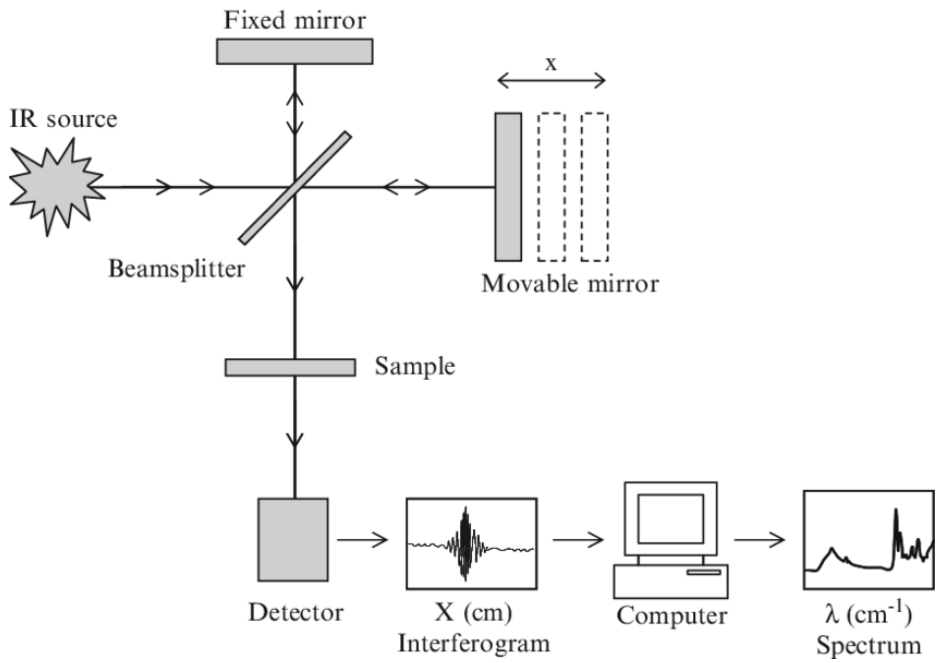

Figure 3.1. Graphical scheme of a Fourier transform infrared (FTIR) spectrometer.[16]

The IR beam is emitted by the energy source (usually a rare-earth oxide or SiC heated up to 1500 K), passes through a slit (the width regulating the amount of energy hitting the sample) and enters the Michelson interferometer. There, it is divided into two beams: one directed towards a fixed mirror, the other one towards a moving mirror. Reflected beams then recombine and, depending on the position of the movable

mirror, they experience constructive or destructive interference. Again, two beams originate from recombination, one directed back to the source and the other one towards the sample section. Some frequencies of the radiation are adsorbed, the remaining are transmitted and reach the detector, which accumulates the signal as an interferogram. Since the scanning time is by the order of 1s, hundreds of signals are accumulated, giving the resulting interferogram. The information carried by the interferogram are decoded by the computer by means of Fourier transformation, which assign to each wavenumber the corresponding peak. The analysis can be performed on both liquid, gaseous and solid samples. In detail, the preparation of solid samples usually prescribes fine grinding, dilution with KBr (chosen as background) up to 0.5 wt.% and production of a pellet.

3.1.3. Analysis of the infrared spectra

The energy of a molecule is the sum of four different contributions:

$$E_{molecule} = E_{electronic} + E_{rotational} + E_{translational} + E_{vibrational} \quad (3.1)$$

The electronic contribution refers to the energy required to allow electronic transitions. This amount of energy is satisfied only as irradiating the molecules with UV or visible light. Rotational energy is provided by microwave absorption. Translational energy is associated with the displacement motion allowed by the thermal energy of the matter. Absorption of IR radiation is responsible for the vibrational contribution: the atoms involved in a chemical bonds are interested by vibrational motion. IR radiation is absorbed only if a change in the dipole moment of the molecule occurs. More specifically, the frequency of the radiation has to be matched by the natural vibration frequency of the molecule resulting in the amplification of the molecular vibration. Two main vibrational modes exist: stretching and bending (**Figure 3.2**).

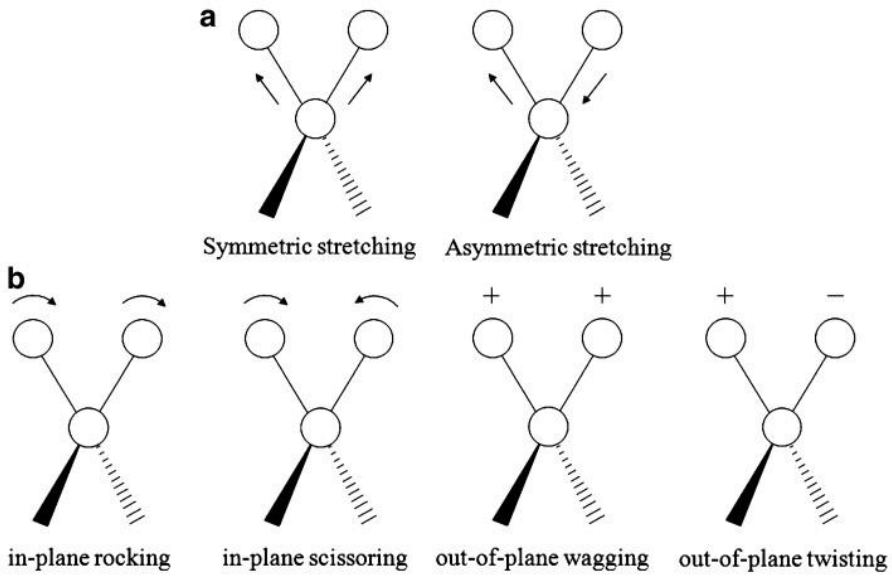

Figure 3.2. Molecular stretching (a) and bending (b) vibrations.[16]

Stretching vibration is characterized by mutual approach and distancing of the atoms along the bond axis. On the other hand, in bending vibrations bond length remains the same but bond angles change. The easiest way to model a chemical bond is to imagine the atoms as two equivalent masses linked by a spring. According to Hook's law, as one atom moves from the equilibrium position by a distance x, the elastic force F is equal to:

$$(3.2)\ F = -kx$$

with k as the elastic constant of the spring. The application of the Newton's principle leads to:

$$(3.3)\ ma = -kx$$

where m is the atomic mass and a is the acceleration. Since $a = \frac{d_x^2}{dt^2}$:

$$(3.4)\ m\frac{d_x^2}{dt^2} = -kx$$

That is the equation of a harmonic oscillator, whose solution is well-known:

$$(3.5)\ x = x_0 \sin(2\pi\upsilon t + \varphi)$$

Substituting x with expression 3.5 in equation 3.4 and calculating the second derivative:

$$(3.6)\ \frac{m}{k} = \frac{1}{4\pi^2\upsilon^2}$$

The fundamental vibration frequency υ is thus calculated as:

$$(3.7)\ \upsilon = \frac{1}{2\pi}\sqrt{\frac{k}{m}}$$

If a diatomic system is considered, the mass of the single atom is replaced by the reduced mass μ:

$$(3.8)\ \mu = \frac{m_1+m_2}{m_1 m_2}$$

Equation 3.7 is rearrangeable to obtain the fundamental vibration wavenumber $\bar{\upsilon}$ considering that $\bar{\upsilon} = \frac{\upsilon}{c}$:

$$(3.9)\ )\ \bar{\upsilon} = \frac{1}{2\pi c}\sqrt{\frac{k}{\mu}}$$

However, the discussion becomes more articulated as extended to multiple atoms molecules. Indeed, the spatial position of every atom is defined by three coordinates, x, y, z, and every independent mode corresponds to a degree of freedom. So, for a N-atomic molecule, 3N degrees of freedom exist. Translational and rotational modes are assigned three degrees of freedom each. Therefore, vibrational modes account for 3N-6 degrees of freedom. For instance, a three-atomic molecule exhibits three vibrational degrees of freedom, one for vibrational bond length for every bond and one for vibrational bond angle. On the other hand, 3N-5 vibrational degrees of freedom are attributed to linear molecules. So, for a diatomic molecule, only one degree of freedom is expected (bond length). The infrared spectrum is determined by assessing the intensity of infrared radiation both before and after traversing the sample. The percentage of transmittance ($\%T$) is defined as:

$$(3.10)\ \%T = \frac{I}{I_0} \cdot 100$$

Where I_0 represents the intensity of the infrared beam before passing through the sample, and I is the intensity after passing through the sample. Absorbance (A) can be derived from the transmittance spectrum using the equation:

$$(3.11)\ A = -\log(\%T)$$

For quantitative analysis, absorbance spectra are widely employed. According to Lambert-Beer's law, if the absorbance (A), path length (d), and molar absorptivity (ε) are known, the concentration (c) of the substance can be determined using the equation:

$$(3.12)\ A = \varepsilon c d$$

The final infrared spectrum, whether in absorbance or transmittance, should be devoid of instrumental and environmental contributions, exclusively showcasing the sample's characteristics. Thus, it is essential to capture a background spectrum beforehand, and the ultimate spectrum should result from normalizing the sample's single beam against the background. This characterization technique brings a lot of advantages, such as:

- It offers a non-destructive approach, delivering a precise measurement method without the need for external calibration.
- Speed enhancement is achieved by collecting a scan every second.
- Increased sensitivity is possible by scanning every second and aggregating scans to ratio out random noise.
- Notably, it boasts greater optical throughput.
- Mechanically, it is simple, featuring only one moving part.

3.1.4. The attenuated total reflectance (ATR) mode

Attenuated Total Reflectance (ATR) serves as a common sampling technique in Fourier-transform infrared spectroscopy (FTIR). Specifically, ATR is grounded in total internal reflection with infrared light and sample interaction occurring exclusively at the point where the radiation is reflected, without the penetration of the IR beam into the sample. A FTIR spectrometer, comprising an IR source, an ATR crystal, and a detector, facilitates ATR analysis. The IR source emits infrared radiation, the ATR crystal, in direct contact with the sample, is responsible for internal reflection, and the detector analyzes the outgoing radiation. Initially, an infrared beam is generated by the IR source and directed to the base of the ATR crystal. The radiation propagates through the crystal until it reaches the surface in contact with the sample. As the crystal and sample possess different refractive indices, the infrared light changes its direction of propagation when transitioning from the crystal to the sample. However, if the crystal has a higher refractive index than the sample and the radiation's angle of incidence exceeds the critical angle, refraction results in total internal reflection, as described in **Figure 3.3**.

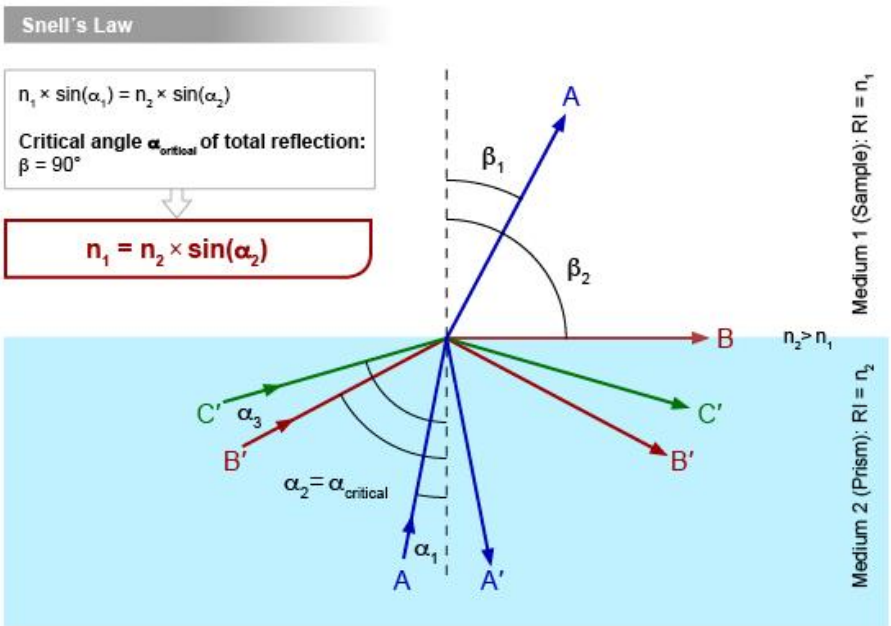

Figure 3.3. Total internal reflection of the light. [17]

Common materials for ATR crystals include zinc selenide (ZnSe), germanium (Ge), and diamond due to their high refractive indices. Zinc selenide is often used for routine applications but is sensitive to acid and alkaline samples and lacks resistance to hard samples; germanium is suitable for samples with high refractive indices, while diamond is an excellent choice due to its hardness and resistance. When the infrared radiation reflects at the contact points (nodes) between the sample and the crystal, a small portion of this light, termed the evanescent wave, penetrates the sample, where it exponentially decays. Typically, this wave can penetrate the sample only for a few microns; penetration depth d_p is expressed as follows:

$$(3.13)\ d_p = \frac{\lambda_c}{2\pi[sen^2\theta - \left(\frac{n_s}{n_c}\right)^2]^{1/2}}$$

Where λ_c is the beam's wavelength, θ is the angle of incidence, n_s and n_c are the refractive indexes of the sample and the crystal, respectively. Specific wavelengths of the evanescent wave are absorbed by the sample depending on its composition. The reflected light lacks these absorbed wavelengths, resulting in attenuation. Finally, the attenuated radiation is analysed by the detector, and the ultimate spectrum is derived.[17]

3.2. Dynamic Light Scattering (DLS)

Dynamic Light Scattering (DLS), also known as photon correlation spectroscopy or quasi-elastic scattering, is an analytical technique used to investigate the diffusion of macromolecules and particles in solution, allowing the calculation of the diffusion coefficient and thus of the hydrodynamic radius of colloidal structures.

(This section is based on the works by J. Stetefeld et. Al,[18] Xu Renliang and W. I. Goldburg[19])

3.2.1. Theoretical background

If a solution containing macromolecules of particles is considered, a monochromatic beam of light is scattered in all direction as it hits these suspended bodies, depending

on both their size and shape. Brownian motion of particles, depending on size, temperature and solvent viscosity, is responsible for intensity fluctuations of scattered light. The analysis of these fluctuations allows to calculate the diffusion coefficient of the systems, which depends on the hydrodynamic radius. Indeed, large particles diffuse slower than small particles, resulting in different positions at the same time. A typical DLS measurement consists of monitoring the Brownian motion of particles under laser irradiation. More specifically, scattered light can undergo either destructive or constructive interference. The latter situation results in an amplified beam producing a detectable signal. The velocity of intensity fluctuations provides information on the diffusion behaviour of the particles. So, a digital autocorrelator correlates fluctuations concerning time. This results in the second-order correlation function $G_2(\tau)$, expressed as an integral of the product of scattering intensities:

$$(3.14) \quad G_2(\tau) = < I(t)I(t+\tau) >$$

where t and $t+\tau$ are the duration of the experiment and the delayed time, respectively. The braces refer to an average of the properties over time t. A normalized function is obtained as follows:

$$(3.15) \quad g_2(\tau) = \frac{<I(t)I(t+\tau)>}{<I(t)>^2}$$

Another correlation function, known as first-order correlation function, correlates relative particle motion using the scattered electric field $< E(t) >$. Canonical and normalized forms are reported below:

$$(3.16) \; G_1(\tau) = < E(t)E(t+\tau) >$$

$$(3.17) \; g_1(\tau) = \frac{<E(t)E(t+\tau)>}{<E(t)>^2}$$

Siegert relation provides the coupling between $g_1(\tau)$ and $g_2(\tau)$, in the hypothesis that photon counting occurs randomly (Gaussian phenomenon):

$$(3.18) \; g_2(\tau) = B + \beta|g_1(\tau)|^2$$

where B and β are the baseline (∼1) and the coherence factor, respectively, the latter depending on both instrument features and scattering properties of the sample. In the case of monomodal particle distribution, exponential decay is expected for $g_1(\tau)$, depending on the decay constant Γ:

$$(3.19)\ g_1(\tau) = e^{-\Gamma\gamma}$$

More specifically, the decay constant Γ is proportional to the translational diffusion coefficient of the particles D_τ, as reported below:

$$(3.20)\ \Gamma = -D_\tau q^2$$

where q is the Bragg wave vector, itself related to solvent refractive index n:

$$(3.21)\ q = \frac{4\pi n}{\lambda}\sin(\theta/2)$$

with λ and θ being the radiation wavelength and the scattering angle (position of the detector), respectively. Therefore, the analytical expression for $g_2(\tau)$ becomes:

$$(3.22)\ g_2(\tau) = 1 + \beta e^{-2D_\tau q^2 \tau}$$

Most used instruments usually fix the scattering angle at 90°, even if backscatter detection systems, with scattering angles close to the incident light (∼180°), help neglect the contribution of rotational diffusion and reduce the effect of dust and large-sized contaminants, since they usually scatter forward most of the light. This strategy is also useful in determining the D_τ for concentrated samples. Stokes-Einstein equation correlates D_τ to the hydrodynamic radius of the particles R_h:

$$(3.23)\ D_\tau = \frac{k_B T}{6\pi\mu R_h}$$

where k_B is the Boltzmann coefficient ($1.380 \cdot 10^{-23}$ Kg·ms^{-2}·K^{-1}), T is the absolute temperature and μ is the viscosity of medium. In particular, R_h is defined as the radius of the sphere that would exhibit the same rate of diffusion as the investigated particle. From D_τ and thus from R_h it is possible to calculate the friction factor f:

$$(3.24)\ f = 6\pi\mu R_h$$

3.2.2. Data analysis

The analysis of DLS data consists on fitting the autocorrelation function $g_2(\tau)$ to obtain the translational diffusion coefficient D_τ and thus the hydrodynamic radius R_h. Two main approaches are proposed: monomodal and non-monomodal distribution methods. The monomodal distribution method, also known as cumulant analysis method, is the simplest strategy to investigate an unknown sample. It is adequate only for Gaussian-like distributions since it provides the mean value of D_τ, not the distribution of D_τ. As previously mentioned, for monomodal systems $g_1(\tau)$ follows a single-exponential decay trend, as reported below:

$$(3.25)\ g_1(\tau) = e^{-2D_\tau q^2 \tau}$$

However, the eventual polydispersity of the system is to be taken into account. Indeed, $g_1(\tau)$ is to me modelled as a sum of several exponential decays with different decay rates. More specifically, Koppel developed the cumulative-generating function $K(-\tau, \Gamma)$:

$$(3.26)\ K(-\tau, \Gamma) = lng_1(\tau)$$

related to the m[th] cumulant of distribution function $k_{(m)}(\Gamma)$ by the following equation:

$$(3.27)\ k_m(\Gamma) = \frac{d^m K(-\tau,\Gamma)^m}{d(-\tau)} \mid -\tau = 0$$

From the Taylor expansion about $\tau = 0$, $K(-\tau, \Gamma)$ can be expressed as follows:

$$(3.28)\ K(-\tau, \Gamma) = -\bar{\Gamma}\tau + \frac{k_2}{2!}\tau^2 - \frac{k_3}{3!}\tau^3 + \frac{k_4}{4!}\tau^4 + \cdots$$

with $\bar{\Gamma}$ as the mean of Γ values.

The transformation of equation 3.22 in logarithmic mode leads to:

$$(3.29)\ ln(g_2(\tau) - B) = ln\beta + 2lng_1(\tau)$$

Substituting expression 3.26 in equation 3.29, a new form for $g_2(\tau)$ is obtained:

$$(3.30)\ ln(g_2(\tau) - B) = ln\beta + 2(-\bar{\Gamma}\tau + \frac{k_2}{2!}\tau^2 - \frac{k_3}{3!}\tau^3 + \frac{k_4}{4!}\tau^4 + \cdots)$$

Equation 3.30 is used to fit the experimental $g_2(\tau)$ vs τ profiles and derive $\bar{\Gamma}$ and k_i parameters. $\bar{\Gamma}$ is the average of decay rates, whereas k_2, k_3 and k_4 represent variance, skewness and kurtosis of measured distributions. Moreover, the ratio between k_2 (variance) and $\bar{\Gamma}^2$ (the square of mean decay rate) gives the polydispersity index (PDI). The cumulant method perfectly suits the sample suspension if the PDI is close to 0.1. For 0.1 < PDI < 0.7, we are in the presence of a quasi-monodisperse sample. For PDI > 0.7, it is better to perform data analysis with non-monomodal distribution methods. Three main strategies are presented. The first method is known as non-negative least squares (NNLS) method and it is used for broad monomodal or multimodal distributions. In this model, which involves Laplace transform of $g_2(\tau)$, decay rates are spaced in a linear or logarithmic form over a range of decay constants Γ_i. b_i model parameters are given by the best fit of data, using the following equation:

$$(3.31)\ \chi^2 = \sum_{j=1}^{N} g_1(\tau_j) - \sum_{i=1}^{M} b_i e^{(-\Gamma_i \tau_j)}]^2$$

with N as the number of data points and M as the number of decay constants. The model also prescribes that Γ_i and b_i are non-negative.

3.2.3. Estimation of R_h

The hydrodynamic radius R_h is estimated thanks to the Stokes-Einstein equation (3.23), which correlates R_h to the translational diffusion coefficient D_τ (the z-averaged value of D_τ in case of a distribution of molecular weights). However, D_τ is derived from fluctuations in scattering intensity that depend on ${R_h}^6$, according to Rayleigh approximation. More specifically, the intensity-weighted distribution for a particle with size *a*, in a bimodal system with N_a molecules of size *a* and N_b molecule of size *b*, is equal to:

$$(3.32)\ \%I_a = \frac{N_a a^6 \cdot 100}{N_a a^6 + N_b b^6}$$

In the hypothesis of homogeneous spherical particles, a smaller estimation of R_h is obtained by converting the intensity-weighted distribution in the volume-weighted distribution, proportional to ${R_h}^3$:

$$(3.33)\ \%V_a = \frac{N_a a^3 \cdot 100}{N_a a^3 + N_b b^3}$$

Even if this strategy is more useful, the contribution of larger particles with higher volume (mass) is overestimated. Therefore, it is possible to evaluate the number-weighted distribution to properly state the contribution of each population of particles:

$$(3.34)\ \%N_a = \frac{N_a \cdot 100}{N_a + N_b}$$

3.2.4. The experimental apparatus

The main components of a DLS instrument are a laser, a properly diluted sample suspension and detector, as shown in **figure 3.5.**

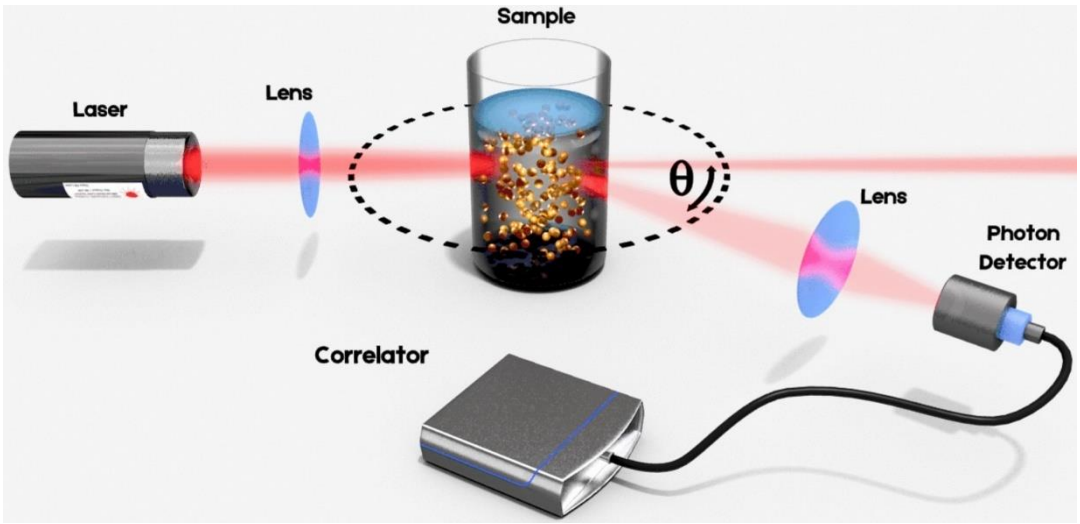

Figure 3.5. Graphical scheme of a typical DLS instrumentation (LS Instruments, Freiburg, Switzerland)

A monochromatic laser beam of known wavelength (usually green light, λ=532 nm), produced from a gas source (He, Ne), is collimated by a lens and hits a diluted sample suspension. The particles scatter light in every direction and the scattered light reaches a phonon detector, positioned at a specific angle with respect to the incident beam direction, known as scattering angle θ. Finally, a correlator elaborates the intensity fluctuations over time and gives the profile of the correlation function. It is important to remember that the intensity of scattered light depends on the refractive indexes of both particles and solvent.

3.3. Electrophoretic light scattering (ELS)

The electrophoretic light scattering (ELS) technique is a variation of DLS. It is based on the detection of the light scattering intensity when the particles exhibit simultaneously Brownian and electrophoretic-driven motion under an oriented electric field. ELS experiments allow to calculate both electrophoretic mobility and zeta potential of colloidal systems.

(This section is based on the work by C. Lunardi et al.[20])

3.3.1. Theoretical background

A charged particle in a liquid medium modifies the charge distribution in the surrounding fluid portion. More specifically, an electrical double layer originates in the immediately close liquid solvent, as described in **Figure 3.6.**

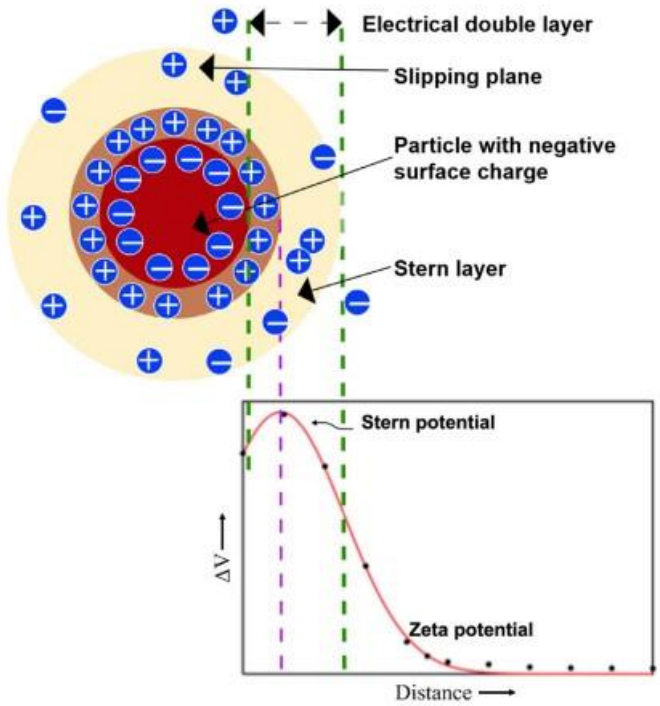

Figure 3.6. Ionic distribution surrounding a negatively charged particle in a liquid medium. Insert shows the profile for the electrical potential with the distance from the charged particle.[21]

In the case of a negatively charged particle, the immediately close solvent layer, known as Stern layer or inner Helmholtz plane, is made of surface-adsorbed ions. The adjacent layer, known as diffuse layer or outer Helmholtz plane, is not strongly bound to the Stern layer. The electrical potential, known as zeta (ζ) potential, at the interface between the Stern and the diffuse layer (slipping plane) is a fundamental parameter in determining the mobility of the colloid, together with the dielectric constant and the viscosity of the fluid. ζ potential contributes to determine the colloidal stability of a suspended particle system. More specifically, according to Derjaguin-Landau- Verwey-Overbeek (DLVO) theory, the balance between van der Waals and electrical forces determines affects the final stability. Henry equation of electrical field allows the calculation of ζ potential:

$$(3.35)\ \frac{U}{E} = \frac{2\varepsilon\zeta F(\kappa a)}{3\mu}$$

The ratio between the particle velocity U and the electric field E is known as electrophoretic mobility ($m^2 \cdot s^{-1} \cdot V^{-1}$), ε is the solvent dielectric permittivity, μ is the viscosity, $F(\kappa a)$ is the dimensionless Henry's function, included in 1-3/2 interval depending on both particle size a and Debye length $\frac{1}{k}$. In detail, $\kappa a \gg 1$ means far larger particle radius than Debye length ($\frac{1}{k} \sim 10\ nm$ for 1 mmolar aqueous solution). In this case, $F(\kappa a) = 3/2$ (Smoluchowski regime) and DLVO theory is correctly applied for $\zeta \leq -50\ mV$. If $\kappa a < 1$, that means small particles (few nm in size), $F(\kappa a) = 1$ (Hückel–Onsager (HO) regime). However, in polar media the application of DLVO theory is allowed by the Smoluchowski approximation, even for small particles, whereas in non-polar solvents Hückel–Onsager (HO) is more accurate. Even if they are often identified with each other, surface charge and ζ potential are not the same thing. Indeed, surface charge is the charge density on particle surface, whereas ζ potential is a measure of the strength or intensity of the electrostatic charge at the shear plane of a colloidal particle when it is subjected to electrophoresis. A higher ζ potential generally indicates a stronger electrostatic repulsion or attraction between the particle and the surrounding medium, influencing the particle's behavior during electrophoresis.

3.3.2. Instrumentation and measurement

A typical experimental apparatus for performing ζ potential measurement is shown in **Figure 3.7.**

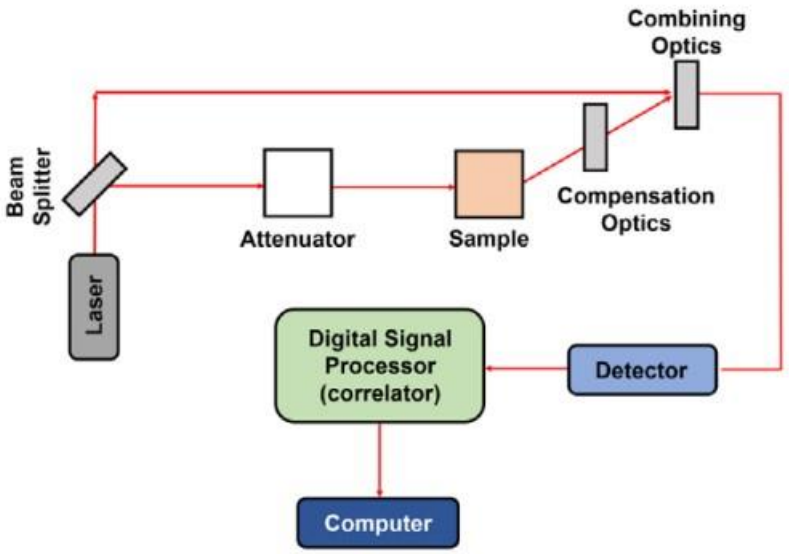

Figure 3.7. Graphical scheme of a ζ potential analyzer.[22]

In detail, a laser source (He-Ne, usually λ=632.8 nm) produces a monochromatic beam that hits the sample particles, which are submitted to an electrical field. The incident light is scattered at frequencies proportional to the Doppler shift (that is the apparent frequency change caused by relative motion between particles and surrounding medium). The amount of emitted photons is split, so that one half is used as reference and the other half is directed to the sample. Reference and sample-hitting beams are finally combined and the Doppler shift is thus determined with respect to the reference beam. In particular, the frequency shift Δf is proportional to particle velocity v, inversely proportional to laser wavelength λ and depends on the scattering angle θ:

$$(3.36)\ \Delta f = \frac{2v\sin(\frac{\theta}{2})}{\lambda}$$

3.4. Nuclear magnetic resonance (NMR)

Nuclear magnetic resonance (NMR) spectroscopy uses radiofrequency waves to extract information about magnetic nuclei. NMR spectroscopy is just one among several spectroscopic approaches commonly employed in biology, chemistry, and

materials science. However, NMR distinguishes itself from other spectroscopic methods in three significant aspects. First, it examines the distribution of nuclei from a specific, user-selected chemical element among the molecules in a sample, broadening its target scope compared to most spectroscopic techniques. Second, NMR signals are responsive to the local environment surrounding the observed nuclei, offering a tool capable of probing the chemical and physical conditions of an atom and delivering more comprehensive information about a given sample than many other spectroscopic methods. Third, NMR demonstrates higher penetration capabilities, while being notably less detrimental compared to alternative spectroscopic approaches.

(This section is based on the work by I. P. Gerothanassis et al.[23])

3.4.1. Theoretical background

A moving charged particle produces a magnetic field. So, it can be modelled as a magnetic dipole associated with a magnetic moment $\boldsymbol{\mu}$. The generated magnetic moment is proportional to the nuclear spin vector $\boldsymbol{I}$:

$$(3.37)\ \boldsymbol{\mu} = \boldsymbol{\gamma I}$$

where the constant $\boldsymbol{\gamma}$ is called gyromagnetic ratio. If an external uniform magnetic field $\boldsymbol{B_0}$ is imposed, the magnetic dipole starts moving describing a conical trajectory, a phenomenon known as Larmor precession. The frequency v_0 of this motion is proportional to the external magnetic field:

$$(3.38)\ v_0 = \frac{|\boldsymbol{\gamma}|\boldsymbol{B_0}}{2\pi}$$

If an additional external field $\boldsymbol{B_1}$ is applied perpendicularly to the plane containing $\boldsymbol{B_0}$ and $\boldsymbol{\mu}$, it exerts a torque on $\boldsymbol{\mu}$, as described by **Figure 3.8.**

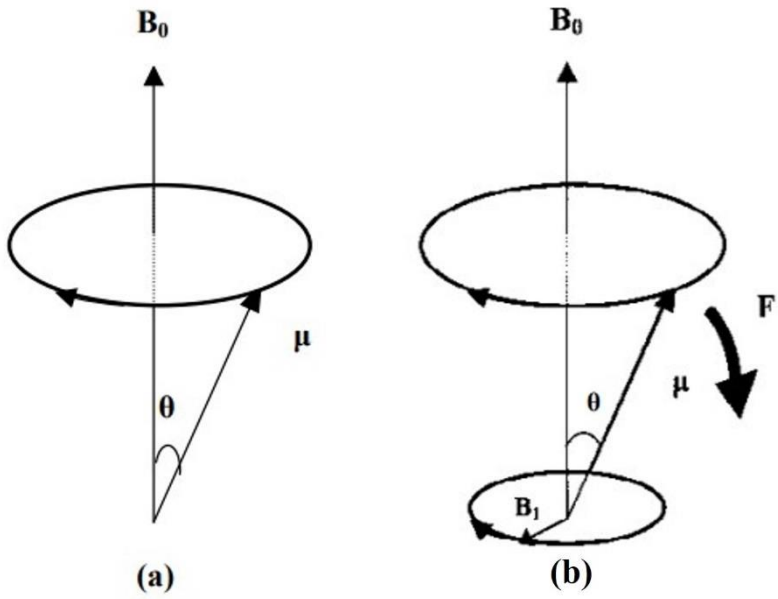

Figure 3.8. Precession of a magnetic moment μ about an applied magnetic field $\boldsymbol{B_0}$ (a). Influence of rotating $\boldsymbol{B_1}$ on $\boldsymbol{\mu}$. When $\boldsymbol{B_1}$ is perpendicular to the $\boldsymbol{B_0}$-$\boldsymbol{\mu}$ plane, a force $\boldsymbol{F}$ arises, aiming to augment the angle between $\boldsymbol{B_0}$ and $\boldsymbol{\mu}$ (b).

Therefore, the simultaneous presence of two perpendicular magnetic fields affects the energy of $\boldsymbol{\mu}$, since the angle θ between $\boldsymbol{B_0}$ and $\boldsymbol{\mu}$ is changed. This condition is described as resonance. Every atomic nucleus has an intrinsic angular momentum $\boldsymbol{P}$ since it is a positively charged particle rotating on its axis. Angular momentum $\boldsymbol{P}$ is quantized:

$$(3.39)\ \boldsymbol{P} = \hbar\sqrt{\boldsymbol{I}(\boldsymbol{I}+\boldsymbol{1})}$$

where $\hbar = \frac{h}{2\pi}$ and $\boldsymbol{I}$ can only have discrete values (1/2, 1, 3/2, 2…up to 7). When a nucleus with angular momentum $\boldsymbol{P}$ and magnetic moment $\boldsymbol{\mu}$ is situated in a stable and powerful magnetic field $\boldsymbol{B_0}$, the angular momentum aligns in a way that its $\boldsymbol{P_z}$ component along the field direction becomes a multiple of ħ, either as an integral or half-integral value.

$$(3.40)\ \boldsymbol{P_z} = m_I\hbar$$

The magnetic or directional quantum number, denoted as m_I, assumes values such as I, I - 1, ..., -I. It is evident that there exist (2I + 1) distinct m_I values, indicating an equal number of potential orientations for the angular momentum and magnetic moment in an external magnetic field $\boldsymbol{B_0}$. For nuclei like ^{1}H and ^{13}C with I =1/2, there are two m_I values (1/2 and -1/2). Consequently, when these nuclei are exposed to an external magnetic field, they can effectively align either with the field (m_I = 1/2) or against it (m_I = -1/2). The energetically more favorable state corresponds to alignment with the field. The energy difference ΔE is directly proportional to the intensity of the applied field $\boldsymbol{B_0}$ at the nucleus **(Figure 3.9)**:

$$(3.41)\ \Delta E = \gamma \hbar |\boldsymbol{B_0}|$$

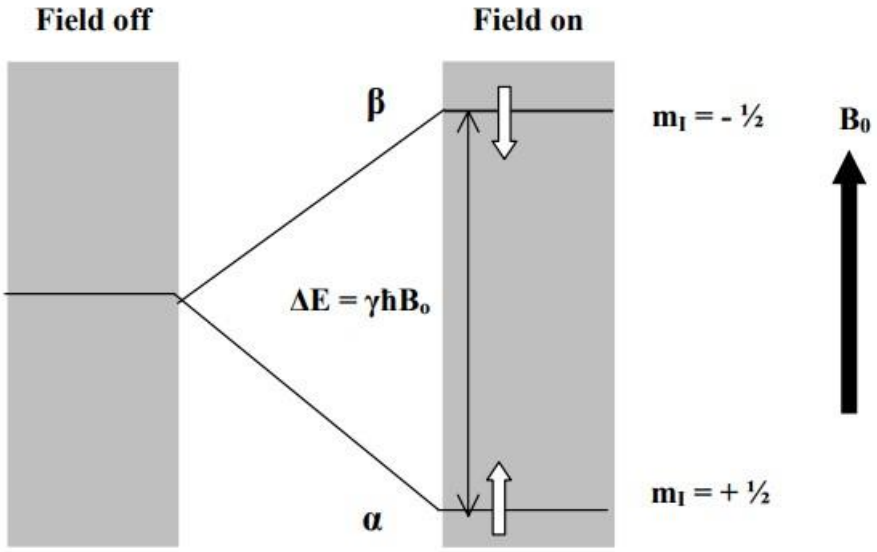

Figure 3.9. Difference in the energy levels of a nucleus in an external magnetic field $\boldsymbol{B_0}$.

So, nuclear magnetic absorption occurs for such radiation frequency v_0 that the external magnetic field $\boldsymbol{B_0}$ satisfies the resonance condition, expressed by equation 3.41. If a nucleus consists of p protons and n neutrons, its overall mass is p + n, its overall charge is +p, and its collective spin arises from the vector combination of the spins of p protons and n neutrons, each having a magnitude of 1/2. Each nuclear

isotope, characterized by a distinct combination of protons and neutrons, possesses its unique total spin value. Unfortunately, the principles governing the vector addition of nuclear spins are not yet fully understood, making it challenging to predict the spin of a specific nucleus in a general sense. For instance, deuterium (^{2}H), an isotope of hydrogen with one proton and one neutron, may exhibit a spin of either 1 or 0, contingent upon the alignment or opposition of the spins of the proton and neutron; however, it is observed to have a spin of 1. Conversely, the helium nucleus (^{4}He), made of two protons and two neutrons, has a spin value of 0. These empirical observations led to the formulation of these rules:

a) If the nucleus has both p and n even, the spin is 0 (^{4}He, ^{12}C, ^{16}O);
b) If the nucleus has both p and n odd, the spin is an integer (^{2}H (I=1), ^{14}N (I=1), ^{10}B (I=3));
c) If the mass of the nucleus is odd, the spin is half-integer (^{1}H (I=1/2), ^{15}N (I=1/2), ^{17}O (I=5/2)).

The alignment of spin magnetic moments in a magnetic field occurs, even though they don't uniformly occupy the lowest energy state due to the competition between thermal motion and the Boltzmann distribution. Assuming the system is in thermal equilibrium with its surroundings, the distribution can be determined using the Boltzmann law. Representing the numbers of particles in the upper and lower levels as n_u and n_l, respectively, and considering T as the absolute temperature, the relationship is expressed as:

$$(3.42)\ \frac{n_u}{n_l} = e^{-\frac{\Delta E}{kT}}$$

where k and ΔE are the Boltzmann constant and the energy gap, respectively. When applying this equation to protons in a magnetic field $\boldsymbol{B_0}$ of 9.4 T (typical value for a NMR measurement), at a temperature of 300 K, the energy gap ΔE is equal to $2.65 \cdot 10^{-25}$ J, kT is equal to $4.41 \cdot 10^{-21}$ J, so that $-\frac{\Delta E}{kT} = 6.4 \cdot 10^{-5}$. This means $\Delta E \ll kT$,

or that the energy to be filled for reorienting the spin is way lower than the thermal energy. In this condition, $e^{-\frac{\Delta E}{kT}} \sim 1 - \frac{\Delta E}{kT}$ and the normalized population difference is derived as:

$$(3.43)\ \frac{n_l - n_u}{n_l + n_u} = \frac{\Delta E}{2kT}$$

The ultimate outcome of this population difference is a magnetization $\boldsymbol{M_0}$ of the sample aligning along the z-axis. In NMR spectroscopy, where the occurrences of upward transitions exceed downward transitions by a ratio of only one in 10^4-10^6, it is akin to detecting just one nucleus in every 10^4-10^6. Consequently, optimizing signal strengths becomes crucial, and this can be achieved, for instance, by employing powerful external magnetic fields $\boldsymbol{B_0}$ to maximize the energy gap ΔE. Likewise, nuclei with substantial gyromagnetic ratios and high natural abundance are preferred, explaining the widespread use of ^{1}H as an NMR nucleus. However, every atomic nucleus is surrounded by an electronic cloud in motion. The external magnetic field $\boldsymbol{B_0}$ affects the motion of the electrons, inducing the circulation of the negatively charged particles within their orbitals, and this results in a secondary magnetic field $\boldsymbol{B'}$opposed to $\boldsymbol{B_0}$. As a consequence, the electron-produced magnetic field shields the nucleus from $\boldsymbol{B_0}$. The intensity of the shielding field is proportional to $\boldsymbol{B_0}$, with the dimensionless constant of proportionality σ known as screening constant. The local magnetic field $\boldsymbol{B_{local}}$ experienced by the nucleus is thus equal to:

$$(3.44)\ \boldsymbol{B_{local}} = \boldsymbol{B_0}(1 - \sigma)$$

The magnetic shielding results in a higher external field being necessary to satisfy the resonance condition in experiments where the magnetic field is varied. Conversely, at a constant field ($\boldsymbol{B_0}$), the resonance condition is achieved at a lower frequency than one might anticipate.

3.4.2. ^{1}H NMR: the spectrum of ethanol

The *^{1}H NMR* spectrum of ethanol is reported in **figure 3.10**. Protons within distinct chemical groups exhibit varying shielding constants, leading to the satisfaction of the resonance condition at different frequencies ν_0. Methyl protons, forming a magnetically equivalent group due to identical CH bonds and shielding, resonate at a frequency determined by their electron density. In contrast, methylene protons, located in a different molecular region with distinct electron density, resonate at a different frequency. The hydroxyl group's proton resonates at yet another field strength, influenced by oxygen's higher electron density compared to carbon.

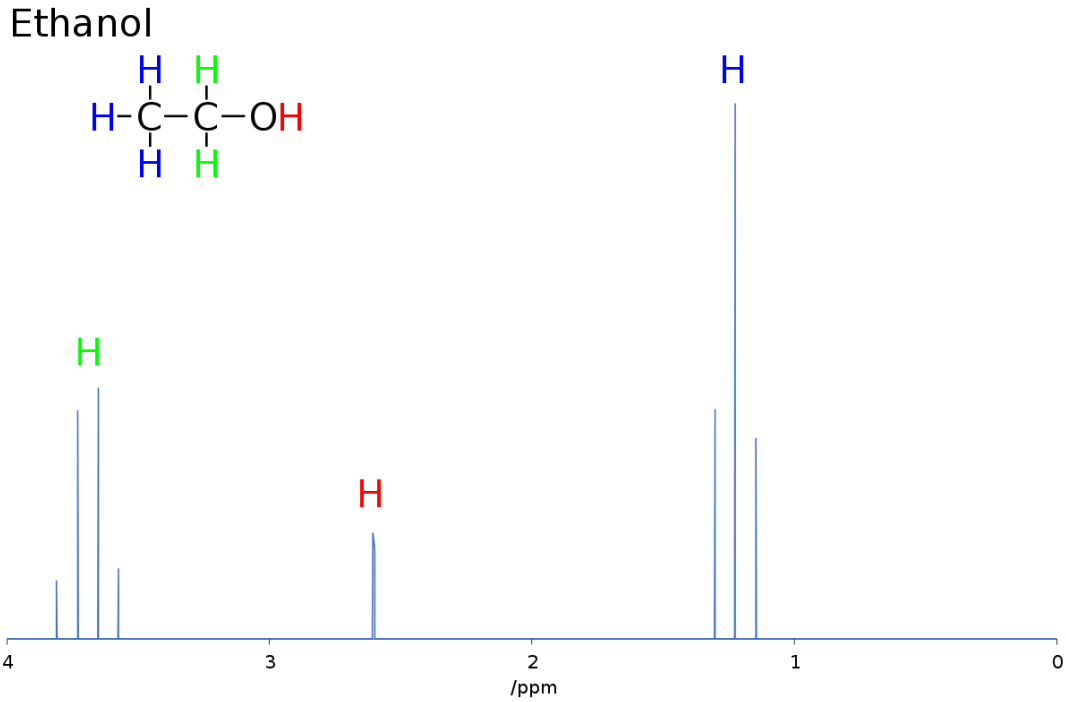

Figure 3.10. ^{1}H NMR spectrum of ethanol. Chemical shifts for methyl, methylene and hydroxyl protons are indicated with blue, green and red H, respectively.

Expecting $\sigma_{CH} < \sigma_{OH}$, the CH hydrogen nucleus precesses with a smaller Larmor frequency than OH in a given applied field. Two crucial aspects of NMR spectroscopy emerge: identical nuclei, like ^{1}H, exhibit different absorption positions in diverse chemical environments, termed chemical shift δ; the absorption peak area

is proportional to the number of equivalent nuclei with the same chemical shift. In ethanol, the group intensities follow a 3:2:1 ratio due to 3 methyl protons, 2 methylene protons, and 1 hydroxyl proton. Chemical shift measurements use the resonance position of the bare proton nucleus as the primary standard, often relative to a standard compound like tetramethylsilane (TMS). δ values, expressed in parts per million (ppm), are positive if the sample absorbs at a higher frequency than the reference at constant field, with a factor of 10^6 scaling the numerical value for convenience:

$$(3.45)\ \delta = 10^6 \frac{\nu_{sample} - \nu_{TMS}}{\nu_{TMS}}$$

3.4.3. Main components of a NMR spectrometer

NMR spectrometers are equipped with three primary components: a superconducting magnet, a probe, and a sophisticated electronic system (console) managed by a workstation, as described in **Figure 3.11**.

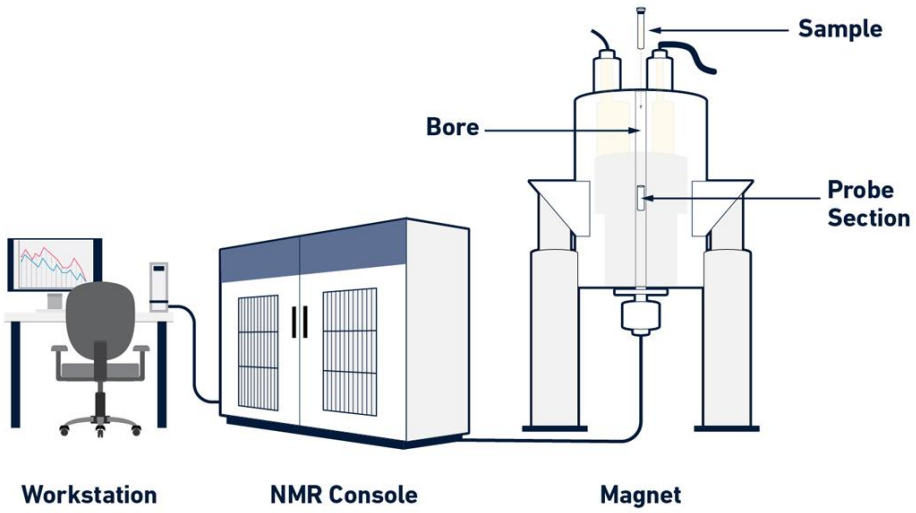

Figure 3.11. Typical apparatus of a NMR spectrometer.[24]

The superconducting magnet generates a robust magnetic field aligning the nuclear spins of atoms within the sample. Modern NMR spectrometers use superconducting

materials in their magnets, necessitating extremely low temperatures (approximately 4 K). Consequently, these spectrometers exhibit a cooling system with an inner jacket filled with liquid helium and an outer jacket containing liquid nitrogen, along with multiple layers of thermal isolating materials. The superconducting magnet encloses a cylindrical chamber known as the "probe," a pivotal instrument component. The sample is inserted into the probe, placing it within the magnetic field's influence. The probe also houses magnetic coils surrounding the sample, serving various functions. These coils are instrumental in delivering radiofrequency pulses, capturing the emitted NMR signal, ensuring magnetic field homogeneity, and applying pulse gradients essential for certain NMR experiments. The spectrometer's electronic system governs all experimental conditions, allowing the adjustment of every NMR experiment parameter via the workstation. This system oversees data acquisition and performs mathematical transformations to generate an NMR spectrum. The spectrum exhibits peaks of varying intensities based on the chemical shift, a magnitude derived from the Larmor frequency of different atomic nuclei within the sample.

3.5. Gas Chromatography (GC)

Chromatography is a separating technique based on physical methods, which provides separation of the components by means of a mobile phase and a stationary phase, driven by variations in the distribution constants of individual sample components between the two phases. The physics state of the phases allows to draw a classification of the chromatographic separation strategies: when the mobile phase is a gas and the stationary phase a solid or liquid, the separation techniques are known as gas-solid chromatography (GSC) or gas-liquid chromatography (GLC), respectively.

(This section is based on the works by P. Cheung,[25] J.M.R. Bélanger et al.,[26] and K. Bartle et al.[27])

3.5.1. Principles of chromatography

In a typical separation stage, a mixture of analytes is introduced as a solution onto the stationary phase, and the mobile phase carries these components through it. Each analyte undergoes equilibration or partitioning between the phases, primarily influenced by its distinct affinity for the stationary phase. Consequently, each analyte possesses a specific equilibrium constant, leading to variations in migration rates. This differential behavior results in the retention of analytes for varying durations on the stationary phase and their subsequent elution from the column at different rates. Each component in the mixture is associated with a unique retention time. This chromatographic approach is commonly referred to as elution chromatography. The relationships between the components of the sample and the mobile and stationary phases can be categorized as either adsorption or absorption. In adsorption chromatography, the sample is drawn to the surface of the phase, typically adhering to the surface of a solid stationary phase. On the other hand, absorption chromatography involves the sample diffusing into the internal structure of the stationary phase. The majority of chromatographic separations typically involve a combination of both adsorption and absorption phenomena. When analytes are eluted from the stationary phase, the representation involves a detection system response plotted against the elution time t or the volume of the mobile phase V (**Figure 3.12**).

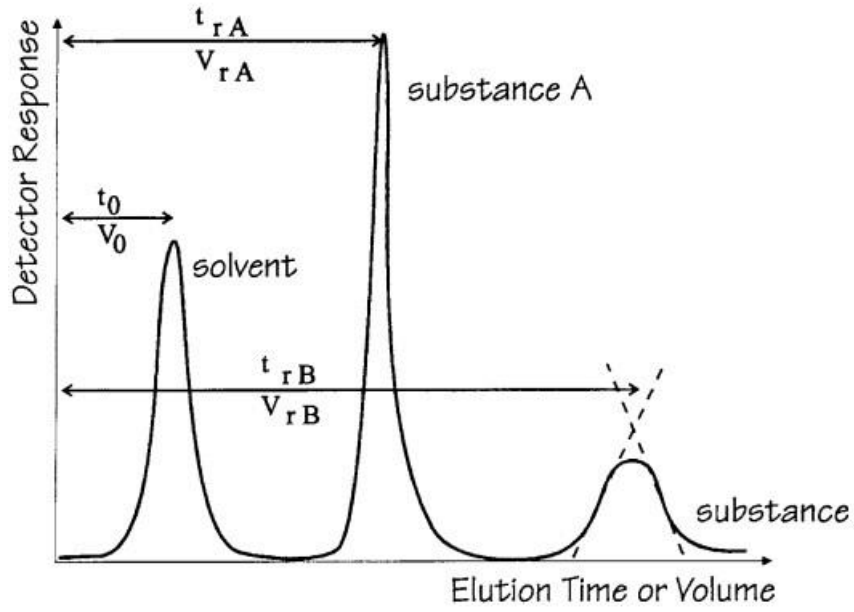

Figure 3.12. Example of a chromatogram originating from the separation of a bicomponent mixture. t_{rA} and t_{rB} refer to the retention times of substances A and B, respectively, whereas t_0 is the time needed by the solvent to travel across the column.[26]

The interchangeability of time and volume on the abscissa is facilitated by the typically constant flow rate F of the mobile phase, where $V = t \cdot F$. Each compound generates a peak characterized by a Gaussian shape and the graphical representation of the elution is called chromatogram. Indeed, not all molecules of a specific component exhibit the same velocity. The midpoint of the elution band signifies the average retention time of the analyte. Certain molecules move at a slower pace, while others move faster. This disparity in velocity arises from the varying occurrences of sorption and desorption of analytes, contributing to the Gaussian profile observed in the detected signal. As previously said, the distribution of the analytes in the two phases is an equilibrium phenomenon, described by the following equation:

$$(3.46)\ K_X = \frac{[X]_s}{[X]_m}$$

where $[X]_s$ and $[X]_m$ are the molar concentration of the analyte X in the stationary and in the mobile phase, respectively, whereas the equilibrium constant K_X is known as partition coefficient. The cumulative volume of the mobile phase V_R necessary for the elution of an analyte includes the volume of the mobile phase V_m and the volume of the mobile phase that passes while the analyte remains stationary ($V_s K_X$). This latter volume is indicative of the analyte's inclination to adsorb onto a specified quantity of stationary phase. V_m is also called dead volume, calculated as $F \cdot t_0$. One of the main parameters in chromatography is the retention time t_r, which is the time needed by the analyte molecules to cross the whole column. However, with t_r one usually refers to the adjusted retention time, which is the original retention time t'_r plus t_M. The ratio $\frac{t'_r}{t_0}$ is termed capacity factor k and quantifies the amount of time the analyte spends in the stationary phase with respect to the time spent in the mobile phase or, alternatively, the total number of moles of X in the stationary phase over the total number of moles of X in the mobile phase. Both the retention time and the width of the peak in the chromatogram W_B determine the number of theoretical plates N:

$$(3.47)\ N = 16\ (\frac{t_r}{W_B})^2$$

Similarly, the effective plate number N_{eff} is calculated as:

$$(3.48)\ N_{eff} = 5.54(\frac{t'_r}{W_{1/2}})^2$$

with $W_{1/2}$ as the width at half peak. As a consequence, the height equivalent to a theoretical plate (HETP) and the height equivalent to one effective plate (H_{eff}) are calculated by dividing the corresponding number of plates for the column length:

$$(3.49)\ HETP = N/L$$

$$(3.50)\ H_{eff} = L/N_{eff}$$

Both the values are expressions of the column efficiency. The lower the column height, the higher the efficiency.

Chromatography is characterized by its dynamic nature. When the analyte traverses the column, concentration gradients emerge, leading to analyte diffusion, a phenomenon known as the kinetic process. Additionally, mass transfer is another significant process during elution. This broadening of bands is quantified in terms of the plate height ($HETP$) and is dependent on the average linear velocity of the mobile phase u. The relationship between $HETP$ and u is described by Van Deempter equation:

$$(3.51)\ HETP = A + \frac{B}{u} + Cu$$

Constant A, used for packed columns, is a measure of the tortuosity of the path a single analyte molecule has to take (eddy diffusion), causing different exit times. Its value approaches zero for open tubular columns under laminar flow conditions. B value accounts for Brownian-like bidirectional diffusion along the column, whereas C is the sum of the contribution of mass transfer in both mobile (Cm) and stationary (Cs) phase and depends on particle size, column diameter and diffusion coefficient. The selectivity or separation factor S pertains to a system's capacity to differentiate between two components, determined by how the analyte distributes between the mobile and stationary phases. Also known as relative retention, as S approaches a value of 1, the separation becomes more challenging. The only means to alter this parameter is by modifying one or both phases. For a bicomponent mixture, the separation factor is calculated as the ratio between the capacity factors:

$$(3.52)\ S = \frac{k_A}{k_B}$$

It can be tuned by properly modifying one or both phases. Resolution R expresses the extent of separation between two components. In chromatography, a minimum

value of $R = 1$ is required for achieving a quantitative separation, indicating a 2% overlap of the peak area. When R reaches 1.5, cross-contamination is minimal, less than one percent (1%), and the peaks are regarded as being at baseline separation. Such separation is particularly crucial in preparative chromatography when obtaining pure compounds is imperative. It is a function of capacity, selectivity, and column efficiency and it can be expressed as follows:

$$(3.53)\ R = 2t_{rB} - \frac{t_{rA}}{W_A} + W_B$$

3.5.2. Main components of a gas chromatography system

In gas chromatography (GC), the separation of vaporized sample components occurs through partitioning between a mobile gaseous phase and either a liquid or solid stationary phase housed in a column. These types are denoted as GLC and GSC, respectively, based on the stationary phase. A typical GC instrument comprises essential components such as a carrier gas supply, sample injection system, separation column, detector, and data recorder, as described in **Figure 3.13**.

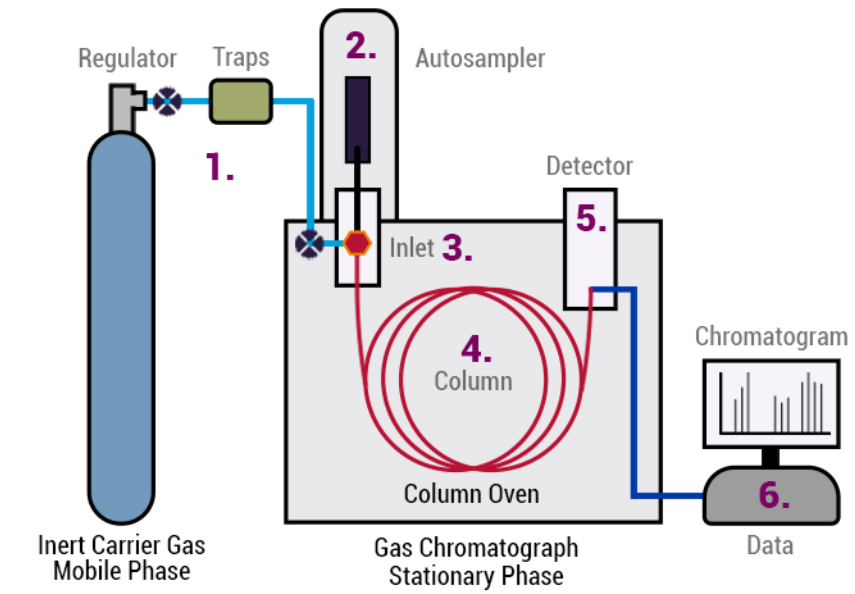

Figure 3.13. Main components of a gas chromatograph.[28]

The mobile-phase gas, termed the carrier gas, must be chemically inert, pure, and free of water, with helium, argon, nitrogen, and hydrogen commonly employed. The injection port, featuring a soft septum for a gas-tight seal, offers various types, including split, splitless, programmed temperature injection, and cold on-column (COC) injectors, tailored to diverse sample and instrumental needs. Most gas chromatographs incorporate ovens to maintain column temperatures between 40°C and 350°C. Temperature-programmed ovens are preferred for enabling separations of chemicals with varying vapor pressures within a single analysis. GC columns are classified as either packed or capillary. Packed columns, typically stainless steel, are filled with inert supports like diatomaceous earth, graphitized carbon, Teflon®, inorganic salts, or glass beads. Capillary columns, on the other hand, lack inert support but feature a stationary phase—a high-viscosity, low-volatility liquid or a thin liquid film coating the inner wall. Capillary columns include WCOT (wall-coated capillary column), SCOT (support-coated open tubular column), and PLOT (porous layer open tubular column). Detectors play a crucial role in sensing effluents from the column and producing a chromatogram record of the chromatography. Various detectors used in GC analysis include flame ionization (FID), thermal conductivity (TCD), electron capture (ECD), flame photometric (FPD), pulsed flame photometric (PFPD), and photoionization (PID) detectors.

3.6. Circular dichroism

Certain biomolecules exhibit molecular asymmetry, meaning their mirror images are not identical. Such molecules are termed chiral. A well-known example is a carbon atom bonded tetrahedrally to four different atoms or groups of atoms. Chirality is also observed in biomacromolecules. For instance, the α-helix, a prevalent helical structure in proteins, is coiled in a right-handed sense. While the majority of polynucleotides exhibit a right-handed helical sense, there are instances of helices winding in a left-handed sense as well.

The interaction between a chiral molecule and polarized light is highly specific and has proven to be a crucial method for characterizing both small and macromolecular structures. Circular dichroism (CD) is a common type of measurement employed to determine the effects of polarized light on asymmetric molecules. CD is defined as the disparity in absorption between left-hand (LCP) and right-hand (RCP) circularly polarized light when interacting with optically active compounds. Although these effects are relatively small, modern instrumentation allows for their accurate measurement. Consequently, the assessment of circular dichroism provides detailed structural and enantiomeric information on proteins, carbohydrates, nucleic acids, pharmaceuticals, liquid crystals, and other substances.

The information contained in this section are mainly taken from the works by Woody R. W. and Ranjbar B. et al.[29, 30]

3.6.1. Physics of the phenomenon

A light beam moving along the y-axis is considered (**Figure 3.14**). In the case of unpolarized light, it propagates in all directions (**Figure 3.14 A)**, while linearly or plane-polarized light is restricted to the z-direction (**Figure 3.14 B)**. On the other hand, circularly polarized light (**Figure 3.14 C**) exhibits rotation in either a clockwise or counterclockwise direction.

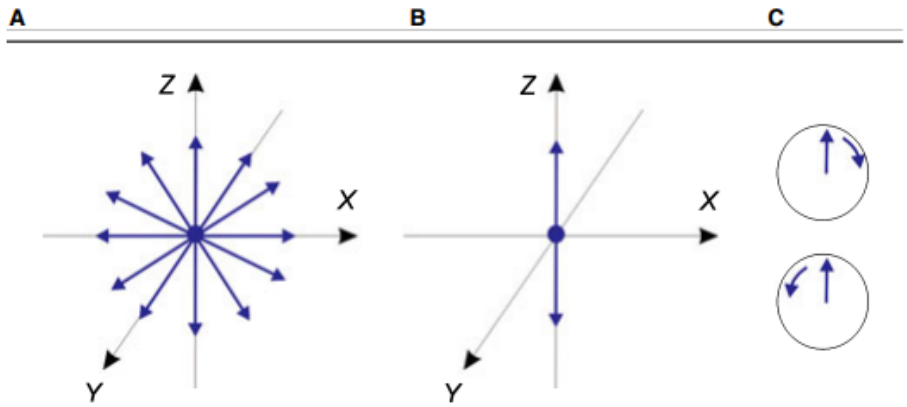

Figure 3.14. Unpolarized (A), linearly/plane-polarized (B) and circularly polarized (C) light beam moving along y-axis.[30]

The absorption of unpolarized light by a sample is expressed through the absorbance A, which is proportional to the molar extinction coefficient ε, according to Lambert-Beer equation. Molar extinction coefficients can be defined similarly for RCP and LCP light, denoted as ε_R and ε_L, respectively. The molar CD $\Delta\varepsilon$, defined as the difference between the extinction coefficients for the two types of circularly polarized light, is given by equation 3.54:

$$(3.54)\ \Delta\varepsilon = \varepsilon_L - \varepsilon_R = \frac{A_L - A_R}{cl}$$

The molar extinction coefficient for unpolarized light is the average of ε_L and ε_R:

$$(3.55)\ \varepsilon = \frac{\varepsilon_L + \varepsilon_R}{2}$$

Typically, $\Delta\varepsilon$ is small in comparison to ε_L, ε_R, and ε. It is possible to define the anisotropy factor g as:

$$(3.56)\ g = \frac{\Delta\varepsilon}{\varepsilon} = 2\frac{\varepsilon_L - \varepsilon_R}{\varepsilon_L + \varepsilon_R}$$

This factor serves as a useful metric indicating the difficulty of measuring CD in the region of a specific absorption band, as g is proportional to the signal-to-noise ratio. Indeed, Δε contributes to the signal, while ε contributes to the noise. The anisotropy factor is typically small, commonly around 10^{-4}. Most commercially available CD instruments measure $\Delta A = A_L - A_R$, which can be readily converted to Δε through equation 3.54. However, instruments are often calibrated in terms of molar ellipticity θ, an angular measure of ΔA:

$$(3.57)\ \theta = 32.98\,\Delta A$$

where θ is in degrees. To eliminate the effects of path length and concentration, the molar ellipticity is defined as:

$$(3.58)\ [\theta] = \frac{100\theta}{lc} = 3298\Delta\varepsilon$$

The units for molar ellipticity are degrees $cm^2/dmol$.

CD proves valuable in assessing conformational changes in macromolecular structures. Consequently, the unfolding of biomolecules like proteins, nucleic acids, and glycosides is gauged by changes in CD spectra, offering insights into the extent of structural modifications. Native proteins typically exhibit characteristic CD spectra, with nuances specific to each protein. The shape of the spectra curve, positive and negative maxima, provides information about the protein's secondary structures. For example, peaks in the 200–250 nm wavelength (known as far-UV region) range indicate α-helical structures, while a 'v'-shaped spectra in the 217–220 nm range suggest β-sheet structures. Reported accuracies for CD analysis are 97% for helices, 75% for beta sheets, 50% for turns, and 89% for other secondary structures. Scans in the near-UV range (250–300 nm) offer insights into tertiary structure, while other parts of the spectrum, such as around 410 nm for heme proteins, may provide additional structural information.

3.6.2. Determination of protein secondary structure

CD spectroscopy in the far-UV spectral range (190–250 nm) is a method for determining protein secondary structure. In this wavelength range, the peptide bond serves as the chromophore, and the signal is generated when it is situated in a regular, folded environment. The peptide chromophore exhibits the weakest energy transition with an $n \rightarrow \pi^*$ transition observed at 210–220 nm, involving non-bonding electrons of oxygen in the carbonyl. Conversely, the strongest energy transition is an absorption band centered at 190 nm due to a $\pi \rightarrow \pi^*$ transition involving the π-electrons of the carbonyl. The α-helix, β-sheet, and random coil structures each contribute to a distinct shape and magnitude of the CD spectrum (**Figure 3.15**).

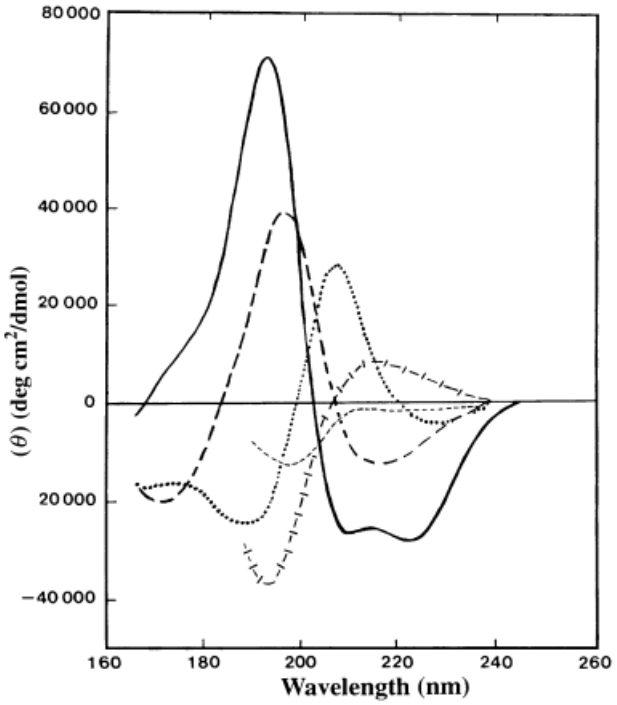

Figure 3.15. Graphs are presented to depict far-UV CD spectra corresponding to different secondary structure types. The representations include a solid line for the α-helix, a long dashed line for antiparallel β-sheet, a dotted line for type I β-turn, a cross-dashed line for extended 3_1-helix or poly(Pro) II helix, and a short dashed line for irregular structure.[30]

To discern secondary structures in proteins, specific features are observed in CD spectra. For instance, the far-UV-CD of a random coil is positive at 212 nm (n → π*) and negative at 195 nm (π → π*). The far-UV-CD of a β-sheet is negative at 218 nm (π → π*) and positive at 196 nm (n → π*). In the case of an α-helix, the exciton coupling of the π → π* transitions results in positive (π → π*) signals perpendicular at 192 nm, negative (π → π*) signals parallel at 208 nm, and a negative shift at 222 nm (n → π*), respectively. The proportion of each secondary structure type in a protein can be estimated by analyzing its far-UV CD spectrum as a sum of fractional multiples of reference spectra for each structural type. However, CD spectra provide an average representation of the entire molecule, making it challenging to pinpoint

which specific residues are involved in a particular portion.Technically, far-UV CD spectra necessitate 20–200 μL of a solution containing 1 mg/mL to 50 μg/mL protein, in a buffer that does not have high absorbance in this spectral region. High concentrations of certain substances, such as dithiothreitol, histidine, or imidazole, which have significant absorbance, should be avoided in the far-UV region. Frequently, it is essential to establish that a modification to a protein results in equivalent conformations for it to perform its function effectively. For instance, following a chemical or genetic modification of a specific protein, CD proves to be a valuable technique for comparing the native and modified forms.

3.6.3. Assessment of the thermal stability of the proteins

Assessment of thermal stability is conducted using CD by tracking changes in the spectrum as temperature increases. In some instances, the entire spectrum in the far- or near-UV CD region is monitored at various temperatures. Alternatively, a specific wavelength can be selected to observe a particular feature of the protein structure, and the signal at that wavelength is continuously recorded as temperature rises. CD is commonly employed to evaluate how solution pH, buffers, and additives like sugars, amino acids, or salts influence thermal stability. Many proteins undergo rapid aggregation or precipitation once they are unfolded (or melted), resulting in irreversible unfolding. The reversibility of the unfolding reaction is assessed by cooling the sample and reheating to observe if the unfolding reaction repeats. Identifying solvent conditions that render unfolding reversible may be more critical for long-term stability (shelf-life) than increasing the melting temperature. If the melting is fully reversible, the melting temperature is directly linked to conformational stability, and the thermodynamics of protein folding can be deduced from CD data. In cases where the protein precipitates or aggregates upon unfolding, the melting reaction becomes irreversible, and the melting temperature reflects the kinetics of aggregation, the solubility of the unfolded form, and the intrinsic conformational stability. Qualitatively, the cooperativity of the unfolding reaction is

measured by the width and shape of the unfolding transition. A highly cooperative unfolding reaction suggests the protein initially existed as a compact, well-folded structure, while a gradual, non-cooperative melting reaction indicates the protein was initially very flexible, partially unfolded, or a heterogeneous population of folded structures (11,12). Concerning the melting of secondary structure, monitoring changes across the entire far-UV CD region helps determine whether the protein loses all, part, or undergoes a conformational change involving a shift in secondary structure at high temperatures. Occasionally, the unfolded form of a protein may exhibit a defined, yet entirely different secondary structure than the native form. Changes in tertiary structure during melting can be tracked by observing alterations in the near-UV CD region. Such studies reveal whether protein melting occurs in a single-step reaction, involving concurrent loss of both secondary and tertiary structure, or a two-step reaction. For example, melting curves for barnase indicated that the decrease in CD at 194 nm with increasing temperature is due to the cooperative melting of secondary structure, while the decrease in CD at 280 nm indicates loss of tertiary structure. The congruence of the 194 and 280 nm melting curves confirms that alterations in secondary and tertiary structures occur concurrently (**Figure 3.16**).

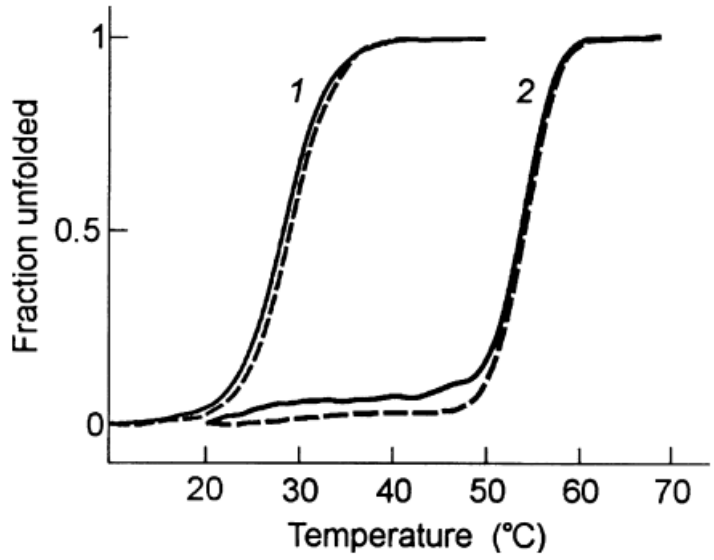

Figure 3.16. Temperature-dependent CD data for barnase are presented in melting curves at two different pH levels: (1) pH 2.4 and (2) pH 5.5. The curves depict the temperature dependence of CD at 280 nm (solid line) and 194 nm (dashed line).[30]

References

(1) *Physical Principles of Electron Microscopy*; 2005.

(2) Wang, Z. L. Characterization of Nanophase Materials. *Particle and Particle Systems Characterization* **2001**, *18* (3), 142–165. https://doi.org/10.1002/1521-4117(200110)18:3<142::AID-PPSC142>3.0.CO;2-N.

(3) Koch, C. C. *Nanostructured Materials : Processing, Properties, and Applications*; William Andrew Pub, 2007.

(4) *Springer Handbook Of Microscopy Hawkes Spence Editors*.

(5) Joy, S. B. D. C.; Ford, B. J. Transmission Electron Microscope. *Encyclopædia Britannica* **2018**.

(6) Ford, B. J.; Joy, D. C.; Bradbury, S. Scanning Electron Microscope. *Encyclopedia Britannica* **2019**, *30*.

(7) Fagerlund, G. *Determination of Specific Surface by the BET Method*.

(8) Schmal, M. *Heterogeneous Catalysis and Its Industrial Applications*.

(9) Barrett, E. P.; Joyner, L. G.; Halenda Vol, P. P.; -RnAtn Apj, R.; Vn-Rn Atn Ac, R. A. *Vp2 = R2AV2-R2AT2 ACi Generalizing Equation (4) and Substituting (6a) for Vm* Yields*.

(10) Fu, S.; Fang, Q.; Li, A.; Li, Z.; Han, J.; Dang, X.; Han, W. Accurate Characterization of Full Pore Size Distribution of Tight Sandstones by Low-Temperature Nitrogen Gas Adsorption and High-Pressure Mercury

Intrusion Combination Method. *Energy Sci Eng* **2021**, *9* (1), 80–100. https://doi.org/10.1002/ese3.817.

(11) Moujijn, J. A.; Van Leeuwen, P.; Van Santen, R. A. Catalysis–Studies Science and Catalysis, Vol. 79. Amsterdam: Elsevier Scientific Publishing Company 1993.

(12) Masel, R. I. *Principles of Adsorption and Reaction on Solid Surfaces*; John Wiley & Sons, 1996; Vol. 3.

(13) Pota, G.; Silvestri, B.; Vitiello, G.; Gallucci, N.; Di Girolamo, R.; Scialla, S.; Raucci, M. G.; Ambrosio, L.; Di Napoli, M.; Zanfardino, A. Towards Nanostructured Red-Ox Active Bio-Interfaces: Bioinspired Antibacterial Hybrid Melanin-CeO2 Nanoparticles for Radical Homeostasis. *Biomaterials Advances* **2023**, *153*, 213558.

(14) Gabbott, Paul. *Principles and Applications of Thermal Analysis*; Blackwell Pub, 2008.

(15) Prime, R. B.; Bair, H. E.; Vyazovkin, S.; Gallagher, P. K.; Riga, A. Thermogravimetric Analysis (TGA). *Thermal analysis of polymers: Fundamentals and applications* **2009**, 241–317.

(16) Ojeda, J. J.; Dittrich, M. Fourier Transform Infrared Spectroscopy for Molecular Analysis of Microbial Cells. *Methods in Molecular Biology* **2012**, *881*, 187–211. https://doi.org/10.1007/978-1-61779-827-6_8.

(17) Anton Paar. *Attenuated Total Reflectance (ATR)*.

(18) Stetefeld, J.; McKenna, S. A.; Patel, T. R. Dynamic Light Scattering: A Practical Guide and Applications in Biomedical Sciences. *Biophysical Reviews*. Springer Verlag December 1, 2016, pp 409–427. https://doi.org/10.1007/s12551-016-0218-6.

(19) Kato, H. Dynamic Light Scattering. *Tanpakushitsu kakusan koso. Protein, nucleic acid, enzyme*. 2004, pp 1676–1680. https://doi.org/10.1119/1.19101.

(20) Lunardi, C. N.; Gomes, A. J.; Rocha, F. S.; De Tommaso, J.; Patience, G. S. Experimental Methods in Chemical Engineering: Zeta Potential. *Canadian Journal of Chemical Engineering*. Wiley-Liss Inc. March 1, 2021, pp 627–639. https://doi.org/10.1002/cjce.23914.

(21) Ohshima, H.; Makino, K. *Colloid and Interface Science in Pharmaceutical Research and Development*; Elsevier, 2014.

(22) Instruments, M. Measuring Zeta Potential–Laser Doppler Electrophoresis. *Malvern Guides* **2015**, 1–2.

(23) Gerothanassis, I. P.; Troganis, A.; Exarchou, V.; Barbarossou, K. *NUCLEAR MAGNETIC RESONANCE (NMR) SPECTROSCOPY: BASIC PRINCIPLES AND PHENOMENA, AND THEIR APPLICATIONS TO CHEMISTRY, BIOLOGY AND MEDICINE*; 2002; Vol. 3.

(24) Zamora Carreras, H. NMR Spectroscopy Principles, Interpreting an NMR Spectrum and Common Problems. *Technology Networks (Analysis and Separation)* **2021**.

(25) Cheung, P. C. K. *Handbook of Food Chemistry*.

(26) Par~, J. R. J.; B~langer, J. M. R. *Chromatography: And Applications Principles*.

(27) Bartle, K. D.; Myers, P. *History of Gas Chromatography +*.

(28) Turner, D. Gas Chromatography – How a Gas Chromatography Machine Works, How To Read a Chromatograph and GCxGC. *Technology Networks (Analysis & Separations)* **2021**.

(29) Woody, R. W. [4] Circular Dichroism. *Methods Enzymol* **1995**, *246* (C), 34–71. https://doi.org/10.1016/0076-6879(95)46006-3.

(30) Ranjbar, B.; Gill, P. Circular Dichroism Techniques: Biomolecular and Nanostructural Analyses- A Review. *Chem Biol Drug Des* **2009**, *74* (2), 101–120. https://doi.org/10.1111/J.1747-0285.2009.00847.X.

Chapter 5

Design of mesoporous nanoscaled supported biocatalysts

Contents

1. Controlling the adsorption of β-glucosidase onto wrinkled SiO_2 nanoparticles to boost the yield of immobilization of an efficient biocatalyst

This section refers to the original version of the paper by Pota, G. et al. *Langmuir*, 2023, *39*(4), 1482-1494. https://doi.org/10.1021/acs.langmuir.2c02861.[1]

1.1. Abstract

β-glucosidase (BG) catalyzes the hydrolysis of cellobiose to glucose, a substrate for fermentation to produce carbon-neutral fuel bioethanol. Enzyme thermal stability and reusability can be improved through immobilization onto insoluble supports. Moreover, nanoscaled matrices allow for preserving high reaction rates. In this work, BG was physically immobilized onto wrinkled SiO_2 nanoparticles (WSNs). The adsorption procedure was tuned by varying BG:WSNs weight ratio in order to achieve the maximum controllability and maximize the yield of immobilization, while different times of immobilization were monitored. Results show that BG:WSNs equal to 1:6 wt/wt provides for the highest colloidal stability, whereas an immobilization time of 24 h results in the highest enzyme loading (135 mg/g of support) corresponding to 80% yield of immobilization. An enzyme corona is formed in 2 h, which gradually disappears as the protein diffuses within the pores. The adsorption into the silica structure cause little changes in the protein secondary structure. Furthermore, supported enzyme exhibits a remarkable gain in thermal stability, retaining complete folding up to 90°C. Catalytic tests assessed that immobilized BG achieves 100% cellobiose conversion. The improved adsorption protocol provides simultaneously high glucose production, enhanced yield of

immobilization and good reusability, resulting in considerable reduction of enzyme waste in the immobilization stage.

1.2. Graphical abstract

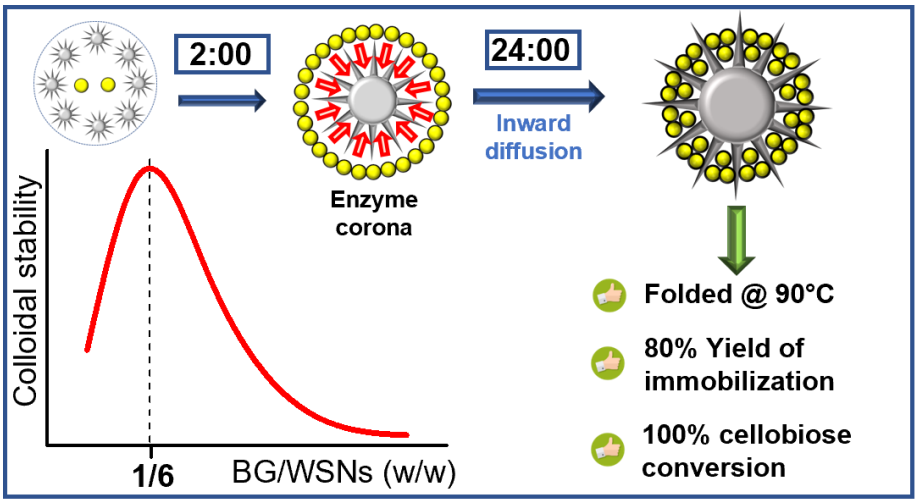

1.3. Introduction

Enzymes are a family of nontoxic, environmentally friendly biomolecules, involved in a plethora of biochemical processes. [2] They are widely used as biocatalysts thanks to their outstanding properties such as milder reaction conditions, higher specificity and selectivity, faster kinetics with respect to traditional catalysts. [2] However, they suffer from intrinsic instability in harsh operative conditions and are expensive.[3] Several technical challenges need to be overcome to make enzymatic processes economically feasible: the high cost of the enzymes, their low thermal and pH stability causing a loss of activity during the process, the inhibition by reactants and products, and difficult recovery.[3] These drawbacks can be overcome by enzyme immobilization. Indeed, immobilization usually results in increased pH, temperature and organic solvent tolerance as well as resistance to proteolytic digestion and denaturants.[4,5] The key issue for enzyme immobilization is the selection of the

immobilization technique and of the appropriate support. Many different immobilization methods are proposed to improve the biocatalyst efficiency. [6] Among them, physical immobilization is the simplest and can be carried out under mild conditions,[7] being based on physical interactions, such as hydrogen bonding, electrostatic forces and hydrophobic interactions between the enzyme and the matrix. With this method, the enzyme activity is often preserved, but the immobilized enzyme can have poor operation stability and be subjected to leaching.[8] For this reason, the choice of a good support is crucial. It should exhibit thermal and mechanical stability, high surface area, adequate pore diameter, biocompatibility, and chemical affinity towards the enzyme, in order to create the optimal microenvironment to preserve protein conformation, activity and ensure reusability. [7] In this context, mesoporous SiO_2 nanoparticles are very performing supports, thanks to a high surface area and tuneable porosity allowing for high loading of guest species. [9–11] Moreover, the great availability of surface hydroxyl groups enables easy chemical functionalization. [12–15] In particular, Wrinkled Silica Nanoparticles (WSNs), which are mesoporous nanoparticles with central-radial pore structure, are gaining great attention as carrier for enzymes since the conical pore shape helps reduce pore blocking.[16] Furthermore, hierarchical trimodal porosity effectively lowers diffusive limitations for both substrate and products.[16] Another important issue is about the colloidal stability of the supported systems that has a significant effect on the catalytic performances of the immobilized enzymes.[17,18] Indeed, fast self-aggregation or precipitation processes in the reaction media can hinder the substrate accessing or induce unfavourable conformational transition of the enzyme on the support,[17,19] thus drastically decreasing the biocatalytic activity. These dynamics are often triggered by the complex behaviour of enzymes in solution since proteins can unfold and aggregate, depending on ionic force and pH values, forming clusters of different size.[20] Hence, robust immobilization on the nanoparticles as well as great colloidal and structural stability appear mandatory to design biocatalysts

with high performances, reduce preparation costs and promote higher reusability. [21,22] Protein-nanoparticle interactions have been extensively studied. [23–25] Most nanoparticles are readily covered by a dynamic layer of proteins when put in contact, generating what is called a protein corona. Not a single kind of interaction can be attributed to protein-surface adsorption, but it rather generates from a complex interplay of polar and nonpolar interaction mechanisms. [23] Both kinds of interaction can be attractive or repulsive, determining the formation of the corona. With porous nanoparticles, the protein corona that possibly forms can later migrate inside the pores.[26] Recently, we have used WSNs as a matrix to immobilize β-Glucosidase (BG) and cellulase.[27,28] BG belongs to glycosyl hydrolase family that finds application in many biotechnological fields. [29,30] It plays a key role in the enzymatic degradation of cellulose, hydrolysing cellobiose to two glucose molecules and allowing to produce sugars that can be fermented in ethanol. The alcohol thus produced can be used as biofuel, with both environmental and geopolitical benefits. [31] Physical immobilization was carried out to attach BG onto WSNs, leading to a performing and stable biocatalyst for the hydrolysis of cellobiose. [27] Adsorption allowed for preserving enzyme native conformation and increasing substrate-enzyme affinity, leading to 100% cellobiose conversion in 2 h. [32] The yield of immobilization (YI), defined as the percentage weight ratio between the adsorbed enzyme and the overall enzyme used in the immobilization step, reached 30%.[27] In a subsequent work dealing with the immobilization of cellulase onto the same nanoparticles, Costantini et al. found out that the YI varies with the enzyme concentration in the adsorption environment following an exponential decay function.[28] This result confirmed what previously observed for lysozyme immobilization into mesoporous silica.[33] Therefore, the lower the enzyme concentration, the higher the YI and thus the lower the enzyme waste. In this work, physical immobilization of BG onto WSNs under diluted conditions was performed. Different enzyme concentrations, corresponding to precise BG:WSN weight ratios, were investigated with the aim to discover the best conditions to limit the self-

aggregation process and enhance the control over the protein-support interaction dynamics. At the same time, the search for the optimal system was intended to optimize the yield of immobilization in order to keep a high enzyme density all over the surface of the nanoparticles. The most stable BG/WSNs systems were tested in the hydrolysis of cellobiose to glucose and compared with the performances of the reference system previously designed.

1.4. Experimental

1.4.1. Materials

Tetraethylorthosilicate (TEOS), urea, cetyltrimethylammonium bromide (CTAB), cyclohexane, anhydrous 2-propanol (ACS reagent), ethanol, hydrochloric acid solution (37.0 % wt. in water), β-glucosidase from almonds (molecular weight 135 kDa for the dimer, product number 49290, specific activity ≥ 4 U/mg, measured as micromole of glucose liberated per minute at pH 5 and 37°C with salicin as substrate), citric acid, trisodium citrate dihydrate, sulfuric acid (95.0-98.0 % wt.), glucose oxidase-peroxidase (GOD-POD) assay kit and potassium bromide were purchased from Sigma-Aldrich (Milan, Italy).

1.4.2. Synthesis of Wrinkled SiO_2 Nanoparticles (WSNs)

The preparation of Wrinkled SiO_2 Nanoparticles (WSNs) was inspired by the synthetic route described by Moon and Lee,[16] which was opportunely modified by using cetyltrimethylammonium bromide (CTAB) instead of cetylpyridinium bromide (CPB) as templating agent for mesopores formation. Also, a more accurate 24-h lasting surfactant removal step was introduced into the preparation protocol. More specifically, 123.68 mL of a solution of IPA and cyclohexane (IPA 3 v/v%) were mixed to an aqueous solution of CTAB (0.01 M) and Urea (0.33 M). The reaction mixture promptly turned from transparent into white. Afterwards, TEOS was added dropwise to the stirred solution for a final concentration of 0.18M. Finally, the reaction system was stirred for 30 min at room temperature and then heated up to 70 ◦C for 16 h. The obtained nanoparticles were centrifuged, washed three times

with ethanol and submitted to acid extraction of the surfactant by dispersion in a HCl-ethanol solution ([HCl] = 1.3 M) for 24h at 70°C. Finally, the nanoparticles were collected by centrifugation and washed three times with ethanol.

1.4.3. Physical immobilization of BG onto WSNs

Physical immobilization of BG onto WSNs was designed following the protocol reported by Califano et al.[27] However, to define the optimal conditions for enzyme adsorption preventing the self-aggregation process, the procedure was carried out in diluted conditions and different concentrations of BG were investigated. More precisely, 3 mg of WSNs were dispersed in 9.5 mL of citric acid/sodium citrate buffer (21 mM, pH=5). 500 μL of each BG solution in buffer were then added to the WSN colloidal suspension. Four BG solutions of different concentrations were tested: 0.6, 1, 1.5, 3 mg/mL, corresponding to precise BG:WSNs weight ratios of 1:10, 1:6, 1:4, 1:2, respectively. Each mixture was kept under mild stirring (400 rpm) at 40 °C for 24 h. Then, 0.6 mL of each prepared BG/WSN mixture was analyzed through Dynamic Light Scattering (DLS) to identify the best immobilization conditions for enhancing the stability of the supported enzyme. Subsequently, to study the time evolution of the most controllable BG/WSNs system (1:6), 0.6 mL of each prepared BG/WSN mixture were withdrawn after 15 min, 2 h, 6 h and 24 h to be analyzed through Dynamic Light Scattering (DLS), Circular Dichroism (CD) and ζ-potential measurements. The prepared samples were named as BG/WSNs_15min, BG/WSNs_2h, BG/WSNs_6h and BG/WSNs_24h. The supported BG/WSNs biocatalysts were collected by centrifugation after double-washing with bi-distilled water to perform catalytic assays as well as other physicochemical analyses. This optimized BG/WSNs system was studied in terms of catalytic performances. The yield of immobilization (YI) was evaluated through thermogravimetric analysis (TGA).

1.4.4. Physicochemical analysis of morphology, size distribution and solution behavior of BG/WSNs

Morphological and dimensional analysis of bare WSNs and BG-loaded WSNs was carried out through Transmission Electron Microscopy (TEM), using a FEI Tecnai G12 Spirit Twin (FEI, Hillsboro, OR, USA) with LaB6 emission source and an acceleration tension of 120 kV. The images are taken with a CCD FEI Eagle 4k camera. The samples to be measured were prepared by soaking the proper copper grid used for TEM measurements (400 mesh with a thin carbon film) into an aqueous suspension of the nanoparticles with concentration set at 0.5 mg/mL.. Time evolution of the colloidal stability and self-aggregation process of the BG/WSNs systems during the immobilization process was monitored by Dynamic Light Scattering (DLS) measurements.[34,35] A home-made experimental set up, composed of a Photocor compact goniometer (Moscow, Russia), a SMD 6000 Laser Quantum 50 mW light source (Laser Quantum, Fremont, CA, USA) operating at 532.5 Å, a photomultiplier (PMT-120-OP/B) and a correlator (Flex02−01D) from Correlator.com (Shenzhen, China) was used. The experimental temperature was fixed to room value (25°C), while the scattering angle θ was set at 130°. A regularization algorithm was used to analyze the correlation function of the scattered intensity (I(t)) reported below as:

$$G^2(\tau) = < I(t)I(t+\tau) >$$

where $G^2(\tau)$ is the correlation function of the scattered intensity I(t) and the angular brackets denote an average over time t. [36] The autocorrelation function is necessary to extract information about the colloidal stability of the nanostructures from the random fluctuation of the scattered intensity. The hydrodynamic radius (R_H) of the nanostructures was calculated as follows:

$$R_H = k_B T/6\eta\pi D$$

where k_B is the Boltzmann constant, T is the absolute temperature, η is the solution viscosity and D is the average diffusion coefficient measured in the DLS experiments. For each sample, twelve acquisitions of the scattering intensities lasting 120 seconds each were collected in order to have a good and reproducible statistics.

ζ-potential measurements were performed to assess the nature of enzyme-support interaction and the influence of the surface charge on the colloidal stability of BG/WSNs nanosystems. About 600 μL of each suspension at different immobilization times were analysed by means of electrophoretic light scattering using a Zetasizer Nano ZSP (Malvern Instruments, England). Each measurement was recorded at 25 °C upon a 30 s equilibration time and the average of three measurements at a stationary level was taken. ζ-potential was calculated by the Smoluchowski model.

1.4.5. Quantification of the enzyme fraction in commercial BG

An estimation of the protein content in the commercial BG was realized through UV analysis, following the procedure first reported by Goldfarb in 1950s.[37] Briefly, a 1 mg/mL BG buffer solution was loaded in a 1 cm path length quartz cuvette and submitted to UV-vis spectrum recording in 240-320 nm range. The enzyme concentration was then calculated following equation (1) derived from the Lamber-Beer law:

$$M=A/(l\cdot\varepsilon) \qquad (1)$$

where M (mol·L-1) is the protein molar concentration, A is the absorbance at 280 nm, l (cm) is the optical length and ε is the BG molar absorptivity ($L\cdot mol^{-1}\cdot cm^{-1}$).

The presence of other protein fractions within the commercial powder was investigated through sodium dodecyl sulphate–polyacrylamide gel electrophoresis (SDS-PAGE).

1.4.6. Evaluation of the yield of immobilization

The yield of immobilization (YI) was determined through Thermogravimetric Analysis (TGA). 10 mg of each dried sample were grinded and loaded into platinum pans to be thermally treated from 30 to 1000 °C under air atmosphere, with a heating rate of 10 °C/min. The decay in the initial weight of each sample was monitored. The enzyme weight fraction contained in the BG/WSNSs samples was calculated as the weight loss between 200 °C and the final temperature over the initial weight, in percentage, minus the organic weight fraction of the bare support. YI was then

evaluated as the percentage ratio between the loaded enzyme and the amount of protein dissolved initially in the adsorption mixture. The activity yield of immobilization YI_E was calculated by the formula $YI_E=(E_i/E_c)*100$, where E_c represents the contacted enzyme activity and E_i the activity expressed by the immobilized enzyme.[38]

1.4.7. Conformational analysis of immobilized BG

Circular Dichroism (CD) was carried out to analyze the structural stability of the supported BG enzyme as well as the evolution of its conformation. For CD analysis, 300 µL of each BG/WSNs suspension were withdrawn from the reactor, poured in a 0.1 cm path length cuvette and analysed using a Jasco J-710 spectropolarimeter equipped with a Peltier thermostatic cell holder (Model PTC-348WI). CD spectra were recorded in 195-250 nm range, with a resolution of 0.5 nm, at both room temperature (25 °C) and reaction temperature (50 °C). Thermal denaturation curves were obtained by heating the samples from 25 °C up to 90 °C, with a heating rate of 1 °C/min and following the CD signal at the fixed wavelength of 222 nm. A Nexus spectrometer equipped with a DTGS (deuterated triglycine sulfate) KBr detector was used to perform FTIR experiments. All the BG/WSNs samples were dried, grinded and pressed into pellets (13 nm in diameter). FTIR spectra were recorded in the 4000-400 cm^{-1} range, choosing a spectral resolution of 2 cm^{-1} and 32 scans for each acquisition. KBr spectrum was chosen as background. The occurrence of any modifications in the protein secondary structure was assessed by gaussian deconvolution of Amide I band, performed by means of GRAMS 32 software. The number of gaussian components and their initial position were determined by the second derivative spectrum.

1.4.8. Catalytic assays

For the hydrolysis of cellobiose to glucose, a cellobiose solution in citric acid/sodium citrate buffer (pH=5, 21 mM) was added to an equal volume of a BG/WSNs suspension in the same medium to have final concentrations of cellobiose and BG

fixed to 1.5 and 0.15 mg/mL, respectively. The system was kept under mild stirring at 50 °C for 24 h. The supernatant with the final obtained product was separated from the supported BG/WSNs biocatalyst by centrifugation (11500 rpm, 10 min) and then was kept in oven (100 °C, 10 min) to thermally inactivate traces of the free enzyme which might had leaked from the support. Finally, the concentration of produced glucose was assessed through the D-glucose oxidase–peroxidase method. [39] In detail, 300 μL of the collected supernatant were diluted to 1:10 v/v with bi-distilled water, mixed to 600 μL of glucose-measuring reagent and kept in a thermostatically controlled water bath at 37 °C. After 30 min, the reaction was stopped by adding 600 μL of sulfuric acid (12 N) and 1.5 mL of the final solution was poured in a 1 cm path length quartz cuvette and underwent absorbance measurement at 540 nm using a SHIMADZU UV-2600i spectrophotometer (Shimadzu, Milan, Italy). The glucose concentration was estimated thanks to a calibration curve. The results were expressed in terms of yield of cellobiose conversion, defined as the concentration (mg/mL) ratio between obtained glucose and initially loaded cellobiose, in percentage. Similarly, the product obtained after 10 min of reaction was also analysed to determine the specific activity of the supported biocatalysts, expressed in U/mg of enzyme. Units (U) indicate the μmoles of glucose produced per minute by a certain amount of enzyme. Experiments were repeated in triplicate.

1.4.9. Operational and thermal stability

Reusability assays were carried out for BG/WSNs_2h and BG/WSNs_24h systems. The biocatalysts were tested in consecutive reaction cycles of 24 h. After each cycle, produced glucose was evaluated as previously described. The biocatalysts were collected by centrifugation and washed twice with bidistilled water before each reaction cycle. The results were expressed in terms of glucose production over the reuse cycles. The occurrence of leakage phenomena affecting the performance of the supported biocatalysts in the consecutive reuses was assessed by TGA measurements. The experimental conditions were the same as those used to evaluate the yield of immobilization. More specifically, the enzyme weight fraction was

estimated before and after the reuse cycle associated to a remarkable loss in terms of glucose production. Both the supported biocatalysts and free BG underwent thermal stability assessment. Briefly, the samples were dispersed (dissolved, in the case of the free enzyme) in citrate buffer, incubated for 1h at a set temperature (60, 70, 80 °C) and then used to perform cellobiose hydrolysis for 24h at 50°C.

The cellobiose conversion obtained without submitting the samples to thermal stress was chosen as reference to evaluate the residual cellobiose conversion (%).

1.5. Results and Discussion

1.5.1. Colloidal behavior and morphology of immobilized BG/WSN

DLS analysis was performed on both naked and BG-loaded WSNs to investigate the colloidal behavior of the systems in aqueous environment as function of the enzyme/nanoparticles ratios and immobilization times. First, a suspension of bare WSNs was analyzed as reference sample. As reported in **Figure 1A**, the hydrodynamic radius distribution shows a polydisperse system with the presence of two populations: the first one is centered at about 290 nm, while the second one is centered at about 2500 nm. This representation emphasizes the presence of large aggregates. Converting the intensity weighted profile into numerical weighted profile, an indication of the relative concentration of the different species in the WSNs suspension is given. This second representation clearly indicates the presence of the most abundant population centered at about 280 nm as hydrodynamic radius.

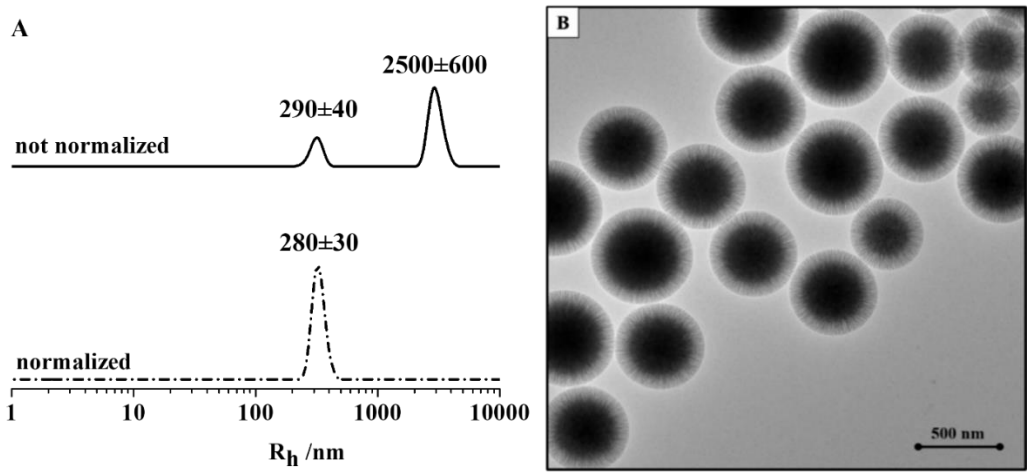

Figure 1. A. Hydrodynamic radius distribution of bare WSNs: intensity weighted profile (solid line) and numerical weighted profile (dashed line). **B**. TEM image of bare WSNs, scalebar=500 nm.

Figure 1B reports TEM micrographs for bare WSNs. The nanoparticles exhibit spherical profiles, with silica fibers spreading radially from the center to the outer surface. The mesoporous structure is made of conical pore channels, with pore size increasing moving outward, as confirmed by the remarkable decrease in contrast with respect to the inner portion of the nanoparticles, where silica skeleton gets thicker. Moreover, this micrograph confirms the presence of silica nanoparticles with size ranging from 450 to 550 nm in diameter, whereas micrometric aggregates are not detected. Therefore, the population of 2500 nm in diameter detected through DLS analysis can be univocally attributed to the presence of clusters of WSNs, confirming that the naked nanostructures tend to aggregate in aqueous solution. As described in the experimental section, different BG:WSNs weight ratios, equal to 1:2, 1:4, 1:6 and 1:10, were considered. In all cases, the immobilization time of 24 h was firstly considered, according to the previously investigated system.[27] The total protein content in the BG commercial powder had been evaluated before the adsorption protocol was started and the estimated value was equal to 24 wt% (see Supporting Information, **Figure S1**). This estimation was considered as correct since SDS PAGE

analysis was performed for 1:6 BG:WSNs ratio (**Figure S2**). Indeed, the images of the gels proved the absence of other proteins besides BG in the commercial product. As a matter of fact, both the profiles of the offered and the immobilized protein (**Figure S2 a, S2 c**) exhibit only one band centered at a molecular weight of about 65 kDa, corresponding to the monomeric form of BG. In fact, SDS PAGE, as known, does not allow detecting oligomeric forms of proteins due to the strong denaturating effect of SDS.[40] No band is detected in the profile of the supernatant (**Figure S2 b**), suggesting almost complete immobilization of the protein.

Therefore, only one quarter of the commercial product is actually made of protein. **Figure S3** displays the autocorrelation functions versus time of BG/WSNs_24h at the considered weight ratios. However, although the self-aggregation and precipitation of greater aggregates occur in all samples, some differences can be observed as function of enzyme/nanoparticles weight ratio. Indeed, by comparing the autocorrelation functions shown in **Figure S3**, a slightly better situation is observed for 1:4 and 1:6 ratios for which the curves tend to reach a plateau condition over time, suggesting that they represent the best conditions capable of promoting greater control of the physical immobilization process of the enzyme onto WSNs. On the other hand, the correlation function of 1:10 w/w sample starts to decay at slightly longer times than the two other systems and does not reach a plateau at value $g^2(t) = 1$, indicating the presence of greater particles, such as large clusters. This could be related to the presence of a very small fraction of WSNs covered with the BG enzyme and, therefore, the prevalence of naked WSNs, which show a greater tendency to self-aggregate and precipitate. Consequently, according to DLS evidence and considering the opportunity to use as low BG amount as possible to make the final biocatalyst, only the system designed by fixing BG:WSN wt/wt equal to 1:6 was further investigated. Four immobilization times (15', 2 h, 6 h and 24 h) were monitored by DLS to study the time evolution of the system during the adsorption process. Considering only the intensity-weighted profiles for both WSNs

and BG/WSNs sample after 15 minutes of immobilization (**Figure 2**), the curves exhibit a population bigger than 2000 nm, but the most significant result is the presence of another population, centered below 500 nm, which is bigger than the corresponding one for bare WSNs. This would suggest that BG is already adsorbed onto WSNs already after the first 15 minutes without gaining colloidal stability.

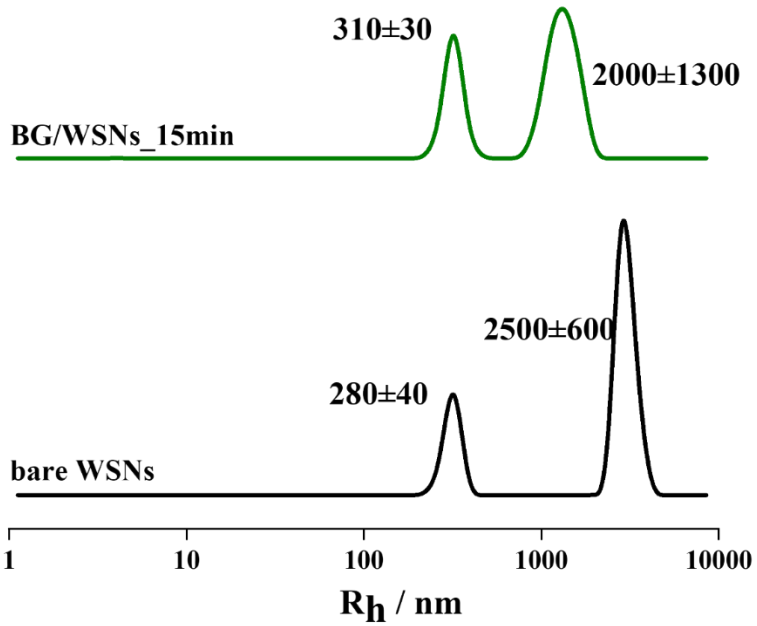

Figure 2. Hydrodynamic radius distribution of bare WSNs (black line) and BG/WSNs_15min weight ratio (olive line).

Unfortunately, due to the rapid evolution of the system also related to the self-aggregation process occurring with the time, it is not possible to make a precise estimation of the size of BG/WSNs at diverse immobilization times. However, a comparison of the correlation functions can be done. As shown in **Figure 3**, no significant differences are observed between the different systems: a slightly better condition should be associated to the BG/WSNs_2h sample, which appears more similar to the BG/WSNs_15min one, while those prepared at longer immobilization times look almost equivalent. Finally, the colloidal stability of the system could be

increasingly worse with time due to aggregation phenomena triggered by adsorbed enzyme.

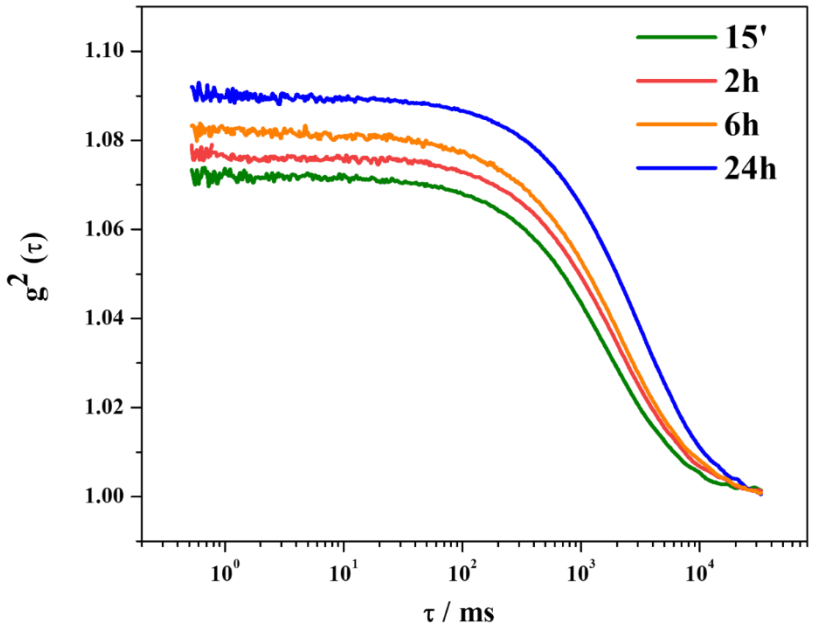

Figure 3. The intensity autocorrelation functions of BG:WSNs weight ratio of 1:6 at different immobilization time: 15 minutes (olive line), 2 h (red line), 6 h (orange line), and 24 h (blue line).

The changes in the morphology of supported biocatalysts occurring during adsorption were investigated through TEM analysis (**Figure 4**). **Figures 4A** and **4B** show lower and higher magnifications of bare WSNs, respectively. As previously said, the pronounced difference in terms of contrast between the core and the border portion of the nanostructure is due to the extended presence of radial pore channels. Micrographs for BG/WSN_15min (**Figure 4C, 4D**) exhibit a decrease in the contrast

difference. In particular, a thin enzyme layer seems to be adsorbed onto the outer surface of the nanoparticles while pores are expected to be only partially filled (**Figure 4D**). Moving onward to 2 h of immobilization, a wide enzyme corona surrounding clusters of nanoparticles becomes visible (**Figure 4E, 4F**). Indeed, 2 h are enough to allow for a consistent amount of protein to be adsorbed externally and start diffusing inward. Protein adsorption could trigger aggregation phenomena, since the enzyme appears organized in extended aggregates enveloping clusters of few nanoparticles (**Figure 4E**). Furthermore, the surfaces of close nanoparticles are bound to each other by enzyme bridges (**Figure 4F**). Complete pore filling seems to be accomplished after 24 h. Indeed, the whole profile of the nanoparticles exhibit a homogeneously dark contrast, suggesting that the protein is completely hosted by the mesopore channels (**Figure 4G**). Moreover, the wide enzyme aggregates, visible in BG/WSNs_2h samples (**Figure 4E, 4F**), disappears, resulting in the absence of a proper protein corona layer of noticeable thickness (**Figure 4H**).

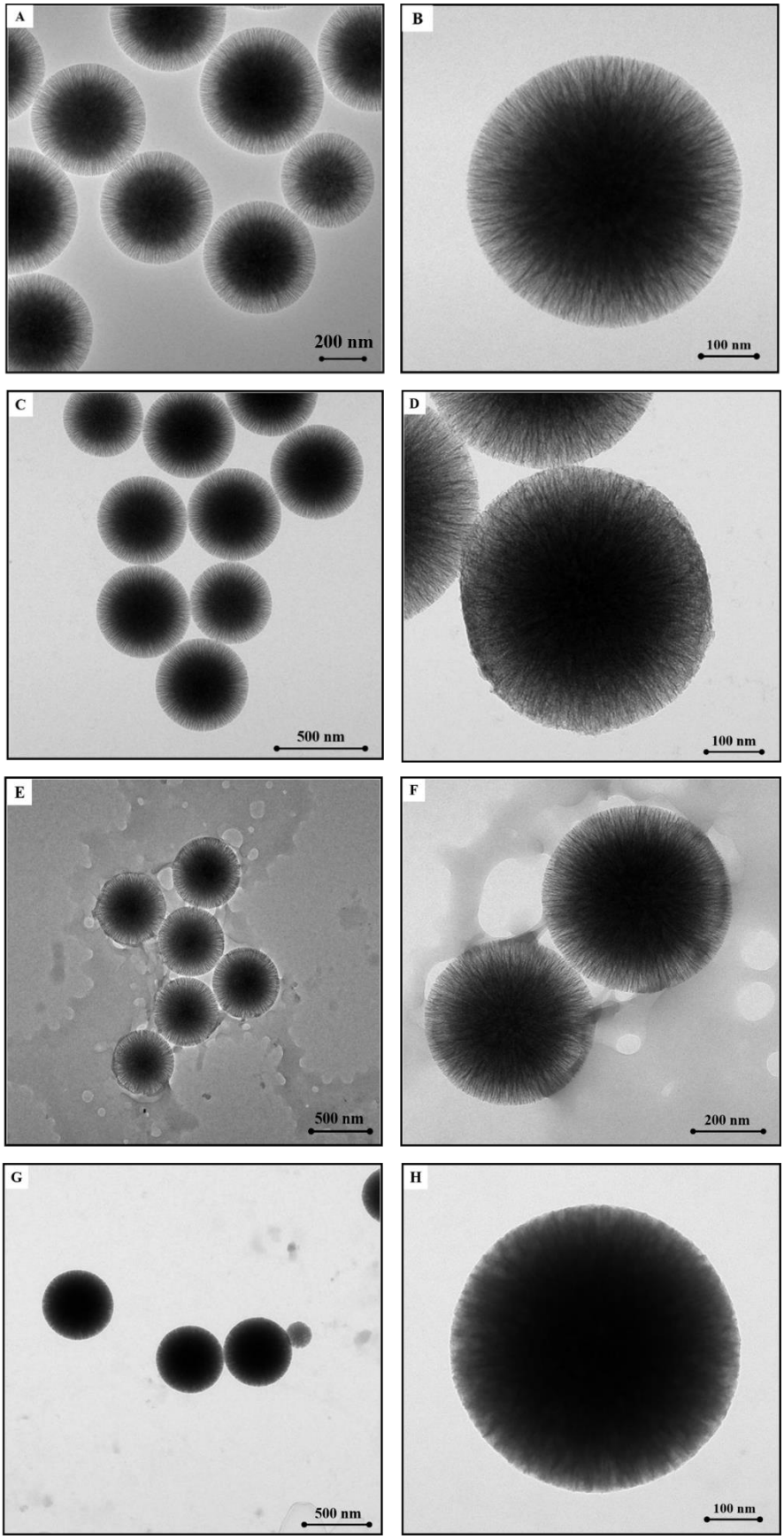
A
200 nm
B
100 nm
C
500 nm
D
100 nm
E
500 nm
F
200 nm
G
500 nm
H
100 nm

Figure 4. TEM images for WSNs (A scalebar=200 nm, B scalebar=100 nm), BG/WSNs_15min (C scalebar=500 nm, D scalebar=100 nm), BG/WSNs_2h (E scalebar=500 nm, F scalebar=200 nm), BG/WSNs_24h (G scalebar=500 nm, H scalebar=100 nm)

A quantitative analysis of TEM images was performed by the Histogram function of the software National Instrument Vision assistant. The Histogram function counts the total number of pixel in each of the 256 grayscale level (zero is black). These intensity profiles were taken along a horizontal line passing through the center of the particle. The results are shown in **Figure 5**. As can be seen, the first maximum, which represents the darkest region of the particle, moves towards smaller pixel values and increases in intensity as the contact time between the enzyme and the support increases. The second maximum, which represents the clearest part, moves significantly towards smaller pixel values (maximum at 120 for WSNs, at 70 for BG / WSNs_15min and BG / WSNs_2h) and almost disappears for BG/WSNs_24h meaning that all the porous structure of the silica skeleton is gradually filled by the protein during the immobilization process.

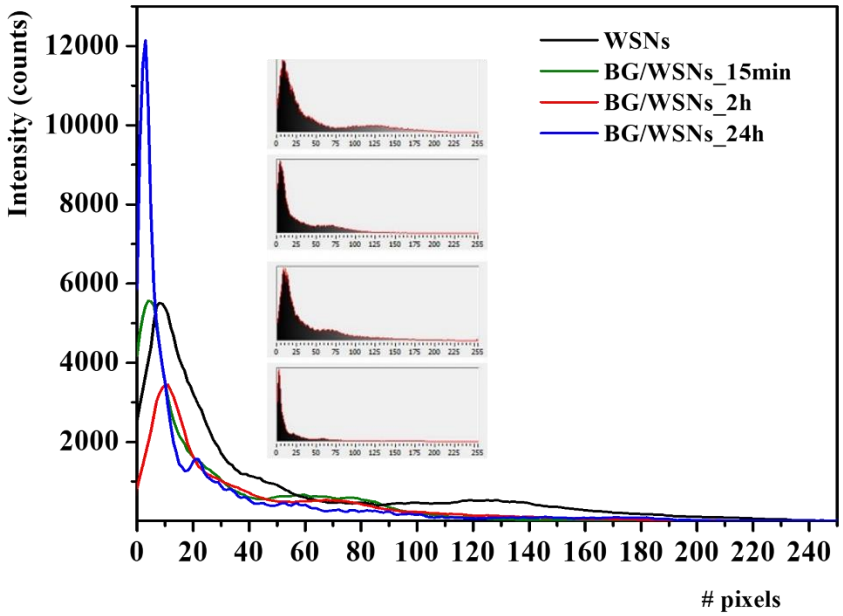

Figure 5. Histogram of grayscale values for WSNs, BG/WSNs_15min, BG/WSNs_2h, BG/WSNs_24h taken along a horizontal line passing through the center of the particle in the TEM images. Inset: normalized histograms with grayscale illustration

ζ-potential measurements assessed that the increasing colloidal instability of BG/WSNs nanosystems over time was due to consistent changes in the surface charge of WSNs and allowed for unveiling the mechanism of interaction between enzyme and support. **Figure 6** shows the evolution of the ζ-potential during the immobilization stage. Bare WSNs exhibit ζ-potential value equal to -7.31 mV. This is an expected result since the isoelectric point (pI) for sol-gel silica is set within 2-3 pH interval [41–45], below pH=5 of citrate buffer used for the immobilization. As the adsorption process goes on, ζ-potential rises with time from -5.35, recorded at 15', up to -1.57 mV, registered after 24 h. This visible trend might be evidence of the protein binding onto the silica surface since commercial BG is positively charged at

pH=5 (pI=7.3, [46]). Previous works had relied on changes in ζ-potential values to monitor protein adsorption kinetics at the interface [47–49]. Therefore, the YI for BG is expected to follow the same trend as the ζ-potential that is the higher the amount of adsorbed protein, the higher the increase in surface potential. In our first work dealing with the physical immobilization of BG onto WSNs, we detected the presence of hydrogen bonding between the enzyme and the silica surface [27]. Results herein described underline that also electrostatic forces give a strong contribution to the protein-silica interaction, since the surface charge seems to be intimately correlated to the enzyme loading.

Moreover, time-dependent aggregation and thus precipitation phenomena detected through DLS analysis could be explained since the system get more and more closer to the condition of zero net charge, for which no electrostatic repulsion helps keep the individual nanostructures separate. This condition does not allow keeping the individual nanostructures separate.

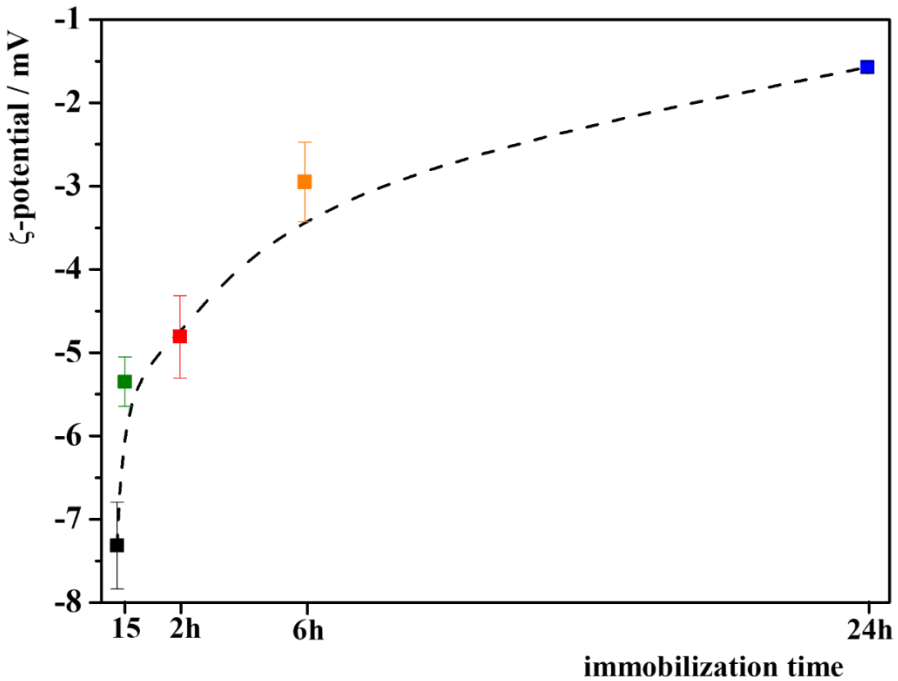

Figure 6. ζ-potential values for BG/WSNs recorded during the adsorption kinetics.

1.5.2. TGA analysis for the estimation of the yield of immobilization

YI of BG/WSNs was estimated through TGA measurements carried out after 2 h and 24 h of immobilization. The reason for choosing these systems is that they were the only ones to load consistent amounts of enzyme, as revealed by TEM images. **Figure 7** reports thermograms for bare WSNs as well as BG immobilized in 2 h and 24 h. WSNs experience a weight loss of 6.8 % in 200-800 °C temperature range, while the values recorded for BG/WSN_2h and BG/WSN_24h are 10.5% and 18.5%, respectively. Thus, the YI for the supported biocatalysts reaches the 23% in 2 h and the 80% in 24 h, corresponding to 38 and 133 mg/g of support, respectively. The presented results confirm that the dilution of both enzyme and support as well as the choice for a lower BG:WSN w/w resulted in the optimization of the immobilization route. In fact, the achieved enzyme loading in 24 h was comparable to that of the reference system namely the biocatalyst similarly produced by Califano et al. [27] using BG:WSNs w/w ratio of 1:2 (133 mg/g vs 150 mg/g) whereas the YI was more than doubled, rising from 30% up to 80%. The feasibility of using TGA analysis for protein content determination was previously assessed. BG:WSN system was tested for protein content with both TGA [27] and the Bradford method, [32] giving exactly the same result of 150 mg/g.

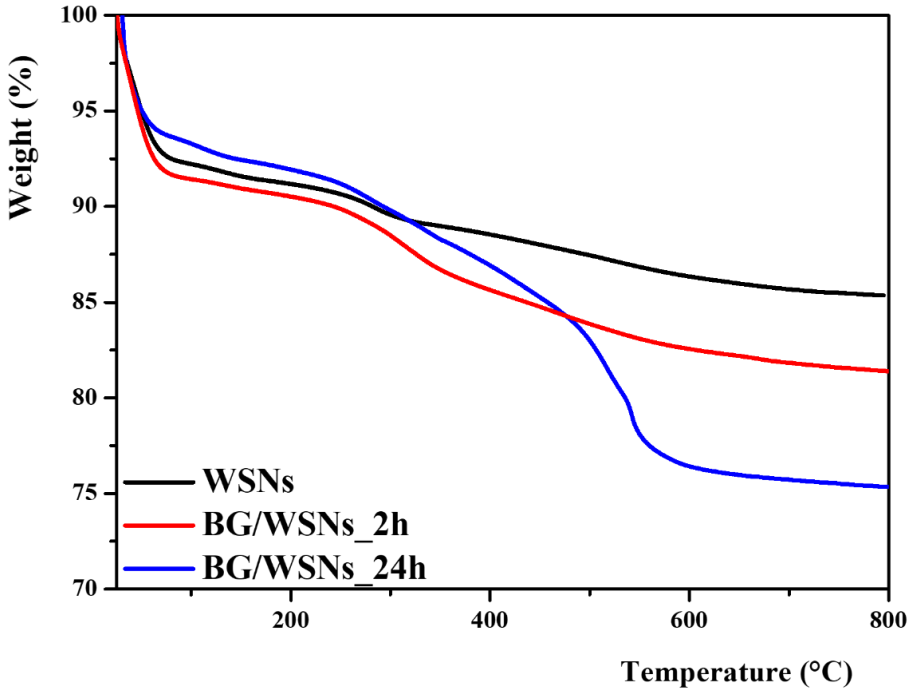

Figure 7. Weight loss profiles for WSNs (black curve), BG/WSNs_2h (red curve), BG/WSNs_24h (blue curve).

Such enhancement in YI was not unexpected. Indeed, it was observed that absorption of cellulolytic enzymes into WSNs follows a Langmuir mechanism which prescribes enzyme monolayer adsorption. [28] According to such mechanism, the amount of immobilized protein rises with the concentration of enzyme in solution until a plateau is reached, when all the binding sites of the support are saturated. Therefore, low enzyme concentrations lead to high YI values since YI follows an exponential decay function.

1.5.3. Conformational analysis of immobilized BG

To analyze the effect of BG immobilization on WSNs at different times on the enzyme conformation, CD spectra of free BG, and BG/WSNs after adsorption at 2h

(BG/WSN_2h) and 24h (BG/WSN_24h) systems were recorded, as shown in **Figure 8.**

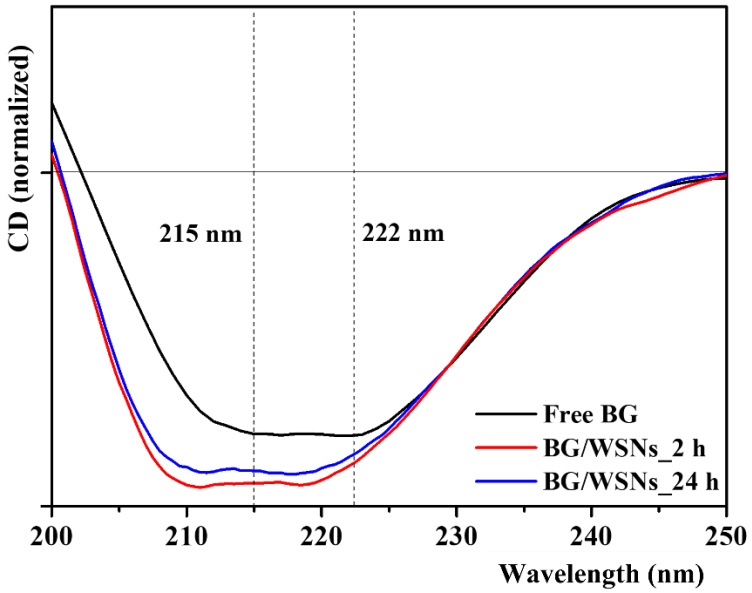

Figure 8. Comparison between CD spectra of free BG (black curve) and BG immobilized on WSNs after 2 h (red curve) and 24 h (blue curve).

The spectrum of the free enzyme showed two minima centered at 215 and 222 nm, suggesting the presence of comparable amounts of β-sheet and α-helix components.[50–53] The spectra of the BG/WSNs systems are similar, but slightly different from that of the free protein. Indeed, the two minima are better resolved and fall at about 210 and 220 nm. These spectral features may suggest a slightly higher presence of α-helices with respect to β-sheets. However, the comparison between the spectra highlights that the enzyme does not unfold and retains its secondary structure when was adsorbed on the nano-silica skeleton in 2 h as well as 24 h. The enzyme in its free form experienced a two-step denaturation phenomenon. In detail, the first step is likely due to rearrangements of the quaternary structure, whereas the second one to the loss of secondary structure, with a melting temperature of 74°C. In fact, it was found that β-glucosidase from almond exist in two isoforms, monomeric and

dimeric, with the dimeric form that performs much better than the monomeric one.[54] Thermal denaturation curves of the immobilized samples (**Figure 9A**) did not exhibit remarkable signs of denaturation up to 90 °C. More specifically, thermal curve of BG/WSN_24h remains flat, indicating that no structural change occurs. Differently, the slight slope exhibited by BG/WSN_2h thermal profile reveals a partial structural modification. Such distinct thermal behaviors could be attributed to the different protein organizations and densities onto the silica skeleton. Indeed, the protein is mostly externally adsorbed over the surface of the nanostructure after 2 h of immobilization and thus free to undergo modifications of quaternary and tertiary structure. On the contrary, the enzyme is best shielded when hosted inside the pores as for BG/WSNs_24h since the pore wall-protein physical interactions ensures conformation rigidity, resulting in a higher improvement of the thermal stability than BG/WSNs_2h.[32] Thermal stabilization of enzymes is particularly important for multimeric enzymes (dimeric in our case) where dissociation of the subunits can produce inactivation.[55] It was argued that for β-glucosidase inactivation may start by subunit dissociation.[56] In our case, immobilization seems to stabilize the quaternary structure of the enzyme. Stabilization of multimeric enzymes by physical adsorption was observed where multipoint enzyme-support interaction exist,[55] due to the presence of several interacting groups on the support surface (i.e -OH for hydrogen bonding and O^- for electrostatic interactions).

The anchoring into the pores of WSNs dramatically improved the thermal stability of the enzyme. The benefits brought by the physical immobilization to the thermal resistance of the enzyme clearly emerges from the comparison between CD spectra of free BG and the most stable supported biocatalyst namely BG/WSNs_24h acquired before and after submitting the sample to a denaturation test (**Figure 9B, 9C**). The free protein experienced a remarkable change in the 200-225 nm range and a very strong decrease in CD intensity, thus confirming that it is mostly unfolded.[57] Differently, immobilized BG exhibited only slight variations in the spectrum profile,

confirming the enhanced rigidity of the protein chains provided by the physical immobilization.

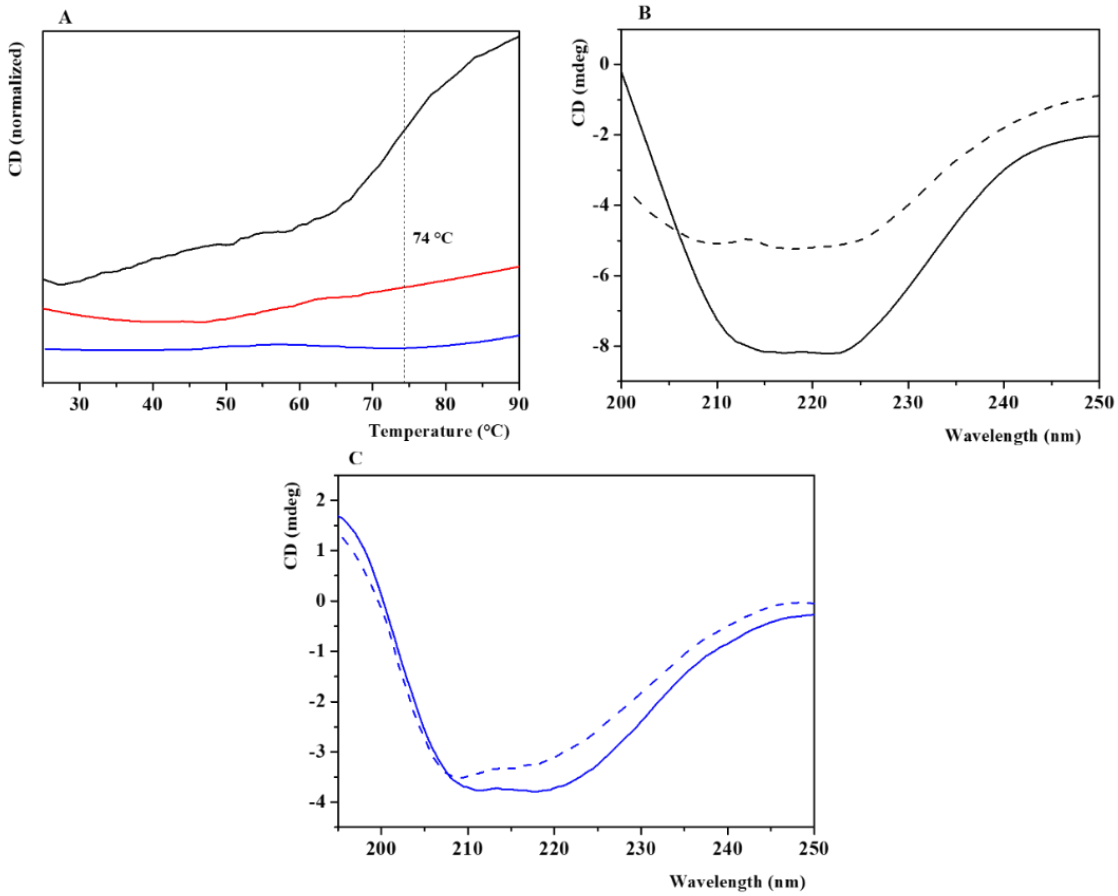

Figure 9. Thermal denaturation curves for free BG (black line), BG/WSNs_2h (red line), BG/WSNs_24h (blue line) (A). Comparison between CD spectra of free BG (B) and BG/WSNs_24h (C) acquired before (dashed curve) and after (solid curve) a thermal denaturation ramp.

The deconvolution of amide I band carried out on FTIR spectrum of BG/WSNs_24h (**Figure S4**) confirmed that the enzyme underwent only little structural modification upon adsorption onto WSNs. As reported in Table 1, the obtained structural pattern

underlines that the optimized system showed more similarities with the original structure of the BG with respect to that observed for the immobilized enzyme at the highest WSNs/BG weight ratio, as previously prepared acting as reference system.[27]

Table 1. Conformational analysis for BG/WSNs_24h compared to free BG and to the reference system. [27,58]

Structure	**Free form**	**BG/WSNs_24h**	**Reference system (BG:WSNs=1:2 t=24h)**
Aggregates		17.1	9.4
β-sheets	30	25.1	34.2
α-helices	34	30.8	20.4
Turns	25	22.0	25.2
Disordered	11	4.9	10.8

Indeed, the percentage of α-helices (30.8%) was higher and closer to the one exhibited by the BG in its free form (34%), just like the difference between the percentage amounts of α-helices and β-sheet,[58] confirming what observed through CD measurements. Moreover, the non-negligible value for aggregate portions could be a consequence of protein rearrangement when adsorbed onto the nanostructure or might occur during the drying process necessary to analyze the samples by FTIR.

1.5.4. Catalytic assays

BG/WSNs_2h and BG/WSNs_24h were both assayed in the hydrolysis of cellobiose to glucose using the same amount of immobilized enzyme.

Table 2 shows the immobilization parameters and activity for the supported biocatalysts, compared to the reference system and to soluble BG.

Table 2. Summary of the immobilization parameters for the supported biocatalysts, compared to the reference system and to soluble BG. [27] [a] The yield of immobilization expressed in terms of activities (YI_E) was measured as the percentage ratio between the activity of the immobilized protein and the activity of the offered protein in the immobilization step. [b] Specific activity (SA) is defined as the recorded activity per mass of BG. [c] Recovered activity (RA) is defined as the recorded activity per mass of support.

Biocatalyst	**YI (%)**	**YI_E (%)[a]**	**Load (mg/g $_{support}$)**	**SA[b] (U/mg_{BG})**	**RA[c] (U/$mg_{support}$)**
BG/WSNs_2h	23	38.2	38	7.77	0.07
BG/WSNs_24h	80	140	133	8.22	0.28
Reference system	30	54.2	150	8.44	0.32
Free BG				4.67	

As can be seen, all the immobilized biocatalysts show hyperactivation, possibly due to an increased concentration of the substrate near the active site.[27] However, for the reference biocatalyst it has been shown that the situation levels off over a longer period: there is a decrease in the rate of the reaction after 60 min for BG_WSN with respect to free BG, probably due to the accumulation of glucose inside the matrix. [27] **Figure 10** shows the histogram reporting the cellobiose conversion achieved by the two biocatalysts in 10 min and 24 h of reaction. Both the biocatalysts allowed for

about 35% cellobiose conversion after 10 min (**Figure 10A**). The specific activities were 7.77 and 8.22 U/mg_{BG} for BG/WSNs_2h and BG/WSNs_24h, respectively (calculated by dividing activity values for the weight of the actual weight of BG contained in the commercial product). Moreover, both the systems pushed cellobiose conversion up to 100% in 24 h (**Figure 10B**). Catalytic assays thus highlight that these biocatalysts exert similar performance as the biocatalyst chosen as reference (activity~8.44 U/mg_{BG}, 100% cellobiose conversion in 24 h), produced by adsorption of BG into WSNs for 24h, fixing enzyme and support concentration to 1 and 2 mg/ml, respectively.[27] The obtained results confirm what assessed by CD analysis that is the enzyme conformation is unaffected or even improved by physical immobilization, leading to performing biocatalysts produced after both 2 h and 24 h of adsorption. Such achievements mean that this modified adsorption route leads to biocatalysts which retain conformation and improved activity, although using only a third of the enzyme needed before in the immobilization step with respect to the reference system designed by Califano et al.[27]

In the end, 24 h is confirmed as the optimal immobilization time. Indeed, it allows for the highest YI (80%), resulting in a consistent enzyme saving. Moreover, enzyme location within the pores is responsible for the highest improvement in protein thermal stability, as assessed by CD analysis (**Figure 9A**). The two-hour adsorption leads to a transient state that is not equilibrium. Actually, it is shown that after 24h the protein corona disappears and the enzyme is mainly located inside the pore. Furthermore, it was found that in porous nanoparticles the proteins of the corona can undergo, during storage, intra-particle migration inside the pores. [26] Therefore, the catalyst is likely to change over time in an uncontrollable way.

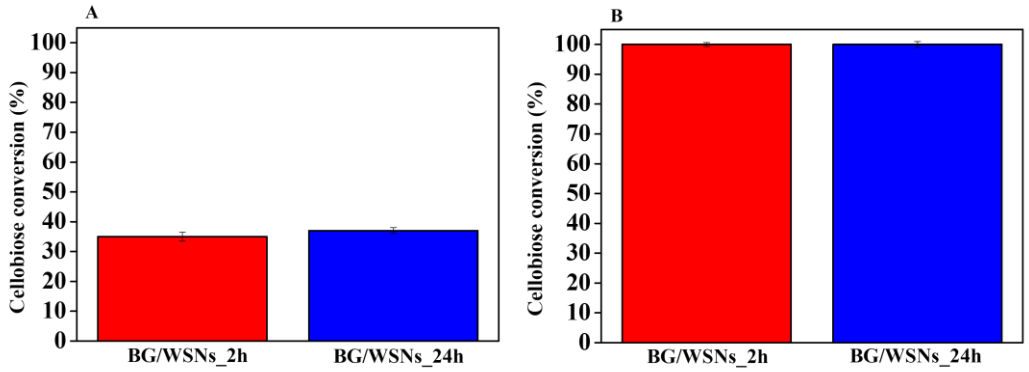

Figure 10. Histograms reporting cellobiose conversion (%) reached by using BG/WSNs_24h and BG/WSNs_2h for 10 min (A) and 24 h (B) reactions.

1.5.6 Operational and thermal stability

The arrangement and organization of the protein over the porous architecture of the silica nanoparticles in the different biocatalysts affect the operational stability, due to conformational variations or leakage phenomena. As a matter of fact, BG/WSNs_24h and BG/WSNs_2h systems exert different performances in terms of reusability, as shown in **Figure 11**.

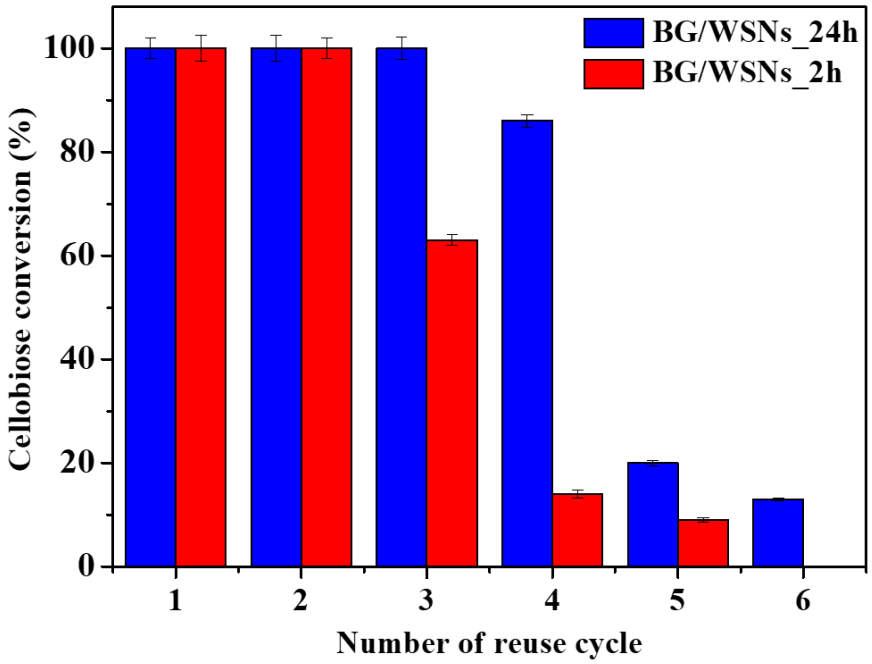

Figure 11. Cellobiose conversion over the number of reuse cycles for BG/WSNs_24h (blue) and BG/WSNs_2h (red).

BG/WSNs_24h biocatalyst exhibits total reusability up to the third cycle, only losing 20% of conversion at the 4th one. Afterwards, the performances of the biocatalyst drop down to about 20% and 15% conversion at the 5th and 6th cycles, respectively. The operational stability of this system was already tested for the reference system: there was no loss of activity after three repeated uses. In the fourth, the yield reduced to 80 and 40% with the fifth reuse.[27] A comparable trend is reported for BG/WSNs_2h. However, it keeps complete conversion only for 2 cycles, losing 40% conversion at the 3rd one. In a similar way as BG/WSNs_2h, after the 3rd cycle it experiences a fall in conversion until losing it all at the 6th reuse cycle. BG/WSNs_24h's higher operational stability can be attributed to the penetration of BG into the pores of the nanostructure. This maximizes the protein-matrix

interaction, reducing the risk of both conformational modifications and leakage phenomena. On the contrary, BG is set mostly over the outer surface of BG/WSNs_2h, being exposed to the release of the external protein layers as long as the reusability tests go on.[59] Indeed, TGA measurements proved that BG/WSNs_2h sample loses almost the 88% of the original enzyme load after 4 reaction cycles whereas only the 20% of protein is released from the pore structure of BG/WSNs_24h.

Figure 12 shows the results of the thermal stability experiments. The bar plot highlights that the immobilized enzyme recovers higher cellobiose hydrolytic activity than its free counterpart upon the incubation a temperature > 60º C, regardless the immobilization time. More specifically, free BG is completely inactivated after incubation at 70°C. On the other hand, the enzyme immobilized for longer times (24 h) is slightly more stable than the enzyme immobilized for shorter times (2h) when both are incubated at 70 ºC. This result confirms the lower stability of the soluble enzyme compared to the immobilized one. Both the supported biocatalysts experienced complete inactivation after incubation at 80°C.

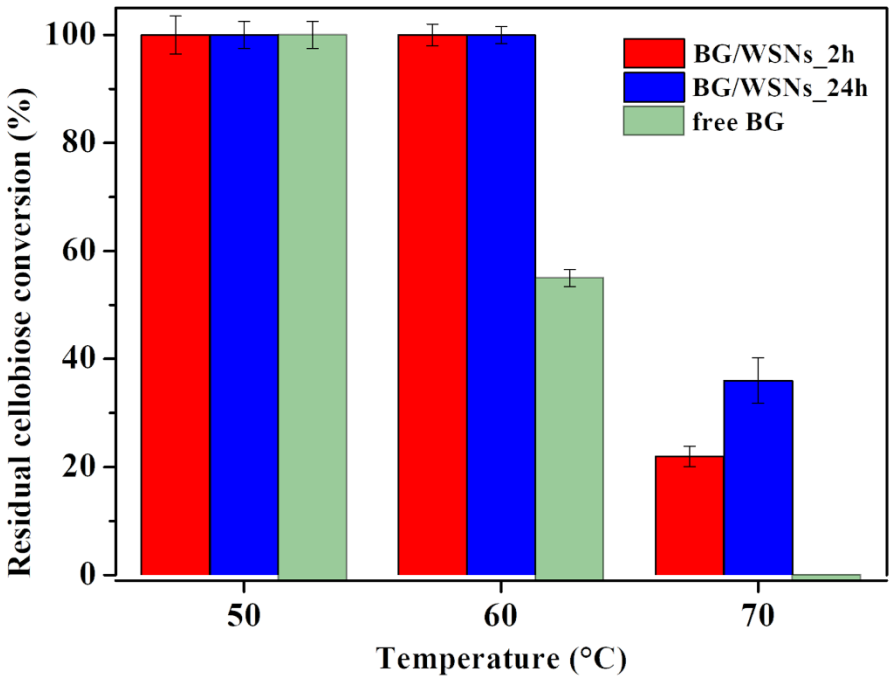

Figure 12. Residual cellobiose conversion (%) over the incubation. Data for reaction without previous incubation (bars at 50°C) were reported for clearer comparison.

1.6. Conclusions

This work is focused on the study of the self-aggregation processes associated to the physical immobilization of BG into WSN with the aim to better control the protein-support interactions and their evolution as function of time and enzyme concentration. Indeed, this behavior is still poorly studied and many aspects related to the enzyme immobilization appear unclear.

In this frame, the optimal adsorption conditions in terms of colloidal stability and yield of immobilization (YI) were found. Specifically, BG:WSNs ratio equal to 1:6 wt/wt leads to the highest controllability of the system, as indicated by DLS analysis. In these conditions, the formation of a protein corona is observed at 2 h and a 23%

YI resulted, as demonstrated by TEM and TGA analyses, respectively. However, the enzyme corona disappears after 24 h as the protein diffuses inward reaching the inner edge of the pores, achieving 80% YI. At the same time, the enzyme conformation only slightly affected by physical immobilization, as confirmed by FTIR and CD measurements. Indeed, a huge gain in thermal stability of the supported enzyme was attested after both 2 h and 24 h of immobilization. More specifically, BG/WSNs_24h preserves almost complete folding even at 90°C thanks to the interactions between the pore walls and the protein established as the enzyme is located inside the pores. Both BG/WSNs_2h and BG/WSNs_24h show complete conversion of cellobiose to glucose after 24 h of reaction at the same enzyme concentration, proving the success of the adsorption protocol in preserving native enzyme secondary structure. The sensitively high YI reached after 24 h points out BG/WSNs_24h to be the best obtained biocatalyst, exerting comparable performances to that previously prepared fixing BG:WSNs equal to 1:2 wt/wt and about 10-fold the support concentration. [27] However, this favorable biocatalytic activity is strongly associated to the enhanced controllability achieved as BG:WSNs wt/wt is set to 1:6 and the protein amount is lowered by one order of magnitude, also guaranteeing a noticeable enzyme saving. Moreover, the new adsorption protocol results in a fully reusable biocatalyst up to the 4^{th} cycle of reaction.

In conclusion, the proposed study underlines the key role of a fine tuning of immobilization processes, in terms of both time and enzyme content onto inorganic supports, to improve colloidal stability and to prevent fast self-aggregation processes as decisive strategies to enhance the enzyme loading and reduce protein waste without undermining the biocatalytic performances.

1.7. Supplementary Materials

S.1. Quantification of the enzyme fraction in commercial BG

The recorded spectrum exhibits a single peak centered at around 280 nm, with absorbance of 0.17 (**Figure S1**). The actual protein molar concentration was calculated by using equation (1) and the estimated value was 1.78×10^{-6} M, being ε and l equal to 95310 $cm^{-1}M^{-1}$ and 1 cm, respectively, corresponding to a mass concentration of 0.24 mg/mL.[46] Thus, only the 24% of the commercial product can be attributed to enzyme macromolecules.

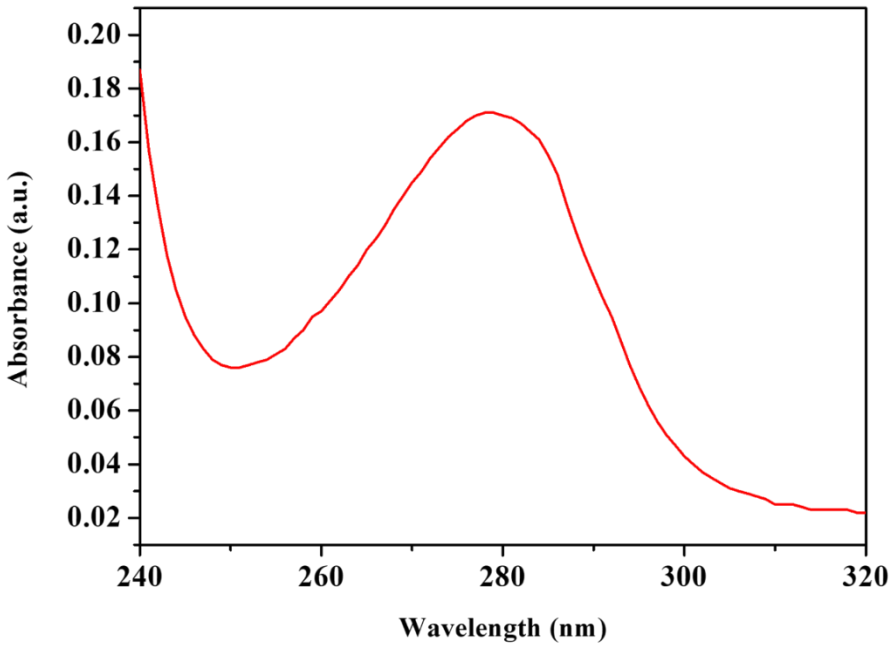

Figure S1. Absorption spectrum for 1 mg/mL BG buffer solution

S.2. Sodium Dodecyl Sulphate - PolyAcrylamide Gel Electrophoresis (SDS-PAGE)

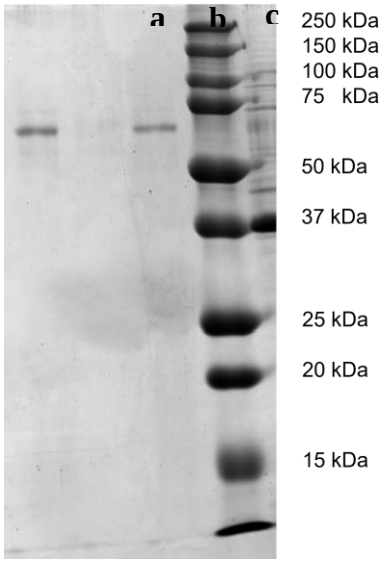

Figure S2. SDS PAGE images for offered BG (a), supernatant (b), immobilized BG (c).

S.3. DLS analysis for different BG/WSNs ratios

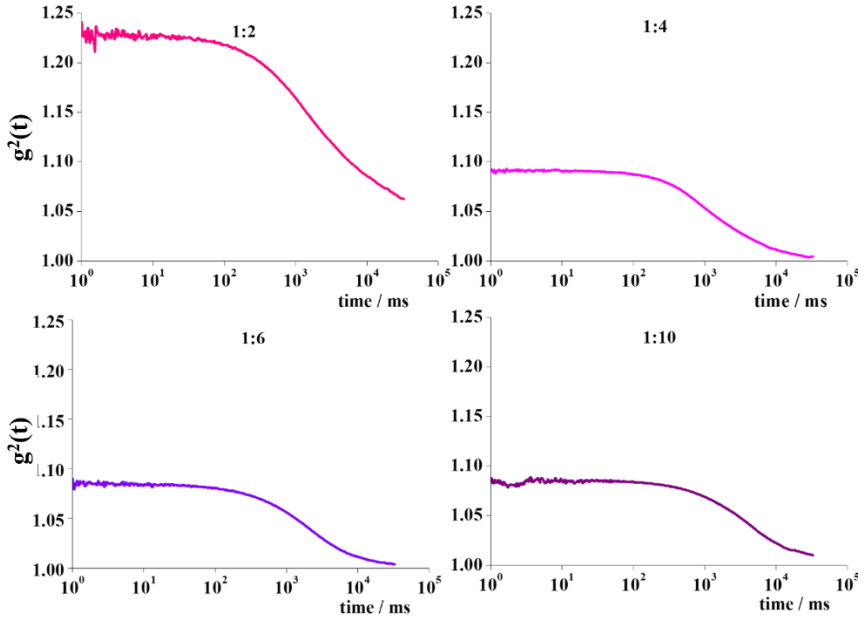

Figure S3. Autocorrelation functions of BG:WSNs weight ratios of 1:2 (pink line), 1:4 (magenta line), 1:6 (violet line), 1:10 (purple line) recorded after 24 h.

S.4. Deconvolution of Amide I band

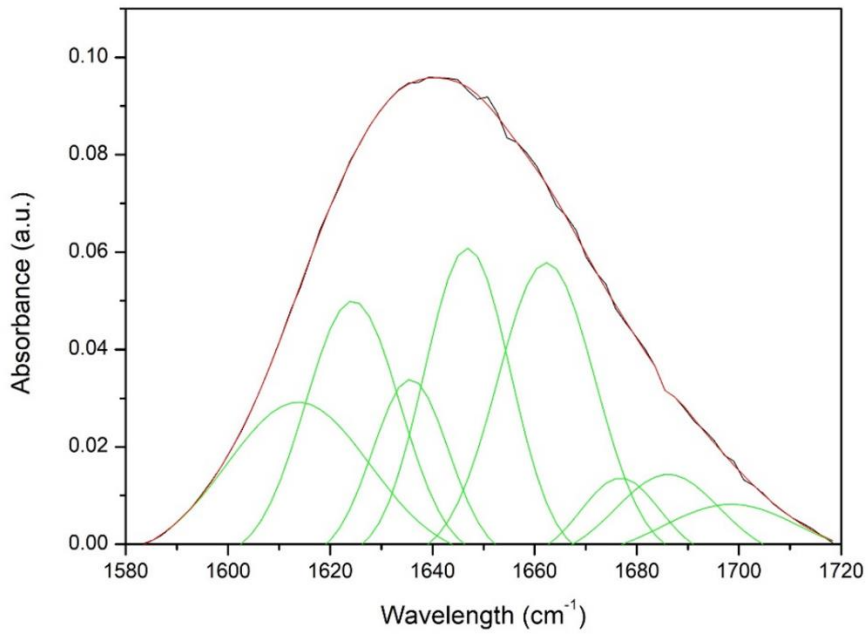

Figure S4. Gaussian deconvolution of Amide I peak for BG/WSNs_24 h sample

2. Co-immobilization of cellulase and β-glucosidase into mesoporous silica nanoparticles for the hydrolysis of cellulose extracted from *Eriobotrya japonica* leaves

This section refers to the original version of the paper by Pota, G. et al. *Langmuir* 2022, 38 (4), 5481-5493.[59]

2.1. Abstract

Fungal cellulases generally contain reduced amount of β-glucosidase (BG), which does not allow for efficient cellulose hydrolysis. To address this issue, we implemented an easy co-immobilization procedure of β-glucosidase and cellulase by adsorption on wrinkled mesoporous silica nanoparticles with radial and hierarchical open pore structure, exhibiting smaller (WSN) and larger (WSN-p) inter-wrinkle distance. The immobilization was carried out separately on different vectors (WSN for BG and WSN-p for cellulase), simultaneously on the same vector (WSN-p), and sequentially on the same vector (WSN-p) in order to optimize the synergy between cellulase and BG. The obtained results pointed out that the best biocatalyst is that prepared through simultaneous immobilization of BG and cellulase on the same vector (WSN-p). In this case, the adsorption resulted in 20% yield of immobilization, corresponding to an enzyme loading of 100 mg/g of support. 82% yield of reaction and 72 μmol/min·g activity were obtained, evaluated for the hydrolysis of cellulose extracted from *Eriobotrya japonica* leaves. All reactions were carried out at a standard temperature of 50°C. The biocatalyst retained 83% of the initial yield of reaction after 9 cycles of reuse. Moreover, it had better stability than the free enzyme mixture in a wide range of temperatures, preserving 72% of the initial yield of reaction up to 90°C.

2.2. Graphical abstract

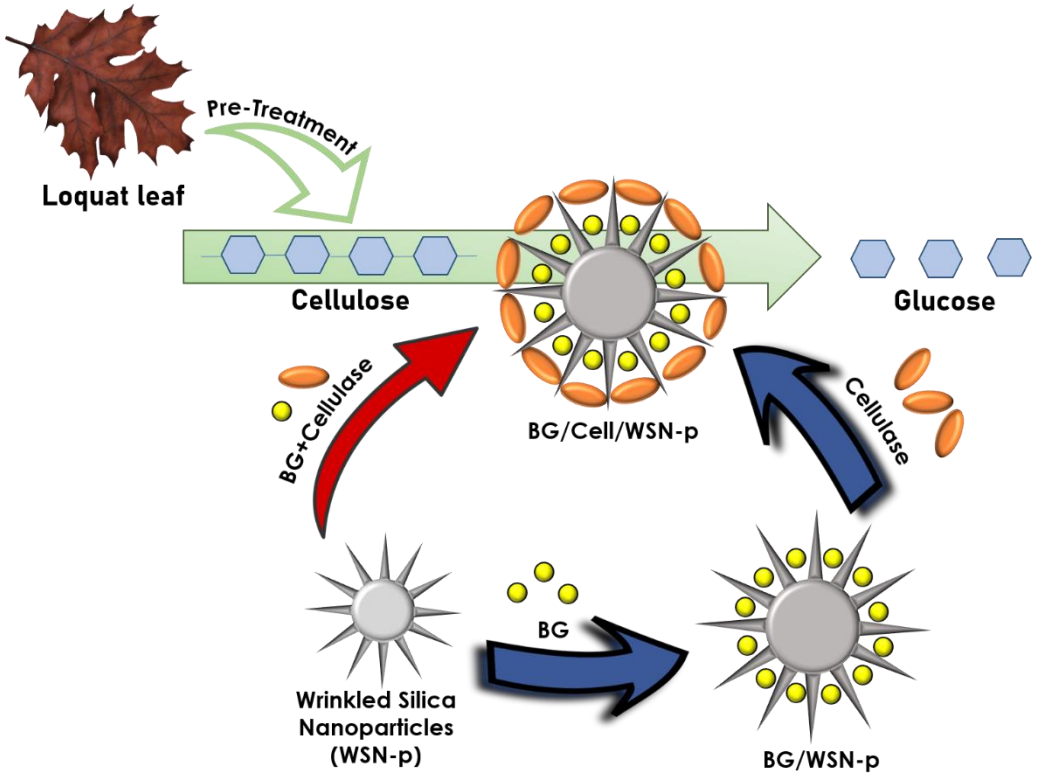

2.3. Introduction

Lignocellulosic agricultural waste biomass is considered a strategic fuel source. In this frame, hydrolysis catalyzed by cellulase enzymes to produce glucose represents a powerful tool. Second generation bioethanol fuel can be obtained by fermentation of glucose derived from lignocellulosic biomass. The use of ethanol instead of gasoline as transportation fuel provides a more complete and cleaner combustion, reducing carbon monoxide, unburned hydrocarbon and particulate emissions.[60,61] Furthermore, bio-derived ethanol used as fuel can help mitigate climate change, being CO_2 neutral.[62] Lignocellulosic biomass is the most abundant non-edible source of glucose, due to its high content of cellulose. It is readily available from industry and agricultural waste with no ethical concern of food competition.[63] Contrary to conventional sources of glucose, i.e. starch, sugar cane and sugar beet, the whole plant can be used to obtain sugars.[64] However, cellulose is much more difficult to

hydrolyze, due to the β-bonds that join the glucose units. This type of bond forces the cellulose macromolecules into a linear conformation. The cellulose chains then join in microfibrils held together by hydrogen bonds, which makes cellulose recalcitrant to enzymatic hydrolysis.[65] In fact, substances such as starch, which contain glucose polymers with α-bonds, serve as energy reserve and glucose is readily available. Cellulose, on the other hand, is a structural polymer, which constitutes the cell wall of plants, and is resistant to biological attack. Furthermore, the cellulose in the biomass is embedded in hemicellulose and lignin in a composite structure. Lignin is a complex phenolic polymer that provides a physical barrier for enzymatic hydrolysis and adsorbs cellulolytic enzymes on its sticky surface.[66,67] For these reasons, the enzymatic hydrolysis of cellulose normally requires a pre-treatment to make it more available to cellulolytic enzymes.[68] The pre-treatment process should efficiently remove lignin and reduce cellulose degree of polymerization and crystallinity, as amorphous cellulose is more readily hydrolyzed by enzymes.[69] Enzymatic hydrolysis of biomass is generally preferred over chemical methods, since it is a green route avoiding toxic reagents and by-products and facilitates downstream processing. The enzymes responsible for the hydrolysis of cellulose are called cellulase. Cellulase, a multi-enzyme system, consists of three types of enzymes, which act synergistically in the decomposition of cellulose. Endo-glucanase (EG) and cellobiohydrolase (CBH) act on insoluble cellulose producing soluble oligomers, i.e. cellobiose and cellotriose. β-glucosidase (BG) hydrolyzes the β-bond of soluble oligosaccharides, leading to the formation of glucose. However, the use of cellulase in soluble form has various drawbacks, mainly related to its intrinsic instability and the difficulty of multiple reuses. In addition, continuous operation is not possible. These are essential issues to offset what is one of the major problems of enzymatic catalysis: the high cost of enzymes.[70] One useful strategy to overcome these limitations is the immobilization of the enzyme on an insoluble support. This allows exploiting the advantages of heterogeneous catalysis, such as

the possibility of reuse and working in continuous operation, but it also has additional benefits. In fact, with a properly designed immobilization protocol, immobilized enzymes can gain stability with respect to harsh environmental conditions, such as high temperatures and pH far from neutral.[71,72] There are several reasons for enzyme stabilization upon immobilization, i.e. the rigidification of the enzyme structure following multipoint attachment or for interaction with the pore walls in porous structures; the seclusion of the enzyme from the external environment by immobilization in porous materials, which protects the enzyme from denaturing factors; or an actual conformational variation due to the interaction with the support, which leads to greater stability.[73] Furthermore, immobilization in some cases can cause an increase in the activity and specificity of the enzyme.[72,74] The increase in the activity of an enzyme as a result of immobilization occurs more rarely. Sometimes it is caused by structural alterations of the enzyme that accidentally increase its activity in a certain reaction, other times it is simply the result of greater stability of the enzyme, so that the activity is higher when measured under drastic conditions. Finally, immobilized enzymes are dispersed on the support surface, which prevents aggregation encountered with free enzymes resulting in a decline in activity.[74] However, immobilization of cellulase is challenging because cellulose is water insoluble. To carry out its catalytic role, cellulase must diffuse to the cellulose surface. Immobilized cellulase have very low mobility, so that diffusion limitations become an issue.[75] For this reason, immobilization of cellulase is often performed with nonporous materials, which have the advantage that the enzyme molecules are on the surface of the carrier and can thus have access to insoluble cellulose.[76] Enzyme orientation is another critical point, since only when the active centre is properly oriented to the medium, the enzyme can perform its catalytic action.[77] Several solutions have been proposed to enhance cellulase flexibility so to favor the right orientation, such as the use of a long spacer arm, immobilization on flexible polymer brush temperature responsive polymers or biomimetic anemone-inspired supports.[78–82] Another problem that must be considered when using cellulase for biomass

conversion is that often BG activity is scarce in the enzymatic cocktail. [83] BG relieves the inhibition exerted by cellobiose on cellulolytic enzymes; hence, its role is essential for efficient hydrolysis of the biomass. All the three enzymes carry out their action interdependently, so that the enzyme composition in the enzymatic cocktail must be well balanced. Co-immobilization of exogenous BG and cellulase is a possible solution. In fact, it was shown that supplementing commercial cellulases with BG increased the yield of glucose.[84] One of the first attempts at co-immobilization of the two systems was done by one-pot entrapment/covalent immobilization in a polyurethane foam.[85]Although the co-immobilized enzymes performed better than cellulase immobilized alone, the reaction yields were far from those obtained with free enzymes. In another study, β-glucosidase and cellulase were simultaneously and covalently co-immobilized on a pH-responsive copolymer. [86] The immobilized enzymes showed better glucose yield (62.69 % after 72 h) compared with the free enzymes in the hydrolysis of micro-crystalline cellulose. More recently, sequential co-immobilization of BG and cellulase was performed on hierarchical microparticles and layered films.[79,87] BG was entrapped in the inner core of a poly(ethylene glycol) layer, cellulase was covalently bound on the outer surface of a brush polymer layer to improve the accessibility of insoluble cellulose to the enzyme and preserve cellulase flexibility. A wide plethora of materials can be used as support for enzyme immobilization. The choice should be guided by different features, such as cost, availability, stability, porosity, surface area and above all the affinity between the enzyme and the carrier.[88] The support for enzyme immobilization can be inorganic (i.e. silica or titania), synthetic organic (mostly polymers) or organic of natural origin. [89–91] Mesoporous silica nanoparticles stand as the adequate supports for enzyme immobilization thanks to their large surface area, narrow pore size distribution, well-defined pore geometry, thermal and mechanical stability. Moreover, they exhibit water insolubility, renewability and toxicological safety. The main technique to produce them is the sol-gel route the mild synthesis conditions allow preparing sophisticated hybrid organic-inorganic systems where the

synergic characteristics and functionalities of a single component extend and improve the properties of the final material.[92,93] Their numerous hydroxyl groups can be activated allowing for enzyme covalent attachment. [94,95] SBA-15 has been the first mesostructured silica material used to immobilize cellulase enzymes thanks to its pore, large enough to host bulky enzymes.[96] FDU-12 materials are particularly well suited for enzyme immobilization due to very large pores and high pore connectivity. Hartono et al. synthesized a series of organo-functionalized FDU-12 with very large pores up to 28 nm for the immobilization of cellulase by physical adsorption. [97] The best biocatalyst showed high activity (70% of the free enzyme activity in the hydrolysis of carboxymethyl cellulose (CMC)). Chang et al. immobilized cellulase from *Trichoderma reseei* by both physical adsorption and covalent binding on synthesized ultra-large pore LP (20-40 nm) silica nanoparticles.[98] The biocatalytic assay was carried out on cellulose oligomers, obtained through a pretreatment with the ionic liquid method.[99] They found that the glucose yields reached by the covalently immobilized biocatalyst was 83.79%, against a glucose yield of approximately 85% provided by free cellulase. Moreover, it showed a high storage stability, giving a glucose yield of 86.56% after 23 days storage at room temperature. In our previous work,[100] we immobilized cellulase by adsorption on wrinkled silica nanoparticles (WSNs). WSN were synthesized by using pentanol as co-solvent (WSN-p), in order to enhance inter-wrinkle distance and properly host the enzyme. The prepared biocatalyst was assayed in the hydrolysis of CMC, providing the same activity as the free enzyme. In this work, BG and cellulase were co-immobilized by a simple adsorption procedure on WSN-p to promote the hydrolysis of cellulose extracted from *Eriobotrya japonica* leaves**.** The choice of the support was guided by two considerations: (i) BG immobilized in WSN showed enhanced activity [28,101,102] and (ii) cellulase immobilized in WSN-p showed the same conversion rate of free cellulase, and good operational stability. [28,101,102]

Despite the undoubted kinetic advantages that there can be in co-immobilizing two or more enzymes that perform simultaneous and synergistic action, this choice is not

always the most appropriate compared to immobilizing these enzymes on different supports. This is because different enzymes can have different stability, size and optimal reaction and immobilization conditions.[71,76] Furthermore, the loading capacity of the support with respect to each enzyme is more limited.[76] However, cellulase and BG have similar stability and optimal reaction conditions.[100,101] The real problem here consists in obtaining a catalyst in which EG and CBH can perform their action on a bulky and insoluble substrate, cellulose. In the present paper, this challenge was faced by developing various and simple immobilization strategies using porous hierarchical supports to immobilize the two enzymes. The morphology of these supports allowed cellulase to easily attack a large and insoluble substrate as cellulose and facilitated the diffusion of the soluble substrate (cellobiose) in the inner pores where BG could act. The immobilization was carried out (i) separately on different vectors (WSN for BG and WSN-p for cellulase) by adsorption of each enzyme on its support in separate batches, (ii) simultaneously on the same vector (WSN-p), by adsorption of the two enzymes on the same support in the same batch of adsorption and (iii) sequentially on the same vector (WSN-p) by adsorbing first BG and then cellulose in a multilayer immobilization. The order for the layered immobilization was chosen to obtain the immobilization of BG in the inner core of the pores and cellulase towards the large pore entry. facilitating cellulase attack.

2.4. Experimental

2.4.1. Materials

Tetraethylorthosilicate (TEOS), urea, cetyltrimethylammonium bromide (CTAB), cyclohexane, pentanol, 2-propanol, ethanol, hydrochloric acid solution (37.0 % wt. in water), Carboxymethylcellulose sodium salt (CMC), acetic acid (99.0 % wt), sodium acetate trihydrate, sodium hydroxide and glucose oxidase-peroxidase (GOD-POD) assay kit, citric acid, trisodium citrate dihydrate, sulfuric acid (95.0-98.0 % wt.) were purchased from Sigma-Aldrich (Milan, Italy). β-glucosidase from almonds (molecular weight 135 kDa for the dimer, product number 49290, specific activity ≥ 4 U/mg, measured as micromole of glucose liberated per minute at pH 5 and 37°C

with salicin as substrate), cellulase from *Trichoderma Reesei* (Product number C0615, specific activity ≥ 5 U/mg solid measured as micromole of glucose liberated from cellulose per hour at 37°C and pH 5) were also acquired from Sigma-Aldrich. Sodium hypochlorite solution (5.0 % wt) was bought from a local supermarket. *Eriobotrya japonica* (loquat) leaves were collected from a private garden in Caserta, Italy.

2.4.2. Cellulose extraction

Cellulose was extracted from *Eriobotrya japonica* leaves following a two-step procedure.[103] Dry leaves were collected from the ground and kept in a ventilated oven at 40°C for 24 h to remove moisture. 2 g of the dried biomass were cut into smaller pieces, put into a dry cloth, grounded to fine pellets and finally dispersed in 60 ml of a sodium hydroxide water solution (4 % wt). The system was kept under stirring at 80°C for 2 h. Afterwards, the suspension was centrifuged and washed three times with bidistilled water. This first step was repeated thrice. The second step aimed at bleaching purified cellulose using a bleaching solution made of equal volumes of distilled water, acetic acid/sodium acetate trihydrate buffer (pH=5) and sodium hypochlorite 1.7 % wt. The solid fraction coming from step one was dispersed into 60 mL of the bleaching solution. The system was kept under stirring at 80°C for 2 h. The samples were collected by centrifugation and washed three times with distilled water. This routine was repeated 4 times. Finally, bleached cellulose was dried in a ventilated oven at 40°C for 24 h. The final product of the extraction was a crispy and fragile white film.

2.4.3. WSNs synthesis

WSNs and WSN-p were synthesized following the procedure described by Moon and Lee using CTAB instead of cetylpyridinium bromide (CPB) as surfactant. [104] The peculiar morphology of WSN-p was achieved replacing 2-propanol with pentanol as co-solvent. Briefly, cyclohexane (oil phase) and a co-solvent (2-propanol and pentanol for WSN and WSN-p, respectively) were added to a water solution of urea and CTAB (surfactant) under stirring. The reaction mixture evolved into a

Winsor III system, characterized by a bicontinuous microemulsion phase stabilized by CTAB. Afterwards, TEOS was added dropwise and the hydrolysis/condensation series of reactions started at the microemulsion interface. The system was kept under stirring at 70°C for 24 h. Subsequently, a surfactant-removal step was carried out dispersing the nanoparticles in a mixture of HCl and ethanol at 70°C for 24 h. The result was the formation of a hierarchical mesoporous silica architecture, with central-radial porous structure. The final product was collected by centrifugation and washed three times with ethanol. Quantitative information of the preparation procedure are reported in our previous works. [100,105]

2.4.4. Optimization of BG/cellulase ratio

BG/cellulase weight ratio was optimized using free cellulase and BG as biocatalysts and CMC as substrate for the hydrolysis reaction. Supplementary BG was needed to enhance the glucose production by pushing forward the conversion of the cellobiose produced as reaction intermediate. First, 4 different enzyme mixtures were tested in the hydrolysis of CMC (concentration set to 2 mg/mL), in order to identify the optimal weight ratio between the enzymes. The composition of each enzyme mixture is reported in **table 1**.

Table 1 Composition of the enzyme mixtures used for the hydrolysis of 2 mg/mL CMC

Enzyme mixture	**BG (mg/mL)**	**Cellulase (mg/mL)**
A	0	2.0
B	0.40	2.0
C	0.67	2.0
D	1.0	2.0

Hydrolysis reactions were carried out in citric acid/sodium citrate buffer (pH = 5, 50 mM) at 50°C, under mild stirring. In details, 5 mL of enzyme mixture (A, B, C and D alternatively) were added to 5 mL of a 20 mg/mL CMC buffer solution. The reaction mixture was withdrawn from the reactor after 24 h, thermally inactivated in oven at 100°C for 10 min and then submitted to spectrophotometric analysis for the determination of glucose concentration. Percentage increment of obtained glucose (Δ glucose) was calculated as follows:

$$\Delta \text{ glucose } (\%) = \frac{c_i - c_A}{c_A} \cdot 100$$

being c_i and c_A the concentration of glucose produced by using as biocatalysts enzyme mixture i (i=B, C, D, alternatively) and enzyme mixture A (that is absolute cellulase).

2.4.5. Enzyme immobilization

BG and cellulase were physically immobilized onto two different matrices: WSN and WSN-p, respectively. Physical immobilization was carried out in citric acid/sodium citrate buffer (pH=5, 50 mM). In both cases, a 4 mg/mL buffer suspension of the support was prepared and mixed with an equal volume of a 2 mg/mL enzyme buffer solution. The system was kept under mild stirring at 40°C for 24 h. Temperature and time of immobilization were optimized in a previous study.[100] The supported biocatalysts (BG/WSN and cellulase/WSN-p) were collected by centrifugation, washed twice with bidistilled water and stored as wet pellets at 4 °C. One-pot co-immobilization was carried out in the same conditions but using a solution containing both enzymes. The support chosen was WSN-p, since it was shown that the secondary structure of cellulase was better preserved in WSN-p than in WSN.[100] Briefly, a solution of BG and cellulase was prepared by dissolving both the enzymes in the same citrate buffer. The enzyme concentration was set to 0.33 mg/mL for BG and 2 mg/mL for cellulase. The aim was to design a supported biocatalyst with the same enzyme composition as enzyme mixture C (**Table 1**).

Afterwards, 16.5 mL of the enzyme solution was added to an equal volume of a 4 mg/mL suspension of WSN-p in buffer and the system was kept under mild stirring at 40°C for 24 h. Finally, the biocatalyst was collected and washed as usual. The concentration ratio between BG and cellulase in the enzyme solution was fixed to 1:6 since we initially assumed that the yield of immobilization of each enzyme, when co-immobilized on WSN-p, remained the same as the one achieved when the proteins are immobilized separately, each on the corresponding support (30% for BG/WSN and 15% for cellulase/WSN-p).[100,101]

Sequential co-immobilization was accomplished by splitting the immobilization process of the two enzymes into two consecutive steps. In the first one, a 0.66 mg/mL BG buffer solution was added to an equal volume of a 4 mg/mL WSN-p buffer suspension. The resulting biocatalyst (SEQ-BG) was collected by centrifugation, washed twice with bidistilled water and dispersed in citrate buffer to a final support concentration of 4 mg/mL. Afterwards, an equal volume of a 2 mg/mL cellulase buffer solution was added to the system. The final biocatalyst was collected, washed and stored as described above. The supported biocatalysts were referred to as SEP-BG/Cell, SIM-BG/Cell and SEQ-BG/Cell, depending on whether they were obtained through separate immobilization, simultaneous (one pot) or sequential co-immobilization, respectively.

The effectiveness of the adsorption for each sample was determined by thermogravimetric analysis (TGA) by subtracting the organic content of each support from the one of the corresponding immobilized biocatalysts. The yield of immobilization (YI %) was calculated as the weight ratio between the adsorbed enzyme and the amount dissolved in the adsorption mixture, in percentage. TGA measurements were repeated after reuse cycles.

2.4.6. Pre-treated Biomass hydrolysis

Both free and supported enzymes were employed in the hydrolysis of pre-treated biomass. The reactions were carried out under mild stirring at 40°C and pH 5. All the catalytic assays were carried out with cellulase concentration set to 1 mg/mL. As

for the case of free enzymes, BG concentration was alternatively set to 0.33 and 0.2 mg/mL for BG:Cellulase wt/wt equal to 0.33 and 0.2, respectively. The amount of supported biocatalyst used in the reaction was similarly selected in order to have cellulase concentration equal to 1 mg/mL. As a consequence, BG concentration was equal to 0.2 mg/mL for SEQ-BG/Cell and included in 0.2-0.33 mg/mL range for SIM-BG/Cell. In details, 10 mg of pre-treated biomass were cut in small pieces and dispersed into 5 mL of each free enzyme mixture. The system was allowed to react for 24 h, kept in a circulating oven (100°C, 10 min) to thermally deactivate the protein and analyzed to determine the obtained glucose concentration. The free enzyme catalyzed hydrolysis reaction was also carried out on the untreated loquat leaf for comparison. Operating conditions (T, time) and cellulase concentration was set the same as above. Briefly, 58 mg of dry loquat leaves were ground into fine pieces and added to 5 mL of BG/Cellulase free enzyme mixture, with BG:Cellulase w/w equal to 1:5. The amount of untreated biomass was chosen in order to have cellulose concentration equal to 2 mg/mL, being loquat leaves chemical composition reported in literature.[106] The reaction was stopped after 24 h and the glucose concentration was estimated as previously reported.

Cellulose hydrolysis was carried out with separately immobilized enzymes on two different vectors (SEP-BG/Cell), one-pot (SIM-BG/Cell) and sequential (SEQ-BG/Cell) co-immobilized enzymes on the same vector. The reaction conditions were the same as the free enzymes but the reaction mixture was centrifuged to separate the biocatalyst before analyzing the glucose concentration. The amount of each supported biocatalyst was chosen in order to reproduce the same composition as the free enzyme mixture. One-pot (SIM-BG/Cell) and sequentially (SEQ-BG/Cell) co-immobilized biocatalysts were similarly tested. Results were expressed in terms of yield of reaction (YR %), calculated as the concentration ratio between glucose and the organic component of substrate, in percentage. The specific activity of both free and supported enzymes was evaluated towards cellulose and expressed as μmoles/minute of obtained glucose per gram of enzyme. The amount of glucose was

measured after 30 min since it was the minimum time for cellulose to be significantly dissolved by enzyme aggression, as confirmed by visual detection. Activity measurements were carried out in the same reaction conditions chosen to evaluate long-time glucose production. Enzyme concentration and operating conditions were almost overlapped to those set for adsorption, thus satisfying the basic requirements for a successful immobilization.[107]

2.4.7. Operational and thermal stability

The operational stability was assessed by submitting the supported biocatalyst to 24h consecutive reaction cycles on pre-treated biomass at 50°C and pH 5. The results were expressed in terms of relative glucose production (%) with the glucose concentration after the 1st reaction cycle chosen as reference. After each reaction cycle, the biocatalyst was collected by centrifugation and washed once with bidistilled water.

Thermal stability evaluation was accomplished by incubating the supported biocatalyst for 1 h at a given temperature (60, 70, 80, 90, 100 °C) before reacting with cellulose for 24 h at 50°C. The yield of reaction obtained without any incubation phase was chosen as reference to evaluate the residual yield of reaction (%) after incubation at temperature x.

2.4.8. Experimental techniques

The evolution of the morphology experienced by the nanosystems during the immobilization steps was investigated through transmission electron microscopy (TEM), using a FEI Tecnai G2 20 Microscope (FEI, Hillsboro,OR, USA).

The enzyme loading of the nanoparticles was assessed by thermogravimetric analysis (TGA). Approximately 10 mg of dried samples were grinded, loaded into a platinum pan and submitted to a temperature ramp from 30 to 1000°C under air atmosphere, with a heating rate of 10 °C/min. The organic weight fraction (O %) of each sample was evaluated as follows:

$$O\ (\%) = \frac{W1-W2}{W1} \times 100 \qquad (1)$$

where W_1 and W_2 refer to the sample weight at 30°C and 1000°C, respectively. The experiments were performed in a TA Instrument Q600SDT apparatus. TGA was also used to estimate the organic weight fraction of the pre-treated biomass. 5 mg of the samples were settled on the bottom of a platinum pan and submitted to the same temperature ramp as the supported biocatalysts under air atmosphere. The percentage contribution of organic compounds within the biomass were calculated following equation 1. The residual weight is attributable to ash fraction.

N_2 adsoprtion/desorption experiments were performed on WSN-p and WSN-p after BG and BG/cellulase adsorption. Experiments were carried out at -196 °C with a Quantachrome autosorb iQ, after degassing for 4 h at 80°C. Specific surface area of the samples was calculated by the Brunauer–Emmett–Teller (BET) method.

The effectiveness of the cellulose extraction process was assessed by Fourier-Transform Infrared Spectroscopy in the attenuated total reflection (ATR) mode, using a Nexus FTIR spectrometer provided with a DuraSam-plIR II accessory equipped with ZnSe crystal. The spectra of pristine and pretreated loquat leaves were recorded in the range 4000 - 525 cm^{-1} at a spectral resolution of 4 cm^{-1}. The spectrum of Whatman® filter paper was acquired for comparison.

FTIR allowed also for detecting the presence of enzyme molecules into the silica nanostructure after each step of sequential immobilization. The spectrometer was equipped with a DTGS (deuterated triglycine sulfate) KBr detector. Pristine WSN-p, SEQ-BG and SEQ-BG/Cell dry powder were grinded, pressed into pellets (13 nm in diameter) and submitted to spectra recording (4000-400 cm^{-1} wavenumber range, 2 cm^{-1} spectral resolution, 32 scans for each acquisition). Blank KBr spectrum was acquired as background.

Glucose (GO) assay kit was used to estimate the concentration of glucose obtained from the reaction. The experimental procedure is the D-glucose oxidase–peroxidase method.[39,108] Aliquots of the reaction product were withdrawn from the reactor and diluted 1:10 with bidistilled water. 300 μL of each diluted solution were poured in

an Eppendorf tube, mixed to 600 μL of glucose-measuring reagent and kept in a thermostatically controlled water bath at 37°C for 30 min. Finally, 600 μL of sulfuric acid (12 N) were added to the system before measuring the absorbance at 540 nm using a SHIMADZU UV-2600i spectrometer. A calibration curve was built in order to calculate the glucose concentration values from the absorbance measurements.

2.5. Results and discussion

2.5.1. Biomass pre-treatment

The recalcitrance of cellulose to biological attack is due both to the presence of lignin and to the compactness of the cellulose fibers, which hinder enzyme penetration.[66] For this reason, a pre-treatment of the biomass is necessary before enzymatic hydrolysis, aimed at eliminating lignin and reducing the degree of crystallinity of the cellulose. In fact, cellulose exists in four polymorphs.[109] Of these, cellulose I occurs in nature, and is made up of rather compact cellulose fibrils, intercalated by amorphous regions. Cellulose II can be obtained by alkaline treatment of cellulose I. [110] Cellulose II is less crystalline than cellulose I, which favors enzymatic hydrolysis. [65] Alkali pre-treatment of the biomass generally offers several advantages over other pre-treatment procedures, such as acid or biological pre-treatments.[65] It requires milder condition and is more environmentally friendly with respect to acid pretreatments, which can also produce toxic substances for hydrolytic enzymes [111] and it can efficiently remove lignin within few hours compared to greener biological pretreatments that can take many days.[112] However, its efficacy depends on the lignin content of the biomass: high lignin content will not be removed effectively.[113] The treatment has in fact proved effective for fibers of the herbaceous plant *Syngonanthus nitens*, with a low content of lignin (6.5%),[103] but not for sugar palm fibers with a lignin content of 13.4%.[114] Lignin content of loquat leaves is estimated to be the 19.2 % of the overall lignocellulosic fraction.[106] A consequent bleaching step was considered necessary to enhance cellulose weight fraction in the pre-treated biomass, in order to make it more available for enzyme aggression.

Figure 1 shows pictures of the various steps used in the pre-treatment of loquat leaves.

Figure 1. Graphical sketch of the biomass pre-treatment procedure.

After the first repetition of the delignification stage, the biomass suspension became wine-colored, due to the release of lignin and other polyphenols pigment. Delignification is achieved through the saponification of ester bonds between lignin and hemicellulose.[115] The bleaching treatment is expected to complete or at least push forward the cellulose purification by eliminating all the coloring compounds untouched by the delignification stage and the remaining lignin. In detail, the decomposition of sodium hypochlorite produces chlorine dioxide (ClO_2), a strong oxidizer. The decomposition of sodium hypochlorite is favored at high temperature and in acidic pH. ClO_2 oxidizes the aromatic rings of lignin producing lower molecular weight compounds, increasing its solubility. The color of the alkali-treated

biomass turned into white soon after the first repetition of the bleaching stage was completed. After the 4th repetition, the recovered bleached biomass appeared as a white pellet easily dispersible in water. This might be a consequence of the partial cellulose depolymerization caused by the oxidizing environment the biomass was submitted to. **Figure 2** shows FTIR spectra of loquat leaf, pretreated biomass and filter paper as a reference for type I crystalline cellulose.

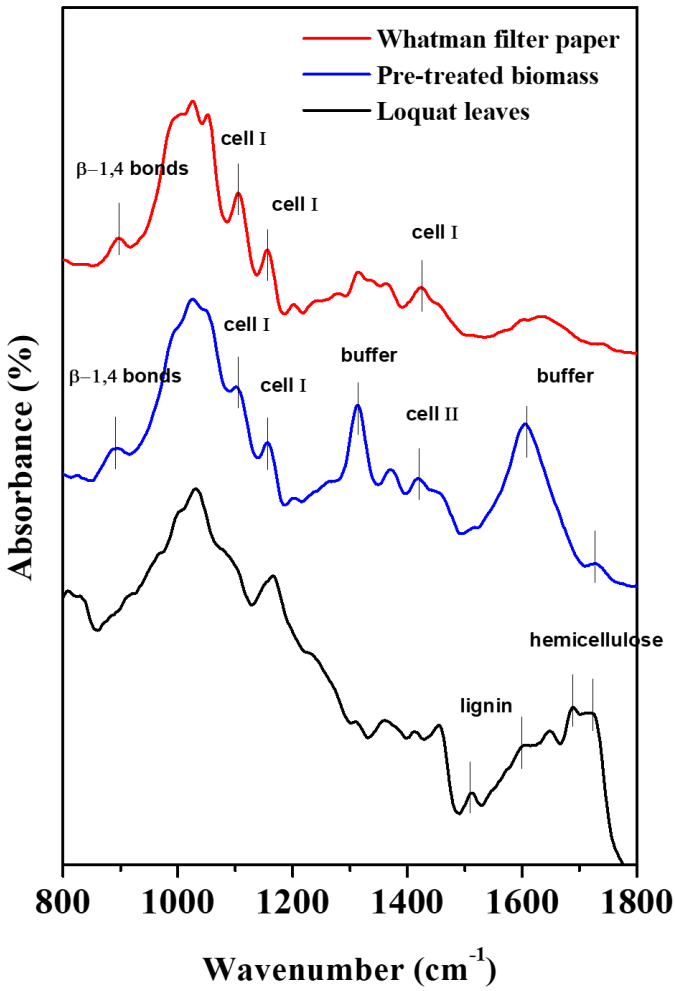

Figure 2. ATR spectra of loquat leaves (black curve), pre-treated biomass (blue curve) and Whatman® filter paper (red curve) displayed in 800-1800 cm^{-1} wavenumber range.

The biomass spectrum has a double peak at 1687 and 1730 cm^{-1}, due to the stretching vibration of the C=O bond of the acetyl groups of the hemicelluloses. The bands at 1603 cm^{-1} belongs to the aromatic skeletal vibrations and the C=C stretching vibrations in lignin; aromatic skeletal vibration of lignin shows also an adsorption band at 1511 cm^{-1} [116]. The band at 1646 cm^{-1} is due to O-H bending vibration of adsorbed water. All the rest of the spectrum is due to the overlapping of the bands of the different biomass components and is therefore difficult to interpret. Following the basic pre-treatment and bleaching, the biomass shows the characteristic cellulose fingerprint between 850 and 1500 cm^{-1}, as can be seen by comparison with the spectrum of the filter paper. In particular, the peaks at 894 cm^{-1} represents -COC vibration at β-glycosidic bond of cellulose,[117] whereas the bands at 1105, 1156 and 1422 cm^{-1} are due to pyranose ring asymmetric stretching, C-O-C asymmetric stretching, and CH_2 symmetric bending vibration of cellulose I.[118] Cellulose I bands at 1105, 1156 cm^{-1} are present in the pre-treated biomass spectrum, indicating that this crystalline form exists within the pre-treated biomass. However, the band at 1422 cm^{-1} is shifted at 1413 cm^{-1}. This shift indicates that part of the cellulose I is transformed into cellulose II and amorphous cellulose.[69] The pre-treatment therefore produces a reduction in the degree of crystallinity of cellulose, making it more accessible to cellulolytic enzymes. The band at 1740 cm^{-1}, present in the spectrum of the pre-treated biomass but not in that of the filter paper, indicates that part of the hemicellulose is still present after the pre-treatment.[69] This fraction will probably not be fully converted by cellulase, as total biodegradation of xylan contained in hemicelluloses requires the action of different enzymes (endo-β-1,4-xylanase, β-xylosidase, and several accessory enzymes).[119]

The two intense peaks that stand out above the spectrum of the pre-treated biomass at 1312 and 1600 cm^{-1} obviously do not belong to any component of the biomass. In fact, neither lignin, nor cellulose, nor hemicellulose show such intense peaks at those wavelength values. These bands could be associated with the presence of the trisodium acetate ions of the buffer loaded in the bleaching solution, which exhibits its most intense absorption at those wavelengths, due to the symmetric and anti-symmetric stretching of COO^-.[120]

2.5.2. Optimization of BG/cellulase weight ratio

Three families of enzymes that work synergistically to convert cellulose to glucose compose cellulase. CBH acts on the free ends of the cellulose chains, releasing mainly cellobiose, thus providing the substrate for BG that hydrolyzes it to glucose. EG is active on amorphous regions of cellulose, randomly cutting internal linkages, creating new free ends for the action of CBH and releasing soluble cellodextrins that will be hydrolyzed by BG. On the other end, the action of BG is essential since cellobiose can severely decrease the rate of cellulose hydrolysis, being an inhibitor of the cellulase complex.[121] The synergy between the three enzymes is expressed on several levels. *Trichoderma reesei* cellulase, the most used fungal cellulase, contains 80% of CBH and 12% of EG.[122] It is therefore clear that BG is insufficient for efficient hydrolysis and cellobiose will accumulate inhibiting the reaction.[83] To obtain a high glucose yield, it is necessary to supplement the enzyme cocktail with additional BG. In literature there are several studies dealing with supplementation of free cellulase with free BG,[122,123] immobilized BG,[124,125] or co-immobilization of BG and cellulase,[79,85–87] using a BG/cellulase ratio of 0.1-0.5. In order to balance the enzyme cocktail improving the glucose yield, we carried out CMC hydrolysis varying the BG/cellulase ratio from 0.2 to 0.5. The results are presented in **Figure 3a**.

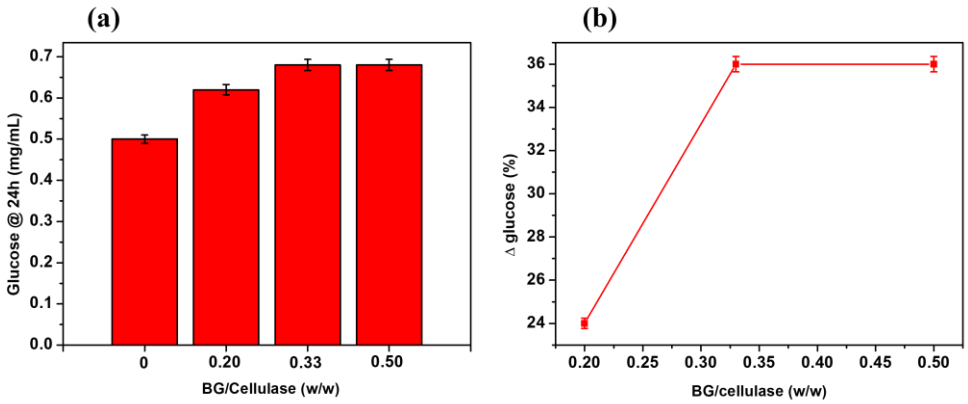

Figure 3. Histograms showing the concentration of glucose in the reaction mixture after 24 h obtained by enzyme mixtures of different compositions (a). Percentage increment of obtained glucose versus BG/cellulase w/w (glucose concentration produced by pure cellulase was set as reference) (b). Each experiment was performed in triplicate.

Histograms report the concentration of the glucose originating from the hydrolysis of CMC (2 mg/mL) in a reaction time of 24 h. Absolute cellulase is responsible for a glucose concentration of 0.50 mg/mL. Glucose concentration rises up to 0.62 mg/mL when BG/cellulase weight ratio is set to 0.20, resulting in 24% increase with respect to the performance of pure cellulase (**Figure 3b**). The percentage enhancement of the glucose production lowers to 9.7% when the weight ratio between the enzymes is pushed up to 0.33 with respect to the case of 0.20 w/w, resulting in 36% overall increase. No further benefits are observed using a BG/cellulase w/w equal to 0.50, meaning that all the cellobiose produced as intermediate is hydrolysed to glucose (**Figure 3b**). Other authors have worked to optimize the enzyme cocktail composition before. For instance, Chakrabarti and Storey obtained a 3-fold higher glucose concentration by degrading CMC (1% w/v) with a mixture of BG (2 U) and cellulase (30 U) with respect to pure cellulase, in solution as well as co-immobilized into a polyurethane foam.[85] Borges et al. proved that supplementing free cellulase (40 FPU/$g_{cellulose}$) with immobilized BG (120

$U/g_{cellulose}$) resulted in 40% higher conversion of sugarcane bagasse to glucose in 96 h.[125] Moreover, supplementing free cellulase with BGs extracted from six different fungi (BG/cellulase = 0.4 w/w) was found to enhance filter paper conversion of 4.22 times.[122].ù The enzyme cocktail composed of 0.50 U/mL BG and 0.75 U/mL cellulase was found to be effective in enhancing corn straw conversion to glucose by 94% with respect to absolute cellulase.[126] Glucose production from the hydrolysis of microcrystalline cellulose was increased by 8.3% after supplementing commercial cellulolytic formulation (5 U/mL cellulase, 0.45 U/mL BG) with 0.40 U/mL of purified BG from *Candida peltate*.[127] Based on literature results and on our experiments, a BG/cellulase ratio comprised between 0.20 and 0.33 w/w can be enough to optimize the biomass hydrolysis yield with the enzymes in immobilized form.

2.5.3. Enzymes co-immobilization

It is widely known that endoglucanase and exoglucanase have high affinity for cellulose surface, which make them easily recoverable by adsorption on fresh cellulose.[128] On the contrary, BG does not adsorb on cellulose. BG should be made readily available where the endoglucanases and exoglucanases have performed their action, to avoid cellobiose accumulation in the proximity of the two enzymes with consequent inhibition. BG will also be inhibited by both cellobiose and its reaction product, glucose. However, at the chosen concentrations (the maximum glucose concentration obtained is approximately 9 mM) the inhibition is limited.[101]

Consequently, we used different co-immobilization strategies to enhance the synergistic action exerted by the enzymes in the hydrolysis reaction of cellulose. As determined by the BG/cellulase ratio optimization tests, we tried to obtain the immobilization in the ratio 0.33 w/w of the two enzymes. To determine the ratio actually obtained, the samples were subjected to thermogravimetric analysis. In particular, the SEQ-BG/Cell sample was analysed after the first adsorption stage (SEQ-BG) and in the second stage of cellulase adsorption on the BG-filled sample (SEQ-BG/Cell). TEM and FTIR investigations were also carried out on bare WSN-

p, SEQ-BG and SEQ-BG/Cell, in order to observe the presence of BG in the nanoparticles and the degree of filling thereof. **Figure 4** reports TEM micrographs for all the nanosystems.

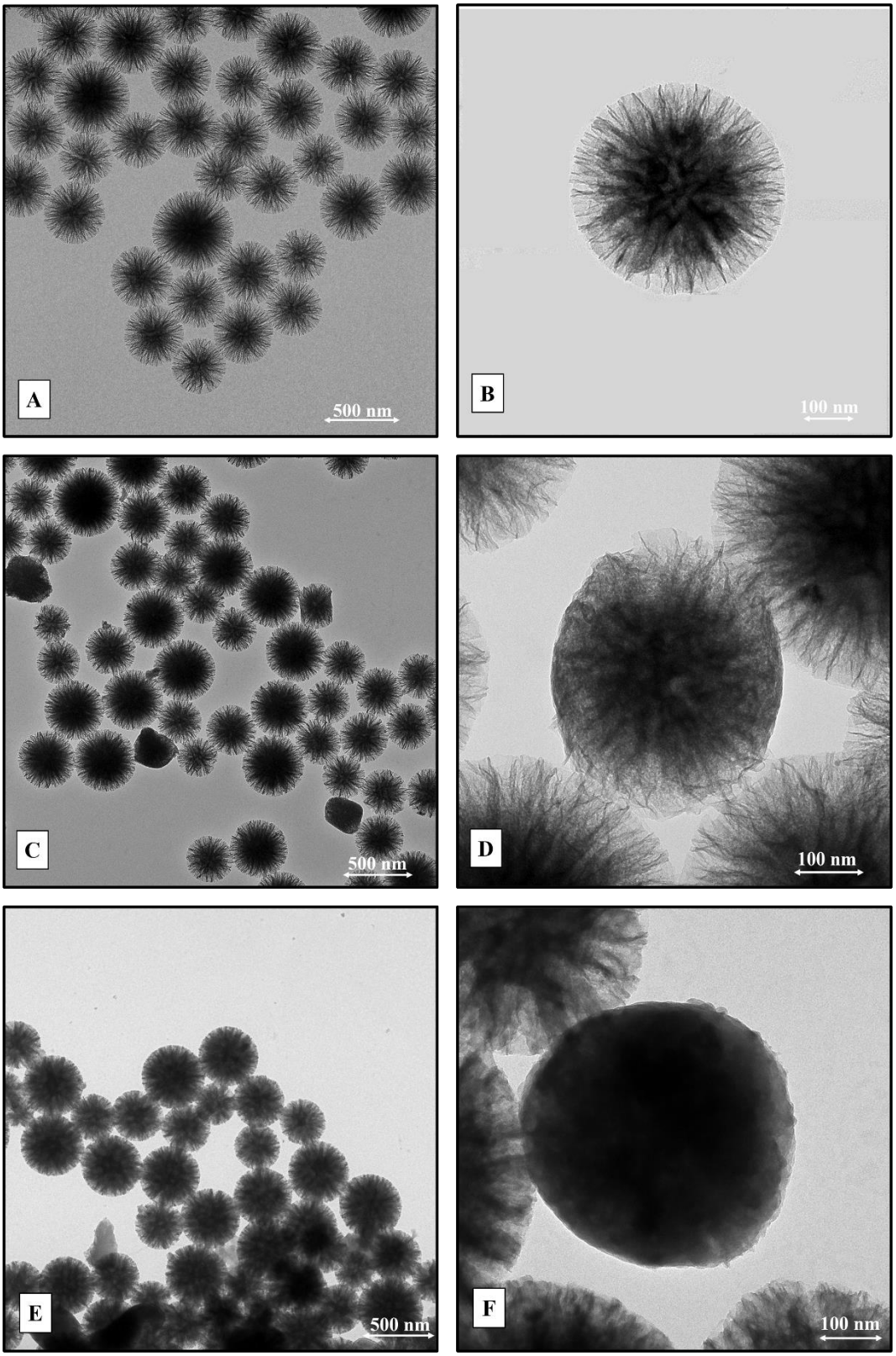
A
500 nm
B
100 nm
C
500 nm
D
100 nm
E
500 nm
F
100 nm

Figure 4. TEM images for WSN-p (A, B), SEQ-BG (C, D) and SEQ-BG/Cell (E, F) taken at lower (500 nm, left column) and higher (100 nm, right column) magnifications.

WSN-p exhibit the well-known profile showing radial silica nanofibers with enhanced inter-wrinkle distance if compared to WSN, as already discussed in our previous study.[100] The image taken at lower magnification (**Figure 4A**) assesses that the nanoparticles appear as a rather monodisperse system with diameter included in 300-500 nm size range. **Figure 4C** and **4D** prove the presence of BG inside the mesopore structure of the silica support due to the increased contrast visible in the inner core of SEQ-BG nanosystems. In particular, BG homogeneously settles along the entire length of pores in WSN-p (**Figure 4D**) during the first immobilization step. Micrographs referring to SEQ-BG/Cell sample (**Figure 4E, 4F**) show that subsequent adsorption of cellulase totally fills the pore structure of the support, as highlighted by the net contrast increase experienced by the nanostructure surface: the immobilized protein almost completely hides the profile of the silica support (**Figure 4F**). However, the overall diameter of the nanostructure does not change after the immobilization process since no protein corona layer of appreciable thickness is formed over the support. The effectiveness of each adsorption stage is confirmed by FTIR spectra reported below in **Figure 5**.

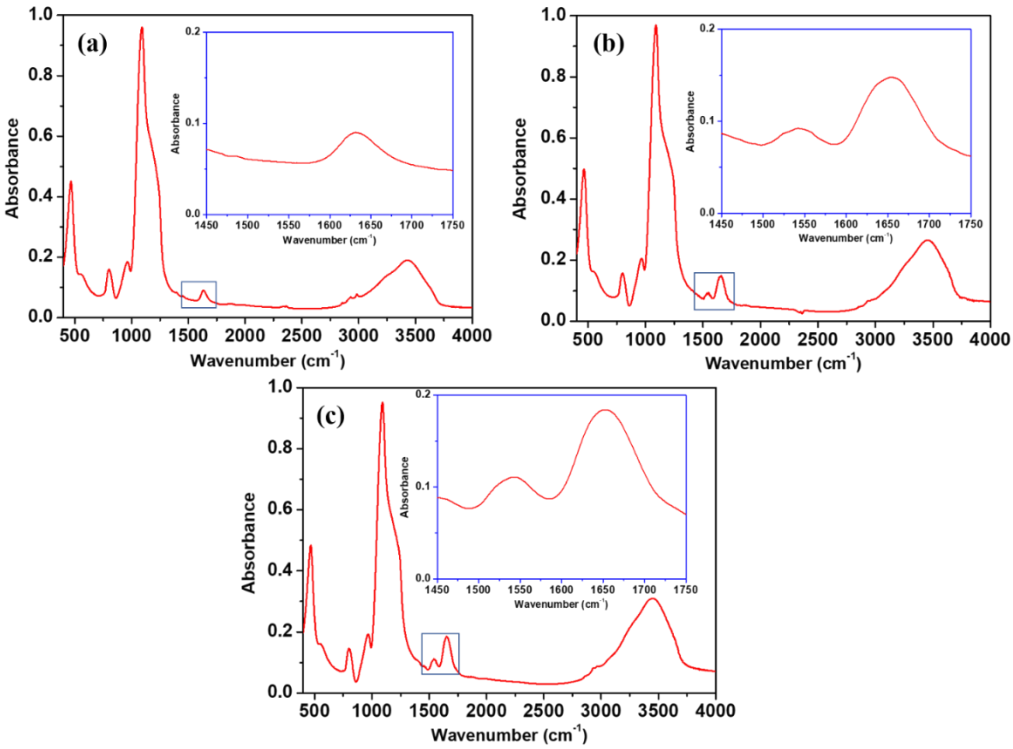

Figure 5. FTIR spectra for WSN-p (a), SEQ-BG (b), SEQ-BG/Cell (c). Insets in blue rectangles show the focus on amide I/amide II region (1450-1750 cm^{-1})

WSN-p exhibit an infrared spectrum which is typical for silica-gel (**Figure 5a**). More specifically, siloxane bridge stretching vibration gives a high band at 1100 cm^{-1} and a smaller band at 800 cm^{-1}, whereas band at 950 cm^{-1} is attributed to non-bridging Si-O stretching. The wide band centred at around 3500 cm^{-1} is assigned to OH stretching for surface silanol groups and adsorbed water.[92] Moreover, Si-O-Si bending corresponds to a band at 470 cm^{-1}.[129] BG immobilization noticeably alters FTIR spectrum of silica nanoparticles (**Figure 5b**). The presence of the protein is confirmed by amide I and amide II bands, which appear in 1450-1750 cm^{-1} wavelength region. The former, produced by stretching vibration of carbonyl groups of peptide bonds [130,131], is slightly displaced respect to its normal position (1650 cm^{-1})[101] due to the overlap with the O-H bending vibration band of adsorbed water (1640

cm^{-1}).[101] The latter, centred at around 1540 cm^{-1}, is due to N-H in-plane bending and C-N stretching vibrations.[130,131] As for the spectrum of SEQ-BG/Cell sample (Figure 5c), it experiences a remarkable increase in the intensity of both amide I and amide II bands, suggesting that the overall amount of enzyme loaded into the silica skeleton has noticeably increased after cellulase adsorption. The amide I band in this spectrum is centred at 1652 cm^{-1}, as it is less affected by the influence of the OH band of the adsorbed water. This wavenumber position is the same as free cellulase,[100] indicating a preserved conformation of the adsorbed cellulase with respect to its native form. The most likely mechanism of physical immobilization is the occurrence of hydrogen bonds between the enzymes and the silica support, as already reported for both BG alone and cellulase.[27,28] For BG, electrostatic interaction plays a role, since the isoelectric point (pI) of β-glucosidase is around 5.5 while silica has a pI around 3.[132] For cellulose the situation is less straightforward, since each individual enzyme composing the enzyme complex has its individual isoelectric point, so that some of them are positively charged and others are negatively charged at pH 5.[133]

Enzyme loading was assessed through TGA for both SEQ-BG and SEQ-BG/Cell, as reported in **table 2**. SEQ-BG sample reached an enzyme loading of 15 mg/g of support. At the end of the process, the total enzyme loading rose up to 90 mg/g of support, corresponding to an overall 15% YI. Therefore, the finally obtained BG/cellulase weight ratio was equal to 0.2, lower than the desired value of 0.33. One-pot co-immobilized SIM-BG/cell sample was submitted to TGA as well, with the aim of monitoring any changes in the overall enzyme loading. The result was 100 mg/g of support, corresponding to 20% YI. Considering that the results for SEQ-BG/Cell was 90 mg/g and that 15 mg/g is BG and 75 mg/g is cellulase, if we suppose that all the extra uptake is BG the ratio BG/cellulose would be 0.33 whereas if we consider that all the extra uptake is cellulase, the ratio would be 0.18. We conclude that we cannot precisely know the BG/cellulase ratio in this sample, but we can assume that it is comprised between 0.2 and 0.33. Finally, the BG/cellulase ratio of

the SEP-BG/Cell sample could be precisely set to 0.33 by mixing the adequate ratio of the two filled vectors.

Table 2. Enzyme loading (mg/g of support) and BG/Cellulase (w/w) for all the biocatalysts.

Biocatalyst	**Enzyme concentration (mg/mL)**	**Enzyme loading (mg/g of support)**	**BG/Cell (w/w)**
SEQ-BG	0.33	15	/
SEQ-BG/Cell	BG: 0.33 Cell: 1	90	0.2
SIM-BG/Cell	BG: 0.17 Cell: 1	100	0.2 – 0.33
SEP-BG/Cell	BG: 1 Cell: 1	BG/WSN: 150 Cell/WSN-p: 75	0.33

Results obtained from N_2 adsorption/desorption experiments point out a progressive filling of the pore structure during sequential immobilization. More specifically, BET surface areas lowered from 544 to 503 to 426 m^2/g, when evaluated for WSN-p, SEQ-BG and SEQ-BG/Cell, respectively. Similarly, total pore volumes decreased from 1.49 to 1.23 to 1.17 cc/g.

2.5.4. Pre-treated biomass hydrolysis

The hydrolysis of the pre-treated biomass is a heterogeneous reaction since the substrate is insoluble while the enzymes are dissolved or suspended in the reaction medium, depending on weather they are in their free or supported form. However, CBH and EG are very prompt in depolymerizing cellulose chains,[134] leading to a

complete disappearance of floating substrate in about 1 h into the reaction medium. Glucose production over time for free BG/cellulase mixture in 1:3 weight ratio is reported in **Figure 6** and compared to that achieved by using SIM-BG/Cell. Free and supported biocatalysts exhibit the same trend, made of a linear region in 0-2 h time interval and of a plateau approached in 24h. Final values for glucose concentration are 9.3 and 7.9 mM, corresponding to 97 and 82% YR for free and supported enzyme mixture, respectively. The difference in terms of long-time performance is slightly higher than that evaluated in short times. Indeed, the activity of SIM-BG/Cell is 72 μmol/min·g and is 10% lower than that of the free enzyme mixtures, which is equal to 80 μmol/min·g.

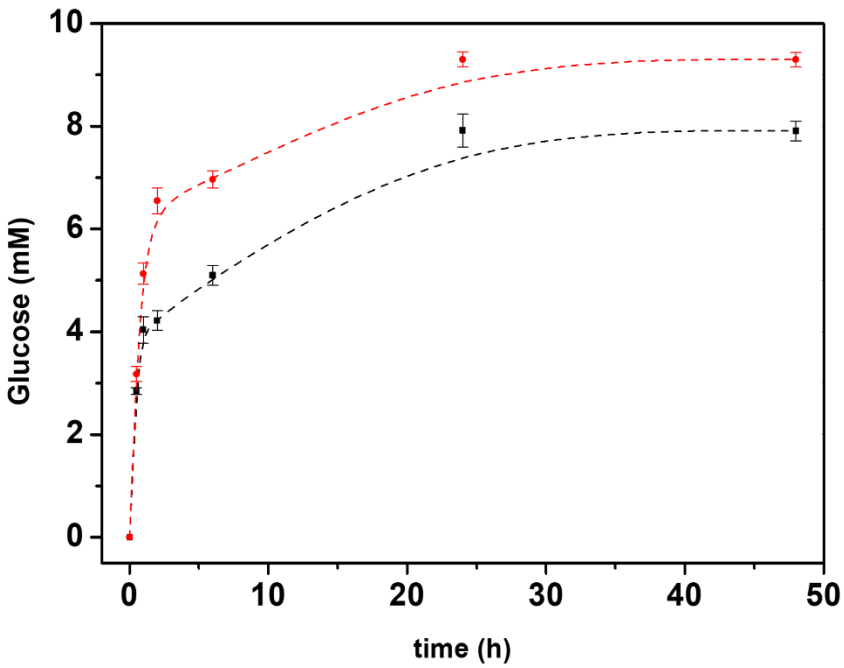

Figure 6. Glucose production over time for free BG:Cellulase 1:3 (w/w) (red) and SIM-BG/Cell (black). Each experiment was performed in triplicate.

Figure 7 shows histograms representing the glucose yield of each tested biocatalyst. Glucose yield (weight %) is obtained after subtracting from the pre-treated biomass total weight the ash fraction, determined by TGA. Free cellulase supplemented with

BG/cellulase 0.33 and 0.2 w/w shows a glucose yield of 97 and 89% respectively. Even in this case, as for the CMC, a small conversion increase is confirmed in the 0.33 sample compared to the 0.2 sample equal to about 9%. BG/Cellulase w/w equal to 0.20 was tested in the hydrolysis of untreated biomass. However, the yield of reaction was only 4%, meaning that pre-treatment is necessary to increase cellulose digestibility.

A dramatic drop in conversion yield occurs for cellulase immobilized on WSN-p (Cell/WSN-p, 28%) and supplemented with 0.33 ratio of BG immobilized on WSN (SEP-BG/Cell, 35%). The yield rises again to 74% by adding 1 mg of free BG during the reaction catalysed by SEP-BG/Cell. This means that the low yield of these two catalysts depends on a BG deficiency in the enzymatic cocktail, which may be due either to an actual absence of BG inside the support (Cell/WSN-p) or to the fact that BG fails to act before the cellobiose accumulates and inhibits the reaction. Cellulase from *Trichoderma reseei* contains at least two CBH, five EG and one BG.[76] Each of them has its own tertiary structure and physical-chemical properties. Adsorption from an enzyme mixture is a rather complicated process. The final surface composition of the support will depend on the molecular weight and shape of the enzymes, their concentration (that account for diffusion from the bulk solution to the support surface) and on their different affinity with the surface (i.e. different isoelectric point of each enzyme).[97] Although the molecular weight of BG is comparable with that of other cellulase enzymes, its concentration is significantly lower (1% wt of the mixture).[76] It is therefore likely that during the immobilization of the cellulase on the WSN, the BG is partially excluded from the process and the enzymatic cocktail obtained on the surface of the support ends up with a serious deficiency of BG activity. This would explain the low glucose yield reached by using Cell/WSN-p. On the other hand, the addition of exogenous BG immobilized on a separate vector (SEP-BG/Cell) only slightly improves the yield, since in this case the BG fails to perform its synergistic action. In fact, with individually immobilized enzymes, the cellobiose produced by CBH must diffuse from the pores of one vector

to those of the other vector, becoming diluted in bulk solution.[135] Meanwhile, in the pores of the support, cellobiose is produced at high rate, and its concentration can be enough to inhibit CBH activity. By adding free BG, the problem is mitigated since it can diffuse freely where cellobiose is being produced.

With the co-immobilized and sequentially immobilized systems, the glucose yield rises to 82 and 72% respectively. Again, we found a difference of about 10% between the two biocatalysts that made us suppose that it could depend on a different BG/cellulase ratio, as reported in table 2. In both cases, the glucose yield is about 15% lower than the respective free references (BG/cellulase free 0.2 for SEQ-BG/Cell and BG/cellulase free 0.33 for SIM-BG/Cell). This may be due to diffusional limitation or pore blocking, because part of the enzyme complex is located deep inside the pores, and cannot be reached by the substrate. In fact, as we will see, the co-immobilized enzyme is very stable. So, we tend to exclude that the decrease in yield may be due to deactivation caused by conformational changes of the polypeptide chains. Moreover, SIM-BG/Cell and SEQ-BG/Cell exerted comparable activities and about only 10% lower than those of the free enzyme mixtures, equal to 72 and 70 μmol/min·g, respectively. The activity of the immobilized biocatalysts scaled in a similar way as conversion with respect to the free enzymes. The results obtained are in agreement with previously available literature results for similar systems. Wang et al. designed a sequential co-immobilization system able to push filter paper conversion to glucose from 40% to 71% in 48 h when integrating cellulase with BG with a BG/cellulase ratio w/w equal to 0.5.[79] Carli et al. covalently immobilized BG and EG either separately and simultaneously on ferromagnetic nanoparticles, finding a 1.6 fold degree of synergism against pre-treated sugarcane bagasse.[136] Song et al. covalently immobilized BG and CBH on superparamagnetic nanoparticles finding a retention of activity equal to 67.1 and 41.5% of the free enzymes respectively.[137] The advantage of our work lies in the higher yields compared to those reported in literature, but also in the straightforwardness of the process, which uses a simple

physical adsorption on easily synthesized nanoparticles. The higher yields obtained in this work may depend on different features of the system: (i) physical adsorption preserves the native conformation of the enzyme, and (ii) wrinkled nanoparticles favour diffusion of the cellulose chains rapidly depolymerized by CBH and EG that have been adsorbed in proximity of the pore openings. Finally, the results obtained confirm the synergistic action of BG and cellulase. When the enzymes are intimately mixed, as in SEQ-BG/Cell and SIM-BG/Cell, BG can immediately hydrolyse the cellobiose produced, preventing its concentration from rising to levels that become inhibitory for CBH.

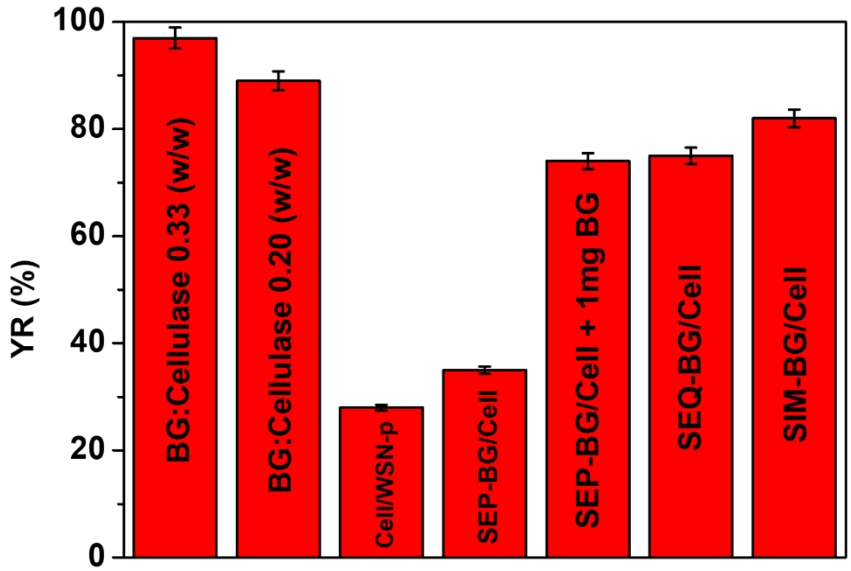

Figure 7. Histograms reporting the yield of reaction obtained by all the selected biocatalysts. Data are shown with error bars. Each experiment was performed in triplicate.

2.5.5. Operational and thermal stability

Operational stability measurements are necessary to assess the reusability of the supported protein in consecutive reaction cycles. The possibility to recover the enzyme from the reaction medium and use it repetitively can balance the high costs associated to the production of the biocatalyst. **Figure 8** reports the relative glucose production histograms for the supported one-pot co-immobilized enzymes (SIM-BG/Cell).

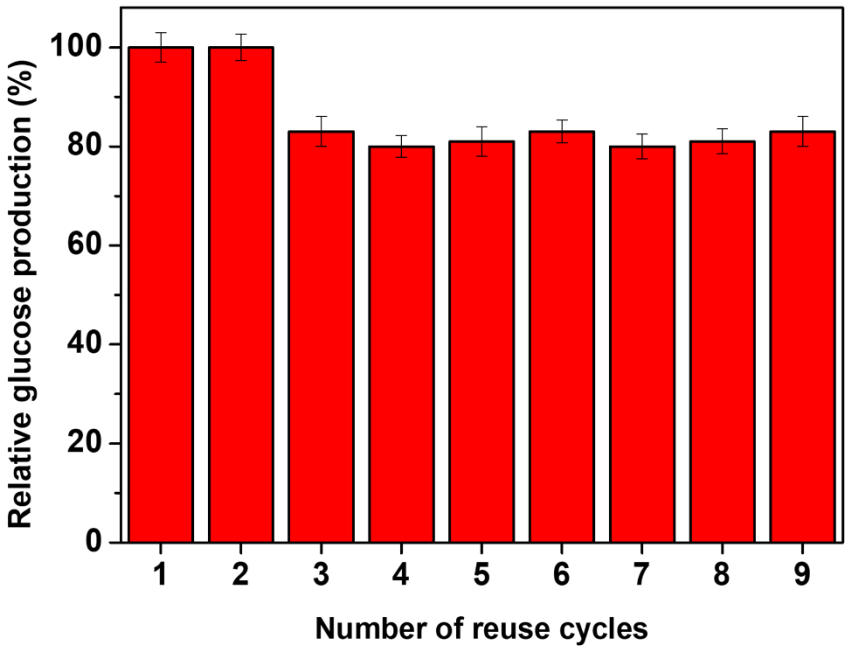

Figure 8. Histograms showing the relative glucose production after each reaction cycle. Each experiment was performed in triplicate.

Results highlight the excellent reusability exerted by the supported biocatalyst, which was reused in 9 consecutive reaction cycles, experiencing only 17% loss in glucose yield. The loss occurs after the second cycle and remains constant up to the 9^{th} cycle. The possible reason for this behavior can be attributed to the mechanism of physical immobilization onto the surface of nanosilica structure. The first enzyme molecules loaded in the adsorption medium diffuse inward into the hierarchical pore

structure and gradually fill the inner core of the nanostructure by interaction with the silica surface.[97,100] When the pores are filled, exceeding enzyme establishes intramolecular aggregates, which do not interact with the inorganic surface. These aggregates are loosely bound to the outer adsorbed enzyme layer and might be easily leached during the reaction,[138] leading to a slight decrease in the catalytic performances in consecutive reuses. The high stability of the co-immobilized enzyme is surprising if compared to what previously found for single-enzyme immobilization: BG adsorbed into WSNs exhibited 40% retention of activity after the 5th reuse cycle,[139] whereas cellulase exhibited a small but gradual loss after the 4th reuse.[100] Several authors reported the remarkable operational stability of the co-immobilized enzyme systems. BG and cellulase co-immobilized onto hierarchical polymeric microparticles exhibited 75% retention of original activity in the hydrolysis of CMC after 10 recycles and 57% retention in the hydrolysis of filter paper after 5 recycles.[79] Co-immobilization of BG and EG resulted in a biocatalyst retaining a relative activity of 80% after the 5th cycle, 2-fold and 8-fold what achieved by single immobilized EG and BG, respectively.[136] The supported multienzyme system introduced in this work exhibits similar or even better reusability performances if compared to the ones cited above but without using any covalent interaction between protein and support. This proves the effectiveness of physical co-immobilization into WSN-p in producing a high performing and reusable biocatalyst. Moreover, the reuse allowed preserving almost all the original enzyme loading as confirmed by TGA measurements, indicating that the leaching falls below the sensitivity threshold of the instrument (in the order of 1 μg).

Thermal stability is also an important feature for industrial use of biocatalysts, where they could be exposed to harsh temperatures. Thermal stability is often improved by protein-support interaction. **Figure 9** reports the comparison between the thermal stability profiles of supported and free enzyme mixture.

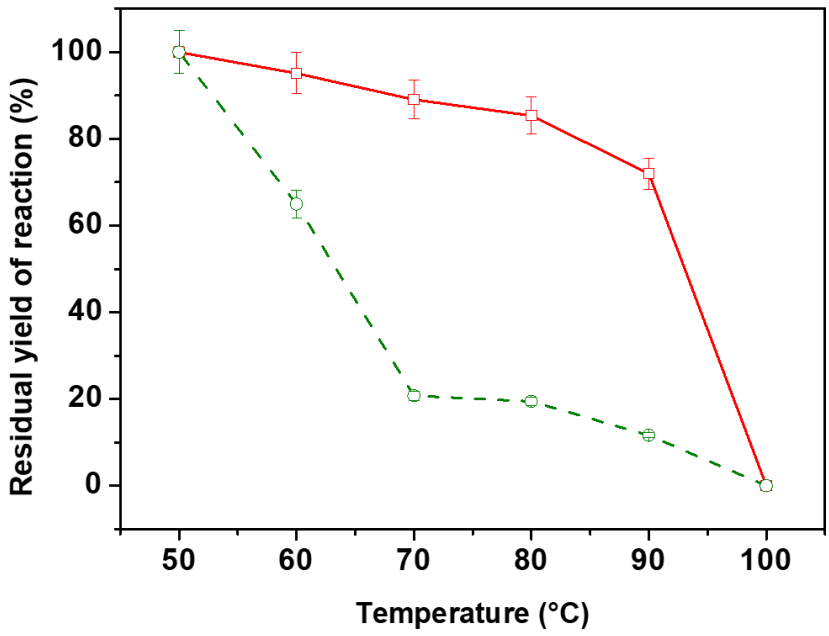

Figure 9. Residual yield of reaction over temperature for supported (red, solid) and free (green, dashed) biocatalyst. Each experiment was performed in triplicate.

Free enzymes experience a rapid decrease of residual yield of rection in 50-70 °C temperature range, suggesting irreversible modification in protein conformation. For temperatures higher than 70 °C, the activity keeps lowering with slower rate to the 0% value, recorded at 100°C. As for supported enzymes, they are remarkably less sensitive to temperature variations as the worsening of the catalytic performances is definitely contained. Indeed, 89% retention of the yield of reaction is recorded at 70 °C, whereas free proteins are almost completely deactivated at the same temperature. Moreover, total 28% loss occurs for such high temperature as 90°C. However, the rising of temperature up to 100°C led to a collapse of the catalytic activity, maybe due to on-off denaturation phenomena. An improvement of enzyme thermal stability upon immobilization has been often observed.[140,141] The interaction of the enzyme with the support can rigidify the enzyme structure by inhibiting the conformational freedom and thermal vibration of the polypeptide chain. In case of enzyme entrapped

in a porous support, the interaction with the pore walls further increases enzyme rigidity.[142] 50°C is confirmed as the optimal temperature for the dual enzyme system.[79] Moreover, the confinement into the silica skeleton is proved to be a proper strategy to preserve the structural pattern of cellulolytic enzymes from thermal denaturation.[102,105]

2.6. Conclusions

In this paper, a simple and efficient strategy to co-immobilize BG and cellulase for enhanced conversion of cellulose to glucose was designed. BG/cellulase ratio was optimized: it was found that a ratio comprised between 0.20 and 0.33 w/w was enough to promote an efficient hydrolysis. The two enzymatic systems where immobilized separately or co-immobilized. The synergistic action of BG and cellulase was maximized when the enzymes were intimately mixed, as obtained in SEQ-BG/Cell and SIM-BG/Cell. In these biocatalysts, BG could hydrolyze cellobiose as soon as it was produced, relieving CBH inhibition. Cellulose hydrolysis yield obtained for SEQ-BG/Cell and SIM-BG/Cell were 72% and 85% respectively. The biocatalysts showed a very good operational stability preserving 83% of the initial yield of reaction up to nine reuses and better stability in a wide range of temperatures than free enzymes, preserving 72% of the initial yield of reaction up to 90°C. This proves the effectiveness of physical co-immobilization of BG and cellulase into WSN-p for industrial application in biorefineries.

3. Tailoring the hydrophobicity of wrinkled silica nanoparticles and of the adsorption medium as a strategy for immobilizing lipase: an efficient catalyst for biofuel production

This section refers to the original version of the paper by Pota et al. *Microporous and Mesoporous Materials*, 2021, 328, 111504. https://doi.org/10.1016/j.micromeso.2021.111504.[15]

3.1. Abstract

Hydrophobic wrinkled silica nanoparticles (WSNs) were obtained by surface functionalization with perfluorodecyltriethoxysilane (PDTES) by chemical vapour deposition (CVD). Surface functionalization was made to design a hydrophobic surface to immobilize lipase in its open active conformation by interfacial activation. Moreover, to modulate the closed/open form equilibrium, favouring the open conformation, n-hexane was added to the water/lipase solution, creating a micro-oily environment. Physicochemical characterization of supports was carried out by solid state ^{29}Si nuclear Magnetic Resonance (NMR), the Brunauer–Emmett–Teller (BET) method, thermogravimetric (TG) analysis, contact angle (CA) measurement, scanning electron microscopy (SEM) and Fourier transform infrared (FT-IR) spectroscopy. Three different supports for physical immobilization of lipase were prepared, differing in the degree of hydrophobicity. The effect of the different hydrophobicity and of the addition of n-hexane on the adsorption of lipase was evaluated. The hyperactivation of the best biocatalyst was tested in the hydrolysis and transesterification of sunflower seed oil and compared to free lipase. The reaction yields were 87% and 75% respectively for hydrolysis, and 93% and 56% respectively for transesterification. The results suggest that both the hydrophobicity of the support and the addition of n-hexane favour the adsorption of lipase in the active conformation.

3.2. Graphical abstract

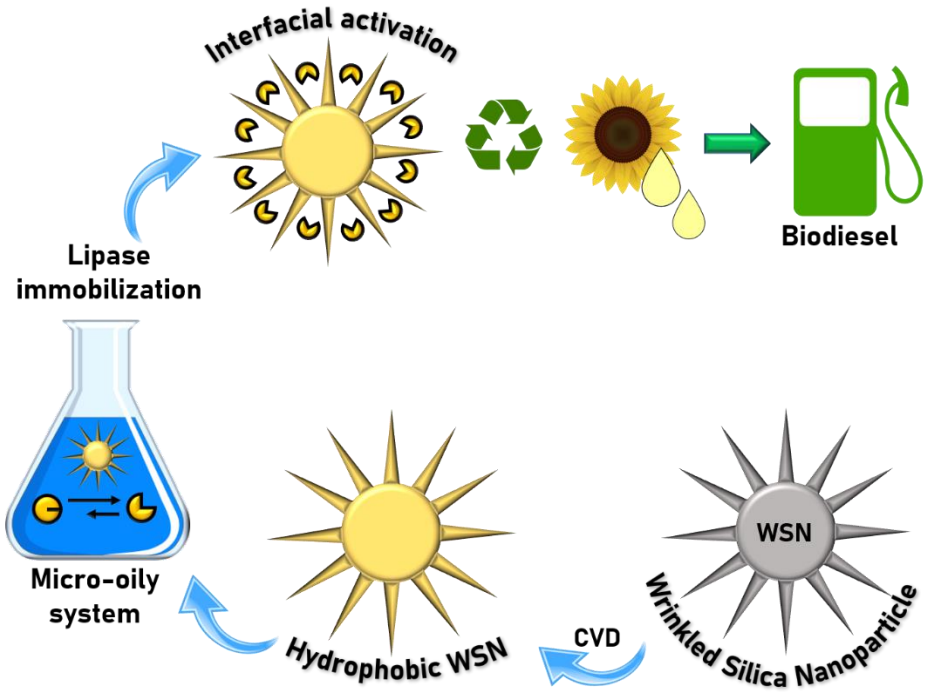

3.3. Introduction

Rapid depletion of fossil fuel sources, together with the increasing impact of greenhouse-gas emissions on climate changes, triggered the search for carbon-neutral biofuels. Biodiesel, consisting of fatty acid alkyl esters, stands as a renewable fuel that has received growing attention in last decades for its use for automotive application.[143] Biodiesel is produced by transesterification of triacylglycerols, a widely available substrate contained in vegetable oils. Transesterification reaction can be catalyzed by lipases (E.C. 3.1.1.3). Lipases are extracted from different sources. They are involved in several biochemical reactions on triacylglycerols, such as hydrolysis and esterifications. Literature is rich of papers dealing with the lipase-catalyzed bioconversion of oils into biodiesel.[144–146] High product purity, easy separation of the byproduct glycerol, lower energy consumption due to mild reaction conditions represent remarkable benefits deriving from the use of lipases in biodiesel production. Moreover, enzymatic transesterification leads to the complete

conversion of free fatty acids (present in low-quality feedstock) to methyl/ethyl esters.[147] The yields of transesterification are usually affected by a series of factors such as lipase stability, specificity, reaction temperature and water content in the reaction medium.[148,149] In particular, lipases specificity can be a problem for biodiesel production, where the full conversion of the triglycerides is required.[150]

Despite many benefits, the commercialization of the enzymatic biodiesel is still hindered by the high cost and low stability of lipases. In order to make it competitive at the industrial level and reach a significant level of applications, it is necessary to overcome these drawbacks and improve recovery as well as recycling of the biocatalyst. To address these deficiencies, lipases can be immobilized on insoluble supports. Enzyme immobilization is the confinement of the enzyme molecules onto/within an insoluble support with retention of its catalytic activity. This methodology allows exploiting the advantages of heterogeneous catalysis. Furthermore, immobilization often results in the improvement of enzyme properties, such as stability, activity and selectivity,[74,151] and decreases the effect of enzyme inhibitors (such as alcohols in case of lipase) and thermal inactivation.[71] Different techniques for enzyme immobilization can be used: adsorption, entrapment, covalent binding, and cross-linking.[152] A successful process of immobilization is expected to guarantee high activity and reusability for the immobilized enzyme, two key features strictly related to the physic-chemical properties of the chosen support.[153] Among all the nanostructured materials suitable for enzyme immobilization, mesoporous silica has recently gained attention as one of the most performing due to its endogenous properties such as low toxicity, high biocompatibility and good stability. High surface area, and tunable pore size and distribution allow high loading of guest species or pollutants. [148,154–156] Moreover, the abundant surface hydroxyl groups enable easy chemical surface functionalization.[92,157,158] Mesoporous silica nanoparticles (MSPs) with radial-oriented microchannels and a conical pore shape are ideal scaffolds for catalytic applications, as the pore structure is accessible to large molecules. This particular morphology allows enzyme molecules to diffuse

smoothly into the pores promoting enzyme loading and minimizing diffusion limitations of reactants and products.[159] The positive outcome of these factors is the enhancement of the catalytic performance of immobilized enzymes.[160] Wrinkled silica nanoparticles (WSNs) belong to this kind of nanoparticles.[104] They have radially widening pores that can easily host functional materials avoiding pore block. Several papers report the choice of WSNs as support for the immobilization of lipase and β-glucosidase so far.[101,102,139,161] The improved catalytic performance exhibited by WSN-supported lipase compared to free enzyme was explained with the good dispersion of active sites inside the pores, due to the radially aligned mesopores of WSNs.[162] Similarly, an improvement of the catalytic performances, together with higher thermal and operational stability, was obtained for WSN-supported β-glucosidase. Even then, this was attributed to the pore shape and the hierarchical pore structure which eliminate diffusive limitations for the substrate, making WSNs optimal hosts of β-glucosidase.[101,139] Generally, lipases immobilization requires the functionalization of the silica particles with hydrophobic moieties and most lipases exhibit full catalytic activity only after interfacial activation. [163] Lipases have a helical loop that covers their active site. In this "closed" conformation, the catalytic site is inaccessible and lipase is inactive. Upon adsorption at a hydrophobic/hydrophilic interface, the loop changes its conformation giving rise to the "open" active from.[164] Therefore, it is preferable to immobilize lipase in the open-lid active conformation. [165] This is possible by using hydrophobic supports. Lipase undergoes interfacial activation during immobilization on hydrophobic support similarly to what happens when lipase is at the interface with its natural substrate.[166,167] Furthermore, due to the mechanism of interfacial activation, lipases tend to form dimers in aqueous solution through the interaction of the active centres of two molecules in the open form, which are in equilibrium with the monomer.[167,168] The dimeric form is less active than the monomeric one and immobilization on hydrophobic supports causes a shift of the dimer/monomer equilibrium of the lipase towards the monomer form, which is readily adsorbed in the open form. For these

reasons, lipase activity sensibly improves when the protein is immobilized on hydrophobic supports.[167–169] For biodiesel production, the use of hydrophobic support is also favorable because the accumulation of hydrophilic compounds during the transesterification reaction, i.e. glycerol or water, can lead to enzyme deactivation. Glycerol can hinder the lipase activity by creating a hydrophilic shell around the enzyme that prevents the hydrophobic substrate to diffuse to the active site.[170] This effect can be reduced in several ways, for example by using ultrasounds,[171] molecular sieves or hydrophobic supports.[172–174] In this work, *Candida rugosa* lipase (CRL) was physically immobilized onto hydrophobic functionalized WSNs to preserve its native conformation and catalytic activity. Immobilization was carried out using a ternary system lipase/water/n-hexane (a micro-oily environment). This was possible because it was found that a 0.2% wt. solution of lipase in water can solubilize small quantities of the oil phase forming a clear solution.[175] The addition of n-hexane was made to modulate the equilibrium between the open and the closed form of lipase. In fact, it was found that some water insoluble organic solvent (i.e. hexane) can induce the opening of the lid increasing lipase activity.[176] Lipase adsorption on hydrophobic supports is enhanced when the open form of the lipase is favored in solution. For example, using octyl agarose as support, it was found that the lipase immobilization rate increased when the ionic strength decreased.[165,177] At high ionic strength, the closed form is favored because the open form exposes a large hydrophobic pocket, and lipase/lipase dimers are stabilized. That is, the closing/opening equilibrium of lipase can be modulated by altering the adsorption medium and the adsorption rate on hydrophobic surfaces increases when the equilibrium is shifted towards the open form. Similar results have been obtained which show how the composition of the lipase adsorption medium on hydrophobic supports alters its properties, probably for its structural flexibility due to the presence of the lid.[178] In fact, it was found that immobilization of lipases with small lids, unable to fully isolate the active center to the medium, is not influenced by the medium composition, unlike to what happen with the immobilization of

lipases with larger lids.[179] Despite hexane may compete with the surface of the support in the adsorption process, it must be considered that lipases generally have a high character of hydrophobicity, especially when they are in open form, as shown in **Figure 1**. When the lid is open, a large hydrophobic surface is exposed around the catalytic tunnel, so that the interaction with the solid surface is still possible even if the active site is interacting with hexane. The adsorption on the solid surface stiffens the lipase structure so that this conformational state is maintained after immobilization on hydrophobic supports. The WSNs surface was modified using perfluorodecyltriethoxysilane (PDTES) as the hydrophobic agent. We have prepared three kinds of samples using a different amount of PDTES, which have shown a different level of hydrophobicity. The enzyme derivatives were used both for triglyceride hydrolysis and transesterification reactions (reaction schemes are shown in **Figure S1**).

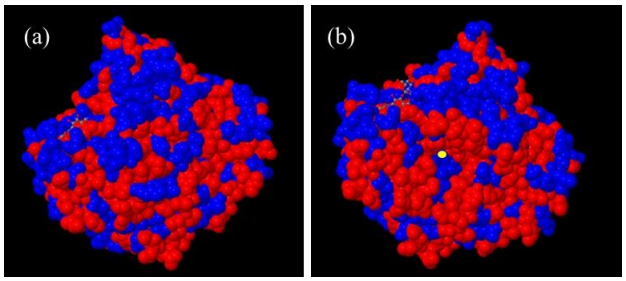

Figure 1. Candida rugosa lipase surface structure. (a) closed form and (b) open form. Red: hydrophobic amino acids, blue: hydrophilic other amino acids, yellow: catalytic Ser 209 (RCSB Protein Data Bank).

3.4. Experimental

3.4.1. Materials

Tetraethyl orthosilicate (TEOS), cetyltrimethylammonium bromide (CTAB), urea, cyclohexane, isopropanol, ethanol (ACS reagent, anhydrous), hydrochloric acid (37 wt.% in water), distilled water, perfluorodecyltriethoxysilane (PDTES), lipase from *Candida Rugosa*, n-hexane, and Span® 80 were bought from Sigma-Aldrich (Milan)

and used as purchased. Sunflower oil high-oleic (SOHO) (density 0.92 g/cm^3, 786 g/mol average molecular weight) was purchased from a local supermarket. [180]

3.4.2. Synthesis and surface hydrophobization of Wrinkled Silica Nanoparticles

Wrinkled Silica Nanoparticles (WSNs) were synthesized as previously described and following the procedure described by Moon and Lee with slight modifications. [104 101] More specifically, CTAB was used as the surfactant instead of cetylpyridinium bromide (CPB) and a more accurate surfactant removal procedure was carried out. Hydrophobic WSNs were produced by chemical vapor deposition (CVD), as described in **Figure 2**. 50 mg of WSNs were homogeneously settled on a Petri dish by drop casting of a WSNs-ethanol dispersion. After the evaporation of the solvent, the dried nanoparticle surface underwent CVD process. The Petri dish was placed on a heating plate at the temperature of 100°C. 5 mL of PDTES-ethanol solution was settled dropwise close to the external borders of the Petri dish. The whole system was rapidly covered by a ceramic dome with an exhaust beak, allowing the hydrophobic solution to evaporate completely. To obtain WSNs with different hydrophobicity behaviours, 1%, 5% and 10% by volume of PDTES in ethanol solution were used. Three samples were named WSN1, WSN5, and WSN10, where the percentage in the acronyms refers to the volume concentration of PDTES-in-ethanol solutions used during the CVD process. PDTES/WSN weight ratio was set to 1.7, 8.5, and 17 for WSN1, WSN5, WSN10, respectively. Finally, silanized nanoparticles were scratched off the Petri dish and ground to obtain a fine powder that was subsequently used for physical immobilization.

3.4.3. Preparation of hydrophobic coated surfaces

To evaluate the hydrophobic properties of functionalized WSNs, a set of coated glass slides was prepared to perform surface wettability measurements. Briefly, 12 mm diameter circular glass slides were hydrophilized by oxygen plasma etching (2 minutes at 0.5 mbar) to activate glass silanol groups. The activation of the glass

surface is needed to lower the water contact angle and improve the affinity with WSN water dispersion. 150 μL of 67 mg/mL WSNs aqueous suspension was placed dropwise on the surface of the supports to have a coating of 8.85 mg/cm^2. Finally, the glass slides were dried in a aerated oven at 100 ˚C for 20 min, obtaining dried supports with 10 mg of nanoparticles that homogenously covered the surface of each support. WSN-coated supports were submitted to CVD using the same experimental apparatus reported above. In this case, 1 mL of PDTES-in-ethanol solution was used. 1%, 5%, and 10% in volume of PDTES in ethanol solutions were used for hydrophobization and the coated surfaces were named as the nanoparticles settled onto them (WSN1, WSN5, and WSN10, respectively).

3.4.4. Physical-chemical characterization

3.4.4.1. Scanning Electron Microscopy (SEM)

A FEI Nova NanoSEM 230 (FEI, Hillsboro, Oregon, USA) was used to collect Scanning Electron Microscopy (SEM) images, at an accelerating voltage of 10 kV. A WSN suspension in ethanol was ultra-sonicated for 10 mins, settled on an aluminum support of 70 μm in thickness and dried at room temperature. Before the analysis, the samples were coated with a Platinum layer of about 10 nm, which corresponds to the thickness of the platinum coating on the quartz sensor.

3.4.4.2. N_2 physisorption

Bare and functionalized WSNs were submitted to N_2 adsorption/desorption analysis to determine the specific surface area and the pore structure. The samples were degassed for 10 h at 0.03 mbar and 100°C. Afterwards, a Micromeritics TriFlex instrument was used to collect N_2 adsorption/desorption isotherms with 10-second equilibration time. Brunauer–Emmett–Teller (BET) method was chosen to calculate the specific surface area, whereas the application of Barrett–Joyner–Halender (BJH) model on the adsorption branch of the isotherm provided the pore size distributions and pore diameter.

3.4.4.3. Measurement of surface wettability

A Dataphysics OCA 30 instrument was exploited to detect the wettability, the contact angle (CA), the roll-off angle and the contact angle hysteresis (CAH) of nanoparticles. In particular, as concerns the contact angles as well as the roll-off angles of distilled water were both measured at around 21 °C. To estimate the contact angle hysteresis, the titlted plane methodology was adoperated and CAH was measured as the contact angle that a droplet of distilled water shows when is posed on an inclined plane and starts descending.[181] In detail, the tilting of the solid sufaced leads to the deformation of the droplet and thus the contact angle hysteresis was calulated as the difference between the advancing and the receding contact angles. The contact angle was also estimated in case of diiodomethane. The data of weattability collected by using diiodomethane and water were subsequently deployed to determine the surface free energy of hydrophobic solid surfaces through the Owens, Wendt, Rabel, and Kaelble (OWRK) method. [182] In particular, all the CAs were evaluated by posing liquid droplets with a valume ranging from 6 to 9 µl on the surface.

3.4.4.4.Thermogravimetric (TGA) analysis

TGA analysis of WSN samples was carried out to assess the degree of functionalization and efficiency of silanization as well as the amount of enzyme loaded onto the nanoparticles. 10 mg of sample was analysed in a TA Instrument simultaneous thermoanalyser SDT Q600 within the temperature range of 25 °C to 1000 °C with a heating rate of 10 °C/min. The organic content in bare WSNs and functionalized WSNs was evaluated following equation 1, where W_1 and W_2 are the sample weight at 200 °C and 1000 °C respectively.

$$\text{Organic content } (\%) = \frac{W1-W2}{W1} \times 100 \quad (1)$$

3.4.4.5. Fourier-Transform Infrared (FTIR) Spectroscopy

Fourier transform infrared (FT-IR) spectroscopy was performed with a Nexus FT-IR spectrometer equipped with a DTGS KBr (deuterated triglycine sulfate with potassium bromide windows) detector. Samples were prepared by pelleting in KBr

and the spectra were recorded in the range 4000 - 400 cm^{-1} at a spectral resolution of 2 cm^{-1}. The spectrum of each sample was corrected by subtracting of the spectrum of blank KBr. Curve fitting of the amide I band of L-WSN5 and LWSN5-w was performed by GRAMS/32 (Galactic Industries Corporation, Salem, NH, U.S.A.) as a linear combination of Gaussian components. The number and position of components were taken from the second derivative spectrum. Second derivative spectra were obtained following the Savitsky–Golay method (3rd-grade polynomial, five points of smoothing). Initial values of bandwidths and intensities were automatically generated.

3.4.4.6. ^{29}Si Nuclear Magnetic Resonance

The cross-polarization (CP) magic-angle spinning (MAS) NMR spectra of starting material WSNs and functionalized WSNs (WSN10) were recorded using a 7 mm CP MAS probe on a Bruker Avance III 400 NMR spectrometer equipped with a wide-bore 9.4 T magnet, corresponding to 1H and ^{29}Si Larmor frequencies of 400.2 and 79.5 MHz, respectively. A detailed description of the procedure can me found in the experimental section of the work by Stojanovic et al.[183]

3.4.5. Lipase immobilization onto WSN

The whole procedure from WSNs hydrophobization to lipase adsorption is schematically shown in **Figure 2**. Lipase was physically immobilized onto bare WSNs and hydrophobic WSNs from a ternary oil-water-enzyme medium and a binary water-enzyme solution (the latter only for sample WSN5). In detail, 25 mg of the enzyme were dissolved in 25 mL of distilled water under magnetic stirring for 30 min. 200 μL of n-hexane was added dropwise to the water-enzyme solution. No phase separation was observed after the addition of hexane. Subsequently, 50 mg of nanoparticles were added to the adsorption mixture and then diluted with 12.5 mL distilled water to improve the nanoparticle dispersion. The system was kept under stirring for 24 h as previously determined by Califano et al. to immobilize β-glucosidase enzyme on WSNs.[101] The supported biocatalysts were recovered by

centrifugation and washed twice with distilled water to remove the non-adsorbed enzymes. The samples obtained after lipase immobilization were named L-WSN, L-WSN1, L-WSN5, L-WSN10 based on the type of wrinkled silica supports used L-WSN5-w was immobilized in distilled water without the addition of n-hexane. The enzyme immobilization in each sample was determined by TGA analysis by subtracting the organic content of each support from the one of the corresponding biocatalysts. The yield of immobilization (YI %) was calculated as the weight ratio between the adsorbed enzyme and the amount dissolved in the adsorption mixture. The enzyme conformation on the nanoparticle surface was investigated by FTIR spectroscopy.

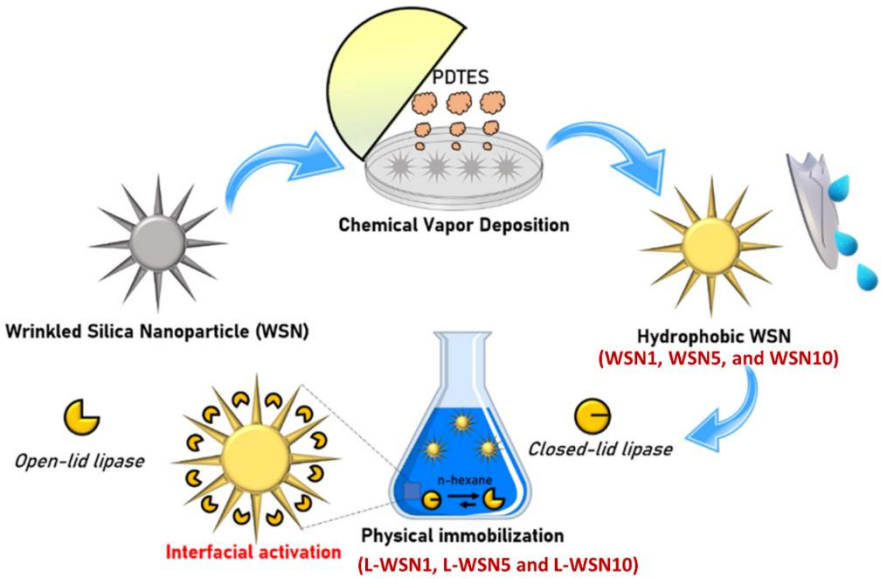

Figure 2. Graphical sketch of the overall experimental route for production of supported biocatalysts.

3.4.6. Catalytic Assay

3.4.6.1. Hydrolysis of sunflower seed oil

Free and supported lipase were tested for room temperature hydrolysis of triglycerides into free fatty acids and glycerol. Typically, 500 µL of Span® 80 was mixed with 10 mL of SOHO sunflower oil (source of vegetable triglycerides) in a 25

mL conic flask. For the free enzyme, 2 mL of a lipase aqueous solution of three different concentrations, 0.4, 0.56, and 0.8 mg/mL were added dropwise to the mixture under stirring to obtain a white water-in-oil emulsion. The amount of water was chosen to ensure an oil-to-water 1:10 molar ratio. After 48 hr, the reaction mixture was transferred to a separating funnel and 50 mL of n-hexane was added to it for extraction of glycerol (bottom) and oil phase (top). Finally, the resulting glycerol was recovered by centrifugation and dried overnight in an oven at 80°C. The yield of the reaction (YR%) was determined as per equation 2. Where, $n_{glycerol}$ and $n_{triglycerides}$ refer to the moles of product and substrate, respectively.

$$YR(\%) = (n_{glycerol}/n_{triglycerides}) \cdot 100 \quad (2)$$

For the immobilized enzyme, only 0.56 mg/mL lipase concentration was tested. Prior to the extraction of glycerol, the biocatalyst was recovered by centrifugation. The chemical nature of the reaction product (e.g. glycerol) was evaluated through FTIR spectroscopy in the attenuated total reflection (ATR) mode by using DuraSam-plIR II accessory equipped with ZnSe Crystal.

3.4.6.2. Operational Stability

The immobilized biocatalyst was subjected to seven consecutive catalytic cycles (each 48h) for evaluation of its reusability. Each reaction was carried out under standard assay conditions. After each cycle, the solution was centrifuged to recover the catalyst and the supernatant underwent the same experimental route to determine the amount of glycerol produced. The yield after the first cycle of the reaction was used as the reference (e.g. 100% conversion).

3.4.6.3. Transesterification of sunflower seed oil

Free and supported lipase were tested as biocatalyst for the transesterification between ethanol and SOHO sunflower seed oil into esters of fatty acids and glycerol. For both free and immobilized lipase, the enzyme concentration was maintained at 0.56 mg/mL. 9.2 g (10 mL) of sunflower seed oil were mixed with 500 μL of Span80 surfactant and 2 mL of ethanol was used for the reaction. To minimize ethanol

inhibition of lipase, the ethanol addition was partitioned in a three-step batch ethanolysis. In particular, a third of the overall ethanol volume (about 700 μL) was added dropwise to the oil-surfactant mixture under stirring. Subsequently, the chosen amount of enzyme was dispersed into the reaction mixture. The remaining ethanol volume was added in two equal aliquots after three and six hours, respectively. The reaction was carried out for 48h at room temperature. The yield of the reaction was determined as previously reported for the hydrolysis reaction.

3.5. Results and discussion

Considering the high available surface area and easy dispersibility wrinkled silica nanoparticles were considered as the support and were synthesized by the method reported earlier [105]. However, it is well known that immobilization of lipase is favoured by the hydrophobicity of the surface.[165] Therefore, WSNs were functionalized by CVD using PDTES as a precursor. To evaluate the effect of functionalization on properties of WSNs, different concentration (1, 5 and 10%) of PDTES was used during CVD.

3.5.1. Scanning electron microscopy (SEM) analysis

Analysis of pristine WSN sample under SEM revealed the formation of spherical nanoparticles with a highly porous structure (**Figure 3a**). The average diameter of WSNs was found to be 300 nm with a uniform distribution. No dimensional and geometric differences are noted between the samples WSN, WSN1, and WSN5 (**Figure 3a-c**). However, in the case of WSN10, the presence of small pseudospherical clusters was observed (**Figure 3d**).

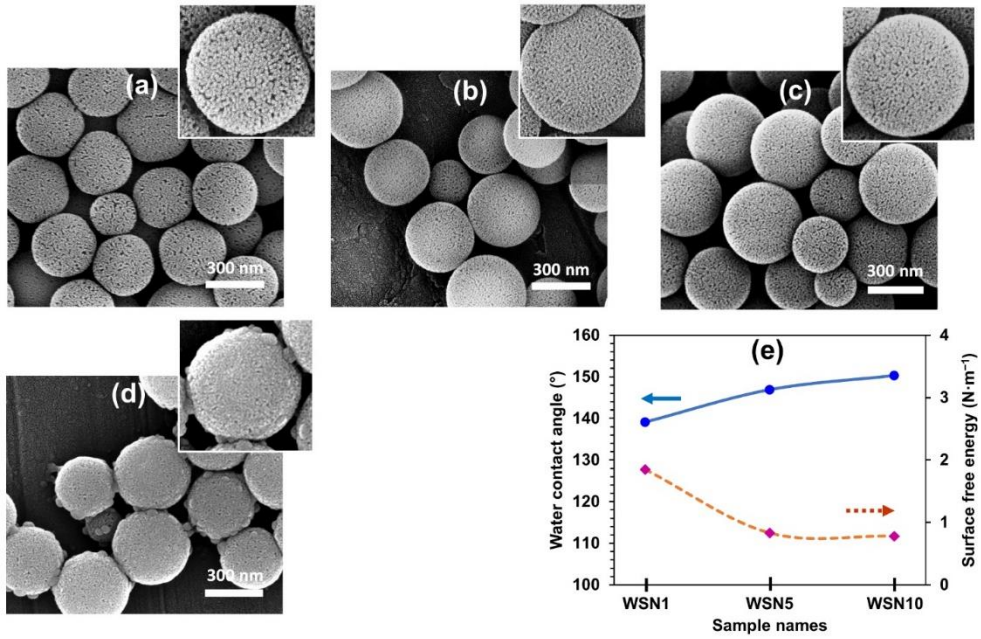

Figure 3. SEM images of (a) **WSN**, (b) **WSN1**, (c) **WSN5**, (d) **WSN10,** and (e) figure showing the contact angle (CA) and surface free energy (SFE) of pristine and functionalized WSNs.

3.5.2. Hydrophobic properties of functionalized WSNs.

As a measure of successful functionalization, contact angle (CA), contact angle hysteresis (CAH), and roll-off angle were measured after uniformly depositing WSNs on a circular glass slide of 12 mm in diameter. According to the CA (θ), a surface can be classified as super hydrophilic when θ≈ 0° (using water as the liquid). When, θ < 90° the surface is hydrophilic and surface is hydrophobic at θ > 90°. [184,185] CA of functionalized WSNs indicate their excellent hydrophobicity (Figure 3e). In particular, both WSN5 and WSN10 can be considered as super-hydrophobic (**Figure 3e** and **Table S1**). Notably, CAH and roll-off angles attain very low values (**Table S1**), which explains the hierarchical surface texture formed due to the nanometric roughness present on the surface of the WSNs. The hydrophobicity obtained during this study (**Table S1**) highlights the efficiency of the CVD treatment.

The surface free energy (SFE) of WSNs was also measured to eliminate the effect of liquids used for measurement on CA. The determination of SFE in necessary to achieve a complete comprehension of the wettability properties of surfaces. In particular, the Owens, Wendt, Rabel, and Kaelble (OWRK) model equation can be applied for the estimation of SFE and its components (e.g. dispersive and polar). [184,186–188] The values of SFE were evaluated by the OWRK method and are listed in Table S2. The values of these three parameters obtained in the case of functionalized WSNs are much lower than the reported values obtained following the same procedure. [189,190] A low affinity with polar substances results in low values for the polar term of surface free energy, which is beneficial since lipase adsorption is boosted by hydrophobic surfaces as functionalized WSN. A high degree of hydrophobicity after functionalization of WSN (e.g. WSN1, WSN5, and WSN10) makes these supports suitable for lipase immobilization via interfacial adsorption, because of the well-known interaction between the open conformation of the enzyme with hydrophobic surfaces. It is reported that the immobilization of lipases on hydrophobic matrices with extended porous structure usually results in an enhancement of the activity of lipases. [168,172,191] Adsorption is based on physical interactions between the enzyme and the silica nanostructure, such as van der Waals forces, and ionic interactions.

3.5.3. N_2 adsorption-desorption measurements

The specific surface area of the synthesized WSNs was calculated from the low-pressure range (0.07 to 0.30 of p/p_0) of the N_2 sorption isotherm (**Figure 4a**). The pore size distribution was evaluated from the adsorption part of the isotherm (**Figure 4b**). The adsorption-desorption isotherm shows the WSN samples have type IV pore structure with a small H3 hysteresis starting from $p/p_0 = 0.9$, which is ascribed to a presence of mesoporous structure with open ends slit shape,[104] but from the BJH analysis (**Figure 4b**), micropore is the dominated pore structure. The BET surface area and total pore volume of the four samples are displayed in **Figure 4c**. **Figure**

4c shows a non-monotonous profile, with WSN5 showing the maximum surface area and pore volume.

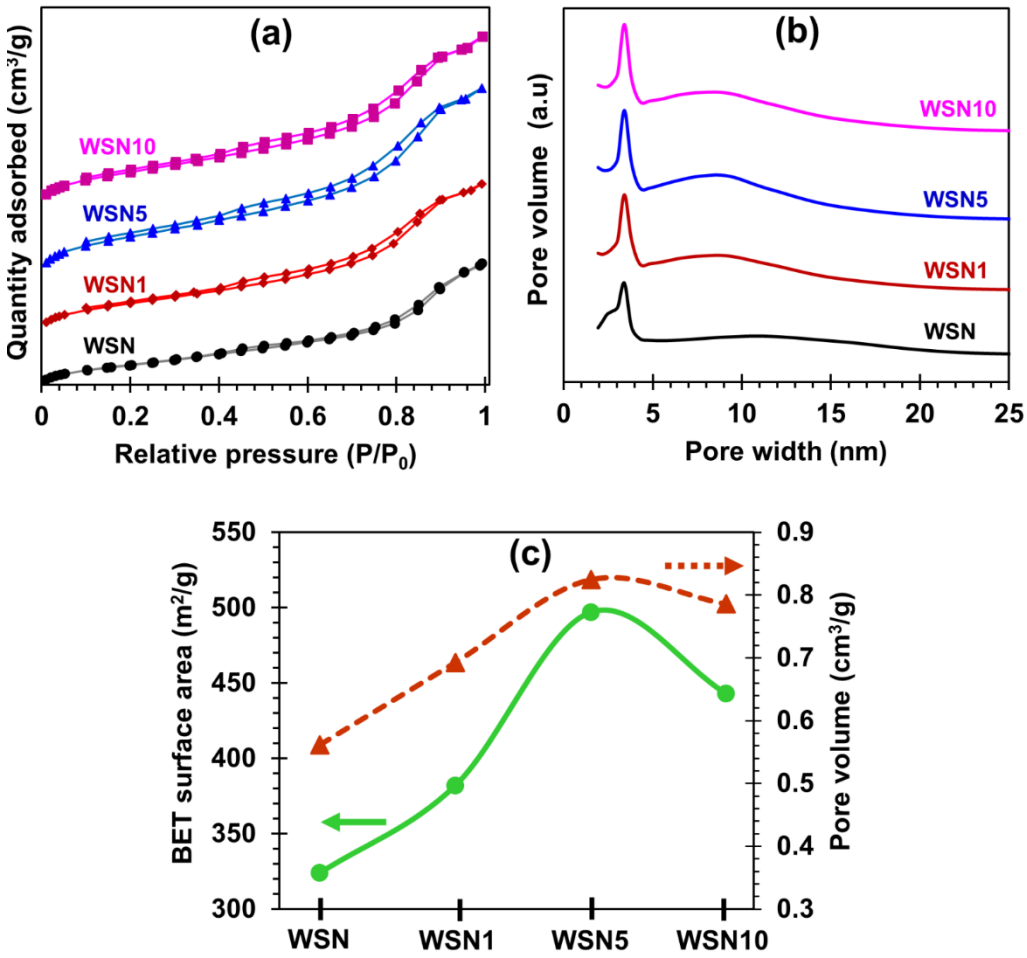

Figure 4. (a) N_2 adsorption–desorption isotherm and the sorption of all curves starts from 0 cm^3/g at $p/p_0=0$. (b) pore size distribution, and (c) change in surface area and pore volume with hydrophobic functionalization of WSNs.

Figure 4b shows that all samples have a narrow pore size distribution centred at 3.5 nm, and a broad peak around 10 nm corresponding to the average inter-wrinkles distance. The peak at 3.5 nm indicates that the wrinkles are mesoporous and the average inter-wrinkled distance decreases from 10 nm to 8.5 nm going from the

WSN sample to WNS1. However, further functionalization does not lead to any change in inter-wrinkle distance. This means that a part of the PDTES is deposited on the outer surface of the particles,[192] and the deposition increases with increase in concentration of PDTES solution during CVD. Concentrations ≥1%, all the excess goes to the external surface. The anchoring of PDTES onto the surface of WSNs might be responsible of the enhancement of surface area as long as the space between the silane groups and the surface is sufficiently wide to adsorbe N_2 molecules.[193] Post synthetic functionalization of mesoporous silica mainly results in the modification of the outer particle surface and near the pore entrances since these sites are easily accessible.[194] This is the possible reason for the increase in the surface area up to a PDTES concentration of 5%. The decrease in the surface area of WNS10 is due to the blocking of some pores, which is clearly visible in the SEM image (**Figure 3d**). The hydrophobization process does not influence the size of the smallest pores, so it can be said that those pores remain empty.

3.5.4. NMR spectra of non-functionalized and functionalized WSN

The functionalization of WSNs with PDTES is shown in **Figure 5a**. To confirm the reaction between siloxane groups of WSNs and PDTES solid-state ^{29}Si NMR analysis of pristine WSNs and WSN10 was performed (**Figure 5b**). For both samples, broad ^{29}Si MAS NMR resonances at -92, -101, and -110 ppm were attributed to the Q_2, Q_3, and Q_4 silica species, with the Q_2- and Q_3-groups localized at the surface.[195] While only the Q_n groups are visible in the WSN starting material, additional resonances were observed at -58 and -67 ppm in the case of WSN10. They are assigned to the T_3 and T_2 groups, respectively, which originate from silica atoms in PDTES.[196] A barely visible shoulder at ~ -53 ppm could be due to a low proportion of T_1 groups. Successful grafting of PDTES to WSNs is accompanied by the increase in relative signal intensity of Q_4 and the simultaneous decrease of the Q_2 resonance (**Figure 5b**). Both observations are consistent with the functionalization of WSNs with PDTES.[196]

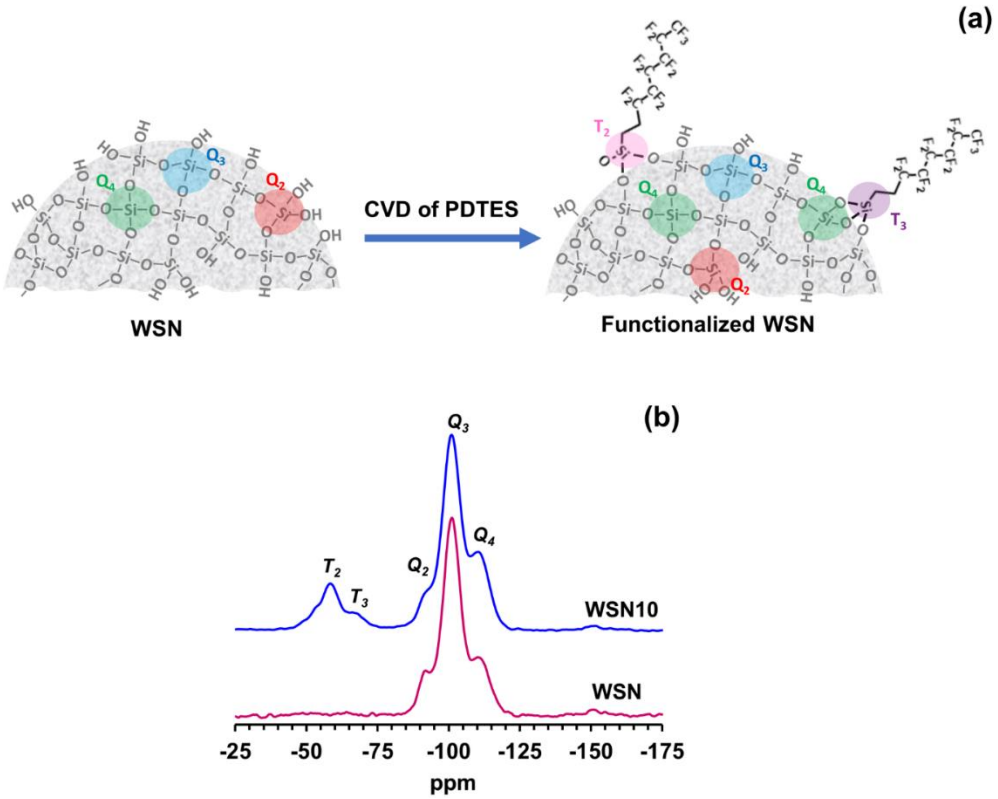

Figure 5. (a) Simplified schematic representation showing grafting of PDTES on the WSNs during the CVD process. (b) ^{29}Si CP MAS NMR spectra of unfunctionalized WSNs and after hydrophobic functionalization of silica nanoparticles (WSN10).

3.5.5. Lipase adsorption

A lipase adsorption experiment was carried out using water-lipase-n-hexane ternary system for all prepared WSN supports. For the WSN5, which is the most promising due to its highest surface area, adsorption was also carried out from a binary system consisting of lipase and water only. Lipase content, lipase loading per gram of support, and adsorption efficiency were determined from the TGA thermogram. The amount of enzyme adsorbed initially decreases (WSN1) due to the decrease in the average pore size, then increases to reach the maximum for WSN5 (**Figure 6a**). This can be attributed to the increase in the specific surface area and hydrophobicity. Adsorption from water alone on the WSN5 support shows a lower uptake (68 vs. 80

mg/g of support) (**Table S3**). In the case of WSN10**,** a decrease in lipase adsorption can be due to blockage of pore entrance during functionalization, which can be seen in the SEM image of WSN10 (**Figure 3d**).

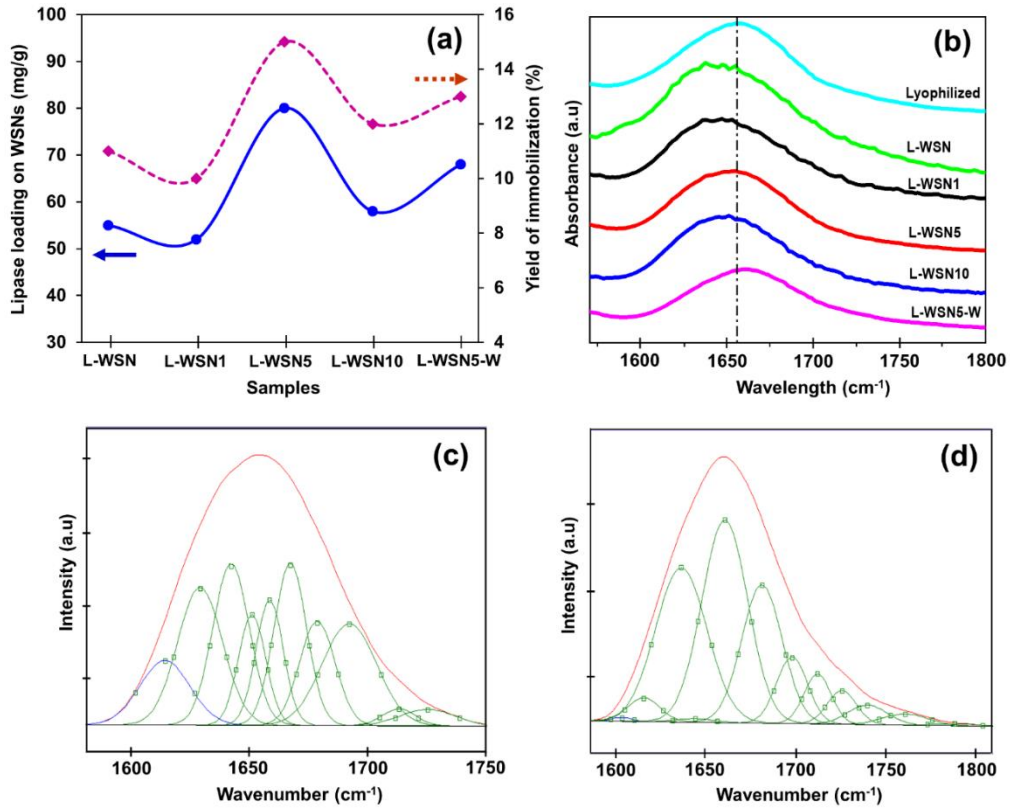

Figure 6. (a) Lipase loading (mg/g) and yield of immobilization (%) for all the supported biocatalysts. FT-IR spectra with (b) focus on amide I region of lyophilized lipase, lipase adsorbed on WSNs, WSN1-10 from water/hexane, and adsorbed on WSN5 from water. (c) Experimental and calculated curves with best fits by Gaussian components of amide I band from L-WSN5 and from (d) L-WSN5-w.

One of the main objectives of a well-designed immobilization process is to keep the secondary structure of the enzyme unaltered and to maintain the activity of lipase. It is worth mentioning here that during the immobilization, the enzyme can experience relevant changes in the conformation due to the interaction with the support or crowding effect, when enzyme molecules are forced into a small space.[197] To observe

such conformational changes in lipase, FTIR spectroscopy was applied.[198–200] Quantitative information on the secondary-structure of the lipase was obtained by analysing the amide I absorption band in the range of 1600–1700 cm^{-1}. This band is generated by the C=O stretching vibration of the peptide group and is very sensitive to the molecular geometry, hydrogen bonding pattern, and dipole interactions along the secondary structures. The amide I band originates from the overlapping of several peaks associated to different structural elements such as α-helices, β-sheets, turns, and irregular structures. These secondary structures can be obtained by deconvolution of the amide I band into Gaussian components through curve fitting.[201]

Table 1. Peak attribution of Amide I band for L-WSN5 and L-WSN5-w.

Peak position L-WSN5 [cm^{-1}]	Peak position L-WSN5-w [cm^{-1}]	Attribution
1614.1 ± 3.9	1616.1 ± 2.6	Aggregates
1629.1 ± 3.7	1628.6 ± 10.7	B-sheets
1642.4 ± 2.5		α-
	1638.5 ± 4.1	helices/unordered
1651.3 ± 8.6	1649.7 ± 1.2	α-helices
1658.8 ± 4.1	1659.4 ± 9.8	α-helices
1667.7 ± 5.1	1670.6 ± 5.0	β-turns
1679.2 ± 11.9	1683.1 ± 6.7	Aggregates
1693.8 ± 13.6	1693.1 ± 2.8	β-sheets/turns

Figure 6b shows the FTIR spectra (range of 1550-1850 cm^{-1}) of all samples with immobilized lipase on WSNs and lyophilized lipase. All adsorbed lipase from the ternary system lipase-water-hexane shows a shift of the amide I band toward lower wavenumber, possibly due to aggregation.[175,202] The shift is minimum in the case of L-WSN5 (**Figure 6b, Table S4**). Lipase adsorbed from a water solution (L-WSN5-w) shows a shift of the amide I band toward higher wavenumbers. It can be assumed that in cases with only a small shift of the amide I band compared to the FT-IR spectrum of the native enzyme, a comparatively similar secondary structure of the bound enzyme should be present. FT-IR analysis pointed out that L-WSN5 is the biocatalyst in which the secondary structure of the protein is best preserved and the amount of uptake lipase is the highest. L-WSN5 and L-WSN5-w were then selected for subsequent studies. The amide I band fitting procedure described in the experimental section was applied to L-WSN5 and L-WSN5-w spectra. **Figure 6c, d** displays the experimental and calculated curves with best Gaussian fit components. The position and the assignment of the Gaussian components of the amide I band are summarized in **Table 1**. [203,204] The amount of the different secondary structures were estimated by the area underneath each Gaussian band/the total area of the peaks between 1600 and 1700 cm^{-1} (**Table 2**). In both cases, except for a certain degree of aggregation, the secondary structure of the polypeptide seems quite preserved. A slight decrease of α-helix content and a slight increase in random-coil (unordered) structures in L-WSN5-w indicates a higher degree of unfolding compared to L-WSN5. On the other hand, hydrogen-bonded aggregates are higher in the case of L-WSN5. The increase in the β-turn content in L-WSN5-w also indicates a change in the secondary structure.[205]

Table 2. Secondary structure elements of L-WSN5 and LWSN5-w, compared to a literature case. *[198,206]

Secondary structure elements	L-WSN5 [%]	L-WSN5-w [%]	Literature* [%]
Aggregates	19.1	12.9	5
β-sheets	24.7	25.2	26
α-helices	25.8	19.7	33
β-turns	22.2	29.6	27
Unordered	8.0	10.0	9

3.5.6. Catalytic assays

Three different free lipase concentrations (0.40, 0.56, and 0.80 mg/mL) were used for the hydrolysis of sunflower seed oil to evaluate the minimum amount of enzyme needed to achieve the maximum conversion at a fixed substrate concentration. To assess that triglycerides were converted after 48h, the ATR spectrum of the product was collected (**Figure S2**). The comparison with a reference spectrum confirmed that glycerol was produced.[207] 0.40 mg/mL concentration led to 56% conversion of the substrate after 48 h (**Figure 7a**), while the yield of the reaction was enhanced to 76% by increasing the lipase concentration to 0.56 mg/mL. No significant improvement of the substrate conversion was detected with a further increase in the enzyme concentration to 0.80 mg/mL.

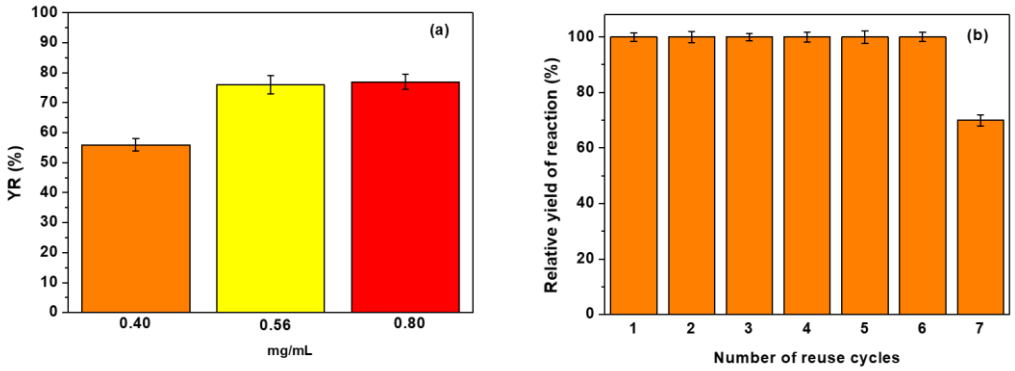

Figure 7. (a) Yield of reaction for different enzyme concentrations. (b) The relative yield of reaction histograms over the number of cycles of reaction.

Thus, 0.56 mg/mL was identified as the enzyme amount needed to reach the regime conversion of 76%. This result led us to study the catalytic activity of supported catalysts keeping the lipase concentration in the reaction solution at 0.56 mg/mL. Only L-WSN5 and L-WSN5-w were subjected to a catalytic reaction. Interestingly, L-WSN5 achieved 87% conversion within 48 h. This is similar to what was reported in the literature for immobilized lipase for esterification of oleic acid with methanol.[162] Nevertheless, the transesterification of raw material, natural oils, is much more complex than the esterification of a simple fatty acid. The first difficulty originates from the heterogeneous chemical composition of natural oils.[150] Indeed, they are composed of triglycerides whose structure contains a number of fatty acids. Furthermore, since transesterification is a three-step reaction, significant conversion rates are achievable only if the enzymes exhibit activity also towards diglycerides and monoglycerides formed as reaction intermediate.[208] The results of the hydrolysis highlight inactive-to-active conformational changes of lipase when adsorbed at a hydrophobic/hydrophilic interface. Therefore, the physical interaction with silanized WSNs was found to be a successful method of immobilization and activation of lipase to achieve the high activity. This result is not surprising, since lipase immobilized on hydrophobized silica particles often showed hyperactivation.[163,209,210] However, L-WSN5-w was only able to achieve only 45% conversion at the same experimental condition. The lower hydrolytic activity is due to a change in the secondary structure of lipase during immobilization from water, which is also in agreement with FTIR analysis. However, the secondary structure modification in L-WSN5-w is small and would not alone justify such a reduction in hydrolysis yield. Another contribution can be due to the higher concentration of lipase molecules immobilized in closed form with respect to L-WSN5 (for the lower concentration in solution) and inhibition of the interfacial activation caused by the interaction with

the support. This result confirms the key role played by the oil phase in the immobilization phase, even if it is present in very small amounts. Transesterification tests were carried out for free enzyme and L-WSN5. The free enzyme was able to produce 600 mg of glycerol from 9.2 g of sunflower oil, corresponding to a yield of reaction equal to 56%. The yield of the transesterification reaction was in this case lower than that of the hydrolysis reaction. The possible reason is the well-known inhibitory effect of short chain alcohols such as methanol and ethanol on lipase activity.[211,212] L-WSN5 was able to produce 1 g glycerol, corresponding to a YR (%) of 93%. In this case, the yield of transesterification was higher than the yield of hydrolysis. This is probably due to the different partitioning of ethanol between the surfactant/oil solution and the microenvironment of the immobilized lipase.[213] The immobilized lipase can be exposed to a lower concentration of ethanol with respect to the bulk oil phase, due to the low affinity of the hydrophobized WSNs with polar short-chain alcohols. Moreover, the hydrophobic WSNs are probably better dispersed in the non-polar oil phase than in presence of excess water, as in the hydrolysis environment. Finally, these results confirm the hyperactivation of lipase. The results of catalytic assays for both hydrolysis and transesterification reactions are summarized in **Table 3**.

Table 3. Yield of reaction (YR %) for hydrolysis and transesterification reported for free lipase**,** L-WSN5 and L-WSN5-w biocatalysts.

Sample	Hydrolysis YR [%]	Transesterification YR [%]
Free lipase	76	56
L-WSN5	87	93
L-WSN5-w	45	/

Operational stability tests were carried out using **L-WSN5** to assess the reusability of the supported biocatalysts. From **Figure 7b** it can be seen that the catalyst maintains its activity for the hydrolysis of triglycerides up to 6th cycle. Reusability tests performed on lipase immobilized on unfunctionalized WSNs showed a gradual decrease of activity with increasing recycling time, ascribed to the leaching of immobilized lipase during successive hydrolysis reactions. On the other hand, lipase immobilized on hydrophobic supports often shows optimal recycling.[209] Indeed, the higher the hydrophobicity of the surface, the stronger is the lipase-support affinity. So, desorption from a hydrophilic matrix is easier if compared to the case of a hydrophobic support.[214] In the seventh cycle, a decrease in conversion to 70% was obtained, which can be attributed to a detectable loss of catalyst after repeated recovery operations. For this reason, any further measurements were considered unreliable.

3.6. Conclusions

In this work, lipase was immobilized by adsorption on hydrophobic WSNs. WSNs were hydrophobized using perfluorodecyltriethoxysilane (PDTES) in different amounts. The adsorption was carried out from a micro-oily environment (water-n-hexane). WSN1, WSN5 and WSN10, showed excellent hydrophobicity. The obtained results made these substrates suitable candidates for lipase immobilization via interfacial adsorption, allowing preferentially lipase immobilization on the support in the open conformation. The analysis of amide I band of the FTIR spectra pointed out that the native conformation of lipase was better preserved in the biocatalyst LWSN5. This result highlighted an important role played by n-hexane in the water/lipase solution used for lipase adsorption, favoring loading and stabilizing the native conformation. The best biocatalyst obtained (LWSN5) was tested in both the hydrolysis and transesterification of triglycerides and compared to free lipase. The yields of hydrolysis was 87% for supported lipase, compared to a yield of 76% for free lipase. Similarly, the transesterification yield achieved by L-WSN5 **(**93%) was higher than free lipase (56%). Finally, recycling study carried out using 7

consecutive cycles demonstrated the easy recoverability of the immobilized biocatalyst system and its practical application potential.

3.7. Supplementary materials

S1. Hydrophobic properties of functionalized WSNs

Table S1. Contact Angle (CA), contact angle hysteresis (CAH) and roll-off angle for the wrinkled silica nanoparticle (WSN) systems treated with ethanol solution of a hydrophobizing agent at three different volume concentration 1, 5 and 10 vol% (e.g. WSN1, WSN5 and WSN10).

Sample	CA (water) [°]	CA (CH_2I_2) [°]	Roll-off Angle [°]	Advancing Angle [°]	Receding Angle [°]	CAH [°]
WSN10	150.3 ± 1.6	138.7 ± 1.2	6.4 ± 0.14	160.3 ± 2.0	146.7 ± 0.8	13.7 ± 2.0
WSN5	146.9 ± 0.4	138 ± 0.9	4.8 ± 0.08	160.3 ± 1.2	146.7 ± 1.4	13.9 ± 1.2
WSN1	139.1 ± 1.2	128.1 ± 3.0	36 ± 0.97	*Not detectable (N.D.)**	*N.D.*	*N.D.*

* N.D. = roll-off angle is higher than the plate tilting angle

Table S2. Surface free energy (SFE), dispersive component of SFE and polar component of SFE for the wrinkled silica nanoparticle (WSN) systems treated

with ethanol solution of a hydrophobizing agent at three different volume concentration 1, 5 and 10 vol% (e.g. WSN1, WSN5 and WSN10).

Sample	Surface free energy [$N \cdot m^{-1}$]	Dispersive component of SFE [$N \cdot m^{-1}$]	Polar component of SFE [$N \cdot m^{-1}$]
WSN10	0.78 ± *Non detectable (N.D.)*	0.77 ± *N.D.*	0.01 ± *N.D.*
WSN5	0.83 ± *N.D.*	0.75 ± *N.D.*	0.07 ± *N.D.*
WSN1	1.85 ± *N.D.*	1.67 ± *N.D.*	0.18 ± *N.D.*

S2. Lipase adsorption

Table S3. Enzyme weight (%), enzyme (mg) per gram of support, yield of immobilization (%) for all the supported biocatalysts.

	Enzyme [wt %]	Enzyme/g of support [mg/g]	Yield of immobilization [%]
LipaseWSN	5.2	55	11
LipaseWSN1	4.9	52	10
LipaseWSN5	7.4	80	15
LipaseWSN10	5.0	58	12
LipaseWSN5-water	6.0	68	13

Table S4. FTIR peak position of the amide I band for all adsorbed lipase, compared with that of lyophilized lipase. The exact position of the peak was taken with the find-peak function of Origin Pro software.

	Peak position [cm^{-1}]
Lyophilized lipase	1658.4
LipaseWSN	1645.0
LipaseWSN1	1645.0
LipaseWSN5	1654.7
LipaseWSN10	1650.8
LipaseWSN5-water	1660.4

S.3 Catalytic assays

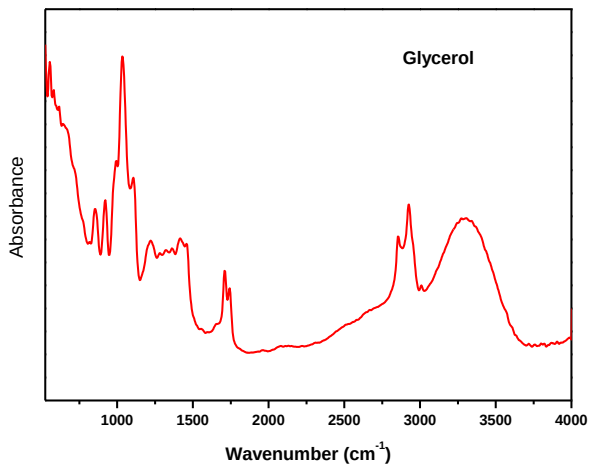

Figure S1. ATR spectrum of Glycerol produced by transesterification and hydrolysis reactions.

4. Deciphering the immobilization of lipases on hydrophobic Wrinkled Silica Nanoparticles

Giulio Pota[1], Daniel Andrés-Sanz[2], Marta Gallego[2], Giuseppe Vitiello[1,3], Fernando López-Gallego[2,4*], Aniello Costantini[1*], Valeria Califano[5].

[1] Department of Chemical, Materials and Production Engineering, University of Naples Federico II, Piazzale Tecchio 80, 80125 Fuorigrotta, Naples, Italy.

[2] Center for Cooperative Research in Biomaterials (CIC biomaGUNE), Basque Research and Technology Alliance (BRTA), 20014 Donostia-SanSebastián, Spain

[3] CSGI, Center for Colloid and Surface Science, Sesto Fiorentino (FI), Italy.

[4] IKERBASQUE, Basque Foundation for Science, 48013 Bilbao, Spain

[5] Institute of Science and Technology for Sustainable Energy and Mobility (STEMS), National Research Council of Italy (CNR), Viale Marconi 4, 80125 Naples, Italy.

*Corresponding author: anicosta@unina.it, flopez@cicbiomagune.es.

Submitted to International Journal of Biological Macromolecules

4.1. Abstract

In this work, the physical immobilization of two different types of lipases, namely from *Candida antarctica B* (CALB) and *Rhizomucor miehei* (RML), into hydrophobic wrinkled silica nanoparticles (WSNs) is investigated. The carriers are hydrophobized by chemical vapor deposition with perfluorodecyltriethoxysilane (PDTES). Both proteins are homogeneously distributed inside the pore architecture of the nanoparticles, as confirmed by Transmission Electron Microscopy (TEM) and Energy Dispersive X-ray (EDX) measurements. We find that the maximum enzyme load of CALB is 2 times larger than that obtained for RML. Furthermore, Fourier

Transform Infrared Spectroscopy (FTIR) confirms the preservation of the enzyme secondary structure after immobilization for both enzymes. The experimental adsorption isotherms are correctly fitted by the Langmuir model, resulting in a binding constant (K_L) for RML 4.5-fold higher than that for CALB, indicating that the former binds more strongly to the nanoparticles than the latter. Kinetic analysis reveals a positive correlation between enzyme load and RML activity unlike CALB where activity decreases along the enzyme load increases. Immobilization is also able to enhance the thermal stability of both lipases. Finally, the resulting heterogeneous biocatalysts are tested for the hydrolysis of ethyl-3-hydroxybutyrate. The results show that free CALB outperforms RML in this hydrolytic reaction. However, the immobilization had opposite effects on both lipases. Immobilized CALB yielded 20% less 3-HBA than free lipase, while immobilized RML increases 3-fold the 3-HBA yield when compared with the free enzyme. The improved performance of immobilized RML can be explained due to the interfacial hyperactivation undergone by this lipase when immobilized on the superhydrophobic surface of H-WSNs.

4.2. Graphical abstract

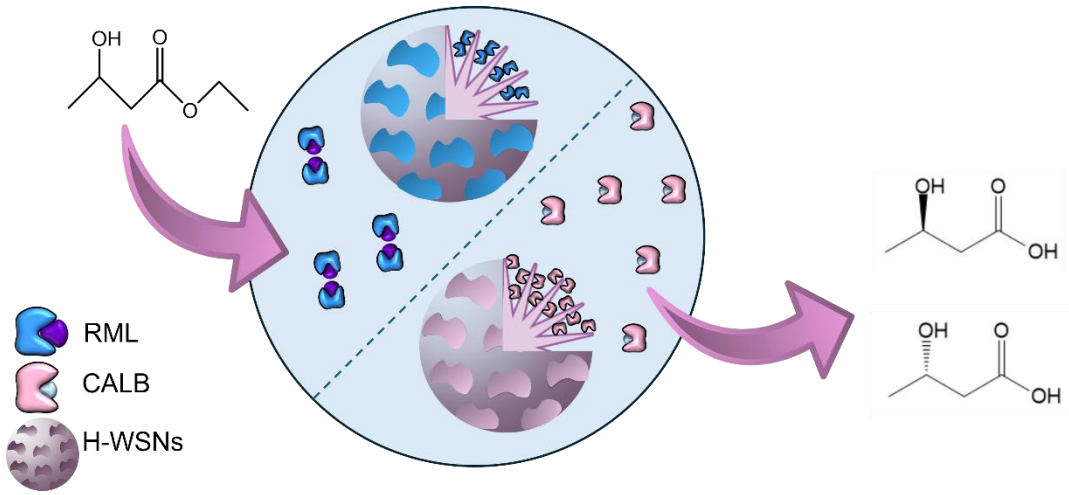

4.3. Introduction

Lipases (E.C. 3.1.1.3, triacylglycerol acyl hydrolases) are one of the most used classes of hydrolases due to the wide range of binding substrates, the extractability from several sources, the high selectivity and the cofactor-less catalysis.[215] As regards this class of hydrolases, they are involved in a plethora of biochemical pathways such as transesterification and hydrolysis of triglycerides to produce biodiesel and free fatty acids, respectively. [216,217] Moreover, pharmaceutical and agrochemical companies employ lipases for the kinetic resolution of racemates.[218] The use of lipase in organic synthesis using organic solvents was a breakthrough in biocatalysts after the pioneering work of Zaks and Kiblanov.[219] Therefore, starting from the late 80's, lipases have been increasingly used as biocatalysts for the synthesis of esters and polyesters as poly-hydroxyalcanoates, paving the way for the production of sustainable and biodegradable polymeric materials.[220,221] Nevertheless, the scale-up of several enzyme processes is undermined by the low thermal and pH stability of biocatalysts, together with the high cost of production and purification. These drawbacks can be overcome by enzyme immobilization.[222–224] This strategy, if rationally conducted, can improve the enzyme stability, ensuring the enzyme reusability and facilitating the reaction downstream process. Although most of immobilization methods exploit porous microparticles as enzyme carriers due to their handiness and loading capacity, nanomaterials are emerging as carriers for enzymes because they offer a trade-off between the activity and stability of the immobilized enzymes, avoiding internal diffusion restrictions and even augmenting enzyme properties[225]. Indeed, nanoscale structures can confer properties to the immobilized biocatalysts that ease their separability and make them work under quasi-homogeneous catalysis conditions.[19,226] In this framework, mesoporous silica nanoparticles (MSNs) stand as suitable supports for enzyme immobilization due to their high thermal and chemical stability, large surface area, tunable pore size, and easy surface functionalization.[227–229] More specifically, wrinkled silica nanoparticles

(WSNs) that are MSNs with central-radial pore structure recently been used as successful carriers for cellulase immobilization. [16,59] Indeed, their conical pore shape allows avoiding pore blocking by the proteins. Moreover, the hierarchical pore architecture is responsible for facile substrate and product diffusion, reducing inhibition and mass transfer limitation phenomena.[27] Chemical modification can be achieved thanks to the high availability of surface silanol (Si-OH) groups which can easily bind silane-based hydrophobic ligands such as dichlorodimethylsilane, resulting in strongly superhydrophobic surfaces.[230] Lately, WSNs were functionalized with perfluorodecyltriethoxysilane (PDTES) through chemical vapor deposition (CVD) to immobilize lipase from *Candida rugosa*.[15] This functionalization technique can operate at low temperatures, limits the solvent damage to the support and is versatile enough to cover a diversity of solid substrates with thin and uniform layers.[231] The protocol resulted in nanocarriers with finely tuned surface hydrophobicity, offering an ideal support for enhancing lipase functionality. Indeed, the active site of lipases is usually covered by a polypeptide chain called lid, which limits substrate accessibility and thus lipase activity in aqueous solutions.[232] In the presence of hydrophobic surfaces, the lid opens and allows the substrate to bind the active site, following the mechanism of interfacial activation.[233–235] However, lid size is different for each lipase and this means different sensitivity to interfacial activation. Sometimes, the enzyme selectivity can be tuned as well by choosing the proper immobilization strategy since support binding is associated with some conformational modifications that can involve the active site.[4,236] In this work, the lipases from *Candida antarctica B* (CALB) and *Rhizomucor miehei* (RML) were physically immobilized on hydrophobic WSNs. The support was functionalized by CVD and the obtained heterogeneous biocatalysts underwent extended physic-chemical characterization. The immobilization kinetic and thermal stability parameters were calculated to ultimately apply these immobilized enzymes for the hydrolysis of ethyl 3-hydroxy butyrate (E3HB),

investigating their catalytic performance and the enantioselectivity in comparison to their soluble counterparts.

4.4. Materials and methods

4.4.1. Materials

Tetraethyl orthosilicate (TEOS), cetyltrimethylammonium bromide (CTAB), urea, cyclohexane, isopropanol (IPA, ACS reagent, anhydrous), ethanol (ACS reagent, anhydrous), hydrochloric acid (37 wt%), perfluorodecyltriethoxysilane (PDTES), *p*-nitrophenyl butyrate (*p*-NPB), bovine serum albumin (BSA), SYPRO© Orange, dimethyl sulfoxide (DMSO), racemic ethyl 3-hydroxy butyrate (E3HB), racemic 3-hydroxy butyric acid (3HBA), and dichloromethane (DCM) were purchased from Sigma-Aldrich (Madrid, Spain). Tris-HCl was acquired from Fisher Bioreagent (Madrid, Spain). Protein concentration was quantified through Bradford assay, using BSA as standard. Bradford dye reagent was bought from BIORAD (Biorad, Hercules, CA, USA). 96-well microplates were purchased from Avantor (2021, VWR International, LLC). Lipase from *Rhizomucor miehei* (RML, M_w=29.59 kDa,[237] 7.5 mg/mL protein concentration) and Lipozyme CALB (lipase B from *C. antarctica*, CALB, M_w=32.27 kDa,[238] 7.75 mg of protein per mL of extract) were kindly donated by the laboratory of Prof. Roberto Fernández-Lafuente (ICP-CSIC, Madrid, Spain).

4.4.2. Synthesis of wrinkled silica nanoparticles (WSNs)

WSNs were produced following a partially modified wet-chemistry sol-gel route described by Moon and Lee [16]. More specifically, cethylpiridinium bromide (CPB) was replaced by less hazardous cethyl trimethylammonium bromide (CTAB) as a surfactant whereas surfactant removal was accomplished through supplementary acid extraction.[239] In detail, 120 mL of a water solution of CTAB (0.01 M) and urea (0.33 M) were mixed with 120 mL of cyclohexane, acting as a non-polar phase. 3.68 mL of IPA were added dropwise to the generated bicontinuous microemulsion, for a final IPA concentration of 3% v/v. The role of the alcohol is to act as a co-solvent to

modulate the distance between the silica nanofibers and properly tune the pore morphology. Silica formation started soon after dropwise addition of 10 mL of TEOS (0.18 M). The system was kept under vigorous stirring for 30' at room temperature. Afterwards, the reaction mixture was heated up to 70°C and left under stirring for 24 h. Fresh nanoparticles were collected by centrifugation and washed three times with ethanol. Subsequently, acid extraction in HCl-ethanol (HCl 1.3 M) was carried out for 24 h to free the mesopores from CTAB. Finally, WSNs were centrifuged and washed three times with ethanol.

4.4.3. Surface hydrophobization of WSNs

WSNs were surface functionalized with PDTES by chemical vapor deposition (CVD) technique to create a proper hydrophobic site for lipase to be surface activated as immobilized. CVD was carried out as previously described by Pota et al.[15] Briefly, 50 mg of WSNs were dispersed in ethanol and settled onto a petri dish by solvent casting. Afterwards, the petri dish coated by the nanoparticles was moved onto a heating plate and placed inside a bigger petri dish. 5 mL of a PDTES 5% v/v solution in ethanol were poured into the outer petri dish and the temperature of the heating plate was risen up to 100°C. The selected concentration value was previously optimized. More specifically, 5% v/v PDTES provides superhydrophobicity without altering the surface morphology of the nanoparticles, as detected for higher concentrations.[15] As the solution began to evaporate, the system was covered by placing a ceramic mortar with an exhaust beak to allow the vapors to completely flow outside. Hydrophobized WSNs (H-WSNs) were finally recovered by scratching away from the petri dish and stored as a fine powder. The process is reported in **Scheme 1.**

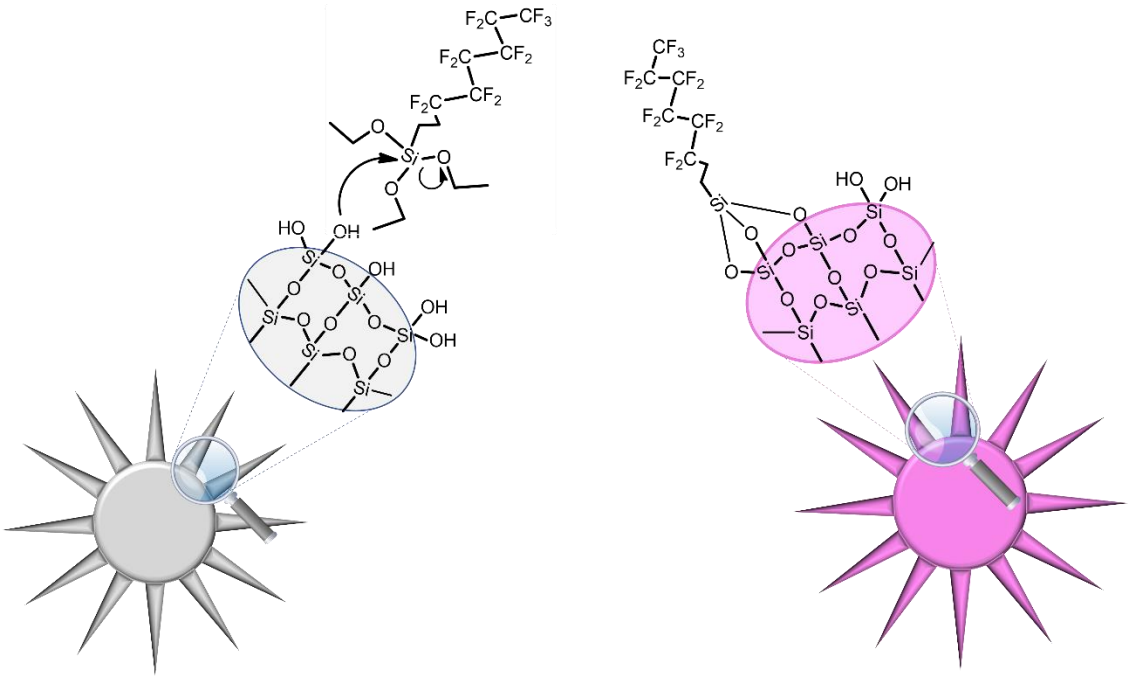

Scheme 1. Graphical sketch describing the attachment of PDTES onto WSNs during CVD process.

4.4.4. Enzyme immobilization

CALB and RML enzymes were physically immobilized into hydrophobized WSNs in sodium phosphate (NaP) buffer (10 mM, pH 7). Briefly, commercial protein stock solutions were diluted with NaP buffer to obtain 1 mL at 1 mg/mL protein concentration. Afterwards, a specific amount of WSNs was dispersed in the enzyme solution. The adsorption mixture was kept under stirring for 24 h. At the end of the immobilization route, supported biocatalysts RML@H-WSNs and CALB@H-WSNs were collected by centrifugation and washed three times with distilled water to remove unbound enzymes. The amount of immobilized protein was assessed through Bradford assay.[240] Different concentrations of nanoparticles were used to perform physical immobilization namely 2, 4, 6 and 10 mg/mL.

4.4.5. Adsorption isotherms study

Adsorption isotherms were built by plotting the protein load at the equilibrium (q_e) over the offered protein per mg of support (C_e). Experimental data were fitted according to the Langmuir function:

$$(1)\ q_e = \frac{q_{max} \cdot C_e}{K_L + C_e}$$

Where q_{max} is the theoretical maximum adsorption capacity (mg/mg of support) whereas K_L is the Langmuir constant (mL/mg of protein). The free energy of immobilization ΔG° (j/mol) is calculated as follows:

$$(2)\ \Delta G^0 = -RTlnK_L$$

where R (j/mol·K) is the universal gas constant and T (K) is the absolute temperature.

4.4.6. Activity measurements

The activity of both free and supported enzymes was measured through *p*-NPB assay. Indeed, lipases catalyze *p*-NPB hydrolysis, leading to *p*-nitrophenol, a yellow product absorbing at 348 nm. This wavelength corresponds to the isosbestic point of *p*-nitrophenol and the molar extinction coefficient ε_{348} is equal to 5150 $M^{-1}cm^{-1}$.[241] In detail, 5 µL of either free or supported enzyme samples were placed in one well of a 96-well microplate. Afterwards, 200 µL of substrate mixture were added to the well and the increase in absorbance was monitored spectrophotometrically employing a Microplate Reader Epoch 2, Agilent (BioTek), CA, USA, for approximately 5 min. The substrate mixture was prepared by dissolving 50 µL of 50 mM *p*-NPB acetonitrile solution in 4.950 mL of sodium-phosphate buffer 50 mM, pH 7. The enzyme activity unit (U), defined as μmol of hydrolyzed substrate per minute, was calculated using Gen 5 software.

4.4.7. Calculation of the parameters of immobilization

The immobilization process was characterized by calculating the following immobilization parameters as done by Santiago-Arcos et al.[242] The protein load is

defined as the mass of immobilized protein (mg) per mg of support. The yield of immobilization Ψ is defined as the percentage of offered protein which is bound to the carrier. It is calculated as mass balance:

$$(3)\ \Psi = \frac{C_O - C_{Sn}}{C_O} \cdot 100$$

where C_0 and C_{Sn} are the concentrations of the protein in the offered solution and in the supernatant, respectively. The theoretical activity of the supported biocatalyst is called immobilized activity *iA*:

$$(4)\ \text{iA}\left(\frac{\text{U}}{\text{mg}}\right) = \text{Offered activity} \cdot \frac{\Psi}{100}$$

The real (measured) activity per mg of carrier of the immobilized protein defines the recovered activity *RA* (U/mg). The relative recovered activity (*rRA*) is defined as the percentage of the theoretical activity retained by the protein after the immobilization:

$$(5)\ \text{rRA}\ (\%) = \frac{\text{RA}}{iA} \cdot 100$$

Finally, the immobilized specific activity *iSA* is obtained normalizing the RA for the actual weight of immobilized protein:

$$(6)\ \text{iSA}\ (\text{U/mg}) = \frac{\text{RA}}{load}$$

4.4.8. Physic-chemical characterization

Functionalized WSNs and supported biocatalysts underwent extended morphological characterization. Transmission electron microscopy (TEM) images were acquired using a JEOL JEM-2100 F (JEOL, Tokyo, Japan) ultra-high resolution microscope at an acceleration voltage of 200 kV. The samples were prepared by placing 3 μL of each sample on a carbon-coated grid and letting it dry before the analysis. Scanning transmission electron microscopy (STEM) analysis was carried out by using a specific high-angle annular dark-field (HAAD) detector in combination with energy dispersive X-ray (EDX) mapping, performed thanks to an Oxford UltimMax EDS detector (Oxford Instruments, Oxon, UK). Size distribution analysis of the

nanostructure was performed using ImageJ software. Fourier transform infrared (FTIR) spectroscopy measurements were carried out using a Nexus FT-IR spectrometer equipped with a DTGS KBr (deuterated triglycine sulfate with potassium bromide windows) detector. The spectra were recorded in 4000-400 cm^{-1} range, with a spectral resolution of 2 cm^{-1}. The powders of dry samples were mixed with KBr (0.5 wt.% sample), accurately ground and pressed into pellets (13 mm in diameter). The spectrum of KBr was used as blank.

4.4.9. Thermal stability analysis

Thermal stability analysis was carried out by incubating both free and supporting biocatalysts at a specific temperature before performing *p*-NPB assay. 30, 40, 50, 60, 70 and 80°C were selected as incubation temperatures. Results were reported as residual activity (%) that is activity measured after incubation over activity at 30°C, in percentage value.

4.4.10. Hydrolysis of racemic E3HB

Free and supported proteins were dispersed in E3HB 200 mM solution in Tris-HCl buffer (pH 7, 10 mM), for a total protein concentration of 60 μg/ mL. The system was kept under stirring for 24h. Immobilized enzymes were separated from the reaction mixture by centrifugation. The amount of produced 3HBA was estimated through Gas Chromatography (GC).

4.4.11. GC analyses

The hydrolysis reaction products were diluted 1:4 v/v with Tris-HCl buffer and analyzed after a derivatization protocol previously described.[243] More specifically, 30 μL of the samples were acidified with 1.5 μL of HCl 6M before extraction with 150 μL of ethyl acetate. 40 μL of the extract, settling at the top of the generated biphasic mixture, were added to 80 μL of a 1:1 v/v mixture of ethyl acetate/N-Methyl-N-tert-butyldimethylsilyltrifluoroacetamide (MTBSTFA) for 1h at 25°C. Finally, GC analysis was performed after drying the samples with $MgSO_4$. The

separation of compounds involved a temperature ramp sequence: initially, the temperature was held at 80 °C for 2.5 minutes and then increased progressively to 225 °C at a rate of 30 °C min^{-1}. Subsequently, it was maintained at this temperature for 7 minutes before a further increase to 300 ºC at a rate of 50 °C min^{-1}, and finally, this temperature was sustained for 0.5 minutes. An internal standard of 2 mM eicosane was added to all samples. The retention time for 3-HBA was determined to be 6.6 minutes. Enantioselectivity assessments followed a similar protocol but utilized 500 µL of the reaction sample and 3 x 500 µL of ethyl acetate for liquid-liquid extraction after acidification with 6 M HCl. The organic phase was concentrated through evaporation in a Speed Vac and then derivatized as previously outlined. Derivatized samples underwent analysis by GC-FID using an Agilent (Agilent, CA, USA) 8890 System with a Beta DEXTM 120 Capillary Column (30 m x 0.25 mm x 0.25 µm), and helium served as the carrier gas. The injector and FID detector temperatures were set at 280 °C and 300°C, respectively. The initial temperature (80 °C) was gradually increased to 150 °C at a rate of 2 °C min^{-1}, held for 5 minutes, and subsequently elevated to 200 ºC at a rate of 20 °C min^{-1}. The oven temperature was maintained at 200 ºC for 2 minutes. Retention times for (R)-3-HBA and (S)-3-HBA were observed at 22.55 and 22.46 minutes, respectively.

4.5. Results and discussion

4.5.1. Physic-chemical characterization

WSNs were chosen as support for enzyme immobilization due to their morphology and physic-chemical features. During the synthesis of these nanoparticles, silica fibers are grown and spread radially from the center of the nanostructure, generating conical-shaped pore with sections increasing moving outward. This feature helps host large macromolecules as proteins avoiding pore blocking. As for the case of lipase immobilization, surface hydrophobization is needed to provide lid opening. In fact, lipases recognize hydrophobic surfaces as if they were their natural substrate, an oil droplet, and get adsorbed in their open form. This interfacial activation often

leads to hyperactivation, that is, immobilized lipases show enhanced activity respect to the free form.[244–246] To that aim, we functionalized the nanoparticles with PDTES (**Scheme 1**) using CVD. The functionalization was confirmed by FTIR spectroscopy (**Figure 1**).

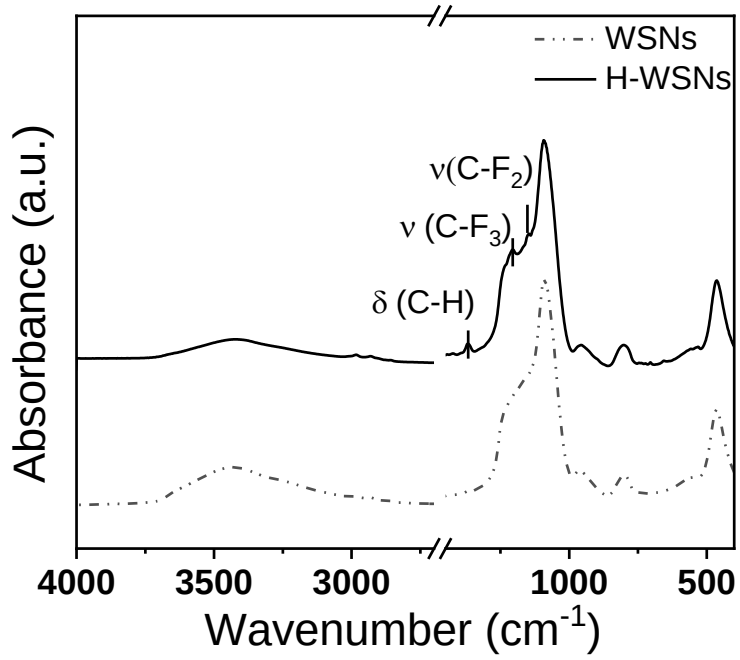

Figure 1. FTIR spectra of bare (dashed) and hydrophobic (solid) WSNs.

Both spectra exhibit the typical features of silica gel.[59] Besides, **Figure 1** shows three bands centered at 1368, 1205 and 1148 cm^{-1} which can be assigned to CH/CH_2 deformation, CF_2 and CF_3 vibration modes respectively, supporting the presence of fluorine moieties onto the silica skeleton.[247] Moreover, the O-H stretching band at 3430 cm^{-1} in the spectrum of H-WSNs experiences a remarkable decrease in intensity, due to the condensation between Si-OH groups of silica surface and the alkoxide groups from PDTES. Different concentrations of H-WSNs were incubated with CALB and RML at fixed protein concentration of 1 mg/mL. For both proteins, the yield of immobilization increases along the WSNs concentration, as more surface

is available for immobilization. In both cases, a plateau is approached at about 10 mg/mL nanoparticle concentration, reaching immobilization yields of 40% and 20% for CALB@H-WSNs and RML@H-WSNs, respectively (**Figure S1**). Then, the enzymes immobilized on the nanoparticles were characterized by TEM-EDX (**Figure 2 A-F)**.

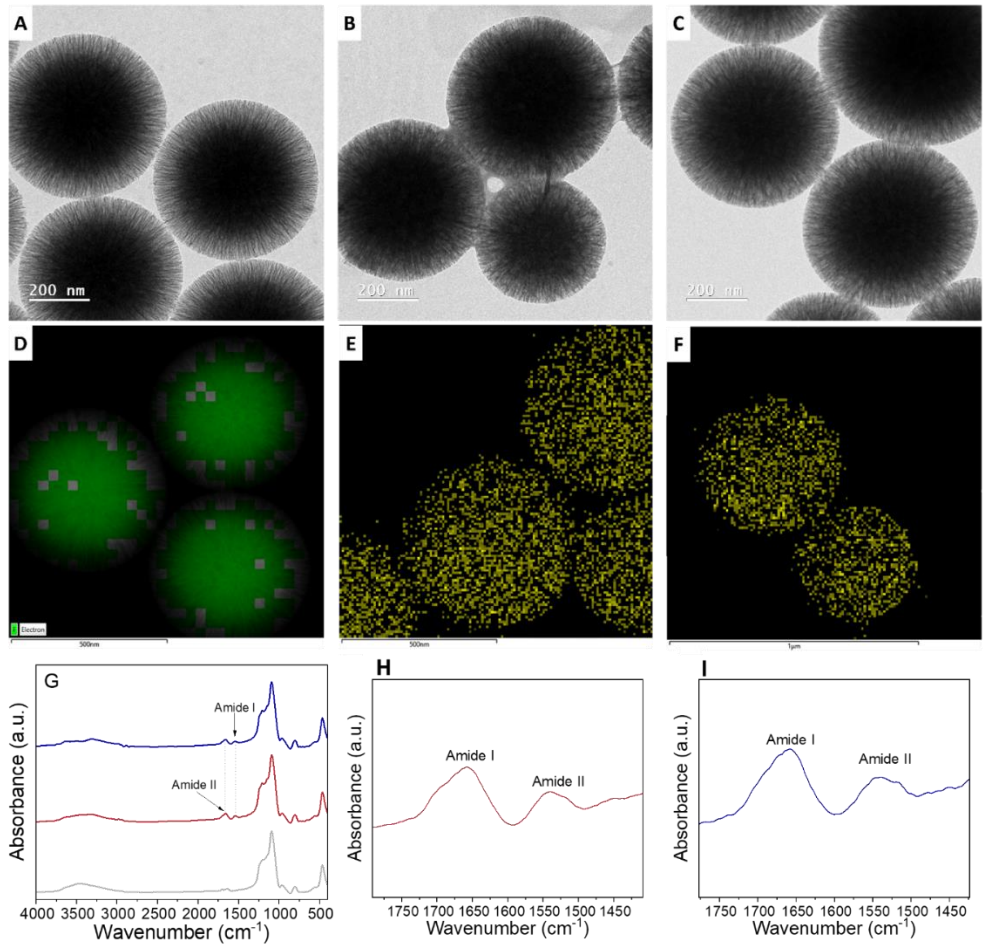

Figure 2. Transmission electron micrographs for H-WSNs (A), CALB@H-WSNs (B), RML@H-WSNs (C). Mapping of fluorine (green) for H-WSNs (D) and of nitrogen (yellow) for CALB@H-WSNs (E) and RML@H-WSNs (F). Comparison between the FTIR spectra of H-WSNs (grey), CALB@H-WSNs (red) and RML@H-WSNs (blue) (G). Amide I and II for CALB@H-WSNs (H)

RML@H-WSNs (I) are highlighted by restricting the wavenumber interval to 1800-1400 cm^{-1}.

Surface hydrophobization on WSNs (**Figure 2A**) resulted in no size increase since the low amount of PDTES used for functionalization was only able to create an undetectable thin layer over the inner and the outer surface of WSNs, as previously demonstrated through SEM measurements.[15] Moreover, most of the silane agent is preferentially grafted inside the pores of the nanostructures rather than onto the outer surface, as confirmed by STEM/EDX mapping (**Figure 2D)**. Adsorption of lipases did not lead to the formation of a protein corona layer in any case (**Figure 2B, C**). As a matter of fact, size distribution analysis (**Figure S2**) confirmed that the diameter of the nanoparticles remained the same after the immobilization. However, some differences between the supported biocatalysts are visible. Indeed, CALB adsorption resulted in interparticle bridging driven by the interaction between the protein chains located on the outer surface of close nanostructures (**Figure 2B**). This fact may cause nanoparticle aggregation due to enzyme-driven interparticle cross-linking. This evidence suggests complete pore filling, allocating some CALB molecules at the outer layer of H-WSNs which are ready to interact with neighbor nanoparticles. On the contrary, RML@H-WSNs nanostructures exhibit no enzyme presence outside the perimeter of each nanoparticle (**Figure 2C**). This suggests a partial pore filling in accordance with the lower immobilization yield achieved with this enzyme. STEM/EDX measurements were performed on both the supported biocatalysts to prove the enzyme physical immobilization. First, EDX spectra confirm the presence of nitrogen within the supported biocatalysts (**Figure S3 B, C**), with respect to the spectrum of H-WSNs which clearly exhibits only Si, O and F peaks (**Figure S3 A**). The atomic count, reported in **Table S1**, shows that the molar amount of N for both the supported biocatalysts is lower than 3% mol, slightly higher for CALB@H-WSNs than RML@H-WSNs, suggesting again a higher enzyme load for the former system. Finally, elemental mapping of nitrogen reveals that both lipases are bound

to the silica skeleton (**Figure 2E** and **2F**). Enzyme confinement into the pore structure of nanoparticles may promote protein conformational changes leading to dramatic worsening of the catalytic performances. To study the changes in the secondary structure of the immobilized lipases, we analyzed them by FTIR spectroscopy (**Figure 2G-I)**. Figure 2G shows an IR fingerprint that confirms the attachment of the lipases on H-WSNs. We observed that the broad band between 3200 and 3600 cm^{-1} decreases in the spectra of both the supported biocatalysts with respect to H-WSNs, meaning lower amounts of exposed silanol groups due to the presence of a protein layer over silica surface. [248] Otherwise, the spectra appear to be almost completely superimposable except for 1400-1700 cm^{-1} region. Indeed, both CALB@H-WSNs and RML@H-WSNs exhibit two small bands centered at around 1655 and 1550 cm^{-1}, which correspond to the typical amide I and amide II bands respectively. Amide I is originated by stretching of carbonyl groups in polypeptides.[249] In this case, it is slightly shifted to higher wavenumbers due to partial overlapping with the adsorbed-water O-H bending band (~1640 cm^{-1}). On the other hand, the out-of-phase combination of the N-H in plane bend and the C-N stretching vibration result in Amide II band.[249] Like for the amide I vibration, the amide II vibration of proteins is hardly affected by side chain vibrations but the correlation between protein secondary structure and frequency is less straightforward than for the amide I vibration. Further focus on high wavenumber regions could lead to notice some different spectral features for both immobilized enzymes . Indeed, a small band rises over -OH stretching contribution at ~ 3300 cm^{-1}. It is the fingerprint of Amide A modes, attributed to N-H stretching.[250] This feature is more visible in RML@H-WSNs, maybe due to the lower amount of adsorbed water with respect to CALB@H-WSNs, resulting in lower -OH stretching band. Gaussian deconvolution of Amide I band was performed to unveil the secondary structure of both the immobilized proteins. Peak attribution is reported in **Figure S4** and results are shown in **Table 1**.

Table 1. Secondary structures of immobilized CALB and RML obtained by deconvoluting Amide I band. Peak attribution was adapted from the protocol prescribed by Yang at al. [251]

	CALB/WSNs (%)	**RML/WSNs (%)**
β-sheet	38	23
Random coil	19	17
α-helix	23	13
β-turns	20	37
Aggregates	/	10

For supported CALB, Amide I band is centered at around 1656 cm^{-1}, which is typical for globular proteins that contain α-helices. This feature, together with the huge amount of β-sheets, confirm the good retention of original lipase conformation, as already observed for immobilization onto silica and nano-TiO_2 carriers.[252] Moreover, the high percentages of unordered and β-turn structures is usually associated with the protein rearrangement after immobilization and solvent removal for performing the analysis.[253] Similar structural rearrangements have been correlated to an enhancement in the specific activity of immobilized lipase towards hydrolysis and transesterification of triglycerides, as previously reported. [15] As regards RML@H-WSNs, Amide I deconvolution unveils the presence of huge amounts of β-turns and β-sheets, as previously observed for RML in solution.[254] Similar results were obtained for RML immobilized onto functionalized silicates and carbon nanotubes.[255] Differently from supported CALB, a non-negligible portion of aggregated structures is presented. This structural rearrangement can be justified by lid-to-lid inter-protein aggregation triggered by hydrophobic interactions. This mechanism is typical of lipases featuring a large lid, such as *Candida rugosa* lipase

(CRL), *Humicola lanuginose* lipase (HLL) and RML itself, that leads to aggregated structures through interfacial activation.[256,257] The occurrence of aggregation in aqueous media could be at the basis of the lower yield of immobilization of RML with respect to CALB which, on the contrary, features only a small lid. Aggregate structure would in fact suffer from restricted diffusion and reduced interaction with the support.

4.5.2. Thermodynamic parameters of the immobilization process

The adsorption isotherms were built to understand the thermodynamics of the immobilization process for both lipases. At different WSNs/enzyme ratios, we calculated the bound enzyme (q_e) and the unbound enzyme concentration (C_e) at the equilibrium based on the immobilization yield reported in **Figure S1**. Afterwards, the experimental data were fitted to the Langmuir adsorption model to derive K_L and q_{max} **(Figure 3)** according to equation (1). [258]

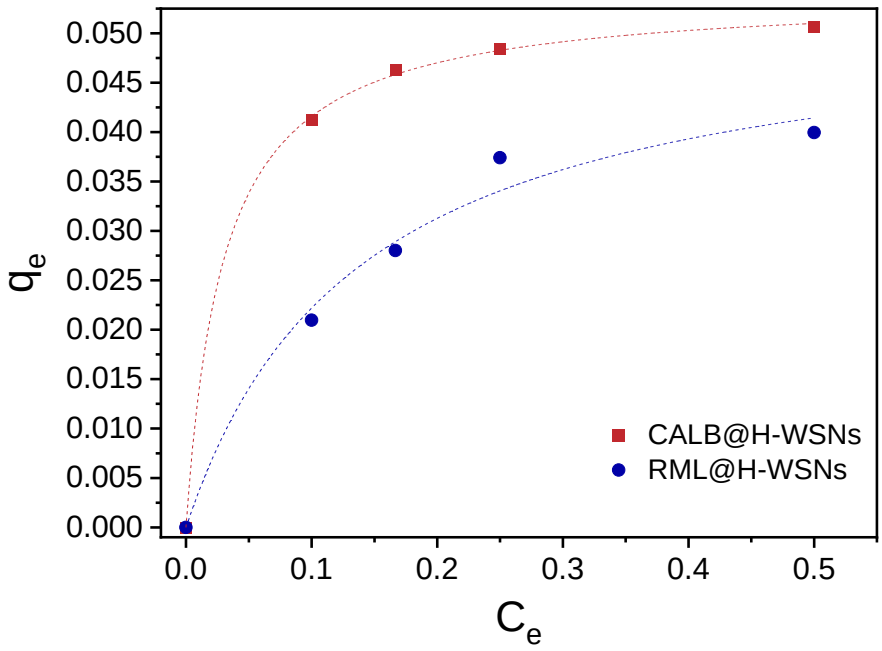

Figure 3. Langmuir-fitted equilibrium isotherm curves for CALB and RML adsorption. The experimental data fit with the Langmuir model with R^2 equal to 0.98 and 0.99 for RML@H-WSNs and CALB@H-WSNs, respectively.

Both Langmuir isotherms exhibit L-2 shape, according to Giles' classification, which is the most common profile for protein adsorption in diluted conditions. [259,260] **Table 2** shows the $\Delta G°$, q_{max} and K_L values for both the supported biocatalysts. The calculation of Langmuir constant K_L allowed to determine the differences in affinity between the two lipases and H-WSNs. As RML is bound to H-WSNs with a higher K_L value than CALB to the same surface, we conclude that RML has higher affinity for the hydrophobic support than CALB. Derived from K_L, we determined a lower $\Delta G°$ value for the absorption of RML to H-WSNs in comparison to CALB through equation (2), supporting the hypothesis of a stronger interaction between the former enzyme and the hydrophobic support. For both the immobilized lipases, the calculated absolute values for $\Delta G°$ are included within the 0-20 kJ/mol range. Such values for free energy of binding are typical of physical protein immobilization phenomena as interfacial activation, driven by van der Walls interactions.[261] The difference in terms of K_L may be explained due to differences in enzyme structures. Indeed, RML lipase exhibits a polypeptide chain called lid which covers the active site and favors the interfacial activation in the presence of hydrophobic surfaces.[262,45] On the contrary, CALB has only a small lid which contributes to interfacial activation mechanism.[263] Therefore, the lower values of $\Delta G°$ found in RML might rely on the strong interactions between the enzyme lid and the H-WSNs, whose superhydrophobic surface may mimic some physicochemical properties found in the natural substrates (fat) of this enzyme family.[264] Despite the different binding thermodynamics, the maximum adsorption capacities q_{max} are similar for both lipases as they have similar molecular size and the surface where they are bound is the same in terms of surface chemistry and morphology.

Table 2. Langmuir-model adsorption thermodynamic parameters and ΔG° of immobilization for the supported biocatalysts

	K_L		q_{max}	ΔG°[j/mol]
CALB/WSNs	0.0299 0.0022	±	0.05405 ± 0.00056	-4901
RML/WSNs	0.1383 0.03917	±	0.0529 ± 0.00549	-8696

4.5.3. Kinetic assessment of the immobilized enzymes

The evaluation of the thermodynamics of enzyme binding was followed by the assessment of the catalytic activity of the two immobilized lipases. The influence of immobilization on enzyme activity at different enzyme loads was investigated by determining both relative recovered activity (*rRA*) and immobilized specific activity (*iSA*) (**Figure 4**). In both the cases, *rRA* and *iSA* share the same trend. In detail, enzyme load positively affects the activity of supported RML (**Figure 4A**) unlike the immobilized CALB, whose recovered activity decreases along the enzyme load (**Figure 4B**).

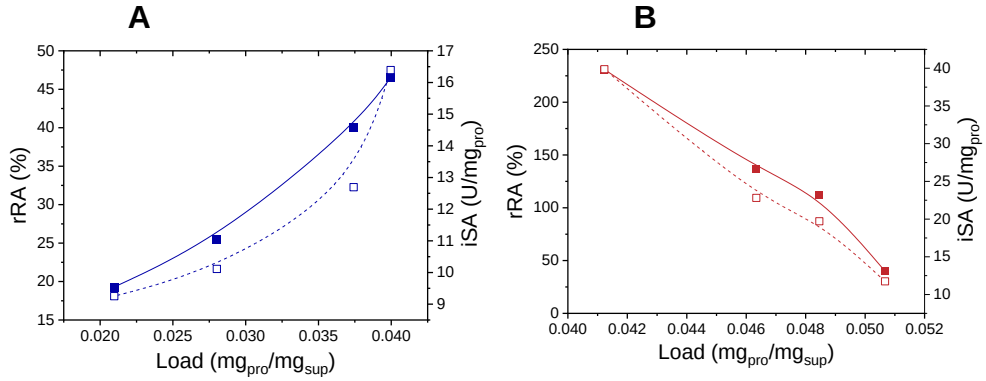

Figure 4. Profiles for percentage relative recovered activity (rRA) and immobilized specific activity (iSA) over the protein load for RML@H-WSNs (A) and CALB@H-WSNs (B), evaluated through para-Nitrophenyl butyrate assay.

For CALB, the effects of hyperactivation after immobilization onto H-WSNs appear clear for low lipase loading, since the immobilized enzyme *(iSA* = 37 U mg^{-1}) was 2.3-fold more active than its soluble counterpart (*iSA* =16 U mg^{-1}), which means a *rRA* of 230%. This recovered activity is 2-3 times higher than the CALB bound onto other highly hydrophobic supports such as triethoxy-octyl-silane-functionalized silica.[265] We suggest that the morphology of WSNs, with conical-shaped radially aligned mesopores, is a suitable environment for the protein to be hosted, since the active sites get widely dispersed into the internal surfaces of the nanostructures. Moreover, the presence of small mesopores and micropores within the silica fibers mitigates mass transfer limitations, allowing easy substrate and product intraparticle diffusion, often resulting in a boosted activity. [239] However, as protein load increases, pores get occluded and the catalysts start to suffer from crowding effect and mass transfer limitations, which meant the *rRA* decreasing to 25% at 0.051 mg_{pro}/mg_{sup} load. [266,267] On the contrary, in the case of RML, immobilization dramatically reduces its specific activity (iSA = 9.24 U·mg^{-1}) in comparison to its free counterpart (SA = 40 U·mg^{-1}). However, RML increases its specific activity with the protein load, benefitting from molecular crowding effects that occurred within the pores, explaining the higher rRA (50%) at 0.040 $mg_{pro}/mg_{sup.}$ This different behavior is attributed to the intramolecular interactions between adjacent proteins which limit conformational rearrangements under test conditions, allowing the protein to preserve the optimal conformation for substrate binding. [269] The opposite effect of crowding on the catalytic performances of the biocatalysts cold be visually justified by TEM images (**Figure 2B, C**). Indeed, the degree of pore filling appears remarkably higher for CALB than for RML, being the latter probably immune from pore occlusion and mass transfer limitations.

4.5.4. Thermal stability assessment

Biocatalysts are very sensitive to temperature overshoots, which can lead to irreversible conformational modification thus undermining the catalytic activity. Moreover, the design of thermally resistant biocatalysts allows to perform reactions at higher temperatures thus improving the kinetics and reducing side problems such as microbial growth and medium viscosity.[270] Therefore, the increase in the thermal stability of the protein is always pursued when immobilizing enzymes. **Figure 5** reports the residual activity of each lipase, in both immobilized and soluble preparations, after their incubation for 1h at different temperatures.

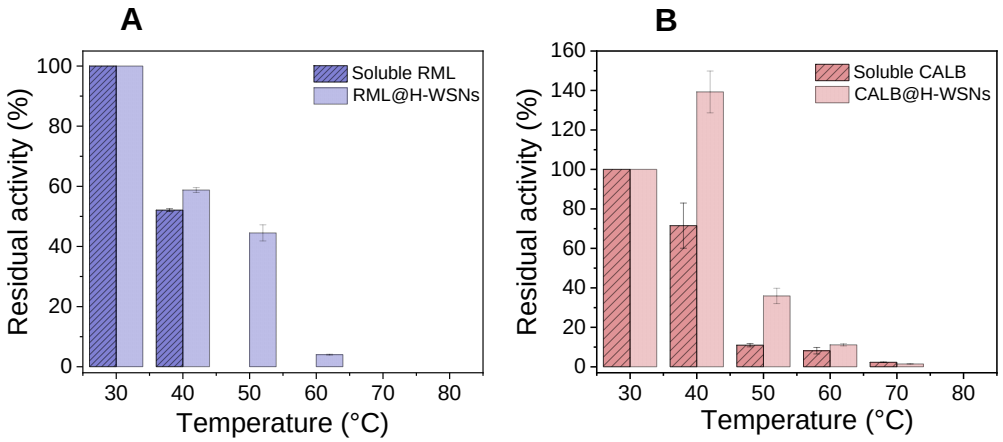

Figure 5. Residual activity of RML (A) and CALB (B) in their free (dark colors) and immobilized (pale colors) forms after 1 hour incubation at different temperatures.

The residual activity of both free lipases is lower than 10% at temperatures higher than 50°C (**Figure 5 A, B**), confirming the achievements of previous reports. [271,272] This means that the catalytic activity and thus the protein conformation is strongly sensitive to small temperature deviations from the optimal temperature 30°C.[273] In contrast, the immobilization of both lipases mitigates their thermal sensitivity, stabilizing them. In the case of RML@H-WSNs, the immobilized enzyme incubated for 1h at 50°C retains 45% of its initial activity before incubation in agreement with

previous findings for silica-immobilized RML.[274] This result is not surprising since WSNs were repeatedly proved to successfully improve thermal stability of hydrolases by hindering thermal vibration of protein chains, due to very strong and effective protein-matrix interactions (hydrogen bonds, electrostatic).[1,59] Likewise, CALB remarkably benefitted from immobilization, even resulting in hyperactivation (140% residual activity) after incubation at 40°C. The reason for this behavior might lie in the reversible conformational modification induced by heat. More specifically, the protein gains structural rigidity in the microenvironment of the silica pores, thus requiring higher activation energy. This means that heat power allows immobilized lipase to rearrange its conformation to properly bind the substrate. [275] Moreover, higher structural rigidity under thermal stress could be provided by enzyme crowding as well. [267]

4.5.5. Hydrolysis of ethyl 3-hydroxybutyrate

The hydrolysis of racemic ethyl 3-hydroxy butyrate (E3HB) was chosen as a model reaction to investigate the potential of these two heterogeneous biocatalysts for an industrially relevant biotransformation. The enantioselective hydrolysis of E3HB is an industrially attractive reaction as enantiomerically pure 3-hydroxy butyric acid can work as precursors of drugs, cosmetics and polymers.[276–278]

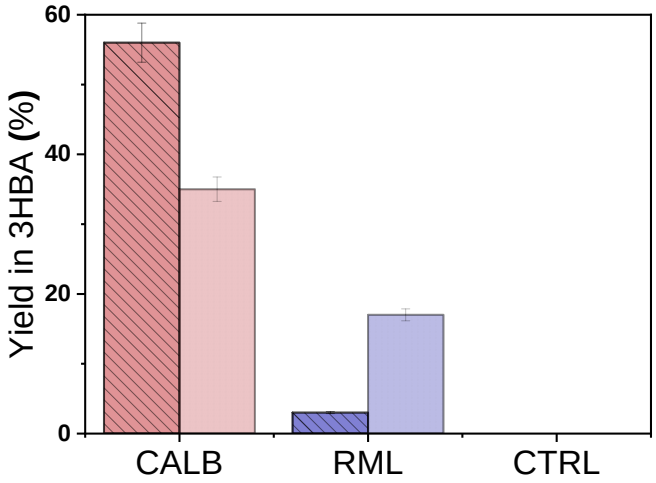

Figure 6. Histograms showing the yield (%) in 3-hydroxybutyric acid of the hydrolysis of racemic ethyl 3-hydroxybutyrate 200 mM in Tris-HCl buffer (pH=7, 10 mM). Darker fill with diagonal lines refers to the soluble protein, whereas lighter dotted fill refers to the immobilized biocatalysts.

Figure 6 shows that CALB outperforms RML in the hydrolysis of E3HB, regardless the enzyme formulation. This result matches with the highest specific activity of CALB compared to RML under aqueous solution. Indeed, it is well known that CALB is one of the most performing enzymes in the enantioselective hydrolysis of esters. [279–282] The very low activity of soluble RML is due to the presence of the lid that almost fully isolates the active site in aqueous reaction media. The attachment onto the fluorine-decorated superhydrophobic surface of H-WSNs may induce the lid opening, enhancing thus the enzyme affinity towards the substrate.[283] On the contrary, CALB exhibits a small lid, thus it undergoes a less pronounced interfacial activation in the presence of small and polar substrates such as E3HB.[284] For the same reason, soluble CALB is more active than soluble RML, due to the active site being more easily accessible even in the closed conformation. Furthermore, the less pronounced tendency to aggregation might contribute to exert high activity even in

the soluble form. Besides the hydrolysis yield, enantioselectivity of the process is also another key parameter to study when an enzyme is immobilized. It is known that the adsorption of lipases to hydrophobic surfaces may alter the enzyme enantioselectivity. Changes in the enantioselectivity are normally explained by enzyme-support interactions.[63–66] **Figure 7** shows how the immobilization mainly affect the enantioselectivity of RML. More specifically, soluble RML is enantioselective towards enantiomer R, being the enantiomeric excess e.e.(R) = 47%. On the contrary, RML@H-WSNs only mild enantioselectivity towards the hydrolysis of (S)-E3HB (e.e.(R) = -17%), suggesting that the protein gains the capacity of converting almost indiscriminately both the enantiomeric forms of E3HB as immobilized, resulting in increased yield of reaction. On the other hand, both soluble and immobilized CALB provide complete hydrolysis of (R)-E3HB. However, both the enantiomers of 3-HBA are produced, maybe due to the higher activity of CALB with respect to RML, which leads to hydrolyze (S)E3HB as soon as all (R)E3HB is consumed. This hypothesis is supported by the evidence of lower (S)3-HBA produced and thus higher enantioselectivity by CALB@H-WSNs, being the e.e.(R) equal to 54% and 42% for supported and soluble protein, respectively. The chromatograms of the reaction products are reported in **Figure S5**.

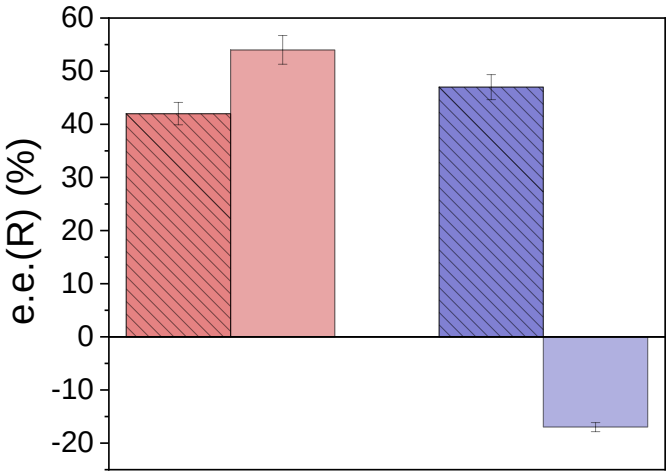

Figure 7. Histograms reporting the enantiomeric excess e.e.(R) % for CALB (in red) and RML (in blue). Darker fill with diagonal lines refers to the soluble protein, whereas lighter dotted fill refers to the immobilized biocatalysts.

4.6. Conclusion

RML and CALB enzymes were successfully immobilized into previously hydrophobized wrinkled silica nanoparticles. CVD technique was able to properly modify the surface properties of the carrier, in order to build a proper environment for lipase to be hosted. The proteins were preferentially loaded inside the pores of WSNs and no protein corona layer was detected. Both the enzymes gained thermal stability due to the high matrix-protein interactions. The presence of a large lid in the secondary structure of RML makes the protein very sensitive to interfacial activation, differently from CALB which has a small lid. The conformational differences between the proteins were translated into different properties of the supported biocatalysts. CALB@H-WSNs experienced a higher maximum load but lower intensity of interaction with the support than RML. Moreover, it severely suffered from enzyme crowding at high enzyme loads and provided lower yield of hydrolysis

as immobilized. On the contrary, the high K_L for RML suggests very strong support binding. The activity of RML benefitted from crowding and the immobilization remarkably boosted the yield of hydrolysis. Moreover, CALB provided the same enantioselectivity towards (R)E3HB whether it was unbound or immobilized, whereas RML changed its selectivity from R-to-S enantiomer as immobilized, even with low enantiomeric excess. In the end, immobilization into WSNs claims to be a successful strategy to design nanoscaled lipase-based biocatalysts. Furthermore, surface modification provides remarkable boosting of RML catalytic performance.

Author Contributions

Conceptualization, F.L.G.; methodology, G.P., F.L.G.; validation, A.C.,V.C., F.L.G.; investigation, G.P., M.G., D.A.S., data curation, G.P.; writing—original draft preparation, G.P., writing—review and editing, V.C., G.V., A.C., F.L.G., supervision, F.L.G., A.C., G.V.; project administration, F.L.G. All authors have read and agreed to the published version of the manuscript.

Funding

The research was partially carried out at the facility of CIC biomaGUNE and partially supported by the Spanish Ministry of Science and Innovation under the Maria de Maeztu Units of Excellence Programme (MDM-2017-0720).

Acknowledgments

FLG acknowledges the funding of IKERBASQUE.

Conflicts of Interest

The authors declare no conflict of interest.

4.7. Supplementary information

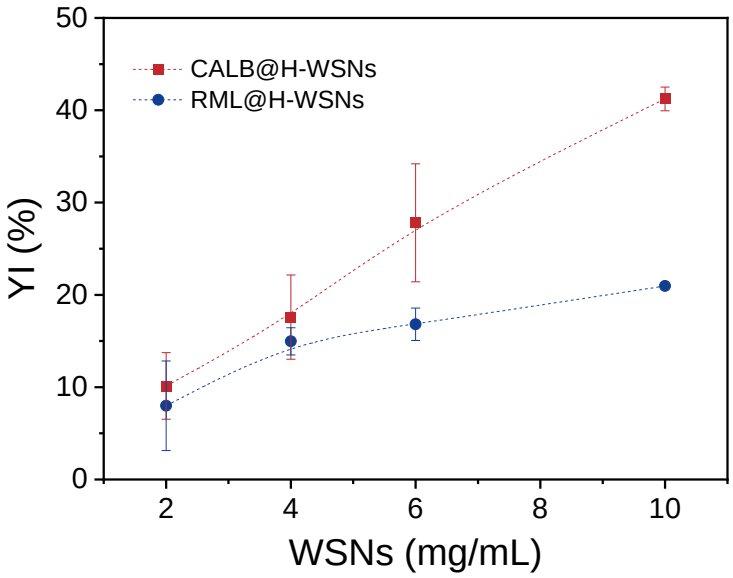

Figure S1. Calculation of the yield of immobilization (YI %) of CALB and RML for different support concentrations, evaluated through Bradford assay.

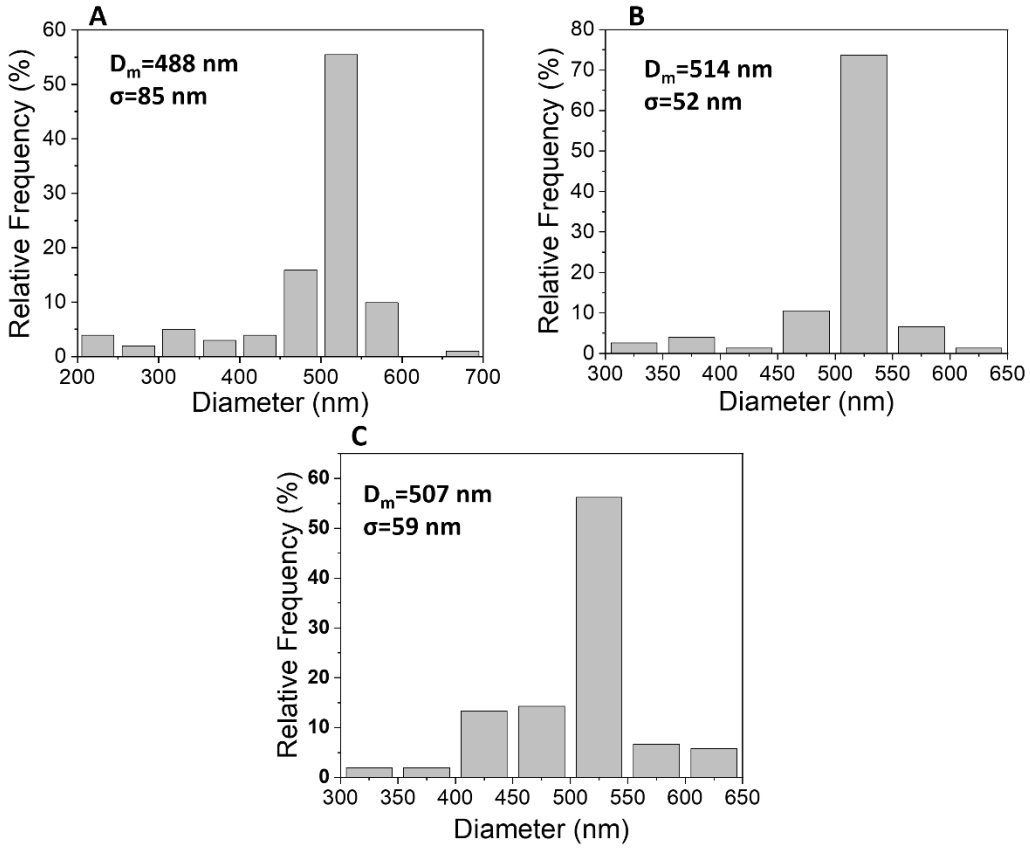

Figure S2. Size distribution analysis for H-WSNs (A), CALB@H-WSNs (B) and RML@H-WSNs (C) carried out through ImageJ software. Mean size and standard deviation were evaluated for a sample of 100 nanoparticles of each sample.

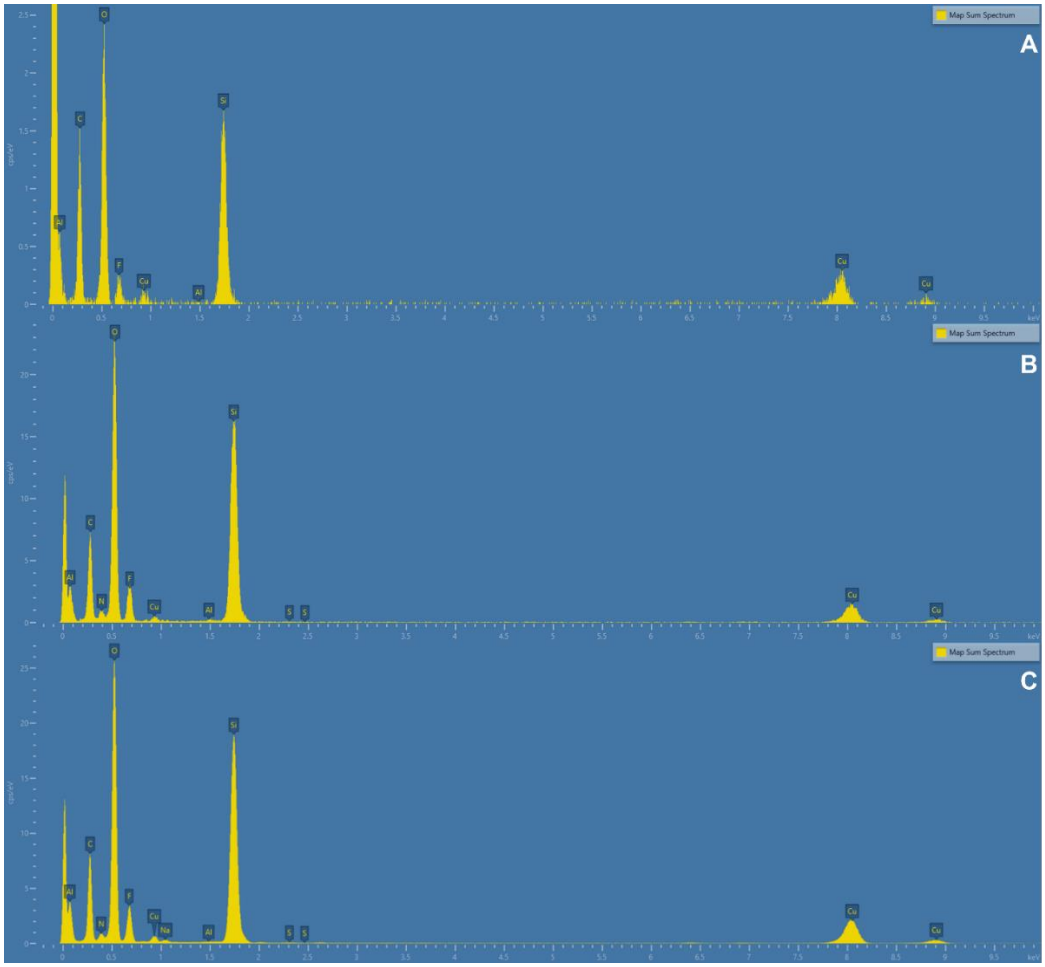

Figure S3. EDX spectrum for H-WSNs (A), CALB@H-WSNs (B) and RML@H-WSNs (C).

Table S1. Atomic molar distribution for bare and functionalized WSNs together with the supported biocatalysts.

Sample	**Si (%)**	**O (%)**	**F (%)**	**N (%)**
WSNs	26.93 ± 2	73.07 ± 2	/	/
Hydr-WSNs	28.27 ± 0.41	65.19 ± 0.32	6.54 ± 0.67	/
CALB/WSNs	28.26 ± 0.53	61.82 ± 0.63	7.70 ± 0.45	2.22 ± 0.29
RML/WSNs	32.38 ± 0.70	59.04 ± 0.45	7.00 ± 0.72	1.58 ± 0.79

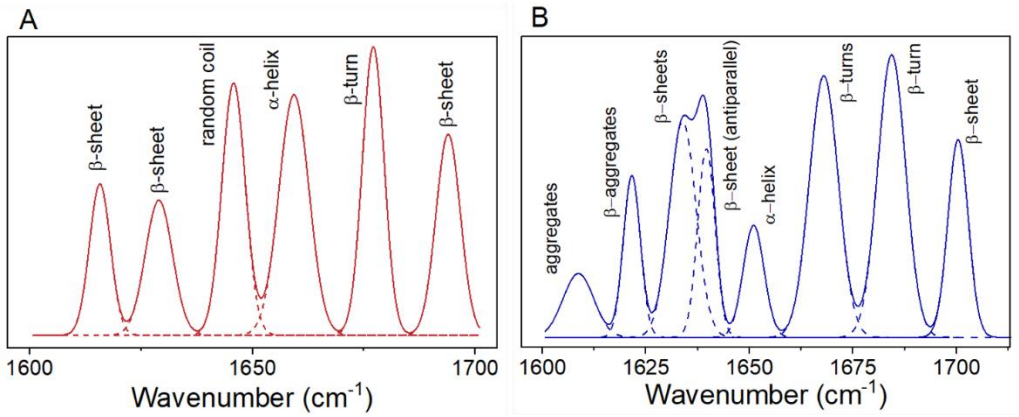

Figure S4. Gaussian deconvolution of the second derivative of Amide I band for CALB@H-WSNs (A) and RML@H-WSNs (B).

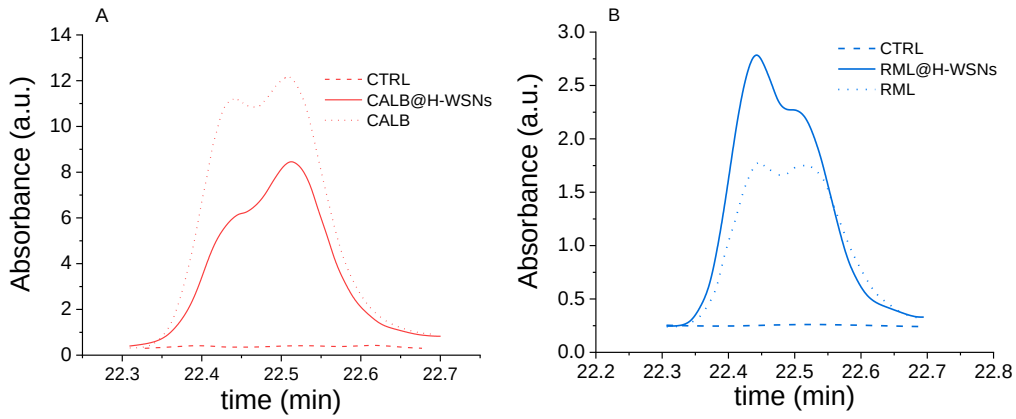

Figure S5. Chromatograms of the reaction products from CALB- (A) and RML- (B) catalyzed hydrolysis of E3HB

5. References

(1) Pota, G.; Gallucci, N.; Cavasso, D.; Russo Krauss, I.; Vitiello, G.; Lopez-Gallego, F.; Costantini, A.; PADUANO, L.; Califano, V. Controlling the Adsorption of B-Glucosidase onto Wrinkled SiO_2 Nanoparticles To Boost the Yield of Immobilization of an Efficient Biocatalyst. *Langmuir 39* (4), 1482–1494. https://doi.org/10.1021/acs.langmuir.2c02861.

(2) Illanes, A. Enzyme Biocatalysis. *Principles and Applications. Editorial Springer-Verlag New York Inc., United States* **2008**, 1–56.

(3) Bommarius, A. S.; Riebel-Bommarius, B. R. *Biocatalysis: Fundamentals and Applications*; John Wiley & Sons, 2004.

(4) Mateo, C.; Palomo, J. M.; Fernandez-Lorente, G.; Guisan, J. M.; Fernandez-Lafuente, R. Improvement of Enzyme Activity, Stability and Selectivity via Immobilization Techniques. *Enzyme Microb Technol* **2007**, *40* (6), 1451–1463.

(5) DiCosimo R, McAuliffe J, Poulose AJ, B. G. Industrial Use of Immobilized Enzymes. *Chem Soc Rev* **2013**, 42, 6437–6474,. https://doi.org/10.1039/c3cs35506c.

(6) Hiep, H.; Kim, M. An Overview of Techniques in Enzyme Immobilization. *Applied Science and Convergence Technology* **2017**, *26* (6), 157–163. https://doi.org/10.5757/ASCT.2017.26.6.157.

(7) Meryam Sardar, R. A. Enzyme Immobilization: An Overview on Nanoparticles as Immobilization Matrix. *Biochemistry & Analytical Biochemistry* **2015**, *04* (02), 1. https://doi.org/10.4172/2161-1009.1000178.

(8) Santos, J. C. S. D.; Barbosa, O.; Ortiz, C.; Berenguer-Murcia, A.; Rodrigues, R. C.; Fernandez-Lafuente, R. Importance of the Support Properties for Immobilization or Purification of Enzymes. *ChemCatChem* **2015**, *7* (16), 2413–2432. https://doi.org/10.1002/cctc.201500310.

(9) Fang, X.; Zhao, X.; Fang, W.; Chen, C.; Zheng, N. Self-Templating Synthesis of Hollow Mesoporous Silica and Their Applications in Catalysis and Drug Delivery. *Nanoscale* **2013**, *5* (6), 2205–2218.

(10) Zou, B.; Song, C.; Xu, X.; Xia, J.; Huo, S.; Cui, F. Enhancing Stabilities of Lipase by Enzyme Aggregate Coating Immobilized onto Ionic Liquid Modified Mesoporous Materials. *Appl Surf Sci* **2014**, *311*, 62–67.

(11) Califano, V.; Costantini, A. Immobilization of Cellulolytic Enzymes in Mesostructured Silica Materials. *Catalysts* **2020**, *10* (6), 706.

(12) Popat, A.; Hartono, S. B.; Stahr, F.; Liu, J.; Qiao, S. Z.; Lu, G. Q. Mesoporous Silica Nanoparticles for Bioadsorption, Enzyme Immobilisation, and Delivery Carriers. *Nanoscale* **2011**, *3* (7), 2801–2818. https://doi.org/10.1039/c1nr10224a.

(13) Gisbert-Garzarán, M.; Vallet-Regí, M. Influence of the Surface Functionalization on the Fate and Performance of Mesoporous Silica Nanoparticles. *Nanomaterials* **2020**, *10* (5), 916.

(14) Slowing, I.; Trewyn, B. G.; Lin, V. S.-Y. Effect of Surface Functionalization of MCM-41-Type Mesoporous Silica Nanoparticles on the Endocytosis by Human Cancer Cells. *J Am Chem Soc* **2006**, *128* (46), 14792–14793.

(15) Pota, G.; Bifulco, A.; Parida, D.; Zhao, S.; Rentsch, D.; Amendola, E.; Califano, V.; Costantini, A. Tailoring the Hydrophobicity of Wrinkled Silica Nanoparticles and of the Adsorption Medium as a Strategy for Immobilizing Lipase: An Efficient Catalyst for Biofuel Production. *Microporous and Mesoporous Materials* **2021**, 111504.

(16) Moon, D.-S.; Lee, J.-K. Tunable Synthesis of Hierarchical Mesoporous Silica Nanoparticles with Radial Wrinkle Structure. *Langmuir* **2012**, *28* (33), 12341–12347.

(17) Abu-Reziq, R.; Alper, H. Magnetically Separable Base Catalysts: Heterogeneous Catalysis vs. Quasi-Homogeneous Catalysis. *Applied Sciences* **2012**, *2* (2), 260–276.

(18) Männel, M. J.; Kreuzer, L. P.; Goldhahn, C.; Schubert, J.; Hartl, M. J.; Chanana, M. Catalytically Active Protein Coatings: Toward Enzymatic Cascade Reactions at the Intercolloidal Level. *ACS Catal* **2017**, *7* (3), 1664–1672.

(19) Kreuzer, L. P.; Männel, M. J.; Schubert, J.; Höller, R. P. M.; Chanana, M. Enzymatic Catalysis at Nanoscale: Enzyme-Coated Nanoparticles as Colloidal Biocatalysts for Polymerization Reactions. *ACS Omega* **2017**, *2* (10), 7305–7312.

(20) Liu, H.-L.; Chen, W.-J.; Chou, S.-N. Mechanisms of Aggregation of Alpha-and Beta-Amylases in Aqueous Dispersions. *Colloids Surf B Biointerfaces* **2003**, *28* (2–3), 215–225.

(21) Sáringer, S.; Rouster, P.; Szilagyi, I. Co-Immobilization of Antioxidant Enzymes on Titania Nanosheets for Reduction of Oxidative Stress in Colloid Systems. *J Colloid Interface Sci* **2021**, *590*, 28–37. https://doi.org/10.1016/j.jcis.2021.01.012.

(22) Sigurdardóttir, S. B.; Lehmann, J.; Grivel, J. C.; Zhang, W.; Kaiser, A.; Pinelo, M. Alcohol Dehydrogenase on Inorganic Powders: Zeta Potential

and Particle Agglomeration as Main Factors Determining Activity during Immobilization. *Colloids Surf B Biointerfaces* **2019**, *175* (November 2018), 136–142. https://doi.org/10.1016/j.colsurfb.2018.11.080.

(23) Wei, Q.; Becherer, T.; Angioletti-Uberti, S.; Dzubiella, J.; Wischke, C.; Neffe, A. T.; Lendlein, A.; Ballauff, M.; Haag, R. Protein Interactions with Polymer Coatings and Biomaterials. *Angewandte Chemie International Edition* **2014**, *53* (31), 8004–8031.

(24) Lynch, I.; Dawson, K. A. Protein-Nanoparticle Interactions. *Nano Today* **2008**, *3* (1–2), 40–47. https://doi.org/10.1016/S1748-0132(08)70014-8.

(25) Camelin, E.; Romero, O.; Piumetti, M.; Ottone, C.; Illanes, A.; Fino, D. Mechanisms of Interaction among Enzymes and Supports. In *Nanomaterials for Biocatalysis*; Elsevier, 2022; pp 105–148.

(26) Diamanti, E.; Arana-Peña, S.; Ramos-Cabrer, P.; Comino, N.; Carballares, D.; Fernandez-Lafuente, R.; López-Gallego, F. Intraparticle Macromolecular Migration Alters the Structure and Function of Proteins Reversibly Immobilized on Porous Microbeads. *Adv Mater Interfaces* **2022**, 2200263.

(27) Califano, V.; Sannino, F.; Costantini, A.; Avossa, J.; Cimino, S.; Aronne, A. Wrinkled Silica Nanoparticles: Efficient Matrix for β-Glucosidase Immobilization. *The Journal of Physical Chemistry C* **2018**, *122* (15), 8373–8379.

(28) Costantini, A.; Venezia, V.; Pota, G.; Bifulco, A.; Califano, V.; Sannino, F. Adsorption of Cellulase on Wrinkled Silica Nanoparticles with Enhanced Inter-Wrinkle Distance. *Nanomaterials* **2020**, *10* (9), 1799. https://doi.org/10.3390/nano10091799.

(29) Ketudat Cairns, J. R.; Esen, A. β-Glucosidases. *Cellular and Molecular Life Sciences* **2010**, *67* (20), 3389–3405.

(30) Ahmed, A.; Batool, K.; Bibi, A. Microbial β-Glucosidase: Sources, Production and Applications. *J Appl Environ Microbiol* **2017**, *5* (1), 31–46.

(31) Yang, B.; Dai, Z.; Ding, S.-Y.; Wyman, C. E. Enzymatic Hydrolysis of Cellulosic Biomass. *Biofuels* **2011**, *2* (4), 421–449.

(32) Califano, V.; Costantini, A.; Silvestri, B.; Venezia, V.; Cimino, S.; Sannino, F. The Effect of Pore Morphology on the Catalytic Performance of β-Glucosidase Immobilized into Mesoporous Silica. *Pure and Applied Chemistry* **2019**, *91* (10), 1583–1592.

(33) Lei, J.; Fan, J.; Yu, C.; Zhang, L.; Jiang, S.; Tu, B.; Zhao, D. Immobilization of Enzymes in Mesoporous Materials: Controlling the

Entrance to Nanospace. *Microporous and mesoporous materials* **2004**, *73* (3), 121–128.

(34) Gallucci, N.; Vitiello, G.; Di Girolamo, R.; Imbimbo, P.; Monti, D. M.; Tarallo, O.; Vergara, A.; Russo Krauss, I.; Paduano, L. Towards the Development of Antioxidant Cerium Oxide Nanoparticles for Biomedical Applications: Controlling the Properties by Tuning Synthesis Conditions. *Nanomaterials* **2021**, *11* (2), 542.

(35) Gallucci, N.; Hmoudah, M.; Martinez, E.; El-Qanni, A.; Di Serio, M.; Paduano, L.; Vitiello, G.; Russo, V. Photodegradation of Ibuprofen Using CeO2 Nanostructured Materials: Reaction Kinetics, Modeling, and Thermodynamics. *J Environ Chem Eng* **2022**, *10* (3), 107866.

(36) Lomakin, A.; Teplow, D. B.; Benedek, G. B. Quasielastic Light Scattering for Protein Assembly Studies. In *Amyloid Proteins: Methods And Protocols*; Sigurdsson, E. . M., Ed.; Humana Press: Totowa, 2005; pp 153–174.

(37) Goldfarb, A. R.; Saidel, L. J. Ultraviolet Absorption Spectra of Proteins. *Science (1979)* **1951**, *114* (2954), 156–157.

(38) Illanes, A.; Wilson, L. Parameters for the Evaluation of Immobilized Enzymes under Process Conditions. *Immobilization of Enzymes and Cells* **2020**, 65–81.

(39) Bergmeyer, H. U.; Bernt, E. UV-Assay with Pyruvate and NADH. In *Methods of enzymatic analysis*; Elsevier, 1974; pp 574–579.

(40) Reynolds, J. A.; Tanford, C. Binding of Dodecyl Sulfate to Proteins at High Binding Ratios. Possible Implications for the State of Proteins in Biological Membranes. *Proceedings of the National Academy of Sciences* **1970**, *66* (3), 1002–1007.

(41) Joseph, B.; Augustine, R.; Kalarikkal, N.; Thomas, S.; Seantier, B.; Grohens, Y. Recent Advances in Electrospun Polycaprolactone Based Scaffolds for Wound Healing and Skin Bioengineering Applications. *Mater Today Commun* **2019**, *19* (May 2018), 319–335. https://doi.org/10.1016/j.mtcomm.2019.02.009.

(42) Mater. Eng. 2017, 1600289, 1600289.Pdf.

(43) Kortesuo, P.; Ahola, M.; Kangas, M.; Jokinen, M.; Leino, T.; Vuorilehto, L.; Laakso, S.; Kiesvaara, J.; Yli-Urpo, A.; Marvola, M. Effect of Synthesis Parameters of the Sol–Gel-Processed Spray-Dried Silica Gel Microparticles on the Release Rate of Dexmedetomidine. *Biomaterials* **2002**, *23* (13), 2795–2801.

(44) Pastor, I.; Ferrer, M. L.; Lillo, M. P.; Gómez, J.; Mateo, C. R. Structure and Dynamics of Lysozyme Encapsulated in a Silica Sol− Gel Matrix. *J Phys Chem B* **2007**, *111* (39), 11603–11610.

(45) Kortesuo, P.; Ahola, M.; Kangas, M.; Yli-Urpo, A.; Kiesvaara, J.; Marvola, M. In Vitro Release of Dexmedetomidine from Silica Xerogel Monoliths: Effect of Sol-Gel Synthesis Parameters. *Int J Pharm* **2001**, *221* (1–2), 107–114.

(46) Grover, A. K.; MacMurchie, D. D.; Cushley, R. J. Studies on Almond Emulsin Bd-Glucosidase I. Isolation and Characterization of a Bifunctional Isozyme. *Biochimica et Biophysica Acta (BBA)-Enzymology* **1977**, *482* (1), 98–108.

(47) Kujda, M.; Adamczyk, Z.; Morga, M.; Sofińska, K. Recombinant Albumin Adsorption on Mica Studied by AFM and Streaming Potential Measurements. *Colloids Surf B Biointerfaces* **2015**, *127*, 192–199.

(48) Rezwan, K.; Meier, L. P.; Rezwan, M.; Vörös, J.; Textor, M.; Gauckler, L. J. Bovine Serum Albumin Adsorption onto Colloidal Al2O3 Particles: A New Model Based on Zeta Potential and UV− Vis Measurements. *Langmuir* **2004**, *20* (23), 10055–10061.

(49) Payerl, C.; Bračič, M.; Zankel, A.; Fischer, W. J.; Kaschowitz, M.; Fröhlich, E.; Kargl, R.; Stelzer, F.; Spirk, S. Nonspecific Protein Adsorption on Cationically Modified Lyocell Fibers Monitored by Zeta Potential Measurements. *Carbohydr Polym* **2017**, *164*, 49–56.

(50) Ahmed, S. S.; Akhter, M.; Sajjad, M.; Gul, R.; Khurshid, S. Soluble Production, Characterization, and Structural Aesthetics of an Industrially Important Thermostable β -Glucosidase from Clostridium Thermocellum in Escherichia Coli. *Biomed Res Int* **2019**, *2019*. https://doi.org/10.1155/2019/9308593.

(51) Holzwarth, G.; Doty, P. The Ultraviolet Circular Dichroism of Polypeptides1. *J Am Chem Soc* **1965**, *87* (2), 218–228.

(52) Greenfield, N. J.; Fasman, G. D. Computed Circular Dichroism Spectra for the Evaluation of Protein Conformation. *Biochemistry* **1969**, *8* (10), 4108–4116.

(53) Monteiro, L. M. O.; Vici, A. C.; Pinheiro, M. P.; Heinen, P. R.; de Oliveira, A. H. C.; Ward, R. J.; Prade, R. A.; Buckeridge, M. S.; de Moraes, M. de L. T. A Highly Glucose Tolerant SS-Glucosidase from Malbranchea Pulchella (Mp Bg3) Enables Cellulose Saccharification. *Sci Rep* **2020**, *10* (1), 1–12.

(54) Caramia, S.; Gatius, A. G. M.; Dal Piaz, F.; Gaja, D.; Hochkoeppler, A. Dual Role of Imidazole as Activator/Inhibitor of Sweet Almond (Prunus Dulcis) β-Glucosidase. *Biochem Biophys Rep* **2017**, *10*, 137–144.

(55) Fernandez-Lafuente, R. Stabilization of Multimeric Enzymes: Strategies to Prevent Subunit Dissociation. *Enzyme Microb Technol* **2009**, *45* (6–7), 405–418.

(56) Vazquez-Ortega, P. G.; Alcaraz-Fructuoso, M. T.; Rojas-Contreras, J. A.; López-Miranda, J.; Fernandez-Lafuente, R. Stabilization of Dimeric β-Glucosidase from Aspergillus Niger via Glutaraldehyde Immobilization under Different Conditions. *Enzyme Microb Technol* **2018**, *110*, 38–45.

(57) Benjwal, S.; Verma, S.; Röhm, K.; Gursky, O. Monitoring Protein Aggregation during Thermal Unfolding in Circular Dichroism Experiments. *Protein Science* **2006**, *15* (3), 635–639.

(58) Perez-Pons, J. A.; Padros, E.; Querol, E. Prediction and Fourier-Transform Infrared-Spectroscopy Estimation of the Secondary Structure of a Recombinant β-Glucosidase from Streptomyces Sp.(ATCC 11238). *Biochemical Journal* **1995**, *308* (3), 791–794.

(59) Pota, G.; Sapienza Salerno, A.; Costantini, A.; Silvestri, B.; Passaro, J.; Califano, V. Co-Immobilization of Cellulase and β-Glucosidase into Mesoporous Silica Nanoparticles for the Hydrolysis of Cellulose Extracted from Eriobotrya Japonica Leaves. *Langmuir* **2022**, *38* (18), 5481–5493.

(60) Catapano, F.; Di Iorio, S.; Magno, A.; Sementa, P.; Vaglieco, B. M. A Comprehensive Analysis of the Effect of Ethanol, Methane and Methane-Hydrogen Blend on the Combustion Process in a PFI (Port Fuel Injection) Engine. *Energy* **2015**, *88*, 101–110.

(61) Catapano, F.; Di Iorio, S.; Luise, L.; Sementa, P.; Vaglieco, B. M. Influence of Ethanol Blended and Dual Fueled with Gasoline on Soot Formation and Particulate Matter Emissions in a Small Displacement Spark Ignition Engine. *Fuel* **2019**, *245*, 253–262.

(62) Califano, V.; Costantini, A. Immobilization of Cellulolytic Enzymes in Mesostructured Silica Materials. *Catalysts* **2020**, *10* (6), 706.

(63) Cherubini, F. The Biorefinery Concept: Using Biomass Instead of Oil for Producing Energy and Chemicals. *Energy Convers Manag* **2010**, *51* (7), 1412–1421.

(64) Venturi, P.; Venturi, G. Analysis of Energy Comparison for Crops in European Agricultural Systems. *Biomass Bioenergy* **2003**, *25* (3), 235–255.

(65) Laureano-Perez, L.; Teymouri, F.; Alizadeh, H.; Dale, B. E. Understanding Factors That Limit Enzymatic Hydrolysis of Biomass. *Appl Biochem Biotechnol* **2005**, *124* (1), 1081–1099.

(66) Avgerinos, G. C.; Wang, D. C. Selective Solvent Delignification for Fermentation Enhancement. *Biotechnol Bioeng* **1983**, *25* (1), 67–83.

(67) Chang, V. S.; Holtzapple, M. T. Fundamental Factors Affecting Biomass Enzymatic Reactivity. In *Twenty-first symposium on biotechnology for fuels and chemicals*; Springer, 2000; pp 5–37.

(68) Alvira, P.; Tomás-Pejó, E.; Ballesteros, M.; Negro, M. J. Pretreatment Technologies for an Efficient Bioethanol Production Process Based on Enzymatic Hydrolysis: A Review. *Bioresour Technol* **2010**, *101* (13), 4851–4861.

(69) Mafa, M.; Malgas, S.; Bhattacharya, A.; Rashamuse, K.; Pletschke, B. I. The Effects of Alkaline Pretreatment on Agricultural Biomasses (Corn Cob and Sweet Sorghum Bagasse) and Their Hydrolysis by a Termite-Derived Enzyme Cocktail. *Agronomy* **2020**, *10* (8), 1211.

(70) Srivastava, N.; Srivastava, M.; Mishra, P. K.; Gupta, V. K.; Molina, G.; Rodriguez-Couto, S.; Manikanta, A.; Ramteke, P. W. Applications of Fungal Cellulases in Biofuel Production: Advances and Limitations. *Renewable and Sustainable Energy Reviews* **2018**, *82*, 2379–2386.

(71) Garcia-Galan, C.; Berenguer-Murcia, Á.; Fernandez-Lafuente, R.; Rodrigues, R. C. Potential of Different Enzyme Immobilization Strategies to Improve Enzyme Performance. *Adv Synth Catal* **2011**, *353* (16), 2885–2904.

(72) Mateo, C.; Palomo, J. M.; Fernandez-Lorente, G.; Guisan, J. M.; Fernandez-Lafuente, R. Improvement of Enzyme Activity, Stability and Selectivity via Immobilization Techniques. *Enzyme Microb Technol* **2007**, *40* (6), 1451–1463.

(73) Rodrigues, R. C.; Berenguer-Murcia, Á.; Carballares, D.; Morellon-Sterling, R.; Fernandez-Lafuente, R. Stabilization of Enzymes via Immobilization: Multipoint Covalent Attachment and Other Stabilization Strategies. *Biotechnol Adv* **2021**, *52*, 107821.

(74) Rodrigues, R. C.; Ortiz, C.; Berenguer-Murcia, Á.; Torres, R.; Fernández-Lafuente, R. Modifying Enzyme Activity and Selectivity by Immobilization. *Chem Soc Rev* **2013**, *42* (15), 6290–6307.

(75) de Oliveira, J. A. R.; da Silva Martins, L. H.; Penteado, E. D.; Kuila, A.; Komesu, A. Microbial Cellulase for the Conversion of Lignocellulosic

Biomass. In *Current Status and Future Scope of Microbial Cellulases*; Elsevier, 2021; pp 59–83.

(76) Hirsh, S. L.; Bilek, M. M. M.; Nosworthy, N. J.; Kondyurin, A.; Dos Remedios, C. G.; McKenzie, D. R. A Comparison of Covalent Immobilization and Physical Adsorption of a Cellulase Enzyme Mixture. *Langmuir* **2010**, *26* (17), 14380–14388.

(77) Han, J.; Luo, P.; Wang, Y.; Wang, L.; Li, C.; Zhang, W.; Dong, J.; Ni, L. The Development of Nanobiocatalysis via the Immobilization of Cellulase on Composite Magnetic Nanomaterial for Enhanced Loading Capacity and Catalytic Activity. *Int J Biol Macromol* **2018**, *119*, 692–700.

(78) Kudina, O.; Zakharchenko, A.; Trotsenko, O.; Tokarev, A.; Ionov, L.; Stoychev, G.; Puretskiy, N.; Pryor, S. W.; Voronov, A.; Minko, S. Highly Efficient Phase Boundary Biocatalysis with Enzymogel Nanoparticles. *Angewandte Chemie* **2014**, *126* (2), 493–497.

(79) Wang, G.; Zhang, K.; Xin, J.-Y.; Zhao, C.-W.; Ma, Y.-H.; Yang, W.-T. Facile Construction of Synergistic β-Glucosidase and Cellulase Sequential Co-Immobilization System for Enhanced Biomass Conversion. *Chinese Journal of Polymer Science* **2020**, *38*, 1277–1285.

(80) Limadinata, P. A.; Li, A.; Li, Z. Temperature-Responsive Nanobiocatalysts with an Upper Critical Solution Temperature for High Performance Biotransformation and Easy Catalyst Recycling: Efficient Hydrolysis of Cellulose to Glucose. *Green Chemistry* **2015**, *17* (2), 1194–1203.

(81) He, B.; Chang, P.; Zhu, X.; Zhang, S. Anemone-Inspired Enzymatic Film for Cellulose Heterogeneous Catalysis. *Carbohydr Polym* **2021**, *260*, 117795.

(82) Bayramoglu, G.; Senkal, B. F.; Arica, M. Y. Preparation of Clay–Poly (Glycidyl Methacrylate) Composite Support for Immobilization of Cellulase. *Appl Clay Sci* **2013**, *85*, 88–95.

(83) Lynd, L. R.; Weimer, P. J.; Van Zyl, W. H.; Pretorius, I. S. Microbial Cellulose Utilization: Fundamentals and Biotechnology. *Microbiology and molecular biology reviews* **2002**, *66* (3), 506–577.

(84) Sternberg, D.; Mandels, G. R. Regulation of the Cellulolytic System in Trichoderma Reesei by Sophorose: Induction of Cellulase and Repression of Beta-Glucosidase. *J Bacteriol* **1980**, *144* (3), 1197–1199.

(85) Chakrabarti, A. C.; Storey, K. B. Enhanced Glucose Production from Cellulose Using Coimmobilized Cellulase and β-Glucosidase. *Appl Biochem Biotechnol* **1989**, *22* (3), 263–278.

(86) Liu, J.; Cao, X. Biodegradation of Cellulose by β-Glucosidase and Cellulase Immobilized on a PH-Responsive Copolymer. *Biotechnology and bioprocess engineering* **2014**, *19* (5), 829–837.

(87) Wang, Y.; Qi, Y.; Chen, C.; Zhao, C.; Ma, Y.; Yang, W. Layered Co-Immobilization of β-Glucosidase and Cellulase on Polymer Film by Visible-Light-Induced Graft Polymerization. *ACS Appl Mater Interfaces* **2019**, *11* (47), 44913–44921.

(88) Jesionowski, T.; Zdarta, J.; Krajewska, B. Enzyme Immobilization by Adsorption: A Review. *Adsorption* **2014**, *20* (5–6), 801–821.

(89) Zdarta, J.; Meyer, A. S.; Jesionowski, T.; Pinelo, M. Multi-Faceted Strategy Based on Enzyme Immobilization with Reactant Adsorption and Membrane Technology for Biocatalytic Removal of Pollutants: A Critical Review. *Biotechnol Adv* **2019**, *37* (7), 107401.

(90) Zdarta, J.; Antecka, K.; Frankowski, R.; Zgoła-Grześkowiak, A.; Ehrlich, H.; Jesionowski, T. The Effect of Operational Parameters on the Biodegradation of Bisphenols by Trametes Versicolor Laccase Immobilized on Hippospongia Communis Spongin Scaffolds. *Science of the Total Environment* **2018**, *615*, 784–795.

(91) Zdarta, J.; Meyer, A. S.; Jesionowski, T.; Pinelo, M. Developments in Support Materials for Immobilization of Oxidoreductases: A Comprehensive Review. *Adv Colloid Interface Sci* **2018**, *258*, 1–20.

(92) Luciani, G.; Costantini, A.; Silvestri, B.; Tescione, F.; Branda, F.; Pezzella, A. Synthesis, Structure and Bioactivity of PHEMA/SiO 2 Hybrids Derived through in Situ Sol–Gel Process. *J Solgel Sci Technol* **2008**, *46* (2), 166–175.

(93) Bifulco, A.; Marotta, A.; Passaro, J.; Costantini, A.; Cerruti, P.; Gentile, G.; Ambrogi, V.; Malucelli, G.; Branda, F. Thermal and Fire Behavior of a Bio-Based Epoxy/Silica Hybrid Cured with Methyl Nadic Anhydride. *Polymers (Basel)* **2020**, *12* (8), 1661.

(94) Zhou, Z.; Hartmann, M. Progress in Enzyme Immobilization in Ordered Mesoporous Materials and Related Applications. *Chem Soc Rev* **2013**, *42* (9), 3894–3912.

(95) Talbert, J. N.; Goddard, J. M. Enzymes on Material Surfaces. *Colloids Surf B Biointerfaces* **2012**, *93*, 8–19.

(96) Takimoto, A.; Shiomi, T.; Ino, K.; Tsunoda, T.; Kawai, A.; Mizukami, F.; Sakaguchi, K. Encapsulation of Cellulase with Mesoporous Silica (SBA-15). **2008**. https://doi.org/10.1016/j.micromeso.2008.05.046.

(97) Hartono, S. B.; Qiao, S. Z.; Liu, J.; Jack, K.; Ladewig, B. P.; Hao, Z.; Lu, G. Q. M. Functionalized Mesoporous Silica with Very Large Pores for Cellulase Immobilization. *The Journal of Physical Chemistry C* **2010**, *114* (18), 8353–8362.

(98) Chang, R. H.-Y.; Jang, J.; Wu, K. C.-W. Cellulase Immobilized Mesoporous Silica Nanocatalysts for Efficient Cellulose-to-Glucose Conversion. *Green Chemistry* **2011**, *13* (10), 2844–2850.

(99) Dadi, A. P.; Varanasi, S.; Schall, C. A. Enhancement of Cellulose Saccharification Kinetics Using an Ionic Liquid Pretreatment Step. *Biotechnol Bioeng* **2006**, *95* (5), 904–910.

(100) Costantini, A.; Venezia, V.; Pota, G.; Bifulco, A.; Califano, V.; Sannino, F. Adsorption of Cellulase on Wrinkled Silica Nanoparticles with Enhanced Inter-Wrinkle Distance. *Nanomaterials* **2020**, *10* (9). https://doi.org/10.3390/nano10091799.

(101) Califano, V.; Sannino, F.; Costantini, A.; Avossa, J.; Cimino, S.; Aronne, A. Wrinkled Silica Nanoparticles: Efficient Matrix for β-Glucosidase Immobilization. *The Journal of Physical Chemistry C* **2018**, *122* (15), 8373–8379.

(102) Sannino, F.; Costantini, A.; Ruffo, F.; Aronne, A.; Venezia, V.; Califano, V. Covalent Immobilization of β-Glucosidase into Mesoporous Silica Nanoparticles from Anhydrous Acetone Enhances Its Catalytic Performance. *Nanomaterials* **2020**, *10* (1), 108.

(103) Siqueira, G.; Abdillahi, H.; Bras, J.; Dufresne, A. High Reinforcing Capability Cellulose Nanocrystals Extracted from Syngonanthus Nitens (Capim Dourado). *Cellulose* **2010**, *17* (2), 289–298. https://doi.org/10.1007/s10570-009-9384-z.

(104) Moon, D.-S.; Lee, J.-K. Tunable Synthesis of Hierarchical Mesoporous Silica Nanoparticles with Radial Wrinkle Structure. *Langmuir* **2012**, *28* (33), 12341–12347.

(105) Venezia, V.; Costantini, A.; Landi, G.; Di Benedetto, A.; Sannino, F.; Califano, V. Immobilization of β-Glucosidase over Structured Cordierite Monoliths Washcoated with Wrinkled Silica Nanoparticles. *Catalysts* **2020**, *10* (8), 889.

(106) Hernández, F.; Madrid, J.; Cerón, J. J.; Pulgar, M. A.; Cid, J. M. Utilisation of Lemon (Citrus Limon) and Loquat (Eribotrya Japonica) Tree Leaves Alone or with NH3-Treated Straw for Goats. *J Sci Food Agric* **1998**, *77* (1), 133–139. https://doi.org/10.1002/(SICI)1097-0010(199805)77:1<133::AID-JSFA12>3.0.CO;2-U.

(107) Boudrant, J.; Woodley, J. M.; Fernandez-Lafuente, R. Parameters Necessary to Define an Immobilized Enzyme Preparation. *Process Biochemistry* **2020**, *90* (November 2019), 66–80. https://doi.org/10.1016/j.procbio.2019.11.026.

(108) Bergmeyer, H. U.; Bernt, E. UV-Assay with Pyruvate and NADH. In *Methods of enzymatic analysis*; Elsevier, 1974; pp 574–579.

(109) Isogai, A.; Usuda, M.; Kato, T.; Uryu, T.; Atalla, R. H. Solid-State CP/MAS Carbon-13 NMR Study of Cellulose Polymorphs. *Macromolecules* **1989**, *22* (7), 3168–3172.

(110) Gautam, S. P.; Bundela, P. S.; Pandey, A. K.; Jamaluddin, J.; Awasthi, M. K.; Sarsaiya, S. A Review on Systematic Study of Cellulose. *Journal of Applied and Natural Science* **2010**, *2* (2), 330–343.

(111) Avci, A.; Saha, B. C.; Dien, B. S.; Kennedy, G. J.; Cotta, M. A. Response Surface Optimization of Corn Stover Pretreatment Using Dilute Phosphoric Acid for Enzymatic Hydrolysis and Ethanol Production. *Bioresour Technol* **2013**, *130*, 603–612.

(112) Mishra, V.; Jana, A. K. Sweet Sorghum Bagasse Pretreatment by Coriolus Versicolor in Mesh Tray Bioreactor for Selective Delignification and Improved Saccharification. *Waste Biomass Valorization* **2019**, *10* (9), 2689–2702.

(113) Sun, Y.; Cheng, J. Hydrolysis of Lignocellulosic Materials for Ethanol Production: A Review. *Bioresour Technol* **2002**, *83* (1), 1–11.

(114) Fitriana, N. E.; Suwanto, A.; Jatmiko, T. H.; Mursiti, S.; Prasetyo, D. J. Cellulose Extraction from Sugar Palm (Arenga Pinnata) Fibre by Alkaline and Peroxide Treatments. In *IOP Conference Series: Earth and Environmental Science*; IOP Publishing, 2020; Vol. 462, p 12053.

(115) Iravani, S.; Varma, R. S. Greener Synthesis of Lignin Nanoparticles and Their Applications. *Green Chemistry* **2020**, *22* (3), 612–636. https://doi.org/10.1039/c9gc02835h.

(116) Cheng, S.; Huang, A.; Wang, S.; Zhang, Q. Effect of Different Heat Treatment Temperatures on the Chemical Composition and Structure of Chinese Fir Wood. *Bioresources* **2016**, *11* (2), 4006–4016.

(117) Hongxia, B.; Yang, Y.; Tu, P. Crystalline Structure Analysis of All-Cellulose Nanocomposites Films Based on Corn and Wheat Straw. *Bioresources* **2021**, *16* (4), 8353–8365.

(118) Yang, Y. P.; Zhang, Y.; Lang, Y. X.; Yu, M. H. Structural ATR-IR Analysis of Cellulose Fibers Prepared from a NaOH Complex Aqueous

Solution. In *IOP conference series: materials science and engineering*; IOP Publishing, 2017; Vol. 213, p 12039.

(119) Saha, B. C. Hemicellulose Bioconversion. *J Ind Microbiol Biotechnol* **2003**, *30* (5), 279–291.

(120) Mohan, J. C.; Praveen, G.; Chennazhi, K. P.; Jayakumar, R.; Nair, S. V. Functionalised Gold Nanoparticles for Selective Induction of in Vitro Apoptosis among Human Cancer Cell Lines. *J Exp Nanosci* **2013**, *8* (1), 32–45.

(121) Singhania, R. R.; Patel, A. K.; Sukumaran, R. K.; Larroche, C.; Pandey, A. Role and Significance of Beta-Glucosidases in the Hydrolysis of Cellulose for Bioethanol Production. *Bioresour Technol* **2013**, *127*, 500–507.

(122) Ng, I.-S.; Tsai, S.-W.; Ju, Y.-M.; Yu, S.-M.; Ho, T. D. Dynamic Synergistic Effect on Trichoderma Reesei Cellulases by Novel β-Glucosidases from Taiwanese Fungi. *Bioresour Technol* **2011**, *102* (10), 6073–6081.

(123) Teugjas, H.; Väljamäe, P. Selecting β-Glucosidases to Support Cellulases in Cellulose Saccharification. *Biotechnol Biofuels* **2013**, *6* (1), 1–13.

(124) Pallapolu, V. R.; Lee, Y. Y.; Garlock, R. J.; Balan, V.; Dale, B. E.; Kim, Y.; Mosier, N. S.; Ladisch, M. R.; Falls, M.; Holtzapple, M. T. Effects of Enzyme Loading and β-Glucosidase Supplementation on Enzymatic Hydrolysis of Switchgrass Processed by Leading Pretreatment Technologies. *Bioresour Technol* **2011**, *102* (24), 11115–11120.

(125) Borges, D. G.; Junior, A. B.; Farinas, C. S.; Giordano, R. de L. C.; Tardioli, P. W. Enhanced Saccharification of Sugarcane Bagasse Using Soluble Cellulase Supplemented with Immobilized β-Glucosidase. *Bioresour Technol* **2014**, *167*, 206–213.

(126) Zhang, Z.; Wang, M.; Gao, R.; Yu, X.; Chen, G. Synergistic Effect of Thermostable β-Glucosidase TN0602 and Cellulase on Cellulose Hydrolysis. *3 Biotech* **2017**, *7* (1), 1–7. https://doi.org/10.1007/s13205-017-0672-2.

(127) Saha, B. C.; Bothast, R. J. Production, Purification, and Characterization of a Highly Glucose- Tolerant Novel β-Glucosidase from Candida Peltata. *Appl Environ Microbiol* **1996**, *62* (9), 3165–3170. https://doi.org/10.1128/aem.62.9.3165-3170.1996.

(128) Qi, B.; Chen, X.; Su, Y.; Wan, Y. Enzyme Adsorption and Recycling during Hydrolysis of Wheat Straw Lignocellulose. *Bioresour Technol* **2011**, *102* (3), 2881–2889.

(129) Silvestri, B.; Luciani, G.; Costantini, A.; Tescione, F.; Branda, F.; Pezzella, A. In-Situ Sol-Gel Synthesis and Characterization of Bioactive

PHEMA/SiO 2 Blend Hybrids. *J Biomed Mater Res B Appl Biomater* **2009**, *89* (2), 369–378. https://doi.org/10.1002/jbm.b.31225.

(130) Barth, A. Infrared Spectroscopy of Proteins. *Biochimica et Biophysica Acta (BBA)-Bioenergetics* **2007**, *1767* (9), 1073–1101.

(131) Kong, J.; Yu, S. Fourier Transform Infrared Spectroscopic Analysis of Protein Secondary Structures. *Acta Biochim Biophys Sin (Shanghai)* **2007**, *39* (8), 549–559.

(132) Gómez, J. M.; Romero, M. D.; Fernández, T. M.; García, S. Immobilization and Enzymatic Activity of β-Glucosidase on Mesoporous SBA-15 Silica. *Journal of Porous Materials* **2010**, *17* (6), 657–662. https://doi.org/10.1007/s10934-009-9335-y.

(133) Sprey, B. Complexity of Cellulases from Trichoderma Reesei with Acidic Isoelectric Points: A Two-Dimensional Gel Electrophoretic Study Using Immunoblotting. *FEMS Microbiol Lett* **1987**, *43* (1), 25–32.

(134) Zhang, D.; Hegab, H. E.; Lvov, Y.; Snow, L. D.; Palmer, J. Immobilization of Cellulase on a Silica Gel Substrate Modified Using a 3-APTES Self-Assembled Monolayer. *Springerplus* **2016**, *5* (1), 1–20.

(135) Arana-Peña, S.; Carballares, D.; Morellon-Sterlling, R.; Berenguer-Murcia, Á.; Alcántara, A. R.; Rodrigues, R. C.; Fernandez-Lafuente, R. Enzyme Co-Immobilization: Always the Biocatalyst Designers' Choice… or Not? *Biotechnol Adv* **2020**, 107584.

(136) Carli, S.; de Campos Carneiro, L. A. B.; Ward, R. J.; Meleiro, L. P. Immobilization of a β-Glucosidase and an Endoglucanase in Ferromagnetic Nanoparticles: A Study of Synergistic Effects. *Protein Expr Purif* **2019**, *160*, 28–35.

(137) Song, Q.; Mao, Y.; Wilkins, M.; Segato, F.; Prade, R. Cellulase Immobilization on Superparamagnetic Nanoparticles for Reuse in Cellulosic Biomass Conversion. *AIMS Bioeng* **2016**, *3* (3), 264–276.

(138) Sprey, B.; Lambert, C. Titration Curves of Cellulases from Trichoderma Reesei: Demonstration of a Cellulase-Xylanase-β-Glucosidase-Containing Complex. *FEMS Microbiol Lett* **1983**, *18* (3), 217–222.

(139) Califano, V.; Costantini, A.; Silvestri, B.; Venezia, V.; Cimino, S.; Sannino, F. The Effect of Pore Morphology on the Catalytic Performance of β-Glucosidase Immobilized into Mesoporous Silica. *Pure and Applied Chemistry* **2019**, *91* (10), 1583–1592.

(140) Verma, M. L.; Rajkhowa, R.; Wang, X.; Barrow, C. J.; Puri, M. Exploring Novel Ultrafine Eri Silk Bioscaffold for Enzyme Stabilisation in Cellobiose Hydrolysis. *Bioresour Technol* **2013**, *145*, 302–306.

(141) Figueira, J. A.; Sato, H. H.; Fernandes, P. Establishing the Feasibility of Using β-Glucosidase Entrapped in Lentikats and in Sol–Gel Supports for Cellobiose Hydrolysis. *J Agric Food Chem* **2013**, *61* (3), 626–634.

(142) Tran, D.N.; Balkus, K. J. Perspective of Recent Progress in Immobilization of Enzymes. *ACS Catal* **2011**, *1*, 956–968.

(143) Di Iorio, S.; Magno, A.; Mancaruso, E.; Vaglieco, B. M.; Arnone, L.; Dal Bello, L. *Engine Performance and Emissions of a Small Diesel Engine Fueled with Various Diesel/RME Blends*; SAE Technical Paper, 2014.

(144) Sarno, M.; Iuliano, M. Highly Active and Stable Fe3O4/Au Nanoparticles Supporting Lipase Catalyst for Biodiesel Production from Waste Tomato. *Appl Surf Sci* **2019**, *474*, 135–146.

(145) Babaki, M.; Yousefi, M.; Habibi, Z.; Mohammadi, M.; Yousefi, P.; Mohammadi, J.; Brask, J. Enzymatic Production of Biodiesel Using Lipases Immobilized on Silica Nanoparticles as Highly Reusable Biocatalysts: Effect of Water, t-Butanol and Blue Silica Gel Contents. *Renew Energy* **2016**, *91*, 196–206.

(146) Babaki, M.; Yousefi, M.; Habibi, Z.; Mohammadi, M.; Brask, J. Effect of Water, Organic Solvent and Adsorbent Contents on Production of Biodiesel Fuel from Canola Oil Catalyzed by Various Lipases Immobilized on Epoxy-Functionalized Silica as Low Cost Biocatalyst. *J Mol Catal B Enzym* **2015**, *120*, 93–99.

(147) Liang, X. Synthesis of Biodiesel from Waste Oil under Mild Conditions Using Novel Acidic Ionic Liquid Immobilization on Poly Divinylbenzene. *Energy* **2013**, *63*, 103–108.

(148) Fang, X.; Zhao, X.; Fang, W.; Chen, C.; Zheng, N. Self-Templating Synthesis of Hollow Mesoporous Silica and Their Applications in Catalysis and Drug Delivery. *Nanoscale* **2013**, *5* (6), 2205–2218.

(149) Poppe, J. K.; Fernandez-Lafuente, R.; Rodrigues, R. C.; Ayub, M. A. Z. Enzymatic Reactors for Biodiesel Synthesis: Present Status and Future Prospects. *Biotechnol Adv* **2015**, *33* (5), 511–525.

(150) Arana-Peña, S.; Carballares, D.; Berenguer-Murcia, Á.; Alcántara, A. R.; Rodrigues, R. C.; Fernandez-Lafuente, R. One Pot Use of Combilipases for Full Modification of Oils and Fats: Multifunctional and Heterogeneous Substrates. *Catalysts* **2020**, *10* (6), 605.

(151) Mateo, C.; Palomo, J. M.; Fernandez-lorente, G.; Guisan, J. M.; Fernandez-lafuente, R. Improvement of Enzyme Activity , Stability and Selectivity via Immobilization Techniques Improvement of Enzyme Activity , Stability and Selectivity via Immobilization Techniques. **2007**, No. May. https://doi.org/10.1016/j.enzmictec.2007.01.018.

(152) NOUROUZIAN, D. Enzyme Immobilization: The State of Art in Biotechnology. **2003**.

(153) Cipolatti, E. P.; Manoel, E. A.; Fernandez-Lafuente, R.; Freire, D. M. G. Support Engineering: Relation between Development of New Supports for Immobilization of Lipases and Their Applications. *Biotechnology Research and Innovation* **2017**, *1* (1), 26–34.

(154) Silvestri, B.; Pezzella, A.; Luciani, G.; Costantini, A.; Tescione, F.; Branda, F. Heparin Conjugated Silica Nanoparticle Synthesis. *Materials Science and Engineering: C* **2012**, *32* (7), 2037–2041.

(155) Zou, B.; Song, C.; Xu, X.; Xia, J.; Huo, S.; Cui, F. Enhancing Stabilities of Lipase by Enzyme Aggregate Coating Immobilized onto Ionic Liquid Modified Mesoporous Materials. *Appl Surf Sci* **2014**, *311*, 62–67.

(156) Sannino, F.; Ruocco, S.; Marocco, A.; Esposito, S.; Pansini, M. Simazine Removal from Waters by Adsorption on Porous Silicas Tailored by Sol–Gel Technique. *Microporous and mesoporous materials* **2013**, *180*, 178–186.

(157) Branda, F.; Bifulco, A.; Jehnichen, D.; Parida, D.; Pauer, R.; Passaro, J.; Gaan, S.; Pospiech, D.; Durante, M. Structure and Bottom-up Formation Mechanism of Multisheet Silica-Based Nanoparticles Formed in an Epoxy Matrix through an In Situ Process. *Langmuir* **2021**, *37* (29), 8886–8893.

(158) Bifulco, A.; Tescione, F.; Capasso, A.; Mazzei, P.; Piccolo, A.; Durante, M.; Lavorgna, M.; Malucelli, G.; Branda, F. Effects of Post Cure Treatment in the Glass Transformation Range on the Structure and Fire Behavior of in Situ Generated Silica/Epoxy Hybrids. *J Solgel Sci Technol* **2018**, *87* (1), 156–169.

(159) Wang, Y.; Du, X.; Liu, Z.; Shi, S.; Lv, H. Dendritic Fibrous Nano-Particles (DFNPs): Rising Stars of Mesoporous Materials. *J Mater Chem A Mater* **2019**, *7* (10), 5111–5152.

(160) Venezia, V.; Sannino, F.; Costantini, A.; Silvestri, B.; Cimino, S.; Califano, V. Mesoporous Silica Nanoparticles for β-Glucosidase Immobilization by Templating with a Green Material: Tannic Acid. *Microporous and Mesoporous Materials* **2020**, *302*, 110203.

(161) Pang, J.; Zhou, G.; Liu, R.; Li, T. Esterification of Oleic Acid with Methanol by Immobilized Lipase on Wrinkled Silica Nanoparticles with Highly Ordered, Radially Oriented Mesochannels. *Materials Science and Engineering: C* **2016**, *59*, 35–42.

(162) Pang, J.; Zhou, G.; Liu, R.; Li, T. Esterification of Oleic Acid with Methanol by Immobilized Lipase on Wrinkled Silica Nanoparticles with

Highly Ordered, Radially Oriented Mesochannels. *Materials Science and Engineering: C* **2016**, *59*, 35–42.

(163) Kalantari, M.; Yu, M.; Liu, Y.; Huang, X.; Yu, C. Engineering Mesoporous Silica Microspheres as Hyper-Activation Supports for Continuous Enzymatic Biodiesel Production. *Mater Chem Front* **2019**, *3* (9), 1816–1822.

(164) Grochulski, P.; Li, Y.; Schrag, J. D.; Cygler, M. Two Conformational States of Candida Rugosa Lipase. *Protein Science* **1994**, *3* (1), 82–91.

(165) Manoel, E. A.; Dos Santos, J. C. S.; Freire, D. M. G.; Rueda, N.; Fernandez-Lafuente, R. Immobilization of Lipases on Hydrophobic Supports Involves the Open Form of the Enzyme. *Enzyme Microb Technol* **2015**, *71*, 53–57.

(166) Knežević, Z. D.; Šiler-Marinković, S. S.; Mojović, L. V. Immobilized Lipases as Practical Catalysts. *Acta periodica technologica* **2004**, No. 35, 151–164.

(167) Fernandez-Lafuente, R.; Armisén, P.; Sabuquillo, P.; Fernández-Lorente, G.; Guisán, J. M. Immobilization of Lipases by Selective Adsorption on Hydrophobic Supports. *Chem Phys Lipids* **1998**, *93* (1–2), 185–197.

(168) Palomo, J. M.; Muñoz, G.; Fernández-Lorente, G.; Mateo, C.; Fernández-Lafuente, R.; Guisán, J. M. Interfacial Adsorption of Lipases on Very Hydrophobic Support (Octadecyl–Sepabeads): Immobilization, Hyperactivation and Stabilization of the Open Form of Lipases. *J Mol Catal B Enzym* **2002**, *19*, 279–286.

(169) Zhuang, W.; Gu, W.; Zhu, Q.; Zhu, J.; Wang, Z.; Niu, H.; Liu, D.; Wu, J.; Chen, Y.; Li, M. Surface Functionalization of Graphene Oxide by Disodium Guanosine 5′-Monophosphate and Its Excellent Performance for Lipase Immobilization. *Appl Surf Sci* **2019**, *492*, 27–36.

(170) Dossat, V.; Combes, D.; Marty, A. Continuous Enzymatic Transesterification of High Oleic Sunflower Oil in a Packed Bed Reactor: Influence of the Glycerol Production. *Enzyme Microb Technol* **1999**, *25* (3–5), 194–200.

(171) Martins, A. B.; Schein, M. F.; Friedrich, J. L. R.; Fernandez-Lafuente, R.; Ayub, M. A. Z.; Rodrigues, R. C. Ultrasound-Assisted Butyl Acetate Synthesis Catalyzed by Novozym 435: Enhanced Activity and Operational Stability. *Ultrason Sonochem* **2013**, *20* (5), 1155–1160.

(172) Rodrigues, R. C.; Virgen-Ortíz, J. J.; Dos Santos, J. C. S.; Berenguer-Murcia, Á.; Alcantara, A. R.; Barbosa, O.; Ortiz, C.; Fernandez-Lafuente, R. Immobilization of Lipases on Hydrophobic Supports: Immobilization

Mechanism, Advantages, Problems, and Solutions. *Biotechnol Adv* **2019**, *37* (5), 746–770.

(173) Séverac, E.; Galy, O.; Turon, F.; Pantel, C. A.; Condoret, J.-S.; Monsan, P.; Marty, A. Selection of CalB Immobilization Method to Be Used in Continuous Oil Transesterification: Analysis of the Economical Impact. *Enzyme Microb Technol* **2011**, *48* (1), 61–70.

(174) Paludo, N.; Alves, J. S.; Altmann, C.; Ayub, M. A. Z.; Fernandez-Lafuente, R.; Rodrigues, R. C. The Combined Use of Ultrasound and Molecular Sieves Improves the Synthesis of Ethyl Butyrate Catalyzed by Immobilized Thermomyces Lanuginosus Lipase. *Ultrason Sonochem* **2015**, *22*, 89–94.

(175) Califano, V.; Bloisi, F.; Perretta, G.; Aronne, A.; Ausanio, G.; Costantini, A.; Vicari, L. Frozen Microemulsions for MAPLE Immobilization of Lipase. *Molecules* **2017**, *22* (12), 2153.

(176) Wongwatanapaiboon, J.; Malilas, W.; Ruangchainikom, C.; Thummadetsak, G.; Chulalaksananukul, S.; Marty, A.; Chulalaksananukul, W. Overexpression of Fusarium Solani Lipase in Pichia Pastoris and Its Application in Lipid Degradation. *Biotechnology & Biotechnological Equipment* **2016**, *30* (5), 885–893.

(177) Lokha, Y.; Arana-Peña, S.; Rios, N. S.; Mendez-Sanchez, C.; Gonçalves, L. R. B.; Lopez-Gallego, F.; Fernandez-Lafuente, R. Modulating the Properties of the Lipase from Thermomyces Lanuginosus Immobilized on Octyl Agarose Beads by Altering the Immobilization Conditions. *Enzyme Microb Technol* **2020**, *133*, 109461.

(178) Arana-Peña, S.; Rios, N. S.; Carballares, D.; Mendez-Sanchez, C.; Lokha, Y.; Gonçalves, L. R. B.; Fernandez-Lafuente, R. Effects of Enzyme Loading and Immobilization Conditions on the Catalytic Features of Lipase from Pseudomonas Fluorescens Immobilized on Octyl-Agarose Beads. *Front Bioeng Biotechnol* **2020**, *8*, 36.

(179) Arana-Peña, S.; Rios, N. S.; Carballares, D.; Goncalves, L. R. B.; Fernandez-Lafuente, R. Immobilization of Lipases via Interfacial Activation on Hydrophobic Supports: Production of Biocatalysts Libraries by Altering the Immobilization Conditions. *Catal Today* **2021**, *362*, 130–140.

(180) Alimentarius, C. Codex Standard for Named Vegetable Oils. *Codex stan* **1999**, *210*, 1–13.

(181) Eral, H. B.; Oh, J. M. Contact Angle Hysteresis: A Review of Fundamentals and Applications. *Colloid Polym Sci* **2013**, *291* (2), 247–260.

(182) Owens, D. K. Some Thermodynamic Aspects of Polymer Adhesion. *J Appl Polym Sci* **1970**, *14* (7), 1725–1730.

(183) Stojanovic, A.; Comesaña, S. P.; Rentsch, D.; Koebel, M. M.; Malfait, W. J. Ambient Pressure Drying of Silica Aerogels after Hydrophobization with Mono-, Di-and Tri-Functional Silanes and Mixtures Thereof. *Microporous and Mesoporous Materials* **2019**, *284*, 289–295.

(184) Kota, A. K.; Kwon, G.; Tuteja, A. The Design and Applications of Superomniphobic Surfaces. *NPG Asia Mater* **2014**, *6* (7), e109–e109.

(185) Parida, D.; Jassal, M.; Agarwal, A. K. Functionalization of Cotton by In-Situ Reaction of Styrene in Atmospheric Pressure Plasma Zone. *Plasma Chemistry and Plasma Processing* **2012**, *32* (6), 1259–1274.

(186) Jiang, S.; Chen, Q.; Tripathy, M.; Luijten, E.; Schweizer, K. S.; Granick, S. Janus Particle Synthesis and Assembly. *Advanced materials* **2010**, *22* (10), 1060–1071.

(187) Fowkes, F. M. Attractive Forces at Interfaces. *Ind Eng Chem* **1964**, *56* (12), 40–52.

(188) Fowkes, F. Determination of Intermolecular Forces by Surface-Chemical Techniques. In *Adhesion*; ASTM International, 1964.

(189) Owens, D. K.; Wendt, R. C. Estimation of the Surface Free Energy of Polymers. *J Appl Polym Sci* **1969**, *13* (8), 1741–1747.

(190) Chibowski, E. J. Surface Free Energy and Wettability of Silyl Layers on Silicon Determined from Contact Angle Hysteresis. *Adv Colloid Interface Sci* **2005**, *113* (2–3), 121–131.

(191) Palomo, J. M.; Filice, M.; Romero, O.; Guisan, J. M. Improving Lipase Activity by Immobilization and Post-Immobilization Strategies. In *Immobilization of Enzymes and Cells*; Springer, 2013; pp 255–273.

(192) Kecht, J.; Schlossbauer, A.; Bein, T. Selective Functionalization of the Outer and Inner Surfaces in Mesoporous Silica Nanoparticles. *Chemistry of Materials* **2008**, *20* (23), 7207–7214.

(193) Lim, M. H.; Stein, A. Comparative Studies of Grafting and Direct Syntheses of Inorganic− Organic Hybrid Mesoporous Materials. *Chemistry of Materials* **1999**, *11* (11), 3285–3295.

(194) Brühwiler, D. Postsynthetic Functionalization of Mesoporous Silica. *Nanoscale* **2010**, *2* (6), 887–892.

(195) Parida, D.; Salmeia, K. A.; Sadeghpour, A.; Zhao, S.; Maurya, A. K.; Assaf, K. I.; Moreau, E.; Pauer, R.; Lehner, S.; Jovic, M. Template-Free Synthesis of Hybrid Silica Nanoparticle with Functionalized

Mesostructure for Efficient Methylene Blue Removal. *Mater Des* **2021**, *201*, 109494.

(196) Adamczyk, A.; Xu, Y.; Walaszek, B.; Roelofs, F.; Pery, T.; Pelzer, K.; Philippot, K.; Chaudret, B.; Limbach, H.-H.; Breitzke, H. Solid State and Gas Phase NMR Studies of Immobilized Catalysts and Catalytic Active Nanoparticles. *Top Catal* **2008**, *48* (1–4), 75–83.

(197) Zaak, H.; Siar, E.-H.; Kornecki, J. F.; Fernandez-Lopez, L.; Pedrero, S. G.; Virgen-Ortíz, J. J.; Fernandez-Lafuente, R. Effect of Immobilization Rate and Enzyme Crowding on Enzyme Stability under Different Conditions. The Case of Lipase from Thermomyces Lanuginosus Immobilized on Octyl Agarose Beads. *Process Biochemistry* **2017**, *56*, 117–123.

(198) Natalello, A.; Ami, D.; Brocca, S.; Lotti, M.; Doglia, S. M. Secondary Structure, Conformational Stability and Glycosylation of a Recombinant Candida Rugosa Lipase Studied by Fourier-Transform Infrared Spectroscopy. *Biochemical Journal* **2005**, *385* (2), 511–517.

(199) Ranaldi, S.; Belle, V.; Woudstra, M.; Rodriguez, J.; Guigliarelli, B.; Sturgis, J.; Carriere, F.; Fournel, A. Lid Opening and Unfolding in Human Pancreatic Lipase at Low PH Revealed by Site-Directed Spin Labeling EPR and FTIR Spectroscopy. *Biochemistry* **2009**, *48* (3), 630–638.

(200) Yang, Y.; Wu, J.; Xiao, T.; Tang, Z.; Shen, J.; Li, H.; Zhou, Y.; Zou, Z. Urchin-like Hierarchical CoZnAl-LDH/RGO/g-C3N4 Hybrid as a Z-Scheme Photocatalyst for Efficient and Selective CO2 Reduction. *Appl Catal B* **2019**, *255* (May), 117771. https://doi.org/10.1016/j.apcatb.2019.117771.

(201) Arrondo, J. L. R.; Muga, A.; Castresana, J.; Goñi, F. M. Quantitative Studies of the Structure of Proteins in Solution by Fourier-Transform Infrared Spectroscopy. *Prog Biophys Mol Biol* **1993**, *59* (1), 23–56.

(202) Aronne, A.; Ausanio, G.; Bloisi, F.; Calabria, R.; Califano, V.; Fanelli, E.; Massoli, P.; Vicari, L. R. M. Structural Characterization of MAPLE Deposited Lipase Biofilm. *Appl Surf Sci* **2014**, *320*, 524–530.

(203) Zhou, Z.; Inayat, A.; Schwieger, W.; Hartmann, M. Improved Activity and Stability of Lipase Immobilized in Cage-like Large Pore Mesoporous Organosilicas. *Microporous and mesoporous materials* **2012**, *154*, 133–141.

(204) Chronopoulou, L.; Kamel, G.; Sparago, C.; Bordi, F.; Lupi, S.; Diociaiuti, M.; Palocci, C. Structure–Activity Relationships of Candida Rugosa Lipase Immobilized on Polylactic Acid Nanoparticles. *Soft Matter* **2011**, *7* (6), 2653–2662.

(205) Soni, S.; Dwivedee, B. P.; Banerjee, U. C. Facile Fabrication of a Recyclable Nanobiocatalyst: Immobilization of Burkholderia Cepacia Lipase on Carbon Nanofibers for the Kinetic Resolution of a Racemic Atenolol Intermediate. *RSC Adv* **2018**, *8* (49), 27763–27774.

(206) Noinville, S.; Revault, M.; Baron, M.-H.; Tiss, A.; Yapoudjian, S.; Ivanova, M.; Verger, R. Conformational Changes and Orientation of Humicola Lanuginosa Lipase on a Solid Hydrophobic Surface: An in Situ Interface Fourier Transform Infrared-Attenuated Total Reflection Study. *Biophys J* **2002**, *82* (5), 2709–2719.

(207) Pitt, F. D.; Domingos, A. M.; Barros, A. A. C. Purification of Residual Glycerol Recovered from Biodiesel Production. *S Afr J Chem Eng* **2019**, *29*, 42–51.

(208) Rodrigues, R. C.; Ayub, M. A. Z. Effects of the Combined Use of Thermomyces Lanuginosus and Rhizomucor Miehei Lipases for the Transesterification and Hydrolysis of Soybean Oil. *Process Biochemistry* **2011**, *46* (3), 682–688.

(209) Kalantari, M.; Yu, M.; Yang, Y.; Strounina, E.; Gu, Z.; Huang, X.; Zhang, J.; Song, H.; Yu, C. Tailoring Mesoporous-Silica Nanoparticles for Robust Immobilization of Lipase and Biocatalysis. *Nano Res* **2017**, *10* (2), 605–617.

(210) Jin, W.; Xu, Y.; Yu, X.-W. Preparation of Lipase Cross-Linked Enzyme Aggregates in Octyl-Modified Mesocellular Foams. *Int J Biol Macromol* **2019**, *130*, 342–347.

(211) Akoh, C. C.; Chang, S.-W.; Lee, G.-C.; Shaw, J.-F. Enzymatic Approach to Biodiesel Production. *J Agric Food Chem* **2007**, *55* (22), 8995–9005.

(212) Christopher, L. P.; Kumar, H.; Zambare, V. P. Enzymatic Biodiesel: Challenges and Opportunities. *Appl Energy* **2014**, *119*, 497–520.

(213) Zoumpanioti, M.; Stamatis, H.; Xenakis, A. Microemulsion-Based Organogels as Matrices for Lipase Immobilization. *Biotechnol Adv* **2010**, *28* (3), 395–406.

(214) Balcao, V. M.; Vieira, M. C.; Malcata, F. X. Adsorption of Protein from Several Commercial Lipase Preparations onto a Hollow-fiber Membrane Module. *Biotechnol Prog* **1996**, *12* (2), 164–172.

(215) de Miranda, A. S.; Miranda, L. S. M.; de Souza, R. O. M. A. Lipases: Valuable Catalysts for Dynamic Kinetic Resolutions. *Biotechnol Adv* **2015**, *33* (5), 372–393.

(216) Kalita, P.; Basumatary, B.; Saikia, P.; Das, B.; Basumatary, S. Biodiesel as Renewable Biofuel Produced via Enzyme-Based Catalyzed Transesterification. *Energy Nexus* **2022**, *6*, 100087.

(217) Salgado, C. A.; dos Santos, C. I. A.; Vanetti, M. C. D. Microbial Lipases: Propitious Biocatalysts for the Food Industry. *Food Biosci* **2022**, *45*, 101509.

(218) Yu, T.; Ding, Z.; Nie, W.; Jiao, J.; Zhang, H.; Zhang, Q.; Xue, C.; Duan, X.; Yamada, Y. M. A.; Li, P. Recent Advances in Continuous-Flow Enantioselective Catalysis. *Chemistry - A European Journal*. Wiley-VCH Verlag May 7, 2020, pp 5729–5747. https://doi.org/10.1002/chem.201905151.

(219) Zaks, A.; Klibanov, A. M. Enzyme-Catalyzed Processes in Organic Solvents. *Proceedings of the National Academy of Sciences* **1985**, *82* (10), 3192–3196.

(220) Sampaio, C. S.; Angelotti, J. A. F.; Fernandez-Lafuente, R.; Hirata, D. B. Lipase Immobilization via Cross-Linked Enzyme Aggregates: Problems and Prospects – A Review. *Int J Biol Macromol* **2022**, *215*, 434–449. https://doi.org/10.1016/J.IJBIOMAC.2022.06.139.

(221) Liu, Y.; Song, L.; Feng, N.; Jiang, W.; Jin, Y.; Li, X. Recent Advances in the Synthesis of Biodegradable Polyesters by Sustainable Polymerization: Lipase-Catalyzed Polymerization. *RSC Adv* **2020**, *10* (59), 36230–36240. https://doi.org/10.1039/d0ra07138b.

(222) Twyman, R. M. ENZYMES| Immobilized Enzymes. **2005**.

(223) Guisan, J. M.; Bolivar, J. M.; López-Gallego, F.; Rocha-Martín Editors, J. *Immobilization of Enzymes and Cells Methods and Protocols Fourth Edition Methods in Molecular Biology 2100*. http://www.springer.com/series/7651.

(224) Chandra, P.; Enespa; Singh, R.; Arora, P. K. Microbial Lipases and Their Industrial Applications: A Comprehensive Review. *Microb Cell Fact* **2020**, *19*, 1–42.

(225) Gupta, M. N.; Kaloti, M.; Kapoor, M.; Solanki, K. Nanomaterials as Matrices for Enzyme Immobilization. *Artificial Cells, Blood Substitutes, and Biotechnology* **2011**, *39* (2), 98–109.

(226) Arabacı, N.; Karaytuğ, T.; Demirbas, A.; Ocsoy, I.; Katı, A. Nanomaterials for Enzyme Immobilization. *Green Synthesis of Nanomaterials for Bioenergy Applications* **2020**, 165–190.

(227) Zhang, Y.; Qi, C.; Tu, J. Fabrication of Hollow Mesoporous Silica-Based Nanoreactors for Enzyme Immobilization: High Loading Capacity,

Effective Protection, and Recyclability. *Mater Today Chem* **2023**, *27*, 101298.

(228) Gößl, D.; Singer, H.; Chiu, H.-Y.; Schmidt, A.; Lichtnecker, M.; Engelke, H.; Bein, T. Highly Active Enzymes Immobilized in Large Pore Colloidal Mesoporous Silica Nanoparticles. *New Journal of Chemistry* **2019**, *43* (4), 1671–1680.

(229) Venezia, V.; Sannino, F.; Costantini, A.; Silvestri, B.; Cimino, S.; Califano, V. Mesoporous Silica Nanoparticles for β-Glucosidase Immobilization by Templating with a Green Material: Tannic Acid. *Microporous and Mesoporous Materials* **2020**, *302*, 110203.

(230) Avossa, J.; Bifulco, A.; Amendola, E.; Gesuele, F.; Oscurato, S. L.; Gizaw, Y.; Mensitieri, G.; Branda, F. Forming Nanostructured Surfaces through Janus Colloidal Silica Particles with Nanowrinkles: A New Strategy to Superhydrophobicity. *Appl Surf Sci* **2019**, *465*, 73–81.

(231) Şakalak, H.; Yılmaz, K.; Gürsoy, M.; Karaman, M. Roll-to Roll Initiated Chemical Vapor Deposition of Super Hydrophobic Thin Films on Large-Scale Flexible Substrates. *Chem Eng Sci* **2020**, *215*, 115466.

(232) Chen, G.; Khan, I. M.; He, W.; Li, Y.; Jin, P.; Campanella, O. H.; Zhang, H.; Huo, Y.; Chen, Y.; Yang, H. Rebuilding the Lid Region from Conformational and Dynamic Features to Engineering Applications of Lipase in Foods: Current Status and Future Prospects. *Compr Rev Food Sci Food Saf* **2022**, *21* (3), 2688–2714.

(233) Verger, R. 'Interfacial Activation'of Lipases: Facts and Artifacts. *Trends Biotechnol* **1997**, *15* (1), 32–38.

(234) Brzozowski, A. M.; Savage, H.; Verma, C. S.; Turkenburg, J. P.; Lawson, D. M.; Svendsen, A.; Patkar, S. Structural Origins of the Interfacial Activation in Thermomyces (Humicola) Lanuginosa Lipase. *Biochemistry* **2000**, *39* (49), 15071–15082.

(235) Zhang, J.; Wang, Z.; Zhuang, W.; Rabiee, H.; Zhu, C.; Deng, J.; Ge, L.; Ying, H. Amphiphilic Nanointerface: Inducing the Interfacial Activation for Lipase. *ACS Appl Mater Interfaces* **2022**, *14* (34), 39622–39636.

(236) Califano, V.; Bloisi, F.; Perretta, G.; Aronne, A.; Ausanio, G.; Costantini, A.; Vicari, L. Frozen Microemulsions for MAPLE Immobilization of Lipase. *Molecules* **2017**, *22* (12), 2153.

(237) Brady, L. , B. A. M. , D. Z. S. , D. E. J. , D. G. G. , T. S. P. , T. J. P. , C. L. , H.-J. B. , N. L. , T. L. *STRUCTURE AND MOLECULAR MODEL REFINEMENT OF RHIZOMUCOR MIEHEI TRIACYLGLYCERIDE LIPASE: A CASE STUDY OF THE USE OF SIMULATED ANNEALING IN PARTIAL MODEL REFINEMENT*.

(238) Uppenberg, J.; Hansen, M. T.; Patkar, S.; Jones, A. *The Sequence, Crystal Structure Determination and Refinement of Two Crystal Forms of Lipase B from Candida Antarctica*.

(239) Pota, G.; Gallucci, N.; Cavasso, D.; Krauss, I. R.; Vitiello, G.; López-Gallego, F.; Costantini, A.; Paduano, L.; Califano, V. Controlling the Adsorption of β-Glucosidase onto Wrinkled SiO2 Nanoparticles To Boost the Yield of Immobilization of an Efficient Biocatalyst. *Langmuir* **2023**.

(240) Kruger, N. J. The Bradford Method for Protein Quantitation. *The protein protocols handbook* **2009**, 17–24.

(241) Lombardo, D.; Guy, O. Effect of Alcohols on the Hydrolysis Catalyzed by Human Pancreatic Carboxylic-Ester Hydrolase. *Biochimica et Biophysica Acta (BBA)-Enzymology* **1981**, *657* (2), 425–437.

(242) Santiago-Arcos, J.; Velasco-Lozano, S.; Diamanti, E.; Cortajarena, A. L.; López-Gallego, F. Immobilization Screening and Characterization of an Alcohol Dehydrogenase and Its Application to the Multi-Enzymatic Selective Oxidation of 1,-Omega-Diols. *Frontiers in Catalysis* **2021**, *1*. https://doi.org/10.3389/fctls.2021.715075.

(243) Cheong, S.; Clomburg, J. M.; Gonzalez, R. Energy-and Carbon-Efficient Synthesis of Functionalized Small Molecules in Bacteria Using Non-Decarboxylative Claisen Condensation Reactions. *Nat Biotechnol* **2016**, *34* (5), 556–561.

(244) Manoel, E. A.; Dos Santos, J. C. S.; Freire, D. M. G.; Rueda, N.; Fernandez-Lafuente, R. Immobilization of Lipases on Hydrophobic Supports Involves the Open Form of the Enzyme. *Enzyme Microb Technol* **2015**, *71*, 53–57.

(245) Fernandez-Lafuente, R.; Armisén, P.; Sabuquillo, P.; Fernández-Lorente, G.; Guisán, J. M. Immobilization of Lipases by Selective Adsorption on Hydrophobic Supports. *Chem Phys Lipids* **1998**, *93* (1–2), 185–197.

(246) Palomo, J. M.; Muñoz, G.; Fernández-Lorente, G.; Mateo, C.; Fernández-Lafuente, R.; Guisán, J. M. Interfacial Adsorption of Lipases on Very Hydrophobic Support (Octadecyl–Sepabeads): Immobilization, Hyperactivation and Stabilization of the Open Form of Lipases. *J Mol Catal B Enzym* **2002**, *19*, 279–286.

(247) Pardal, F.; Lapinte, V.; Robin, J. Modification of Silica Nanoparticles by Grafting of Copolymers Containing Organosilane and Fluorine Moities. *J Polym Sci A Polym Chem* **2009**, *47* (18), 4617–4628.

(248) Zhong, N.; Chen, W.; Liu, L.; Chen, H. Immobilization of Rhizomucor Miehei Lipase onto the Organic Functionalized SBA-15: Their Enzymatic

Properties and Glycerolysis Efficiencies for Diacylglycerols Production. *Food Chem* **2019**, *271*, 739–746. https://doi.org/10.1016/j.foodchem.2018.07.185.

(249) Barth, A. Infrared Spectroscopy of Proteins. *Biochimica et Biophysica Acta (BBA)-Bioenergetics* **2007**, *1767* (9), 1073–1101.

(250) Torii, H.; Tatsumi, T.; Tasumi, M. Effects of Hydration on the Structure, Vibrational Wavenumbers, Vibrational Force Field and Resonance Raman Intensities of N-methylacetamide. *Journal of Raman Spectroscopy* **1998**, *29* (6), 537–546.

(251) Yang, H.; Yang, S.; Kong, J.; Dong, A.; Yu, S. Obtaining Information about Protein Secondary Structures in Aqueous Solution Using Fourier Transform IR Spectroscopy. *Nat Protoc* **2015**, *10* (3), 382–396. https://doi.org/10.1038/nprot.2015.024.

(252) Foresti, M. L.; Valle, G.; Bonetto, R.; Ferreira, M. L.; Briand, L. E. FTIR, SEM and Fractal Dimension Characterization of Lipase B from Candida Antarctica Immobilized onto Titania at Selected Conditions. *Appl Surf Sci* **2010**, *256* (6), 1624–1635. https://doi.org/10.1016/j.apsusc.2009.09.083.

(253) Chronopoulou, L.; Kamel, G.; Sparago, C.; Bordi, F.; Lupi, S.; Diociaiuti, M.; Palocci, C. Structure-Activity Relationships of Candida Rugosa Lipase Immobilized on Polylactic Acid Nanoparticles. *Soft Matter* **2011**, *7* (6), 2653–2662. https://doi.org/10.1039/c0sm00712a.

(254) De Vasconcellos, A.; Paula, A. S.; Filho, R. A. L.; Farias, L. A.; Gomes, E.; Aranda, D. A. G.; Nery, J. G. Synergistic Effect in the Catalytic Activity of Lipase Rhizomucor Miehei Immobilized on Zeolites for the Production of Biodiesel. **2012**. https://doi.org/10.1016/j.micromeso.2012.07.043.

(255) Alagöz, D.; Toprak, A.; Yildirim, D.; Tükel, S. S.; Fernandez-Lafuente, R. Modified Silicates and Carbon Nanotubes for Immobilization of Lipase from Rhizomucor Miehei: Effect of Support and Immobilization Technique on the Catalytic Performance of the Immobilized Biocatalysts. *Enzyme Microb Technol* **2021**, *144*, 109739. https://doi.org/10.1016/J.ENZMICTEC.2020.109739.

(256) M. Palomo, J.; Fuentes, M.; Fernández-Lorente, G.; Mateo, C.; M. Guisan, J.; Fernández-Lafuente, R. General Trend of Lipase to Self-Assemble Giving Bimolecular Aggregates Greatly Modifies the Enzyme Functionality. *Biomacromolecules* **2003**, *4* (1), 1–6. https://doi.org/10.1021/bm025729+.

(257) Salameh, A.; Wiegel, J. *Effects of Detergents on Activity, Thermostability and Aggregation of Two Alkalithermophilic Lipases from Thermosyntropha Lipolytica*; 2010; Vol. 4.

(258) Tu, M.; Pan, X.; Saddler, J. N. Adsorption of Cellulase on Cellulolytic Enzyme Lignin from Lodgepole Pine. *J Agric Food Chem* **2009**, *57* (17), 7771–7778.

(259) Giles, C. H.; MacEwan, T. H.; Nakhwa, S. N.; Smith, D. 786. Studies in Adsorption. Part XI. A System of Classification of Solution Adsorption Isotherms, and Its Use in Diagnosis of Adsorption Mechanisms and in Measurement of Specific Surface Areas of Solids. *Journal of the Chemical Society (Resumed)* **1960**, 3973–3993. https://doi.org/10.1039/jr9600003973.

(260) Latour, R. A. The Langmuir Isotherm: A Commonly Applied but Misleading Approach for the Analysis of Protein Adsorption Behavior. *J Biomed Mater Res A* **2015**, *103* (3), 949–958. https://doi.org/10.1002/jbm.a.35235.

(261) Jaycock, M. J.; Parfitt, G. D. *Chemistry of Interfaces*; Horwood, E., Ed.; John Wiley & Sons, 1986.

(262) Rodrigues, R. C.; Fernandez-Lafuente, R. Lipase from Rhizomucor Miehei as an Industrial Biocatalyst in Chemical Process. *J Mol Catal B Enzym* **2010**, *64* (1–2), 1–22.

(263) Overbeeke, P. L. A.; Govardhan, C.; Khalaf, N.; Jongejan, J. A.; Heijnen, J. J. *Influence of Lid Conformation on Lipase Enantioselectivity*; 2000; Vol. 10. www.elsevier.comrlocatermolcatb.

(264) Verger, R. 'Interfacial Activation'of Lipases: Facts and Artifacts. *Trends Biotechnol* **1997**, *15* (1), 32–38.

(265) Vescovi, V.; Kopp, W.; Guisán, J. M.; Giordano, R. L. C.; Mendes, A. A.; Tardioli, P. W. Improved Catalytic Properties of Candida Antarctica Lipase B Multi-Attached on Tailor-Made Hydrophobic Silica Containing Octyl and Multifunctional Amino-Glutaraldehyde Spacer Arms. *Process Biochemistry* **2016**, *51* (12), 2055–2066.

(266) Klinman, J.; Hammes-Schiffer Editors, S. *Topics in Current Chemistry 337 Dynamics in Enzyme Catalysis*. http://www.springer.com/series/128.

(267) Zaak, H.; Siar, E. H.; Kornecki, J. F.; Fernandez-Lopez, L.; Pedrero, S. G.; Virgen-Ortíz, J. J.; Fernandez-Lafuente, R. Effect of Immobilization Rate and Enzyme Crowding on Enzyme Stability under Different Conditions. The Case of Lipase from Thermomyces Lanuginosus Immobilized on Octyl Agarose Beads. *Process Biochemistry* **2017**, *56*, 117–123. https://doi.org/10.1016/j.procbio.2017.02.024.

(268) Barbosa, O.; Torres, R.; Ortiz, C.; Fernandez-Lafuente, R. The Slow-down of the CALB Immobilization Rate Permits to Control the Inter and Intra

Molecular Modification Produced by Glutaraldehyde. *Process Biochemistry* **2012**, *47* (5), 766–774. https://doi.org/10.1016/J.PROCBIO.2012.02.009.

(269) Fernandez-Lopez, L.; Pedrero, S. G.; Lopez-Carrobles, N.; Gorines, B. C.; Virgen-Ortíz, J. J.; Fernandez-Lafuente, R. Effect of Protein Load on Stability of Immobilized Enzymes. *Enzyme Microb Technol* **2017**, *98*, 18–25.

(270) Longo, M. A.; Combes, D. Analysis of the Thermal Deactivation Kinetics of α-Chymotrypsin Modified by Chemoenzymatic Glycosylation. In *Progress in biotechnology*; Elsevier, 1998; Vol. 15, pp 135–140.

(271) Poojari, Y.; Clarson, S. J. Thermal Stability of Candida Antarctica Lipase B Immobilized on Macroporous Acrylic Resin Particles in Organic Media. *Biocatal Agric Biotechnol* **2013**, *2* (1), 7–11.

(272) Garmroodi, M.; Mohammadi, M.; Ramazani, A.; Ashjari, M.; Mohammadi, J.; Sabour, B.; Yousefi, M. Covalent Binding of Hyper-Activated Rhizomucor Miehei Lipase (RML) on Hetero-Functionalized Siliceous Supports. *Int J Biol Macromol* **2016**, *86*, 208–215. https://doi.org/10.1016/j.ijbiomac.2016.01.076.

(273) Noel, M.; Combes, D. Effects of Temperature and Pressure on Rhizomucor Miehei Lipase Stability. *J Biotechnol* **2003**, *102* (1), 23–32.

(274) Babaki, M.; Yousefi, M.; Habibi, Z.; Mohammadi, M.; Yousefi, P.; Mohammadi, J.; Brask, J. Enzymatic Production of Biodiesel Using Lipases Immobilized on Silica Nanoparticles as Highly Reusable Biocatalysts: Effect of Water, t-Butanol and Blue Silica Gel Contents. *Renew Energy* **2016**, *91*, 196–206.

(275) Spinelli, D.; Fatarella, E.; Di Michele, A.; Pogni, R. Immobilization of Fungal (Trametes Versicolor) Laccase onto Amberlite IR-120 H Beads: Optimization and Characterization. *Process Biochemistry* **2013**, *48* (2), 218–223.

(276) Ren, Q.; Ruth, K.; Thöny-Meyer, L.; Zinn, M. Enatiomerically Pure Hydroxycarboxylic Acids: Current Approaches and Future Perspectives. https://doi.org/10.1007/s00253-010-2530-6.

(277) Seebach, D.; Albert, M.; Arvidsson, P. I.; Rueping, M.; Schreiber, J. V. From the Biopolymer PHB to Biological Investigations of Unnatural β- and γ-Peptides. *Chimia (Aarau)* **2001**, *55* (4), 345–353.

(278) Chiba, T.; Takeshi, N. A SYNTHETIC APPROACH TO (+)-THIENAMYCIN FROM METHYL (R)-3-HYDROXYBUTANOATE. A NEW ENTRY TO (3R, 4R)-3-[(R)-1-HYDROXYETHYL]-4-

ACETOXY-2-AZETIDINONE. *Chem Lett* **1985**, *14* (5), 651–654. https://doi.org/https://doi.org/10.1246/cl.1985.651.

(279) Ghanem, A.; Schurig, V. Lipase-Catalyzed Access to Enantiomerically Pure (R)-and (S)-Trans-4-Phenyl-3-Butene-2-Ol. *Tetrahedron Asymmetry* **2003**, *14* (1), 57–62.

(280) Klomp, D.; Peters, J. A.; Hanefeld, U. Enzymatic Kinetic Resolution of Tropic Acid. *Tetrahedron Asymmetry* **2005**, *16* (23), 3892–3896.

(281) Reis, J. S.; Andrade, L. H. Lipase-Catalyzed Kinetic Resolution of β-Borylated Carboxylic Esters. *Tetrahedron Asymmetry* **2012**, *23* (17), 1294–1300.

(282) Romero-Fernandez, M.; Heckmann, C. M.; Paradisi, F. Biocatalytic Production of a Nylon 6 Precursor from Caprolactone in Continuous Flow. *ChemSusChem* **2022**, *15* (16). https://doi.org/10.1002/cssc.202200811.

(283) Holmquist, M.; Norin, M.; Hult, K. The Role of Arginines in Stabilizing the Active Open-Lid Conformation of Rhizomucor Miehei Lipase. *Lipids* **1993**, *28*, 721–726.

(284) Stauch, B.; Fisher, S. J.; Cianci, M. Open and Closed States of Candida Antarctica Lipase B: Protonation and the Mechanism of Interfacial Activation. *J Lipid Res* **2015**, *56* (12), 2348–2358. https://doi.org/10.1194/jlr.M063388.

Chapter 6

Miniaturized enzyme reactors for continuous flow biocatalysis

Contents

1. Continuous flow biocatalysis

1.1. Flow chemistry: principles and applications

From a decade to now, continuous processing has gained space and importance within the context of chemical industry for two main reasons that are cost containment and sustainability.[1] In detail, continuous flow reactors are usually associated with smaller equipment with respect to their batch counterpart, and characterized by higher degrees of automation which limit human intervention.[2] Moreover, the approach of numbering up which is the possibility to put several reactors working in parallel allows to overcome the problematics related to scale up, namely mass and heat transfer limitations. Safety issues are reduced as well, since enhanced mass and heat transfer together with the manipulation of smaller volumes allow to work with operating conditions (Temperature, pressure, reactivity) impossible to be safely handled in batch. Furthermore, real-time monitoring of the product stream, as well as feedback loop strategies pave the way for enhanced sustainability and cost-efficiency of the processes, resulting in increased yields and savings of reactants and energy.[1,2] Although industrials sectors like petro- and bulk chemical have already experienced continuous operating conditions, only lately continuous processing is becoming popular in fine chemistry and pharma industry too.[3] This growing interest towards flow chemistry was fed also by the suitability of using miniaturized reactors for the design of new catalysts. More specifically, micro- and meso-fluidic reactors gained increasing attention, with the latter usually chosen over the former due to the better matching between productivity and industrial needs.[4] Schematic representations of a flow reactor configuration involving mesoreactors (**A**) or microreactors (**B**) are reported in **Figure 1.1**.

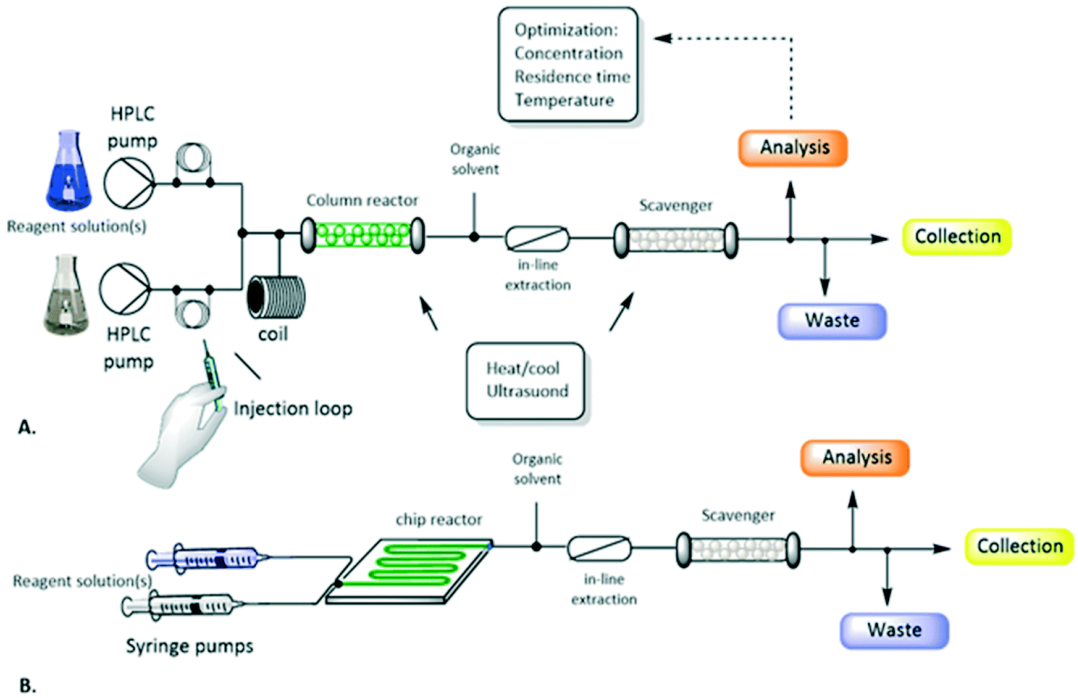

Figure 1.1. Flow diagrams for microfluidic (A) and mesofluidic (B) reactors.[1]

Microfluidic reactors (**Figure 1.1. B**) are usually chips or microtube devices made of glass, plastic or metal, with internal diameter lower than 500 μm and operating volumes of μL range. They usually provide enhanced heat/mass transfer and prompt temperature control.[4] It is suggested that continuous flow systems, primarily leveraging microreactor technology, hold the potential to enhance approximately 50% of all chemical processes.[5] However, short diffusion paths, together with laminar flow regime with very low Reynolds number (*Re*), non-uniform flow profiles, short residence time and high surface area-to-volume ratio, leading to significant surface effects, strongly limit mixing. To overcome these challenges, the

operating set-up has to be adequately complicated, and researchers often employ various strategies such as implementing microscale mixers, creating segmented flow, utilizing active mixing techniques (e.g., acoustic or electrokinetic methods), or designing microreactor geometries that enhance mixing by inducing chaotic advection. Moreover, such small cross-sections are associated with pressure drops and channel obstruction.[4] On the other hand, mesofluidic reactors that are reactors with internal diameter higher than 500 μm provide lower mass and heat transfer, even if the wider cross-sections allow to handle higher flow rates and reduce pressure drops. Furthermore, mixing limitations are usually overcome by turbulent flow regimes or packed-bed configurations.[4] Generally speaking the operative setup of a miniaturized continuous flow reactor includes various pumps (such as HPLC, syringe, peristaltic, or gear centrifugal pumps) designed for the precise and reproducible delivery of solvents and reagents. Additionally, the system incorporates loops for introducing small reagent volumes, mixing tubes serving as the initial point for blending different reagents, temperature-controlled reactors, a back pressure regulator (BPR) for overseeing the overall system pressure, and downstream units responsible for work-up operations, separations (extractors), purifications (scavenger columns), and analysis (spectrophotometers, bench-top NMR, LC/GC-MS).[1]

1.2. Definition of the parameters

The performances of the catalysts used in different transformation routes or in the same reaction pattern performed under different fluid-dynamic conditions are assessed by calculating the following parameters:

(1.1) Reaction yield: $\frac{mol\ of\ product}{mol\ of\ substrate}$

(1.2) Catalyst productivity: $\frac{grams\ of\ product}{grams\ of\ substrate}$

(1.3) Volumetric productivity: $\frac{grams\ of\ product}{Volume \cdot time}$

(1.4) Space-time yield (STY): $\frac{mol\ of\ product}{catalyst\ volume \cdot time}$ [1]

STY is a very critical factor for assessing the potential up-scalability of the continuous flow process, since it gives the amount of product released by a reactor of a particular volume. Depending on the product costs, STY is expected to be higher than 100 $g \cdot L^{-1} day^{-1}$ or higher than 500 $g \cdot L^{-1} day^{-1}$ whether the product is high-value or low-value.[6] The first way to assess the benefits of performing a reaction in continuous regime is to compare the performance of such process with that performed in batch. So, there is the need to introduce the distinction between two different time parameters. Fortunately, certain crucial parameters can be juxtaposed: the reaction time (t) in a batch reactor signifies the duration needed for a potential reaction to reach a specific (predefined) conversion. In continuously operated systems, the residence time (τ) can be employed, defined as the duration for the reagents to traverse through the reactor.[2] Flow biocatalysis gives an important contribution to green chemistry, and the eco-friendliness of chemical processes is described by a series of parameters. The first one is the atom economy (AM):

$$(1.5) \quad AM = \frac{MW_P}{\sum_i MW_{R_i}}$$

where MW_P is the molecular weight of the product and MW_{R_i} is the molecular weight of the i^{th} reactant. It is the most immediate way to measure the sustainability of a process, since it quantifies the waste produced by each step without considering solvents and supplementary chemicals. The actual waste product is quantified by the E factor:

$$(1.6) \quad E = \frac{Kg_{waste}}{Kg_{product}}$$

It is more precise than AM since it includes solvents, auxiliary chemicals and it is suitable for multi-step procedures. More specifically, the closer is E to zero, the more sustainable is the process.[7]

1.3. Fluid-dynamics of miniaturized reactors

The fluid dynamics of a miniaturized reactor is characterized by two dimensionless quantities: the Reynolds number (Re) and the Peclet number (Pe). Re assesses the ratio of inertial to viscous forces in the fluid and is defined by the equation 1.7:

$$(1.7) \quad Re = \frac{vL\rho}{\mu}$$

Here, ρ represents the fluid density, v is the linear velocity of a fluid element, μ is the viscosity, and L is a characteristic size of the system. Re helps determine whether the fluid flow is in a laminar regime ($Re < 2100$) or turbulent ($Re > 2100$). In turbulent flow, chaotic intersections of flow lines result in the formation of vortices (**Figure 1.2**), leading to perpendicular mass and energy transfer with respect to the motion's direction. This promotes mixing and macroscopic heat transfer within the system.

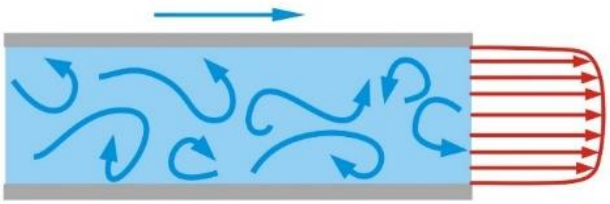

Figure 1.2. Schematic representation of turbulent regime

In the laminar regime, mass transfer occurs solely through diffusion between various planes (**Figure 1.3**). The fluid motion in the laminar regime follows Poiseuille's law:

$$(1.8) \quad Q = \frac{\pi \cdot \Delta P \cdot r_H^4}{8 \cdot \mu \cdot L}$$

Here, ΔP is the pressure difference along the channel, r_H is the hydrodynamic radius, μ is the fluid viscosity, and L is the channel length. In microfluidic systems, Re typically ranges between 10^{-6} and 10^{2}, indicating laminar flow regimes.

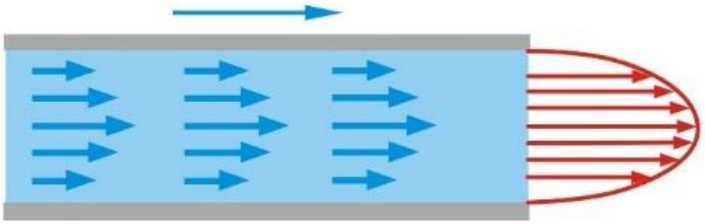

Figure 1.3. Schematic representation of laminar regime

The dimensionless Peclet number (Pe) accounts for the relationship between two transport phenomena, convection and diffusion, expressed as:

$$(1.9) \quad Pe = \frac{v \cdot L}{D_{ij}}$$

Here, v is the velocity of the fluid current, L is the characteristic length of the system, and D_{ij} is the diffusivity of chemical species i in medium j. For $Pe \gg 1$, convection becomes the dominant transport mechanism, and diffusion can be disregarded. Conversely, for $Pe \ll 1$, matter primarily undergoes transport through diffusion, while convection is negligible. When $Pe \sim 1$, both phenomena must be considered for describing matter transport. An alternative method to assess the significance of convection versus diffusion involves examining the characteristic time required for these transport mechanisms. The characteristic diffusion time t_d is estimated as:

$$(1.10) \quad t_d = \frac{L^2}{D_{ij}}$$

While the characteristic convection time (t_c) is given by:

$$t_c = \frac{L}{v} \quad (1.11)$$

A smaller characteristic time indicates a more efficient transport mechanism. Therefore, the Peclet number represents the ratio between the characteristic time of diffusion and that of convection. It becomes evident that for shorter distances, diffusion exhibits shorter characteristic times compared to convection, whereas for longer distances, convection is faster, resulting in shorter characteristic times.[8]

1.4. Miniaturized enzyme reactors

1.4.1. Suitable reactor configurations

The utilization of biocatalysts for driving chemical transformations has become a crucial and influential aspect in both research and industry, particularly in the selective synthesis of essential organic compounds. The integration of knowledge and expertise from chemical reaction engineering and biocatalysis into a concept known as continuous flow biocatalysis has recently garnered significant attention within the scientific community. In general, the advantages of micro flow-reactors, characterized by having at least one dimension below 1 mm inside diameter (*id*) are evident. These advantages include (i) high heat transfer surface to product volume ratios, (ii) effective heat transfer capabilities that are ideal for optimizing reaction conditions, (iii) efficient mixing, (iv) improved flow capacities, (v) lower pressure drops, (vi) absence of channel blockages, and (vii) the potential for preparing multikilogram quantities when mesoreactors are considered.[2] Several continuous

biocatalytic reactor configurations are available, the most popular shown in **Figure 1.4**.

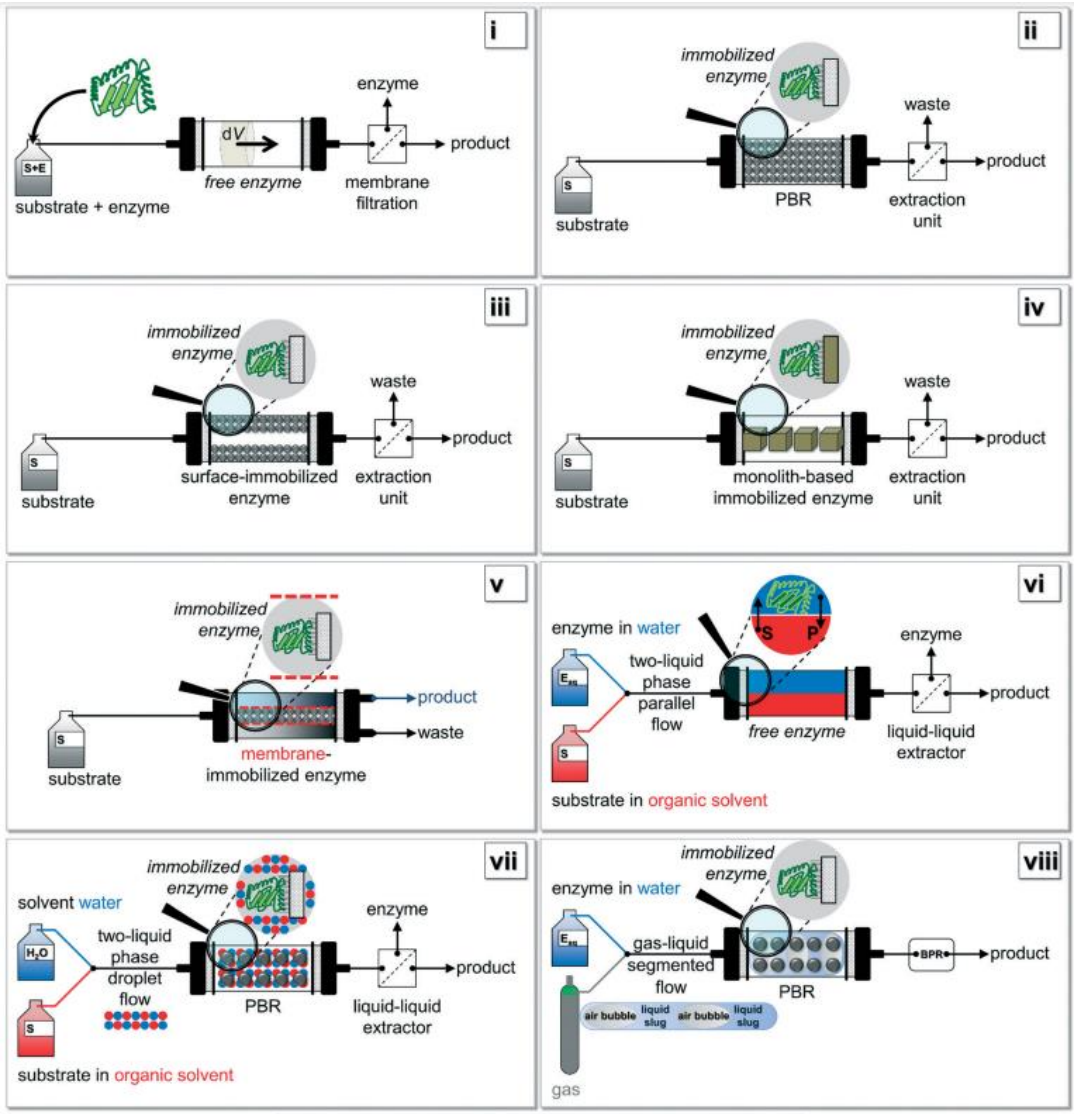

Figure 1.4. Different configurations available for the continuous operation of biocatalytic reactions.[2]

Even if reusability concerns, related to the need to avoid waste and offset the cost of enzyme production and purification, impose to employ immobilized biocatalysts,

biocatalytic processes can be run in continuous with free enzymes as well (**Figure 1.4 i).** The reactor can be considered segregated (plug flow reactor, PFR) and the conversion degree depends on the axial coordinate. In case of water-soluble substrate, in can be pre-mixed with the enzyme and directly fed to the reactor. On the contrary, parallel flow configuration is suitable for non-polar substrates (**Figure 1.4 vi**). The simplest concept among immobilized enzymes in the reactor group involves using a packed-bed reactor (PBR), where the enzyme is directly attached to the packaging material (**Figure 1.4 ii**). To mitigate issues such as high pressure drops and channeling effects in this setup, a reactor with surface-immobilized enzymes can be employed (**Figure 1.4 iii**). Additionally, enzymes can be immobilized onto monolith materials (**Figure 1.4 iv**) or retained using methods like size-exclusion membranes (**Figure 1.4 v**). Immobilized enzymes can also be utilized in configurations within a liquid–liquid system involving immiscible solvents (**Figure 1.4 vii**) or within a gas–liquid system (**Figure 1.4 viii**). In the first case, the two liquids are typically mixed to facilitate droplet flow. In the second case, a segmented air–liquid flow is primarily employed.[2]

1.4.2. Example of mesofluidic reactors

Enzyme cofactors play a significant role in biocatalysis, as many enzymes rely on them to catalyze valuable reactions in organic synthesis. However, the recycling of cofactors often poses a challenge when implementing enzymes at an industrial scale since cofactors are rather expensive. Baumer et al. addressed this challenge by introducing a quasi-stationary recycling system for nicotinamide adenine dinucleotide (phosphate) NAD(P)H that utilizes immobilized Halo-tagged alcohol dehydrogenase from *L. brevis* (HaloTag-LbADH).[9] The researchers established both a simple flow-through system and a closed-loop cofactor regeneration system, providing a thorough comparison between the two setups (**Figure 1.5**). Closed-loop

setup allowed for continuous production and rapid substrate changes, being suitable as model for continuous biocatalytic devices utilizing (co-) substrates that are miscible in organic solvent. In the asymmetric reduction of acetophenone, closed-loop system achieved comparable conversion (96%) with respect to open-loop system (92%) with half the flow rate (30 μL·min^{-1}) using 50 mmol L−1 of substrate and 10% (v/v) 2-propanol. The reactor configuration was employed to run the reduction of three additional substrates, yielding moderate to high space–time yields (STYs) and high to very high turnover numbers (TTNs) with excellent enantioselectivities (>99%). Furthermore, the system exhibited reliability through continuous runs over 32 hours without a loss in performance. This setup illustrates the potential of NADP(H) recycling for continuous operation within biocatalytic processes.[9]

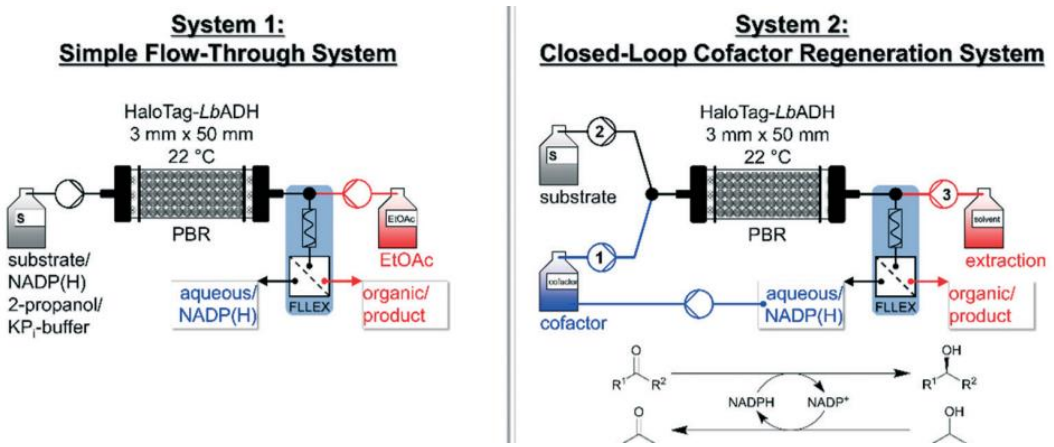

Figure 1.5. Open-loop and closed-loop reactor configurations proposed by Baumer et al.[9]

Other examples of self-sufficient heterogeneous biocatalysts were presented by the group of Lopez-Gallego. More specifically, phosphorylated cofactors (PLP, FAD^{+}, and NAD^{+}) were co-immobilized with enzymes onto the same polyethyleneimine (PEI)-activated solid porous material (**Figure 1.6**). This approach allows for

chemical reactions to occur in aqueous media without the need for the exogenous addition of cofactors. In this configuration, the enzymes and PEI are permanently attached to the solid surface, while the negatively charged cofactors are reversibly adsorbed to the PEI through ion-exchange interactions. NAD^+-bearing biocatalysts were successfully employed in the asymmetric reduction of prochiral ketones in continuous.[10,11]

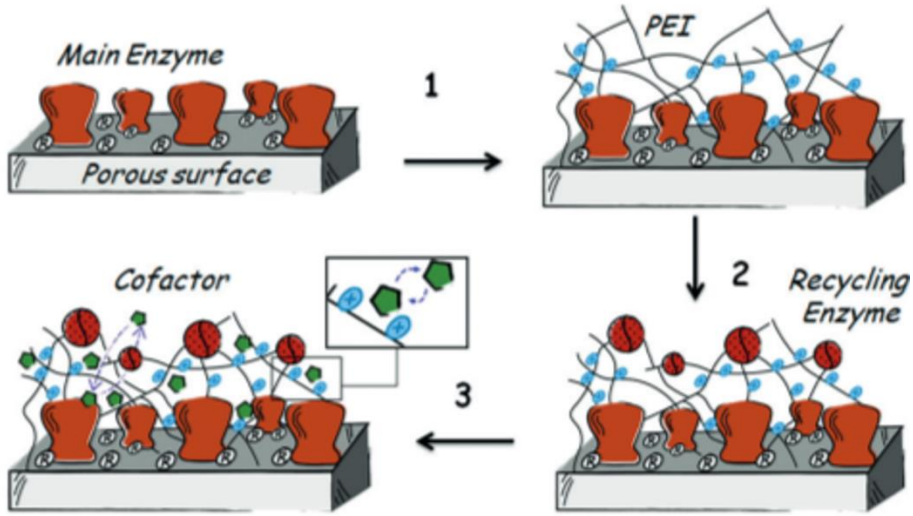

Figure 1.6. Structure of the self-sustaining heterogeneous biocatalyst. The equilibrium between cofactor association and dissociation is illustrated in the inset.[10]

Subsequently, they extended the utilization of self-sufficient heterogeneous biocatalysts, incorporating co-immobilized ω-transaminases and PLP to efficiently operate packed-bed reactors in continuous flow. More specifically, ω-transaminase from *Halomonas elongata* was co-immobilized with PLP onto PEI-coated porous methacrylate-based carriers to run the enantioselective deamination of α-methylbenzyl amine in a PBR. The reaction was performed for up to 50 column volumes at a flow rate of 1.45 $mL \cdot min^{-1}$, resulting in >90% conversion in all cycles without the need for an exogenous addition of cofactor.[12] Currently, the biocatalytic

enantioselective reduction of β-ketoesters is emerging as a significant pathway in chemical processes for obtaining enantiomerically pure β-hydroxyesters. The biosynthesis of these compounds is characterized by mild reaction conditions in terms of temperature and pressure, and it eliminates the need for toxic substrates or metallic catalysts. β-hydroxyesters, which are pivotal building blocks, find applications in the food and pharmaceutical industries for the synthesis of various functional products. The advantages of flow biocatalysis to produce such important chemicals can be properly exploited by choosing the adequate carrier for enzyme immobilization, that means highly porous, chemically and physically stable. Ceramic carriers like zirconium oxide ZrO_2 seems to fulfil these requirements, especially as in the form of a solid membrane. Andrés-Sanz et al. reported the co-immobilization a thermophilic hydroxybutyryl-CoA dehydrogenase (TtHBDH-His) and a formate dehydrogenase (His-CbFDH) into Yttrium-stabilized zirconia (YSZ) solid membrane to perform the asymmetric reduction of ethyl acetoacetate with *in-situ* redox cofactor recycling (**Figure 1.7**). The immobilization is accomplished by coordination interactions between the imidazole groups of His-tags and both Zr and Y atoms. The co-immobilized system successfully achieved in situ recycling of the redox cofactor, maintaining specific productivity with only 0.05 mM NADH and accumulating a TTN of 4000 in 24 hours.[13]

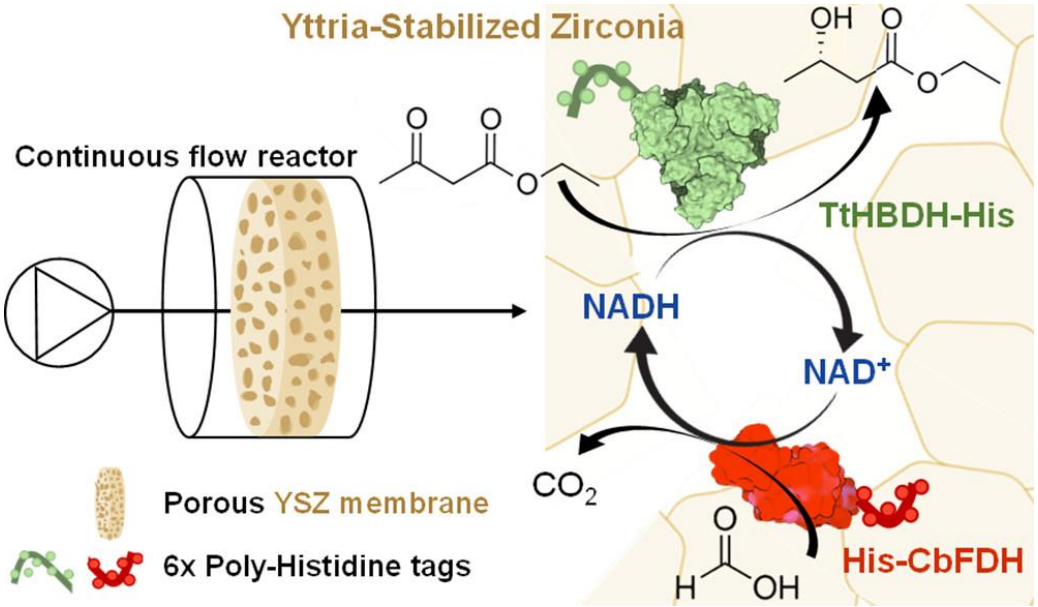

Figure 1.7. Diagram illustrating the arrangement of the flow reactor for the ongoing enantioselective reduction of β-ketoesters, with simultaneous cofactor recycling facilitated by the co-immobilization of TtHBDH-His and His-CbFDH on YSZ membranes.[13]

2. Honeycomb cordierite monolith for the hydrolysis of cellulose

2.1. Cordierite as a suitable carrier material

Cordierite, a ceramic compound consisting of magnesia, silica, and alumina in a 2:3:2 molar ratio, stands as the preferred choice for monoliths, especially in honeycomb structures. Honeycomb monoliths exhibit exceptional mechanical strength and minimal thermal expansion, making them efficient catalytic carriers for the eco-friendly, cost-effective, and versatile production of various valuable

chemicals. Catalytic coatings on cordierite honeycomb monoliths find extensive applications in emission control systems for automotive and stationary energy production, as well as in chemical processing and catalytic combustion. Monoliths are also widely employed in the pharmaceutical industry and enzymatic reactions. In the context of the last considered application, coating monoliths with catalytic material provides several advantages over using the catalyst in free powder form:

1. very high thermal resistance.
2. complete recovery from the reaction mixture.
3. ecological disposal.
4. reduction of costs associated with enzyme purchases.
5. utilization of a very thin (yet effective) active phase layer on the monolith.[14]

2.2. Morphology and properties of cordierite monoliths

2.2.1. Properties of ceramic monoliths

The monolith can be manufactured in various sizes and shapes, commonly adopting circular or oval cross-sectional areas (**Figure 2.1**). The configurations and characteristics of monoliths are defined in relation to their geometric and hydraulic parameters. These structures are crafted from ceramic, metal, or plastic materials, each displaying distinct physical and chemical properties. Metal monoliths enable superior heat transfer and mechanical stability. In the context of the present thesis work, ceramic monoliths are utilized due to their higher porosity, facilitating improved coating adhesion and ensuring good thermal stability. Cordierite monoliths offer several advantageous features over metal or plastic monoliths:

1. Thermal shock resistance attributable to a low coefficient of thermal expansion.
2. Porosity and pore size distribution conducive to easy washcoat application.

3. Compatibility with washcoat and catalysts.[14,15]

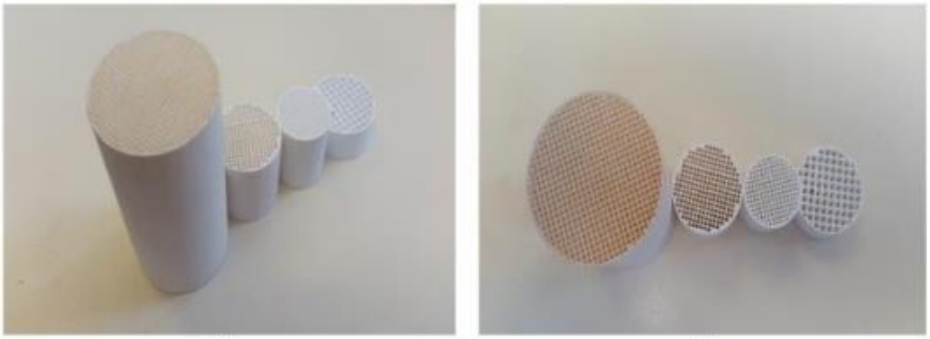

Figure 2.1. Monoliths with different cell density values and pore sizes: (a) side view; (b) top view.

2.2.2. Geometric parameters

The channel geometry has the potential to influence both mass and heat transfer, thereby impacting catalytic performance. A monolith can be analytically characterized using geometric equations (2.1-2.3) and equation 2.4, which describes pressure drops along the channel.

$$\text{(2.1) Cell density} = \frac{1}{L^2}$$

$$\text{(2.2) Open Frontal Area} = \frac{(L-t_w)^2}{L^2}$$

$$\text{(2.3) Geometric Surface Area} = \frac{4(L-t_w)}{L^2}$$

where L is the width/length of channel, t_w is the thickness of the wall.[15] Pressure drops along the channel ΔP are described by Darcy-Weisbach equation:

$$\text{(2.4) } \Delta P = \frac{2fL\rho v^2}{gD_h}$$

where f is the friction factor, D_h is the hydraulic diameter, g is the gravitational acceleration, v is the velocity in the channel and ρ is the fluid density.[16] Monolithic

catalysts typically feature a large open frontal area, resulting in minimal pressure drop. The thickness of the coating can influence the open frontal area, geometric surface, and hydraulic diameter. A thicker coating might potentially decrease the open frontal area, thereby restricting spatial velocities or impeding the diffusion of large reactive molecules within channels. When applying a washcoat to a monolithic structure, several additional crucial factors need consideration, including pH levels, slurry concentration, appropriate calcination, drying procedures, or specific techniques for a required application. The pH of the coating solution affects the uniformity of the coating. The rheological properties of the slurry, including concentration, particle size distribution, and solid content, affect viscosity, impacting adherence and uniformity of the coating. Adhesion and uniformity, in turn, depend on drying time and calcination procedures.[15]

2.3. Catalyst efficiency: comparison between kinetic and diffusive regime

When dealing with porous catalysts, it is essential to consider that the reaction takes place across all available surfaces, both internal and external. Proximity of reagents to the active phase and effective removal of products are critical for the reaction to proceed. Transport phenomena play a pivotal role, and their interaction with the chemical reaction determines the overall system behavior. Therefore, employing a microreactor provides enhanced control over diffusive transport phenomena, hydrodynamics, and intrinsic kinetics.[17] In **Figure 2.2**, you can observe how the small size of the channels helps alleviate restrictions resulting from both external (L_{flow}) and internal (L_{diff}) diffusive transport. Consequently, there is an expansion of the outer surface where the active phase interfaces with reagents and products, leading to improved transport to and from the active phase.

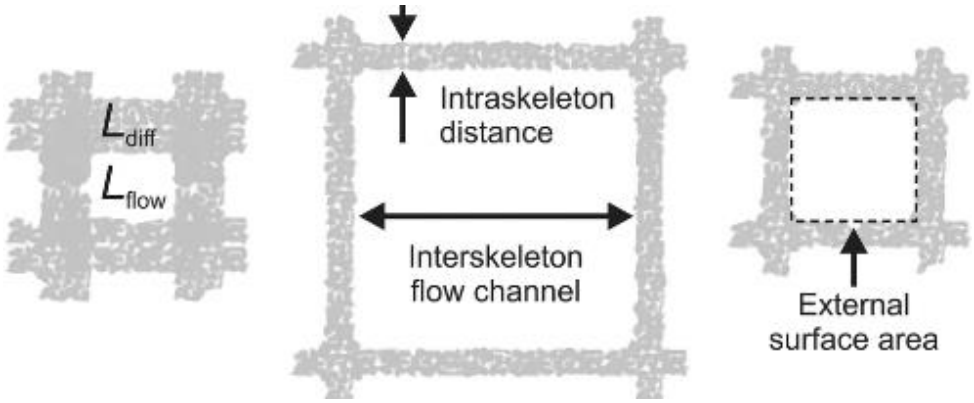

Figure 2.2. Schematic representation of the channel of a monolith.[17]

The effectiveness of a porous catalyst is quantified by the Thiele modulus ϕ, a parameter that incorporates both intrinsic kinetics and diffusion phenomena.[18] This parameter assesses the relative significance of the intrinsic reaction rate and internal diffusive transport, accounting for the constraints imposed by intraporous diffusion on the reacting species. The ϕ is also influenced by the morphology and geometry of the catalyst and can be mathematically expressed by the formula:

$$(2.5)\ \phi = \delta\sqrt{\frac{k\, c_b^{n-1}}{D_{eff}}}$$

Here, δ denotes the average washcoat thickness (proportional to pore size), c_b signifies the concentration of the reactive species on the active phase's surface, and n indicates the order of the chemical reaction. In case of low substrate concentration, enzyme kinetics can be treated as first-order reactions ($n = 1$). The kinetic constant of the reaction is denoted as k, and D_{eff} represents the effective diffusivity. Within a porous catalyst, molecules experience reduced flow compared to normal

conditions, a consequence of the presence of voids. D_{eff} is correlated with the catalyst's void fraction (ε) and the tortuosity parameter (τ) as follows:

$$(2.6)\ D_{eff} = \frac{D \cdot \varepsilon}{\tau}$$

with $\varepsilon = \frac{V_{pores}}{V_{total}}$ and $\tau = \frac{L_m}{L}$. The parameter τ is defined as the ratio of the effective distance traveled by two particles L_m to the net displacement L, which is the distance between the two centers of the particles represented by a straight line. ϕ also depends on temperature, which influences k and D_{eff}.The ratio between the observed reaction rate and the intrinsic reaction rate (in the absence of diffusive phenomena) is expressed by the effectiveness factor η:

$$(2.7)\ \eta = \frac{r_{\text{observed}}}{r}$$

Figure 2.3 shows the effectiveness η as a function of ϕ:

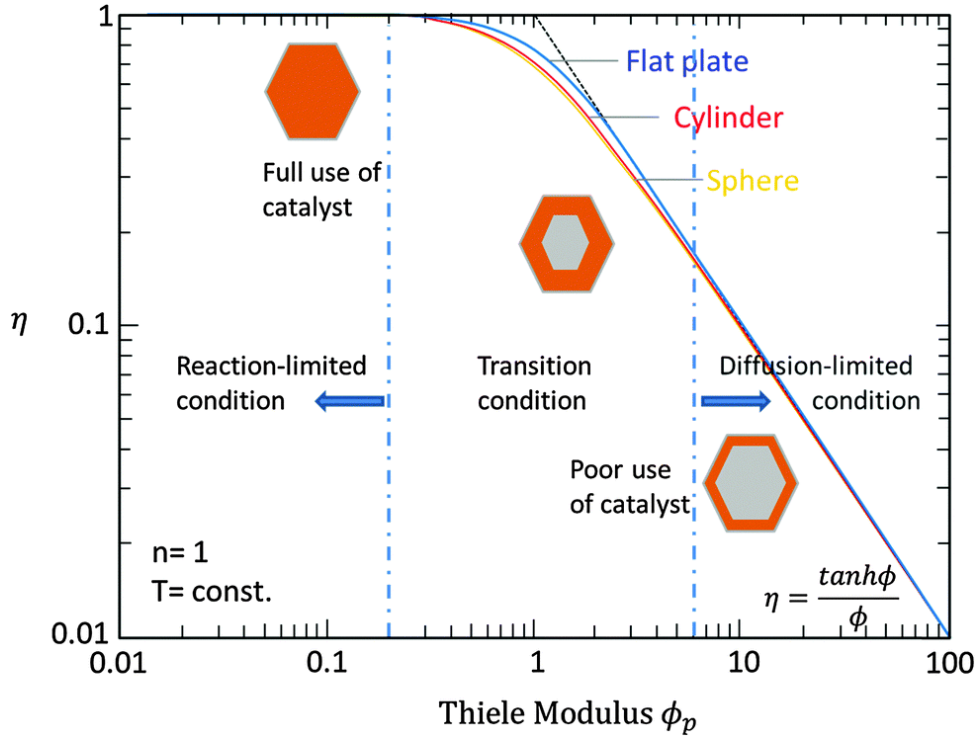

Figure 2.3. Efficiency factor profile over the Thiele modulus for porous catalysts, considering various geometries.[18]

Examining the diagram allows us to make the following observations. $\phi < 0.2$ means $k \ll D_{eff}$. In this condition, the entire catalyst converts the maximum substrate concentration, equivalent to the surface concentration, leading to $\eta \to \infty$ This means that the system is under kinetic control. For $0.2 < \phi < 0.6$, a transitional regime is evident. Finally, $\phi > 0.6$ means $k \gg D_{eff}$. In this case, a pronounced concentration drop occurs due to diffusive limitations, indicating the catalyst operates in a diffusive regime. An analytical expression for ϕ can thus be obtained:

$$(2.8)\ \eta = \frac{\tanh(\phi)}{\phi}$$

The choice of ϕ depends on the specific characteristics of the reaction system, and there isn't a one-size-fits-all optimal value for ϕ. However, in practice, a commonly recommended range for Thiele modulus values is indeed between $0.2 < \phi < 1.2$ Within this range, the kinetic and diffusive regimes are often comparable. This balance can lead to a system that is more cost-effective and efficient, considering a trade-off between the benefits of enhanced reaction rates (kinetic regime) and the limitations imposed by mass transfer and diffusion (diffusive regime). The specific choice of ϕ would still depend on the details of the reaction, the catalyst structure, and the desired outcomes of the process.[18]

2.4. Waschoating the walls of a cordierite honeycomb monolith with cellulase-loaded WSNs for the hydrolysis of cellulose

A strategy to implement a co-immobilization strategy involving cellulase and β-glucosidase (BG) for cellulose hydrolysis is herein presented. Additionally, the goal is to design a miniaturized enzyme reactor for running the enzyme cascade in a continuous flow regime. The mesofluidic reactor was created by immobilizing the enzyme mixture onto wrinkled silica nanoparticles (WSNs) previously deposited on ceramic cordierite monoliths, employing both sequential (SEQ-Mon) and simultaneous (SIM-Mon) methods. Initially, the operational and thermal stability of powder biocatalysts were evaluated. Subsequently, the performance of the IEM was compared to that of the powder biocatalyst in batch, and the optimized reactor configuration was tested under laminar flow regime. This step is crucial for the large-scale implementation of this technology, as continuous reactors are typically employed to achieve higher productivity.

2.4.1. Materials

Tetraethylorthosilicate (TEOS), urea, cetyl trimethyl ammonium bromide (CTAB), cyclohexane, pentanol, 2-propanol,ethanol, hydrochloric acid solution (37.0% wt. in

water), carboxymethylcellulose sodium salt (CMC), acetic acid (99.0% wt.), sodium acetate trihydrate, sodium hydroxide and glucose oxidase-peroxidase(GOD-POD) assay kit, citric acid, trisodium citrate dihydrate, and sulfuric acid (95.0−98.0% wt.) were purchased from Sigma-Aldrich(Milan, Italy).β-Glucosidase from almonds (molecular weight of 135kDa for the dimer, product number 49290, specific activity ≥ 4U/mg, measured as micromole of glucose liberated per minute at pH 5 and 37°C with salicin as substrate) and cellulase from *T. reesei* (product number C0615, specific activity ≥5 U/mg solid measured as micromole of glucose liberated from cellulose per hour at 37°Cand pH 5) were also acquired from Sigma-Aldrich.

2.4.2. Washcoat of cordierite monoliths

The octagonal cordierite monoliths were derived from a single solid block, featuring channels with a square cross-section, each side measuring 1 mm (**Figure 2.4**). Geometrical parameters are reported in **Table 1.**

Table 1. Geometrical parameter of the employed cordierite monoliths.

Parameter	**Value**
Cell density	600 cpsi

Diameter (average)	17 mm
Average weight	0.980 g
Thickness of the channel wall	0.076 mm
Volume	2758 mm^3
Specific surface area	3.574 mm^{-1}
Length	10 mm

Silica nanoscaled coating on the monolith walls was achieved through repeated dip coating in an aqueous suspension containing WSNs at a concentration of 33 mg/ml, following the procedure by Venezia et al.[19] The washcoating procedure enhanced the dispersion of the support onto the monolith, minimizing nanoparticle aggregation compared to using free powder.

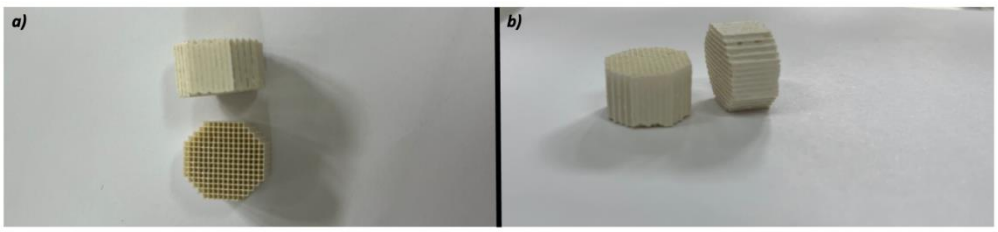

Figure 2.4. Cordierite monoliths a) top view; b) side view.

The conventional approach involves immersing the support into a slurry containing the solid phase, uniformly distributing it on the inner walls of the monolith. Each immersion lasts approximately 15 seconds, with any residue removed through compressed air treatment. Subsequently, the samples are placed in an oven at 120 ºC for 30 minutes to facilitate water evaporation. Calcination of the monoliths involves applying a temperature ramp with a slope of 10 ºC/min up to 450 ºC, maintaining this temperature for 2 hours. The washcoating and calcination steps are repeated

multiple times until the specified mean deposition, determined by weighing, reaches 50 mg. To assess the mechanical robustness and bonding capability of the WSN washcoat, an ultrasonic stability assessment was conducted. Each monolith was immersed in distilled water in a beaker and placed within an ultrasonic bath operating at a frequency of 59 kHz for 10 minutes. Subsequently, the monolith underwent a 30-minute heat treatment in an oven, and its weight post-test was measured. The percentage of weight loss for the sample was determined using the following formula:

$$(2.9)\ w_{loss}(\%) = \frac{w_{pre} - w_{post}}{w_{pre}} \cdot 100$$

where w_{pre} and w_{post} are the weight of the samples before and after the ultrasonic treatment, respectively.

2.4.3. Simultaneous co-immobilization of cellulase and supplementary β-glucosidase onto the washcoat

The concurrent physical immobilization of BG and cellulase into the monolith involved immersing the washcoated monoliths in a citric acid/sodium citrate buffer solution (pH=5), wherein the enzymes had been previously dissolved. The chosen BG/cellulase weight ratio was set at 6:1, mirroring the value selected for the case of nanoparticles in powder. The mixture underwent gentle stirring for 24 hours, with 25 mg of cellulase and 4.16 mg of β-glucosidase included in 25 ml of buffer solution. Subsequently, the monolith was thoroughly washed with distilled water, and the resulting catalyst was denoted as SIM-Mon. **Figure 2.5** illustrates the washcoated support immersed in the enzyme solution.

Figure 2.5. Cellulase/BG adsorption phase into monolith.

2.4.4. Sequential co-immobilization of cellulase and supplementary β-glucosidase onto the washcoat

Sequential absorption of β-glucosidase and cellulase enzymes on the monolith was carried out in the same media as the case of simultaneous co-immobilization. This procedure is made of two steps:

1. In the first step, 8.25 mg of BG were dissolved in 25 ml of citrate buffer in the presence of the monolith. The system is subjected to gentle agitated for 24 h to 40 °C.
2. 25 mg of cellulase were dissolved in 25 ml of citrate buffer in the presence of the monolith. The system is gentle agitated for 24 h to 40 ºC. More specifically, BG/Cellulase weight ratio was fixed to 3:1 wt./wt., again analogously to the powder case. The catalyst was termed as SEQ-Mon

2.4.5. Hydrolysis of Cellulose-Based substrates

2.4.5.1. Case 1: Powder Biocatalysts

The hydrolysis reaction was performed using a concentration of Whatman® filter paper (FP) at 2 mg/ml in a total reaction volume of 5 ml. Specifically, SIM-BG/Cell or SEQ-BG/Cell were dispersed in 2.5 ml of citrate buffer, which was then mixed with 2.5 mL of a suspension at a concentration of 4 mg/mL. The system underwent gentle stirring for 24 hours at a temperature of 50 ºC. At specified time intervals (10 min, 30 min, 1 h, 2 h, 4 h, 6 h, and 24 h), aliquots were withdrawn, subjected to an oven treatment (10 min at 100 ºC) to deactivate the protein, and centrifuged to separate the biocatalysts. Glucose concentration was determined using the glucose oxidase-peroxidase assay kit. The same reaction protocol was employed, replacing FP with carboxymethyl cellulose sodium salt (CMC). Since FP is neither soluble nor stable in aqueous solutions, evaluating the behavior of the supported proteins towards a soluble substrate like CMC was essential to transpose the system to a continuous flow mesoreactor operating under laminar regime ($Re \ll 2100$).

2.4.5.2. Case 2: Monolith (Batch)

The hydrolysis reaction was conducted using an FP concentration of 2 mg/ml in a total reaction volume of 5 ml. The system was gently agitated for 24 hours at a temperature of 50 ºC. At specified time intervals (10 min, 30 min, 1 h, 2 h, 4 h, 6 h, and 24 h), aliquots were withdrawn, and the glucose evaluation procedure described above was applied. The same reaction protocol was also followed, replacing FP with CMC.

2.4.5.3. Case 3: Monolith (Continuous Flow)

The CMC solution was introduced to the reactor via a peristaltic pump at a fixed speed, correlated with a volumetric flow rate (Q= 15 μL/min). Specifically, the volumetric flow rate was chosen in relation to the equivalent batch time, fixed at 4 hours in this case. The contact time (τ) was defined as:

$$(2.10)\ \tau = \frac{w_{cat-m}}{Q}$$

where w_{cat-m} is the biocatalyst mass in the monolithic reactor, and Q is the flow rate. For ease of comparison between batch and continuous tests, a batch-equivalent contact time (t_{batch}) was defined as:

$$(2.11)\ t_{batch} = \frac{\tau V_{batch}}{w_{cat-p}}$$

where w_{cat-p} is the biocatalyst mass used in the batch experiments, and V_{batch} is the volume of the solution. All tests were conducted at a constant temperature of 50 ºC, using a thermostatic bath. A volume of approximately 2 mL, corresponding to the volume of the monolith, was considered transitory and discarded.

2.4.5.4. Reactor configuration

Continuous hydrolysis experiments with CMC were conducted within a laboratory-scale flow microreactor. This setup featured a peristaltic pump for liquid flow control, a Pyrex tube to house the monolith, and a temperature-controlled tank. The reactor was configured in an upflow mode, ensuring a consistent bottom-up liquid flow. The graphical sketch in **Figure 2.6** depicts the arrangement of the installation.

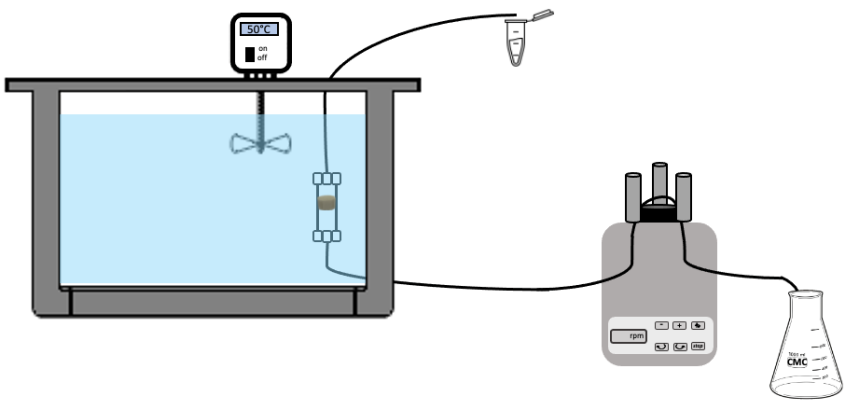

Figure 2.6. Graphical scheme of the reactor configuration

2.4.6. Results

Figure 2.7 illustrates the kinetics curve for supported biocatalysts produced through simultaneous (SIM-BG/cell) and sequential (SEQ-BG/cell) immobilization on WSNs in the hydrolysis of 2 mg/mL filter paper (FP) suspension.

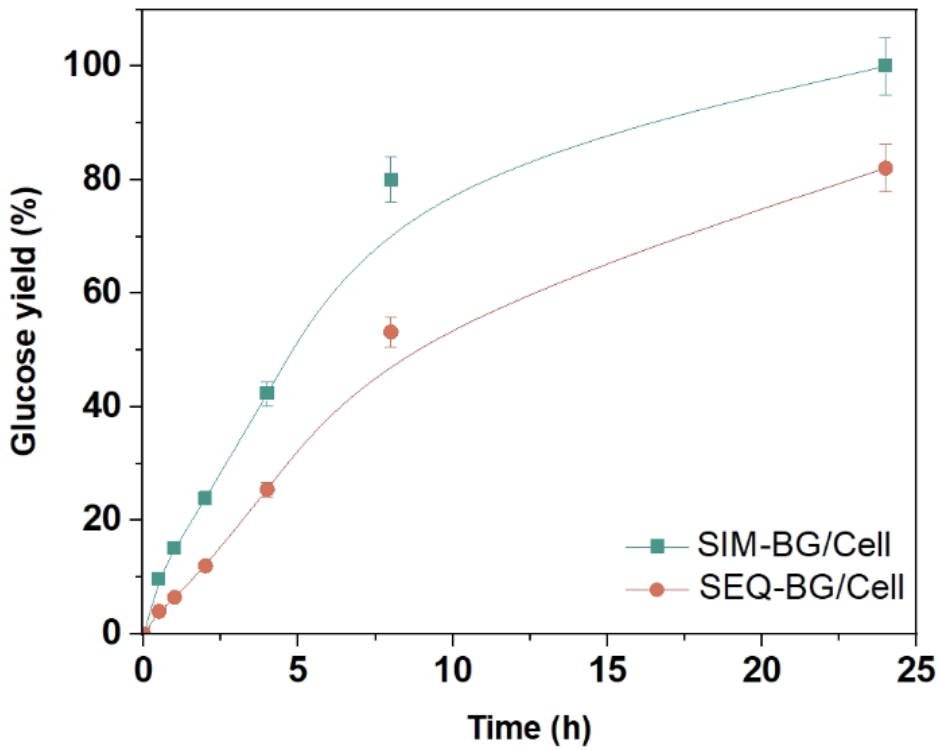

Figure 2.7. Glucose yield profiles over time for SIM-BG/Cell and SEQ-BG/Cell.

Data indicate that, for both biocatalysts, kinetic curves exhibit linear behavior up to 4 hours, followed by an approach to a plateau, resulting in 100% and 82% glucose yield for SIM-BG/cell and SEQ-BG/cell, respectively. The superior performance can be attributed to the enhanced yield of immobilization achieved through simultaneous co-immobilization, as detailed in a previous paper.[20] Furthermore, this immobilization strategy likely achieves a BG/cellulase wt./wt. close to the optimized value of 0.33. Thus, it is evident that simultaneous enzyme immobilization on WNS offers advantages, enabling higher conversion values. Evaluation of operational stability is crucial for assessing the ability of the supported protein to be reused in sequential reaction cycles. Retrieving the enzyme from the reaction solution and employing it repeatedly can mitigate the high cost associated with biocatalyst production. **Figure 2.8** displays histograms depicting the relative glucose production for SIM-BG/cell **(A)** and SEQ-BG/cell **(B)** within a single reaction vessel.

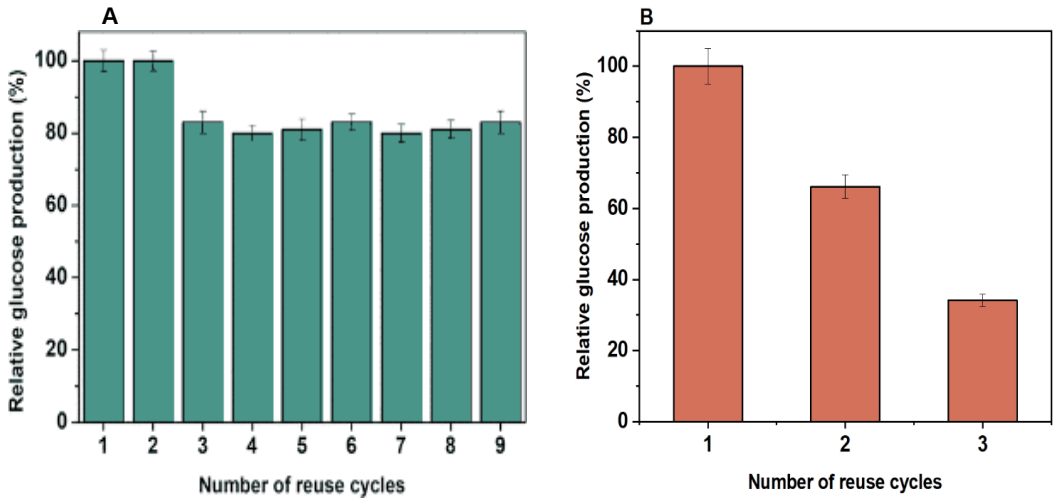

Figure 2.8. Histograms reporting the operational stability for SIM-BG/Cell (A) and SEQ-BG/Cell (B)

The results highlight the excellent reusability demonstrated by the simultaneously co-immobilized biocatalyst, employed for nine consecutive reaction cycles, with only a 17% reduction in glucose yield. This reduction becomes apparent after the second cycle and remains consistent through the ninth cycle. The process of physically immobilizing enzymes onto the nanosilica structure's surface leads to intramolecular aggregates, resulting in a slight decline in catalytic performance during successive reuses as these aggregates are detached.[21] The supported multienzyme system exhibits excellent reusability performances, confirming the effectiveness of simultaneous physical co-immobilization into WSN in producing a high-performance and reusable biocatalyst. In contrast, the sequentially immobilized biocatalyst in **Figure 2.8 B** shows a significant loss in relative glucose production, collapsing to 30% after three reaction cycles. The reason could be attributed to the modification of the surface charge of the nanoparticles during sequential immobilization steps. Protein adsorption is mainly driven by differences in surface charge between silica (*pI*~2.2) and proteins (*pI*~7) at pH 5. In one-pot immobilization, both enzymes experience maximum interaction with the support. In sequential immobilization, the support surface charge becomes less negative, resulting in reduced electrostatic interaction between cellulase and support.[22]Additionally, partial filling of the pores by BG could reduce the available surface for cellulase attachment, and a consistent aliquot of this protein may be adsorbed onto previously immobilized layers of BG.[20,23,24] Enzyme-to-enzyme intermolecular interactions are weak, leading to easier enzyme leaching during consecutive reaction cycles. Both enzyme-immobilized monoliths were tested in the hydrolysis of FP for 24 hours to compare the performances of proteins when loaded into free or immobilized WSNs in batch. For both samples, the conversion is relatively low, reaching a maximum of 37% for SIM-Mon, as reported in **Figure 2.9**.

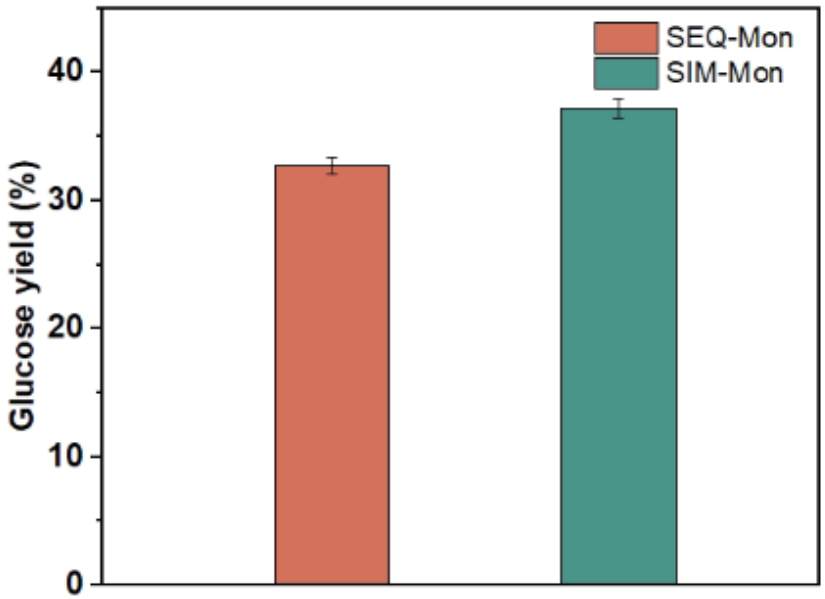

Figure 2.9. Glucose yield for SEQ-Mon and SIM-Mon in 24 h, using FP as substrate.

This result is unsurprising since FP is not water-soluble, and the adsorption strategy prescribes that proteins are adsorbed into a washcoat of nanoparticles. This likely results in a consistent loss in overall enzyme load, leading to remarkable reductions in glucose yield due to mass transfer limitations. The operational stability of enzyme-loaded monoliths was investigated to assess the possibility of implementing a continuous flow reactor. Both SIM-Mon and SEQ-Mon samples were tested in consecutive reaction cycles for 24 hours using filter paper as a substrate, as reported in **Figure 2.10**. Both monoliths exhibit good conversion retention after 2 reaction cycles, with relative glucose yield reaching 73% and 95% for SIM-Mon and SEQ-Mon, respectively. However, the third reuse coincides with a consistent conversion drop, almost halved for SEQ-Mon and decreased to 60% for SIM-Mon. This

behavior could be attributed to progressive enzyme leakage, facilitated by different concurrent factors. Limited accessibility of the nanoparticles' pores, due to washcoating, and insufficient controllability of washcoat thickness and morphology with the dip coating technique could result in irregular and rough superimposed layers of nanoparticles, considerably reducing overall pore exposition to offered proteins.

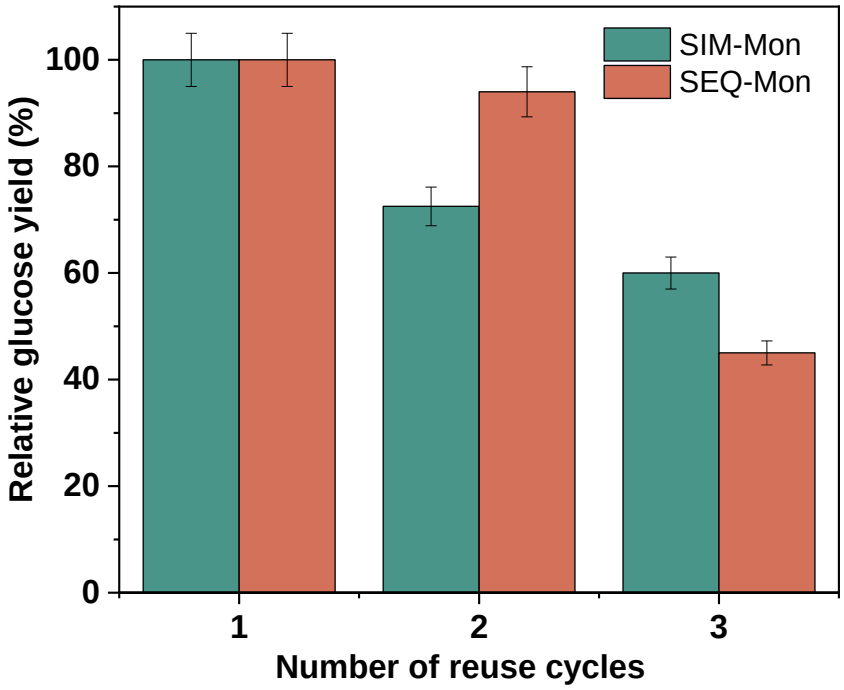

Figure 2.10. Operational stability histograms for SIM-Mon and SEQ-Mon

Following these differences in operational stability, further studies were carried out only for SIM-Mon. All attempts to compare the performances of dispersed and

washcoated biocatalysts faced the problem of the insolubility of FP cellulose, severely compromising glucose yield by the monoliths. Moreover, the transposition of the reaction cascade from batch to continuous flow requires perfect substrate stability to avoid mass transfer limitations and phase separation. Therefore, CMC sodium salt was chosen as a soluble substrate, and a conversion test was carried out using SIM-Mon as a biocatalyst due to the higher glucose yield as converting FP. The results reported in **Figure 2.11** highlight the high affinity between enzyme and substrate, resulting in almost complete conversion in 2 hours. The remarkably high conversion at a short time confirms the good choice of the substrate, indicating the absence of diffusive limitations and the possibility to carry out tests in continuous flow reactors.[24]

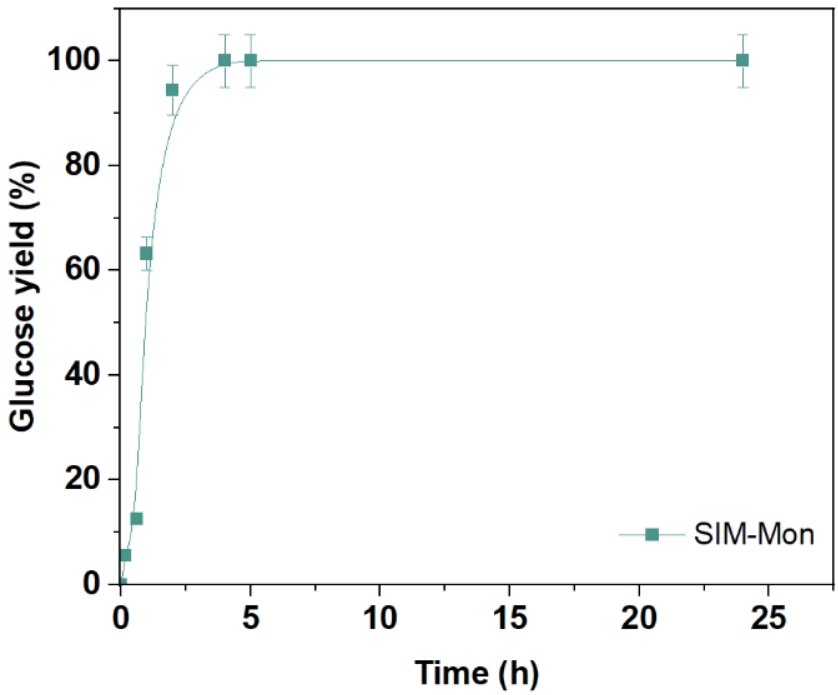

Figure 2.11. Reaction course for SIM-Mon using CMC as substrate

Preliminary catalytic tests under continuous flow regime were conducted with SIM-Mon as a biocatalyst, with a fixed flow rate of 15 μL/min, corresponding to a $t_{batch} = 4h$ hours, sufficient to achieve 100% conversion in batch conditions. As shown in **Figure 2.12**, the first reaction cycle resulted in a 40% glucose yield, whereas at the second reuse, the calculated conversion was 75% lower. The relatively contained CMC conversion after the first cycle, together with the collapse experienced at the second reuse, supports the hypothesis of consistent enzyme loss, even under very low Re ($\sim$30). Therefore, further efforts must be planned to improve the immobilization strategy and reduce enzyme leakage.

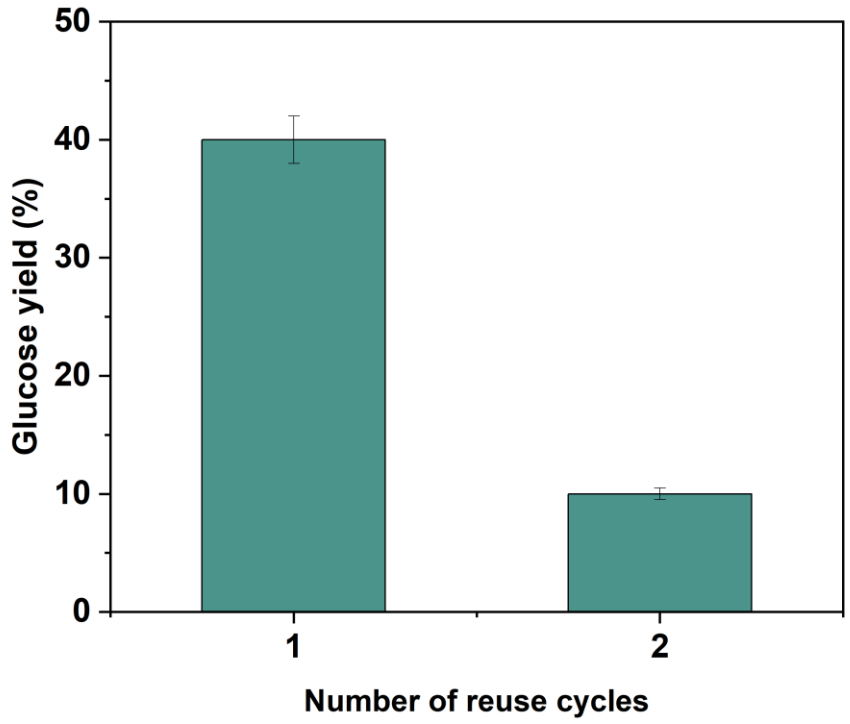

Figure 2.12. Glucose yields reached for SIM-Mon at 15 μL/min

2.4.7. Conclusions

The supported biocatalysts have demonstrated great ability to convert cellulose. Specifically, regarding yield and considerations of operational stability, the simultaneous immobilization strategy, SIM-BG/cell, outperforms the sequential immobilization approach (SEQ-BG/cell). The immobilization protocols were transferred to ceramic monoliths on which a washcoat of WSNs was previously carried out, to design a miniaturized reactor capable of continuous operation. The monoliths were examined in batch, revealing the need to modify immobilization methods due to significant enzyme losses, hindering the system's transition from batch to continuous operation. Nevertheless, preliminary tests conducted with a continuous microreactor have shown the possibility of cellulose conversion under laminar conditions. Therefore, future investigations could focus on the optimization of the immobilization process, more specifically in increasing enzyme concentrations and coating the outer surface of the monolith to convey enzymes into the channels only. An investigation under these conditions has already been carried out, increasing the concentration of enzymes by 5 times and coating the monolith with Teflon, resulting in a 70% glucose yield. Finding a pretreatment to increase the colloidal stability of cellulose in an aqueous suspension. With the increasing spread of biorefinery processes, biomass conversion should be possible without chemical modification of the extracted cellulose, aiming for complete circularity.

3. Sequential enzymatic cascade for the continuous and divergent biotransformation of β-ketoesters into enantiomerically pure β-hydroxy acids

3.1. Lipase enzymes in chemical synthesis

Lipase enzymes, owing to their remarkable catalytic properties, have become indispensable contributors to the realm of chemical synthesis. More specifically, the pioneering work by Zaks and Klibanov assessed the stability of lipases in organic solvents together with their versatility in catalyzing a variety of chemical reactions involving carboxylic acid derivatives such as esterification, aminolysis, acyl exchange, transesterification, and oximolysis (**Scheme 1**).[25] Indeed, even if a specific quantity of water molecules is necessary for enzymatic activity, the primary determinant influencing the impact of organic solvents does not seem to be their interaction with the enzyme molecule directly, but rather their interaction with the enzyme-bound water. However, this water is tightly associated with the enzyme.[25]

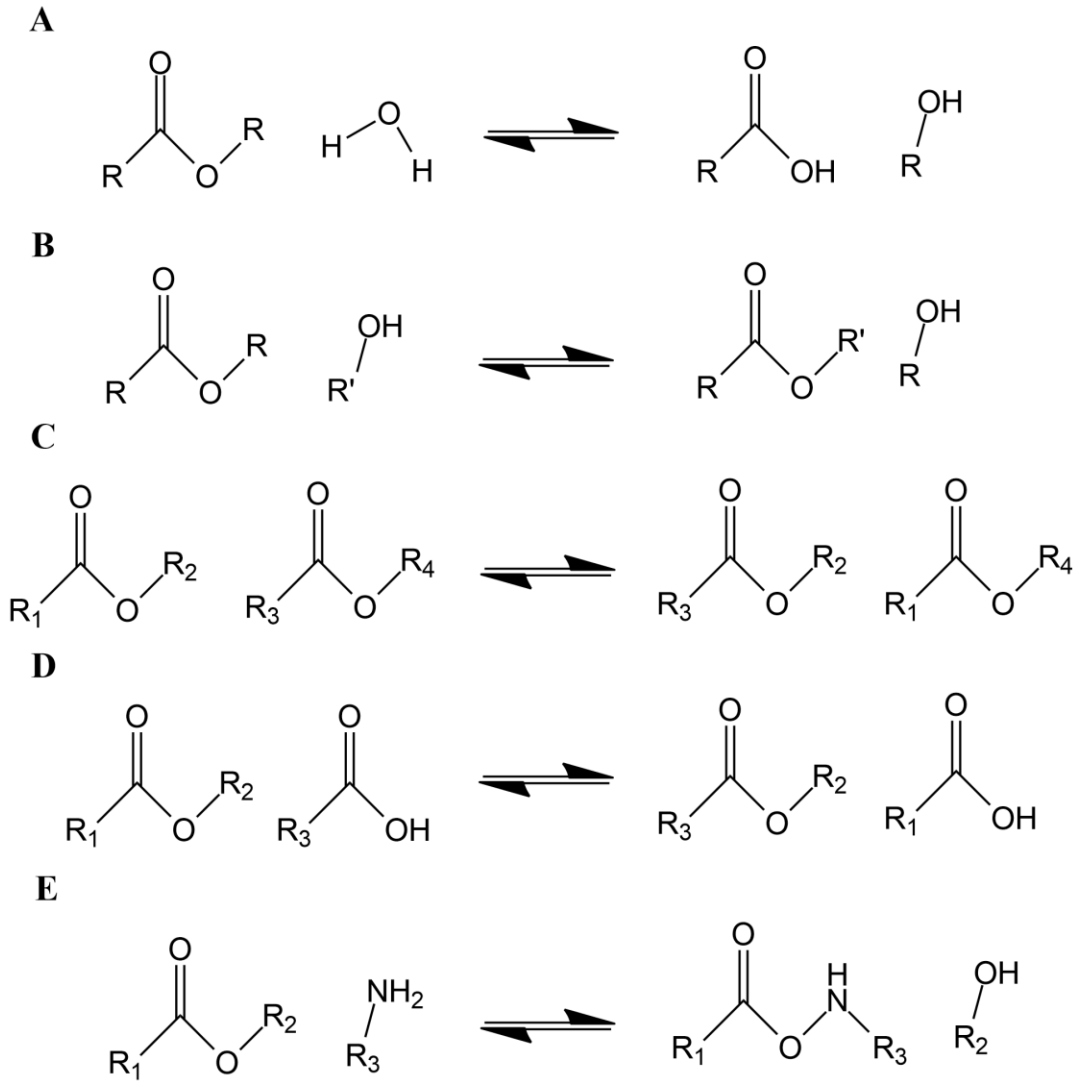

Scheme 1. List of the possible lipase-catalyzed reactions: hydrolysis (A), alcoholysis (B), interesterification (C), acidolysis (D), aminolysis (E).

The adaptability of lipase enzymes to diverse reaction conditions, including non-aqueous solvents and mild temperatures, enhances their applicability, providing a robust and sustainable foundation for synthetic pathways. As biocatalysts, lipases not only facilitate greener and more efficient processes but also contribute

significantly to the development of sustainable methodologies for chemical synthesis. All these factors contribute to motivate the growing industrial interest towards lipases, pushing the global enzyme market to the impressive value of 590.2 million $.[26] Indeed, lipases widely used by food, paper, textile, energy and pharmaceutical companies. Notably, lipases exhibit high regio- and stereoselectivity, making them pivotal in the resolution of racemic mixtures and the production of enantiomerically pure compounds, a critical aspect in the pursuit of chiral synthesis. In detail, in this section the application of lipase as a multifunctional catalyst for the enantioselective hydrolysis β-hydroxyester is discussed.

3.2. The importance of hydroxyacids

Enantiomerically pure β-hydroxyesters can be obtained through the asymmetric biocatalytic reduction of β-ketoesters, as previously reported in paragraph 1. This method of biosynthesis offers advantages such as mild reaction conditions in terms of temperature and pressure, and it eliminates the need for toxic substrates or metallic catalysts.[27,28] Ethyl (R)-3-hydroxybutyrate finds application in the synthesis of β-lactamases inhibitors,[29] whereas its S-isomer serves as a crucial intermediate for the production of carbapenems and insect pheromones.[30] Moreover, β-hydroxyesters, derived from this process, serve as pivotal building blocks in the food and pharmaceutical industries for the synthesis of functional products.[31] More specifically, lipase can provide the enantioselective hydrolysis of β-hydroxyesters to obtain enantiopure β-hydroxyacids.[32–34] Hydroxy acids are naturally present in plants such as sugarcane, tomatoes, oranges, lemons, grapes, and apples, as well as in animal tissues. Throughout history, civilizations have utilized certain hydroxy acids, found in crude plant extracts, for the treatment of various inflammatory diseases, primarily attributed to the presence of salicylic acid as an active component.[35] In the

cosmetic sector, hydroxy acids are utilized to address skin conditions like photoaging, acne, pigmentation disorders, and psoriasis.[36] The primary classification is based on the position on the hydroxy group in the molecule (**Figure 3.1**).

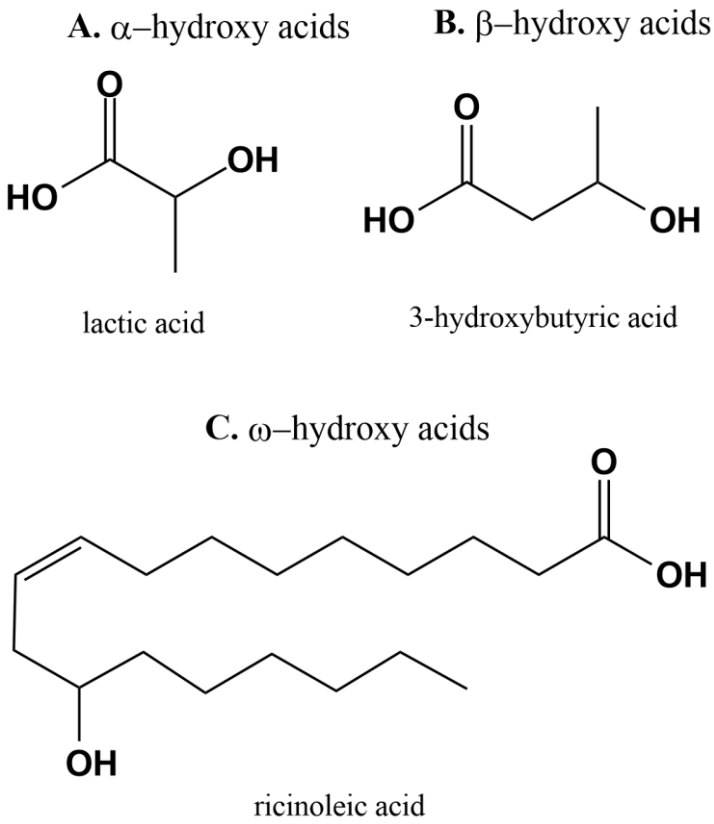

Figure 3.1. Lactic, 3-hydroxybutyric and ricinoleic acids as examples of α-(A), β-(B) and ω-(C) hydroxyacids.

α-hydroxyacids have the hydroxy group attached to the carbon atom adjacent to the carboxylic acid group, like lactic acid (**Figure 3.1 A)**. β-hydroxyacids have the hydroxy group separated by two carbon atoms from the carboxylic acid group. They are used as starting materials to synthesize vitamins, antibiotics, and some other optically active bioactive compounds.[37] The most famous is ethyl 3-hydroxybutyrric

acid (**Figure 3.1 B**), potentially suitable as monomer for the synthesis of polyhydroxyalkanoates (PHAs) like poly-hydroxy butyrate (PHB). The rest of aliphatic hydroxyacids are termed as ω-hydroxyacids, like ricinoleic acid (**Figure 3.1 C**).

3.3. Synthesis of polyhydroxyacids

3.3.1. Catalysts

Polyhydroxyacids are obtained by the polymerization of hydroxyacid-derived building blocks. The polymerization of hydroxy acid monomers is a highly versatile process, and its outcome is significantly influenced by the specific monomer and catalyst types employed. The polymerization mechanism involves electrophilic activation of the carbonyl group, followed by attack from the alcohol group, leading to the formation of an intermediate that releases water after a proton transfer. Due to the reversible nature of this reaction, water removal is crucial for pushing the conversion and guiding the equilibrium toward the ester. High vacuum and elevated temperatures are typically applied to facilitate water removal. The ability of polymers formed by the self-condensation of hydroxy acids to be fully recycled in a Circular Economy approach is a noteworthy feature, as the polymerization is reversible. Properly selecting conditions enables the polymer–monomer equilibrium to favor the monomer species, facilitating the recovery of initial monomers. While polyesters derived from hydroxy acids can be produced without a catalyst, the inclusion of a catalyst is strongly recommended to enhance reaction rates and achieve higher molecular weight (M_w) values in shorter durations.[38] Catalysts for hydroxy acid polymerization encompass metals, organic materials, and enzymes, each serving specific roles in the process. Inorganic catalysts, usually transition-metal based (Ti, Sn), exhibit high activity and stability. However, their use is associated with

racemization, discoloration and racemization. Organic catalysts, such as 1,3-propanedisulfonic acid (PSA) and 1,5-naphthalene disulfonic acid (NSA), organic catalysis has become increasingly popular, driven by its cost-effectiveness and versatility. In comparison to metals, organo-catalysts typically demonstrate enhanced tolerance to moisture and air. However, to match the superior activity of metallic counterparts, higher catalyst loadings and extended reaction times are often necessary. On the other hand, lipase biocatalyst allows for reaching high stereo- and chemo-selectivity with mild reaction conditions and without toxic residues, providing a good platform for green and complex polymer synthesis.[39]

3.3.2. Polymerization routes

PHAs stand out as a particularly captivating class of polymeric materials, drawing significant attention due to their distinctive qualities such as biocompatibility and biodegradability. Notably, these polymers find extensive applications in bioengineering, drug delivery systems, and packaging. Various synthetic approaches have been explored to tailor the structure and properties of polyesters. Within the spectrum of polyester synthesis methods, three primary modes of lipase-catalyzed synthesis of aliphatic linear polyesters are prominent, namely ring-opening polymerization (ROP) of lactones (**Scheme 2A**) and polycondensation strategies. More specifically, polycondensation (SN_2 reaction with water as leaving molecule) can occur between diacids and diols (**Scheme 2B**) or as self-condensation between hydroxyacids or their corresponding esters (**Scheme 2C)**.[39,40]

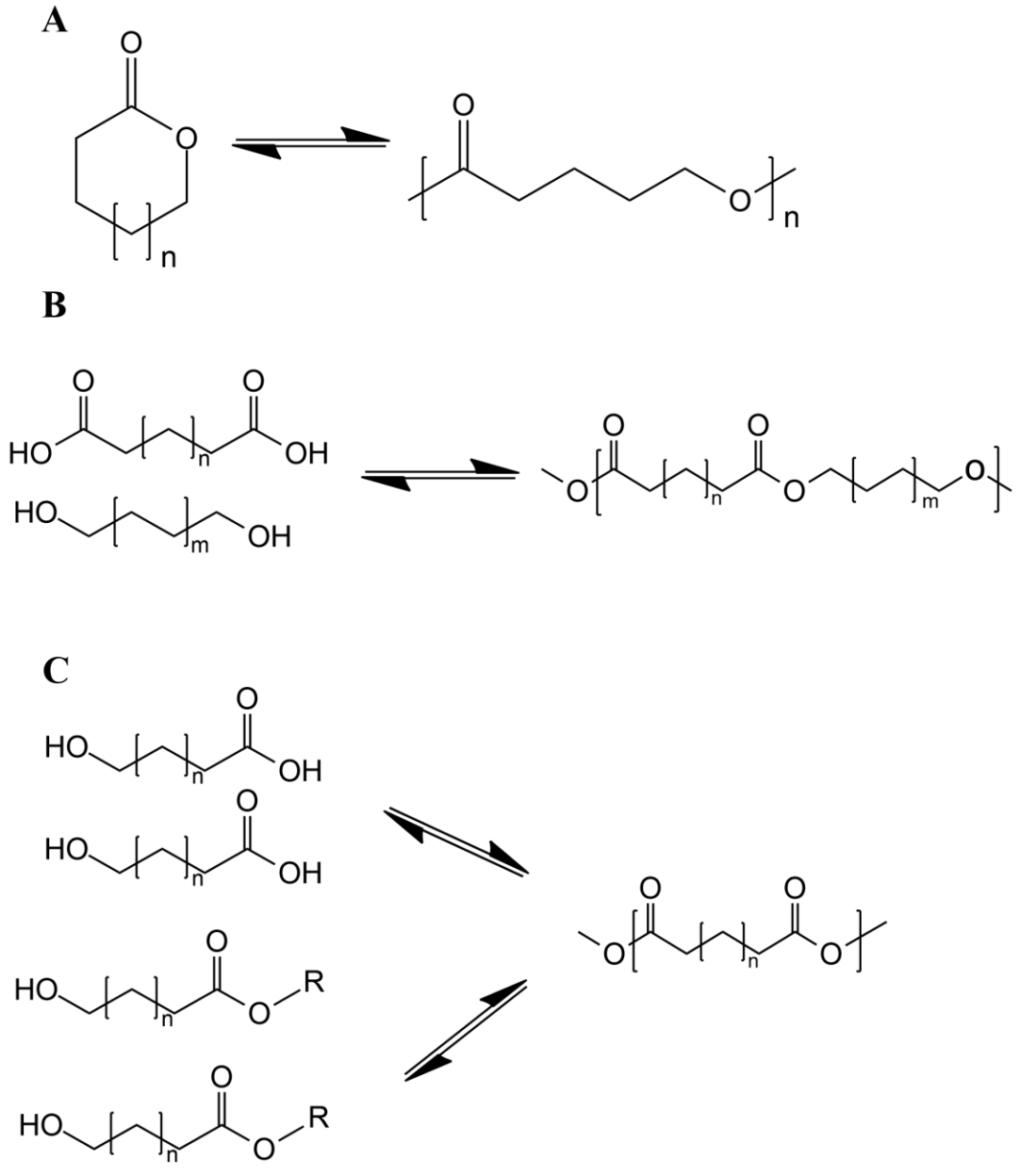

Scheme 2. Schematic representation of lipase-catalyzed polymerization.

3.3.3. Lipase-catalyzed synthesis of PHB

Following poly (aspartic acid-co-hydroxyalkanoates) (PAHAS), poly(β-hydroxy acids) (PBHAs) stand as the second most significant biopolyesters derived from hydroxy acids. β-Hydroxy acids serve as intriguing synthetic targets, serving as precursors for the production of poly(3-hydroxybutyrate) (P3HB or PHB). PHB exhibits exceptional oxygen barrier properties and rapid biodegradability. Notably, PHB shares similar mechanical characteristics with PET but is less hydrophobic, positioning it as a promising and sustainable material for packaging.[41] Industrial bioproduction involves the fermentation of glucose by the bacterium *Alcaligenes eutrophus*, although certain Gram-positive (G+) and Gram-negative (G−) bacterial species can also produce PHB under specific conditions of nutrient scarcity.[42] This biological process yields an optically active biopolymer with a well-defined configuration. However, enzymatic polymerization allows for the synthesis of PHB with high stereo-regularity, contributing to improved material properties. While the enzymatic production of PHB may not be as widely adopted on an industrial scale as some other methods, ongoing research and advancements in enzyme engineering continue to enhance the feasibility and efficiency of enzymatic PHB production.[39,40] In 1995, Gerngross and Martin reported the first enzymatic cell-free synthesis of polyhydroxybutyrate (PHB) using purified PHA synthase (also known as class III lipase), the pivotal enzyme in PHA biosynthesis responsible for polymerizing monomeric hydroxyalkanoate substrates. The in vitro polymerization system produced PHB with a molecular mass exceeding $10 \cdot 10^6$ g/mol, surpassing the typical mass of PHAs extracted from microorganisms by an order of magnitude.[43] Jedlinski and colleagues documented the regioselective ring-opening polymerization of (S)-β-butyrolactone. This process involves the inversion of configuration, from (S) to (R), and can be achieved using a particular supramolecular complex with (R)-3-hydroxybutyric acid sodium salt as the initiator. The outlined synthesis of biomimetic poly-(R)-3-hydroxybutyrate results in polymer analogs akin to the

natural PHB produced in both eukaryotic and prokaryotic living organisms.[44] ROP is by far more popular than polycondensation in enzyme-catalysis synthesis of PHAs. The first reported example of PHB-based co-polymer was reported by Debuissy et al. In their study, the enzymatic synthesis of fully biobased poly(3-hydroxybutyrate-co-butylene succinate) (poly(HB-co-BS)) copolyesters was carried out using Candida antarctica lipase B (CALB) in solution, employing either a one-step or a two-step process from 1,4-butanediol, diethyl succinate, and hydroxylated poly(3-hydroxybutyrate) oligomers (PHB-diol). The two-step process yielded copolyesters with higher molar masses (M_w up to 18.000 g/mol), surpassing the one-step process ($M_w \sim$ 8000 g/mol), without thermal degradation. Notably, the choice of solvent, such as diphenyl ether, influenced molar masses compared to dibenzyl ether or anisole. Immobilized CALB-catalyzed copolyesters exhibited thermal stability up to 200 °C. [45] Kakasi-Zsurka and colleagues documented a lipase-catalyzed reaction involving 3-hydroxybutyric acid and d-glucono-lactone. This process resulted in a blend of linear and cyclic oligomers with moderate molecular weights. The most effective biocatalyst, Novozyme 435, facilitated the creation of novel oligomeric compounds. These compounds featured gluconolactone units incorporated into the oligomeric chain, eliminating the need for prior sugar derivatization or acid monomer activation. The highest polymerization degrees, reaching up to 9 for the copolymer and 10 for the 3-hydroxybutyric acid homopolymer co-product, were attained under solventless conditions.[46] Even if continuous-flow biocatalysis, as previously said, is claiming the attention of the scientific community, there is a limited number of studies documenting the application of solid-supported enzymes in exploring organic synthesis or polymerization reactions. This scarcity is likely attributed to the challenges associated with loading immobilized enzyme beads into microreactors and the

notable increase in pressure drop across microchannels caused by the rising viscosity of polymer products.

3.3.4. Continuous-flow enzymatic polymerization

Continuous-flow enzymatic polymerization is mainly reported for producing polycaprolactone (PCL). Kundu et al. demonstrated solid-supported enzyme-catalyzed polymerization in a continuous-flow mode, focusing on the ring-opening polymerization of ε-caprolactone (CL). They utilized immobilized Candida Antarctica Lipase B (CALB) as a biocatalyst in an aluminium microchannel reactor, promoting contact between reactants and enzymes. The microreactor exhibited enhanced enzyme availability, lower enzyme leaching, and a significantly higher apparent rate constant compared to the batch reactor under the same enzyme loading and temperature conditions.[47] Zhu et al. developed a PTFE tubular microreactor for the enzymatic chemoselective ring-opening polymerization of ε-caprolactone and δ-valerolactone in continuous flow. This approach resulted in improved thiol fidelity, faster polymerization rates, and narrower molecular weight distributions compared to batch operations. The integration of an enzyme-packed microreactor system allowed for the preparation of thiol-terminated block copolymers by adjusting the monomer introduction sequence. Subsequently, they integrated enzymatic protecting-group-free ring-opening polymerization, radical polymerization, and nanoparticle synthesis in a continuous-flow system, successfully preparing amphiphilic poly(N-vinylpyrrolidone)-b-CL and poly(ε-caprolactone)-protected silver nanoparticles.[48]

3.4. Enzyme cascade reactions in continuous

In batch processes, employing sequential reactions is laborious and necessitates manual adjustments, along with work-up and purification steps between each stage. Conversely, in flow systems, these sequential reactions can be modularly integrated. Theoretically, if a series of stepwise reactions can utilize the same solvent or implement an exchanging solvent mechanism, the optimized reactions can be conducted consecutively. This modular approach allows for the telescoping of reactions, where the reaction mixture from the first step becomes the reagent for the next, enabling a streamlined sequence. This adaptability facilitates cascade design with varying reaction conditions, as certain flow systems permit different reactors to operate under distinct conditions such as temperature, pH, and ionic strength. For instance, pH adjustments can be made through the addition of acids or bases, a second reagent can be introduced between reactors, and concentrations can be modulated by adding a diluting factor. While achieving this ideal scenario may pose challenges due to the necessity of quenching reactions, working up intermediates, and purifying the stream between transformations, integrating other enabling technologies allows for in-line filtration, extraction, distillation, and purification to maintain a continuous flowing sequence. Automation through dedicated connected software further streamlines these steps. With meticulous process design, continuous flow systems provide precise control with minimal manual operator intervention and manipulation.[4]

3.5. Continuous and divergent biotransformation of β-ketoesters into enantiomerically pure β-hydroxy acids

Enzymatic cascades stand as bio-inspired suitable strategies for chemical biosynthesis. Indeed, the high costs of expression and purification are widely rewarded by extreme product purity and enantio-selectivity. In particular, some

enzymes exhibit high versatility, being able to catalyze one reaction rather than another depending on the reaction media. This study was focused on the design of a series of packed bed enzyme reactors for the selective transformation of ethyl acetoacetate (EAA) into (R)3-Hydroxybutyrric acid (HBA).

3.5.1. Reactor set-up

The reactor configuration consists of a series of PBR (**Figure 3.2**). The former is filled with ketoreductase from *Lactobacillus kefir* (LKKred) immobilized onto agarose beads; the latter is filled with Novozyme 435 that is *Candida albicans* lipase B (CALB) immobilized onto methacrylate beads.

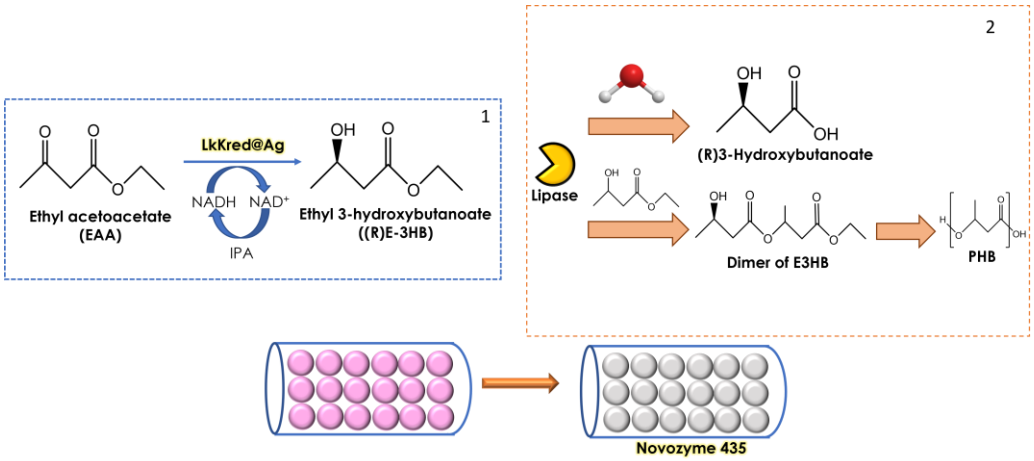

Figure 3.2. Reactor set-up for the series of LKKred-(1) and N435-(2) filled PBRs.

The first reactor is fed with EAA by a syringe pump. The substrate is dissolved in either Tris buffer (pH= 7) or hexane depending on the desired product, whether it's HBA or PHB. Indeed, the first step always results in the selective reduction of EAA into ethyl-3-hydroxybutyrate (E3HB), whereas lipase can catalyze either hydrolysis or self-condensation of the intermediate. Different flow rates were investigated, and the final products were analyzed by gas chromatography. The system was kept working continuously to assess the operational stability.

3.5.2. Results

3.5.2.1. Enantioselective reductive hydrolysis of EAA to (R)-3-HBA

The first step of the enzyme cascade, that is the hydrolysis of EAA to E3HB, was investigated and the effect of substrate concentration, choice of solvent and 2-propanol (IPA) concentration was first assessed in batch (**Figure 3.3**).

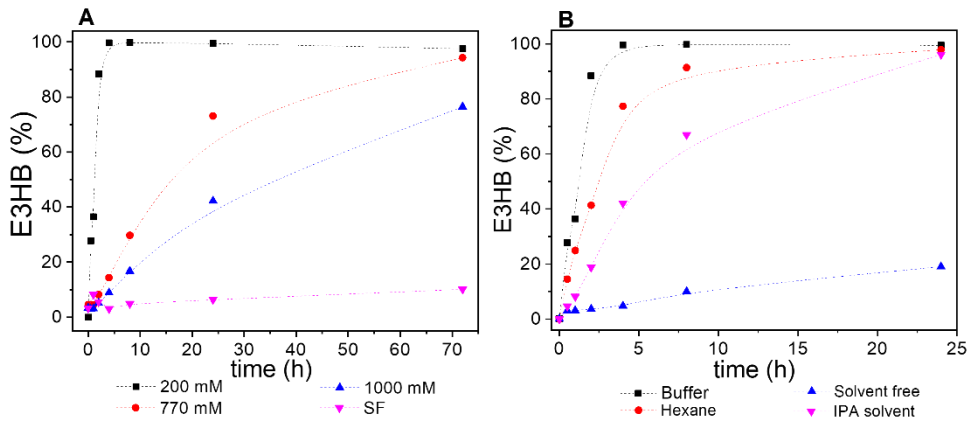

Figure 3.3. Reaction time-courses of the asymmetric reduction of acetoacetate (EAA) into ethyl (R)-3-hydroxybutyrate (3-HBE) catalyzed by HB-KRED. (A) Effect of the substrate concentration. 0.2 M EAA was mixed with 5% IPA, 0.7 and 1.1 M with 10% IPA, and the solvent free (6.24 M EAA) with 20% IPA in Tris-HCl pH7 at 25ºC. (B) Effect of solvent. 0.2 mM of EAA and 5% IPA are mixed under all solvent conditions but when pure IPA was used as solvent. In the buffer sample, 10 mM Tris-HCl at pH 7 was used.

Data reported in **Figure 3.3 A** show that the higher the substrate concentration, the slower the kinetics. Indeed, complete EAA conversion to E3HB is accomplished in 2 h for EAA 200 mM, whereas 72 h are required for EAA 770 mM. Furthermore, solvent-free conditions result in massive substrate inhibition, allowing only for 10%

conversion in 72 h. The influence of the solvent on the catalytic performances of the protein was a mandatory step to verify the feasibility of the reactor series to provide for the polymerization of E3HB intermediate, which is expected to be performed in non-polar solvents. Hexane was selected as model solvent due to the higher hydrophobicity index, which should favor self-condensation of the hydroxyester over hydrolysis.[49] Reaction progress over time confirms that hexane only slightly affect the selective reduction of EAA, achieving complete conversion in 24 h (**Figure 3.3 B**). More specifically, the presence of a non-polar reaction environment does not alter the capacity of co-factor regeneration, allowing HB-KRED to properly work with 5% IPA. Furthermore, IPA was tested as only solvent and the system was able to achieve complete conversion, even if slower than the case of hexane. Again, solvent-free conditions strongly limit E3HB production. As previously said, a proper volume of IPA is required for cofactor regeneration, since HB-KRED catalyzes the oxidation of 2-propanol (electron donor) to acetone for reducing NAD^+ to NADH.[50–52] However, the amount of alcohol has to be properly selected since high volumes of 2-propanol might exert denaturing effects on the biocatalyst.[53] 2-propanol %v vas tuned along with EAA concentration to monitor the effect on the reaction kinetics (**Figure S1**). IPA v% does not significatively alter EAA conversion as substrate concentration is fixed to 200 mM, being 3% (molar excess equal to 2) enough to obtain full conversion in 24 h. Very similar profile is obtained with EAA 770 mM and IPA 6% (equimolar condition), whereas remarkably slower kinetics are reported for IPA 20% (molar excess equal to 3) suggesting the negative effect on protein conformation, strongly limiting substrate binding at short times. The two steps of the cascade were then tested separately in continuous in two independent PBRs loaded with HB-KRED and HB-CALB (**Figure S2**), and both the reactors seem to exert good conversion at all the selected flow rates. Therefore, the systems were finally

coupled and tested continuously, as described by the graphical sketch in **Figure 3.4 A**.

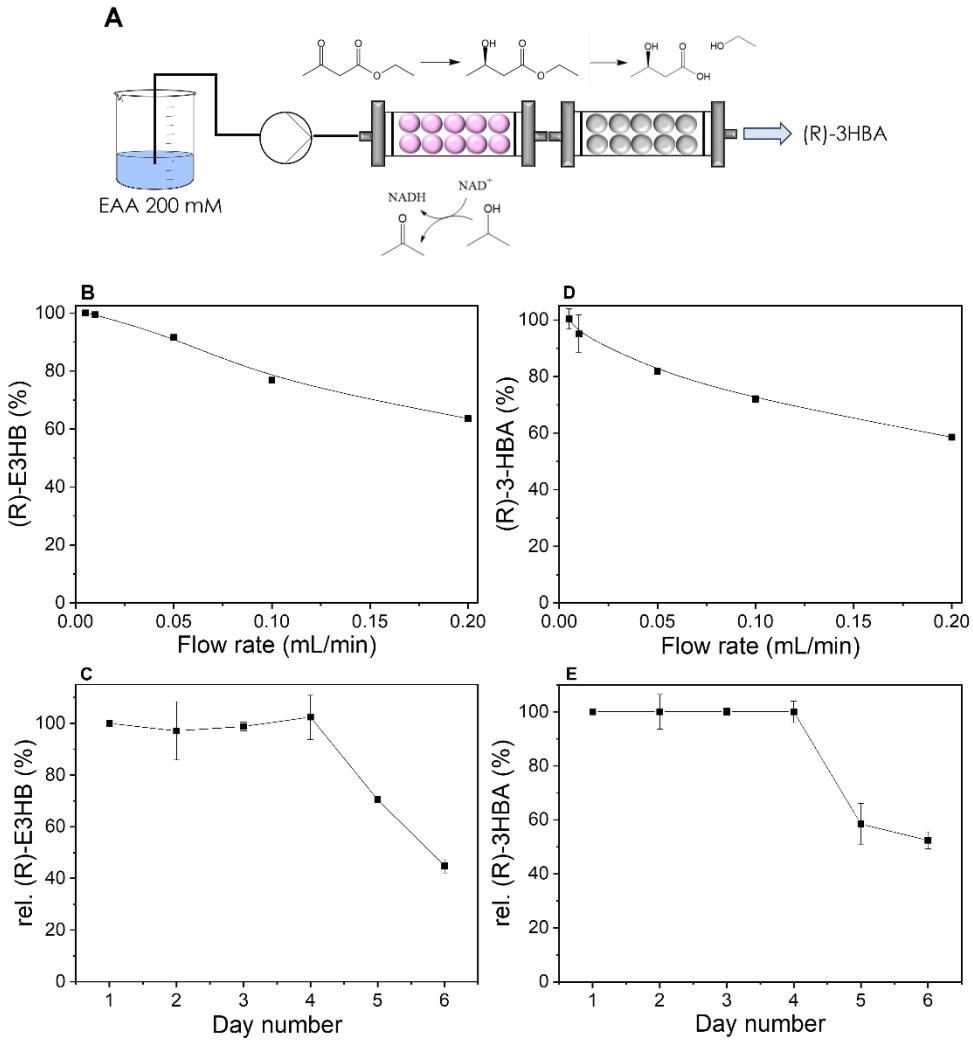

Figure 3.4. Continuous transformation of EAA into (R)-3HBA through two telescoped PBRs loaded with HB-KRED (1st reactor) and HB-CALB (2nd reactor) (A). Yield of (R)-3HBE (B) and (R)-3HBA (D) at different flow rates. The telescoped PBRs were flushed with 200 mM EAA and 5% IPA in 10 mM Tris-HCl

pH 7 at different flow rates. Operational stability of the telescoped flow-system monitoring the yield of (R)-3HBE (C) and (R)-3HBA (E) at the outlet of the first and second PBR, respectively. The telescoped PBRs were flushed with 200 mM EAA and 5% IPA in 10 mM Tris-HCl pH 7 at 0.01 mL min^{-1} at 25ºC.

Both PBRs share similar trends for the degree of conversion against the flow rate, with yield in (R)-3HBA decreasing from 100% to 60% as the flow rate is 20-fold enhanced, from 10 to 200 μL/min (**Figure 3.4 D**). Since the amount of product Therefore, the overall space-time yield (STY) for the telescoped reactors reaches the remarkable value of 68 g/L·h for the highest flow rate, that means in residence time reduced to 14 min. The enantioselectivity of the reaction series was clearly demonstrated through chiral GC analysis, as reported in **Figure S3**. More specifically, the chromatogram of the reaction product is completely overlapped to that of (R)-3HBA. Finally, telescoped reactors were continuously run at 10 μL/min flow rate to assess the operational stability. In detail, aliquots of the outlets from both the PBRs were collected, in order to unveil the eventual causes of the conversion decay. Results are exiting since 100% yield of reaction is preserved by both the reactors after 4 days of uninterrupted work. At day 6, the relative yield in 3-HBA decays to 50% (**Figure 3.4 E**), maybe as a consequence of the worse performances of HB-KRED from reactor 1, as visible in **Figure 3.4 C**.

3.5.3. Conclusions

Herein, a series of two telescoped PBRs to obtain (R)-HBA from EAA was successfully designed. In summary, hydrolytic reaction series result in STY of 68 g/L·h for 200 μL/min flow rate, with chiral gas chromatography confirming

enantioselectivity of the process. Operational stability was impressive, maintaining 100% yield after four days of continuous operation at 10 µL/min. The overall results highlight the promising performance and stability of the telescoped reactors in enantioselective reductive hydrolysis.

3.5.4. Supplementary material

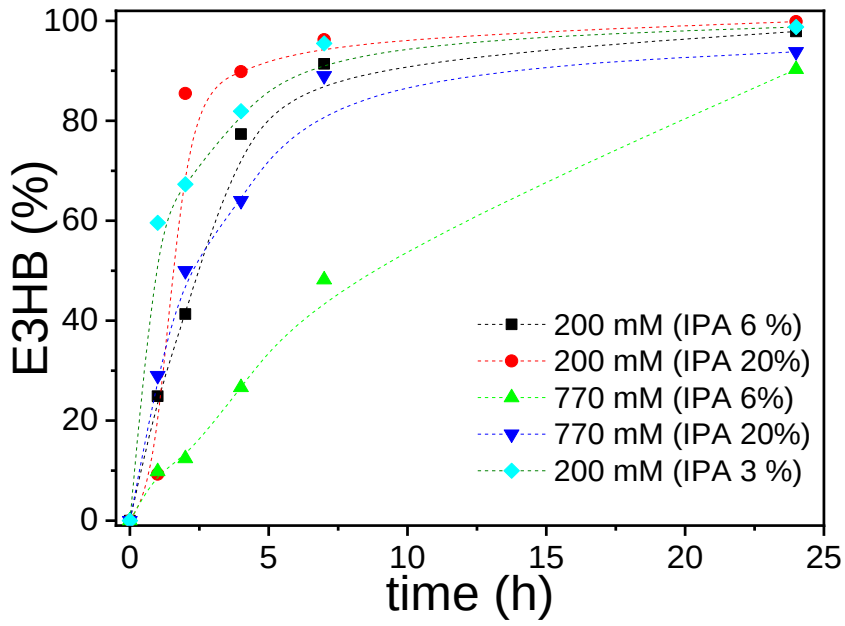

Figure S1. Reaction time-courses of the asymmetric reduction of acetoacetate (EAA) into ethyl (R)-3-hydroxybutyrate (3-HBE) catalyzed by HB-KRED at different IPA molar excess. The IPA molar excess regarding EAA ranges 1 to 14 using 10 mM Tris-HCl buffer at pH 7. All reaction were performed in batch with 100mg/mL (w/v) of HB-KRED at 25º C.

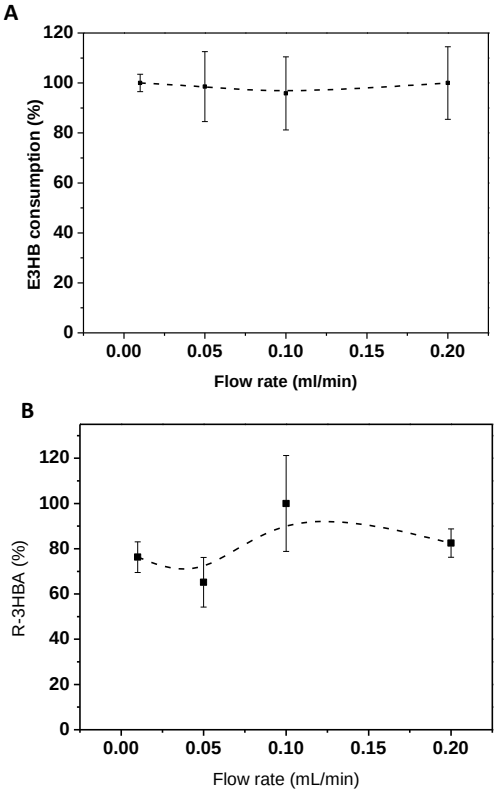

Figure S2. Flow ramp for the asymmetric reduction of EAA (A) and the hydrolysis of (R)-3-HBE (B) catalyzed in two independent PBRs loaded with HB-KRED and HB-CALB, respectively. 200 mM of either EAA or (R)-3-HBE were flushed at 0.01-0.2 mL min^{-1} through both PBRs in presence of 5% IPA at 25ºC and pH 7.

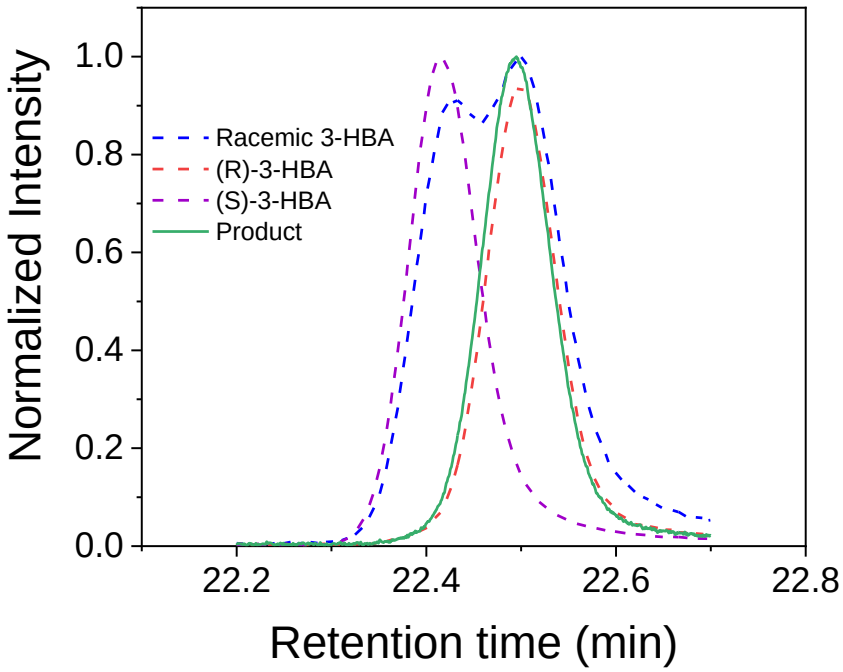

Figure S3. Chiral chromatograms of the reaction crude collected from the outlet of the two telescoped PBRs reported in **Figure 3.4**. The intensity of all samples was normalized to the areas of the R isomer. Racemic mixture of 3HBA (dashed blue), (R)-3HBA standard (dashed red), (S)-3HBA standard (dashed purple). Reaction crude (solid green).

4. References

(1) Benítez-Mateos, A. I.; Contente, M. L.; Roura Padrosa, D.; Paradisi, F. Flow Biocatalysis 101: Design, Development and Applications. *Reaction Chemistry and Engineering*. Royal Society of Chemistry April 1, 2021, pp 599–611. https://doi.org/10.1039/d0re00483a.

(2) De Santis, P.; Meyer, L. E.; Kara, S. The Rise of Continuous Flow Biocatalysis-Fundamentals, Very Recent Developments and Future Perspectives. *Reaction Chemistry and Engineering*. Royal Society of Chemistry December 1, 2020, pp 2155–2184. https://doi.org/10.1039/d0re00335b.

(3) Badman, C.; Cooney, C. L.; Florence, A.; Konstantinov, K.; Krumme, M.; Mascia, S.; Nasr, M.; Trout, B. L. Why We Need Continuous Pharmaceutical Manufacturing and How to Make It Happen. *J Pharm Sci* **2019**, *108* (11), 3521–3523. https://doi.org/10.1016/J.XPHS.2019.07.016.

(4) Tamborini, L.; Fernandes, P.; Paradisi, F.; Molinari, F. Flow Bioreactors as Complementary Tools for Biocatalytic Process Intensification. *Trends in Biotechnology*. Elsevier Ltd January 1, 2018, pp 73–88. https://doi.org/10.1016/j.tibtech.2017.09.005.

(5) Roberge, D. M.; Ducry, L.; Bieler, N.; Cretton, P.; Zimmermann, B. Microreactor Technology: A Revolution for the Fine Chemical and Pharmaceutical Industries? *Chem Eng Technol* **2005**, *28* (3), 318–323. https://doi.org/10.1002/CEAT.200407128.

(6) Liese, A.; Seelbach, K.; Wandrey, C. *Industrial Biotransformations*; John Wiley & Sons, 2006.

(7) Sheldon, R. A. Metrics of Green Chemistry and Sustainability: Past, Present, and Future. *ACS Sustain Chem Eng* **2018**, *6* (1), 32–48. https://doi.org/10.1021/ACSSUSCHEMENG.7B03505/ASSET/IMAGES/LARGE/SC-2017-03505Y_0001.JPEG.

(8) Rossetti, I.; Compagnoni, M. Chemical Reaction Engineering, Process Design and Scale-up Issues at the Frontier of Synthesis: Flow Chemistry.

Chemical Engineering Journal **2016**, *296*, 56–70. https://doi.org/10.1016/J.CEJ.2016.02.119.

(9) Baumer, B.; Classen, T.; Pohl, M.; Pietruszka, J. Efficient Nicotinamide Adenine Dinucleotide Phosphate [NADP(H)] Recycling in Closed-Loop Continuous Flow Biocatalysis. *Adv Synth Catal* **2020**, *362* (14), 2894–2901. https://doi.org/10.1002/ADSC.202000058.

(10) Velasco-Lozano, S.; Benítez-Mateos, A. I.; López-Gallego, F. Co-Immobilized Phosphorylated Cofactors and Enzymes as Self-Sufficient Heterogeneous Biocatalysts for Chemical Processes. *Angewandte Chemie International Edition* **2017**, *56* (3), 771–775. https://doi.org/10.1002/ANIE.201609758.

(11) Benítez-Mateos, A. I.; San Sebastian, E.; Ríos-Lombardía, N.; Morís, F.; González-Sabín, J.; López-Gallego, F. Asymmetric Reduction of Prochiral Ketones by Using Self-Sufficient Heterogeneous Biocatalysts Based on NADPH-Dependent Ketoreductases. *Chemistry – A European Journal* **2017**, *23* (66), 16843–16852. https://doi.org/10.1002/CHEM.201703475.

(12) Benítez-Mateos, A. I.; Contente, M. L.; Velasco-Lozano, S.; Paradisi, F.; Lo, F. Self-Sufficient Flow-Biocatalysis by Coimmobilization of Pyridoxal 5′-Phosphate and ω-Transaminases onto Porous Carriers. **2018**. https://doi.org/10.1021/acssuschemeng.8b02672.

(13) Andrés-Sanz, D.; Diamanti, E.; Silvo, D. Di; Gurauskis, J.; López-Gallego, F. Selective Coimmobilization of His-Tagged Enzymes on Yttrium-Stabilized Zirconia-Based Membranes for Continuous Asymmetric Bioreductions. *Cite This: ACS Appl. Mater. Interfaces* **2022**, *14*, 4285–4296. https://doi.org/10.1021/acsami.1c20738.

(14) Williams, J. L. Monolith Structures, Materials, Properties and Uses. *Catal Today* **2001**, *69* (1–4), 3–9. https://doi.org/10.1016/S0920-5861(01)00348-0.

(15) Govender, S.; Friedrich, H. B. Monoliths: A Review of the Basics, Preparation Methods and Their Relevance to Oxidation. *Catalysts 2017, Vol. 7, Page 62* **2017**, *7* (2), 62. https://doi.org/10.3390/CATAL7020062.

(16) Brown, G. O. The History of the Darcy-Weisbach Equation for Pipe Flow Resistance. *Proceedings of the Environmental and Water Resources History* **2002**, 34–43. https://doi.org/10.1061/40650(2003)4.

(17) Haas, C. P.; Müllner, T.; Kohns, R.; Enke, D.; Tallarek, U. High-Performance Monoliths in Heterogeneous Catalysis with Single-Phase Liquid Flow †. *Cite this: React. Chem. Eng* **2017**, *2*, 498. https://doi.org/10.1039/c7re00042a.

(18) Hartmann, M.; Schwieger, W.; Machoke, A. G. Featuring Work from the Research Groups of Professor Catalytic Test Reactions for the Evaluation of Hierarchical Zeolites. *Chem. Soc. Rev* **2016**, *45*, 3313. https://doi.org/10.1039/c5cs00935a.

(19) Venezia, V.; Costantini, A.; Landi, G.; Di Benedetto, A.; Sannino, F.; Califano, V. Immobilization of β-Glucosidase over Structured Cordierite Monoliths Washcoated with Wrinkled Silica Nanoparticles. *Catalysts* **2020**, *10* (8), 889.

(20) Pota, G.; Sapienza Salerno, A.; Costantini, A.; Silvestri, B.; Passaro, J.; Califano, V. Co-Immobilization of Cellulase and β-Glucosidase into Mesoporous Silica Nanoparticles for the Hydrolysis of Cellulose Extracted from Eriobotrya Japonica Leaves. *Langmuir* **2022**, *38* (18), 5481–5493.

(21) Ramírez-Ramírez, L. G.; Zazueta-álvarez, D. E.; Fileto-Pérez, H. A.; Reyes-Jáquez, D.; Núñez-Núñez, C. M.; la Rosa, J. de D. G. De; López-Miranda, J.; Vázquez-Ortega, P. G. Improvement in the Thermostability of a Recombinant β-Glucosidase Immobilized in Zeolite under Different Conditions. *Molecules* **2022**, *27* (13). https://doi.org/10.3390/molecules27134105.

(22) Pota, G.; Gallucci, N.; Cavasso, D.; Russo Krauss, I.; Vitiello, G.; Lopez-Gallego, F.; Costantini, A.; PADUANO, L.; Califano, V. Controlling the Adsorption of B-Glucosidase onto Wrinkled SiO_2 Nanoparticles to Boost the Yield of Immobilization of an Efficient Biocatalyst. *Langmuir 39* (4), 1482–1494. https://doi.org/10.1021/acs.langmuir.2c02861.

(23) Hartono, S. B.; Qiao, S. Z.; Liu, J.; Jack, K.; Ladewig, B. P.; Hao, Z.; Lu, G. Q. M. Functionalized Mesoporous Silica with Very Large Pores for Cellulase Immobilization. *The Journal of Physical Chemistry C* **2010**, *114* (18), 8353–8362.

(24) Costantini, A.; Venezia, V.; Pota, G.; Bifulco, A.; Califano, V.; Sannino, F. Adsorption of Cellulase on Wrinkled Silica Nanoparticles with Enhanced Inter-Wrinkle Distance. *Nanomaterials* **2020**, *10* (9), 1799. https://doi.org/10.3390/nano10091799.

(25) Zaks, A.; Klibanov, A. M. Enzyme-Catalyzed Processes in Organic Solvents. *Proceedings of the National Academy of Sciences* **1985**, *82* (10), 3192–3196.

(26) Chandra, P.; Enespa; Singh, R.; Arora, P. K. Microbial Lipases and Their Industrial Applications: A Comprehensive Review. *Microb Cell Fact* **2020**, *19*, 1–42.

(27) Zheng, G. W.; Xu, J. H. New Opportunities for Biocatalysis: Driving the Synthesis of Chiral Chemicals. *Curr Opin Biotechnol* **2011**, *22* (6), 784–792. https://doi.org/10.1016/J.COPBIO.2011.07.002.

(28) Cui, Y. H.; Wei, P.; Peng, F.; Zong, M. H.; Lou, W. Y. Efficient Biocatalytic Stereoselective Reduction of Methyl Acetoacetate Catalyzed by Whole Cells of Engineered E. Coli. *RSC Adv* **2018**, *8* (18), 9970–9978. https://doi.org/10.1039/C8RA00883C.

(29) Clark, J. S.; Fessard, T. C.; Whitlock, G. A. A Concise Enantioselective Synthesis of the Fungal Metabolite (+)-Decarestrictine L. *Tetrahedron* **2006**, *62* (1), 73–78. https://doi.org/10.1016/J.TET.2005.09.144.

(30) Mori, K. Synthesis of Optically Active Pheromones. *Tetrahedron* **1989**, *45* (11), 3233–3298. https://doi.org/10.1016/S0040-4020(01)81007-3.

(31) Gamenara, D.; Domínguez de María, P. Candida Spp. Redox Machineries: An Ample Biocatalytic Platform for Practical Applications and Academic Insights. *Biotechnol Adv* **2009**, *27* (3), 278–285. https://doi.org/10.1016/J.BIOTECHADV.2009.01.005.

(32) Ghanem, A.; Schurig, V. Lipase-Catalyzed Access to Enantiomerically Pure (R)-and (S)-Trans-4-Phenyl-3-Butene-2-Ol. *Tetrahedron Asymmetry* **2003**, *14* (1), 57–62.

(33) Klomp, D.; Peters, J. A.; Hanefeld, U. Enzymatic Kinetic Resolution of Tropic Acid. *Tetrahedron Asymmetry* **2005**, *16* (23), 3892–3896.

(34) Reis, J. S.; Andrade, L. H. Lipase-Catalyzed Kinetic Resolution of β-Borylated Carboxylic Esters. *Tetrahedron Asymmetry* **2012**, *23* (17), 1294–1300.

(35) Kornhauser, A.; Coelho, S. G.; Hearing, V. J. Clinical, Cosmetic and Investigational Dermatology Dovepress Applications of Hydroxy Acids: Classification, Mechanisms, and Photoactivity. *Clin Cosmet Investig Dermatol* **2010**, *2010*, 3–135. https://doi.org/10.2147/CCID.S9042.

(36) Tang, S. C.; Yang, J. H. Dual Effects of Alpha-Hydroxy Acids on the Skin. *Molecules 2018, Vol. 23, Page 863* **2018**, *23* (4), 863. https://doi.org/10.3390/MOLECULES23040863.

(37) Świzdor, A.; Panek, A.; Milecka-Tronina, N.; Kołek, T. Biotransformations Utilizing β-Oxidation Cycle Reactions in the Synthesis of Natural Compounds and Medicines. *OPEN ACCESS Int. J. Mol. Sci* **2012**, *13*, 13. https://doi.org/10.3390/ijms131216514.

(38) Ajioka, M.; Enomoto, K.; Suzuki, K.; Yamaguchi, A. Basic Properties of Polylactic Acid Produced by the Direct Condensation Polymerization of Lactic Acid. *Bull Chem Soc Jpn* **1995**, *68* (8), 2125–2131.

(39) Gabirondo, E.; Sangroniz, A.; Etxeberria, A.; Torres-Giner, S.; Sardon, H. Poly (Hydroxy Acids) Derived from the Self-Condensation of Hydroxy Acids: From Polymerization to End-of-Life Options. *Polym Chem* **2020**, *11* (30), 4861–4874. https://doi.org/10.1039/d0py00088d.

(40) Liu, Y.; Song, L.; Feng, N.; Jiang, W.; Jin, Y.; Li, X. Recent Advances in the Synthesis of Biodegradable Polyesters by Sustainable Polymerization: Lipase-Catalyzed Polymerization. *RSC Adv* **2020**, *10* (59), 36230–36240. https://doi.org/10.1039/d0ra07138b.

(41) McAdam, B.; Fournet, M. B.; McDonald, P.; Mojicevic, M. Production of Polyhydroxybutyrate (PHB) and Factors Impacting Its Chemical and

Mechanical Characteristics. *Polymers 2020, Vol. 12, Page 2908* **2020**, *12* (12), 2908. https://doi.org/10.3390/POLYM12122908.

(42) Rehm, B. H. A. Polyester Synthases: Natural Catalysts for Plastics. *Biochemical Journal* **2003**, *376* (1), 15–33. https://doi.org/10.1042/BJ20031254.

(43) Gerngross, T. U.; Martin, D. P. Enzyme-Catalyzed Synthesis of Poly[(R)-(-)-3-Hydroxybutyrate]: Formation of Macroscopic Granules in Vitro. *Proceedings of the National Academy of Sciences* **1995**, *92* (14), 6279–6283. https://doi.org/10.1073/PNAS.92.14.6279.

(44) Jedliński, Z.; Kowalczuk, M.; Adamus, G.; Sikorska, W.; Rydz, J. Novel Synthesis of Functionalized Poly (3-Hydroxybutanoic Acid) and Its Copolymers. *Int J Biol Macromol* **1999**, *25* (1–3), 247–253. https://doi.org/10.1016/S0141-8130(99)00039-2.

(45) Debuissy, T.; Pollet, E.; Avérous, L. Enzymatic Synthesis of a Bio-Based Copolyester from Poly (Butylene Succinate) and Poly((R)-3-Hydroxybutyrate): Study of Reaction Parameters on the Transesterification Rate. *Biomacromolecules* **2016**, *17* (12), 4054–4063. https://doi.org/10.1021/ACS.BIOMAC.6B01494.

(46) Kakasi-Zsurka, S.; Todea, A.; But A.; Paul, C.; Boeriu, C. G.; Davidescu, C.; Nagy, L.; Kuki, Á.; Kéki, S.; Péter, F. Biocatalytic Synthesis of New Copolymers from 3-Hydroxybutyric Acid and a Carbohydrate Lactone. *J Mol Catal B Enzym* **2011**, *71* (1–2), 22–28. https://doi.org/10.1016/J.MOLCATB.2011.03.004.

(47) Kundu, S.; Bhangale, A. S.; Wallace, W. E.; Flynn, K. M.; Guttman, C. M.; Gross, R. A.; Beers, K. L. Continuous Flow Enzyme-Catalyzed

Polymerization in a Microreactor. *J Am Chem Soc* **2011**, *133* (15), 6006–6011. https://doi.org/10.1021/ja111346c.

(48) Zhu, N.; Huang, W.; Hu, X.; Liu, Y.; Fang, Z.; Guo, K. Enzymatic Continuous Flow Synthesis of Thiol-Terminated Poly(δ-Valerolactone) and Block Copolymers. *Macromol Rapid Commun* **2018**, *39* (8), 1700807. https://doi.org/10.1002/MARC.201700807.

(49) Song, H.; Zhao, Y.; Zhang, Y.; Kong, W.; Xia, C. Synthesis of Polyhydroxyalkanoates by Polymerization of Methyl 3-Hydroxypropionate in the Catalysis of Lipase. *Cuihua Xuebao/Chinese Journal of Catalysis* **2012**, *33* (3), 432–438. https://doi.org/10.1016/S1872-2067(11)60336-7.

(50) Amidjojo, M.; Weuster-Botz, D. Asymmetric Synthesis of the Chiral Synthon Ethyl (S)-4-Chloro-3-Hydroxybutanoate Using Lactobacillus Kefir. *Tetrahedron Asymmetry* **2005**, *16* (4), 899–901. https://doi.org/10.1016/J.TETASY.2005.01.013.

(51) Inoue, K.; Makino, Y.; Itoh, N. Purification and Characterization of a Novel Alcohol Dehydrogenase from Leifsonia Sp. Strain S749: A Promising Biocatalyst for an Asymmetric Hydrogen Transfer Bioreduction. *Appl Environ Microbiol* **2005**, *71* (7), 3633–3641. https://doi.org/10.1128/AEM.71.7.3633-3641.2005/ASSET/21F6547C-787F-4287-87EF-101F8C9D4DAF/ASSETS/GRAPHIC/ZAM00705558900T6.JPEG.

(52) Wang, H.; Wei, D.; Yang, Z.; Fu, H.; Ye, W.; Xie, Y.; Liu, Q. Efficient Asymmetric Synthesis of Chiral Alcohols Using High 2-Propanol Tolerance Alcohol Dehydrogenase SmADH2 via an Environmentally

Friendly TBCR System †. *Cite this: Catal. Sci. Technol* **2020**, *10*, 70. https://doi.org/10.1039/c9cy01794a.

(53) Bull, H. B.; Breese, K. Interaction of Alcohols with Proteins. *Biopolymers* **1978**, *17* (9), 2121–2131. https://doi.org/10.1002/BIP.1978.360170907.

Chapter 7

Conclusions and future outlooks

Contents

1. Conclusions

The present PhD thesis reported successful strategies to design supported nanoscaled biocatalysts and to implement continuous-flow enzymatic processes for green chemistry applications. Wrinkled silica nanoparticles (WSNs) emerged as ideal supports for protein immobilization, in this case for cellulases and lipases, due to a combination of morphological and chemical features. As a matter of fact, the possibility to tune pore size and the interwrinkle distance by varying the co-solvent in the synthesis step allowed to properly host huge loads of cellulase and supplementary β-glucosidase, necessary for increasing the amount glucose produced from cellulose hydrolysis.[1] The mechanisms of β-glucosidase physical immobilization was thoroughly investigated through a number of physic-chemical techniques and the protein load was remarkably increased by enhancing the colloidal stability of the support during adsorption.[2] Moreover, proper surface hydrophobization was accomplished thanks to the wide availability of silanol groups. Indeed, lipase immobilization was carried out onto hydrophobic WSNs through interfacial activation, resulting in a performing biocatalyst for biodiesel production.[3] The same immobilization route was used to bind two different lipases, in order to unveil the thermodynamics of enzyme adsorption and to monitor eventual changes in the enantioselectivity after immobilization. This activity was carried out at the Heterogeneous Biocatalysis Lab, headed by Dr. Fernando Lopéz-Gallego, from CIC biomaGUNE (Donostia/San Sebastian, Spain) In all these case, reusable and thermally stable biocatalysts were obtained only through physical immobilization, that means without the use of chemical linkers and activators.

The last part of the thesis work was dedicated to the implementation of miniaturized enzyme reactors. A series of two packed bed reactors (PBRs) loaded with supported ketoreductase and lipase was implemented to perform the telescoped multi-enzyme

enantioselective hydrolysis of a β-ketoester to a β-hydroxyacid under continuous flow, resulting in a performing and reusable reactor configuration. This activity was also conducted at the Heterogeneous Biocatalysis Lab. Moreover, preliminary studies for the translation of cellulose hydrolysis from batch to continuous flow were carried out by attaching cellulase-loaded WSNs onto the walls of a cordierite monoliths.

In conclusion, the reported results confirm the suitability of enzyme immobilization as a fundamental strategy to encourage the industrial scalability of biocatalytic processes and to convert traditional chemical routes into more sustainable examples.

2. Future outlooks

As clearly noticeable, most of the thesis work was spent in developing nanobiocatalysts to be used in batch systems.

However, the last section was dedicated to the implementation of miniaturized enzyme reactors for continuous flow biocatalysis, and this will definitely be the future direction of my work. First, a more solid and stable immobilization route should be selected to design cellulase-loaded washcoated monoliths. A suitable solution could be the introduction of a chemical immobilization route, prior surface functionalization and activation of WSNs. Indeed, the optimization of cellulose hydrolysis under continuous flow is a mandatory requirement for developing a more complex reactor series, designed for transforming the lignocellulosic biomass into bioethanol, after the fermentation of glucose by Saccharomycetes fungi. Further work should be done to enrich the potential of the series of PBRs developed to perform the telescoped enzyme cascade. Indeed, the heterogeneity of the possible lipase-catalyzed reactions would allow to increase the versatility of the reactor configuration. More specifically, other products of chemical interest could be obtained, such as poly-hydroxyalkanoates, since lipase can provide the condensation

of hydroxyesters in organic solvents. As a matter of fact, preliminary studies assessed the capacity of the system to produce small oligomers of PHB, even if more accurate analyses are to be carried out to quantify the amount of produced polymer and to increase the molecular weight.

References

(1) Pota, G.; Sapienza Salerno, A.; Costantini, A.; Silvestri, B.; Passaro, J.; Califano, V. Co-Immobilization of Cellulase and β-Glucosidase into Mesoporous Silica Nanoparticles for the Hydrolysis of Cellulose Extracted from Eriobotrya Japonica Leaves. *Langmuir* **2022**, *38* (18), 5481–5493.

(2) Pota, G.; Gallucci, N.; Cavasso, D.; Krauss, I. R.; Vitiello, G.; López-Gallego, F.; Costantini, A.; Paduano, L.; Califano, V. Controlling the Adsorption of β-Glucosidase onto Wrinkled SiO2 Nanoparticles To Boost the Yield of Immobilization of an Efficient Biocatalyst. *Langmuir* **2023**.

(3) Pota, G.; Bifulco, A.; Parida, D.; Zhao, S.; Rentsch, D.; Amendola, E.; Califano, V.; Costantini, A. Tailoring the Hydrophobicity of Wrinkled Silica Nanoparticles and of the Adsorption Medium as a Strategy for Immobilizing Lipase: An Efficient Catalyst for Biofuel Production. *Microporous and Mesoporous Materials* **2021**, 111504.